

①

COMPONENT PART NOTICE

THIS PAPER IS A COMPONENT PART OF THE FOLLOWING COMPILATION REPORT:

TITLE: Aircraft Dynamic Loads due to Flow Separation (Les Contraintes Aerodynamiques
Imposees aux Aeronefs par le Decollement de l'Ecoulement).

TO ORDER THE COMPLETE COMPILATION REPORT, USE AD-A229 916.

THE COMPONENT PART IS PROVIDED HERE TO ALLOW USERS ACCESS TO INDIVIDUALLY AUTHORED SECTIONS OF PROCEEDING, ANNALS, SYMPOSIA, ETC. HOWEVER, THE COMPONENT SHOULD BE CONSIDERED WITHIN THE CONTEXT OF THE OVERALL COMPILATION REPORT AND NOT AS A STAND-ALONE TECHNICAL REPORT.

THE FOLLOWING COMPONENT PART NUMBERS COMPRISE THE COMPILATION REPORT:

AD#: P006 218 thru AD#: P006 231
AD#: _____ AD#: _____
AD#: _____ AD#: _____

Accession For	
NTIS GRA&I	<input checked="" type="checkbox"/>
DTIC TAB	<input type="checkbox"/>
Unannounced	<input type="checkbox"/>
Justification	
By _____	
Distribution/ _____	
Availability Codes	
Dist	Avail and/or Special
A-1	

DTIC FORM 463
MAR 85

DISTRIBUTION STATEMENT A
Approved for public release; Distribution Unlimited

OPI: DTIC-TID

BTIC FILE COPY

AGARD-CP-483

AGARD-CP-483

AD-A229 916

AGARD

ADVISORY GROUP FOR AEROSPACE RESEARCH & DEVELOPMENT

7 RUE ANCELLE 92200 NEUILLY SUR SEINE FRANCE

AGARD CONFERENCE PROCEEDINGS No.483

Aircraft Dynamic Loads due to Flow Separation

(Les Contraintes Aérodynamiques Imposées aux
Aéronefs par le Décollement de l'Écoulement)

BTIC
ELECTE
NOV 16 1990
S E D

NORTH ATLANTIC TREATY ORGANIZATION



DISTRIBUTION AND AVAILABILITY
ON BACK COVER

DISTRIBUTION STATEMENT A

Approved for public release;
Distribution Unlimited

90 11 16 002

AGARD-CP-483

NORTH ATLANTIC TREATY ORGANIZATION
ADVISORY GROUP FOR AEROSPACE RESEARCH AND DEVELOPMENT
(ORGANISATION DU TRAITE DE L'ATLANTIQUE NORD)

AGARD Conference Proceedings No.483

Aircraft Dynamic Loads due to Flow Separation

(Les Contraintes Aérodynamiques Imposées aux Aéronefs
par le Décollement de l'Ecoulement)

Papers presented at the 70th Meeting of the AGARD Structures and Materials Panel,
held in Sorrento, Italy on 1st—6th April 1990.

The Mission of AGARD

According to its Charter, the mission of AGARD is to bring together the leading personalities of the NATO nations in the fields of science and technology relating to aerospace for the following purposes:

- Recommending effective ways for the member nations to use their research and development capabilities for the common benefit of the NATO community;
- Providing scientific and technical advice and assistance to the Military Committee in the field of aerospace research and development (with particular regard to its military application);
- Continuously stimulating advances in the aerospace sciences relevant to strengthening the common defence posture;
- Improving the co-operation among member nations in aerospace research and development;
- Exchange of scientific and technical information;
- Providing assistance to member nations for the purpose of increasing their scientific and technical potential;
- Rendering scientific and technical assistance, as requested, to other NATO bodies and to member nations in connection with research and development problems in the aerospace field.

The highest authority within AGARD is the National Delegates Board consisting of officially appointed senior representatives from each member nation. The mission of AGARD is carried out through the Panels which are composed of experts appointed by the National Delegates, the Consultant and Exchange Programme and the Aerospace Applications Studies Programme. The results of AGARD work are reported to the member nations and the NATO Authorities through the AGARD series of publications of which this is one.

Participation in AGARD activities is by invitation only and is normally limited to citizens of the NATO nations.

The content of this publication has been reproduced
directly from material supplied by AGARD or the authors.

Published September 1990

Copyright © AGARD 1990
All Rights Reserved

ISBN 92-835-0582-4



Printed by Specialised Printing Services Limited
40 Chigwell Lane, Loughton, Essex IG10 3TZ

Preface

To achieve high manoeuvrability, modern combat aircraft are required to operate under post-stall flight conditions at incidences beyond the steady stall angle of attack. Under such separated flow conditions, aircraft structures are subject to buffet induced vibrations leading, in turn, to random-type dynamic loads. These loads are often totally ignored or underestimated during the original design process giving rise to problems in a large portion of today's high-performance aircraft. Moreover, for aircraft operating under transonic flow conditions, the strong aerodynamic pressure fluctuations associated with the occurrence of shock waves may also cause heavy buffeting responses and thus limit the cruise Mach numbers of civil aircraft.

The Specialists' Meeting was intended to provide a "state-of-the-art" review of all types of separated-flow dynamic problems to be encountered in present and future aircraft. In particular, the Meeting concentrated on the following topics:

- Evaluation of aerodynamic buffet input characteristics,
- In-flight and wind tunnel buffeting measurements and
- Aeroelastic buffeting prediction techniques.

These Conference Proceedings, commissioned by the AGARD Structural Materials Panel, contain the technical papers presented at the Specialists' Meeting and a Technical Evaluation Report.

Préface

Pour atteindre la grande manoeuvrabilité qui leur est demandée, les avions de combat modernes doivent évoluer dans des conditions de vol en post-décrochage à des incidences supérieures à celle du décrochage stationnaire.

Dans de telles conditions de décollement de l'écoulement, les structures d'avion sont soumises à des vibrations déclenchées par le tremblement, qui créent à leur tour des charges dynamiques aléatoires. Il arrive souvent que ces charges soient sous-estimées voire même totalement méconnues par ceux qui sont responsables de l'étude originale. Ceci est à l'origine de bon nombre de problèmes posés par les avions à hautes performances d'aujourd'hui.

La réunion fera le point de l'état actuel des connaissances des problèmes du décollement de l'écoulement en dynamique des structures dans la mesure où ils se posent pour les avions actuels et futurs. En outre, pour un avion évoluant dans des conditions d'écoulement transsonique, les très fortes fluctuations de pression associées à la présence d'ondes de choc risquent de provoquer de fortes réactions de tremblement limitant ainsi les nombres de Mach en croisière des avions civils.

La réunion de spécialistes a fait le point de l'état actuel des connaissances des problèmes du décollement de l'écoulement dans la mesure où ils se posent pour les avions actuels et futurs.

La réunion a traité en particulier les sujets suivants:

- l'évaluation des charges dynamiques induites par l'excitation due au tremblement
- les méthodes de détermination des forces de tremblement en vol et en soufflerie
- les techniques aéroélastiques de prévision du tremblement.

Ce compte-rendu de conférence, établi à la demande du Panel AGARD des Structures et Matériaux, contient les communications techniques présentées lors de la réunion de spécialistes, ainsi qu'un rapport d'évaluation technique.

Structures and Materials Panel

Chairman: Prof. Dr-Ing. Hans Förching
Direktor der DLR Institut für Aeroelastik
Bunsenstrasse 10
D-3400 Göttingen
Germany

Deputy Chairman: Mr Samuel L. Venneri
Director, Materials & Structures
Division (Code RM)
Office of Aeronautics & Space Technology
NASA Hq
Washington DC 20546
United States

SUB-COMMITTEE ON AEROELASTICITY

Chairman: Prof Dr-Ing. H.Förching
Direktor der DLR Institut für Aeroelastik
Bunsenstrasse, 10
D-3400 Göttingen
Germany

Members:	L.Chesta	IT
	E.H.Dowell	US
	R.Freyman	LU
	E.Fuente Tremps	SP
	V.Giavotto	IT
	J.J.Glaser	CA
	J.J.Kacprzynski	CA
	R.Labourdette	FR
	R.F.O'Connell	US
	N.Sandsmark	NO
	P.Satini	IT
	O.Sensburg	GE
	C.W.Skingle	UK
	A.F.Tovar de Lemos	PO
	S.L.Venneri	US
	R.J.Zwaan	NL

PANEL EXECUTIVE

Mr Murray C.McConnell — UK

Mail from Europe:
AGARD—OTAN
Attn: SMP Executive
7, rue Ancelle
92200 Neuilly sur Seine
France

Mail from US and Canada:
AGARD—NATO
Attn: SMP Executive
APO New York 09777



Tel: 33(1) 47 38 57 90 & 57 92
Telex: 610176 (France)
Telefax: 33(1) 47 38 57 99

Accession For	
NTIS GRA&I	<input checked="" type="checkbox"/>
DTIC TAB	<input type="checkbox"/>
Unannounced	<input type="checkbox"/>
Justification	
By _____	
Distribution/	
Availability Codes	
Dist	Avail and/or Special
A-1	

Contents

	Page
Preface/Préface	iii
Structures and Materials Panel	iv
Technical Evaluation Report D.G.Mabey	T
SESSION I – AERODYNAMIC BUFFET INPUT CHARACTERISTICS	
Wind Tunnel Investigation and Flight Tests of Tail Buffet on the CF-18 Aircraft by B.H.K.Lee, D.Brown, M.Zgela and D.Poirel	1
A Unified Approach to Buffet Response of Fighter Aircraft Empennage by M.A.Ferman, S.R.Patel, N.H.Zimmerman and G.Gesternkorn	2
Effects of Trailing-Edge Flap on Buffet Characteristics of a Supercritical Airfoil by B.H.K.Lee	3
Experimental Investigation of Buffet Onset and Penetration on Supercritical Airfoil at Transonic Speeds by E.Stanewsky and D.Basler	4
Experimental Investigations of Buffet Excitation Forces on a Low Aspect Ratio Trapezoidal Half-Wing in Incompressible Flow by P.Bublitz and H.Zingel	5
Experimental Investigation and Semi-Empirical Prediction of the Dynamic Response of a Low-Aspect-Ratio Trapezoidal Wing due to Flow Separation by H.Zingel	6
Unsteady Aerodynamic Forces on an Oscillating Wing at High Incidences and Flow Separation by H.W.Försching	7
The Forward Mounted Spoiler as a Source of Buffet Excitation by P.G.Myers and D.L.Birdsall	8
Investigation of a Semi-Empirical Method to Predict Limit Cycle Oscillations of Modern Fighter Aircraft by J.J.Meijer and R.J.Zwaan	9
SESSION II – IN-FLIGHT AND WIND TUNNEL BUFFETING MEASUREMENTS	
Interaction between the Canard and Wing Flows on a Model of a Typical Combat Aircraft by D.G.Mabey, B.L.Welsh and C.R.Pyne	10
Predictions of F-111 Tact Aircraft Buffet Response A.M.Cunningham Jr and C.F.Coe	11
The Effect of Wing Planform on Low-Speed Buffet by S.J.Zan and D.J.Maull	12
Nouvelle Méthode de Détermination des Forces de Tremblement en Soufflerie par R.Destuynder et R.Barreau	13

Reference

SESSION III – AEROELASTIC BUFFETING PREDICTION TECHNIQUES

Forces Aérodynamiques Couplées dues au Décrochage Instationnaire sur une Aile de Grand Allongement Oscillant à Grande Amplitude par J.J.Costes et D.Petot	14
Unsteady Separated Flow Phenomena Causing Self-Excited Structural Oscillations by L.E.Eriksen	15
Unsteady Airloads Due to Separated Flow on Airfoils and Wings by J.W.Edwards	16

EVALUATION REPORT ON AIRCRAFT DYNAMIC LOADS DUE TO FLOW SEPARATION

by

D. G. MABEY
 Senior Principal Scientific Officer
 Dynamics Laboratory
 Royal Aerospace Establishment
 Bedford MK41 6AE
 United Kingdom

SUMMARY

This paper presents a review of the 70th meeting of the AGARD Structures and Materials Panel. Some conclusions are drawn and recommendations made for future research.

1. INTRODUCTION

"Aircraft Dynamic Loads due to Flow Separation" was the topic considered at the 70th meeting of the Structures and Materials Panel (SMP) of AGARD, held at Sorrento, Italy from 2-4 April 1990. A wide range of aerodynamic and structural problems in this area was identified previously in a specially commissioned pilot paper (Ref. 1). This pilot paper was widely circulated and used as the basis for the call for papers for this meeting. Although 20 papers were selected originally, only 16 featured in the final programme.

In this Technical Evaluation Report on the meeting, brief notes and comments are made in section 2 on the individual papers, in an attempt to give the reader a general indication of the content of the meeting. (Generally these notes will be in the order in which the papers were presented). In section 3 an attempt is made to discuss the presentations in a broader context and to identify areas where future research might be fruitful. Some conclusions are suggested in section 4.

Dynamic loads due to flow separation for both combat and transport aircraft represent important and controversial topics: the views expressed are solely those of the author.

2. SYNOPSIS OF PAPERS

Paper No 1 relates to a wind tunnel and flight investigation of tail buffet and buffeting on the CF-18 aircraft (the Canadian version of the F-18). Measurements are presented of overall forces, fluctuating pressures (buffet excitation) and structural responses (buffeting). A significant feature of the wind tunnel tests was the careful choice of roughness used to fix transition (Ref. 2) to ensure that flow separations on the model develop in the same way as in flight. An important feature of the flight buffeting is that the bending response of the fins is "in-phase" (Paper No 1, Fig 43). The LEX fence provides a significant reduction in buffet (Paper No 1, Fig 25) and buffeting (Paper No 1, Fig 19). However, the paper gives no indication as to how long it took the aircraft manufacturer to determine the position and size of the LEX. Although fin accelerations and total dampings were presented, the buffet excitation parameter in the fin bending modes was not calculated, as requested in Ref. 1.

Paper No 2 (not presented) also related to a directly comparable investigation of fin buffeting on the F-18 aircraft. The authors suggest that fin buffeting may be predicted from either a simple analogue model (representing the principal modes of interest - first and second bending for the F-18) or by integrating the unsteady pressures measured on a rigid fin. However, the authors make no discussion of the difficulty of establishing the aerodynamic damping in the modes. For the analogue model, it is assumed (though not stated explicitly) that the correct aerodynamic damping can be achieved by representing the correct ratio of aerodynamic/structure stiffness as well as the frequency parameter. The rigid fin provides no estimate of aerodynamic damping and levels appropriate to attached flow have been assumed when predicting the response (again this is not stated explicitly). This is unlikely to be a good assumption because of the tremendous variations in the vortex field (eg Fig 12 of Paper No 16). Again, the buffet excitation parameter was not calculated.

Paper No 3 relates to a wind tunnel investigation of the effect of a trailing-edge flap on the buffet characteristics of a supercritical aerofoil. Although transition was not fixed, the Reynolds number was judged sufficiently high (20×10^6) to ensure a turbulent shock wave/boundary layer interaction. Shock oscillations induced by separation (in the frequency range from 50-80 Hz) are well below the lowest modal frequency (140 Hz) of the stiff force balance. (However readers should be cautioned that the rms \bar{C}_p measurements include effects of the balance modes and a tunnel resonance.

These terms, of course, would not occur in flight). Somewhat surprisingly, for a fixed Mach number the shock oscillation frequency does not change with the angle of incidence; this is inconsistent with observations on another supercritical aerofoil which are described now.

Paper No 4 also relates to the buffet on a supercritical aerofoil. Here the prime objective was to measure the buffet onset on a typical supercritical aerofoil (the CAST 7) and to see how this changed as Reynolds number was varied over a wide range (about 2.5×10^6 to 25×10^6). Most of the measurements were made with free transition but a few comparative measurements were made with fixed transition. Shock oscillations were observed after buffet onset (cf Paper No 3), driven by the interaction of the complex flow at the foot of the shock (ie the bubble) and at the trailing-edge. With free transition the shock frequency decreased with increasing Reynolds number. Comparative measurements with fixed transition were not available but would have been of great interest. In these experiments the shock oscillation frequency varied with the angle of incidence, in contrast to the measurements of Paper No 3.

Papers No 5, 6, and 7 relate primarily to investigations of the buffet and buffeting on a low aspect ratio, trapezoidal wing. Hence for brevity these three papers are considered together. The half model has a NACA 64-A-005 section (which has a sharp leading edge) and was tested both with and without a strake. Interest was centred mainly on flows separated from the sharp leading edge at high angles of incidence, and hence no roughness was applied to fix transition, although for these low speed tests the Reynolds number was only 2.4×10^6 . The model was intended to be stiff but was provided with freedom to move in pitch or roll. Even without the strake the wing flow is highly three-dimensional (Paper No 4, Fig 7) yet despite this, the overall forces and the buffeting (Paper No 6, Fig 1) are the same in character as those observed on aerofoils with a sharp leading edge. Analysis of the measurements shows (Paper No 7) that the aerodynamic forcing associated with the separated flow is unaffected by the relatively small amplitudes of model motion. However, the motion dependent aerodynamic forces (which generate aerodynamic damping) are affected strongly by flow separations. Hence these variations in aerodynamic damping need to be scaled carefully from model to flight tests, as demonstrated previously (Ref.3). It should be recalled that half model tests can represent only symmetric modes. Hence although the pitching mode excited here should be appropriate to an aircraft, the rolling mode cannot be. In addition it should be noted that because of the high level of unsteadiness in the open jet tunnel, the model has a significant response under attached flow conditions (Paper No 6, Fig 1).

Paper No 8 provides a simple description of a forward mounted spoiler as a source of buffet excitation on a wing at low speeds. The spoiler creates a bubble which is almost two-dimensional so that the steady and fluctuating pressures agree well with those observed previously (Ref 4). No large change in steady lift occurs until the bubble reattachment point reaches the trailing edge of the wing.

Paper No 9 describes an investigation of a semi-empirical method to predict Limit Cycle Oscillations (LCO) on modern fighter aircraft. The method is essentially quasi-static and can be applied to both rigid body and structural modes of aircraft. Comparison of Figs 3 and 4 of Paper No 9 indicate how important the flows on the outboard section of a wing are to the development of LCO. Although the LCO's discussed occur in the transonic speed range, LCO may occur also due to vortex movements (Ref 5) and transition movements (Ref 6). The method of Paper No 9 should predict these types of LCO as well.

Paper No 10 shows how the interaction between the canard and wing flows on a model of a typical combat aircraft is controlled by the canard effective incidence, α_c . The measurements include overall forces, steady and fluctuating pressures, canard buffeting and wing buffeting. All these measurements can be related with α_c .

Paper No 11 provides a summary of what must surely be the most comprehensive flight-tunnel comparison of buffet and buffeting ever made (Ref 7) - that on the TACT-F 1-11. For this relatively stiff aircraft, the effects of static and dynamic aeroelastic distortion are small, and scale effects are also small. The buffet excitation was judged independent of the wing motion, both in flight and the wind tunnel, consistent with other research (Paper No 7 and Ref 3). In flight an LCO occurred in the wing torsional mode which did not occur on the wind tunnel model. A full explanation for this apparent anomaly has been given by quasi-steady theory (Ref 5).

Paper No 12 describes the effect of varying aspect ratio and sweep on buffeting at low speeds with well separated flows. The wing aspect ratios varied from 8-4, with sweep angles of 0° , 20° and -20° . For the frequency parameters, $n = fc/U > 0.1$ typical of wing bending at low speeds, the buffet excitation parameter in the first wing bending mode is about $\sqrt{nG(n)} = 0.003$ to 0.004 consistent with previous measurements in wind tunnels and in flight. For frequency parameters much lower (which would normally be inappropriate for the bending mode) the levels of $\sqrt{nG(n)}$ were appreciably higher. Increases in excitation at such low frequency parameters could be important for rigid body motions.

Paper No 13 discusses the problems of predicting the buffeting forces on the wings of a transport aircraft. High Reynolds numbers are required, and 12×10^6 can be achieved at reasonable kinetic pressures on large half models when tested in the ONERA S-1 Tunnel at Modane. Hence the effects of static aeroelastic distortion are of reasonable magnitudes and can be estimated. Paper No 13 makes 3 important observations, not made elsewhere during the meeting:

- (i) Great care is needed to establish "buffet-onset" on a transport aircraft because what is prescribed in the air-worthiness regulations is a particular level of response at a particular point - normally the pilot's seat. In contrast, in a wind tunnel test buffet onset is normally synonymous with incipient separation. A very different "buffet onset" might be obtained from the buffeting response, of say, an engine nacelle.
- (ii) For a transport aircraft wing buffeting can be reduced by Active Control Technology if a control can be placed in a region where the flow is still attached after buffet onset.
- (iii) When exciting a transport wing in pitch, very large oscillations can develop at transonic speeds, immediately after the onset of flow separation (Paper No 13, Fig 14).

Paper No 14 gives a theory to predict the coupled aerodynamic forces due to unsteady stall on a high aspect ratio wing oscillating in pitch at high amplitudes. The method gives good results for unswept, swept back and swept forward wings but is limited to frequency parameters of $n = fc/U < 0.1$.

Paper No 15 provides a reminder of some unsteady separated flows causing self-excited oscillations, including the well known and important example of the "trays" on the space shuttle.

Paper No 16 provides a timely review of the unsteady airloads due to separated flow on aerofoils and wings, and of the attempts to predict these flow by Computational Fluid Dynamics (CFD). Successful predictions have been made for shock oscillations on a rigid, 18% thick bi-convex aerofoil and also for aileron buzz on the P-80 aircraft. However, attempts to simulate the LCO bending oscillation observed on a high aspect ratio supercritical wing at transonic speeds have not yet been successful. The author also considers the prospects for the prediction of buffet excitation on aircraft configurations with twin fins. He concludes that an increase in computing speed by 3 orders of magnitude will be essential before such techniques become practical.

3. DISCUSSION

It is convenient to discuss the findings of this meeting under 3 general headings: theoretical results, experimental results and discussion of some general shortcomings.

With regard to the theoretical results, the most impressive advance since the publication of the pilot paper (Ref 1) has been the prediction of LCO, for which 2 rather similar quasi-steady methods are now available (Paper No 9 and Ref 5). However, the LCO oscillation in bending of the NASA wing has not yet been predicted successfully (Paper 16). The meeting has also confirmed that the linear model for the prediction of buffeting works well as long as the modal aerodynamic damping appropriate to the separated flow can be measured. The aerodynamic damping can be measured either in an ordinary, nominally rigid wind tunnel model (made of aluminium in preference to steel to give larger motion) or by oscillating a nominally rigid wing (as in the experiments cited (Papers No 5,6,7)). However, Edwards showed (Paper No 16) that we are a long way from being able to use CFD techniques to predict either the aerodynamic damping or the buffet excitation.

Ref 1 issued two specific challenges to the CFD community. The first, the prediction of shock oscillations on bi-convex wings - is well established. However, despite this success with thin-layer Navier Stokes codes, this method has not been applied as a matter of routine to more realistic supercritical aerofoils or NACA or RAE aerofoils. The second challenge to the CFD community was the prediction of the buffet excitation caused by a bubble (represented at this meeting by Paper No 8). It is sad to record that no author attempted this computation.

With regard to the experimental results, a wide range of problems was addressed including variations in wing aspect ratio, sweep, section, Mach number and angle of incidence; fin buffeting at high angles of incidence and canard/wing interaction. However, although there were many interesting new measurements, some presentations gave an impression which can only be expressed adequately by the French phrase "déjà vu". With respect to the very important question of fin buffeting, it was alarming to learn that "some fins fail after only 300 hours of flying time". In the author's view such a low life is unlikely to be indicative of random scatter in fatigue testing, as one structural engineer suggested. It is more likely to be indicative of a very sensitive flow on the aircraft which has been adversely affected by some minor imperfection, eg a small misalignment of the fuselage nose. This important aspect of fin buffeting was not addressed, but the effect of the small LEX fence on the F-18 is significant (Paper 1).

Opinions are likely to differ with regard to the shortcomings of the meeting. In the author's view the most serious was the failure to use the consistent and logical notation carefully specified (Ref 1). The prediction of aircraft dynamic loads due to flow separation is an extremely difficult problem. Why persist in making it more difficult by refusing to present results in non-dimensional forms which can be compared easily? For example, it would have been invaluable to compare the independent measurements on virtually the same aircraft in Papers No 1 and 2 in terms of the buffet excitation parameter, but this was not done. AGARD has had a consistent notation for measurements of pressure fluctuations (Ref 8) since 1958 and for the buffet excitation parameter (Ref 1) since 1988.

Similarly there was often a marked reluctance to present results in terms of a frequency parameter. Of course, in many problems there is uncertainty about the best choice for the reference length for the problem in question. This is a particularly interesting and difficult question for fin buffeting (both in experiment and in prediction attempts). For aerofoils the chord is generally used whereas for a bubble the local bubble length can be used even for a swept bubble (Paper No 10). Taking an aerofoil as a simple example, it is much better to have a frequency parameter

$$n = \frac{fc}{U}, \quad (1)$$

$$\text{or} \quad \nu = \frac{2\pi fc}{U}, \quad (2)$$

$$\text{or} \quad k = \frac{\pi fc}{U}, \quad (3)$$

than a frequency, f , in HZ. This may mean a great deal to a pilot's comfort or to the fatigue life of the structure, but it is of little interest to an aerodynamicist striving to establish the physics of the problem.

Another common shortcoming was a general failure to address the question "How sensitive will this flow be to variations in Reynolds number?" Fig 3 of Paper No 4 for an NLR supercritical aerofoil suggests that even with fixed transition large scale effects can persist at Reynolds numbers up to 25×10^6 . Hence it could be dangerous to suggest (as in Paper No 13) that there is a universal, minimum test Reynolds number which will ensure full scale results. It follows that much more attention should be given to the ways in which transition is fixed, and to careful comparisons with transition free measurements (where appropriate). This was illustrated in Paper No 4 and advocated in the AGARD Manual on this topic (Ref 9). Ideally wind tunnel tests and CFD computations should include some variation in Reynolds number. Very often the CFD specialist rests content at successfully predicting an incipient flow separation on an aerofoil at, say $M = 0.85$, $R = 1.5 \times 10^6$. The aeronautical engineer would like him to make the calculations also at $R = 15 \times 10^6$ and 150×10^6 . This philosophy will become particularly important with respect to the prediction of the aerodynamic characteristics of hypersonic vehicles. In an attempt to clarify the controversial question of the simulation of scale effects, Ref 1 suggested that the meeting should include a special session devoted entirely to unsteady measurements in cryogenic wind tunnels, which allow scale effects and the effects of aeroelastic distortion to be distinguished (Ref 10). Unfortunately not one paper was submitted in this area. No papers were submitted on flap or cavity buffeting.

In summary, the main achievement is the prediction of Limit Cycle Oscillations (LCO) and some interesting new experiments. The main failure is the reluctance to adopt a common notation and also to take an adequate account of scale effects both in experiments and computations. Perhaps these omissions could be remedied by another meeting on this topic in 5 years time, when we might "Torna a Sorrento" with advantage.

4. CONCLUSIONS AND RECOMMENDATIONS

This review suggests 3 main conclusions and 4 recommendations.

The conclusions are:

- (1) Useful progress has been made in the prediction of Limit Cycle Oscillations.
- (2) The linear model for the prediction of buffeting has been verified carefully in both wind tunnels and flight tests.
- (3) Aerodynamic damping in separated flows depends on the mode shape, frequency parameter, Mach number and angle of incidence. Hence it cannot currently be predicted theoretically.

The recommendations are:

- (1) The AGARD notation for buffet excitation and buffeting response should be adopted, so that aerodynamicists can acquire a better understanding of the separated flows giving dynamic loads.
- (2) Much greater attention should be given to establishing the magnitude of possible scale effects, both in experiments and calculations.
- (3) Special tests in cryogenic wind tunnels should be made to distinguish between genuine scale effects and the effects of aeroelastic distortion. Such measurements would be of equal interest for landing configurations (say at $M = 0.2$) or cruise configurations (say at $M = 0.85$).
- (4) Researchers should be careful to assess and remove any tare effects of flow unsteadiness in wind tunnels which will not occur in flight.

REFERENCES

- 1 D.G. Mabey Some Aspects of Aircraft Dynamic Loads due to Flow Separation
AGARD R-750 (1988)
- 2 G.E. Erickson et al Experimental Investigation of the F/A-18 Vortex Flows at
Subsonic through Transonic Speeds
AIAA 89-2222 (1989)
- 3 G.F. Butler The Prediction of Buffeting Response in Flight from Wind-
J.G. Jones Tunnel Measurements on a Model of Conventional Construction
RAE Technical Report 84-045 (1984)
- 4 D.G. Mabey Analysis and Correlation of Data on Pressure Fluctuations
in Separated Flow
AIAA J. Aircraft 9 (9), pp 642-645 (1972)
- 5 A.M. Cunningham Practical Problems - Airplanes
Chapter 3 of Unsteady Transonic Aerodynamics,
Vol 120, Progress in Astronautics and Aeronautics
(published by AIAA) pp 75-132 (1989)
- 6 D.G. Mabey Aeroelastic Oscillations Caused by Transitional Boundary
Layers and their Attenuation
AIAA J. Aircraft Vol 24, 7, pp 463-469
- 7 C.F. Coe Predictions of F 1-11 TACT Aircraft Response and Correlations
A.M. Cunningham of Fluctuating Pressures Measured on Aluminium and Steel
Models and the Aircraft
NASA CR 4069 (1987)
- 8 T.B. Owen Techniques of Pressure Fluctuation Measurements Employed in
RAE Low Speed Wind Tunnel
- 9 AGARD Fluid Boundary Layer Simulation and Control in Wind Tunnels
Dynamics Panel AGARD AR-224 (1988)
- 10 D.G. Mabey Some Remarks on Dynamic and Aeroelastic Model Tests in
Cryogenic Wind Tunnels
NASA CR 145029 (1975)

WIND TUNNEL INVESTIGATION AND FLIGHT TESTS OF
TAIL BUFFET ON THE CF-18 AIRCRAFT

by

B.H.K. Lee, D. Brown
National Aeronautical Establishment
National Research Council, Ottawa, Ontario, Canada

and

M. Zgela, D. Poirel
Directorate Aerospace Support Engineering
National Defence Headquarters, Ottawa, Ontario, Canada

SUMMARY

Investigations of tail buffet on the CF-18 have been conducted at the National Aeronautical Establishment (NAE) and the Aerospace Engineering Test Establishment (AETE). Flow visualization of the vortex burst phenomenon was carried out in a low speed water tunnel using a modified 1/72 scaled plastic model. In wind tunnel tests, a rigid 6% model was used for measurements in the NAE 5ft x 5ft Trisonic Tunnel. Unsteady pressure measurements on the vertical fin were made by means of 24 fast response transducers on each surface. Results of the acceleration experienced by the fin are presented. The vortex flow structure was studied with the aid of a 49 pressure-sensor-rake mounted behind the fin. In addition to measuring steady pitot pressure values, to deduce pressure contours, unsteady pressure fluctuations were obtained from 13 fast response transducers. The LEX was also instrumented with pressure orifices and fast response transducers. The investigation was carried out with LEX fences 'on' and 'off' to note their effect on tail buffet loads. Flight tests have been conducted at AETE on a test aircraft with accelerometers installed on the vertical fins and horizontal stabilators and strain gauges mounted on the aft fuselage structures and fin root attachment stubs. Flight test data are presented showing the effectiveness of the LEX fence in reducing aft fuselage structural response to buffet loads.

LIST OF SYMBOLS

A_j	area of jth panel on vertical fin
A_T	total surface area of fin
\bar{c}	wing mean aerodynamic chord (8.29 inches for wind tunnel model)
\bar{c}_f	vertical fin mean aerodynamic chord (5.03 inches for wind tunnel model)
c_f	local chord of fin
C_M	aircraft steady pitching moment coefficient (moment axis 23.79 inches from nose for wind tunnel model)
C_M'	rms value of aircraft pitching moment coefficient
$C_{N'}^{\prime}$	vertical fin normal force coefficient, positive outboard
C_{NI}'	rms value of normal force coefficient on vertical fin inboard surface
C_{NO}'	rms value of normal force coefficient on vertical fin outboard surface
C/C_c	structural damping ratio
C_p	steady pressure coefficient
C_p'	rms value of pressure coefficient
L	length of aircraft from nose to jet exhaust plane (39.1 inches for wind tunnel model)
M	free stream Mach number
p_i	steady pressure on vertical fin inboard surface
p_o	steady pressure on vertical fin outboard surface
p_{irmsj}	rms value of pressure on vertical fin inboard surface on the jth panel
p_{ormsj}	rms value of pressure on vertical fin outboard surface on the jth panel
q	free stream dynamic pressure
$Re_{\bar{c}}$	Reynolds number based on \bar{c}
X, Y, Z	aircraft co-ordinate system measured from the nose

x_f, y_f, z_f fin co-ordinate system
 x_v, y_v, z_v vortex rake co-ordinate system
 α angle of incidence

INTRODUCTION

Modern combat aircraft must be capable of flying under conditions of separated flows in order to achieve high manoeuvrability. The F/A-18 through the use of advanced digital flight control systems, the optimized positioning of its horizontal and vertical fins and its multiple high lift aerodynamic devices can sustain controlled flight up to 50° angle-of-attack (AOA). Its enhanced agility has resulted in the development of Air Combat Manoeuvre (ACM) tactics focussed on high AOA flight regimes.

The leading edge extension (LEX) is prominent among the high lift devices and has been credited with a large increase in maximum lift coefficient over that which would be obtained without the LEX. The rolled-up vortex that originates at the sharp edge of the LEX results in an increase in lift and the induced high velocity flow on the wing upper surface delays C_{Lmax} to a higher AOA than would be obtained in the absence of the LEX. Manoeuvrability in this flow regime is also enhanced by the interaction of the vortical flow with the tail control surfaces.

Aircraft structures under such conditions are subject to random aerodynamic loads arising from pressure fluctuations due to flow separations and/or impact of vortical flows on the structures. The loads are difficult to measure in flight, but a fairly good estimate can be predicted using wind tunnel rigid model unsteady pressure measurements (Refs. 1-3). An example of this type of severe random aerodynamic loading is found in the CF-18 vertical tail buffeting when the highly turbulent flows, resulting from bursting of the LEX vortices, impact the vertical fins. The effect of buffet loads on structural integrity of the vertical fins is currently a major concern. However, some alleviation of buffet loads has been achieved through a modification of the LEX by the addition of a stream-wise fence.

A number of studies on high angle-of-attack aerodynamics and the effect of the vortical flow on vertical tail buffeting has appeared in recent years (Refs. 4-7). These investigations focus mainly on the measurements of steady forces and pressures on the LEX (Ref. 4), laser light sheet measurements of the vortex structure (Ref. 4) as well as velocity flow field surveys (Ref. 6), water tunnel experiments on vortex burst phenomenon (Ref. 7) and some limited wind tunnel fin pressure measurements and vertical tail acceleration data from flight tests (Ref. 5).

This paper presents some preliminary results of an investigation of tail buffeting on the CF-18 aircraft in three parts.

Part I describes the water tunnel experiments and gives some data on the vortex burst locations.

Part II discusses results from a wind tunnel programme carried out at the NAE. In the wind tunnel studies, unsteady pressure measurements on the vertical fin of a rigid 6% model of the CF-18 were carried out to provide aerodynamics data for structural loads prediction. One of the vertical fins was instrumented with fast response pressure transducers on each surface to measure the unsteady pressures. The fin was also instrumented with strain gauges and an accelerometer for response measurements.

In studies of aero-structural interaction, usually pressures are measured on the structures and the loads are then computed. For different structural configurations, or when the aerodynamic conditions are varied, the measurements have to be repeated. To explore the feasibility of predicting the salient features of buffet loads on the CF-18 vertical fin, from knowledge of the aerodynamics in the vicinity of the fin, the dynamics of the flow field were also measured using a multi-tube vortex rake. The LEX was instrumented with pressure orifices and fast response transducers to provide information on the flow field beneath the LEX vortex. All the measurements were carried out with the LEX fences 'on' and 'off' so as to investigate the effect of modifying the vortical flow on tail buffet loads. Flow visualization, using oil streaks, was carried out to show the effect of the LEX fence on the vertical fin and horizontal stabilator surface streamlines. Results are given for $M = 0.6$, $Re_c = 3.38 \times 10^6$, $q = 3.95$ psi and α from 0° to 35°.

Part III deals with flight tests conducted at the AETE located at the Canadian Forces Base Cold Lake, Alberta, using test aircraft CF-188701 that was specially instrumented for that purpose. Accelerometers were installed on the port engine, vertical fins and horizontal stabilators for dynamic studies. Aft fuselage structures and fin root attachment stubs were also strain gauged to assess the effectiveness of the LEX fence in reducing dynamic stress during flight in areas of the flight envelope where fatigue damage is significant. Flight test data are presented showing the effectiveness of the LEX fence in reducing aft fuselage structural response to the buffet loading. A summary of the flight test methodology is presented.

PART I WATER TUNNEL EXPERIMENTS

I.1 Description of the NAE Water Tunnel and Experimental Procedures

The NAE flow visualization water tunnel (Figure 1) is located at the Low Speed Aerodynamics Laboratory. It resembles a conventional closed circuit wind tunnel and is constructed of mild steel plate. A total of 350 gallons of water are contained in the tunnel. The contraction ratio is 4 and the contraction modifies the cross-section from circular at the settling chamber to rectangular at the working section which is 10 inches wide, 13 inches high and 32 inches long. Glass plates form the front and bottom sides, while the back wall contains a 10.25 inches diameter turntable, with a retaining ring, calibrated in degrees. Removable plates close the working section on the top. Two aircraft models were used. They were sting mounted mounted from the top of the working section on a bracket which was attached to the turntable by an arm outside the working section, one model seen in side view and the other in plan view. The angle-of-attack could be adjusted from the outside of the water tunnel. A general view of the facility is shown in Figure 1.

Water velocities in the working section can be varied from 0.2 feet per second to 10 feet per second with good control and measuring accuracy.

The corresponding unit Reynolds numbers are $1.3 \times 10^4/\text{ft}$ and $6.5 \times 10^5/\text{ft}$ respectively based on a water temperature of 20°C. The light source is a 1200 watts high pressure quartz mercury vapour lamp and it is located below the working section. For flow visualization, a dye of synthetic, inorganic chemical is used which has the property of emitting visible light of constant intensity when illuminated by a uniform source of radiant energy of the proper wavelength. Still photographs and video are used for recording the flow phenomena.

The aircraft models used were built from 1/72 scale plastic kits available from hobby shops. The dimensions were checked and found to be sufficiently accurate for these type of tests. The models were modified to provide a leading-edge flap angle of 35° and the intake was blocked and faired with plasticene. The model was painted black to avoid light reflections. Dye dispensing holes were located below the junction of the leading-edge extension with the fuselage.

I.2 Results

Figure 2 shows a side and plan view of the model at $\alpha = 30^\circ$ and $Re_c = 5000$ (based on a model wing mean aerodynamic chord of 1.92 inches). The location where the vortex breaks down and the subsequent highly turbulent flow impacting on the vertical fins are shown. The axial positions of the vortex burst at different α are given in Figure 3 which shows results from water tunnel (Ref. 8), wind tunnel and flight tests (Ref. 4) at various Mach numbers and Reynolds numbers. A straight line can be drawn through these data. It was noted in Ref. 4 that at low speeds the results are independent of M and Re_c . The separation is fixed by geometry at the sharp leading-edge extension and compressibility effects do not effect the vortex core breakdown until at transonic conditions when shock waves appear on the wing and interact with the vortex flows.

PART II WIND TUNNEL EXPERIMENTS

II.1 Test Facility

The measurements were performed in the 5ft x 5ft transonic test section of the NAE trisonic blowdown wind tunnel which is briefly described in the following.

With the transonic test section the Mach number range is 0.4 to 1.4. The Reynolds number depends on the selection of a run stagnation pressure level. At $M = 0.6$ the range would, typically be from 5×10^6 to 12×10^6 per ft and the corresponding run times would be 42 to 12 seconds.

The walls of the test section are perforated by 0.5 inch diameter holes inclined at 30° to the flow direction which allow pressure and flow communication between test section and a 12 ft diameter, 16 ft long plenum chamber. The wall porosity which is variable between 0.5% and 6% of the wall area (by means of sliding throttle plates) was set at 4% for the measurements.

Sting mounting of models from a vertically translating strut is provided. A linkage mechanism controls a pitch angle change from -11° to 22° and models may be rolled 360° . For these measurements the model was supported on an offset sting (11° crank angle) which gave a model incidence range from 0° to 33° . Sting bending under load resulted in approximately a 2° increment pitch angle for the Mach number range tested.

Free stream stagnation and static pressures are measured by means of Parascientific Inc. Digiquartz pressure transducers with an uncertainty of ± 0.01 psia. Stagnation temperature is measured by means of a resistance thermometer ($\pm 0.5^\circ\text{C}$) located in the settling chamber where stagnation pressure is also sensed.

The wind tunnel is equipped with a subsonic/ transonic Mach number control system composed of hydraulically driven chokes that protrude into the flow, through floor and ceiling, downstream of the test-section. The system is capable of controlling the test Mach number for $M \leq 0.95$ to an accuracy of 0.003 over the angle-of-attack excursion of the model. For control at transonic/supersonic speeds ($0.95 \leq M \leq 1.2$) the re-entry flaps at the diffuser entry are adjusted to influence the flow out of the plenum chamber.

II.2 Model Design and Construction

The model used was a sting-mounted 6% scale F/A-18 shown in Figure 4. It consists of three major pieces, namely an aluminum alloy nose section, with integral strakes (LEX) equipped with removable fences and a single place canopy; a stainless steel centre fuselage with integral wings; and a stainless steel rear fuselage. These parts are designed with close tolerance spigotted joints and are dowelled and bolted together. The centre fuselage is bored to accept a 1.5 inch diameter Able Corp. sting balance.

Leading- and trailing-edge flaps are fastened to the wings by simple bolted lap joints with dowel pins for accurate assembly. In the model tested, the leading- and trailing-edge flap deflections were set at 35° and 0° respectively.

The vertical fins are fastened to a steel insert that in turn is bolted to the rear fuselage. The horizontal stabilators are made with integral spindles that are clamped in a fitting that is fixed in the rear fuselage. The stabilator angle was set at -9° for this investigation.

Through-flow air intakes and flow passages are provided with removable internal chokes. The flow passages terminate in D-shaped exits on each side of the support sting.

Models of the AIM 9 missiles were fixed to the wing tips for the measurements.

II.3 Instrumentation

II.3.1 Nose Section

For these measurements, the starboard side of the nose section was modified to incorporate 84 surface pressure orifices and 4 fast response EndevCo 8515B (50 psia) pressure transducers. The pressure orifices have a

diameter of 0.02 inch and are distributed as follows: canopy centreline - 16 (15 connected); upper fuselage side - 12 (11 connected); upper LEX, inner row - 16; upper LEX, outer row - 8; lower fuselage side - 20 (18 connected); lower LEX - 12. The positions of the orifices on the upper surfaces are indicated in Figure 5 and the co-ordinates of those on the upper LEX are given in Table 1.

Orifice pressures were measured using five PSI electronically scanned pressure modules that were contained in a cavity under the canopy. Connectors were made using Teflon tubing. Each module contains 16 differential pressure transducers (± 45 psi). Reference pressure from an accurately measured nitrogen source outside the wind tunnel was led via flexible Teflon tubing to the nose cavity. During operation the transducers were subjected to increasing and decreasing calibration pressures immediately before each wind tunnel blowdown. Electrical wirings from the modules were led out of the nose section to a terminal block mounted on the main wing section as illustrated in Figure 6.

The fast response pressure transducer locations are also indicated in Figure 5. These are installed beneath the LEX surface. Connection to the surface is by means of a very short (0.03 inch) passage of 0.020 inch diameter which gives a high frequency response. Table 2 gives the co-ordinate positions of the transducers.

11.3.2 Instrumented Vertical Fin

For these measurements the standard starboard fin was replaced by an extensively instrumented fin, designed to measure dynamic pressures at 24 positions directly opposite to each other on each surface. In the construction 48 EndevCo 8515B (50 psia) absolute pressure transducers are embedded under the surface and pressure is sensed via 0.02 inch diameter passages, whose length varies from 0.014 to 0.025 inch. In addition, 4 strain gauges (Figure 7) are installed near the fin root at approximately half chord and an accelerometer (EndevCo Model 25, $\pm 500g$) is mounted 4.35 inches (75% span) from the root at $1/3$ local chord behind the leading edge. Positions of the instrumentation are shown in Figure 7. The transducers are numbered in Figure 8 for later reference and their locations are given in Table 3.

The fin is composed of two parts, one an insert, that are dowelled and bolted together. Pockets for the instrumentation and wiring are milled in each. The tip of the insert is very thin and in this region heavy duty steel staples were used to clamp the two together. Body filler was used to fill small surface cavities that resulted from this procedure. Figure 9 shows the assembly of transducers with wiring prior to joining the two parts of the fin.

Pressure calibration of the transducers was effected by fitting a gas-tight 'glove' over the entire fin 'in situ' on the model, thus subjecting each transducer to a common pressure from a nitrogen supply.

11.3.3 Vortex Rake

This instrument consists of a square array of 49 stagnation pressure measuring tubes supported, at 1 inch intervals, by two 6 inches x 6 inches frames. The rake was designed to achieve minimum flow blockage and yet be sufficiently rigid to withstand the high vibration levels from shed vortices of the model aircraft at high angles of incidence. Approximately 3 inches behind the support frames the 0.095 inch diameter tubes (0.071 inch bore) are gathered into a square bundle and housed in a square tube. This was clamped to the model support sting so as to place the face of the array a short distance (approximately 0.6 inch) behind the starboard fin and orientated at 20° to the aircraft model reference line as indicated Figure 10.

Thirteen of the 45 active tubes (the corner tubes were not connected) were devoted to dynamic pressure measurements and the remainder to sensing steady pressures. These tubes are distributed on the vertical and horizontal centrelines of the array as denoted in Figure 10. High frequency response was obtained by cementing $1/16$ inch diameter Kulite differential pressure transducers (XCW-062, ± 25 psi) just inside the tips of the 0.071 inch bore tubes. The reference side of these transducers was connected via 0.02 inch bore stainless steel tubing lying inside the 0.071 inch bore tubing of the rake to a pressure manifold, located in the base of the sting, which was connected to an external pressure source. Wiring from the transducers was led out alongside the reference pressure tube to electrical connectors mounted on the side of the sting.

The 32 steady pressure stagnation tubes were made by cementing short pieces of 0.070 inch O.D., 0.033 inch I.D. tubes inside the 0.071 inch bore tubing to form a 1 inch long tip. The tips were connected to two 16-transducer PSI electronically scanned pressure modules, that were also housed in the base of the sting, by 0.032 inch O.D., 0.02 inch I.D. stainless steel tubing cemented inside the tips of the rake tubes.

Internal chamfers of 40° included angle were machined in the ends of both dynamic and steady pressure tubes to reduce the directional sensitivity of the rake, since it was required to operate over a 35° angle-of-incidence range. The rake was aligned with the free-stream direction when the model incidence angle was 20°.

Accelerometers were installed at the upper corner of the rake closest to the model centreline to measure vibration levels.

Figure 11 illustrates some of the features of the construction of the rake and its mounting on the sting. Figure 12 shows the F/A-18 model with underwing stores (only a clean wing configuration was used in this investigation) and the vortex rake mounted.

II.3.4 Model Preparation

Boundary layer transition trips were installed following the scheme laid down in Reference 4. Rows of epoxy cylinders (0.045 inch diameter on 0.1 inch centres, 0.002 inch high) were applied 0.4 inch behind the leading edges of the LEX, wings, intakes, fins and horizontal stabilizers, on both surfaces. In addition a ring was applied around the nose, 0.4 inch behind the tip and a longitudinal row was fixed on the underfuselage centreline from nose to the intakes' station. Figure 6 shows the placement on the LEX and upper wing surfaces.

II.2 Results and Discussion

II.2.1 Surface Flow Visualization

The surface shear stress patterns on the vertical fin inboard and outboard surfaces and the horizontal stabilizer upper surface are shown in Figure 13. The angle of incidence was 30°, $M = 0.6$ and the fence was installed on the LEX. The oil-dot flow visualization technique permitted the skin friction lines to be located from the oil streaks and hence the surface streamlines can be determined (Ref. 9). These figures show quite large upflow on the inboard surface of the vertical fin and outflow on the horizontal stabilizer upper surface. The vertical fin outboard surface shows some upward movement of the surface streamlines in the vicinity of the fin-fuselage junction especially near the trailing edge. The surface streamlines were constructed from the oil streaks and are shown in Figure 14. The LEX fence has a strong effect on increasing the upflow velocity on the inboard vertical fin while on the horizontal stabilizer, the streamlines seem to have a smaller outflow velocity component with the fence 'on'.

II.2.2 Balance Data

Some representative results of the effect of the LEX fence on the aircraft steady and unsteady pitching moment are shown in Figures 15 and 16. The measurements were made with the vortex rake removed. The data are given at $M = 0.6$ and α varies from 0° to 35°. The steady moment coefficient with the fence 'on' and 'off' is almost identical except for values of α between 10° and 22.5° where a small difference in C_M is observed. The scatter in the C_M measurements is fairly large in the range of α between 15° and 25°. Video photography of the aircraft model during the wind tunnel tests showed much larger motion at these values of α than at other angles of incidence. The LEX fence has little influence on C_M until α is sufficiently large when the vortex burst is close to the tail. This angle is approximately 10° as observed from Figure 3. The benefit of the LEX fence in reducing the pitching moment fluctuations is clearly demonstrated in Figure 16. A reduction in the moment fluctuations also implies a reduction in the lift unsteadiness.

II.2.3 Pressure Measurements on LEX Upper Surface

Steady pressure measurements along the inboard and outboard rows of orifices on the LEX upper surface are shown in Figure 17 for $\alpha = 30^\circ$. The

axial vortex burst positions with the fence 'off' obtained from the straight line drawn through the experimental points in Figure 3 are also shown in the figure for $\alpha = 25^\circ$, 30° and 35° . At $\alpha = 30^\circ$ (Figure 17), the vortex burst is ahead of the fence. At these test conditions ($M = 0.6$, $\alpha = 30^\circ$), the pressure at the first orifice on the outboard row at $X/\bar{c} = 2.16$ has been affected before the influence of the fence is felt by inboard row of orifices.

The axial locations of the fast response transducers are shown in Figure 17. The values of C_p' are given in Figure 18 where the curves are displaced 0.025 of a unit upwards to avoid overlapping. At $\alpha = 10^\circ$, the first two transducers show a peak without the fence while with fence 'on', the peak disappears. It is not clear why the pressure fluctuations behave in this manner. At each transducer location, the value of α when C_p' starts to increase rapidly corresponds to the angle of incidence when the vortex burst is located near that transducer. The burst position can be determined approximately from Figure 3. For transducers 1 and 2, the effect of the fence is to lower the pressure fluctuations for values of α above those when the vortex has burst. A peak at $\alpha = 10^\circ$ is also observed at the third transducer with the fence 'off'. A large increase in C_p' is detected when the fence is 'on'. This peak in C_p' is due to the vortex generated by the fence which causes an increase in pressure fluctuations. At the fourth transducer which is located downstream of the fence trailing edge, the values of C_p' are consistently larger than those without the fence when α is between 5° and 25° .

II.2.4 Vertical Fin Data

II.2.4.1 Accelerometer Results

The rms values of the accelerometer placed in the vertical fin (Figure 7) are shown in Figure 19. The effect of the fence in modifying the flow structure after vortex breakdown causes a significant decrease in the acceleration felt by the fin. At $\alpha = 30^\circ$ an acceleration level of about 140 g without the fence is noted in the figure. With the LEX fence 'on' a decrease of 20 g is detected.

II.2.4.2 Steady Pressure Distributions

The steady C_p distributions on the vertical fin inboard surface are shown in Figure 20. The C_p curves for each row of transducers are displaced upwards to avoid overlapping. The baseline is marked in the figure and the row number (Figure 8) of the transducers under consideration is given in parenthesis. The effect of the fence is to decrease the steady state pressures on the fin to values below those with the fence 'off'. The difference is more pronounced in the middle of the fin than at the tip.

On the outboard surface of the vertical fin, the C_p distributions are given in Figure 21. The fence has little influence in modifying the steady pressures.

Figure 22 shows the normal force C_N acting on the fin. This force is obtained by the following equation

$$C_N = \sum_{j=1}^{24} (P_{Ij} - P_{Oj}) A_j / q A_T \quad (1)$$

and is positive outboard. The areas A_j for each panel are shown in Figure 8. It is assumed that the pressure measured by the each transducer is constant throughout the panel. For values of α up to about 20° , the force changes sign from negative to positive. A maximum in C_N is observed at α approximately 30° .

II.2.4.3 Unsteady Pressure Fluctuations

The unsteady pressure fluctuations C_p' on the vertical fin inboard surface are shown in Figure 23. The $C_p' = 0$ baseline is displaced upwards for

each row of transducers to avoid overlapping. The effect of the fence in lowering the pressure fluctuations is more pronounced near the fin leading edge and progressively diminishes towards the trailing edge for transducers rows 1, 2 and 3. As the tip of the fin is approached, the decrease in C_p' is more uniform along the fifth and sixth rows of transducers.

Figure 24 shows the pressure fluctuations on the outboard surface of the vertical fin. A much smaller decrease in pressure fluctuations is observed with the fence 'on' than in the previous figure. In fact for the first two rows of transducers, there is an increase in C_p' for X_f greater than approximately 40% of the local chord. The fence is more effective in lowering C_p' closer to the tip of the fin.

The unsteady normal force fluctuation on the fin outboard surface is given by the following equation

$$C_{NO}' = \sum_{j=1}^{24} P_{Ormsj} A_j / q A_T \quad (2)$$

and a similar expression can be used for the inboard surface by replacing P_{Ormsj} with P_{Irmsj} . It is assumed in the above equation that P_{Ormsj} is constant on each panel and the fluctuating pressures are perfectly correlated on the panel but uncorrelated between adjacent panels. The decrease in normal force fluctuations on both surfaces of the vertical fin with the LEX fence 'on' is shown in Figure 25. On the outboard surface, a maximum C_{NO}' is detected at α approximately 30° , while on the inboard surface it appears that a maximum C_{NI}' is not reached even at α as high as 35° . A larger decrease in normal force fluctuations with the fence 'on' is noted for the inboard surface for α greater than about 22.5° .

II.2.5 Vortex Rake Results

The vortical flow constant total pressure contour lines behind the vertical fin are shown in Figures 26 and 27 at α about 30° with the fence in the 'off' and 'on' positions. The centre of the low pressure region is located outboard of the vertical fin in both figures. It appears that with the fence 'on' the constant pressure contour lines are more compressed in the vertical direction. Inboard of the fin, a low pressure region is also detected with the fence 'on'. The pressure fluctuations C_p' obtained from the mid-horizontal and vertical rows of unsteady transducers are also included in these two figures. The C_p' is smallest in the centre of the vortex system and increases towards the edges of the rake. With the fence 'on', the magnitude of the pressure fluctuations increase gradually outboard of the fin following the pattern of the elongation of the steady pressure contour lines.

To study the distortion of the vortical flow without the interference of the vertical fins and horizontal stabilator, the tail section of the model aircraft was removed. The vortical flow structure is shown in Figures 28 and 29 with the fence in the 'off' and 'on' positions. The effect of the fence on 'compressing' the steady pressure contour lines is quite pronounced. Again, the lowest C_p' is located in the center of the low pressure region. The rms pressure fluctuations are quite similar for these two figures.

PART III GVT AND FLIGHT TESTS

III.1 Background

Faced with early structural failures and a rapid accumulation of fatigue damage to the vertical fin and attachment structures, resulting from the buffet, loading throughout the F/A-18 fleet, the manufacturer (McAair) implemented, in 1984, an interim solution relying entirely upon structural modifications (Figure 30), in an attempt to reduce the dynamic stresses in critical areas. However, it was soon realized that the structural enhancement alone would not be sufficient to provide full life of the vertical fin under current in-service usage, the dynamic stresses still being too severe.

Engineering studies and wind tunnel tests were performed on a series of LEX configurations that appeared to provide a substantial reduction in dynamic loading of the vertical fins. The M68 trapezoidal fence (8.3 x 32.1 inches) was selected because of its better effectiveness in reducing the vertical fin dynamic loading. Follow-on testing was carried out to investigate the effect of the final production design of the M68 trapezoidal fence on aft fuselage dynamic load environment, LEX fence support structure, acoustic noise, engine mount load and aircraft handling qualities. Approximately 85 flights were flown by the manufacturer, accumulating approximately 3000 test points. As a result of this testing, the US NAVY adopted the LEX fence as a retrofit for its fleet of F-18. Similarly, the LEX fence modification was implemented on all Canadian Forces CF-18 aircraft. The production fence installation is shown in Figure 31.

Subsequent to the modifications to the LEX the Canadian Forces decided to assess independently the effectiveness of the LEX fence modification in reducing the fatigue damage in the aft fuselage under representative CF usage. The AETE was tasked to undertake a flight test programme to investigate the CF-18 aft fuselage dynamic loading environment.

The objectives of the flight test program were: a) to measure the structural response of the vertical fins, horizontal stabilators, port engine aft attachment hanger and F404 engine, both with and without the LEX fence attached, to characterize the buffet load alleviation; b) to determine the extent of dynamic load transfer, due to vertical fin buffet environment, into the surrounding aft fuselage structure as a means to identify possible fatigue in critical components; c) to gather aft fuselage strain data at designated locations in order to provide correlation with existing damage tolerance and/or fatigue life estimates; d) to assess the validity of the vertical fin dynamic load tracking philosophy; e) to assess the effectiveness of the MSDRS AOA and q tracking software in collating accurate in-service usage data; and f) to develop a dynamic load spectrum representative of CF usage.

This part of the paper will address the methodology and gives some preliminary results of the dynamic response of the tail in flight under buffet conditions.

III.2 Ground Vibration Test

In order to establish the baseline dynamic characteristics of the vertical fin prior to flight testing, a ground vibration test (GVT) was performed at AETE. The objectives of this ground test program were to: a) establish the structural dynamic characteristics of the CF188 vertical fin structures with the interim structural modifications implemented in 1984; and b) perform strain measurements at the frame attachment stubs to determine the distributions and magnitude of the dynamic strains for each of the significant modes.

Testing was carried out on two different aircraft: CF188708, which has a lightweight aft fuselage, and CF188701 which is an early production aircraft with heavyweight aft fuselage. The difference in weight between the two is in the order of 200 lbs. Both aircraft had the structural modifications shown in Figure 30 embodied. The reason for the testing of two aircraft was that CF188701 being AETE's fully instrumented aircraft would be used for flight testing, while CF188708 being a squadron aircraft would be structurally representative of the overall Canadian fleet. The GVT showed that there were negligible differences in tail dynamic properties and dynamic stresses at the root between the two configurations. Only results for the flight test aircraft are presented.

In the test programme, the Force-Normal Mode (FNM) method and the Frequency Response Function (FRF) method were used. The first method was primarily utilized in a multi-exciter environment when the fin structure was either excited symmetrically or antisymmetrically, using a pair of electromagnetic exciters. The second technique was used when a single exciter was utilized to excite the structure asymmetrically. A pseudo-random excitation, within the frequency band of 0-100 Hz, was used to gather FRF plots to roughly identify the modes and related frequencies. Once the modal frequencies had been identified, mode mapping was performed and modal parameters measured using the FNM method for dual shaker excitation and the FRF method for single shaker excitation. Symmetric and antisymmetric sine-dwell excitation as well as pseudo-random asymmetric excitation of the left fin were used to excite the structure and investigate modal responses. The response was monitored at four reference locations designated by KS16, KS01, KT16, and KT01 in Figure 32. Linearity of the structure was also

verified by measuring the modal frequencies at different force levels. Modal damping was estimated using both the time decay traces and the 3dB bandwidth method. Root strain measurements were performed for the modes of interest under the same type of excitation used for the mode shape mapping but with excitation forces increased up to 100 lbf. Strain gauges were installed on the left and right vertical fin attachment stubs at FS 557.5, FS 566.0, FS 575.5, FS 580.5, FS 590.5, and FS 598.0.

III.3 Flight Test

III.3.1 Data Acquisition and Processing

Flight testing was carried out using AETE test aircraft CF-188701 specially instrumented for the purpose. The on-board instrumentation system is an FM (Frequency Modulation) and PCM (Pulse Code Modulation) system in which all parameters being monitored (digital or analogue) are encoded into either a serial PCM data stream or an FM multiplex for subsequent recording.

The aircraft test instrumentation can handle up to 64 channels of analogue data. For testing purposes and because of limitations in the data collector bit rate and sampling frequency requirements, a maximum of 54 analogue channels were encoded in the PCM and divided as follows: 11 channels to monitor fuel quantities, in the various internal and external tanks; 16 channels to monitor engine and aft fuselage accelerations and 27 channels to monitor aft fuselage strain gauges. Connections to the signal conditioners, installed in the aircraft nose to the aft fuselage strain gauges and charge amplifiers, utilized routes of existing spare wiring installed during manufacture of the aircraft. Additional wiring in the port engine bay area was added for this project.

Data was stored using the on-board MARS 2000 analogue recorder and for the flight test portion of the project was telemetered to the ground station for real time monitoring and back up storage. The basic instrumentation system is illustrated in Figure 33.

A large number of flight parameters available from the 1553 data BUS was gathered from the flight control computers and inertial navigation system, via the data BUS interface unit, including all MSDRS strain sensors. The data was collected into a single NRZ-L PCM stream at 400 kbps. Sampling rate was set at 606.06 samples/sec for the analogue data and 20.02 samples/sec for most of the flight parameters. This provided a recording capability of 30 minutes of flight data.

The MARS 2000 tape was removed from the on-board recorder after every flight. Tape integrity was verified to ensure that the data had been properly recorded prior to post processing. The PCM data was reformatted to VAX compatible tape and then further processed using the relevant aircraft calibration data file to yield data in engineering units. Following each mission, key measurands (all accelerometers and critical strain gauges) were verified to ensure serviceability. Once a key measurand was found to be unserviceable, a decision had to be made whether or not the unserviceability justified halting the test activities to rectify the problem. As is often the case with a flight test programme, the final decision is one of compromise, where measurand necessity is carefully weighed against other constraints.

III.3.2 Strain Gauge Installation

A total of 27 strain gauges and associated bridge completion networks were installed at selected areas of the aft fuselage. The strain gauge instrumentation was applied only to aft fuselage frames and longerons as well as port and starboard vertical fin attachment stubs. The port engine aft hanger attachment was also instrumented to measure loads. This installation required careful routing of the wiring in the engine bay area.

All gauges used were temperature compensated, 350 Ω AE gauges of 0.125 inch grid length. They were bonded in place at room temperature using an M-Bond 2000 adhesive. The power was a 5 volt DC supply. This type of gauge and the bonding method has been extensively used at AETE and has proved to be highly reliable. Accurate data can be obtained up to 18 months after installation in moderate strain areas. All gauges were protected from the environment using a rubber sealant.

The installation was performed by removing access doors, panels and covers and did not require major alteration to the structure.

III.3.3 Accelerometers Installation

Ten accelerometers were installed on the aft fuselage structure, the horizontal stabilators and vertical fins while six more were installed on the port engine structure to measure engine responses. The locations of the aft fuselage accelerometers are shown in Figures 34 and 35. Vertical fins and horizontal stabilator accelerometers were bonded externally to the structure and micro-dot cable connections extending from the accelerometers to the aft fuselage access location were routed spanwise along the surface in areas where flow disturbance would have small effects. The micro-dot cables were secured to the surface using a rubber sealant compound. The bonding compound is usually an epoxy-based adhesive or a dental cement. Because of the high vibration and temperature environment the engine accelerometers were attached to the hard points of the engine structures, using specially manufactured brackets. All charge amplifiers were installed underneath door 63L, located on top of the dorsal deck area.

III.3.4 Flight Test Matrix and Methodology

To fulfil the test objectives two test matrices were flown. The first matrix involved the execution of a set of controlled manoeuvres to quantify the improvement in dynamic loading in each of the AOA and q band currently used for aft fuselage fatigue tracking. This test matrix also included a stress survey of the aft fuselage in an attempt to verify the LEX fence effects on manoeuvre and steady state stresses. A second test matrix was designed to quantify the improvement due to the LEX fence in a more realistic scenario of actual Air Combat Manoeuvres and Ground Attack operations.

The initial test matrix was constructed in terms of achieving specific conditions of AOA and q parameters. Table 4 shows the standard AOA and q matrix currently used for tracking aft fuselage dynamic loading. For fleet usage characterization and individual aircraft tracking, time spent in the different AOA and q boxes is collated and summed for each aircraft in the fleet. Table 4 is generated from the code 66 report provided by the CF-18 MSDRS reporting system. CF in-service usage statistics provided the basis for test matrix design.

To achieve the required AOA and q conditions, a set of controlled manoeuvres were flown. Testing was concentrated in areas of the AOA and q matrix where most of the fatigue damage was shown to occur with secondary attention directed at areas of reported low damage. These bands are indicated on Table 4 by the highlighted areas inclusive of mode 1 and mode 2 damages.

A total of 45 test points composed the final AOA and q test matrix. Test altitudes were set between 10,000ft MSL and 30,000ft MSL with most of the flying carried out at 10,000ft MSL. Test point tolerances were kept within $\pm 1^\circ$ AOA, ± 10 KCAS and $\pm 1,000$ ft of the desired test conditions. Each test point was repeated three times to enable an accurate statistical analysis of the structural response in each band to be obtained. Table 5 gives the test points flown for the AOA and q testing. The aircraft was flown in the modified fighter escort configuration shown under ACM in Figure 36. An additional 30 test points were flown to investigate the LEX fence effects on both steady state and manoeuvre induced stresses in the aft fuselage. This stress survey was carried out by flying typical MIL-Spec manoeuvres that were to induce significant stress levels (ie. design loads) in the aft fuselage. Table 6 provides the test points flown for this part of testing.

The current aft fuselage fatigue tracking methodology assumes that the fatigue damage induced by buffet loading can be entirely characterized by the knowledge of time spent in the different AOA and q bands during service usage. This, of course is based on the assumption that the magnitude and frequency content of the dynamic loading are well known for each of the AOA and q bands and can be properly superimposed to the steady state and manoeuvre loading components.

The second test matrix was designed to verify the validity of these assumptions and, if required, to improve on the methodology. By flying a series of ACM missions it was believed that buffet load conditions more representative of service usage would be induced: the rigor of controlled testing being removed and the pilots left to exercise their creative flying abilities.

ACM flights were carried out with and without the LEX fence to obtain baseline pre-LEX fence buffet data. A total of 13 ACM missions, representative of in-service operations, were flown of which 8 were with and

5 without the LEX fence. Mission length averaged approximately 55 minutes of which about 10 minutes were spent above 10° AOA. They were flown in the modified fighter escort configuration. Three missions had to be reflown, the buffet data and time spent above 10° AOA showing lack of aggression in the ACM engagements, which rendered them unrepresentative. In addition to the ACM missions, three Ground Attack missions representative of CF operations were flown to increase the database for low altitude buffet and to investigate engine responses and aft attachment hanger loading which have been reported as more severely affected by low level weapon delivery manoeuvres than air combat manoeuvres. These were flown for two store configurations shown in Figure 36.

Flight testing started in July 1989 and was complete by late September 1989. A total of 33 missions were flown to support the two test matrices for a total of approximately 31.6 flying hours.

III. 4 Results and Discussion

III.4.1 Ground Vibration Test

Figure 37 shows a typical FRF plot for the anti-symmetric pseudo-random excitation. The FRF identifies clearly the different modes in the vicinity of amplitude peaks with $\pm 90^\circ$ phase difference between the structural response measured in 'g' and the exciting force signal.

For antisymmetric excitation, five modes can be identified. The symmetric and asymmetric excitations only triggered 3 and 4 modes respectively. It was found that the modes at 11.25 Hz and 14.25 Hz had very strong contributions from the aft fuselage lateral bending (AFLB) and aft fuselage torsion (AFT) with strong response of the horizontal stabilator and were identified as such. The fifth mode or Mode 3 as identified in the figure does not contribute significantly in fatigue damage and was therefore not investigated.

The modal frequencies and corresponding damping parameters for the three different excitation methods and modes of interest are presented in Table 7. The strain measurements confirmed that the interim modification (added cleat) had resulted in dynamic stresses re-distribution at the fin root attachment stubs. In particular the following observations are noted: a) Mode 1 dynamic stresses were relatively unaffected by the cleat modification in the uncleaned frame at FS 557.5, FS 566.0 and FS 575.5; and b) Mode 2 dynamic stresses were increased by a factor of two for the uncleaned frames. It was also noted that the dynamic strains ratios, that is, the microstrain-per-g calculated for each resonance, had similar values regardless of the excitation technique used.

III.4.2 Flight Test

Figure 38 compares power spectral density obtained from test data at 134 KCAS, 25° noseboom AOA, for the vertical fin KT01 and KS01 accelerometers with LEX fence 'on'. For this condition, sustainable buffet conditions were achieved in the AOA and q band of [26°, 28°], [75, 125] psf. Responses for the vertical fins show maximum amplitude at approximately 15.9 Hz for mode 1 and 44.9 Hz for mode 2 which is consistent with ground vibration data.

Figure 39 shows similar data for the KQ64 and KR64 accelerometers located in the horizontal stabilators where peak responses at approximately 14.2 Hz and 45.5 Hz are observed.

Figures 40 and 41 show filtered mode 2 response for the KS16 and KT16 accelerometers, within the same AOA and q band with the LEX fence 'off' and 'on' respectively. The reduction in buffet load is evident: with LEX fence 'off' the results show a peak acceleration of approximately 450 g while a maximum amplitude of 200 g is detected with the LEX 'on'. An overall reduction in the response level is also observed. Mode 1 showed similar trends as shown by Figures 42 and 43. For the AOA and q band of [30°, 32°] and [175, 225] psf a peak amplitude of 110 g for the LEX fence 'off' condition can be seen while peak response of 35 g are observed for LEX fence 'on' configuration.

In Figures 40-43, the asymmetry in amplitude response between the left and right fin can be noted. The magnitude of the response fluctuates in a random manner.

CONCLUSIONS

The following conclusions can be drawn from the water tunnel and wind tunnel investigations:

1) At low speeds the vortex burst position is independent of M and Re_c . Flight, wind tunnel and water tunnel data on the variation of the burst position with α can be collapsed into a straight line.

2) Surface shear stress patterns at high α show large upflow and outflow on the vertical fin inboard surface and horizontal stabilator upper surface respectively. The surface streamlines on the vertical fin outer surface is mainly in the free stream direction except near the fin-fuselage junction.

3) The LEX fence has little influence on the steady balance measurements. Fluctuating quantities, such as unsteady lift and pitching moment, are reduced with the fence 'on'.

4) At high α above 25° there is a large increase in the unsteady pressure fluctuations on the upper surface of the LEX.

5) Measurements taken at an α of 30° show an acceleration level of about 140 g at a position approximately 75% span from the root at 1/3 chord behind the leading edge of the vertical fin. With the LEX fence 'on' a decrease of 20 g was detected.

6) Steady pressure measurements on the vertical fin show the normal force to decrease significantly with the LEX fence 'on'. Fluctuating pressures are also reduced with the fence installed and the effect is more pronounced on the inner surface.

7) Total pressure contours of the vortical flow behind the vertical fins show the centre of the low pressure region to be located outboard of the fins. With the fence 'on' the contour lines are more compressed in the vertical direction.

The following conclusions are obtained from GVT and flight tests:

8) GVT shows mode 1 dynamic stresses to be relatively unaffected by the cleat modification in the uncleaned frame at FS 557.5, FS 566.0 and FS 575.5. There is an increase by a factor of two in Mode 2 dynamic stresses for the uncleaned frames.

9) Flight tests show that maximum acceleration responses at the vertical fins and horizontal stabilators occur at approximately 15 Hz and 45 Hz. Both modes 1 and 2 have a large reduction in peak acceleration with the LEX fence 'on'.

ACKNOWLEDGEMENTS

The wind tunnel investigations were supported in part by the Department of National Defence. Messrs. N. Tang and M. Plosenski carried out the wind tunnel data reduction. Mr. R.L. Wardlaw made available the water tunnel for flow visualization studies. Special appreciation to the AETE staff for conducting the flight tests.

REFERENCES

1. Mullans, R.E. and Lemley, C.E., "Buffet Dynamic Loads During Transonic Maneuvers", Air Force Flight Dynamics Laboratory, Tech. Rept. AFFDL-TR-72-46, Sept. 1972.
2. Lee, B.H.K., "A Method for Predicting Wing Response to Buffet Loads", J. Aircraft, Vol. 21, Jan. 1984, pp.85-87.
3. Lan, C.E. and Lee, I.G., "Investigation of Empennage Buffeting", NASA CR-179426, January 1987.
4. Erickson, G.E., Hall, R.M. Banks, D.W., Del Frate, J.H., Schreiner, J.A., Harley, R.J. and Pulley, C.T., "Experimental Investigation of the F/A-18 Vortex Flows at Subsonic Through Transonic Speeds, Invited Paper", AIAA-89-2222, 1989.

5. Zimmerman, N.H., Ferman, M.A. and Yurkovich, R.N., "Prediction of Tail Buffet loads for Design Application", Paper 89-1378-CP, AIAA/ASME/ASCE/AHS/ASC 30th Structures, Structural Dynamics and Materials Conference, Mobile, Alabama, April 1989.

6. Sellers, W.L. III, Meyers, J.F. and Hepner, T.E., "LDV Surveys Over a Fighter Model at Moderate to High Angles of Attack", SAE Technical Paper Series 881448, October 1988.

7. Wentz, W.H.Jr., "Vortex-Fin Interaction on a Fighter aircraft", AIAA-87-2474, AIAA 5th Applied Aerodynamics Conference, Monterey, CA., August 1987.

8. Pollock, N., Aeronautical Research Laboratory, Melbourne, Australia, "Private Communication", August, 1989.

9. Peake, D.J and Tobak, M., "Three-Dimensional Interactions and Vortical Flows with Emphasis on High Speeds", AGARDograph AG 252, July, 1980.

Table 1. Pressure Orifice Locations on LEX

Orifice No. (Figure 5)	X/ \bar{c}	Y/ \bar{c}	Orifice No. (Figure 5)	X/ \bar{c}	Y/ \bar{c}
29	1.662	0.253	41	2.458	0.253
30	1.728	0.253	42	2.524	0.253
31	1.794	0.253	43	2.590	0.253
32	1.861	0.253	44	2.657	0.253
33	1.927	0.253	45	2.160	0.355
34	1.993	0.253	46	2.226	0.355
35	2.060	0.253	47	2.292	0.355
36	2.126	0.253	48	2.358	0.355
37	2.192	0.253	49	2.425	0.355
38	2.259	0.253	50	2.491	0.355
39	2.325	0.253	51	2.557	0.355
40	2.391	0.253	52	2.623	0.355

Table 2. Pressure Transducer Locations on LEX

Transducer No.	X/ \bar{c}	Y/ \bar{c}
1	1.894	0.263
2	2.126	0.297
3	2.392	0.335
4	2.590	0.364

Table 3. Pressure Transducer Locations on Vertical Fin

Transducer No. (Figure 8)	X _f / \bar{c}_f	Y _f / \bar{c}_f	Transducer No. (Figure 8)	X _f / \bar{c}_f	Y _f / \bar{c}_f
1	0.252	0.141	13	0.924	0.578
2	0.453	0.141	14	1.061	0.578
3	0.653	0.141	15	1.197	0.578
4	0.853	0.141	16	0.888	0.816
5	1.053	0.141	17	0.971	0.816
6	0.434	0.339	18	1.072	0.816
7	0.605	0.339	19	1.174	0.816
8	0.776	0.339	20	1.100	0.985
9	0.947	0.339	21	1.177	0.985
10	1.119	0.339	22	1.236	0.985
11	0.651	0.578	23	1.180	1.035
12	0.788	0.578	24	1.230	1.035

Table 4 CF-18 Flight Dynamics Spectrum Report

NOSE BOOM ALPHA	DYNAMIC PRESSURE (psf)										TOTAL
	0	40	75	125	175	225	300	350	400	3000	
	40	75	125	175	225	300	350	400	3000	UP.	
< - 0.	25	3	24	10	0	0	1	5	17	0	85
0. - 2.	18	90	438	76	200	2105	2681	2042	4086	0	11736
2. - 4.	2	270	258	339	1300	626	119	99	147	0	3260
4. - 6.	0	587	139	565	293	131	67	66	95	0	1943
6. - 8.	0	500	74	108	85	69	19	25	51	0	931
8. - 10.	3	75	130	65	95	60	39	33	29	0	529
10. - 12.	1	21	22	19	13	15	9	3	2	0	105
12. - 14.	0	21	17	9	6	21	7	4	2	0	87
14. - 16.	1	33	14	8	7	25	7	5	0	0	100
16. - 18.	0	47	16	15	24	21	16	3	0	0	142
18. - 20.	0	26	9	14	7	2	2	1	0	0	61
20. - 22.	0	16	13	16	4	1	1	0	0	0	51
22. - 24.	0	29	8	11	3	1	2	0	0	0	54
24. - 26.	6	39	15	5	1	10	3	0	0	0	79
26. - 28.	3	0	5	2	0	1	1	0	0	0	12
28. - 30.	0	0	2	5	2	4	0	0	0	0	13
30. - 32.	0	1	0	2	0	1	0	0	0	0	4
32. - 34.	1	1	9	2	0	0	0	0	0	0	13
34. - 36.	0	0	0	0	0	0	0	0	0	0	0
36. - 38.	0	0	0	0	0	0	0	0	0	0	0
38. - 40.	0	0	0	0	0	0	0	0	0	0	0
40. - 42.	1	0	1	0	0	0	0	0	0	0	2
42. - 44.	0	0	0	0	0	0	0	0	0	0	0
ABOVE 44.	0	0	1	0	0	0	0	0	0	0	1
TOTALS	61	1759	1195	1271	2040	3093	3074	2286	4429	0	19208

Blocks Read : 360
 Records Processed : 3844
 Continuous Time Discontinuities : 0
 MCl OFP Identification : 87X+

Table 5 AOA and q Test Points

Test point Manoeuvres Number		Altitude	Airspeed	FCES AOA
		(FEET MSL)	(KCAS)	(DEG)
1	Symmetrical Pushdown	10,000	335	1.4
2	Symmetrical Pushdown	10,000	450	1.4
3	Symmetrical Pushdown	10,000	245	4.0
4	Level constant g-turn	10,000	245	8.4
5	Symmetrical Pushdown	10,000	105	12.0
6	Stabilized g-turn	10,000	390	13.8
7	Level constant g-turn	10,000	220	15.5
8	Stabilized g-turn	10,000	335	15.5
9	Level constant g-turn	10,000	220	19.1
10	Stabilized g-turn	10,000	245	19.1
11	Stabilized g-turn	10,000	275	19.1
12	Level constant g-turn	10,000	220	20.8
13	Stabilized g-turn	10,000	245	20.8
14	Stabilized g-turn	10,000	275	20.8
15	Level constant g-turn	10,000	165	22.6
16	Stabilized g-turn	10,000	220	22.6
17	Stabilized g-turn	10,000	245	22.6
18	Stabilized g-turn	10,000	275	22.6
19	Level flight	10,000	135	24.4
20	Level constant g-turn	10,000	165	24.4
21	Stabilized g-turn	10,000	220	24.4
22	Stabilized g-turn	10,000	245	24.4
23	Stabilized g-turn	10,000	275	24.4
24	Level constant g-turn	10,000	135	26.1
25	Level constant g-turn	10,000	165	26.1
26	Stabilized g-turn	10,000	220	26.1
27	Stabilized g-turn	10,000	245	26.1
28	Level constant g-turn	10,000	135	27.9
29	Stabilized g-turn	10,000	165	27.9
30	Stabilized g-turn	10,000	220	27.9
31	Level flight	10,000	105	29.7
32	Level constant g-turn	10,000	135	29.7
33	Stabilized g-turn	10,000	165	29.7
34	Stabilized g-turn	10,000	220	29.7
35	Stabilized g-turn	10,000	165	29.7
36	Stabilized g-turn	10,000	165	31.4
37	Stabilized g-turn	10,000	320	36.7
38	Stabilized g-turn	10,000	335	26.1
39	Level flight	30,000	350	1.4
40	Level constant g-turn	30,000	225	15.5
41	Stabilized g-turn	30,000	285	19.1
42	Level flight	30,000	135	24.4
43	Stabilized g-turn	30,000	250	26.1
44	Stabilized g-turn	30,000	350	26.1
45	Stabilized g-turn	30,000	175	31.4

Table 6 Stress Survey Test Points

Test point Number	Manoeuvres	Altitude	Airspeed	MACH #
		(FEET MSL)	(KCAS)	
46	1 g 360° roll	5,000	390	.65
47	Rolling Pull-out	5,000	390	.65
48	Symmetric Pull-up	5,000	390	.65
49	to Nz limit	5,000		
50	1 g 360° roll	5,000	460	.75
51	rolling Pull-out	5,000	460	.75
52	Symmetric Pull-up	5,000	460	.75
53	to Nz limit	5,000		
54	1 g 360° roll	5,000	520	.85
55	Rolling Pull-out	5,000	520	.85
56	Symmetric Pull-up	5,000	520	.85
57	to Nz limit	5,000		
58	1 g 360° roll	5,000	580	.95
59	Rolling Pull-out	5,000	580	.95
60	Symmetric Pull-up	5,000	580	.95
	to Nz limit	15,000		
61	1 g 360° roll	15,000	380	.75
62	Rolling Pull-out	15,000	380	.75
63	Symmetric Pull-up	15,000	380	.75
64	to Nz limit			
65	1 g 360° roll	15,000	430	.85
66	Rolling Pull-out	15,000	430	.85
	Symmetric Pull-up	15,000	430	.85
67	to Nz limit			
68	1 g 360° roll	15,000	490	.95
69	Rolling Pull-out	15,000	490	.95
	Symmetric Pull-up	15,000	490	.95
70	to Nz limit			
71	1 g 360° roll	25,000	360	.85
72	Rolling Pull-out	25,000	360	.85
73	Symmetric Pull-up	25,000	360	.85
	to Nz limit			
74	1 g 360° roll	3,000	620	.99
	1 g 360° roll	10,200	610	1.06
75	Wind-up turn	8,500	540	.94
76	Symmetric Pull-up	2,500	610	.95
	to Nz limit			
	Level Acceleration V_L	10,000	V_L	V_L
	Level Acceleration V_L	20,000	V_L	V_L
	Level Acceleration V_L	30,000	V_L	V_L

Table 7 CF-188701 GVT Modal Parameters

EXCITATION		SYMMETRIC		ANTISYMMETRIC		ASYMMETRIC	
FRF PEAK#	MODE	FREQ (Hz)	DAMP (C/Cc)	FREQ (Hz)	DAMP (C/Cc)	FREQ (Hz)	DAMP (C/Cc)
1	AFLB	NI	-	11.25*	-	11.25*	-
2	AFT	NI	-	14.75*	-	NI	-
3	MODE 1	15.21♦	.021■	15.23♦	.019■	15.40♦	.016
4	MODE 2	45.27♦	.031■	45.47♦	.042■	45.33♦	.021■
5	MODE 3	96.75*	-	96.80*	-	96.85*	-

NOTES

- NI = means mode peak not identified
 (*) = FRF gathered using pseudo-random excitation at 21.5 lbf rms
 (♦) = sine-dwell excitation at 60.0 lbf rms
 (■) = averages taken from a number of measurements

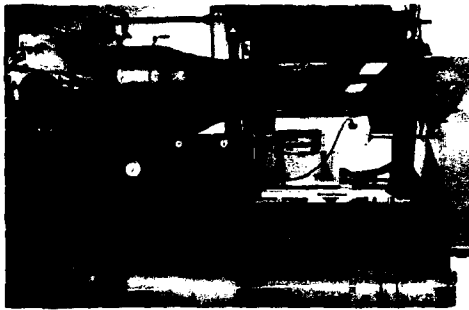


Figure 1 General View of NAE Water Tunnel



Figure 2 (a) Side View, (b) Plan View of Model and Vortex at $\alpha = 30^\circ$

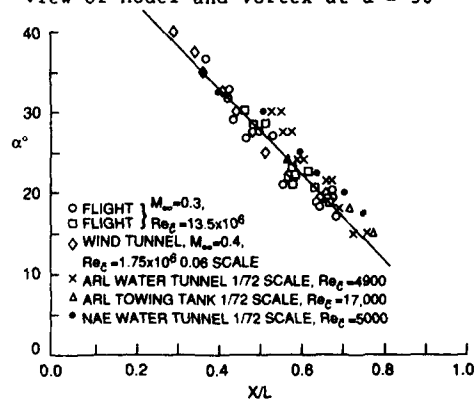


Figure 3 Axial Positions of Vortex Breakdown

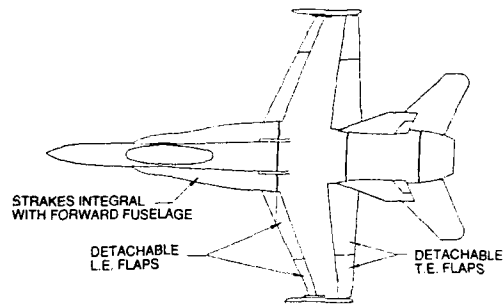


Figure 4 F/A-18 Model Features

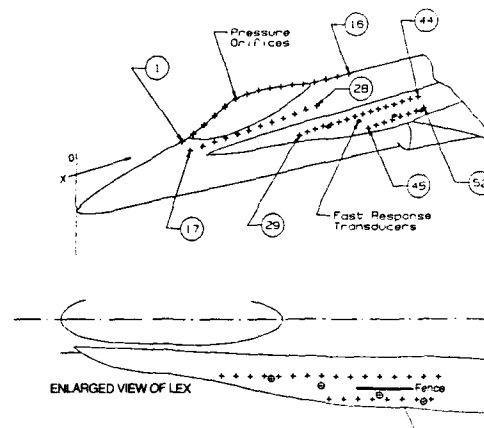


Figure 5 Forward Fuselage and LEX Pressure Orifice Locations



Figure 6 Pressure Instrumentation in Nose Cavity

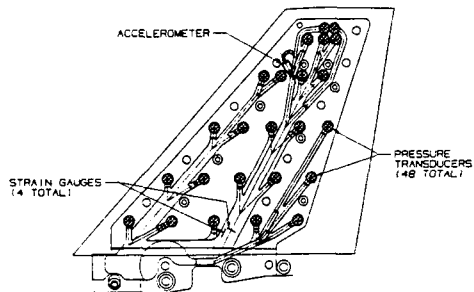


Figure 7 Fin Instrumentation Layout

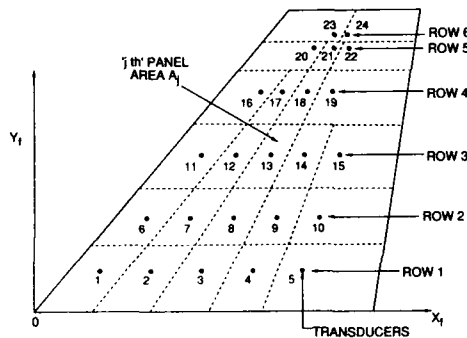


Figure 8 Fin Pressure Transducer Locations

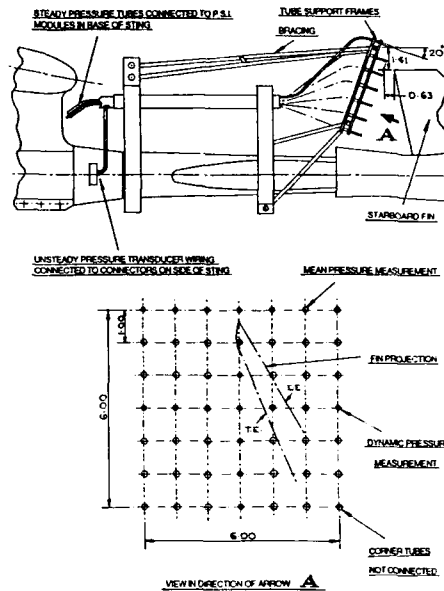


Figure 10 Vortex Rake Arrangement

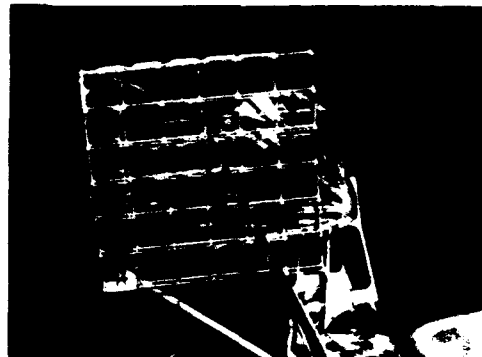


Figure 11 Vortex Rake Mounting behind Fin

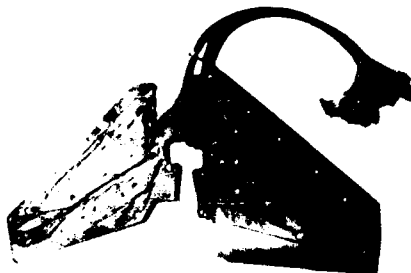
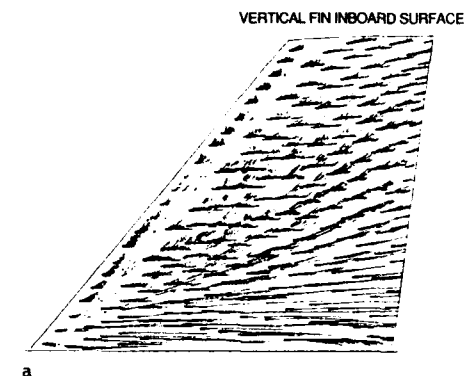


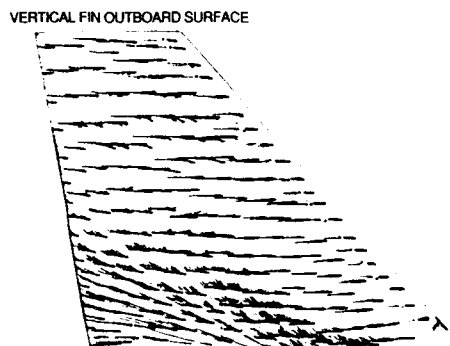
Figure 9 Exposed View of Fin with Wiring



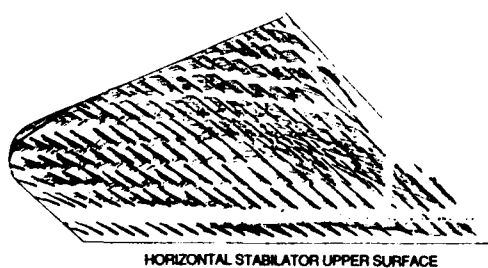
Figure 12 F/A-18 Model with Vortex Rake



a

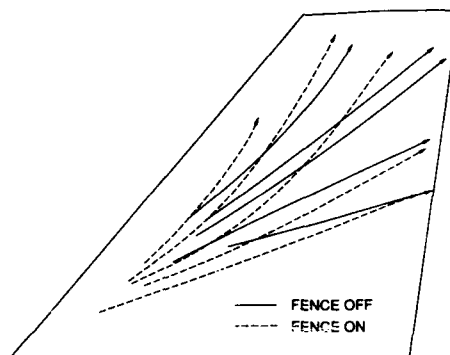


b



c

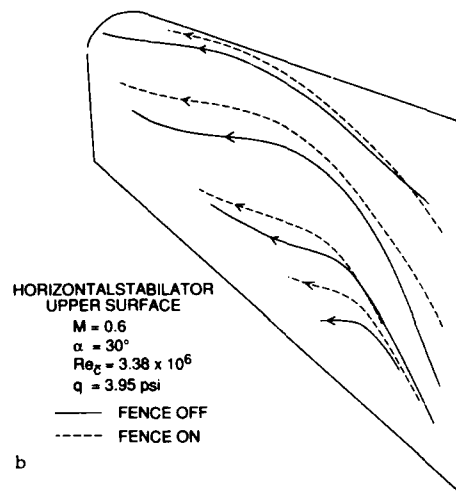
Figure 13 Oil Streaks on
(a) Vertical Fin Inboard Surface,
(b) Vertical Fin Outboard Surface,
(c) Horizontal Stabilator Upper
Surface. $M = 0.6$, $\alpha = 30^\circ$, $Re_c = 3.38 \times 10^6$, $q = 3.95$ psi



VERTICAL FIN INBOARD SURFACE

 $M = 0.6$, $\alpha = 30^\circ$, $Re_c = 3.38 \times 10^6$, $q = 3.95$ psi

a

HORIZONTAL STABILATOR
UPPER SURFACE
 $M = 0.6$
 $\alpha = 30^\circ$
 $Re_c = 3.38 \times 10^6$
 $q = 3.95$ psi

— FENCE OFF
 - - - FENCE ON

b

Figure 14 Surface Streamline
(a) Vertical Fin Inboard Surface,
(b) Horizontal Stabilator Upper
Surface. $M = 0.6$, $\alpha = 30^\circ$, $Re_c = 3.38 \times 10^6$, $q = 3.95$ psi

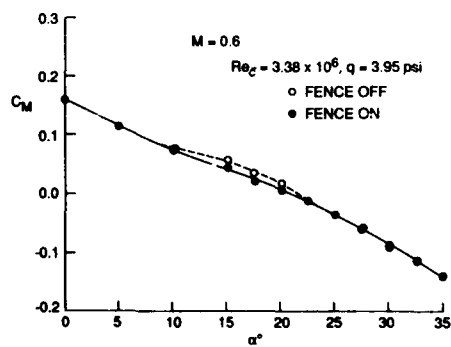
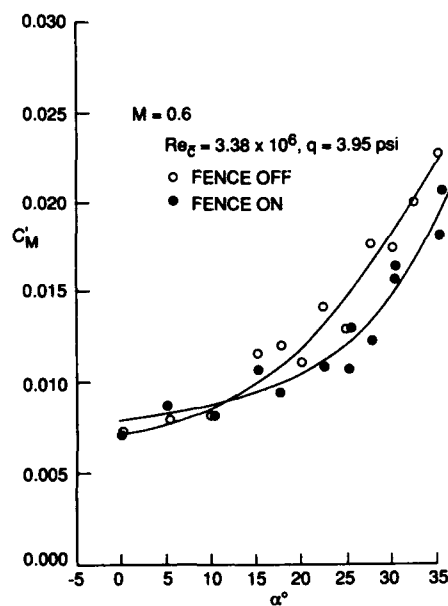
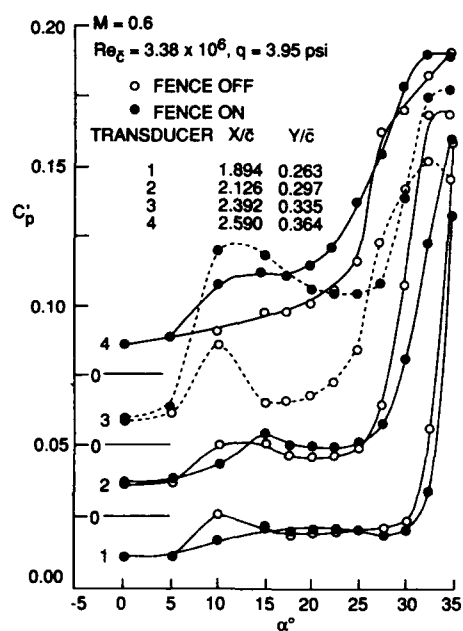
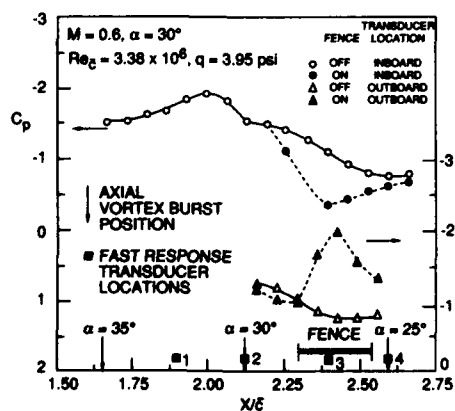
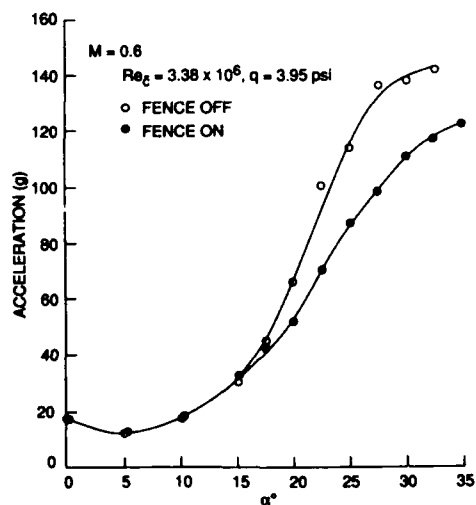


Figure 15 C_M versus α

Figure 16 C_M' versus α Figure 18 C_p' versus α on LEX Upper Surface^PFigure 17 C_p Distributions on LEX Upper Surface^PFigure 19 Vertical Fin Acceleration versus α

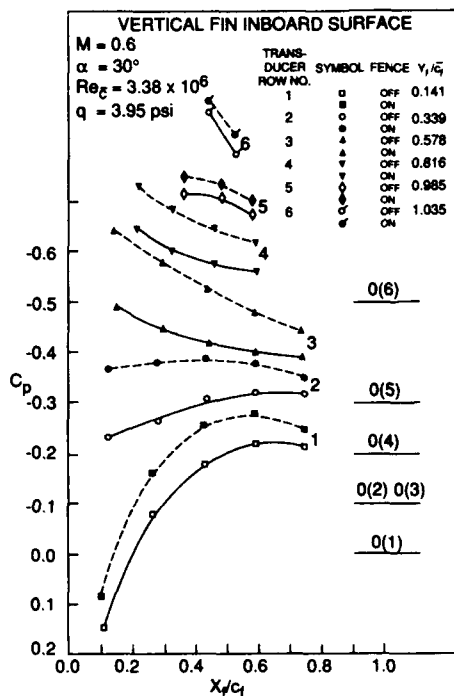


Figure 20 C_p Distributions on Vertical Fin Inboard Surface

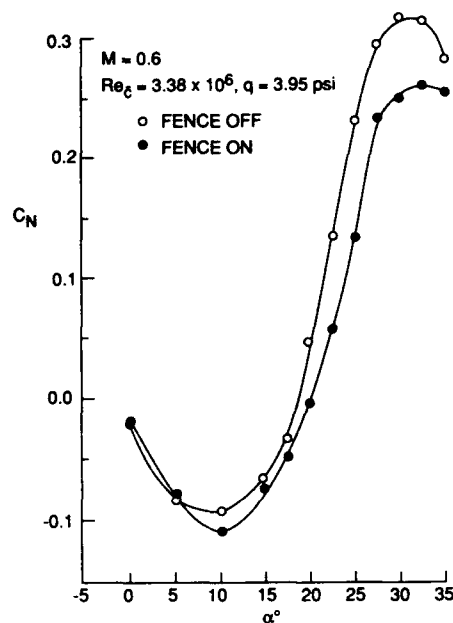


Figure 22 Vertical Fin C_N versus α

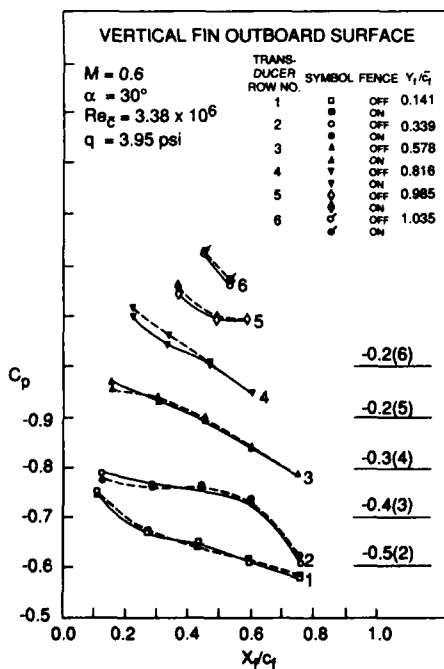


Figure 21 C_p Distributions on Vertical Fin Outboard Surface

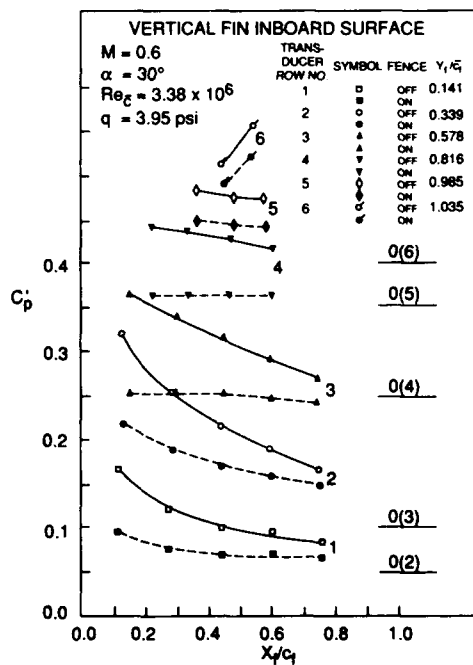


Figure 23 C_p' Distributions on Vertical Fin Inboard Surface

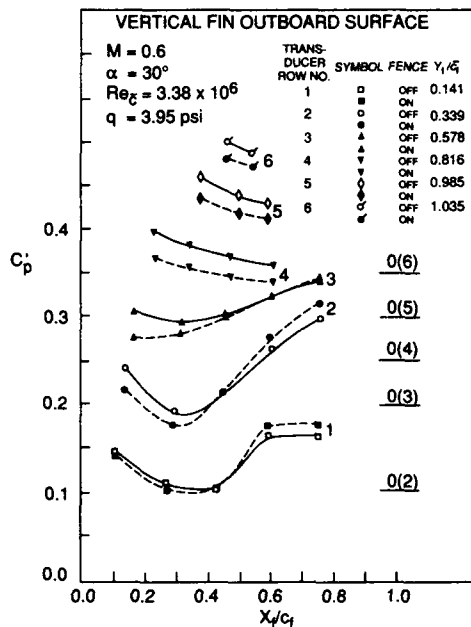


Figure 24 C_p' Distributions on Vertical Fin Outboard Surface

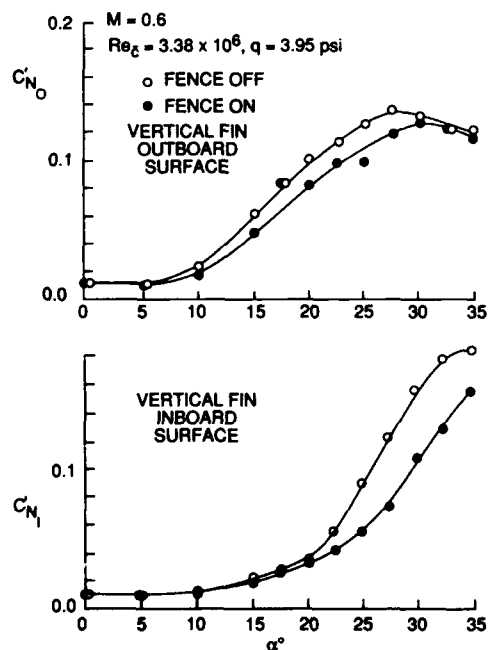


Figure 25 C_N' versus α on Vertical Fin Outboard and Inboard Surfaces

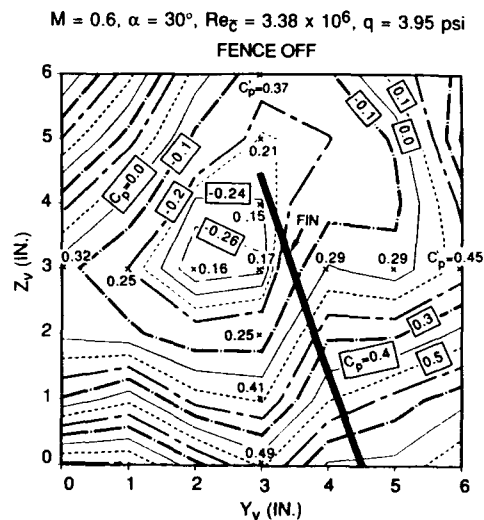


Figure 26 Total Pressure Contours behind Vertical Fin with LEX fence 'off'

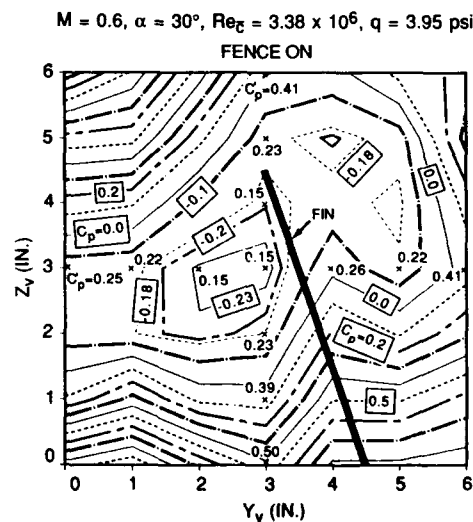


Figure 27 Total Pressure Contours behind Vertical Fin with LEX fence 'on'

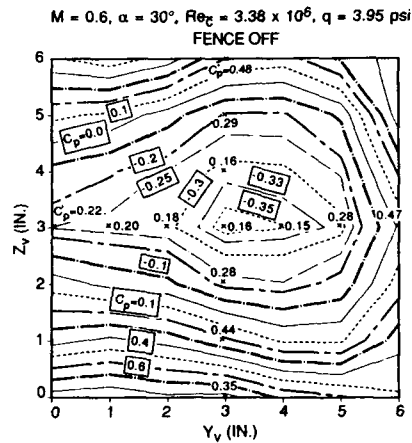


Figure 28 Total Pressure Contours with Tail Section Removed and LEX fence 'off'

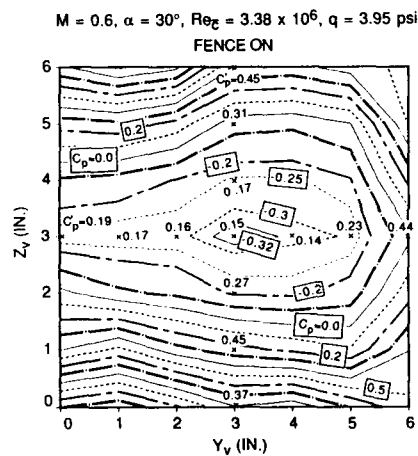


Figure 29 Total Pressure Contours with Tail Section Removed and LEX fence 'on'

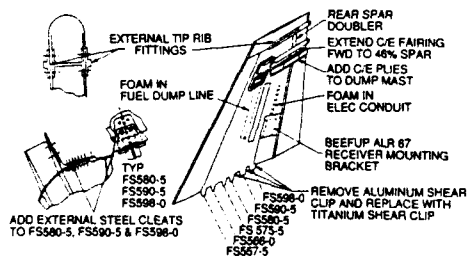


Figure 30 Vertical Fins Structural Enhancement

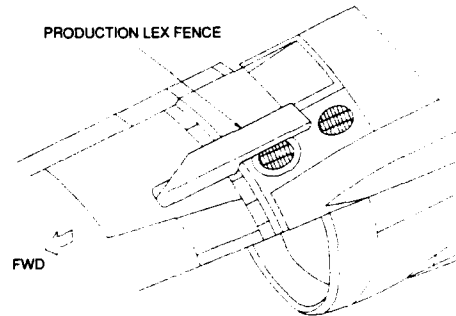
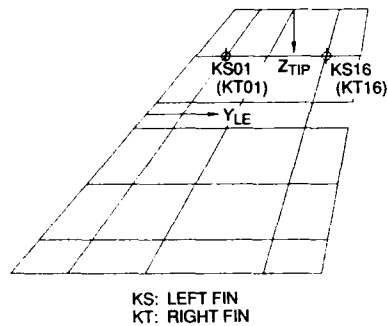


Figure 31 M68 Trapezoidal Lex Fence



LOCATION	YLE (IN.)	ZTIP (IN.)
KS16	48.20	9.00
KS01	10.93	10.50
KT16	48.20	9.00
KT01	10.93	10.50

Figure 32 CF-188701 GVT Reference Locations

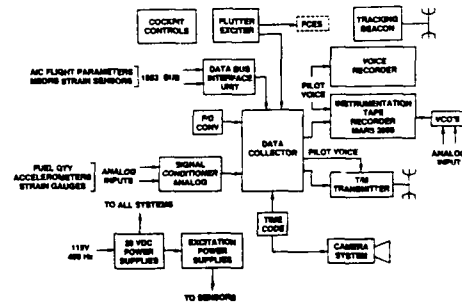


Figure 33 CF-188701 Basic Instrumentation System

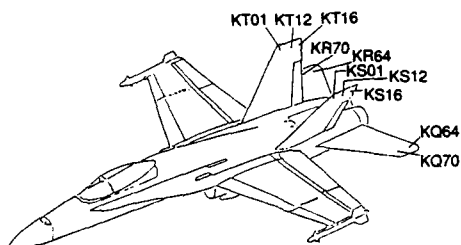
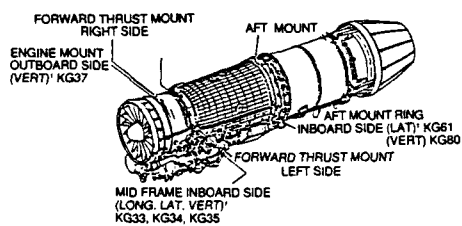


Figure 34 AFT Fuselage Accelerometer Installation



(1) NOTE: ACCELEROMETER LOCATED SIMILAR POSITION BUT OPPOSITE SIDE SHOWN

Figure 35 F404 Port Engine Accelerometer Installation

TESTED CONFIGURATIONS	CONFIGURATION									
		1	2	3	4	5	6	7	8	9
ACM	1	☐				⊕				☐
GA	1		●			⊕		⊕	☐	
	2		●	⊕				⊕	⊕	

⊕ 330 USG FUEL TANK
☐ AIM-9L/M MISSILE
● SUU-5005
⊕ WING PYLON

Figure 36 CF-18 Weapon Stations

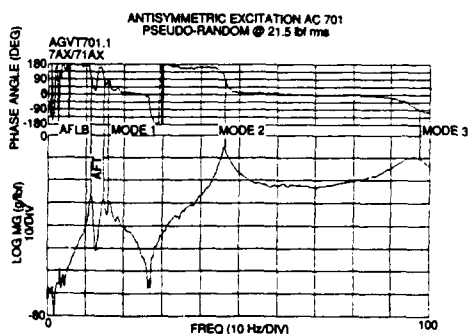


Figure 37 CF-188701 GVT Frequency Response Function

SAMPLING FREQ.: 606.06 Hz FFT LENGTH: 1024
WINDOW LENGTH: 512

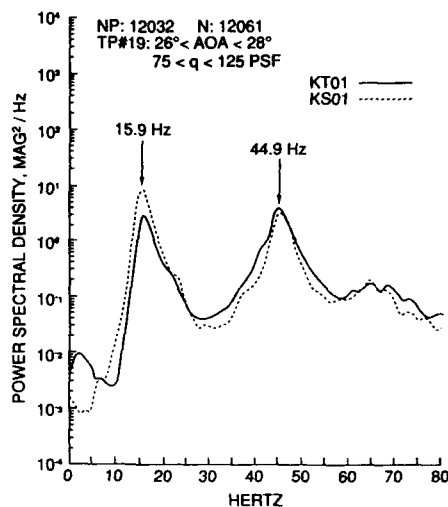


Figure 38 Power Spectral Density at Locations KS01 and KT01

SAMPLING FREQ.: 606.06 Hz FFT LENGTH: 1024
WINDOW LENGTH: 512

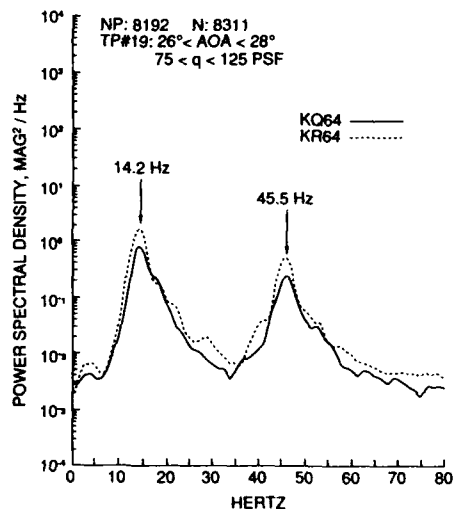


Figure 39 Power Spectral Density at Locations KQ64 and KR64

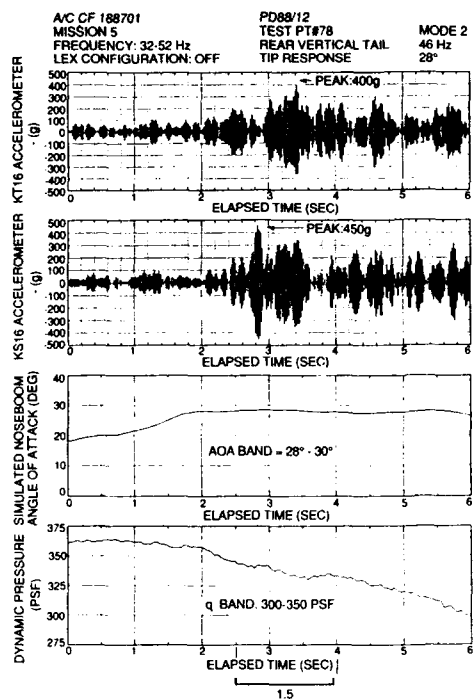


Figure 40 Mode 2 Response at
Locations KS16 and KT16 : LEX Fence
Off

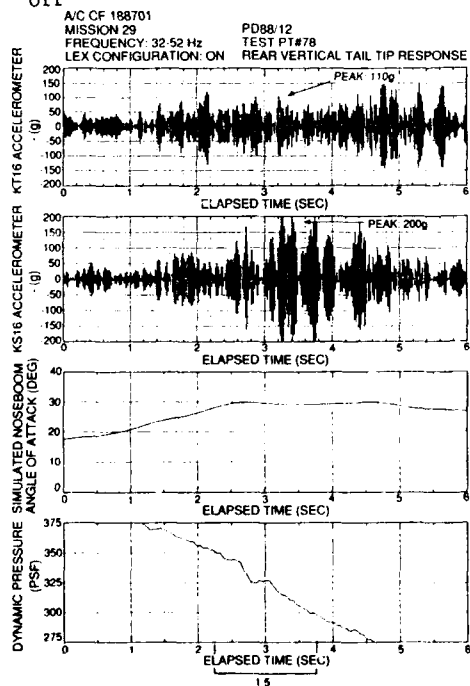


Figure 41 Mode 2 Response at
Locations KS16 and KT16 : LEX Fence
On

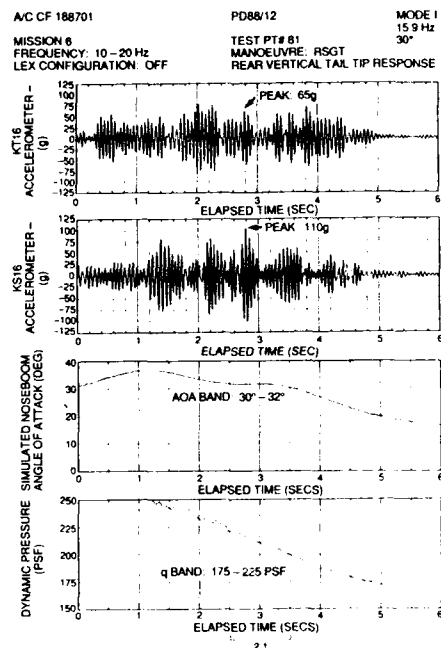


Figure 42 Mode 1 Response at
Locations KS16 and KT16 : LEX Fence
Off

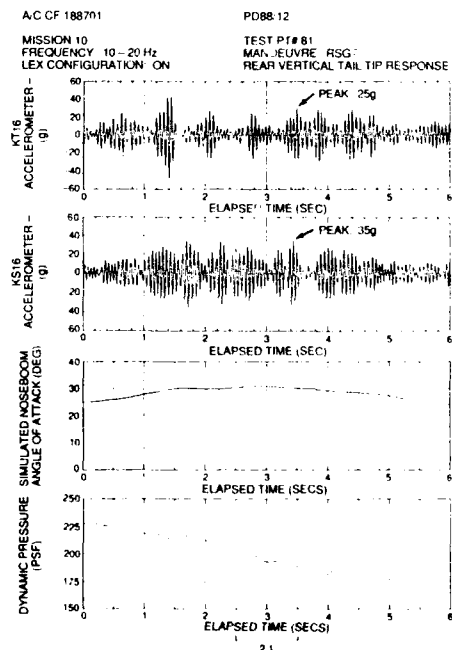


Figure 43 Mode 1 Response at
Locations KS16 and KT16 : LEX Fence
On

A UNIFIED APPROACH TO BUFFET RESPONSE OF FIGHTER AIRCRAFT EMPENNAGE

by

M.A.Ferman, Principal Tech Specialist
 S.R.Patel, Engineer
 N.H.Zimmerman, Principal Tech Specialist (retired)
 McDonnell Aircraft Company
 McDonnell Douglas Corporation
 St. Louis, MO
 United States

and

Gordon Gerstenkorn, Project Engineer
 Naval Air Development Center
 Warminster, PA 18974-5000
 United States

Abstract

A unified approach has been derived for predicting buffet response of fighter aircraft empennage operating in high angle of attack maneuvering conditions. Since the advent of high angle of attack flight using controlled vortex flows, incidences of severe structural stress, and in some cases, damages have resulted. This has been pronounced on twin tailed aircraft, including McDonnell's F-15 and F/A-18 aircraft which required structural beef-ups to their empennage. Two concepts are shown for predicting buffet response of empennage. The first approach uses elastically scaled models in wind tunnel tests to provide full scale prediction. The second approach is based on calculations using measured pressure data from wind tunnel tests. The latter method is more versatile. Detailed applications are shown for the F/A-18 empennage, while other applications at McDonnell are noted. This work covers many years and is believed to be a mature approach.

List of Symbols & Nomenclature

a	acceleration
AOA	angle of attack
BM	Bending Moment
c_p	pressure coefficient
f_p	natural frequency
l, L	length
m	mass
M	Moment
PSD	power spectral density
CSD	Cross Power Spectral Density
psf	pounds per square foot
r	radial distance from vortex core
RMS	Root Mean Square
q, Q	dynamic pressure
T	Torque, or Transfer Function
TM	Torsional Moment
v	velocity
CRAD	Contracted Research and Development
IRAD	Internal Research and Development
α	Angle of Attack

Subscripts

a	aircraft scale
m	model scale
n	n th mode

Comments

Bar over symbol means RMS value.
 Two bars over a symbol means PSD.

Background and Introduction

One of the earliest buffet investigations, by Frazer and Duncan, Reference 1, concerned an accident that resulted in the destruction of a small transport aircraft in England in 1930. They showed the accident to be caused by buffet. The aircraft had been drawn upward by up-drafts from a tall cloud which caused the angle of attack to increase sharply, resulting in buffet. Frazer evaluated buffet and flutter through theory and tests and concluded that buffet damaged the wing struts causing the destruction of the aircraft. For empennage buffet, one of the earliest incidents was reported in References 2 and 3 in 1933. The severe vibration of a McDonnell pursuit plane was traced to tail buffet produced by turbulent flow from the wing and fuselage. Hood and White produced improvements by introducing wing fillets, engine cowl, and other devices to smooth the airflow over the tails. Abdrashitov, Reference 4, also investigated many facets of tail buffet, including causes and cures. He used both theory and test to conduct a thorough evaluation for that era (late 30's).

A large number of wing buffet studies occurred between 1940 and 1968 because of increased flight speeds, References 5 through 8. Since 1968, aircraft design emphasis has been on agility and high angle of attack maneuvering. As a consequence, there has been renewed interest in tail buffet. References 9 through 11 describe some of the new endeavors. There have been a rash of severe environmental effects on other newer aircraft operating at high angles of attack, especially twin tailed aircraft.

A precursor of this paper (Reference 12) is amplified here with major new work from internal research and development (IRAD) at McDonnell. The presentation of Reference 12 summarized a Navy sponsored program (1986-1987), Ref. 13. McDonnell's current internal research on buffet began in 1983 and continues today. Methods used on earlier vehicle studies were steadily improved from the GAM-72 missile (1958) to the Mercury Atlas (1966), Reference 14 to the F-4 (1972), Reference 5. Our method is now believed to be mature and more accurate.

Basics of the Empennage Buffet Phenomena

The vortical flow pattern on the F/A-18 aircraft at a high angle of attack flight condition is shown in Figure 1. Under conditions of high humidity, the vortex from the LEX can be seen, as is shown in the figure. In this case, the aircraft is at approximately 28 degrees angle-of-attack, and the vortex is well defined. It is tightly wound until it reaches the intersection between the wing and the fuselage. At this point, vortex burst occurs. Burst is the point where the tangential component of the velocity transitions from a $1/r$ variation, as is seen in a classical vortex, to one that is proportional to r , where r is the radius from the core. The burst vortex then travels aft and upward, impinging on the vertical tail. The burst vortex flow is associated with an expanded flow regime compared to the tightly wound unburst regions, and exhibits larger pressure oscillations.

The vertical tails, when exposed to the LEX vortex wake, experience very high buffeting pressures with resulting high dynamic response levels. These high responses were not anticipated when the aircraft was designed. Flight test data indicated dynamic response levels exceeding 500G's at the most critical combination of angle of attack and dynamic pressure. This high dynamic response has caused damage to the tails and was the main reason for this investigation into methods that could be used to predict empennage buffet loads of the type experienced on the F/A-18.

Two methods were developed, both of which rely on buffet dynamic data obtained from wind tunnel model tests. Wind tunnel data was the starting point because the available aerodynamic methods, including Computational Fluid Dynamics (CFD) codes, were not capable of predicting the unsteady pressures in the vortex region of the flow over the F/A-18 tails. Figure 2 shows a sketch of vortical flow over a 12% wind tunnel model. Flow visualization was achieved employing nitrogen enriched steam that was injected into the vortex. Videotape data was used to produce the sketch. It is seen that the flow here is a good replication of the flight test. Thus, wind tunnel experiments can correctly produce the vortex flow field. The wind tunnel data is augmented with our large data base of experimental data from flight tests and earlier general wind tunnel tests to form the basis of the prediction techniques.

It is anticipated that CFD methods ultimately will be able to predict the vortex flow field. When this happens, the methods developed here can be used with the CFD predictions to predict buffet response.

Our experience shows that buffet is basically an incompressible flow phenomenon. This is because empennage buffet occurs at high angles of attack, and this can be attained only at relatively low dynamic pressure without exceeding the design limit load of the aircraft. Figure 3 is a plot of peak RMS buffet pressure as a function of dynamic pressure for the F/A-18 vertical tails. Superimposed on this curve are the angles of attack associated with the various buffet levels. As can be seen, maximum buffet pressure levels occur with high angles of attack but with low dynamic pressure. Maximum buffet pressures occur for the dynamic pressure range between 300 to 400 psf where the aircraft can sustain the high angles of attack necessary to cause empennage buffet. At higher dynamic pressures, the aircraft cannot attain the required angles of attack without exceeding the design limit load of the aircraft. These conditions can be contrasted to those where wing buffet occurs. Wing buffet is usually considered to be a high dynamic pressure, transonic phenomenon.

Method Development

The conceptual approaches of the two methods developed are shown in Figure 4. One method, the "flexible tail method" uses a flexible wind tunnel model similar to that which might be used for a flutter test. The tunnel results are scaled to predict the aircraft. The other method, the "rigid tail pressure method," uses the unsteady test pressures on a rigid tail in calculations to predict full scale response. Both methods make use of our own scaling laws to predict aircraft data from model data. In both cases, MCAIR flight and wind tunnel data bases were used to validate the methods.

For the development of the flexible tail method, buffet loads were measured during the buffet condition in the wind tunnel and were scaled to aircraft size. The data was then compared to the corresponding data obtained from the aircraft. If the two sets of data matched it was assumed that the scaling laws were valid; if not, an additional pass was made through the scaling procedures. This process was repeated until suitable scaling laws were validated. The flexible tail method has the advantage that buffet loads are obtained directly. It has the disadvantage that a physical model is required for each design to be evaluated. This method was fully matured in the Navy contract, Ref. 13.

For the development of the rigid tail pressure method, unsteady pressures were measured during the buffet condition on a rigid wind tunnel model. These pressures were scaled to aircraft size and used with a finite element model of the empennage to predict the buffet loads. Once again, these loads were compared to those measured on the aircraft for validation. This method has the advantages that only a rigid model of the structure is required in tunnel tests. Once the buffet pressures are obtained, they can be used with a finite element model of the surface to predict buffet response. Thus, this method is useful for evaluating changes to the structure. Also, it can be applied early in the aircraft design

cycle to account for buffet effects before design details are finalized. This method was matured more recently in McDonnell's IRAD, whereas it was only a supplementary approach in the Navy CRAD.

o Buffet Pressure Measurements

Before a detailed discussion of the two methods to predict response is presented, the buffeting pressures will be described. Measurements of these pressures were made on a 12 percent scale wind tunnel model of the F/A-18 vertical tail and stabilator. Pressure data were taken on both sides of the stabilator and vertical tail models.

Figure 5 presents a plot of RMS buffet pressure as a function of dynamic pressure as measured on the wind tunnel model for a particular transducer pair and for a fixed angle of attack. The data show that the buffeting pressures are indeed a linear function of dynamic pressure if the other parameters can be fixed. They also indicate that the buffeting pressure can be presented in terms of a non-dimensional buffet pressure coefficient, C_p .

Typical results are given in Figure 6 for a single pressure transducer on the vertical tail for various angles of attack. The pressure transducer was located at the 60 percent span station and at the 45 percent chord station. Pressure data were taken on both sides of the panel and the difference between them was computed. Data are presented here for angles of attack of 24, 32, 36, and 52 degrees.

In each case shown, the buffet pressure has a very distinct peak which shifts to a lower frequency as angle of attack is increased. The RMS for each case is also shown. The overall RMS pressure has a peak value at approximately 32 degrees AOA for the F/A-18 vertical tail. Thus, both the RMS buffet pressure and spectrum shape are functions of angle of attack. In addition, the data presented here is for only one location on the tail. In order to use this pressure data for calculating dynamic response, pressures PSD's and cross PSD's from several other location are required. Such PSD's were measured and the trends are similar to those presented here.

Figure 7 shows how the buffet pressures change with dynamic pressure for 32 degrees AOA. This data is for the same pressure transducer pair for which data was presented in Figure 6 and from which it was shown that the maximum RMS buffet pressures occur at this angle of attack. It can be seen that both the RMS value of the buffet pressure and also the spectrum shape are functions of the dynamic pressure. The spectrum data shows that the peak pressure moves to a higher frequency as dynamic pressure is increased. Further, it was found that the RMS pressure is a linear function of dynamic pressure. Once again this data is for a particular location on the tail and for one angle of attack. Measurements must be taken at several locations on the tail and at other angles of attack in order to use this data in buffet response calculations.

These data were also used to develop scaling laws for the buffet pressure spectrum. An example of the application of these scaling laws is shown in Figure 8. In the top half of the figure two buffet pressure spectra are shown for different dynamic pressure conditions. In the bottom half of the figure both spectra have been non-dimensionalized and they collapse to almost identical curves. For the horizontal axis the non-dimensional parameter is the reduced frequency, fl/v . For the vertical axis, the non-dimensional parameter is the buffet pressure coefficient, C_p . This is important since it shows that buffet pressures measured in the wind tunnel can be scaled to predict those obtained in flight. The data that must be measured in the tunnel are buffeting pressures for the angle of attack range of interest and for enough positions on the tail to predict the dynamic response. The effect of velocity is to shift the peak in the pressure spectrum and this can be accounted for through scaling with the parameter fl/v .

The peak in the pressure spectrum can tune to different structural modes depending on angle of attack and velocity. This was observed in the wind tunnel test data and is illustrated in Figure 9. Both of these plots are for the same speed. However, the upper plot is for an angle of attack of 24 degrees and the lower plot is for an angle of attack of 52 degrees. Both show a bending moment response and a buffet pressure spectrum that is consistent with the test condition. From the upper plot in the figure, the peak in the buffet pressure spectrum corresponds to a frequency of approximately 42 Hz and is coincident with a structural resonance at that frequency. Consequently, a very strong structural response is shown at 42 Hz. As the angle of attack is increased, the peak in the buffet spectrum shifts to a lower frequency and at 52° angle of attack corresponds to a frequency of about 15 Hz. Thus, the mode at this frequency is excited and becomes the dominant response.

For the F/A-18, this modal tuning by the buffet PSD shape turned out to be very important. Observations from flight test showed that for the vertical tail buffet response, the amplitude in the first bending mode at approximately 15 Hz was almost independent of dynamic pressure. However, the response in the second bending mode at approximately 43 Hz increased at a rate that was greater than a linear function of dynamic pressure. This data is indicated in Figure 11. However, if the variation in the buffet pressure spectrum with air speed is accounted for, the solid lines shown in the figure can be predicted. This data further shows the value of the buffet pressure spectrum data.

o Flexible Tail Response Method

The flexible tail method requires a wind tunnel model tail surface that has been dynamically scaled to match the resonant frequencies and mode shapes of the actual tail surface. The scaling here is very similar to that used to design flutter model tails. Test conditions for the tunnel must be selected such that the scaled dynamic pressure simulates the dynamic pressure at the required flight condition. This requirement is based on the need to scale the spectral content of the buffet pressure data to the flight conditions that are being simulated. With appropriately calibrated strain gages, bending moments and torques can be measured directly and then scaled to match those that would be seen by the aircraft in flight. Figure 11 compares typical results obtained using this method with data obtained from flight. The plot shows the non-dimensional RMS buffet bending moment coefficient as a function of angle of attack for measurements taken from the wind tunnel model and from the aircraft. The model data have been scaled to match aircraft data using the relationship between aircraft and model root-mean-square moments:

$$\tilde{M}_A = \left\{ (l_A/l_m)^2 (m_A/m_m) (f_{na}/f_{nm})^2 \right\} \tilde{M}_m$$

The moments are non-dimensionalized to coefficient form by dividing by ql^3 .

The aircraft data is represented by the solid symbols and the predicted data, model scaled to aircraft, is represented by the open symbols. While there is scatter in both sets of data, the model data is indeed representative of that seen on the aircraft. In general, the comparisons show that the scaling laws are reasonably accurate in predicting RMS bending moment data observed in flight tests.

Figure 12 compares RMS acceleration as measured on the aircraft in flight with data obtained by using the scaling procedures. In this case the scaling relationship for converting model accelerations, to aircraft levels, is given as

$$\bar{a}_a = [(l_a/l_m) (f_{na}/f_{nm})^2] \bar{a}_m$$

Once again there is scatter in both sets of data but, as in the previous figure, the predicted data is representative of what is seen on the aircraft in flight.

Both of the previous figures addressed scaling of the RMS values of the bending moments and the accelerations. Attention is now turned to scaling of the spectrum levels of these two quantities. Shown in Figure 13 is a plot of bending moment PSD as measured on the F/A-18 stabilator in flight and as measured on the model and scaled to match aircraft data. In this case the stabilator has two resonances in the 40 to 50 Hz range.

The main mode excited is the second bending mode which has a resonant frequency at about 48 Hz on the aircraft and at about 45 Hz on the model. The amplitude of this response is predicted reasonably well. The lower resonance at approximately 43 Hz is the pitch/rotation mode. While this mode is excited on the aircraft, it is not excited as well on the model. Consequently, if this mode were required in the response calculation, the method would not do a good job. The reason the pitch/rotation mode is not excited as well on the model as on the aircraft is not understood at this time.

The first bending mode at 16 Hz is predicted closely, however. The RMS value of each PSD is also shown on the figure. The model data was scaled as described on the previous figure and falls within the scatter of the RMS data. The scaling to be applied to predict bending moment PSD spectrum levels can be written as

$$\bar{M}_a = [(l_a/l_m)^4 (m_a/m_m)^2 (f_{na}/f_{nm})^3] \bar{M}_m$$

Scaling of the frequencies may also be required and can be written as

$$f_a = (f_{na}/f_{nm}) f_m$$

In general the spectrum is predicted well enough for engineering purposes. The response in the critical mode is correctly predicted. The small error in the frequency of the peak response is due to the physical model's inadequately simulating the aircraft.

A PSD of acceleration as measured on the F/A-18 in flight and as determined from scaling from model data is shown in Figure 14. The vertical tail has two modes of interest as far as buffet response is concerned. These are the first bending mode at approximately 16 Hz and the second bending mode at approximately 45 Hz. As can be seen from the figure, the second bending mode is predicted reasonably well by scaling the data from the model to the aircraft. The first bending mode, however, leaves something to be desired. The response peak from the flight data appears to be abruptly cut off, as though some of the data were lost. However, from a response standpoint, the peak level in the dominant mode is correctly predicted. The scaling for the acceleration at a spectrum level is given as

$$\bar{a}_a = [(l_a/l_m)^2 (f_a/f_m)^3] \bar{a}_m$$

The frequency may also have to be scaled depending on how the model was constructed. The frequency scaling parameter is that defined during the discussion of Figure 14.

In summary the flexible tail method requires a dynamically scaled model that is constructed in much the same way as a flutter model tail. The tail is instrumented with strain gages that are calibrated to read bending moments and torques directly. The velocity at which the tail is tested must be selected by scale factors to match the corresponding buffet conditions in flight. If these conditions can be satisfied, then the method has the advantage that it gives a direct reading of the buffet loads. It has the disadvantage of requiring a more complicated flutter model type tail that may not be available early in an aircraft design program. Structural changes in this actual design might require a new model to be run.

o Rigid Pressure Response Method

The Rigid Pressure method utilizes the unsteady pressures measured from the rigid model during wind tunnel tests. In this method only data from a rigid aircraft model is required to predict aircraft dynamic response. This method also has the advantage of its use early in the design stages of an aircraft when only a rigid aerodynamic performance model is available. Rigid pressures obtained from this model can be used to obtain initial estimates of the buffet response loads using the Rigid Pressure calculation scheme. The Rigid Model buffet design concept is shown in Figure 15. The rigid wind tunnel pressures, in the form of pressure PSDs, are scaled to full aircraft levels using the pressure scaling equation:

$$P_a = (l_a/l_m) (\rho_a/\rho_m)^2 (V_a/V_m)^3 P_m$$

at the corresponding frequencies:

$$f_a = [(V_a/V_m)/(l_a/l_m)] f_m$$

These scaled-up pressures are then applied to a well correlated finite element model of the empennage surface in order to calculate aircraft dynamic response. Well correlated here means a model that accurately predicts ground vibration test (GVT) data.

Since we are concerned with a primary lifting surface undergoing general bending and torsion motions during buffet excitation, the oscillatory aerodynamics must be included in the problem. The oscillatory aerodynamics cannot be readily obtained from the rigid measurements made in the wind tunnel; hence, an unsteady aerodynamic code which can accurately compute aerodynamic damping and stiffness is required.

We can now state the mathematical equation to be solved as:

$$M\ddot{x} + C\dot{x} + Kx = \rho A \ddot{x} + 1/2 \rho V B \dot{x} + (1/2) \rho V^2 D x + F(t)$$

Where M, C, K represent structural mass, stiffness and damping. The A, B, and D are equivalent aerodynamic terms. F(t) is a general forcing function.

Since buffet is random, we use Power Spectral Density, PSD, type relations where response of a coordinate is commonly expressed as:

$$PSD_x = T^2 PSD_F$$

The transfer function, T, is defined as:

$$T = \frac{1}{(\omega^2 M + i\omega C + K) + (\omega^2 \rho A - i(1/2)\rho V B - (1/2)\rho V^2 D)}$$

T^2 is the square of the transfer modulus obtained by multiplying T by its complex conjugate, T^* . So

$$T^2 = T \cdot T^*$$

We can also find the root mean square, rms, values of the coordinate x by the relation:

$$X_{rms} = [\int PSD_x d\omega]^{1/2} = [\int T^2 PSD_F d\omega]^{1/2}$$

Though not shown here are cross spectral densities, CSDs, which can also be included in the analysis. They result from the pressure field influence from point-to-point on the upper surface and on the lower surface. These effects were considered in our approach, and the CSDs that were available were included in the calculation. They showed little effect. Also, due to the lack of complete CSD data in many cases, they were omitted.

NASTRAN was used as the analytical tool for the Rigid Pressure calculation technique as shown in Figure 16. NASTRAN was chosen because of its versatility and its widespread acceptance by many analysts. A vibration model is first established, which is well correlated with results from ground vibration tests. The measured rigid pressure PSDs are then scaled-up to aircraft levels using the scaling equations discussed previously. These pressure PSDs are converted to force PSDs, $\rho A P$, before being submitted to the NASTRAN data file. Cross Power Spectra of force are likewise computed for the measured data and submitted to the NASTRAN data file. The unsteady aerodynamics used for buffet response calculations was initially strip-theory aerodynamics which was calculated externally by a separate FORTRAN program. The program calculates the aerodynamic damping and stiffness matrices which are then added to their structural counterparts via the built-in matrix procedure in NASTRAN, the Direct Matrix Abstraction Program (DMAP). In our effort to improve the Rigid Pressure method we have reached a point where all calculations are done completely within NASTRAN. This has several advantages over the initial method. The transfer function relating response to the buffet pressures now includes the unsteady aerodynamics computed in NASTRAN. Also, a very important advantage is that the Doublet-Lattice aerodynamic theory can be used with very little effort in input as opposed to our modified strip theory used before. The NASTRAN method matches the V-w condition accurately in this transfer function. Our strip method used measured lift curve slopes, $C_{L\alpha}$ which is quite descriptive of the actual flow.

For evaluation of the Rigid Pressure method, we chose the F/A-18 Horizontal and Vertical tails. We used the fully correlated NASTRAN models used by the F/A-18 project for flutter studies. These models are essentially "beam-rod" models i.e. the models consist of beam elements which represent the elastic axis with the correct bending and torsion distributions. The mass, center of gravity, and moment of inertias are also accurately represented in the models.

Using the full scale F/A-18 horizontal stabilator "beam-rod" model with scaled-up wind tunnel pressures, buffet analyses were performed for angles of attack from 16° to 20°. Inboard and outboard root mean square (rms) moments, and tip acceleration were calculated for a frequency range of 0 Hz to 120 Hz. This frequency range captures the first five modes of the stabilator. Buffet response was computed using the externally calculated strip theory aerodynamics and the Doublet-Lattice theory. The responses computed using both theories were compared to each other, to scaled-up responses from wind tunnel tests, and to available flight test data. This type of comparison is shown by means of PSDs in Figure 17 for an angle of attack of 20°. As can be seen fairly good correlation is obtained between the calculated responses and the measured responses. The Doublet-Lattice aerodynamics also gives better results than the strip theory aerodynamics. Model response data was obtained from the wind tunnel tests by means of measurements taken on a flexible tail. The F/A-18, being twin-tailed, allows us to equip the model with a rigid tail for obtaining pressures, and a flexible tail for obtaining response data, such as, moments and accelerations. All wind tunnel data obtained was from an F/A-18 12% model. The wind tunnel moment PSD data is scaled-up to aircraft level using the scaling equation:

$$M_a = [(l_a/l_m)^4 (m_a/m_m)^2 (f_{na}/f_{nm})^3] M_m$$

and

$$f_a = (f_{na}/f_{nm}) f_m$$

The model root mean square (rms) values are scaled to aircraft values using the scaling equation:

$$\tilde{M}_a = [(l_a/l_m)^2 (m_a/m_m) (f_{na}/f_{nm})^2] \tilde{M}_m$$

These moments can be non-dimensionalized to coefficient form by dividing by ql^3 . This is shown in Figure 18 for inboard and outboard moments comparing again calculated response (doublet-lattice and strip theory), model scaled-up using the above equations, and available flight test data. While there is scatter in the data, the calculated values, especially the doublet-lattice values, show fairly good agreement with the scaled-up model values and the flight test values.

Buffet analysis was also performed for the F/A-18 vertical tail using the NASTRAN "beam-rod" model. Analysis was done only with doublet-lattice aerodynamics. Moment PSDs are shown in Figure 19 for calculated versus model moments scaled-up to aircraft level for an angle of attack of 32° . Again, fairly good agreement is obtained. The rms moment coefficients are shown in Figure 20 for an angle of attack range of 18° to 52° for calculated responses, model scaled up, and available flight test responses. Again there is some scatter among the data, but fairly good agreement of the calculated and measured values is achieved.

In summary, the Rigid Pressure method only requires pressures obtained from rigid wind tunnel models in order for one to compute dynamic response. It can be used very early in the design cycle when a flexible model may not be available. It can also be used during inservice operations when design changes are made where the finite element model could be adjusted to accommodate the design change, and buffet response can be re-calculated. This application of the Rigid Pressure method has been quite useful on the F/A-18 and F-15 projects. Recent work on the F/A-18 has used a detailed finite element model whereby local skin and spar dynamic stresses and strains were computed due to buffet loading. This type of application has already been used on the F-15 project for the vertical tail with considerable success. The F-15 project is now using the method in analyzing buffet response in the outer wing panel. The rigid pressure method was used to help assess constrained layer damping applications to reduce buffet response in Reference 15.

CONCLUSION

A unified approach to prediction of buffet response of fighter aircraft empennage is shown. One method uses flexible wind tunnel model data scaled to full size prediction. It is bolstered by another more analytical method called the rigid pressure method. The latter employs scaled wind tunnel pressures in calculations of full size prediction. While the scaled flexible model method is probably slightly more accurate, the rigid pressure method is probably more general. It can be employed as soon as tunnel models are available for general aerodynamics, and permits rapid assessment of structural changes, damping treatment, etc. The accuracy is as good as tunnel-to-tunnel variations and within repeatability of test point-to-point within a given test. This latter method has found considerable application at McDonnell in the past three years. More work is needed to handle transient behavior, nonlinearity and more accurate representations of torsional mode aerodynamic damping.

ACKNOWLEDGEMENTS

This paper represents many years of research including McDonnell IRAD and government sponsored CRAD. Many people contributed to the work shown here; the authors, thus express sincere thanks to Rudy Yurkovich, Clarence Perisho (retired), Chris Smith, Jim Hess, and Milt Hieken of McDonnell Aircraft Co., and Tom Hess of NADC.

REFERENCES

1. "The Accident Investigation Sub-committee on the Accident to the Aeroplane G-AAZK at Meopham, Kent, England on 21 July 1930," British R & M 1360, January 1931.
2. White, J. A. and Hood, M. J., "Wing - Fuselage Interference, Tail Buffeting and Flow About the Tail of a Low Wing Monoplane," NACA Report 482, 1933.
3. Hood, M. J. and White, J. A., "Full Scale Wind Tunnel Research on Tail Buffeting and Wing-Fuselage Interference of a Low Wing Monoplane," NACA TN-460, 1933.
4. Abdrashitov, G., "Tail Buffeting," NACA TM-1041, February 1943 (Translated from Russian, Report 395 from the Central Aero-Hydromechanical Institute, Moscow, 1939).
5. Mullans, R. E. and Lemley, C. E., "Buffet Dynamic Loads During Transonic Maneuvers," AFFDL-TR-72-46, September 1972.
6. Coe, F. C. and Cunningham, A. M., "Predictions of F-111 TACT Aircraft Buffet Response and Correlations of Fluctuating Pressure Measurements on Aluminum and Steel Models and the Aircraft," NASA CR 4069, May 1987.
7. Lee, B. H. K., "Aeroelastic Response of an Aircraft Wing to Random Loads," National Aeronautical Report (Canada), LR 613, NCR 21230, April 1983.
8. Lee, B. K. K. and Ohman, L. H., "Unsteady Pressure and Force Measurements Associated with Transonic Buffeting of a Supercritical Airfoil," Aeronautical Note (Canada), NAE-AN-18, NCR 22448, June 1983.
9. Roos, H. N. and Waymon, G. F., "Testing for Severe Aerodynamically Induced Vibration Environments," Fifty-Third Shock and Vibration Symposium, October 1982.
10. Triplett, W. E., "Pressure Measurements on Twin Vertical Tails in Buffeting Flows," AFWAL Report AFFDL-TR-82-3015, April 1981.
11. Lan, C. E. and Lee, I. G., "Investigation of Empennage Buffeting," NASA Contractor Report 179476, January 1987.
12. Zimmerman, N. H., Ferman, M. A., Yurkovich, R. N., and Gerstenkorn, G., "Prediction of Tail Buffet Loads for Design Applications", 30th SDM, Mobile, AL., 3-5 Apr 89
13. Zimmerman, N. H. and Ferman, M. A., "Prediction of Tail Buffet Loads for Design Application," Report No. NADC-880434-60, July 1987.
14. Schweiker, J. W. and Davis, R. E. "Response of Complex Shell Structures to Buffeting Flows," Journal of Spacecraft and Rockets, Vol. 3, No. 11, Nov. 1966
15. Yurkovich, R. N., "Application of Constrained Layer Damping to the F/A-18 Horizontal Tail", Damping 1989 Conference, 8-10 Feb 1989, West Palm Beach, FL.



Figure 1. F/A-18 Aircraft at High Angle-of-Attack Showing Vortex From the Leading Edge Extension and Wing Tips

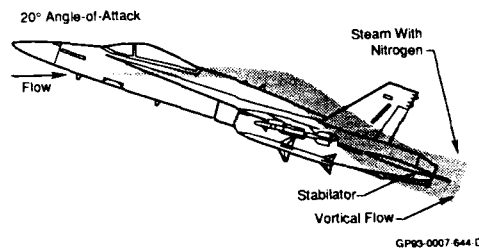


Figure 2. 12% Wind Tunnel Model of F/A-18 Showing Vortical Flow From Leading Edge Extension

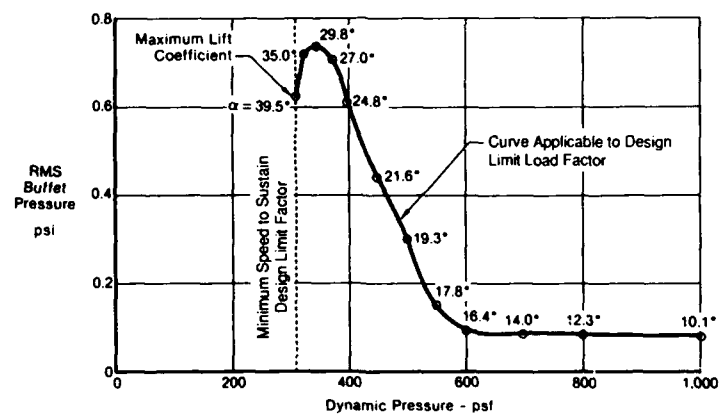


Figure 3. Representative Variation of Buffet Pressure With Dynamic Pressure at Design Limit Load Factor

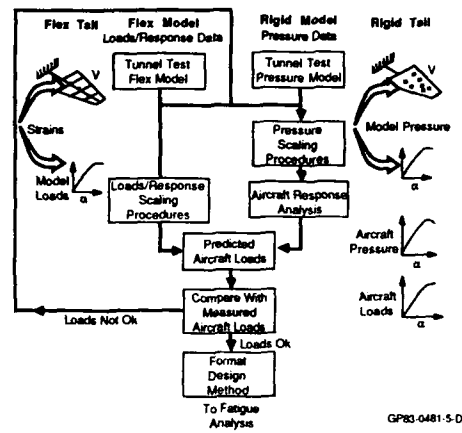
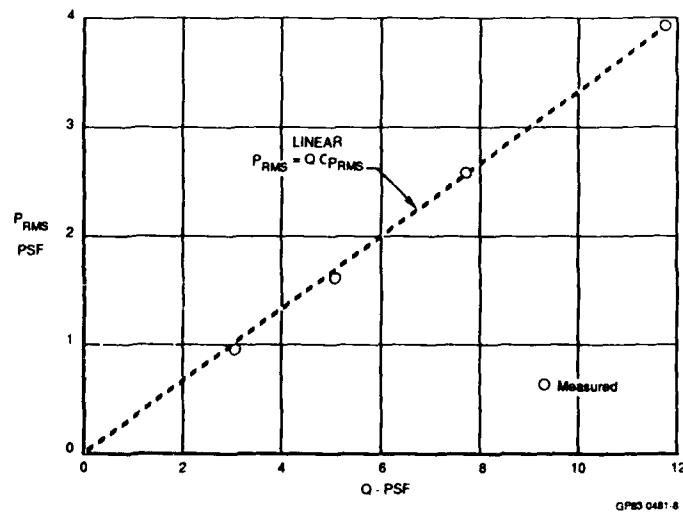


Figure 4. Buffet Load Prediction Methods

Figure 5. Validation Check of RMS Buffet Pressure Scaling
F/A-18 Vertical Tail 12% Wind Tunnel Model

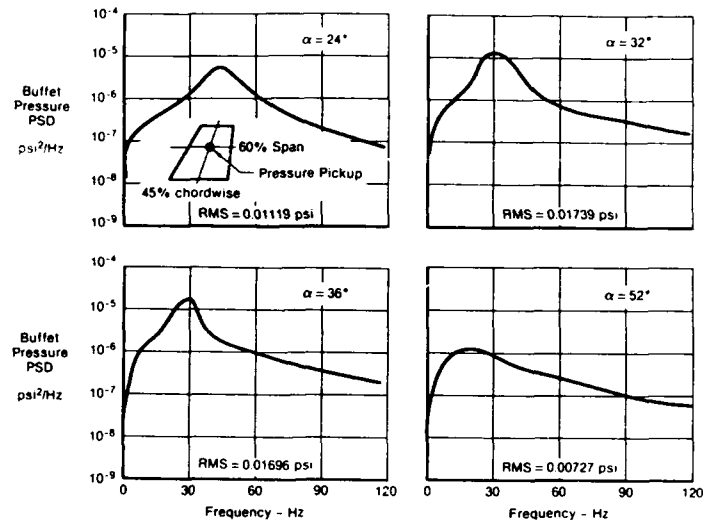


Figure 6. Validation of Pressure Characteristics
With Angle-of-Attack
F/A-18 Vertical Tail 12% Wind Tunnel Model ($Q = 7.5$ PSF)

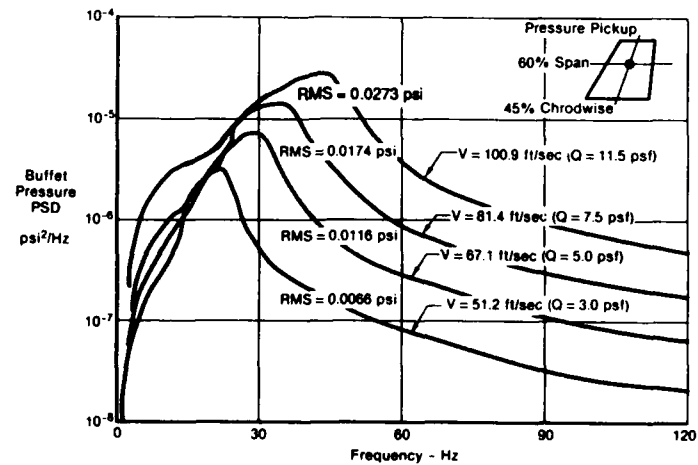
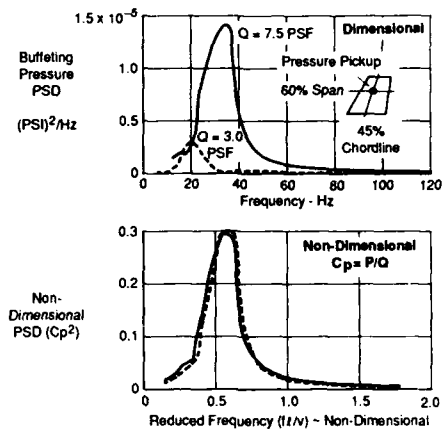
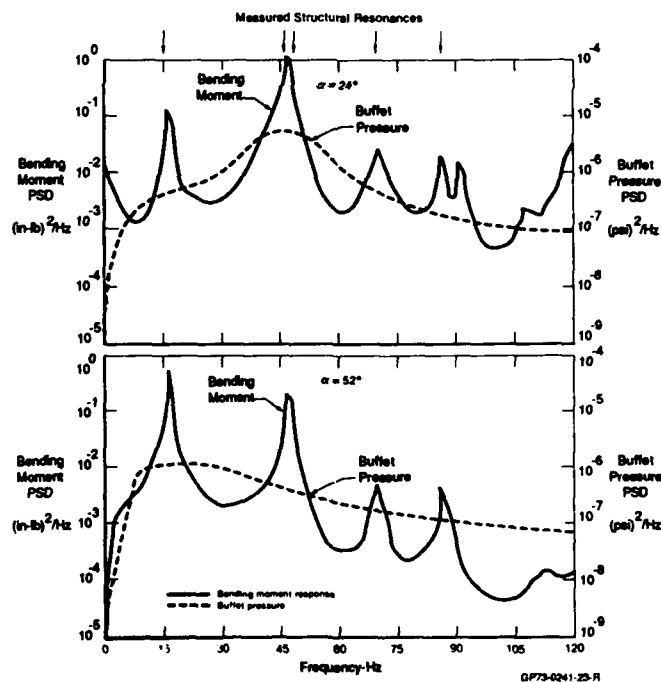


Figure 7. Validation of Buffet Pressure Scaling
Characteristics With Airspeed
F/A-18 Vertical Tail 12% Wind Tunnel Model $Q = 7.5$ PSF



GP3-0007-301

Figure 8. Validation Check of Buffet Pressure PSD Scaling
F-18 Vertical Tail 12% Wind Tunnel Model



Q73-0241-25-R

Figure 9. Explanation of Buffet Response Variation
With Angle-of-Attack
FA-18 Vertical Tail Bending Moment 12% Wind Tunnel Model
 $V = 81.5 \text{ Ft/Sec}$ ($Q = 7.5 \text{ PSF}$)

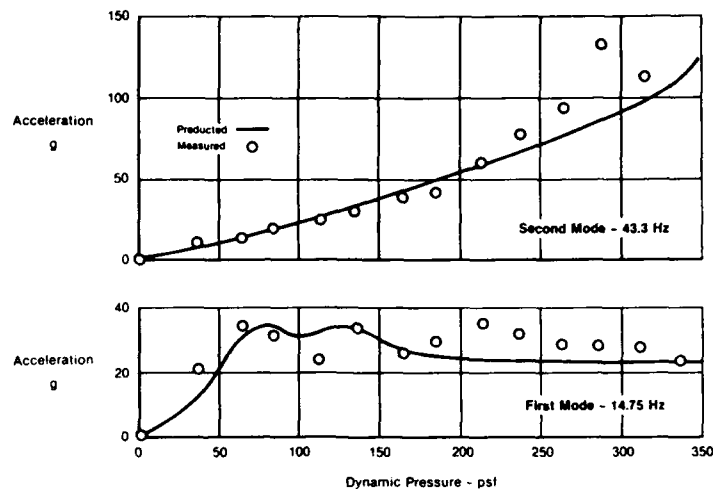


Figure 10. Comparison of Prediction Modal Trends
With Flight Measurements for F/A-18 Vertical Tail
 $\alpha = 32^\circ$ Altitude = 15,000 ft

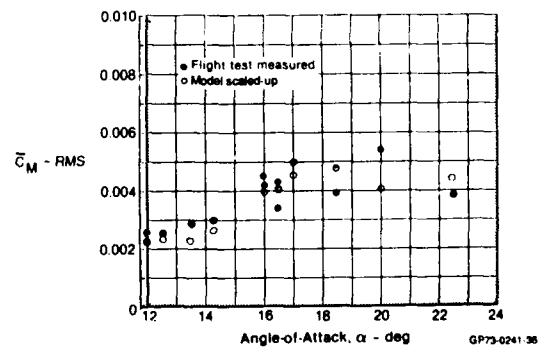


Figure 11. Buffet Correlation Study for F/A-18 Stabilator
Outboard Bending Moment

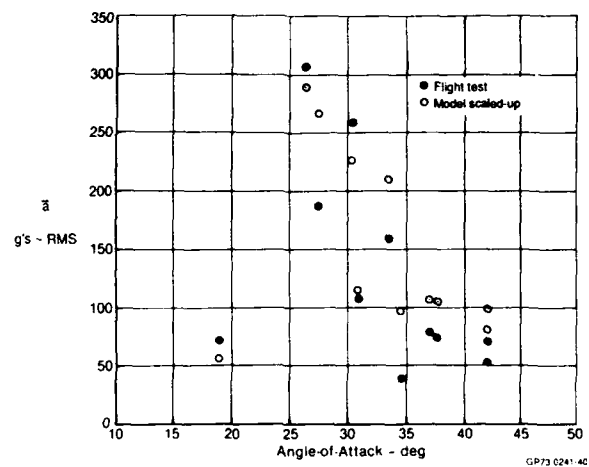


Figure 12. Buffet Correlation Study F/A-18 Vertical Tail
Air Tip Acceleration

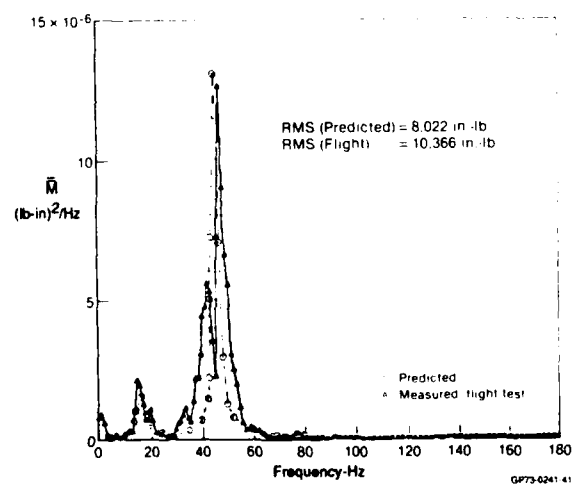


Figure 13. Comparison of Predicted vs Measured PSD
for F/A-18 Stabilator Bending Moment Outboard
 $\alpha = 20^\circ$ $Q = 450$ psi Altitude = 9,700 ft

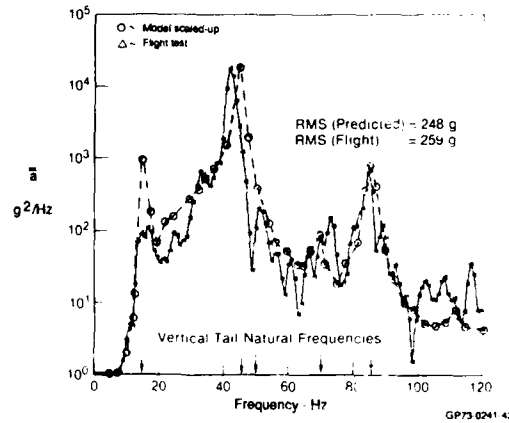


Figure 14. Comparison Between Predicted and Measured Aft Tip Acceleration PSD

$\alpha = 35.0^\circ$ $Q = 356$ psf Altitude = 15,500 ft

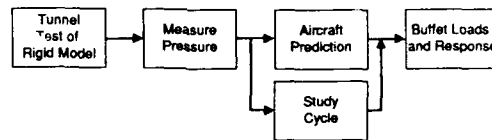


Figure 15. Rigid Pressure Design Cycle

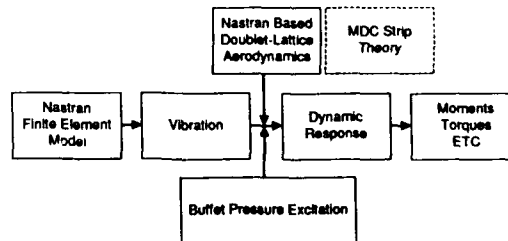


Figure 16. Nastran Based Buffet Response Calculation Technique

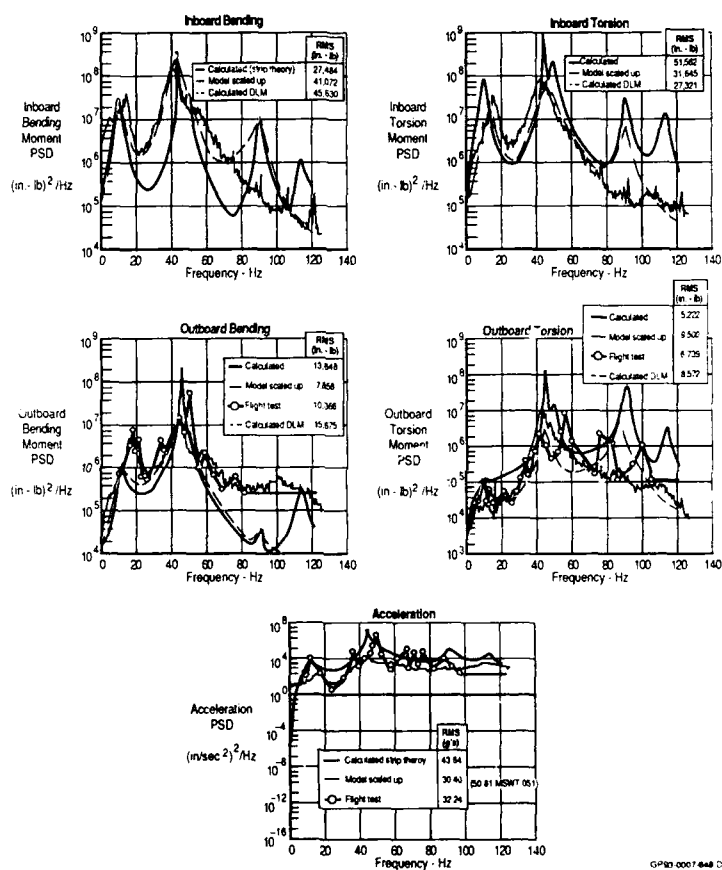


Figure 17. Comparison of Measured Flight Test vs Predicted Buffet Response
Rigid Model Pressure Method, F/A-18 Stabilator, A.O.A. = 20°

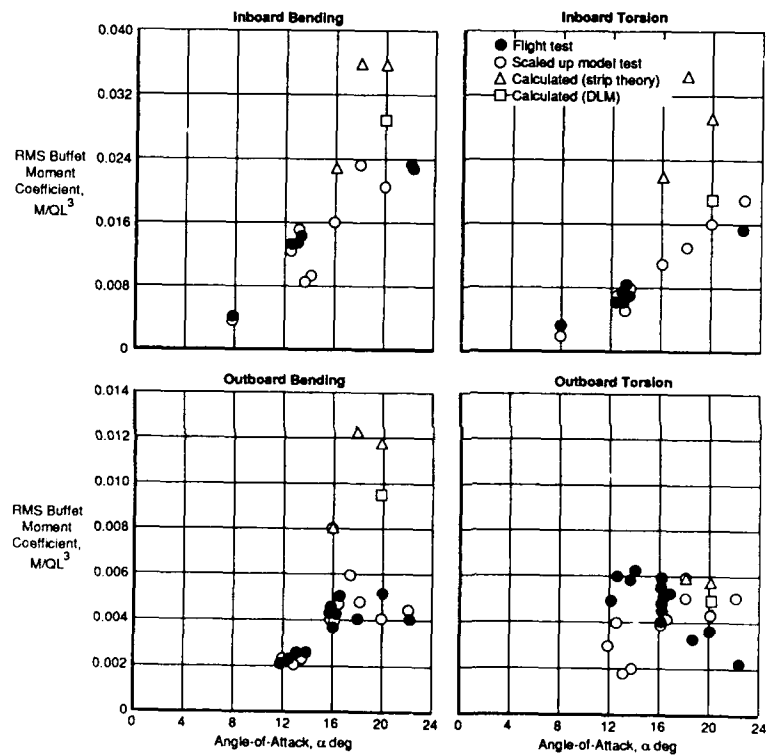


Figure 18. F/A-18 Stabilator Buffet Correlation Study

GP93-0007 649-D

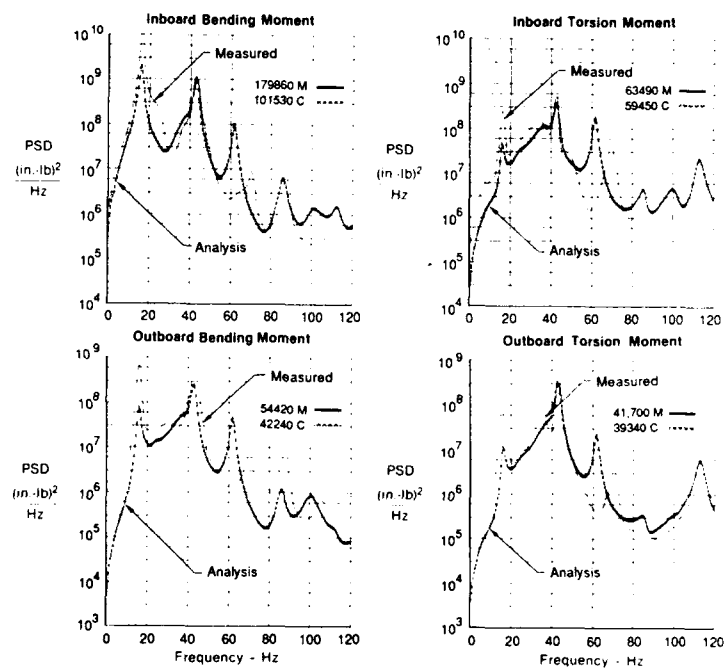


Figure 19. F/A-18 Vertical Tail Buffet Response (PSDs)
Scaled Model Data vs Predicted Data
AOA = 32°

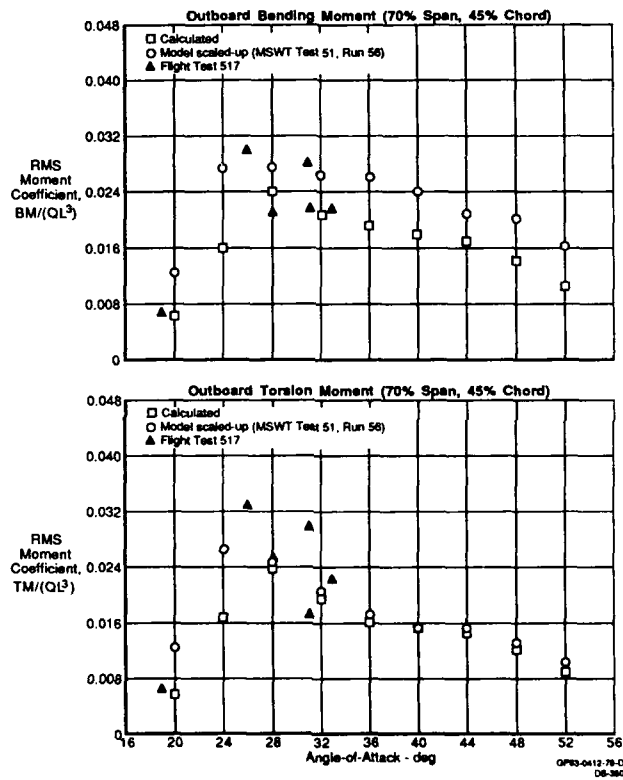


Figure 20. F-18 Vertical Tail Buffet Response Moment Coefficients For Angle-of-Attack Variations

EFFECTS OF TRAILING-EDGE FLAP
ON BUFFET CHARACTERISTICS OF A SUPERCRITICAL AIRFOIL

by
B.H.K. Lee
National Aeronautical Establishment
National Research Council
Ottawa, Ontario, Canada, K1A 0R6

SUMMARY

The buffet characteristics of a 16% thickness-to-chord ratio supercritical airfoil were investigated in the High Reynolds Number Two-Dimensional Test Facility of the National Aeronautical Establishment. The trailing-edge flap dimension was 13.5% chord and it was deflected at various angles to study the effect of modifying the downstream pressure on controlling flow separation over the airfoil. The unsteady normal force was measured and the buffet boundary was determined from the divergence of the fluctuating normal force. The investigation was conducted quite deep into the buffet regime. Spectral analyses of the normal force were carried out and the frequencies of shock wave oscillations were measured. They were found to be Mach number dependent and varied between 50-80 Hz for $M = 0.612$ to 0.792 . The effects of varying the flap angles on the shock wave position and drag of the airfoil were also investigated. Results for an off-design Mach number of 0.612 were given in some details.

LIST OF SYMBOLS

b	model span
C_D	drag coefficient from wake integration
C_D'	function when integrated over the width of the wake gives total drag
C_L	lift coefficient from balance measurements
C_{Lmax}	maximum lift coefficient
$C_{L\alpha}$	lift-curve slope
C_N	fluctuating normal-force coefficient from balance measurements
C_N'	rms value of normal-force coefficient
C_p	pressure coefficient
C_{pTE}	trailing-edge pressure coefficient
c	chord length
M	Mach number
M_D	drag rise Mach number
M_{DES}	design Mach number
q_∞	free stream dynamic pressure
t_w	maximum thickness of airfoil
w	thickness of wake
x	distance measured from airfoil leading-edge
x_s	shock wave position
y	distance traversed by wake probe, perpendicular to flow direction
α	angle of incidence
δ	flap angle

1. INTRODUCTION

In performing maneuvers inside the subsonic and transonic flight envelope, fighter aircraft often fly in the buffet regime for a significant amount of time. The buffet loads due to flow separation on the wing may cause serious fatigue problems and have an important impact on the structural integrity of the aircraft. In addition, maneuverability, performance and handling qualities are often degraded. Delay of separation or increasing the airplane buffet onset normal force coefficient to as large a value as possible is highly desirable.

Some early flight tests showed buffet could be alleviated or reduced through deflections of leading- and trailing-edge flaps. The results reported by Monaghan and Friend (Ref.1) were for the F-8C aircraft having wing section

designed for subsonic flows while the F-104 test aircraft used in Friend and Sefic's (Ref.2) investigation has supersonic airfoil design. In both cases, the wing was fairly thin. The effectiveness of using leading- and trailing-edge flaps for buffet alleviation were quite different in the two aircraft configurations. The results showed that for the F-8C, leading-edge flaps were more effective while for the F-104 the use of trailing-edge flaps gave better improvements in raising the buffet boundaries.

Aside from the two earlier studies with airfoils of conventional design, it appears that little or no research has been carried out on the use of flaps to control buffet of supercritical airfoils. To gain better insight into the effects of flaps on buffet intensities and delay of buffet onset at transonic conditions, flight tests or wind tunnel investigations of supercritical airfoils with flaps are required. An understanding of the manner in which a flap can modify flow separation over the airfoil is useful in assessing the effectiveness or feasibility of deploying a flap as a passive means of buffet control.

An investigation on the effects of a trailing-edge flap on buffet characteristics of a 16% thick supercritical airfoil was carried out in the NAE High Reynolds Number Two-Dimensional Test Facility. The airfoil was used in a previous joint NAE-Boeing Canada (de Havilland Division) research and development program in the study of airfoil design for drag reduction (Ref.3). The design conditions for this airfoil were for a cruise Mach number of 0.72 and lift coefficient of 0.6. The original airfoil was modified by replacing the rear section with a trailing-edge flap of dimension approximately 13.5% chord. The installation of a leading-edge flap was considered to be much more complex and would alter the airfoil design characteristics. To control separation the simplest way is to change the downstream pressure by use of a trailing-edge flap.

In an earlier paper (Ref.4) some results from this investigation were described. Buffet onset boundaries with different flap deflection angles were given. Most of the results on the characteristics of the buffet flow were presented at the design Mach number. In this paper some further results are described and behaviour of the flow at an off-design Mach number of 0.612 is discussed in some detail.

2. MODEL, INSTRUMENTATION AND DATA PROCESSING

The airfoil was made of aluminium having a chord of 12 in. and a span of 15 in. The thickness-to-chord ratio was 16%. The flap dimension was approximately 13.5% chord, and the trailing-edge thickness was 0.1% chord. There were 79 pressure orifices on the model surface for static pressure measurements: 43 of them were located on the airfoil upper surface and 23 on the lower surface. On the flap, there were 13 pressure orifices with 6 on either side and one at the trailing edge. Their locations on the airfoil are shown in Figure 1. The drag of the airfoil was obtained using a traversing wake rake with pitot probes at four spanwise locations which were approximately 18 in. downstream of the airfoil trailing edge. In this experiment, only the two centrally located probes were used and their average was taken for drag measurements.

The lift and pitching moment were determined from a side-wall balance. In addition to the steady-state values of the balance outputs, the fluctuating quantities were also measured. The rms value of the normal force is presented in nondimensional form given by

$$C_N' = N_{rms} / q_{\infty} bc \quad (1)$$

Spectral analyses of the balance outputs were also performed. The signal was sampled at 1.6 kHz and analysed digitally on a computer using the IEEE routine PMPSE (Ref.5) to give power spectra and autocorrelation functions. A fast Fourier transform (FFT) block size of 256 and a signal duration of 2s were chosen in all the analyses. A few longer duration runs of 10s were performed and an FFT block size of 1024 was used.

As reported in Ref.4, wind-off tests on the response of the force balance to impulse excitation were carried out and four natural frequencies were detected at about 140, 215, 320 and 360 Hz. These were much larger than the peak excitation frequencies observed under buffet conditions which varied from approximately 50 Hz at $M=0.612$ to 80 Hz at $M=0.792$.

Distributed suction was applied through porous plates to regions of the tunnel side walls in the vicinity of the model. The amount of suction was selected so as to minimize any three-dimensional effects.

All the tests were performed at a chord Reynolds number of approximately 20 million with free transition. At design conditions, flow visualization using a thin film of oil containing a dye which fluoresced in ultra-violet light showed transition to occur on the upper surface at less than 5 percent chord from the leading edge. The Mach numbers in this investigation varied between 0.612 to 0.792 and the flap angle settings were $\delta = 0^\circ, 4^\circ, 8^\circ, 14^\circ, -4^\circ$ and -8° . The standard convention of positive flap deflection in the downward position and negative in the upward position was adopted. The maximum value of the angle of incidence was 10° .

3. RESULTS AND DISCUSSIONS

3.1 Lift and Normal Force Fluctuations from Balance Measurements

For this supercritical airfoil it is noted from the C_L versus α curves that up to moderate angles of attack and M greater than the drag rise value M_D (determined from the criterion $dC_D/dM = 0.1$) at design conditions, C_L does not usually reach a maximum. However, below M_D a value of C_{Lmax} is detected. The C_L versus α curves at M_{DES} are shown in Figure 2 for different δ . A C_{Lmax} is detected in all cases and the effect of the flap is to shift the curves either upwards to the left or downwards to the right depending on the sign of the flap angles. The value of α where C_{Lmax} occurs decreases as δ changes from negative to positive values. It varies from approximately 4.8° at $\delta = -8^\circ$ to 2.4° at $\delta = 14^\circ$. The increase in lift for positive flap angles is quite significant. This is also true for Mach numbers below and above its design value as discussed in Reference 6. At higher M , a C_{Lmax} is usually not detected and the C_L versus α curves are similar to those shown in Figure 3 for $M = 0.772$.

The effects of changing flap angles on the fluctuating normal force were also given in Reference 6 where results of C_N' variations with C_L for different M were shown. When C_N' is plotted against α , it is found that for M less than $M_D = 0.75$, C_N' reaches a maximum and then decreases with further increase in α . For larger M , the curves of C_N' increase monotonically with α with much smaller magnitudes.

To show the behaviour of C_N' with M for different flap angles, results are given in Figure 4 at $\alpha = 4^\circ$. Similar curves can be obtained for different α . For a given δ , C_N' increases with M and reaches a maximum. Its magnitude increases with positive δ and decreases with negative δ . Also, changing δ from negative to positive angles results in a smaller value of M where the maximum of C_N' occurs.

3.2 Buffet Boundaries

In Figure 5 C_N' is plotted versus C_L with $\delta = 0^\circ$. For supercritical airfoils, the curve for $M = 0.712$ is typical of the behaviour of C_N' with C_L when a C_{Lmax} in the lift versus α curve is present. At higher M when a C_{Lmax} is not observed, C_N' varies with C_L in a manner shown by the curve for $M=0.772$. To determine the C_L at buffet onset, the procedure used is to obtain a smooth C_N' versus C_L curve either by the use of a spline or fitting manually. C_L at buffet is then determined by noting the point on the curve with a slope of $dC_N'/dC_L = 0.1$. This value is arbitrarily chosen. When buffet onset is primarily due to trailing-edge separation, the results are found to be consistent with those derived using the trailing-edge pressure divergence criterion. Figure 6 shows the variations of C_N' and C_{pTE} with α for $M = 0.722$ and $\delta = 0^\circ$. The values of α

at buffet onset determined from trailing-edge pressure divergence and the present method are indicated. The slope $dC_N'/d\alpha$ is related to dC_N'/dC_L by the following expression

$$dC_N'/d\alpha = 0.1 C_{L\alpha} \quad (2)$$

where $C_{L\alpha}$ is obtained from steady lift vs α curves. Experience at NAE in testing supercritical airfoils shows that it is more convenient to use the fluctuating normal force from a balance to determine buffet onset. Installation of a pressure orifice close to or at the trailing edge to measure pressure divergence is cumbersome and often not feasible for airfoils with thin trailing edge. Also, it is often necessary to obtain trailing-edge pressure data over a wide range of incidence below buffet onset in order to define a baseline to locate α when trailing-edge pressure divergence occurs.

For conventional airfoils, it is often possible to designate in the C_L versus M plot regions of mild, moderate or heavy buffeting. For supercritical airfoils such as the one investigated in this paper, buffet onset occurs so close to C_{Lmax} for M near or less than M_{DES} that it is not too meaningful to assign a degree of severity, except when M is greater than some value, for example, M_D for this particular airfoil. Figure 7 shows the buffet onset boundary at different values of δ together with curves for two buffet intensities expressed in terms of constant C_N' . At $\delta = 0^\circ$ the curves lie below the buffet onset boundary at Mach numbers less than 0.72 and 0.75 for $C_N' = 0.05$ and 0.1 respectively. This is due to the behaviour of the C_N' variations with C_L , where for $M < 0.75$ a decrease in C_L is detected when C_N' increases above its value at buffet onset. For higher Mach numbers the curves lie above the buffet onset boundary since C_N' increases with C_L monotonically. Also shown in Figure 7 are the values of C_{Lmax} for those values of M where a maximum in C_L can be detected. For positive δ the curves for $C_N' = 0.05$ and 0.1 cross the buffet boundary at M near 0.72, while for negative δ the value of M is close to 0.75.

It is seen that the buffet boundary curves can be raised appreciably and there are large increments in lift with positive changes in δ . C_L at buffet onset decreases rapidly for $M > M_{DES}$. At $M = 0.75$, which corresponds to the drag rise Mach number M_D at design C_L , this airfoil shows small gains in the buffet boundary by the use of flaps. Further increase in Mach number again shows an increase in the lift before encountering buffet. The drag rise curves are also included in these figures and they are described in section 3.6.

3.3 Power Spectra of Balance Normal Force

Figures 8 and 9 show the effect of varying α on the normal force power spectra at $\delta = 0^\circ$ and $M = 0.672$ and 0.752 respectively. On the upper right hand corner of the figures, the buffet boundary is plotted for reference (instead of C_L , α is sometimes plotted vs M for the buffet boundary). The peaks in these figures at approximately 140, 215, 320 and 360 Hz correspond to the natural frequencies of the force balance (Ref.4). The disturbance at 420 Hz is from the wind tunnel (Ref.7). The peaks having frequencies of 55 Hz at $M = 0.672$ and 75 Hz at $M = 0.752$ represent shock wave oscillations on the upper surface of the airfoil. They have been identified in a related study (Ref.8) on the periodic shock motion as due to shock-boundary layer interaction. In that investigation a model of the self-sustained shock oscillations for the Bauer-Garabedian-Korn (BGK) No.1 supercritical airfoil was proposed. The propagation velocity of the pressure disturbance due to the shock motion was measured experimentally. Using this velocity, the oscillating shock frequencies were calculated and they were found to be in good agreement with the measured values. The shock oscillation frequencies for the present airfoil derived from normal force spectra are 50-80 Hz for M between 0.612 and 0.792. At $M = 0.672$ and $\alpha = 9^\circ$, it can be seen from the normal force spectra shown in Figure 8 that discrete frequency shock wave oscillations are not present. A slight decrease in the shock strength is noticeable in Figure 9 at $M = 0.752$ and $\alpha = 5.546^\circ$.

Beyond the buffet onset boundary, the shock wave strengthens as α is increased. For a given M , there is an α above which the shock starts to weaken.

A maximum value of α can be found where periodic shock motion is not detected. The flow conditions when shock oscillations occur are shown in Figure 10 for $\delta = -4^\circ$. The variations of C_N' with α for this δ are given in Figure 11 for three Mach numbers and they show that the value of α where C_N' is a maximum decreases with increasing M. The locations inside the shock oscillation region when C_N' reaches a maximum are shown in Figure 10. Results for other values of δ show similar behaviour.

3.4 Shock Wave Positions

When the shock wave is oscillating its locations determined from C_p plots falls within the range of positions that occur during one pressure scan cycle of approximately 2.5s. At severe buffet conditions locating the shock position is difficult. The manner in which shock position is measured in Reference 9 is followed in this study and there is certain degree of arbitrariness in this definition for large oscillating shock motion. However, the results using Reference 9 definition of the shock position are consistent and measurements are relatively easy to carry out.

The effects of δ on shock position x_s/c are shown in Figure 12 for three values of M. Except for the highest M tested at 0.792 which shows x_s/c to decrease with α , it is seen from the results for the other two M values that x_s/c increases with α initially and reaches a maximum before decreases slowly. Except for large M, the effect of a trailing-edge flap is to move the shock position further downstream for positive δ and upstream for negative δ by varying the pressure behind the shock wave. The shock position is difficult to measure for high M. Only data for three values of δ at M = 0.792 are shown. The results for other δ indicate the shock position is quite similar for all positive δ while for negative δ the shock occurs further downstream in contrast to an upstream movement for the lower M cases.

The variations of x_s/c with M is illustrated in Figure 13 for $\alpha = 3^\circ$. The curves show the shock position to move downstream with increasing M until a maximum x_s/c is reached. From then onwards it moves gradually upstream. Similar trends are observed when the shock locations at buffet onset are plotted against M for various flap angles as shown in Figure 14. At higher M (eg 0.792) the measurements of the shock location become difficult and are not very accurate.

3.5 Trailing-Edge Pressure Measurements

In this investigation the trailing-edge pressure was measured as the airfoil incidence was increased to fairly large values beyond the buffet onset value. Some of the results presented in Reference 6 are replotted here in the form of C_{PTE} versus M as shown in Figure 15. The incidence α is fixed at 4° and the effect of varying δ is illustrated. Similar curves are obtained for other values of α . The value of M where divergence of C_{PTE} at a given α can be determined from this type of plots.

From the trailing-edge pressure coefficient versus α or C_L plots, buffet severity can be represented by ΔC_{PTE} . This is obtained by noting the value of the trailing-edge pressure C_{PTEdiv} when divergence occurs (onset of buffet). As the airfoil moves deeper into the buffet regime, buffet severity can be measured in terms of C_{PTE} as

$$\Delta C_{PTE} = C_{PTE} - C_{PTEdiv} \quad (3)$$

The buffet intensity from normal force fluctuation measurements is denoted in terms of C_N' as

$$\Delta C_N' = C_N' - C_{NB'} \quad (4)$$

where C_{NB}' denotes the value of C_N' at buffet onset. Figure 16 shows the relationship between $\Delta C_N'$ and ΔC_{PTE} for three values of M , namely, at M_{DES} and two values of M above and below M_{DES} . Only data using three values of δ are shown in order that the figure will not be unduly crowded. There is a maximum in $\Delta C_N'$ for the lower values of M tested and this is due to a easily detectable C_N' maximum in the graphs plotted against C_L or α . At higher M , C_N' maximum is difficult to locate. From observing the results for other M values tested, it was noted that in the neighbourhood of M_{DES} much larger changes in $\Delta C_N'$ with ΔC_{PTE} occur than at M lower or higher than M_{DES} . In the range of M near M_{DES} the effects of flaps result in larger $\Delta C_N'$ changes with ΔC_{PTE} . The results for M smaller or greater than M_{DES} do not show any particular trend of the effect of the flaps on $\Delta C_N'$.

3.6 Drag Measurements

The drag polar was determined from wake measurements and at the design C_L , M_D (using a criterion based on a value of $dC_D/dM = 0.1$) was 0.75.

At the design C_L of 0.6, C_D versus M is plotted in Figure 17. Below M_D , small flap angles ($\delta = \pm 4^\circ$) do not increase the drag significantly. However, the drag of the airfoil with 8° and 14° flaps shows a fairly large increase above that for $\delta = 0^\circ$. For off-design conditions at $C_L = 0.4$, the increase in drag for the 8° and 14° flaps are quite large. At $C_L = 0.8$, drag increase for negative flap angles is much larger than for positive angles of the same magnitude.

For a given C_L the drag coefficient at the drag rise Mach number is plotted in Figure 18. At the design $C_L = 0.6$, the $\delta = 0^\circ$ case gives the lowest drag at the drag rise Mach number of 0.75. The variations of M_D with C_L for different flap deflections are shown in Figure 19.

3.7 Results at Off-Design Mach Number

In Reference 4, some results on the characteristics of this airfoil at the design Mach number were given. In this paper the behaviour of the airfoil at off-design conditions are discussed and the Mach number chosen is 0.612.

The static pressures are shown in the form of C_p plots given in Figure 20. The profiles are taken from pressure scans close to $\alpha = 6.5^\circ$. The pressure irregularity at $x/c = 0.087$ was due to a partially blocked orifice. The shape of the pressure profile between x/c 0.2 to 0.4 for positive δ is typical for airfoils when shock induced separation with reattachment occurred. This type of flow separation for supercritical airfoils was studied and discussed in Reference 10.

The trailing-edge pressure variations with α as the buffet regime is penetrated is shown in Figure 21. The values of the α indicated in Figure 20 are marked in Figure 21 as 'a', 'b'..... 'f'. It is seen that at $\delta = -8^\circ$, the airfoil is not experiencing buffet and at $\delta = -4^\circ$, the value of α is very close to that at buffet onset. For the other values of δ the airfoil is operating inside the buffet regime.

The corresponding variations of C_N' with α is shown in Figure 22. The curves are displaced by 0.02 of a unit upwards to avoid overlapping. Using the divergence of C_N' as the buffet onset criterion, it can be seen from this figure that the airfoil is operating at buffet conditions for δ equal or greater than 0° . The peak in C_N' is a characteristic behaviour when a C_{Lmax} is presented.

The corresponding power spectra of the balance normal force are shown in Figure 23. The curves are displaced 10 db downwards so that they will not overlap. The appearance of a shock wave with frequency of approximately 50 Hz begins at a value of $\delta = 0^\circ$ and the intensity of this shock increases with increasing δ .

Some representative results for the wake profiles are given in Figure 24. The growth of the wake with different flap settings corresponding to the α given in Figure 20 is shown for a wake traverse 1.75 inches from the tunnel center line. The distance y traversed by the wake probe is normalized with respect to the airfoil chord. C_D' on the horizontal scale is proportional to the total pressure drop. The integral of C_D' over the width of the wake gives the total drag. From the previous figures, the airfoil is just inside the buffet regime at $\delta = 0^\circ$. As δ is increased, the wake profiles become more unsteady. C_D' shown are between values that occur in one pressure scan. The duration of a scan depends on the width of the wake and the traversing speed, but will not exceed a maximum value of 2.4s. The wake thickness determined from the wake profiles at a value of $C_D' = 1\%$ of its maximum value (Ref.4) show the rapid thickening of the wake as the flow separation becomes more severe with a resulting increase in buffet intensity.

4. CONCLUSIONS

A 16% thick supercritical airfoil with a trailing-edge flap was investigated in the NAE Two-Dimensional Test Facility at a chord Reynolds number of approximately 20 million. The investigation was carried out quite deep into the buffet regime and the effects of flap deflection on lift increment and buffet severity were analyzed. The results can be summarized as follows:

- (1) The onset of buffet can be determined quite accurately from plots of C_N' versus C_L at values of C_L where the slope of the curve is 0.1. This value for the slope is found to give consistent results which agree quite well with values derived from the criterion using the trailing-edge pressure divergence for flow conditions when buffet onset is primarily due to trailing-edge separation.
- (2) Buffet boundaries can be raised appreciably by positive deflections of the trailing-edge flap. The buffet onset boundaries for this supercritical airfoil occur very close to and in some cases correspond to C_{Lmax} when $M < M_{DES}$. To identify regions of different degree of severity in the C_L versus M plot, such as mild, moderate and heavy buffeting as in conventional airfoils is not too meaningful.
- (3) The shock positions are determined from the steady state C_p measurements. For Mach numbers near or less than the design value the shock initially moves downstream with increasing angle of incidence to a maximum downstream position before moving slowly back upstream. For higher Mach numbers, only upstream motion of the shock is detected. At the lower Mach numbers, positive flap angles cause the shock to move further downstream while the opposite is true for negative flap deflections.
- (4) Spectral analyses of the balance normal force outputs show shock oscillations at about 50-80 Hz between $M=0.612$ and 0.792 inside the buffet regime. The magnitudes of the fluctuating normal force have quite large values near the "elbow" of the buffet onset curve. As the Mach number increases to higher values, the fluctuations in normal force decrease and the shock waves become more steady.
- (5) Intrusion into the buffet regime and the resulting buffet severity can be represented either by the decrease in trailing-edge pressure ΔC_{PTE} or increase in magnitude of the fluctuating normal force $\Delta C_N'$. For Mach numbers near the design value, much larger changes in $\Delta C_N'$ with ΔC_{PTE} are observed than for other values of M . Whereas C_{PTE} decreases continuously with α , C_N' reaches a maximum and then decreases as the incidence is further increased except for high M where a maximum value in C_N' is difficult to determine. C_N' is a more accurate indicator of buffet severity.
- (6) At the design C_L small flap angles do not increase the drag significantly for $M < M_D$. For off-design conditions ($C_L = 0.8$) the drag rise is much larger for negative flap angles than for positive angles of the same magnitude. The wake profiles show large unsteady fluctuations at conditions beyond the buffet onset boundary. Positive flap angles increase the wake thickness while negative angles have the opposite effect.

5. REFERENCES

1. Monaghan, R.C. and Friend, E.L., "Effects of Flaps on Buffet Characteristics and Wing-Rock Onset of an F-8C Airplane at Subsonic and Transonic Speeds," NASA TM X-2873, Aug. 1973.
2. Friend, E.L. and Sefic, W.J., "Flight Measurements of Buffet Characteristics of the F-104 Airplane for Selected Wing-Flap Deflections," NASA TN D-6943, Aug. 1972.
3. Eggleston, B., Poole, R.J.D., Jones, D.J. and Khalid, M., "Thick Supercritical Airfoils with Low Drag and Natural Laminar Flow," J. Aircraft, Vol. 24, June 1987, pp. 405-411.
4. Lee, B.H.K. and Tang, F.C., "Transonic Buffet of a Supercritical Airfoil with Trailing-Edge Flap," J. Aircraft, Vol. 26, May 1989, pp. 459-464.
5. Rabiner, L.R., Schafer, R.W. and Dlugos, D., "Periodogram Method for Power Spectrum Estimation," Programs for Digital Signal Processing, Edited by The Digital Signal Processing Committee, IEEE Acoustic, Speech and Signal Processing Society, IEEE Press, New York 1979.
6. Tang, F.C. and Lee, B.H.K., "Wind Tunnel Investigation of the Buffet Characteristics of a Supercritical Airfoil with Flap at a Reynolds Number of 20 million," National Research Council of Canada, NAE-LTR-5X5/0179, August 1988.
7. Lee, B.H.K., Ellis, F.A. and Bureau, J., "Investigation of the Buffet Characteristics of Two Supercritical Airfoils," J. Aircraft, Vol. 26, August 1989, pp. 731-736.
8. Lee, B.H.K., "Oscillatory Shock Motion Caused by Transonic Shock-Boundary Layer Interaction", AIAA Journal (to be published).
9. Blackerby, W.T. and Cahill, J.F., "High Reynolds Number Tests of a C-141A Aircraft Semispan Model to Investigate Shock-Induced Separation," NASA CR-2606, October 1975.
10. Lee, B.H.K., "Investigation of Flow Separation on a Supercritical Airfoil," J. Aircraft, Vol. 26, November 1989, pp. 1032-1037.

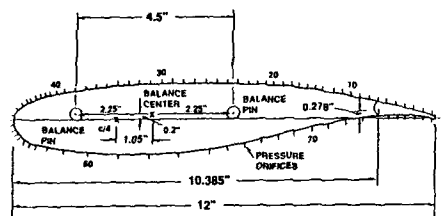


Fig.1 Schematic of 16% thickness-to-chord ratio supercritical airfoil

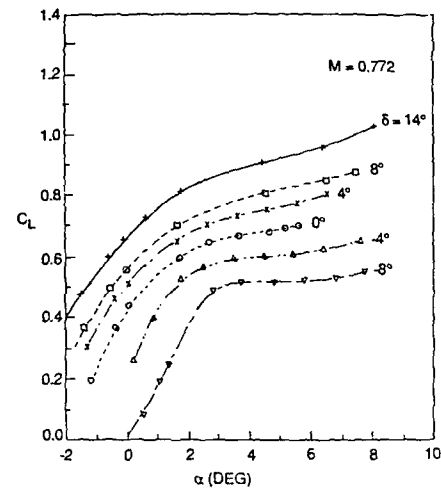


Fig.3 C_L vs α at $M = 0.772$ and various flap angles

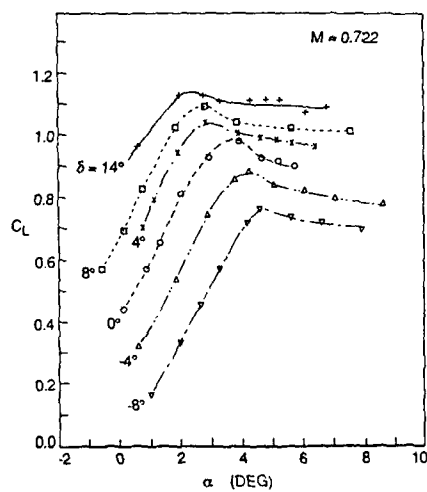


Fig.2 C_L vs α at $M = 0.722$ and various flap angles

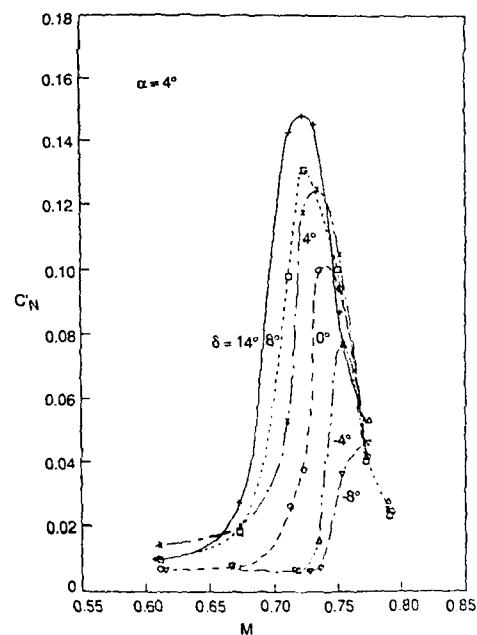


Fig.4 C_N' vs M at $\alpha = 4^\circ$ and various flap angles

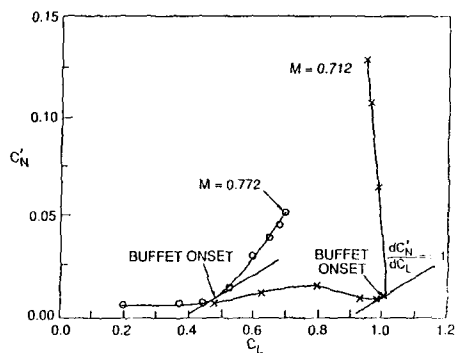


Fig. 5 C_N' vs C_L at $\delta = 0^\circ$,
 $M = 0.712$ and 0.772

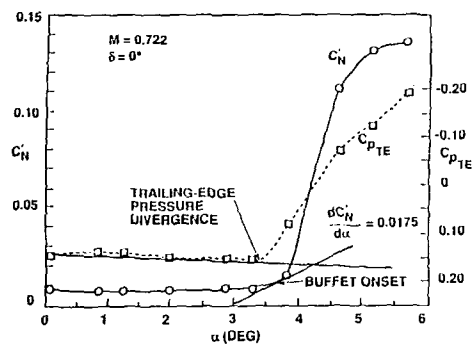


Fig. 6 Comparison of buffet onset
determined from divergence of
balance normal force fluctuations
and trailing-edge pressure

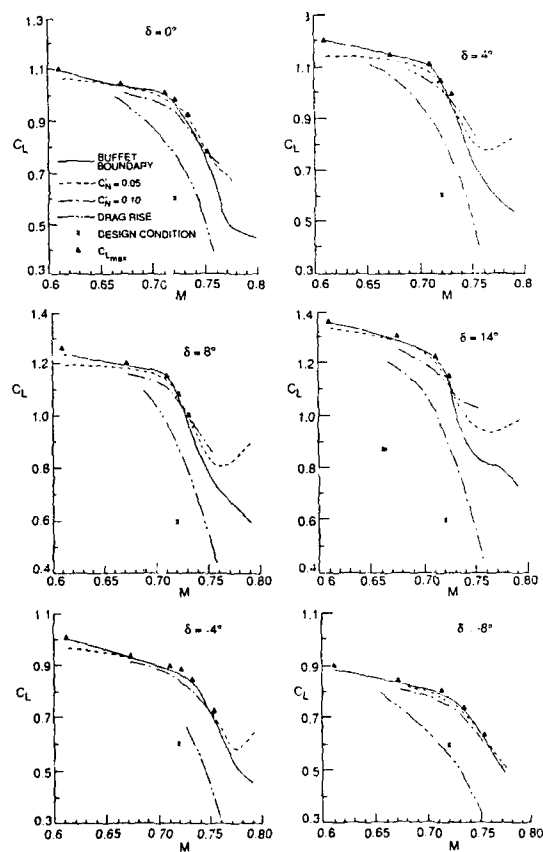


Fig. 7 Buffet boundaries for various
flap angles

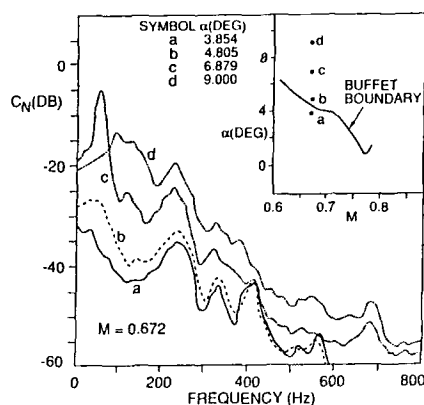


Fig 8 Variations of normal force power spectra with α at $M = 0.672$ and $\delta = 0^\circ$

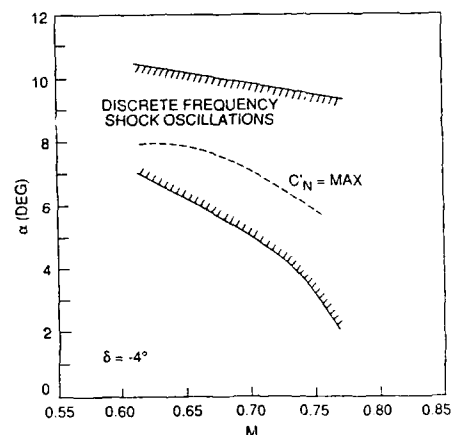


Fig.10 Region of discrete frequency shock wave oscillations at $\delta = -4^\circ$

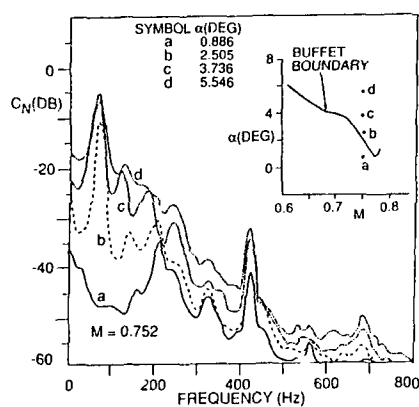


Fig.9 Variations of normal force power spectra with α at $M = 0.752$ and $\delta = 0^\circ$

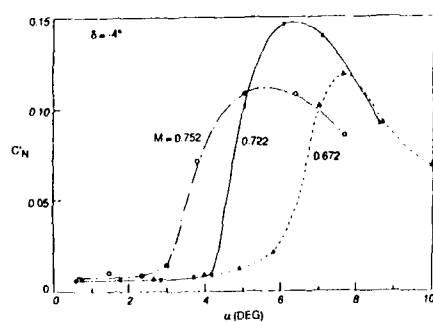


Fig.11 Variations of C'_N with α at $\delta = -4^\circ$

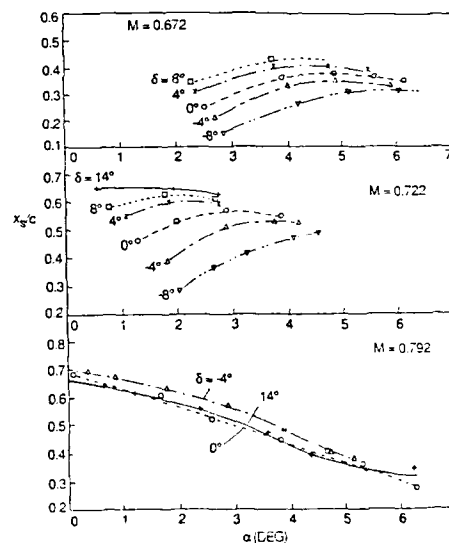


Fig.12 Shock positions vs α for different values of δ at $M = 0.672$, 0.722 and 0.792

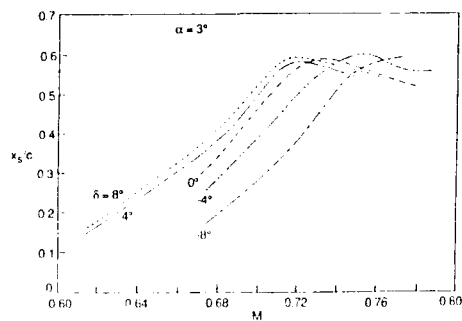


Fig. 13 Shock positions vs M at $\alpha = 3^\circ$ for various flap angles

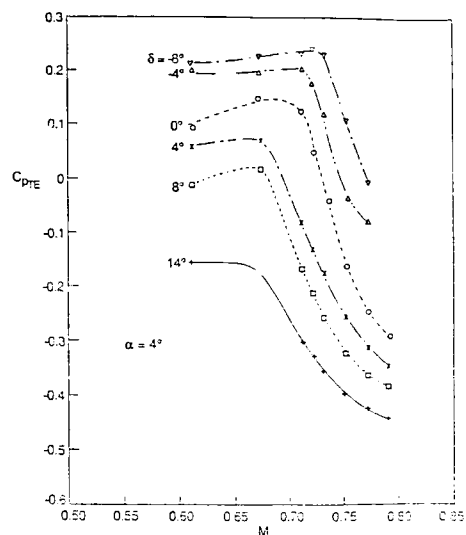


Fig. 15 C_{pTE} vs M at $\alpha = 4^\circ$ for various flap angles

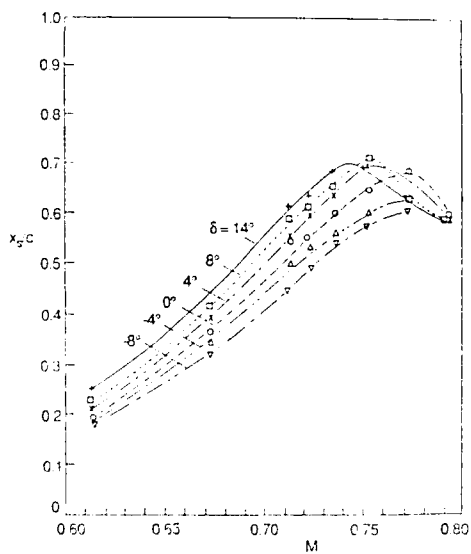


Fig. 14 Shock positions at buffet onset vs M for various flap angles

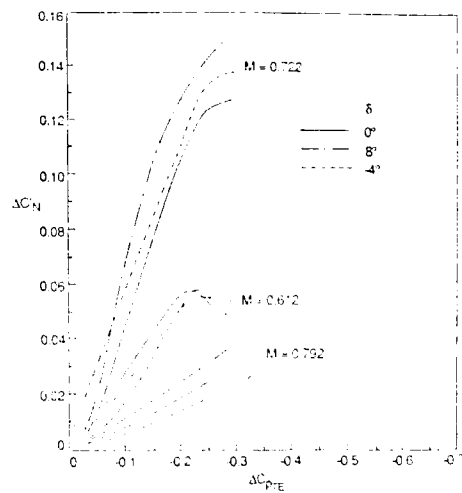


Fig. 16 $\Delta C_N'$ vs ΔC_{pTE} at $M = 0.612$, 0.722 and 0.792 and $\delta = -4^\circ$, 0° and 8°

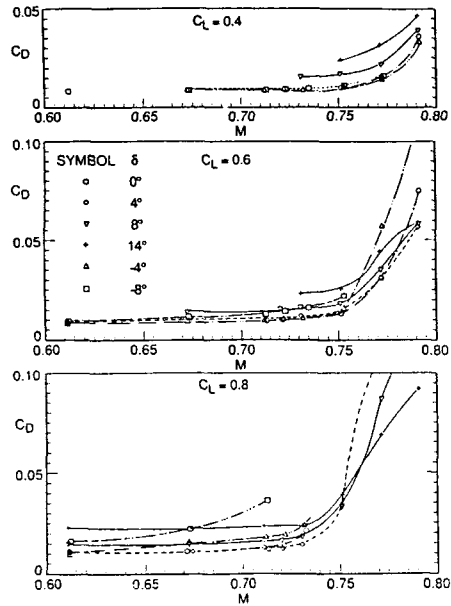


Fig.17 C_D vs M at $C_L = 0.4, 0.6$ and 0.8 for various flap angles

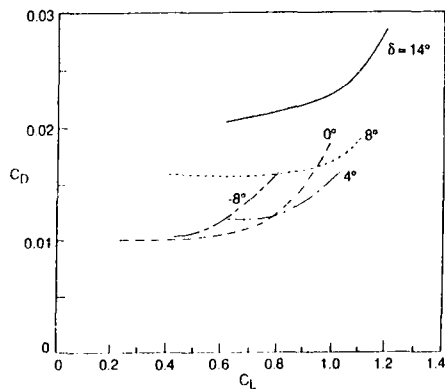


Fig.18 C_D vs C_L at $M = M_D$ for various flap angles

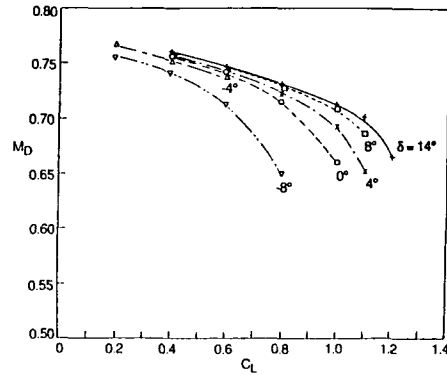


Fig.19 M_D vs C_L for various flap angles

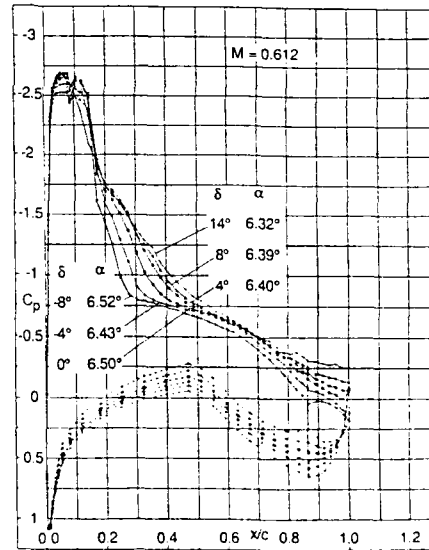


Fig.20 C_p distributions at $M = 0.612$ for various flap angles

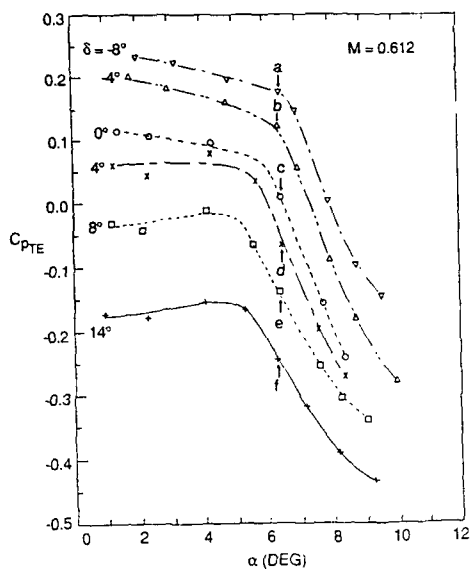


Fig. 21 C_{pTE} vs α at $M = 0.612$ for various flap angles

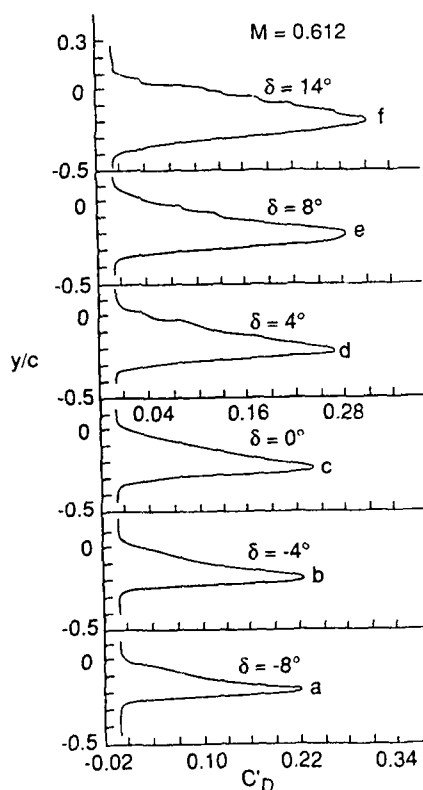


Fig. 24 Wake profiles at $M = 0.612$ and α approximately 6.5° for various flap angles

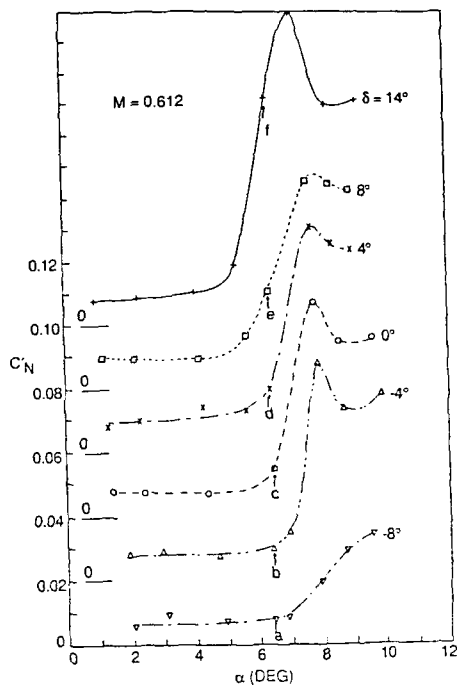


Fig. 22 C_N' vs α at $M = 0.612$ for various flap angles

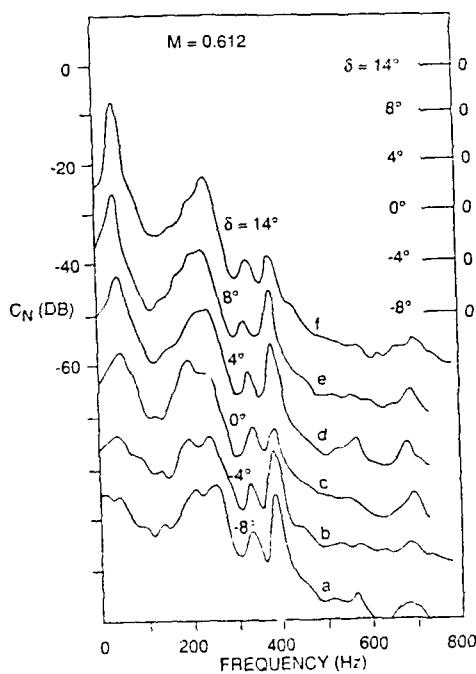


Fig. 23 Power spectra of balance normal force at $M = 0.612$ and α approximately 6.5° for various flap angles

EXPERIMENTAL INVESTIGATION OF BUFFET ONSET AND PENETRATION ON A SUPERCRITICAL AIRFOIL AT TRANSONIC SPEEDS

by

E. Stanewsky

Deutsche Forschungsanstalt für Luft- und Raumfahrt
Institut für Experimentelle Strömungsmechanik
3400 Göttingen, FRG

and

D. Basler

Holtronic, GmbH
8011 Ottersberg, FRG

ABSTRACT

An experimental investigation was carried out on the supercritical airfoil CAST 7/DOA1 to determine the influence of three parameters: Mach number, angle of attack and most of all Reynolds number, on the buffet process and especially on the shock oscillation frequency and amplitude. For this investigation, the model was equipped with regular pressure orifices, dynamic pressure transducers and hot-film sensors, the latter utilized to determine transition location and regions of separation. The flow field was observed by a holographic high-speed, real-time interferometer. The analysis of the results revealed that the buffet process is essentially driven by the interaction of the upper surface shock wave with the boundary layer, especially as it influences the development of the shock-induced separation bubble, and the resultant change in flow conditions at the airfoil trailing edge and that, within the domain of intensive buffet, the shock oscillation frequency decreases with Reynolds number while the amplitude increases. It was furthermore found that the amplitude of the shock oscillation, hence the magnitude of the change in the dynamic load on the airfoil, seems to be dependent on the airfoil geometry.

INTRODUCTION

Transonic airfoil flow is characterized at the design point by the presence of a large supersonic region on the upper surface terminated by an isentropic compression or a weak shock wave. Increasing Mach number or angle of attack beyond the design point leads to the development of stronger shocks which initially only thicken the upper surface boundary layer; however, dependent on the severity of the rear adverse pressure gradients, a trailing edge separation may already develop, **Figure 1**. A further increase in shock strength causes the boundary layer to separate at the foot of the shock and the development of a shock-induced separation bubble. Again, there may or may not be a trailing edge separation. Raising angle of attack or Mach number still further causes the shock-induced separation bubble to spread downstream while, at the same time, rear separation may slowly move upstream [1]. Joining of the two separated regions or the shock-induced separation bubble reaching the trailing edge, i.e., the attainment of total separation on the airfoil, may lead to the commencement of shock oscillations, a condition commonly referred to as airfoil or wing buffet.

The buffet boundary is the boundary in the lift (or angle of attack) and freestream Mach number plane separating conditions where the flow is essentially attached- or only partly separated- and where the flow is totally separated and dominated by shock oscillations and correspondingly large pressure fluctuations, **Figure 2**. For a transport aircraft, the buffet boundary sets the performance limit since the margins in lift and freestream Mach number between

the cruise point and said boundary, i.e., ΔC_L and ΔM_∞ , indicated in **Figure 2**, are prescribed and must be adhered to; for a fighter airplane, the buffet boundary is a boundary only in the sense that it indicates when unsteady phenomena commence and the performance of the aircraft, e.g., as a weapons platform, starts to deteriorate. The accurate prediction of the buffet boundary- as well as the flow development within the buffet domain- is, therefore, important for both types of aircraft.

Accurate prediction means in the transonic Mach number range that the influence of the Reynolds number on the flow development must be well known since the flow development about transonic airfoils or wings may be very sensitive to changes in Reynolds number- or, more generally, to changes in the state and condition of the boundary layer upstream of the upper surface shock- especially in the presence of strong shock waves and separation [1,2]. This is demonstrated in **Figure 3** where the Reynolds number dependence of maximum lift and the lift coefficient at buffet onset is depicted for two transonic Mach numbers: At fixed transition conditions, the lift coefficient at buffet onset increases by about 25 percent as the Reynolds number is increased from 2×10^6 to 30×10^6 , i.e., from a Reynolds number typical of most conventional transonic wind tunnel tests to a Reynolds number close to flight conditions. With transition left free, very favorable results are obtained at low Reynolds numbers which is due to the fact that the shock boundary layer interaction is transitional with transition occurring in the shock-induced laminar separation bubble and the turbulent boundary layer reattaching immediately. An increase in Reynolds number causes the transition point to move upstream with a corresponding drop in lift coefficient down to the fixed transition level; the latter is a strong indication of the importance of the boundary layer condition on the flow development.

The knowledge and understanding of the effect of the Reynolds number- or, more generally, the state and condition of the boundary layer- on the actual buffet process and characteristic parameters of this process, such as shock oscillation frequency and amplitude, is still rather limited. The preliminary experimental investigation described here was, therefore, carried out to investigate, in addition to the influence of Mach number and angle of attack, especially the effect of viscous conditions on the buffet process. The final objective of the continuing investigation is, however, to find a way to simulate the full-scale buffet process at the low Reynolds numbers of conventional wind tunnels and/or to extrapolate low Reynolds number results to flight conditions.

The present paper constitutes a supplementary analysis to Reference 3.

THE EXPERIMENTAL SET-UP

The supersonic airfoil CAST 7/DOA1 was utilized for the present investigation [4,5]. The flow about this airfoil was found to be very sensitive to viscous changes and a large body of data is available for this airfoil at steady flow conditions [6]. The airfoil model with a chord of $c = 100\text{mm}$ was instrumented as shown in Figure 4: Surface pressure orifices to determine the average pressure distribution, surface flush-mounted dynamic pressure transducers to record the pressure fluctuations at the various chord locations and surface hot-film sensors mainly utilized to detect transition and separation locations. Density distributions in the (unsteady) flow field and "flow visualization" were obtained by a holographic high-speed, real-time interferometer whose set-up relative to test section and model is illustrated in Figure 5; a detailed description of the system is given in Reference 7.

The tests were conducted in a transonic test section with slotted top and bottom walls, especially designed to fit an existing (hypersonic) Ludwig-tube facility [7]. Characteristic data of the test set-up were: test section height to chord ratio $h/c = 3$, test section width to chord ratio $B/c = 1.5$, test section length to chord ratio $L/c = 10$, wall open area ratio $\tau = 3.2$ percent. The tunnel width to chord ratio selected was found to provide "two-dimensional" flow patterns over 50 percent of the model span. The run time of the Ludwig-tube facility was 0.34s. The short duration may only cause a problem in that the model surface temperature does not adjust to the adiabatic recovery temperature in the time available. Surface temperatures were not measured during the investigation; however, it was generally assured that the charge temperature of the tube was such that adiabatic conditions could be expected on the model surface.

It was mentioned above that the flow field surrounding the airfoil model was observed by holographic interferometry. From the interferograms, recorded by a high-speed camera, the shock movements, shock strength- qualitatively represented by the extent of the shock into the flow field- and the time-dependent boundary layer development were obtained. Density variations and hence the exact path of propagation of disturbances within the flow field during the buffet process were not yet evaluated. Figure 6 shows, as an example of the type of information available, interferograms representing instances during one cycle of the shock oscillation, viz., the upstream movement of the shock. It can be observed that during this movement the shock strength- or the height of the shock- first increases, then decreases, while the boundary layer thickness at the trailing edge for instance, continuously increases. A detailed analysis of the relation between shock movement, shock strength and boundary layer development and their role within the buffet process will be presented below.

The variables of the investigation were the freestream Mach number, the angle of attack and the state and condition of the boundary layer, the latter varied by changing the Reynolds number and, in some instances, by artificially fixing boundary layer transition near the leading edge of the airfoil.

VISCOSITY AND THE BUFFET-DRIVING MECHANISM

One should consider first some typical time-averaged pressure distributions, here at a constant Mach number of $M_\infty = 0.775$ and a Reynolds number of $Re = 8 \times 10^6$, with increasing angle of attack going from a pre-buffet state to a condition beyond buffet onset, Figure 7. The upper surface pressure distribution is characterized by a strong expansion near the leading edge followed by a plateau-type pressure distribution over the mid-section of the airfoil, which is of some consequence to the magnitude of the shock movement at steady as well as unsteady conditions,

a relatively strong shock wave and fairly large rear adverse pressure gradients making the airfoil susceptible to trailing edge separation. There are in the present context two more characteristic features to be considered: the shock wave moves upstream with increasing angle of attack, here beginning at $\alpha > 2^\circ$, and at the same time there is a rapid drop in trailing edge pressure. Decreasing trailing edge pressure indicates a strong thickening of the boundary layer at the trailing edge and it is likely that either separation starts to develop at the trailing edge or the shock-induced separation bubble has reached this position. As a consequence, conditions (especially the angle) under which the flow leaves the trailing edge region are being altered, i.e., there is essentially a decambering of the airfoil, which causes circulation to be reduced and the shock to move upstream. It can also be seen that the pressure rise due to the shock spreads at $\alpha = 4^\circ$ over a much larger chord distance than at either $\alpha = 2^\circ$ or $\alpha = 3^\circ$ which indicates a strong shock oscillation with the pressures being averaged by the orifices and the pressure leads to the transducers. The close coupling between conditions at the trailing edge and shock location and strength is believed to be part of the mechanism driving the shock oscillations responsible for buffet.

The close relation between shock location and the boundary layer thickness at the trailing edge, here normalized by the thickness for attached flow conditions, is also demonstrated in Figure 8 where the time dependence of these quantities is depicted. One observes- without going into the details of disturbance propagation- that the most forward shock location corresponds closely to a state in time where the boundary layer at the trailing edge reaches its maximum thickness, while the most aft location of the shock is associated with an attached or nearly attached boundary layer at the trailing edge. The shock oscillation frequency was, at the freestream conditions considered, i.e., a Mach number of $M_\infty = 0.77$, an angle of attack of $\alpha = 3^\circ$ and a Reynolds number of $Re = 6 \times 10^6$ with transition fixed at 9 percent chord, determined to be $f = 140\text{Hz}$ which is verified by the spectral density distribution depicted in the inset to Figure 8.

The buffet-driving mechanism can probably best be understood by closely examining one cycle in the shock movement. For that purpose, the thickness of the boundary layer at the trailing edge and the shock strength, represented, as mentioned above, by the height the shock extends into the flow field (h_s), are plotted as a function of the shock location, Figure 9. It is indicated in the top diagram that during the latter stages in the downstream movement of the shock, the strength of the shock increases, a process that continues during the subsequent forward movement until a certain position on the airfoil is reached. During the remainder of the forward movement, the shock strength decreases. The bottom plot shows that during the whole process of upstream movement the boundary layer thickness at the trailing edge increases. It is believed that the thickening of the boundary layer at the trailing edge and the corresponding drop in trailing edge pressure is driving the shock upstream since the shock must adjust its position according to the trailing edge pressure similar to the flow behavior in a supersonic diffuser [8], i.e., the communication between trailing edge and shock is a direct one. A thickening of the boundary layer at the trailing edge also causes, however, as already mentioned, a decambering of the airfoil and consequently a reduction in circulation. This, in turn, should result in a decrease in the extent of the supersonic region and hence in shock strength. Why is the shock strength then increasing as the shock moves forward? One reason or contributing factor is certainly the shock movement itself: Due to the forward propagation of the shock, the relative velocity between incoming flow and shock increases thus increasing the shock strength. (The reduction in shock velocity, as the most forward position is being approached, similarly contributes to the subsequent decrease in shock strength.) One

must, however, also consider that the change in circulation is a process only initiated at the trailing edge. The pressure disturbances generated here must travel via the lower surface, where the flow is being accelerated due to the pressure drop at the trailing edge, to the leading edge region where, as a result, a change in stagnation point location will occur. Only then will the "new" flow field develop on the upper surface. This process will, of course, take longer than the direct communication between trailing edge and shock via the upper surface. The increase in shock strength during the initial upstream movement of the shock may, therefore, be, at least in part, a result of the thinner trailing edge boundary layer present during the downstream progression of the shock wave. A detailed analysis of the interferograms is anticipated to give a more precise picture of the various paths of disturbance propagation and the corresponding response in the flow field development.

The increase in boundary layer thickness at the trailing edge is essentially caused by the increase in shock strength and the development of shock-induced separation reaching the trailing edge. There is, of course, a delay between the onset of separation at the foot of the shock and the time the separation bubble reaches the trailing edge. This can best be seen in the upper diagram where the shock strength is reduced during the latter stages of the forward movement, i.e., shock-induced separation disappears, while the trailing edge boundary layer thickness still increases. Only after a certain time has elapsed will the reduced shock strength be felt at the trailing edge and the downstream movement of the shock will be initiated. Note that the growth rate of the separation bubble is believed to be an essential factor in determining the frequency of the shock oscillation and thus, in part, responsible for the Reynolds number dependence of the buffet process. We will return to this topic later.

The decrease in shock strength during the downstream movement of the shock and the simultaneous reduction in trailing edge boundary layer thickness, causing the downstream progression, is again believed to be a consequence of the shock movement itself, here reducing the relative velocity between the incoming flow and the shock wave, and the different paths disturbances generated at the trailing edge take: the direct way to the shock within the upper surface flow field determining shock location, and the route via the lower surface to the leading edge determining, in part, shock strength.

In the preceding discussion we considered the buffet process associated with a turbulent shock boundary layer interaction. Since the influence of the state of the boundary layer on buffet is also of interest, a brief look at a laminar interaction case seems advisable. A laminar interaction- or a transitional interaction where transition to turbulent flow occurs in the laminar separation bubble with a subsequent immediate turbulent reattachment- distinguishes itself from the turbulent interaction by the existence of a weak forward oblique shock caused by the laminar separation bubble which might extend quite some distance upstream of the main (or rear) leg of the shock. Figure 10 shows for such a test case the time-dependent positions of the forward and rear leg, respectively, of the shock together with the normalized trailing edge boundary layer thickness. One sees that the buffet process is quite similar to the turbulent one just described and there are only two features where further attention should be drawn to: During the downstream movement of the shock, i.e., during a period where the strength of the shock was judged to decrease by considering the extent of the shock into the flow field, the forward shock collapses, i.e., separation disappears. This is a confirmation of the correctness of the flow field analyses given above. Considering the output of the dynamic pressure transducer located on the upper surface at 35 percent chord, one may, as indicated in Figure 10, easily draw the wrong conclusions concerning the frequency of the shock oscillation since both, the forward

and the rear leg of the shock pass over this transducer. This emphasizes the strong need for time-resolving flow visualization.

Before proceeding with the analysis of viscous effects on the buffet process it is deemed beneficial to discuss briefly the relation between shock oscillation frequency, the amplitude of the shock movement and the average shock location and trailing edge pressure, Figure 11. One observes that, as the angle of attack is increased beyond, say, 2.5° , the trailing edge pressure starts to decrease due to the development of separation and the shock movement (change in average shock location) as a result starts to slow down and then reverses. In this incidence range, i.e., prior to the actual buffet onset, the shock oscillates with a relatively high frequency and low amplitude. Increasing the angle of attack causes separation to become more severe, the average shock location shifts more rapidly upstream, the oscillation frequency decreases while the amplitude of the shock oscillation rapidly increases until a full buffet state is reached. It can be seen that at these conditions the shock has moved upstream by almost 10 percent from its most rearward position and the trailing edge pressure coefficient has dropped to $C_{PE} = -0.05$, the latter indicating that the criterion " $C_{PE} = 0.05$ " for the onset of buffet is quite conservative. An increase of angle of attack within the domain of heavy buffet ($\alpha \geq 4^\circ$) causes the amplitude to decrease while the frequency increases again.

Concerning the amplitude of the shock oscillation it seems that it is in essence determined by the average shock location and the change in shock location for a given disturbance (corresponding to a $\Delta\alpha$) at the trailing edge: At $\alpha = 3^\circ$ a given $\Delta\alpha$ only results in a small change in shock location; at $\alpha = 4^\circ$ this change is large, while at $\alpha = 5^\circ$ the change in shock location seems to decrease again. The occurrence of the maximum amplitude corresponds, by the way, to a condition where the flow alternates between attached and totally separated whereas at incidences reasonably far below or above the angle of maximum amplitude only either attached or totally separated flow prevails.

ANALYSIS OF VISCOUS EFFECTS ON BUFFET

The two important parameters of the buffet process, i.e., the amplitude and frequency of the shock oscillation, are likely to be dependent on Reynolds number or some characteristic boundary layer parameter since this process is so closely tied to the development of separation. Considering first the dependence of the reduced frequency on Reynolds number for angles of attack well within the buffet domain, one observes that the reduced frequency, based on the chord length, generally decreases with increasing Reynolds number, Figure 12. This holds for the two angles of attack considered, viz. $\alpha = 4^\circ$ and 5° , as well as for the three Mach numbers depicted, viz. $M_\infty = 0.74, 0.76$ and 0.78 . Note that the shock oscillation frequency increases with Mach number.

Before proceeding, let us first consider the data point at $Re = 6 \times 10^6$ and transition fixed at 9 percent of the chord. Increasing the Reynolds number generally reduces the boundary layer or displacement thickness upstream of the shock. It will be shown later that this seems instrumental in reducing the shock oscillation frequency. Forcing transition near the leading edge is very likely to generate a boundary layer upstream of the shock that is thicker than the one for free transition. The reduced frequency at $Re = 6 \times 10^6$ and fixed transition should, therefore, by the above arguments, be higher than the one for free transition. However, one must remember that a thicker boundary layer interacting with the shock also causes a more severe decambering of the airfoil and hence a reduction in circulation with a more forward average shock position. This is verified in Figure 13, where the pressure distributions at $M_\infty = 0.760$ and a Reynolds number of $Re = 6 \times 10^6$ are depicted for free and fixed transition. In

the case of fixed transition the distance between shock location and trailing edge is noticeably larger- hence the lower frequency. Taking the shock location into account by basing the reduced frequency on the distance between the (average) shock location and the trailing edge, it can be seen, **Figure 14**, that the thicker boundary layer upstream of the shock is indeed associated with the higher frequency which is in support of the Reynolds number dependence discussed above.

The present results on the Reynolds number dependence of the shock oscillation frequency are supplemented in **Figure 15a** by data of Reference 9 obtained over a Reynolds number range between $Re = 15 \times 10^6$ and 30×10^6 . The reduced frequency is here, for lack of other information, again formed with the chord length c . One observes that the trend given by the present results, i.e., a decrease in the reduced frequency with Reynolds number, is sustained by the results for the Garabedian and Korn airfoil up to a Reynolds number of $Re = 30 \times 10^6$ which is close to the flight Reynolds number of a large transport aircraft. Moreover, the frequencies determined for the CAST 7-DOA1 airfoil at angles of attack of $\alpha = 4^\circ$ and 5° are very close to the ones for the Garabedian and Korn airfoil at corresponding Reynolds numbers.

Turning now to the amplitude of the shock oscillation, hence the load variation on the airfoil, one can see that the amplitude increases with Reynolds number, a trend opposite to the one observed for the oscillation frequency, **Figure 15b**. Note that these opposing trends always seem to hold, no matter whether the dependency on Mach number, angle of attack or Reynolds number is concerned. In **Figure 16b** we use again present results and results of Reference 9, now for two different airfoils. The increase of the shock oscillation amplitude is similar for all three airfoils considered and is sustained up to the highest Reynolds number investigated. Contrary to the frequency, differences in the amplitude level for the three airfoils considered exist, however. These differences are most pronounced between the two supercritical airfoils CAST 7 and Garabedian and Korn on one hand and the conventional airfoil NACA 0012 on the other hand. They can possibly be explained by characteristic differences in the geometry, hence in the flow development: In the case of the NACA 0012 airfoil, shock-induced total separation occurs very suddenly with the shock wave being relatively close to the trailing edge and without the prior development of a separation bubble. The flow behavior should, therefore, be similar to the one for the supercritical airfoil CAST 7 at higher angles of attack where during the buffet or shock oscillation process reattachment, as indicated previously, no longer takes place, and where the amplitude decreases with angle of attack. Furthermore instrumental in reducing the shock oscillation frequency may be the pressure or Mach number distribution upstream of the shock which in the case of the classical NACA 0012 airfoil is not of the plateau type but is characterized by a continuous acceleration immediately up to the shock. The shock movement in response to pressure changes at the trailing edge can, therefore, be small since small movements result, due to the larger shock-upstream gradients, in relatively large changes in pressure immediately downstream of the shock [10].

It is believed and some evidence was given above, that the development of the shock-induced separation bubble is an essential factor in determining the shock oscillation frequency. This would provide an explanation for the trend in the Reynolds number dependence of the shock oscillation frequency- being at the same time further evidence- by the following arguments: Increasing the Reynolds number generally means decreasing the boundary layer thickness or any other thickness parameter of the boundary layer upstream of the shock. Such a decrease can also be achieved by moving, at a sufficiently low Reynolds number, a boundary layer tripping device, say, from 7

percent chord to 30 percent chord as is indicated in **Figure 16**. The two different boundary layer thicknesses (or trip locations) cause, as can also be seen in **Figure 16**, quite a pronounced difference in the development of the shock-induced separation bubble with increasing shock-upstream Mach number, i.e., increasing shock strength. Essential in the present context is that in the case of the thicker boundary layer the bubble grows much faster and reaches, for instance at $M_i = 1.35$, almost double the extent of the one present for the thinner boundary layer. Although these results were obtained for steady, pre-buffet conditions, it is judged that similar differences will occur in the dynamic buffet process. This implies that for the lower Reynolds number and thicker boundary layer the shock-induced separation bubble will reach the trailing edge much faster, once separation has occurred, thus generating the higher frequency.

The preceding discussion was concerned with conditions at $\alpha = 4^\circ$ and $\alpha = 5^\circ$, i.e., conditions well within the buffet domain. At an angle of attack of $\alpha = 3^\circ$ we are in the vicinity of the buffet boundary and might, dependent on Mach number (or Reynolds number), be at pre- or post-buffet-onset conditions. Such a situation is illustrated in **Figure 17**: At the Mach number of $M_\infty = 0.78$, the reduced frequency decreases with Reynolds number, as was the case for $\alpha = 4^\circ$ and 5° , while at the lower Mach numbers of $M_\infty = 0.76$ and $M_\infty = 0.74$ the trend is opposite, i.e., the shock oscillation frequency increases with Reynolds number. The right-hand diagram of **Figure 17** indicates, using the criterion of $C_{p_{tr}} = 0.05$ as the definition of the buffet boundary, that $M_\infty = 0.78$ corresponds to a post-buffet- and $M_\infty = 0.74$ and $M_\infty = 0.76$ to a pre-buffet-onset state. The higher Reynolds number is, at the latter conditions, most likely to result in a higher average velocity in the boundary layer resulting, in turn, in higher convection speeds of disturbances generated at the foot of the shock and, therefore, in the increased shock oscillation frequency.

CONCLUSION AND FUTURE TESTS

An analysis of the results of an experimental investigation of the buffet process and its dependence on viscous effects on a supercritical airfoil has led to the following conclusions:

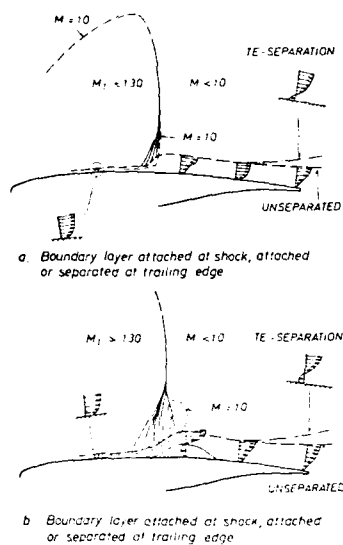
1. The buffet process seems to be driven by the interaction of the flow conditions at the trailing edge, which control shock location and, at least in part, via the circulation, the shock strength, and conditions at the shock which affect separation.
2. The development of the shock-induced separation bubble seems to play a major role in determining the buffet frequency and the dependence of that frequency on Reynolds number.
3. The buffet frequency decreases with Reynolds number while the amplitude increases. This trend is substantiated by other investigations up to a Reynolds number of $Re = 30 \times 10^6$.
4. The shock oscillation amplitude is dependent on the type of pressure distribution (plateau or strong gradients) prevailing upstream of the upper surface shock, hence on airfoil geometry.

A large number of data concerning the unsteady density distribution in the flow field around the airfoil has been obtained during the course of the present investigation. Foremost on the list of future work is the evaluation of these data with respect to the different paths disturbances generated at the trailing edge take to affect the overall buffet process. This task may also require more detailed tests. Further tests, mainly in a transonic cryogenic Ludwig-tube, will also be carried out to

1. determine boundary layer parameters (displacement thickness, momentum thickness, shape factor) of dominant influence on the buffet process in order to be able to simulate high Reynolds number flow at the low Reynolds numbers of conventional wind tunnels.
2. find means to eliminate buffet by boundary layer control and
3. determine the Reynolds number dependence up to full-scale conditions.

REFERENCES

- [1] E. Stanewsky, "Shock Boundary Layer Interaction", In *Boundary Layer Simulation and Control in Wind Tunnels*, AGARD-AR-224, April 1988, pp.271-305.
- [2] A. Elsenaar, T.W. Binion, E. Stanewsky, "Reynolds Number Effects in Transonic Flow", AGARDograph No. 303, Dec. 1988.
- [3] E. Stanewsky, D. Basler, "Mechanism and Reynolds Number Dependence of Shock-induced Buffet on Transonic Airfoils", IUTAM Symposium Transsonicum III, Springer-Verlag Berlin Heidelberg, 1989, pp. 479-488.
- [4] P.Kühl, H.Zimmer, "The Design of Airfoils for Transport Aircraft with Improved High-Speed Characteristics", Dornier GmbH, Report 74/16 B, 1974.
- [5] E. Stanewsky, H.Zimmer, "Development and Wind Tunnel Investigation of Three Supercritical Airfoils for Transport Aircraft", Z. Flugwiss. 23 (1975), Heft 7/8, pp. 246-256.
- [6] A. Elsenaar (Chairman), "Two-dimensional Transonic Testing Methods: Final Report of the GART-EUR Action Group AD (AG 02)", GARTEUR/TP-011 (NLR TR 83086 L), July 1981.
- [7] D. Basler, "Experimental Investigation of the Convection of Shock-induced Disturbances on Transonic Airfoils", DFVLR-FB 87-28, July 1987.
- [8] H.H. Pearcey, "Some Effects of Shock-induced Separation of Turbulent Boundary Layers in Transonic Flow Past Aerofoils", A.R.C. Technical Report, R & M No. 3108, 1959.
- [9] N. Hirose, H. Miwa, "Computational and Experimental Research on Buffet Phenomena of Transonic Airfoils", IUTAM Symposium Transsonicum III, Springer-Verlag Berlin Heidelberg, 1989, pp. 489-499.
- [10] J.F. Cahill, "Simulation of Full-scale-flight Aerodynamic Characteristics by Tests in Existing Transonic Wind Tunnels", AGARD-CP-83, 1971, pp. 20/1 to 20/8.



Transonic viscous-inviscid interaction

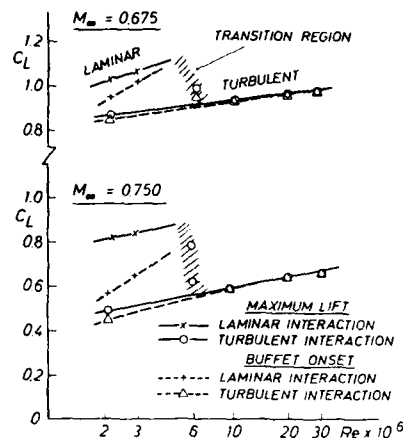


Figure 3: Reynolds number dependence of maximum lift and buffet onset for a supercritical airfoil (Ref. 2)

Figure 1: Flow and boundary layer development on a transonic airfoil

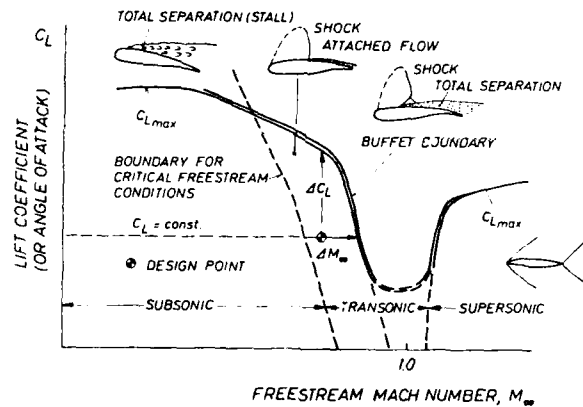


Figure 2: The transonic buffet boundary

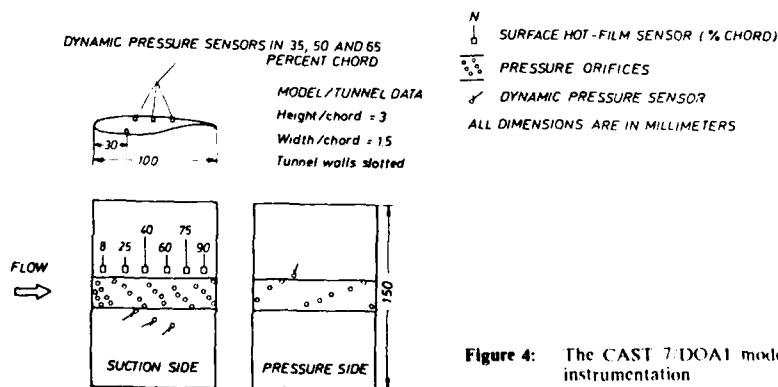


Figure 4: The CAST 7/DOA1 model and instrumentation

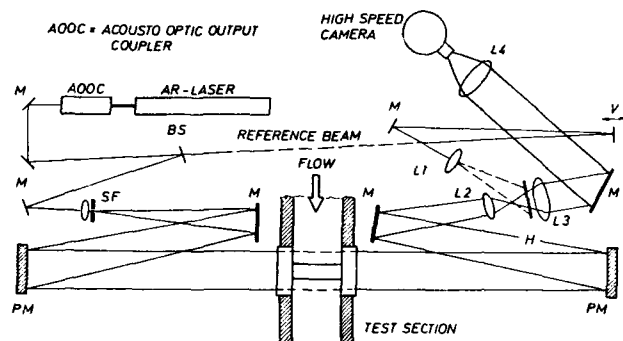


Figure 5: The set-up of the high-speed, real-time holographic interferometer

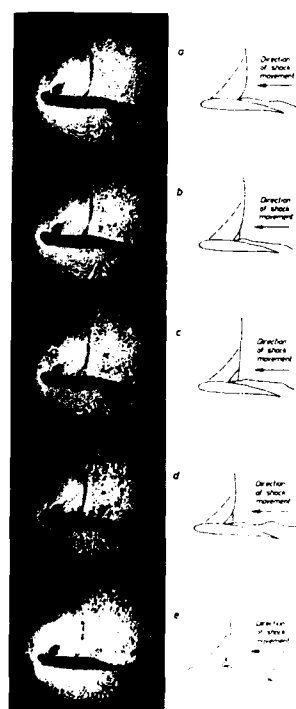


Figure 6: The unsteady flow field observed by holographic interferometry

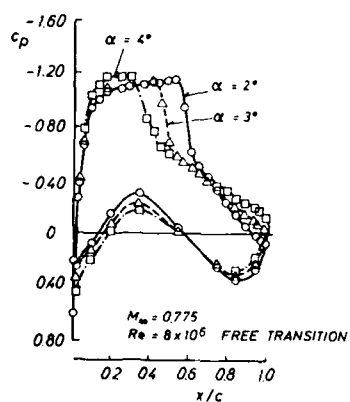


Figure 7: Averaged pressure distributions at pre- and post-buffet onset conditions

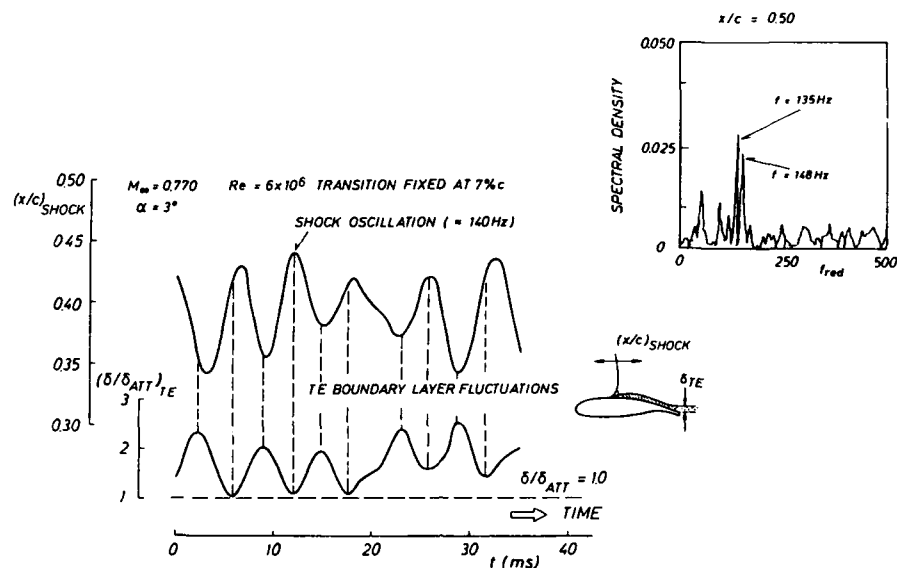


Figure 8: Shock oscillation and trailing edge boundary layer fluctuations in the presence of a turbulent upper surface boundary layer

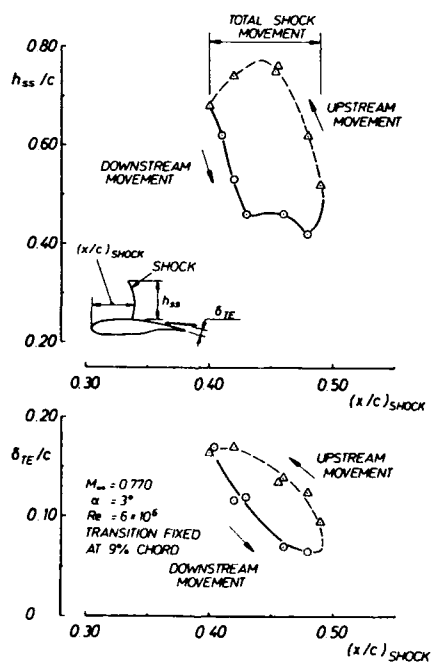


Figure 9: Relation between shock movement, shock strength and trailing edge boundary thickness

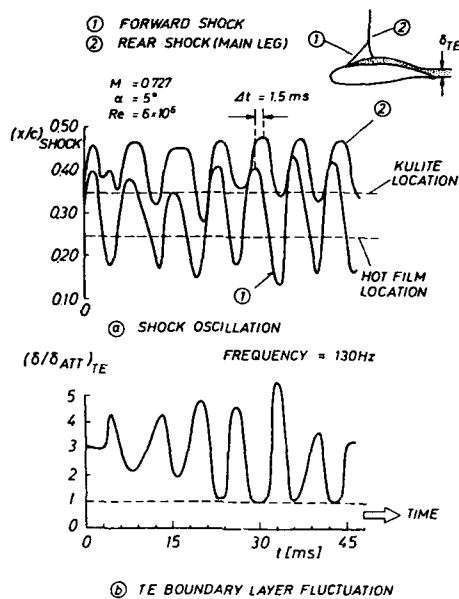


Figure 10: Shock oscillation and trailing edge boundary layer fluctuations for an initially laminar upper surface boundary layer

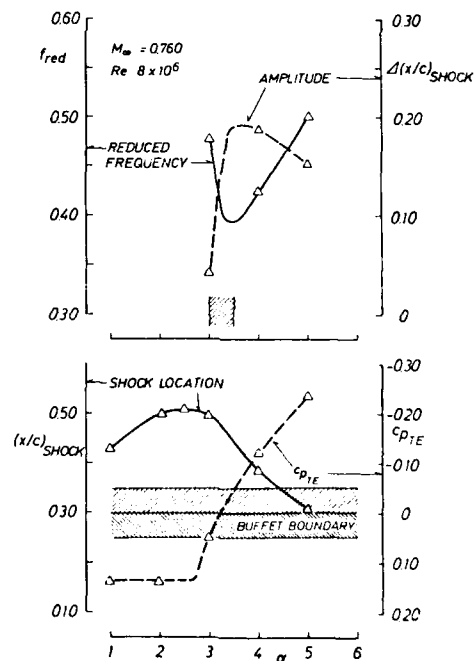


Figure 11: Shock oscillation frequency and amplitude, shock location and trailing edge pressure relative to the buffet boundary

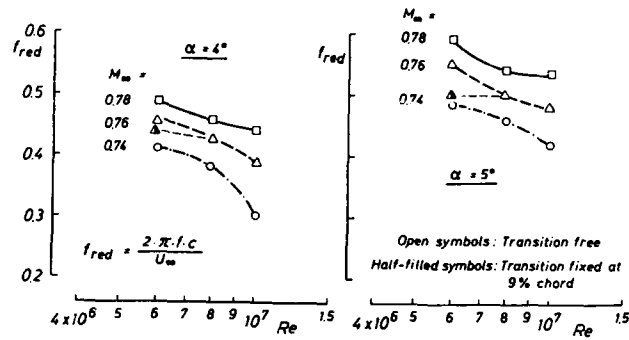


Figure 12: Dependence of the reduced shock oscillation frequency $f_{red} = 2\pi f c / U_\infty$ on Reynolds number

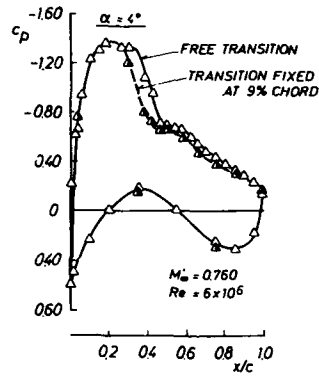


Figure 13: Comparison of pressure distributions for two different boundary layer thicknesses upstream of the shock

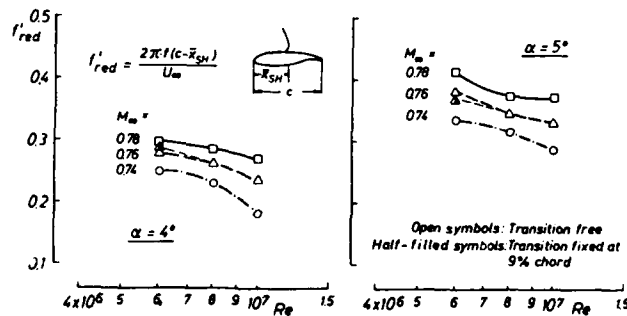


Figure 14: Dependence of the reduced shock oscillation frequency $f'_{red} = 2\pi f (C - \bar{x}_{SH}) / U_\infty$ on Reynolds number

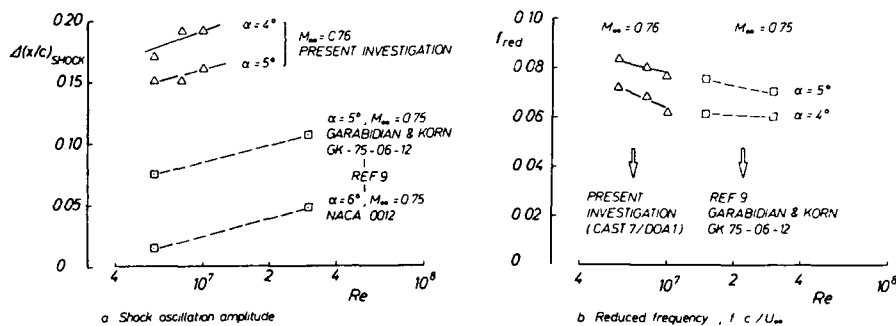


Figure 15: Reynolds number dependence of shock oscillation frequency and amplitude for various types of airfoils

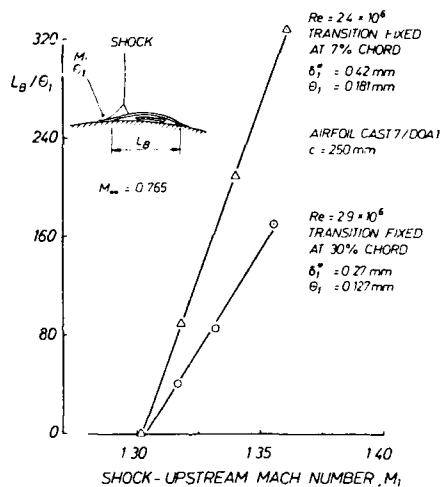


Figure 16: Extent of the shock-induced separation bubble for two different initial boundary layer thicknesses

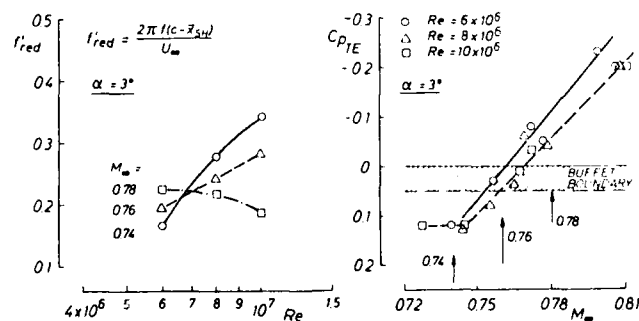


Figure 17: Reynolds number dependence of the reduced shock oscillation frequency f_{red} for pre- and post-buffet onset conditions

Experimental Investigations of Buffet Excitation Forces
on a Low Aspect Ratio Trapezoidal Half Wing
in Incompressible Flow

by

P. Bublitz

DLR - Institute for Aeroelasticity
Göttingen, Fed. Rep. of Germany

H. Zingel, Deutsche Airbus GmbH
Bremen, Fed. Rep. of Germany

Abstract:

This paper addresses the problem of determining the steady and unsteady airloads on swept wings of low aspect ratios at high incidences. Despite great progress in the field of computational fluid dynamics (CFD), this problem is not yet accessible to computer-supported methods, at least with respect to unsteady airloads. First, the information will be discussed which is necessary for buffeting prediction. The reasons for performing pressure measurements are outlined. Then, a brief description of the test set-up and instrumentation will be given. The steady and unsteady test results will be presented and their strong mutual interdependency will be demonstrated. The question as to whether it is possible to separate the unsteady pressures due to flow separation from those due to oscillatory motion of the model will be answered on the basis of experimental results. The usefulness of such investigations and their limitations with respect to the buffeting problem will be discussed.

1. Introduction

In a paper often quoted since it appeared, W.B. Herbst [1] reported that *supermaneuverability* can be achieved by combined application of different *key technologies* such as digital fly by wire, thrust to weight ratio greater than one, thrust vector control and, last but not least, delta wings to penetrate the post-stall regime. At that time numerous publications already existed on delta wings and/or hybrid wing configurations. The latter consisted of a moderately swept basic wing equipped with lift augmentation systems (LAS) as strakes etc., see for instance W. Staudacher [2] or W. Baumert [3]. Most of these investigations concentrated on steady state wings up to high incidences. Their aim was to select wing planforms producing greater lift at very high angles of attack. This could be achieved by using flow separations in the form of concentrated conical vortices emanating from highly swept leading edges. The majority of the above mentioned publications was devoted to experimental work. To a lesser extent the problem was attacked theoretically, see for example Ref. [4]. Controlled flow separation can have undesirable, as well as desirable, consequences. Problems arise in flight mechanical and aeroelastic fields. The former are associated with asymmetry or the breakdown of the conical vortices and shall not be further discussed in the present context. The latter are due to secondary vortex formation and/or turbulent mixing processes causing more or less stochastic pressure fluctuations, which can lead to forced vibrations of the aircraft structure. These, in turn, can produce motion-induced unsteady airloads. Hence, we are confronted with a dynamic response problem which can turn into a stability problem depending on the complex motion-induced pressures involved. In the terminology proposed by D.G. Mabey in his survey paper [5], the unsteady aerodynamic driving forces due to flow separation are called buffet, whereas the stochastic dynamic response in this case is denoted buffeting. In the same paper he gives a thorough review of the efforts undertaken to solve the problem and presents many valuable general results. One conclusion which must be drawn from his presentation is that every new design has to be checked individually with respect to its post-stall capability. On the other hand, he states that investigations of unsteady phenomena at high angles of attack on steady models with superimposed forced oscillations are inadequate with respect to real aircraft. Real aircraft perform transient maneuvers which are not simulated by experiments on steady models. This argument is supported by the experimental results of M. Jarrah and H. Ashley [6]. These authors reveal that transient airloads exceed the corresponding steady ones by about 50%. This phenomenon, due to the time delay involved in vortex formation with respect to aircraft motion, has been known for a long time from straight wings and helicopter blades and is referred to as Kramer's effect [7] or dynamic stall. Here, the pitch rate plays an extremely important role and, without doubt, great effort is called for in the investigation of actual cases. At present this can only be done experimentally. On the other hand, experimental data for the steady case still seems to be valuable in the validation of mathematical calculations. The present experimental investigations were stimulated by J. Becker's theoretical work [8].

2. Theoretical Considerations

In preparing the respective experiments it was necessary to define the information to be acquired. Since the fundamental considerations are given in detail in Refs. [9,10], only a brief survey shall be given here, the mathematical equations will be left out, because they can also be found in Refs. [11,12]. The aircraft structure is assumed to behave linearly so that it can be described by means of its modal quantities such as eigenfrequencies, eigenmodes, generalised masses and global damping parameters. At high angles of attack the lifting surfaces of an aircraft create steady as well as unsteady airloads due to flow separation - the buffet forces, which are of more or less stochastic character. These, in turn, may lead to irregular time-dependent forced oscillations of the disturbing airframe, referred to as buffeting [5]. In a mathematical sense, this process establishes a dynamic response problem in which the unsteady airloads due to flow separation represent the external driving forces and are independent of the elastomechanical system. Once the airframe is buffeting, it induces motion dependent unsteady airloads. This process has been known for a long time for smooth flow and plays an important role in relation to the flutter problem. Here, the motion-induced external airloads are dependent on the oscillating lifting system influencing it simultaneously in such a manner that they determine the dynamic behaviour as well as the other internal forces including inertia, restoring and damping forces. Their mutual interaction results in a mathematically complex eigenvalue problem defining the stability of the system. While for smooth flow, potential-theoretical methods exist to calculate the motion-induced airloads, these have to be determined experimentally in separated flows. It is especially important to analyse the extent to which the unsteady pressures due to flow separation are interfering with the motion induced, since these can have a great influence on the modelling of the buffet problem. From the preceding explanations, it becomes evident that statistical measuring and evaluation methods have to be applied, as was already proposed a long time ago [13,14]. Another point is that it was decided to employ a semi-rigid test set-up. That means, the wing was designed to be so stiff that its lowest eigenfrequency was sufficiently beyond the highest frequency of forced oscillations or the eigenfrequency of the model-suspension spring system. This arrangement should minimise the influence of an elastic wing structure on the motion-induced pressures.

3. Model and Test Set-Up

The tests were carried out on a half model consisting of a wing and a dummy fuselage. The planform of the basic wing was trapezoidal and of low aspect ratio. It could optionally be equipped with a strake. Its geometric dimensions can be seen in Fig. 1 and were proposed by MBB-Munich. During the first test phase fourteen *in situ* pressure transducers were installed on the suction surface and ten on the pressure surface at each of two measuring cross-sections, CS1 and CS2. These cross-sections were located at the relative spanwise positions $\eta = 0.36$ and $\eta = 0.64$, respectively. In addition, six accelerometers were installed. The position of four of these are indicated by B_1 to B_4 . In a second test phase, the number of *in situ* pressure transducers was increased to a total of eighty-three at seven measuring cross-sections in order to gain deeper insight into the local pressure distributions, see Fig. 2 of Ref. [11]. The half model was mounted on a turntable which served to adjust the steady mean angles of attack in the range $0^\circ < \alpha < 40^\circ$. About the mean angles of attack the wing could be excited to forced oscillations by means of an electro-hydraulic exciter in the range of angular amplitudes $0^\circ < \hat{\alpha} < 4^\circ$ and in the frequency range $0 \text{ Hz} < f < 18 \text{ Hz}$. Because the dummy fuselage remained at rest during the oscillations of the wing, the unavoidable gap between them was sealed by a sheet of aluminium, see Fig. 2. All tests were performed in the $3 \times 3 \text{ m}^2$ low speed wind tunnel of the DLR research center in Göttingen, which has a maximum speed of about 60 m/s. Since the corresponding Mach number is $\text{Ma} < 0.2$, the flow could be considered incompressible. The other relevant similarity parameters such as Reynold's number and reduced frequency covered the ranges $0 < \text{Re} < 2 \cdot 10^6$ and $0 < \omega^* < \approx 1.0$, respectively, based on the mean chord as a reference length, $\bar{c} = c_m = 0.61 \text{ m}$, see Fig. 1.

The equipment necessary to control the unsteady forced motions of the model, on the one hand, and for data acquisition and evaluation, on the other hand, can be seen in the functional block diagram, Fig. 3. Since this diagram is self-explanatory, only a few comments shall be made here. The measuring amplifiers for the 50 piezo-resistive pressure transducers actively compensated the temperature drift. The computer incorporated analogue anti-aliasing low-pass filters to reject higher frequency components of the random signals beyond 128 Hz. The implemented software was suitable to calculate the following information from the experimental data gathered: steady mean values, RMS values, spectral decomposition by means of Fourier-transformation (FFT), power spectral densities, cross-power spectral densities and coherence functions. During Test Phase 1 only a DEC PDP 8 computer was available. Thus, most of the data had to be stored in an analogue recorder and had to be computed off-line after the experiments. Only rather limited on-line and, consequently, quick-look capabilities were given. Test Phase 2 could be performed with a DEC VAX 750 computer in connection with a very fast array processor AP/20 and a disk storage capacity of 300 MByte. This improved the data acquisition and evaluation considerably. Test Phases 1 and 2 differed also with respect to other conditions.

During Test Phase 1 the wing configurations "with" and "without" rakes were tested. The oscillatory motion of both configurations was, however, restricted to the pitch motion about the quarter-line axis of the basic trapezoidal wing - and others parallel to it.

Phase 2 concentrated on the determination of the unsteady airloads necessary for buffet prediction. This task requires a dense distribution of pressure sensors to achieve reasonably good information about the local pressure distributions, especially in the case of flow separation. Due to the lack of an adequate number of pressure transducers for the strake, it was decided to limit the investigations to the basic trapezoidal wing. Therefore, it may be considered a more fundamental investigation with respect to complex high lift generating configurations. Test Phase 2 also differed from Test Phase 1 concerning the oscillatory motion of the wing. The pitch axis was normal to the wind direction and crossed the quarter-point only at the wing root. Hence, the outer parts of the wing performed a combined pitch-heave motion with respect to their quarter point. In addition, the wing could be excited to roll oscillations. This has to be kept in mind when comparing the results of both test phases.

4. Test Results

4.1 Steady Pressure Distributions and Global Forces

A synopsis of the steady pressure distributions on the half wing with strake as functions of the angle of attack in the range $5^\circ < \bar{\alpha} < 40^\circ$ can be seen in Fig. 4. At 5° the influence of the strake vortex is already perceptible on the upper side of the inboard cross-section CS1, whereas the outboard cross-section CS2 still shows the typical potential-theoretical pressure distribution. As the incidence increases, the vortex produced by the strake grows, which is reflected by a hump in the pressure distributions on the suction surface in both cross-sections. At $\bar{\alpha} = 27.5^\circ$ this vortex is burst and the flow completely separated from the outboard wing, as indicated by the constant pressure distribution on the suction surface. The fact that it does not even vanish at the trailing edge proves the Kutta Condition to be no longer valid. A further increase in the angle of attack also leads to complete flow separation from the inboard wing. Over the entire range of angles of attack $0^\circ < \bar{\alpha} < 40^\circ$, the pressures at the pressure surface increase continuously.

The respective steady pressure distributions on the basic trapezoidal wing are shown in Fig. 5. Only for $\bar{\alpha} = 5^\circ$ are the pressure distributions on the inner and outer wing those predicted by potential-theory.

For increasing incidences, the flow starts to separate from the suction surface considerably earlier than for the wing with strake, see Fig. 4. In both cases, however, flow separation first occurs at the outer parts of the wing and subsequently spreads over the inner parts, which can be seen more easily in Fig. 6, where the pressure distributions represented were measured at a greater number of spanwise cross-sections. On the other hand, since in both cases the pressures on the suction surface diminish while the pressures on the pressure surface increase, the final lift force caused by each of them is equal to approximately fifty percent. In smooth flow a lifting surface is sustained preponderantly by suction forces. The flow phenomena responsible for this development can be seen in Fig. 7. This figure illustrates the rather complex vortex structures on the suction surfaces with the aid of oil-flow patterns. For more detailed explanations, see Refs. [11, 15]. The differently shadowed areas will be discussed below in context with the coherence of unsteady pressure distributions. The effect of the aforementioned steady pressures on the steady global forces and moments can be seen in Figs. 8 and 9. In Fig. 8 the lift coefficients are plotted as functions of the angle of attack for wings with and without strakes, respectively; these results are very similar to those measured in the present case, see Ref. 16. This information reveals impressively the influence of the strake vortex on the lift force. Fig. 9 presents the global lift, pitch and roll coefficients versus mean angles of attack. Comparison of the lift coefficients in Fig. 8 and Fig. 9 for the wing without strake shows good agreement.

4.2 Unsteady Pressure Distributions on the Wing at Rest

With regard to the buffeting problem, the unsteady pressure distributions resulting from flow separation are of special interest. Fig. 10 illustrates the development of the unsteady pressures on the suction surface as a function of the steady angle of attack in terms of amplitude spectra. These represent the frequency content of the unsteady pressures. At $\alpha = 5^\circ$, i.e. for attached flow, pressure fluctuations of relatively low frequency only occur near the leading edge, where the steady mean pressures exhibit the suction peak, see Figs. 5,6. Otherwise, the flow is observably smooth. As the incidence increases and the flow separates, the amplitude spectra assume a broad band character indicating that flow separation occurs randomly. However, in the amplitude spectra, especially at the outer cross-section and for higher angles of attack, humps are discernable, as shown in Fig. 11. (The spectra in Fig. 11 are smoother due to the longer integration time.) These humps may be due to almost periodic vortex shedding. They occur predominantly in the range of angles of attack $15^\circ < \bar{\alpha} < 35^\circ$ and are shifted inversely to lower frequencies as the incidence increases. In any case, the existence of amplitude spectra and their correlated power spectral densities (PSD) implies more or less randomly exciting airloads due to flow separation, the so-called buffet forces. Their effectiveness is closely tied to the interdependence between the local pressure fluctuations in space and time. A measure of their correlation is the so-called coherence function, which is restricted to values $0 < \Gamma < 1$.

Zero coherence signifies that two events are completely uncorrelated, whereas $\Gamma = 1$ means full correlation. For the buffeting problem, it follows that highly correlated unsteady pressures are the most effective ones. Fig. 12 shows a selected example of coherence functions along the indicated cross-section. The reference pressure transducer can be recognised by its total coherence. Obviously, the coherence decreases as the distance of the other transducers from the reference transducer increases. With the exception of the pressure transducers near the leading edge, all others show maximum coherence at about 40 Hz. Compare the respective amplitude spectra in Fig. 11! An overview of the coherence distributions and their magnitudes for different angles of attack can be seen in Fig. 7. A more sophisticated presentation can be found in Ref. 17. Nevertheless, it is interesting to note the manner in which the coherence on the suction surface is affected by the local flow phenomena in connection with the increasing angles of attack.

4.3 Unsteady Pressure Distributions on the Oscillating Wing.

With respect to the buffeting problem, the unsteady airloads due to the oscillatory motion of the wing are of great importance because the mathematical model of the buffeting phenomenon is strongly dependent on them. The first question is to what extent the unsteady pressures due to flow separation are influenced by the motion-induced pressures and vice versa. The answer indicates whether the airloads due to separation can be considered as external driving forces and whether the motion-induced pressures can be attributed solely to the oscillating airframe. Only if their mutual interference is negligibly small is the buffeting problem amenable to mathematical treatment. An inspection of Figs. 13 and 14 reveals that the oscillatory motion only has a little influence on the unsteady pressures due to flow separation because the peaks at the frequency of the forced oscillation scarcely alter the amplitude spectra in both cases. A further question concerns the aerodynamic damping on airframes oscillating in separated flows. While this damping can be calculated for attached flows, it can thusfar only be determined experimentally for separated flows. To this end, a digital vector component analysis was performed on the first harmonic of the motion induced pressures. A typical result can be seen in Fig. 15 - valid for the pressure surface at the indicated cross-section. At first glance, it becomes evident that the real as well as the imaginary parts are strongly stamped by the flow phenomena, as depicted in Fig. 7. The vortex positions are reflected in the respective pressure distributions. Throughout, the imaginary parts are larger than those for the steady mean angle of attack $\bar{\alpha} = 5^\circ$. An exception can be seen for $\bar{\alpha} = 10^\circ$, where the integral value may be smaller. In any case, the aerodynamic damping in separated flow can hardly be estimated on the basis of potential theory. More information on this point can be found in Refs. [11,12].

5. Conclusions

Experiments were performed to investigate the pressure distributions necessary for the buffeting prediction of a low aspect ratio trapezoidal wing. The main results of this investigation can be summarized as follows.

The steady mean pressure distribution is dependent on the mean angle of attack in such a way that for increasing incidences the flow separates first at the tip of the wing and extends subsequently over the complete suction surface of the wing. The development of the associated coupled vortex system leads finally to a lift force which is caused in almost equal parts by suction and pressure forces.

Flow separation produces on the suction surface stochastic pressure fluctuations of wide band frequency contents, which can have more or less periodic constituents. Their frequencies decrease inversely with the increasing angles of attack, predominantly in the range $15^\circ < \bar{\alpha} < 35^\circ$.

The coherence of these unsteady pressures - which is of great importance for the buffeting problem - is clearly affected by the local flow phenomena.

The unsteady pressures due to the oscillatory motions of the wing scarcely interfere with those resulting from flow separation and vice versa.

The damping airloads on oscillating airframes in separated flow are throughout higher than predicted by potential-theory except for special angles of attack.

Due to the complexity of the flow phenomena involved, the above results can be applied only to the configuration investigated.

Further investigations in this field have to take into account the transient flight maneuvers of full-scale aircraft.

6. Bibliography

- [1] Herbst, W.B.: *Future Fighter Technologies*. Journal of Aircraft, Vol. 17, No. 8, Aug. 1980, pp. 561-598.

- [2] Staudacher, W.: *Verbesserung der Manöverleistungen im hohen Unterschall*. DLR-Mitteilung 73-04 pp. 5-1 - 5-21, see also MBB-Report UFE-896-72 (Ö).
- [3] Baumert, W.: *Messungen am Prinzipmodell Flügel und Strake bei symmetrischer Anblasung*. DLR Internal Report, Göttingen, 1975.
- [4] Hoeimakers, H.W.M.; Vaastra, W.; Verhaagen, N.G.: *On the Vortex Flow over Delta and Double-Delta Wings*. NLR MP 82018U (1982).
- [5] Mabey, D.G.: *Some Aspects of Aircraft Dynamic Loads Due to Flow Separation*. AGARD R-750, 1987, pp. 1-25.
- [6] Jarrah, M.; Ashley, H.: *Impact of Flow Unsteadiness on Maneuvers and Loads of Agile Aircraft*. AIAA 89-1282.
- [7] Kramer, M.: *Die Zunahme des Maximalauftriebes von Tragflügeln bei plötzlicher Anstellwinkelvergrößerung (Böeneffekt)*. Zeitschrift für Flugtechnik und Motorluftschiffahrt (ZFM) 23 (1932) pp. 185-189.
- [8] Becker, J.: *Bewegungsinduzierte Luftkräfte bei abgelöster Strömung und ihre Übertragung auf die Ermittlung der Strukturresonanz*. Dissertation (Ph.D. Thesis) TU München, 1983.
- [9] Bublitz, P.: *Messung der instationären Drücke und Kräfte bei abgelösten Strömungen*. DGLR-Jahrbuch, 1979, pp. 073-1-073-44.
- [10] Bublitz, P.: *Measurement of the Unsteady Aerodynamic Loading on Wings at High Angles of Attack*. Proceedings of the Colloquium Honoring H.G. Küssner on the Occasion of His 80th Birthday. DLR-Institute for Aeroelasticity, 1980.
- [11] Försching, H.: *Unsteady Aerodynamic Forces on an Oscillating Wing at High Incidences and Flow Separation*. AGARD-Specialists' Meeting on Aircraft Dynamic Loads Due to Flow Separation. Sorrento, Italy, 1990.
- [12] Zingel, H.: *Experimental Investigation and Semi-Empirical Prediction of a Low Aspect Ratio Trapezoidal Wing Due to Flow Separation*. AGARD-Specialists' Meeting on Aircraft Dynamic Loads Due to Flow Separation. Sorrento, Italy, 1990.
- [13] Krumhaar, H.: *Zusammenfassender Bericht über neuere Untersuchungen zur Frage der Böenbelastungen von Flugzeugen*. Mitt. der MPI u. AVA, No. 21, 1958.
- [14] Liepmann, H.W.: *On the Application of Statistical Concepts to the Buffeting Problem*. Journal of the Aeronautical Sciences, Vol. 19, No. 12, Dec. 1952, pp. 793-800.
- [15] Zingel, H.: *On the Prediction of the Aeroelastic Behaviour of Lifting Systems Due to Flow Separation*. DGLR-Report 89-01.
- [16] Wedemeyer, E.: *Stable and Unstable Vortex Separation*. AGARD Conf. Proc. 247, 1979, pp. 13-1 - 13-10.
- [17] Försching, H.; Zingel, H.: *Motion-Induced Unsteady Airloads on an Oscillating Low-Aspect-Ratio Trapezoidal Half-Wing in Separated Flow*. Journ. of Fluids and Struct. Vol. 2, No. 6, Nov. 1988, pp. 515-539.

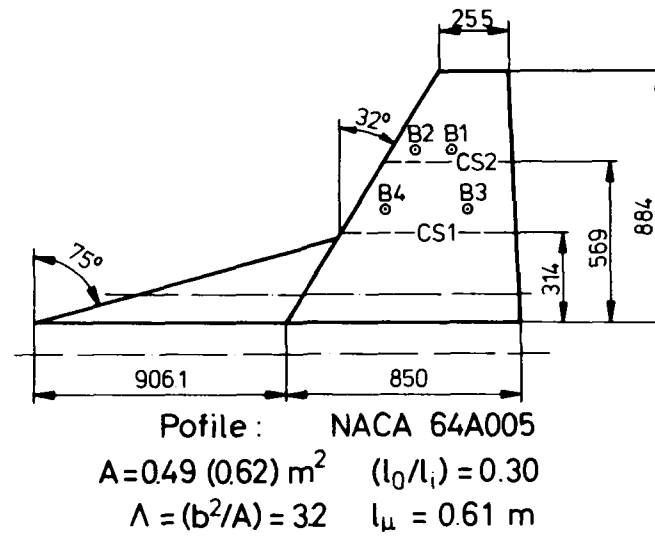


Figure 1. Geometry of the test wing.



Figure 2a. Wing with strake in the working cross-section of the 3x3 m² low-speed wind-tunnel.



Figure 2b. Basic trapezoidal wing in the working cross-section of the $3 \times 3 \text{ m}^2$ low-speed windtunnel.

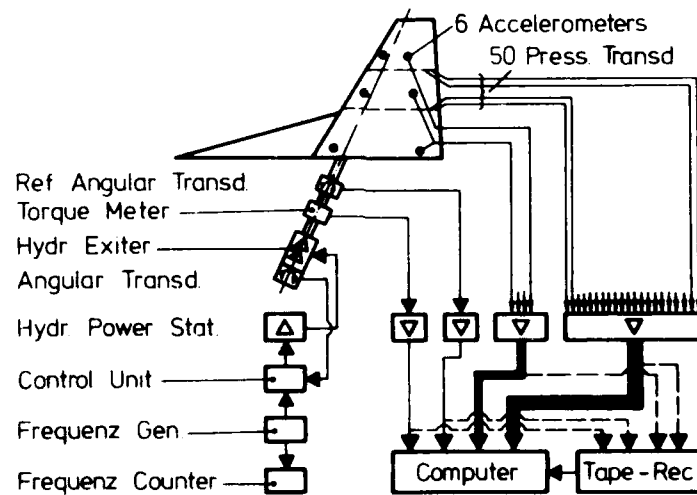


Figure 3. Schematic functional block diagram of the electronic equipment.

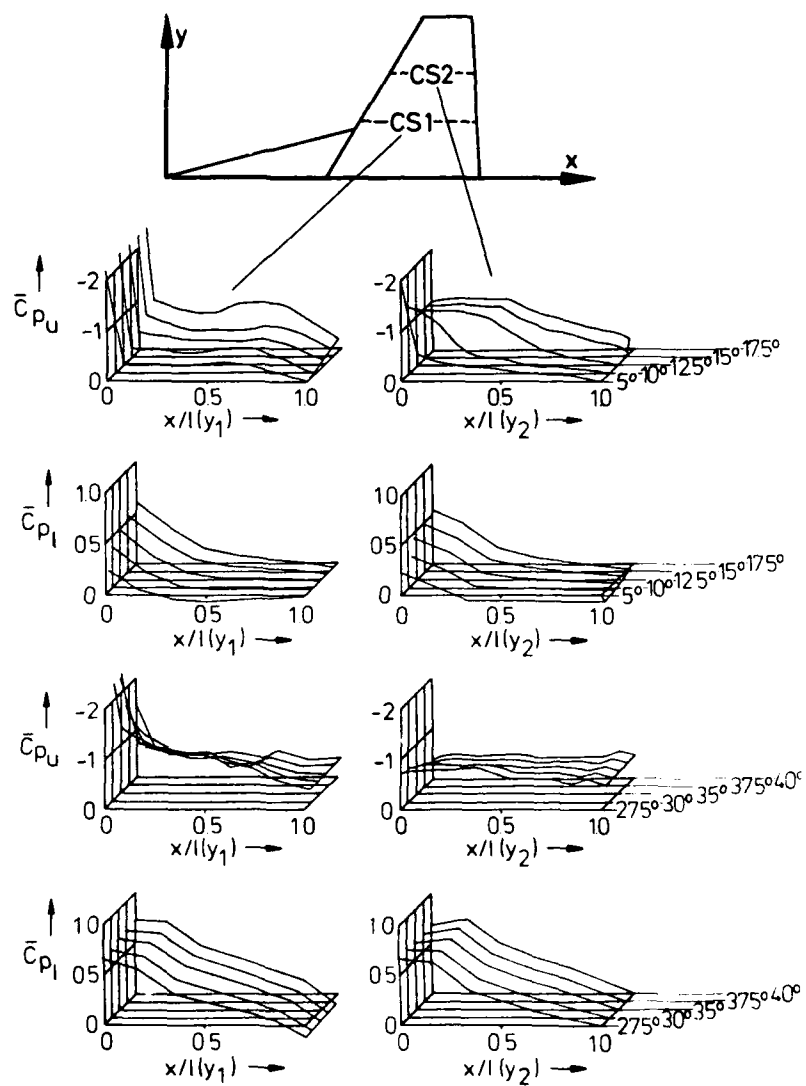


Figure 4. Steady mean pressure coefficients \bar{c}_p as functions of the angle of attack $\bar{\alpha}$ for the wing with strake, $Re = 2 \cdot 10^6$.

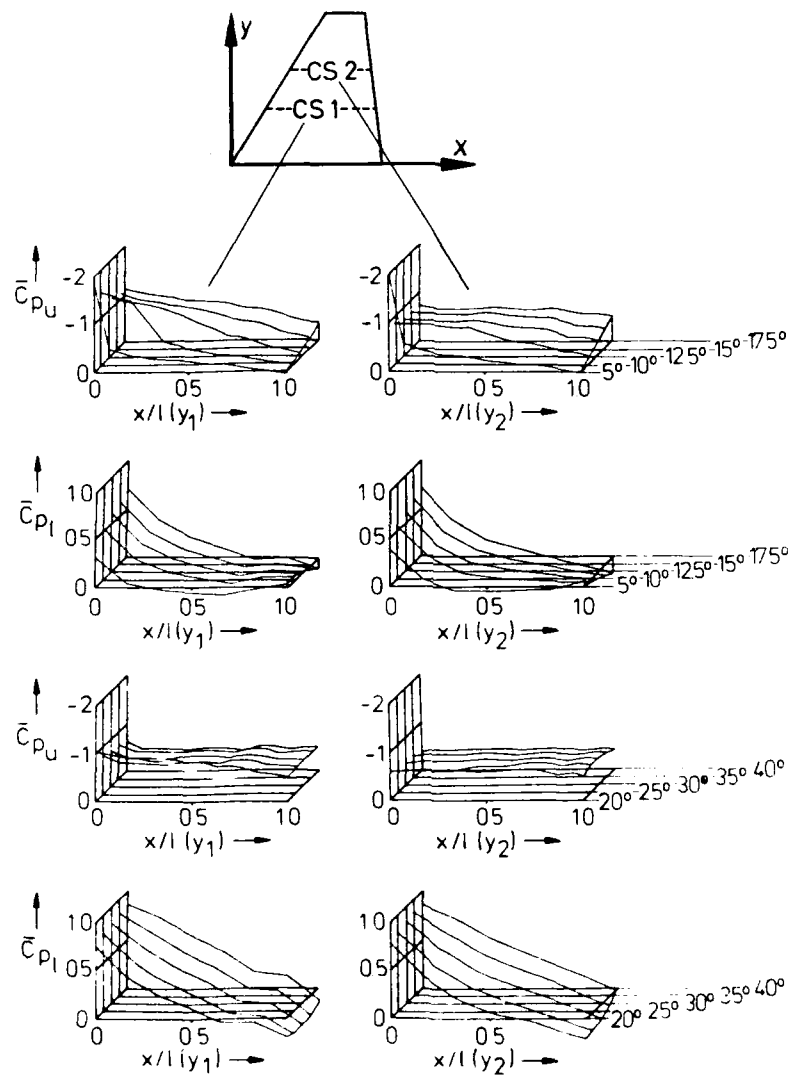


Figure 5. Steady mean pressure coefficients \bar{c}_p as functions of the angle of attack α for the wing without strake, $Re = 2 \cdot 10^6$.

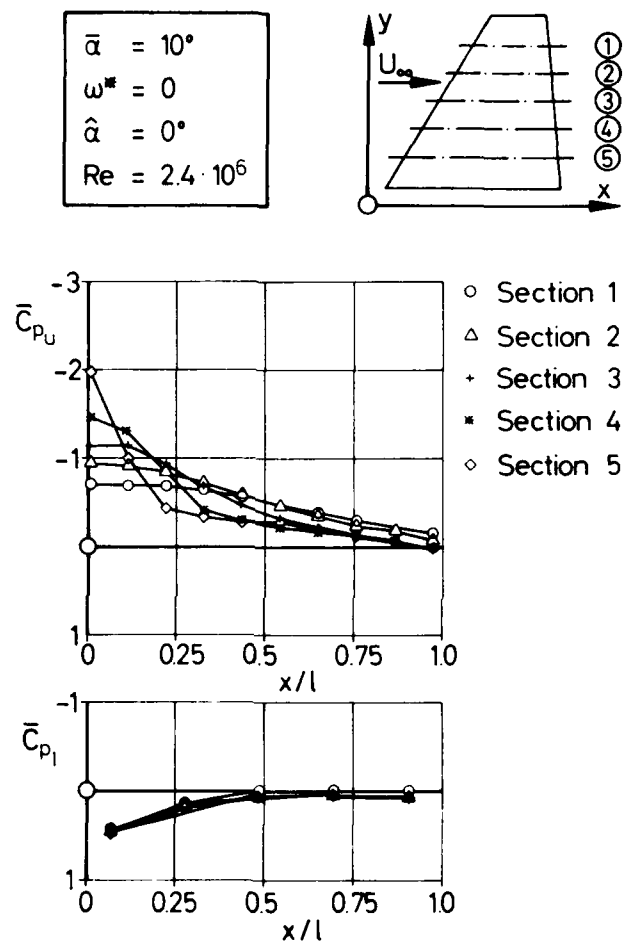


Figure 6. Steady mean pressure coefficients \bar{c}_p at $\bar{\alpha} = 10^\circ$, $Re = 2.4 \cdot 10^6$.

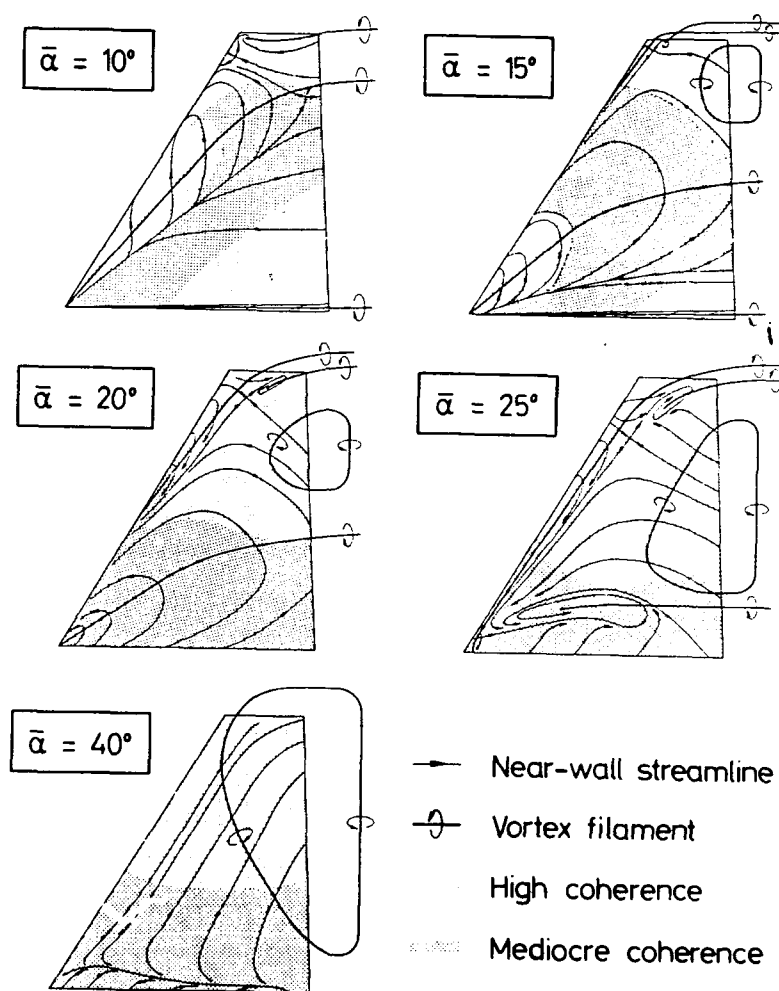


Figure 7. Phenomenological explanation of the flow characteristics on the suction surface of the wing for $Re = 2.4 \cdot 10^5$.

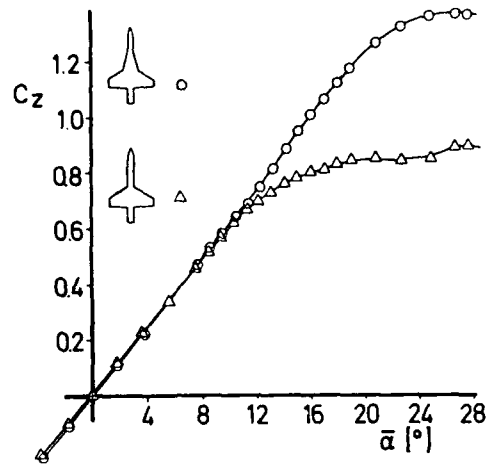


Figure 8. Lift coefficients c_l versus steady mean angle of attack $\bar{\alpha}$.
 \triangle wing without strake \circ wing with strake

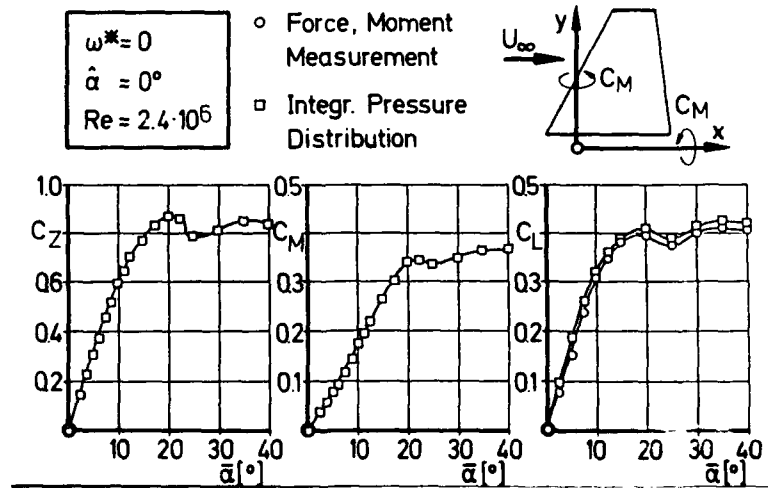


Figure 9. Normal force c_z , pitch c_m , roll c_l coefficients versus mean angle of attack $\bar{\alpha}$.

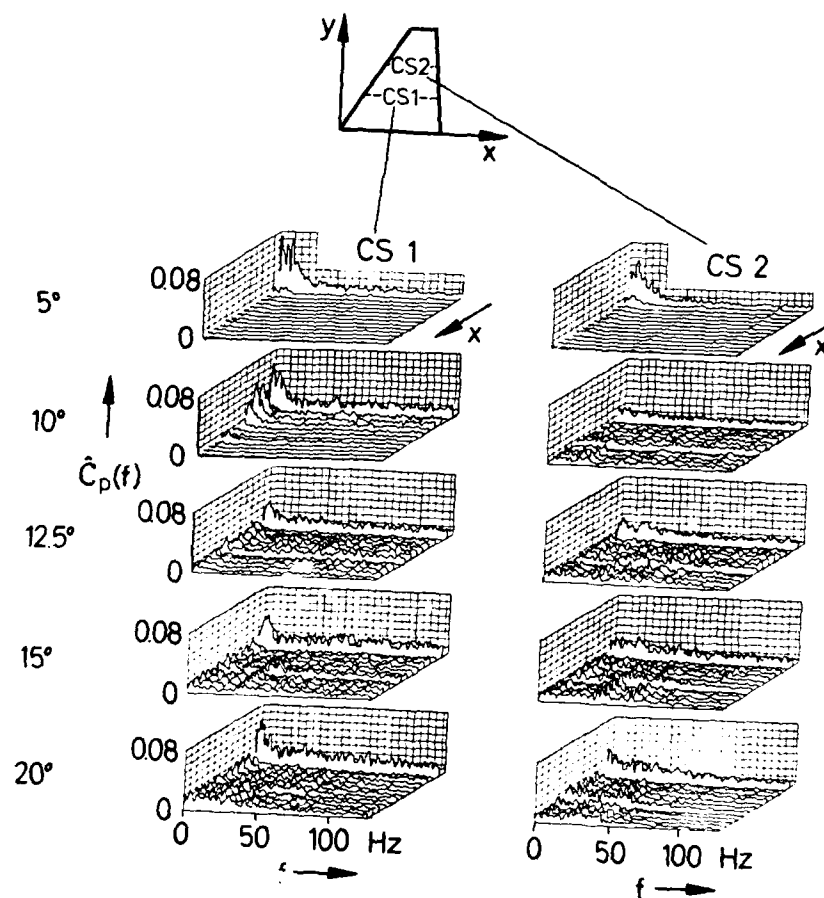


Figure 10.

Amplitude spectra $\hat{C}_p(f)$ of pressure fluctuations for stationary wing without strake as functions of $\bar{\alpha}$; $Re = 2 \cdot 10^6$.

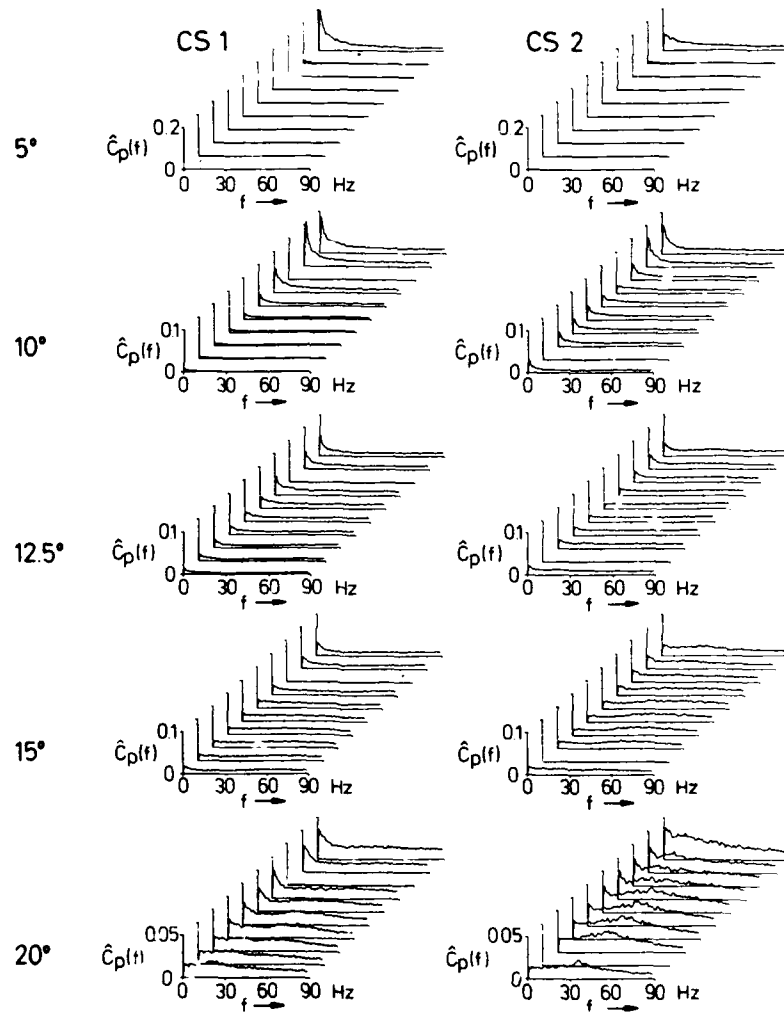


Figure 11. Amplitude spectra $\hat{c}_p(f)$ of pressure fluctuations for stationary wing without strake as functions of α ; $Re \approx 2.4 \cdot 10^5$; Test Phase 2.

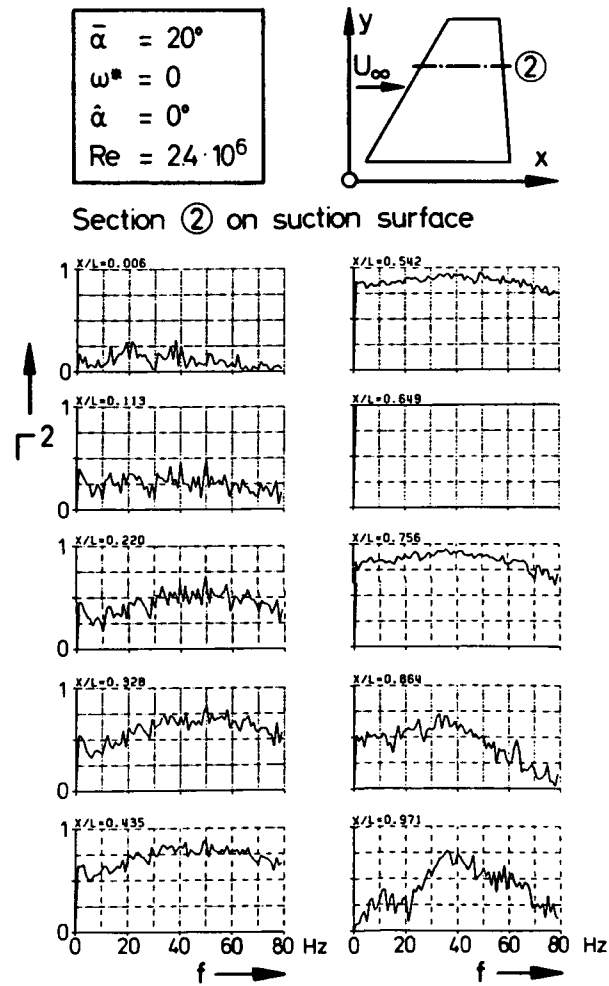


Figure 12. Coherence functions Γ^2 of the pressure fluctuations $\Gamma^2(f)$, cross-section ②
 $\bar{\alpha} = 20^\circ$; $Re = 2.4 \cdot 10^6$.

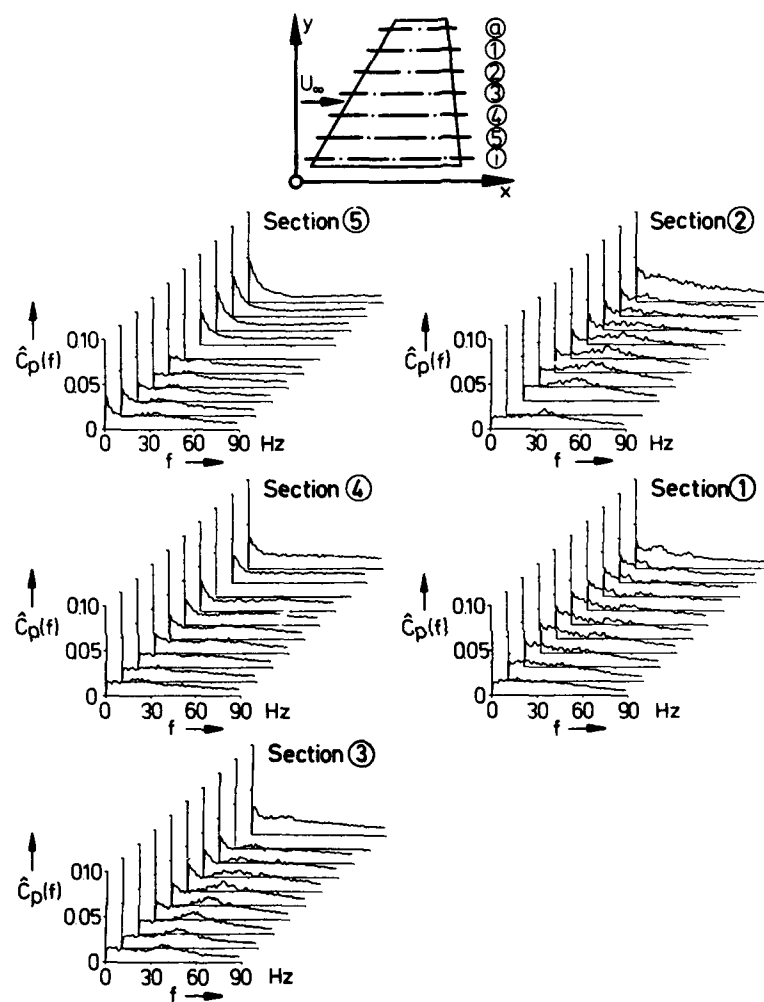


Figure 13.

Amplitude spectra $\hat{c}_p(f)$ on the suction surface of the stationary wing $\bar{x} = 20^\circ$ and for $Re = 2.4 \cdot 10^6$.

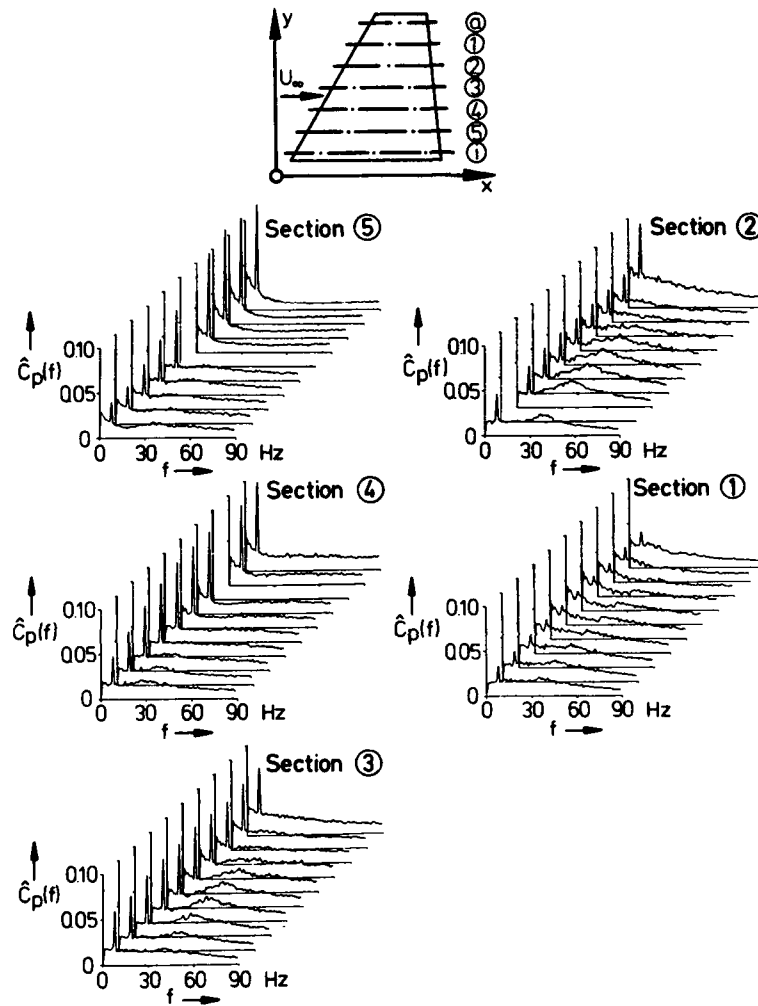


Figure 14. Amplitude spectra $\hat{c}_p(f)$ on the suction surface of the oscillating wing in pitch at $\bar{\alpha} = 20^\circ$ and for $Re = 2.4 \cdot 10^5$; $f = 8$ Hz; $\omega^* = 0.51$; $\bar{\alpha} = 1^\circ$.

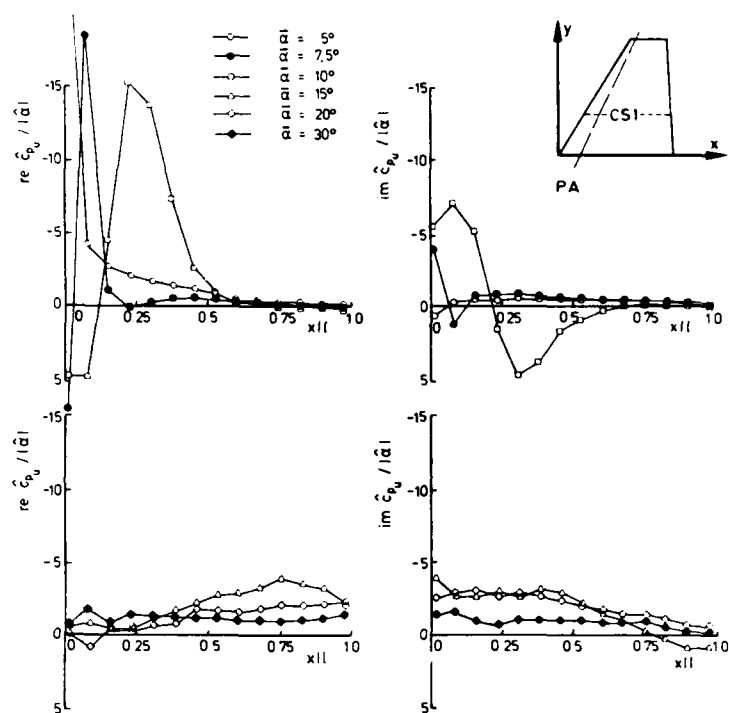


Figure 15a. Complex unsteady pressures induced by forced oscillations.
 $\text{Re} = 2 \cdot 10^6$; $\hat{\alpha} = 1^\circ$; $f = 4 \text{ Hz}$; $\omega^* = 0.3$

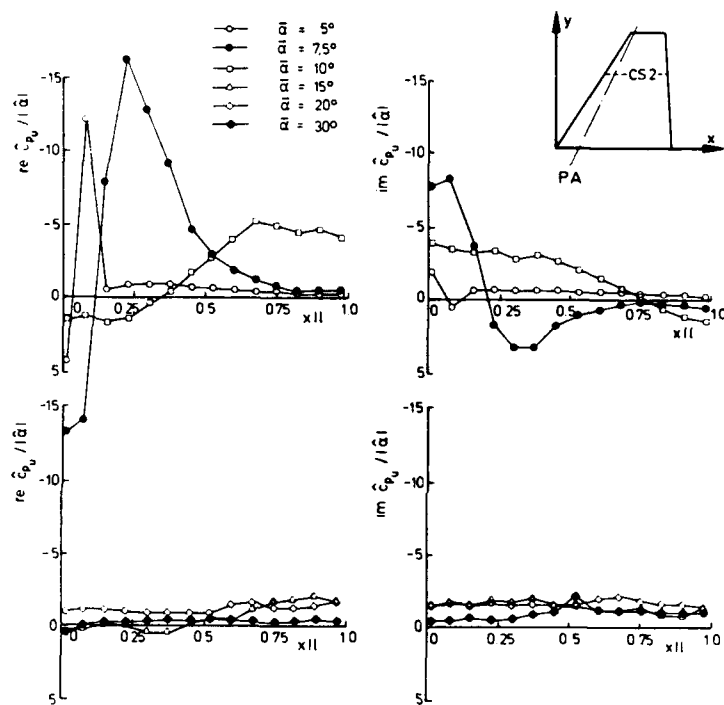


Figure 15b. Complex unsteady pressures induced by forced oscillations.
 $Re = 2 \cdot 10^6$; $\hat{\alpha} = 1^\circ$; $f = 4$ Hz; $\omega^* = 0.3$

EXPERIMENTAL INVESTIGATION AND SEMI-EMPIRICAL PREDICTION OF THE DYNAMIC RESPONSE OF A LOW-ASPECT-RATIO TRAPEZOIDAL WING DUE TO FLOW SEPARATION

by

H. Zingel
Deutsche Airbus GmbH
Huenefeldstr 1-5
D-2800 Bremen
Germany

Summary

The buffet response of a low-aspect-ratio trapezoidal half-wing model was measured in the low speed wind tunnel of the DLR-Research Center in Göttingen at different model natural frequencies of pitch and roll both separately and coupled and at different angles of incidence up to 40 degrees. On the basis of linear aeroelastic equations of motion and measured structural dynamic and unsteady aerodynamic input data, the buffet response was calculated and compared with the measurement. The comparison shows a satisfactory coincidence. Consequently the adopted way for the semi-empirical calculation of the buffet response proves to be practicable.

List of Symbols

a) Geometrical parameters

$e_n(P)$		Unity vector normal to the aircraft surface
l_i	[m]	Wing chord at the wing root
l_{μ}	[m]	Reference wing chord
O	[m ²]	Surface
S	[m ²]	Wing area
x, y, z	[m]	Cartesian co-ordinate system, see Figure 2
α_0		Steady state angle of incidence
λ		Wing taper
Λ		Wing aspect ratio
φ		Leading edge sweep angle

b) Elastomechanical parameters

$H_r(P, \omega)$	[1/N]	Vector of the transfer function of the r^{th} natural mode
$H_r^*(P, \omega)$	[1/N]	Vector of the conjugated complex transfer function
K_r	[Nm]	Generalized stiffness of r^{th} natural mode
M_r	[Nms ²]	Generalized mass of the r^{th} natural mode
$q_r(t)$		Generalized co-ordinate of the r^{th} natural mode
$S_u(P, \omega)$	[m ² s]	Diagonal matrix of the power spectral density of the displacement $u(P, t)$, see Equation (12)
$u(P, t)$	[m]	Vector of the displacement of the aircraft structure at the location $P(x, y, z)$
$\alpha(t)$		Pitch angle
$\hat{\alpha}$		Pitch angle amplitude
α_r		Pitch angle of the rigid body mode r
$\hat{\alpha}_{RMS}$		RMS value of the pitch angle
$\gamma(t)$		Roll angle
$\hat{\gamma}$		Roll angle amplitude
$\gamma_{d,r}$		Damping ratio of the r^{th} natural mode, elastomechanical constituent
$\gamma_{d,r,tot}$		Total damping ratio of the r^{th} natural mode
γ_r		Roll angle of the rigid body mode r

$\hat{\gamma}_{rms}$		RMS value of the roll angle
$\Phi_r(P)$	[m]	Vector form of the r^{th} natural mode shape
ω^*		Reduced frequency, see Equation (2)
ω_r	[1/s]	Natural circular frequency of the r^{th} natural mode

c) Aerodynamic parameters

A_{rs}	[Nm]	Aerodynamic force parameter, see Equations (5) and (6)
$c_l(t)$		Roll moment coefficient
$\hat{C}_{L,Y}^M$		Unsteady roll moment coefficient
$\hat{C}_{M,\alpha}^M$		Unsteady pitch moment coefficient
$C_z(t)$		Normal force coefficient
\hat{L}_α^M	[Nm]	Motion-induced roll moment of a harmonic pitch vibration
\hat{L}_Y^M	[Nm]	Motion-induced roll moment of a harmonic roll vibration
$\hat{M}_{\alpha,\alpha}^M$	[Nm]	Motion-induced pitch moment of a harmonic pitch vibration
$\hat{M}_{\alpha,Y}^M$	[Nm]	Motion-induced pitch moment of a harmonic roll vibration
$\hat{D}_s^M(P)$	[Pa]	Motion-induced pressure of the s^{th} natural mode at the location $P(x,y,z)$
$p^D(P,t)$	[Pa]	Pressure fluctuations, independent of motion, at the location $P(x,y,z)$
$Q_r^M(t)$	[Nm]	Generalized motion induced aerodynamic force of the r^{th} natural mode, see Equation (9)
$Q_r^D(t)$	[Nm]	Generalized aerodynamic driving force of the r^{th} natural mode, see, Equation (10)
Re		Reynolds number, see Equation (1)
$S_\alpha(\omega)$	[s]	Power spectral density of the pitch angle $\alpha(t)$
$S_\alpha^{**}(\omega^*)$		Non-dimensional power spectral density of the pitch angle $\alpha(t)$, see Equation (3)
$\underline{S}_p^D(P_1, P_2, \omega)$	[Pa ² s]	Diagonal matrix of the cross spectral density of the pressures $p^D(P_1, t)$ and $p^D(P_2, t)$
$S_{Q_r, r_s}(\omega)$	[N ² m ² s]	Cross spectral density of the generalized aerodynamic driving forces $Q_r^D(t)$ and $Q_{r_s}^D(t)$, see Equation (11)
U_∞	[m/s]	Free stream velocity
ν	[m ² /s]	Kinematic viscosity

d) Other parameters and symbols

f	[Hz]	Frequency
$im(\cdot)$		Imaginary part of a complex quantity
N		Number of natural modes
$re(\cdot)$		Real part of a complex quantity
t	[s]	Time
T	[s]	Integration time
ω	[1/s]	Circular frequency ($= 2\pi f$)

e) Indices

M	Motion-induced
---	----------------

D	Excitation, caused by separation
r	r th natural mode
RMS	RMS value
s	s th natural mode
α	Pitch vibration
γ	Roll vibration
$(\hat{\cdot})$	Amplitude value

1 Introduction

Separated flows cause vibrations of aircraft structures; these are referred to as buffeting. For transport aircraft the flight envelope is limited due to the buffet boundary, whereas fighter type aircraft have to operate at separated flow conditions beyond the buffet boundary, by which the manoeuvrability is increased (see for example W. B. Herbst [1]). The principle of the dynamic aircraft response due to flow separation is shown in Fig. 1, using some results of wind tunnel experiments on a low-aspect-ratio trapezoidal half-wing at subsonic speed. The normal force coefficient slope $-\partial C_N / \partial \alpha_0$ decreases when flow separation starts. At the same angle of incidence the roll moment fluctuations, expressed by their root mean square values $C_{L, \text{rms}}$, increase first smoothly, then more rapidly, due to the progress of the flow separation with increasing incidence. As a consequence of these roll moment fluctuations the wing responds with structural vibrations, which are expressed in this case by the roll angle response $\hat{\gamma}_{\text{rms}}$. More details of the wind tunnel test results will be discussed later in this paper.

One basic requirement to operate an aircraft beyond the buffet boundary is to know the intensity of buffeting, that is the aircraft vibration level due to buffet loads. For that a large number of methods have been developed, which vary widely in terms of accuracy and the effort required. D.G. Mabey [2] determines the bending moment at the wing root of a conventional wind tunnel model by wind tunnel tests and thus draws a qualitative conclusion on the structural vibrations of the corresponding aircraft. P.W. Hanson [3] determines the structural vibrations due to flow separations on a dynamically scaled wind tunnel model. Although this method is very accurate, it requires complicated model construction and is therefore very expensive. Of great practical importance is a calculation method for determining the structural vibrations due to flow separation. But it will be not possible in the foreseeable future to calculate the unsteady aerodynamic forces on an aircraft at separated flow. For this reason, semi-empirical methods of calculation have been developed. In these methods, unsteady aerodynamic loads measured on conventional wind tunnel models are introduced into aeroelastic equations of motion. This work is summarized by H. Försching [4], [5].

At DLR-Research Center in Göttingen an extensive test program recently had been carried out on a low-aspect-ratio trapezoidal half-wing at subsonic speed. Measured were

- o the pressure fluctuations due to flow separation on the whole wing surface simultaneously, which gave the buffet forces,
- o the unsteady motion-dependent pressures on the harmonically oscillating model, which gave the aerodynamic stiffness and damping,
- o the structural vibration response (buffet response) of the wind tunnel model, which was elastically supported in the wind tunnel.

These test results were summarized by H. Zingel [6]. A more detailed discussion of the problems and results will be given in this Specialists' Meeting by P. Bublit [7] and H. Försching [8], who deal with the test results on the aerodynamic point of view, whereas in this paper some details of the measured buffet response of the wind tunnel model will be discussed. Moreover, on the basis of linear aeroelastic equations of motion and the measured buffet forces and motion-induced airloads, semi-empirical calculations of the buffet response have been carried out, both for the case of a single degree of freedom vibration in pitch and roll and for the case of a two degrees of freedom vibration in pitch and roll. The semi-empirical calculation will be compared with the measured buffet response.

2 Experimental Determination of the Dynamic Aeroelastic Response Behaviour

2.1 Test Arrangement

In a wind tunnel experiment the dynamic aeroelastic response of a low-aspect-ratio trapezoidal half-wing was measured at subsonic speed in the Göttingen 3mx3m low speed wind tunnel. Maximum Reynolds number was

$$Re = \frac{U_\infty l_\mu}{\nu} = 2.4 \cdot 10^6. \quad (1)$$

The main objective of these experiments was to provide measured dynamic response amplitudes which can be used for assessing a dynamic response calculation. In addition, the test results provide insights into the way in which the dynamic response of the model depends on structural dynamic and aerodynamic parameters.

The wind tunnel model and the test arrangement are shown in Fig. 2. The model was manufactured as an integral unit in aluminium alloy. This gives a high level stiffness and a low model weight so that the natural frequencies of the model are high and outside the frequency range investigated (below 20 Hz). The wind tunnel model is elastically restrained by leaf springs in such a way that it can execute pitch and roll vibrations - either separately or coupled. The spring parameters can be varied by means of movable supports and exchangeable leaf springs so that the natural frequencies of the wing/suspension system can be changed in the range of 4 Hz < f < 16 Hz, that is the reduced frequency range of $0.25 < \omega^* < 1.02$ with

$$\omega^* = \frac{2\pi f l_w}{U_\infty} \quad (2)$$

In analysing the investigations, the main concern is the structural deflection in the pitch $a(t)$ and roll $y(t)$ rigid body motion. These are converted into non-dimensional power spectral densities

$$S_a^*(\omega^*) = \frac{U_\infty}{l_w} S_a(\omega^*) \quad (3)$$

and non-dimensional amplitude spectra

$$\hat{a}(\omega^*) = \sqrt{\frac{1}{\pi} S_a^*(\omega^*) \Delta\omega^*} \quad (4)$$

$S_a(\omega^*)$ is the power spectral density of $a(t)$ and $\Delta\omega^*$ is a function of the signal length T that was analysed, referring to Shannons theorem (see for example J.S. Bendat, A.G. Piersol [9]).

A ground resonance test was carried out on the test arrangement described. Fig. 3 shows as a typical example the natural vibration modes of a configuration with the natural frequencies $f_a = 16.1$ Hz, that is the pitch mode, and $f_y = 7.8$ Hz, that is the roll mode. The pitch mode has a pronounced part of roll motion which gives a nodal line leaving the wing at the trailing edge, whereas the roll mode is nearly a pure roll motion. The portion of roll motion in the pitch mode and vice versa the portion of pitch motion in the roll mode is directly correlated to the vicinity of the natural frequencies. The location of the nodal line is correlated to the relation of the natural frequencies. That means, in the case of a larger roll frequency related to the pitch frequency, the nodal line of the pitch mode will leave the wing at the leading edge, opposite to the case shown in Fig. 3. (For more details see H. Zingel [5]).

2.2 Wind Tunnel Test Results

An example of the wind tunnel experiments is shown in Fig. 4 with the amplitude spectra of the dynamic pitch response $a(\omega^*)$ for the configuration with the natural frequencies $f_a = 16.1$ Hz and $f_y = 7.8$ Hz (corresponding to the reduced frequencies 1.02 and 0.49). The angle of incidence is varied in the range between 0° and 40°. The amplitude spectra are characterised by a marked peak at the resonance frequency of the pitch vibration mode and a smaller peak at the resonance frequency of the roll vibration mode. The narrow peak at the resonance frequency of the pitch vibration mode indicates weak damping, whereas the wide peak at the resonance frequency of the roll vibration mode indicates a high level of damping. An increase in the resonance peaks is found up to an incidence of about 20°. Above this angle, the pitch angle amplitudes decrease.

The RMS-values of the dynamic pitch response $\hat{a}_{1, RMS}$ in the pitch mode (index 1 always corresponds to the pitch mode whereas index 2 always corresponds to the roll mode) considered in Fig. 4, are plotted in Fig. 5 as a function of the angle of incidence α_0 . The RMS values are formed over the frequency range in the vicinity of the resonance frequency over a band of $\Delta\omega^* = 0.127$ (corresponding to $\Delta f = 2$ Hz). In order to obtain amplitude values, the results are multiplied by $\sqrt{2}$. Fig. 5 shows that the RMS values of the pitch response $\hat{a}_{1, RMS}$ increase when the flow separation starts at an incidence of 5°. The pitch response reaches a maximum at an incidence of 20° and then decreases again to almost the level found at attached flow.

The dependence of the RMS values of dynamic response on incidence is in the same manner as the aerodynamic force fluctuations, as shown in Fig. 1 for the dynamic roll response $\hat{y}_{1, RMS}$ and the roll moment fluctuations $\hat{C}_{l, RMS}$. From the practical point of view the results in Fig. 5 means that an aircraft is excited to strong structural vibrations when it flies at maximum lift (compare Fig. 1). Beyond maximum lift, the structural vibrations due to flow separation are relatively small.

The RMS values of the pitch angle fluctuations $\hat{a}_{1, RMS}$ for a pure pitch mode with the natural frequency of $f_a = 16.1$ Hz are also plotted in Fig. 5. These are generally smaller

than the RMS values of the pitch angle fluctuations for the previously considered coupled configuration. Coupling of pitch and roll vibration in this case leads to an increase in the dynamic pitch response. Furthermore, the RMS values of the pitch response $\hat{q}_{1,RMS}$ of a configuration with the natural frequencies $f_0 = 15.4$ Hz and $f_1 = 10.7$ Hz are plotted in Fig. 5. In this case, the RMS values of the dynamic pitch response $\hat{q}_{1,RMS}$ are even larger than in the case of the configuration with $f_0 = 16.1$ Hz and $f_1 = 7.8$ Hz.

The coupling of the pitch and roll vibrations in the natural modes is more pronounced, indicated by a nodal line leaving the trailing edge of the wing more near the wing root. This is due to the fact that the natural frequencies are closer together.

The RMS values of the roll angle fluctuation $\hat{\gamma}_{2,RMS}$ of some configurations are considered in Fig. 6 as a function of incidence. In the case of the pure roll vibration with $f_1 = 12$ Hz ($\omega^* = 0.76$), the RMS value of the roll angle $\hat{\gamma}_{2,RMS}$ increases slowly at first when flow separation begins (at angles of incidence above 5°) and then increases more rapidly at larger incidences (in excess of 10°). After reaching a maximum at an incidence of 20° , the RMS value of the roll angle drops again to approximately attached flow level, similar to the pitch response in Fig. 5.

If the conditions of the suspension are selected in such a way that pitch vibration is possible in addition to roll vibration, then - if the pitch natural frequency is smaller than the roll natural frequency ($f_0 = 8.1$ Hz and $f_1 = 11.5$ Hz) - larger vibration amplitudes are achieved over the whole incidence range than are obtained in the case of an uncoupled roll vibration. If, on the other hand, the pitch natural frequency is larger than the roll natural frequency ($f_0 = 15.4$ Hz and $f_1 = 10.7$ Hz) the RMS values of the roll response $\hat{\gamma}_{2,RMS}$ are substantially smaller than in the case of an uncoupled roll vibration.

It can be concluded that the response amplitudes of the pitch vibration increases, if the nodal line of the pitch mode is leaving the wing surface at the wing trailing edge. This is the same for the roll response in the roll vibration mode. This response behaviour is directly correlated with the aerodynamic damping. In the case of a nodal line leaving the wing surface over the wing trailing edge, the rotation angle ratio α/γ becomes negative (compare Fig. 3). This gives a reduction of the total aerodynamic damping, expressed by the imaginary part of the unsteady aerodynamic force parameter

$$A_{rs} = \int \int_{(0)} \Phi_r^T(P) p_s^M \underline{e}_n(P) dO; \quad r = 1, 2, \dots, N; \quad s = 1, 2, \dots, N \quad (5)$$

in the general formulation and

$$A_{rs} = \alpha_r \alpha_s \dot{M}_{25,r}^M + \alpha_r \gamma_s \dot{M}_{25,\gamma}^M + \gamma_r \alpha_s \dot{L}_\alpha^M + \gamma_r \gamma_s \dot{L}_\gamma^M; \quad r = 1, 2; \quad s = 1, 2 \quad (6)$$

in the formulation for the special case considered. $\Phi_r(P)$ is the r^{th} natural vibration mode, $p_s^M(P)$ is the motion-induced pressure at the location $P(x, y, z)$ on the surface of the structure considered, caused by a vibration with the s^{th} natural vibration mode. $\underline{e}_n(P)$ is the unity vector normal to the surface. \dot{M}_{25}^M is the pitch moment and \dot{L}^M is the roll moment.

3 Semi-Empirical Calculation of the Dynamic Aeroelastic Response Behaviour

3.1 Equations of Motion

It is generally accepted to describe the dynamic response problem due to flow separation applying the so-called linear forced oscillation approach, which is shown schematically in Fig. 7. The aerodynamic forces are sub-divided into forces induced by motion and those induced by flow separation. The aerodynamic forces caused by flow separation act as driving forces and lead to structural vibrations. It will be assumed, that this vibrations, if they are small, do not affect the driving forces. Additionally it will be assumed that there is a linear relationship between the motion-induced aerodynamic forces and the aircraft vibration. The validity of these assumptions was already shown by H. Zingel [6] and by P. Bublitz [7] and H. Försching [8] in their contributions to this Specialists' Meeting.

It is common practice to analyse dynamic aeroelastic problems by using modal parameters and generalized co-ordinates. The displacement vector $\underline{u}(P, t)$ of an aircraft structure will be represented by superimposing the N vibration modes $\Phi_r(P)$:

$$\underline{u}(P, t) = \sum_{r=1}^N \Phi_r(P) q_r(t) \quad (7)$$

In this, $q_r(t)$ is the generalized co-ordinate of the r^{th} vibration mode. A system of linear differential equations of motion will be formulated:

$$M_r \ddot{q}_r(t) + \gamma_{d,r} \omega_r M_r \dot{q}_r(t) + K_r q_r(t) - Q_r^M(t) = Q_r^D(t); \quad r = 1, 2, \dots, N. \quad (8)$$

In this expression, M_r is the generalized mass of the r^{th} vibration mode, $\gamma_{d,r}$ is the damping ratio of the r^{th} vibration mode and K_r is the generalized stiffness. The system of equations, Equation (8), is coupled by the generalized motion-dependent aerodynamic forces $Q_r^M(t)$. These are obtained by superimposing the unsteady aerodynamic force parameters $A_{r,n}$, as described by Equation (5), using

$$Q_r^M(t) = \sum_{n=1}^N A_{r,n} q_n(t); \quad r = 1, 2, \dots, N. \quad (9)$$

Formally, the definition of the generalized aerodynamic driving forces $Q_r^D(t)$ is entirely analogous:

$$Q_r^D(t) = \int \int \int_{(0)} \Phi_r^T(P) p^D(P, t) \Phi_n(P) dO; \quad r = 1, 2, \dots, N. \quad (10)$$

$p^D(P, t)$ is the pressure caused by flow separation at the location $P(x, y, z)$ on the surface of the aircraft. These pressures are stochastic quantities and thus have to be treated by statistical means (see for example J.S. Bendat, A.G. Piersol [9]). A cross spectral density of the generalized driving force is formed in a manner analogous to the generalized excitation in Equation (10):

$$S_{Q_{rs}}(\omega) = \int \int \int_{(0)} \int \int_{(0)} \Phi_r^T(P_1) S_{pD}(P_1, P_2, \omega) \Phi_s(P_2) dO dO; \quad r = 1, 2, \dots, N; \quad s = 1, 2, \dots, N. \quad (11)$$

In this $S_{pD}(P_1, P_2, \omega)$ is the matrix of the cross spectral density of the pressure signals $p^D(P_1, t) \Phi_n(P_1)$ and $p^D(P_2, t) \Phi_n(P_2)$. The dynamic response problem is now formulated by means of the so-called input-output relation

$$\underline{S}_n(P, \omega) = \sum_{r=1}^N \sum_{s=1}^N \underline{H}_r^*(P, \omega) \underline{H}_s^T(P, \omega) S_{Q_{rs}}(\omega) \quad (12)$$

In this, $\underline{S}_n(P, \omega)$ is the diagonal matrix of the power spectral density of a deflection $\underline{u}(P, t)$ of the aircraft structure considered at the location $P(x, y, z)$. $\underline{H}_r(P, \omega)$ is the transfer function of the r^{th} vibration mode, which can be determined from Equation (8).

Equation (12) is the fundamental equation for the semi-empirical calculation of the aeroelastic structural response, which will be used on the wind tunnel model considered in Section 2, this having two degrees of freedom. An equation for the power spectral density $S_a(\omega)$ of the pitch angle fluctuations $\alpha(t)$ and for the power spectral density $S_\gamma(\omega)$ of the roll angle fluctuations $\gamma(t)$ is obtained. The aerodynamic data necessary to perform a dynamic response calculation were measured in a wind tunnel test on the same model described in Section 2. The measurement procedure and test results are described by H. Zingel [6] and will be presented and discussed by P. Bubltz [7] and H. Försching [8] in their contributions to this Specialists' Meeting. The structure dynamic parameters of the wind tunnel model were measured in a ground vibration test as described in Section 2.

3.2 Results of the Calculation

3.2.1 One Degree of Freedom Configurations

In the following the results of the semi-empirical calculation of the dynamic wind tunnel model response will be discussed and compared with the measurements described in Section 2. First the wind tunnel model oscillating in one degree of freedom will be considered. Fig. 8 shows the spectra of the pitch angle response amplitudes $\hat{\alpha}(\omega^*)$ of the wind tunnel model with the natural frequency $\omega_n^* = 0.76$ for selected incidences $\alpha_0 = 0^\circ$; 10° ; 20° ; and 40° . The comparison of measurement and calculation shows a good coincidence. The calculation gives larger amplitudes in the region of the resonance frequency.

The RMS values $\hat{\alpha}_{\text{RMS}}$ for the case considered in Fig. 8 are plotted against the incidence α_0 in Fig. 9. Measured and calculated pitch response values agree well. Differences between measurement and calculation are relatively large at large angles of incidence in excess of 30° . Also plotted in Fig. 9 is the roll angle response $\hat{\gamma}_{\text{RMS}}(\alpha_0)$ for the wing model with the natural roll frequency $\omega_{\gamma}^* = 0.76$. The comparison of measurement and

calculation is very similar to the case of the pitch response. The calculated roll angle response $\hat{\gamma}_{\text{res}}$ is larger than the measurement at very low angles of incidence at attached flow conditions.

In order to indicate the influence exerted by the aerodynamic stiffness or inertia and the aerodynamic damping, when compared with the corresponding structural dynamic terms, the resonance frequencies $f_{a,R}$ and $f_{y,R}$ and the total damping ratios $\gamma_{a,a,\text{tot}}$ and $\gamma_{a,y,\text{tot}}$, together with the corresponding structural dynamic parameters f_a , f_y and $\gamma_{a,a}$, $\gamma_{a,y}$ are plotted in Fig. 10 against the angle of incidence α_0 for a pitch vibration with $\omega_a^* = 0.51$ and a roll vibration with $\omega_y^* = 0.51$. In the case of the pitch vibration the motion-dependent unsteady aerodynamic forces lead to a resonance frequency $f_{a,R}$ which is somewhat larger than the natural frequency f_a . That means, the motion-induced unsteady aerodynamic forces act as aerodynamic stiffness. In the case of the roll vibration, the unsteady motion-induced aerodynamic forces act as inertia forces and reduce the resonance frequency $f_{y,R}$ relative to the natural frequency f_y . In the lower part of the diagram, the total damping ratios $\gamma_{a,a,\text{tot}}$ and $\gamma_{a,y,\text{tot}}$ are plotted against the incidence α_0 . The aerodynamic constituent of the system damping far outweighs the structural dynamics damping constituents $\gamma_{a,a}$ and $\gamma_{a,y}$.

In Fig. 11 the motion induced pitch moment coefficients $\text{re } \hat{C}_{M,a}^M$ and $\text{im } \hat{C}_{M,a}^M$ and the roll moment coefficients $\text{re } \hat{C}_{M,y}^M$ and $\text{im } \hat{C}_{M,y}^M$ are plotted against the incidence α_0 for the cases $\omega_a^* = 0.51$ and $\omega_y^* = 0.51$. The curves of the real parts of the pitch and roll moment coefficients corresponds to the curves of the resonance frequencies $f_{a,R}$ and $f_{y,R}$ in Fig. 10 including the different signs. Also the curves of the imaginary parts of the pitch and roll moment coefficients corresponds to the damping curves in Fig. 10.

3.2.2 Two Degrees of Freedom Configurations

The calculated dynamic structural response of the two degrees of freedom configurations will be considered below and compared with the measurements from Section 2. The spectra of the pitch angle amplitudes $\hat{\alpha}(\omega^*)$ for the configuration with the natural frequencies of $f_a = 16.1$ Hz and $f_y = 7.8$ Hz are shown in Fig. 12 for various angles of incidence. Calculation produces larger amplitudes than measurement for all incidences at the frequency of the pitch mode. The pitch amplitudes from measurement and calculation agree well at the frequency of the roll mode, but the measurement shows a frequency shift, particularly at large angles of incidence, which does not appear from the calculation. It appears unlikely that the aerodynamic stiffness term can be responsible for a shift in the resonance frequency of the order of the value determined. The reason for the frequency shift can be associated with a change in the model suspension stiffness due to the appearance of aerodynamic forces.

The RMS values of the pitch angle amplitudes $\hat{\alpha}_{1,\text{RMS}}$ and $\hat{\alpha}_{2,\text{RMS}}$ are plotted against the angle of incidence α_0 in Fig. 13 for the same configuration. As already has been shown in Fig. 12, the calculation gives larger amplitudes in the resonance frequency of the pitch mode for all angles of incidence. Measurement always gives larger amplitudes than calculation in the roll mode.

Fig. 14 shows the RMS values of the roll angle fluctuation $\hat{\gamma}_{1,\text{RMS}}$ and $\hat{\gamma}_{2,\text{RMS}}$ against the angle of incidence α_0 . The calculation produces larger values than measurement in both the pitch and the roll vibration modes. The discrepancy between measurement and calculation in the roll mode is approximately the same as that of the one degree of freedom case in Fig. 9.

The resonance frequencies $f_{a,R}$ and $f_{y,R}$ and the total damping ratios $\gamma_{a,a,\text{tot}}$ and $\gamma_{a,y,\text{tot}}$ are plotted against the angle of incidence in Fig. 15 for the configuration considered before. The resonance frequency $f_{a,R}$ only changes slightly relative to the natural frequency of the elastomechanical system f_a . The total damping ratio $\gamma_{a,a,\text{tot}}$ is very small relative to the pure pitch vibration (see Fig. 10). In the incidence range between 10° and 25° , the total damping ratio $\gamma_{a,a,\text{tot}}$ is smaller than the damping ratio of the elastomechanical system $\gamma_{a,a}$. This means that the unsteady motion-induced aerodynamic forces no longer have a damping effect in this range of incidence but act, in fact, against the damping. Superimposing the roll vibration on the pitch vibration has in this case the effect that the unsteady motion-induced aerodynamic forces resulting from the coupling reduce the aerodynamic damping and, in fact, cause a change in sign of the aerodynamic damping term. These relationships have already been discussed when considering the measured dynamic response in Section 2 and are here confirmed by consideration of the damping.

The resonance frequency $f_{y,R}$ and the total damping ratio $\gamma_{a,y,\text{tot}}$ of the roll vibration mode are approximately equal to that of the one degree of freedom comparative case in Fig. 10, because the vibration mode of the two degrees of freedom system has only a small pitch vibration superimposed on the roll vibration (see Fig. 3).

4 Conclusion and Outlook

The buffet response of a low-aspect-ratio trapezoidal half-wing was measured in the low speed wind tunnel of the DLR-Research Center in Göttingen. The maximum structural vibrations occurred just at the angle of incidence of maximum lift. Beyond the maximum lift, in the post-stall range, the structural vibrations are relatively small. The coupling of pitch and roll vibrations had a quite substantial influence on the amplitu-

des of the buffet response.

A calculation of the wind tunnel model buffet response was carried out on the basis of linear aeroelastic equations of motion. All the necessary input data were derived experimentally. The structural dynamic quantities of the wind tunnel model were derived in a ground vibration test, the aerodynamic driving forces were measured on the wind tunnel model at steady incidence and the motion-induced unsteady airloads were measured on the harmonically oscillating wing. The buffet response was calculated for one and two degrees of freedom and shows in general a satisfactory coincidence with the measured buffet response. Consequently the adopted way for the semi-empirical calculation of the buffet response proves to be practicable.

Differences between calculated and measured buffet response are due to inaccuracies of the measured structural dynamic quantities, the measured unsteady airloads and the measured buffet response. Additional uncertainties came from the approximations of the linear forced oscillation model approach.

Improvements seem to be possible in a more expended instrumentation of the wind tunnel model to have a better approximation of the distribution of both the motion-induced airloads and driving airloads due to flow separation. Further wind tunnel experiments seem to be usefull to investigate the applicability of the presented semi-empirical buffet response calculation procedure on the more practical relevant high subsonic and transonic flow region on fighter type aircraft just as on transport aircraft.

5 References

- [1] Herbst, W.B.: Future Fighter Technologies. J. Aircraft 17 (1980) 8, 561-566.
- [2] Mabey, D.G.: An Hypothesis for the Prediction of Wing Buffeting from Dynamic Tests on Wind Tunnel Models. RAE TR 70-189 (1970).
- [3] Hanson, P.W.: Evaluation of an Aeroelastic Technique for Predicting Airplane Buffet Loads. NASA TN D-7066 (1973).
- [4] Försching, H.: Aeroelastic Buffeting Prediction Techniques - A General Review. VKI Lecture Series 1981-4, 1981; published as DFVLR-FB 81-15 (1981).
- [5] Försching, H.: Aeroelasticity at Separated Flow. Concepts and Prospects. In: International Symp. on Aeroelasticity. DGLR-Report 82-01 (1982), pp 1-10.
- [6] Zingel, H.: Zur Bestimmung des aeroelastischen Verhaltens von Auftriebssystemen infolge von Strömungsablösung. DFVLR-FB 86-35 (1986). On the Prediction of the Aeroelastic Behaviour of Lifting Systems due to Flow Separation. ESA-TT-1042 (1987).
- [7] Bublitz, P., Zingel, H.: Experimental Investigation of Buffet Excitation Forces on a Low Aspect Ratio Trapezoidal Half-Wing in Incompressible Flow. AGARD Specialists' Meeting on Aircraft Dynamic Loads Due to Flow Separation, Sorrento, Italy, 1-6 April 1990.
- [8] Försching, H.W.: Motion-Induced Unsteady Airloads in Separated Flow. AGARD Specialists' Meeting on Aircraft Dynamic Loads Due to Flow Separation, Sorrento, Italy, 1-6 April 1990.
- [9] Bendat, J.S., Piersol, A.G.: Random Data: Analysis and Measurement Procedures. New York: Wiley Interscience, 1971.

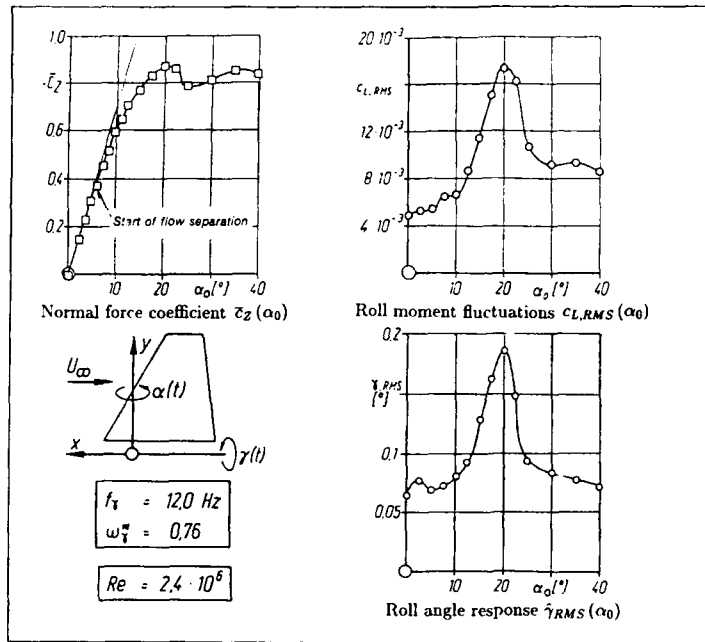


Fig.1: Principle of dynamic response due to flow separation (*buffeting*)

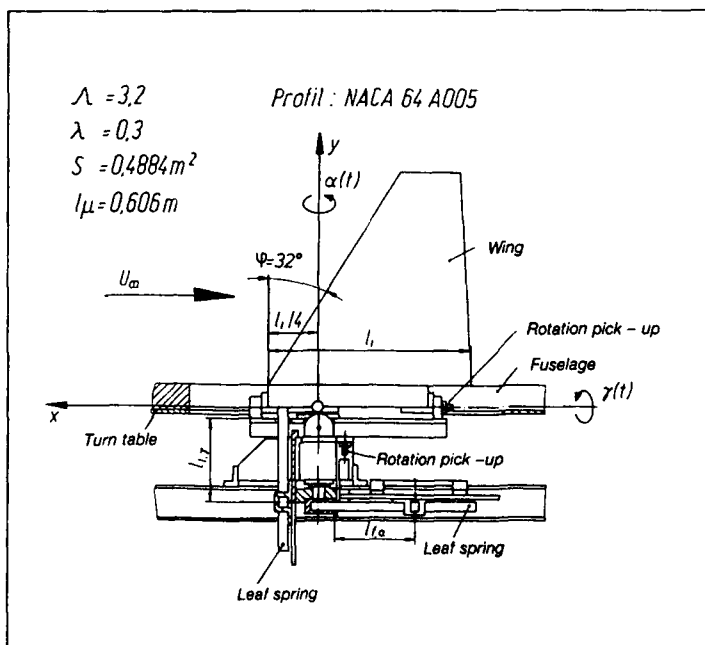


Fig.2: Geometry and elastic suspension of the wind tunnel model

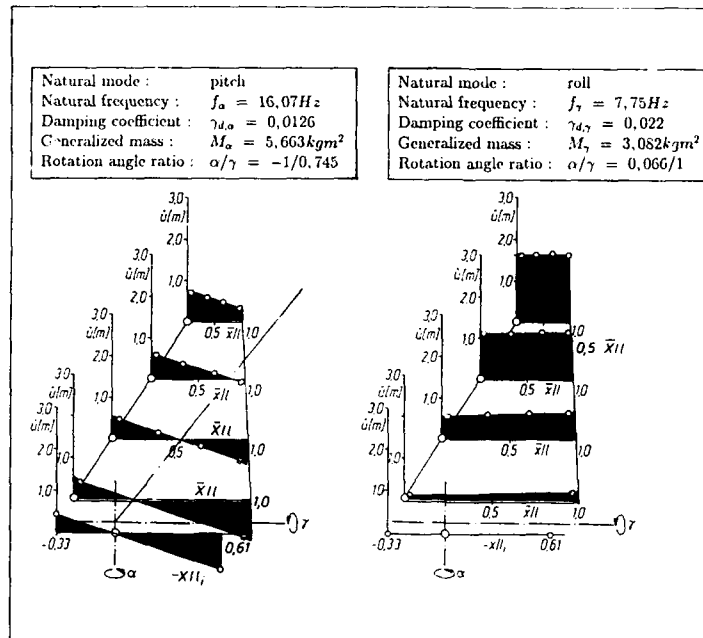


Fig.3: Natural modes of the coupled configuration with $f_\alpha = 16,07 \text{ Hz}$ and $f_\gamma = 7,75 \text{ Hz}$

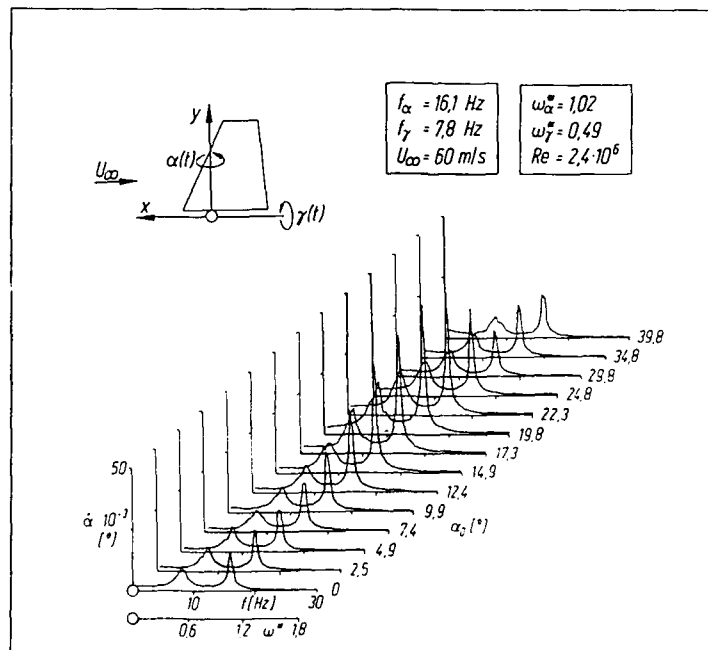


Fig.4: Amplitude spectra of the pitch angle $\dot{\alpha}(\omega^*)$; $\omega_\alpha^* = 1,02$, $\omega_\gamma^* = 0,49$; measurement

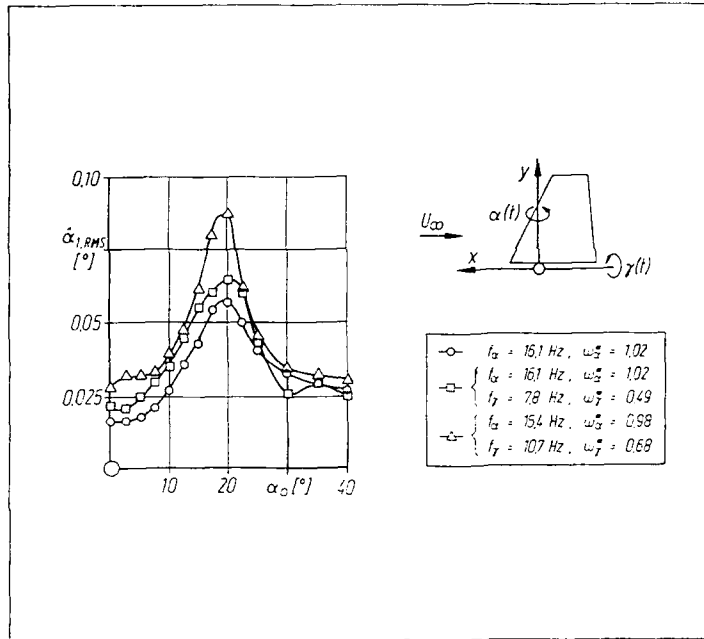


Fig. 5: RMS - values of the pitch angle $\hat{\alpha}_{1,RMS}(\alpha_0)$; measurement

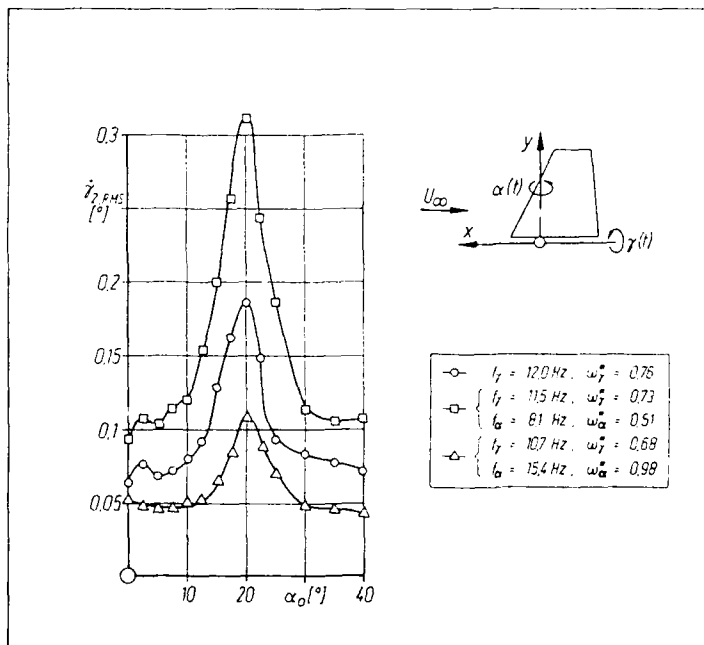


Fig. 6: RMS - values of the roll angle $\hat{\gamma}_{2,RMS}(\alpha_0)$; measurement

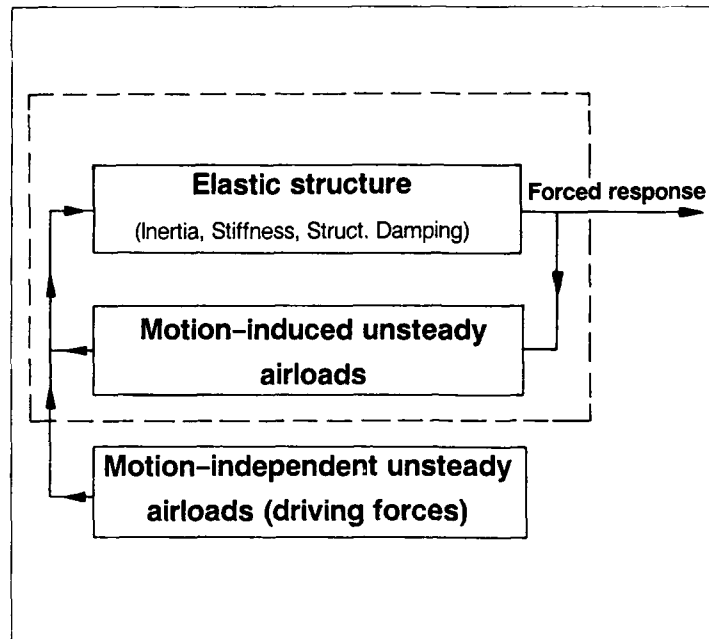


Fig. 7: Aeroelastic functional diagram of the forced oscillation model approach

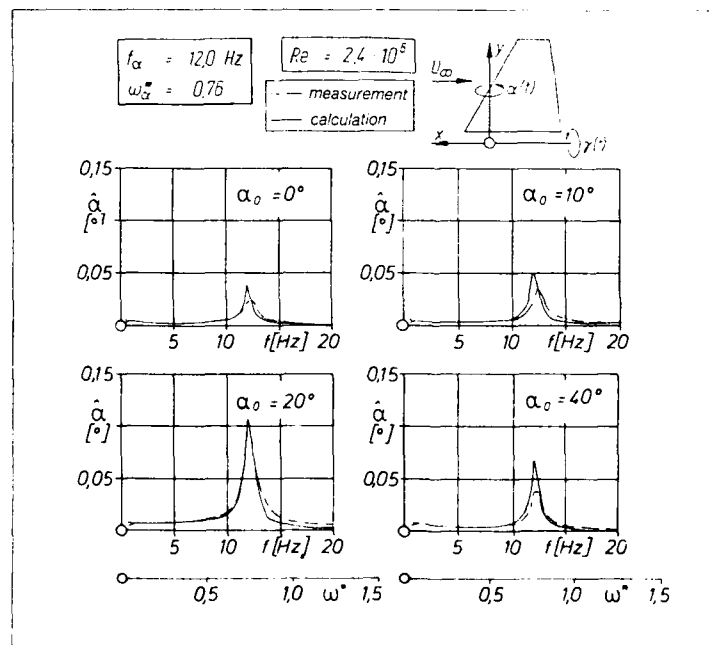


Fig. 8: Amplitude spectra of the pitch angle $\hat{\alpha}(\omega^*)$; $\omega_{\alpha^*} = 0.76$; comparison of measurement and calculation

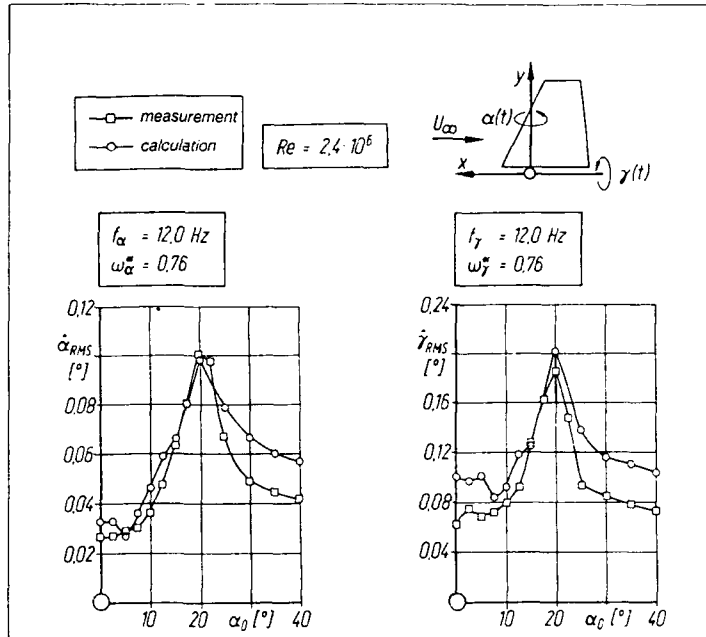


Fig. 9: RMS values of the pitch angle $\dot{\alpha}_{RMS}(\alpha_0)$ and the roll angle $\dot{\gamma}_{RMS}(\alpha_0)$: $\omega_\alpha^* = 0.76$; $\omega_\gamma^* = 0.76$; comparison of measurement and calculation

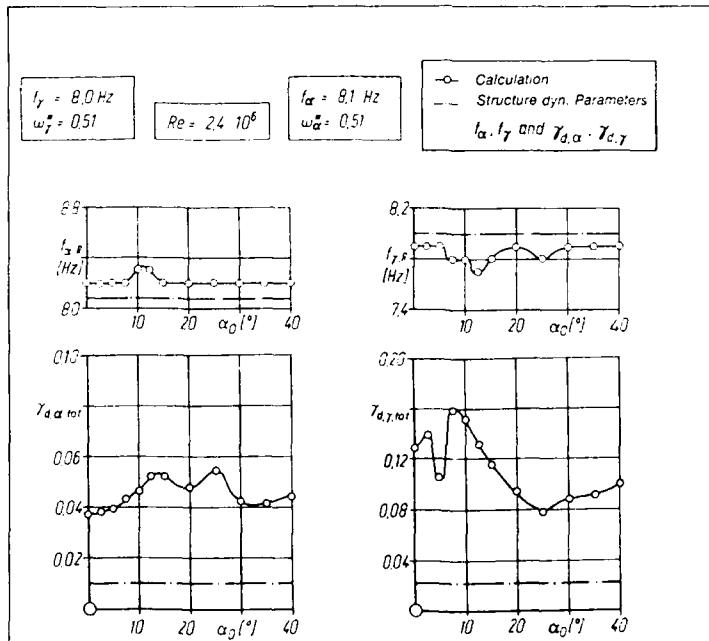


Fig. 10: Resonance frequencies $f_{\alpha,R}(\alpha_0)$ and $f_{\gamma,R}(\alpha_0)$ and total damping coefficients $\gamma_{d,\alpha,tot}(\alpha_0)$ and $\gamma_{d,\gamma,tot}(\alpha_0)$; $\omega_\alpha^* = 0.51$; $\omega_\gamma^* = 0.51$

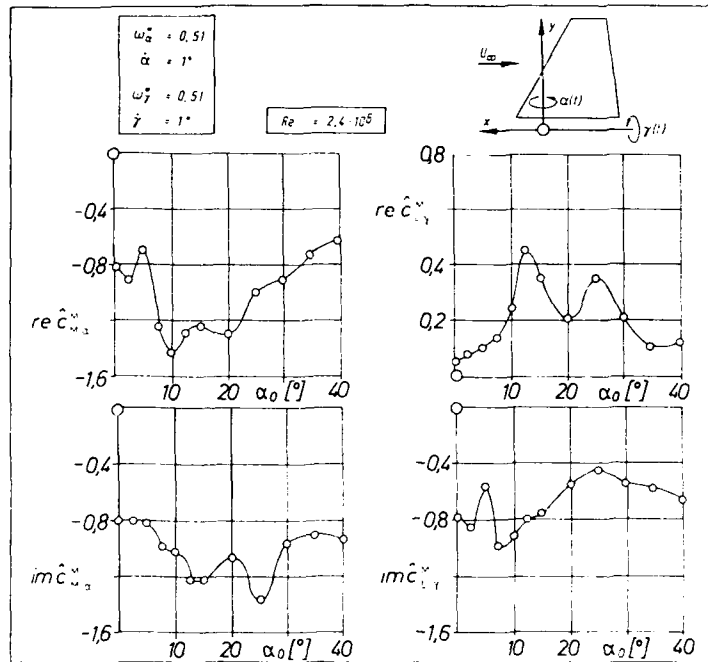


Fig.11: Unsteady pitch moment coefficient $\hat{c}_{M,\alpha}^*(\alpha_0)$ and roll moment coefficient $\hat{c}_{L,\gamma}^*(\alpha_0)$

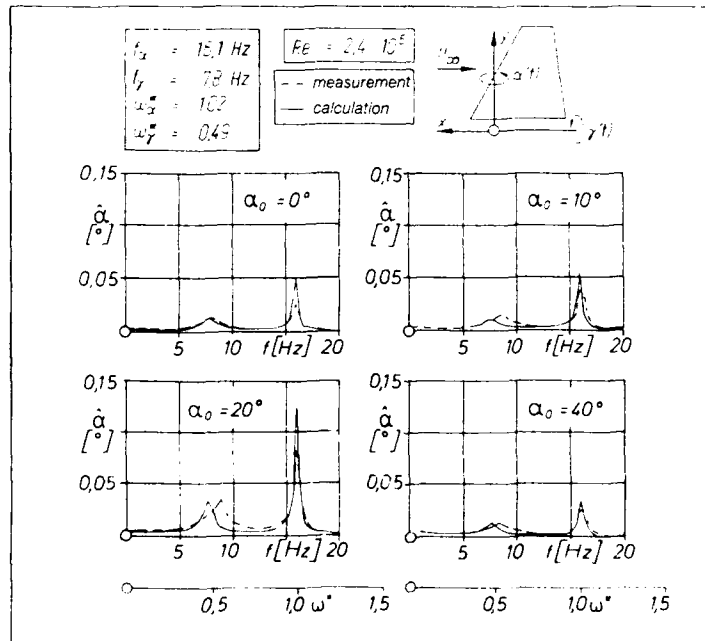


Fig.12: Amplitude spectra of the pitch angle $\dot{\alpha}(\omega^*)$; $\omega_{\alpha}^* = 1.02$; $\omega_{\gamma}^* = 0.49$; comparison of measurement and calculation

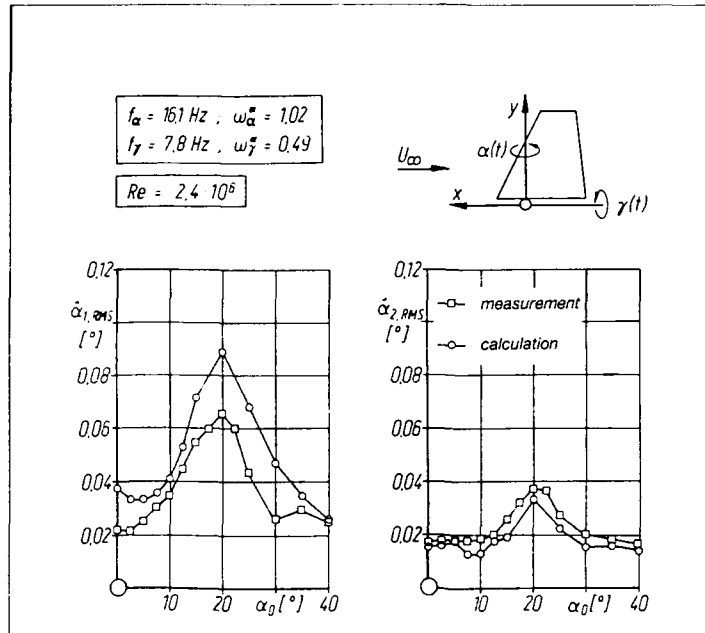


Fig.13: RMS - values of the pitch angles $\dot{\alpha}_{1,RMS}(\alpha_0)$ and $\dot{\alpha}_{2,RMS}(\alpha_0)$; $\omega_\alpha^* = 1.02$; $\omega_\gamma^* = 0.49$; comparison of measurement and calculation

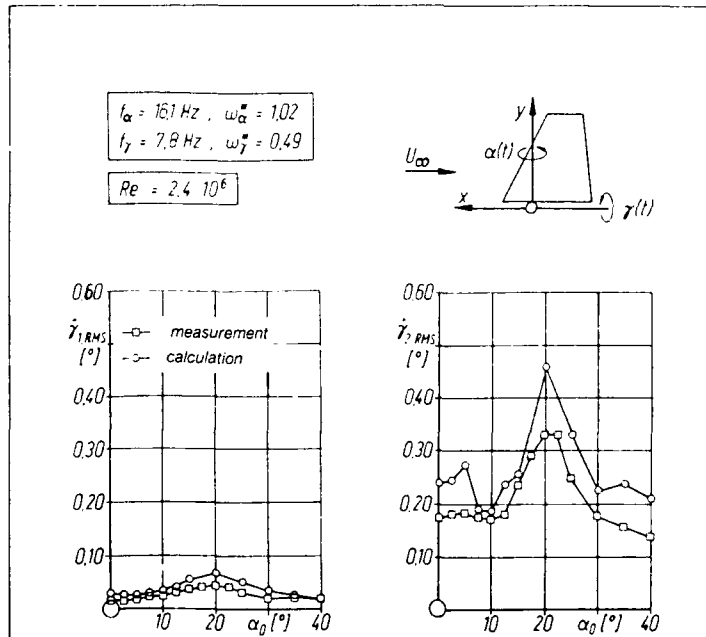


Fig.14: RMS - values of the roll angles $\dot{\gamma}_{1,RMS}(\alpha_0)$ and $\dot{\gamma}_{2,RMS}(\alpha_0)$; $\omega_\alpha^* = 1.02$; $\omega_\gamma^* = 0.49$; comparison of measurement and calculation

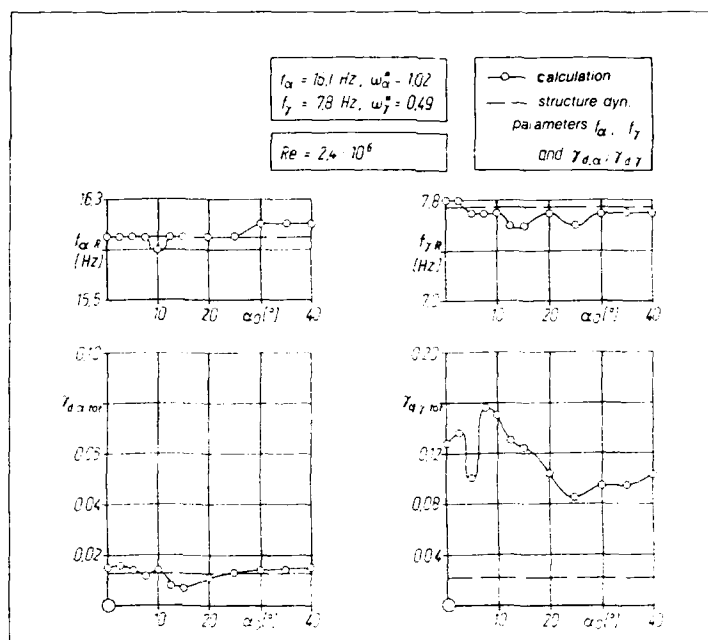


Fig. 15: Resonance frequencies $f_{a,R}$ and $f_{y,R}$ and total damping coefficients $\gamma_{d,a,tot}(\alpha_0)$ and $\gamma_{d,y,tot}(\alpha_0)$; $\omega_a^* = 1.02$; $\omega_y^* = 0.49$

Unsteady Aerodynamic Forces on an Oscillating Wing at High Incidences and Flow Separation

by
H.W. Försching

DLR - Institute for Aeroclasticity
Göttingen, Fed. Rep. of Germany

Summary:

Based on wind tunnel measurements on a low-aspect-ratio trapezoidal half-wing model in incompressible flow, some characteristic features of motion-induced unsteady airloads at high incidences and flow separation are presented and discussed. Special emphasis is placed on the effect of the motion of the wing on the flow separation processes and on the investigation of the interactions between the separated flow phenomena on the stationary wing and the motion-induced unsteady airloads on the oscillating wing. It is shown that these airloads are strongly affected by the flow separations and that their prediction from inviscid potential-flow theory may lead to rather unrealistic results in buffeting response calculations.

List of Symbols

A_{ri}	generalized motion-induced unsteady airload, see Eq.(2)
$c(y)$	local chord of the wing
\bar{c}	mean chord of the wing, see Eq.(7)
$\hat{c}_{M,\alpha}^M$	amplitude of motion-induced unsteady aerodynamic pitching moment due to harmonic pitching oscillations $\alpha(t)$
$\hat{c}_{M,\gamma}^M$	amplitude of motion-induced unsteady aerodynamic rolling moment due to harmonic rolling oscillations $\gamma(t)$
$c_p(t)$	unsteady aerodynamic pressure coefficient, see Eq.(3)
\bar{c}_p	steady mean value of aerodynamic pressure coefficient $c_p(t)$, see Eq.(3)
$\hat{c}_{p,P}^M$	amplitude of the aerodynamic pressure fluctuations at point P , see Eq.(4)
$\hat{c}_{p,\alpha}^M$	amplitude of motion-induced unsteady aerodynamic pressure coefficient due to harmonic pitching oscillations $\alpha(t)$, see Eq.(10)
$\hat{c}_{p,\gamma}^M$	amplitude of motion-induced unsteady aerodynamic pressure coefficient due to harmonic rolling oscillations $\gamma(t)$, see Eq.(11)
f	frequency of oscillation
\hat{I}_r^M	amplitude of motion-induced unsteady aerodynamic rolling moment $I(t)$ due to harmonic rolling oscillations $\gamma(t)$
Ma	Mach number
\hat{M}_α^M	amplitude of motion-induced unsteady aerodynamic pitching moment $M(t)$ due to harmonic pitching oscillations $\alpha(t)$
$P(x, y, z)$	point at location (x, y, z)
$p(t)$	unsteady aerodynamic pressure
$\mathbf{p}^M(P, \omega, Ma, \alpha_0)$	vector of motion-induced unsteady airload per unit area
p_∞	freestream aerodynamic pressure
\hat{p}_α^M	amplitude of motion-induced unsteady aerodynamic pressure due to harmonic pitching oscillations $\alpha(t)$
\hat{p}_γ^M	amplitude of motion-induced unsteady aerodynamic pressure due to harmonic rolling oscillations $\gamma(t)$
q_r	generalized coordinate of the r^{th} natural mode shape
q_∞	freestream dynamic pressure $= \rho U_\infty^2 / 2$

S	(integration) surface
$S_p(P, \omega, \alpha_0)$	power spectral density of the pressure coefficient $c_p(P, t, \alpha_0)$
$S_p^*(P, \omega^*, \alpha_0)$	non-dimensional form of $S_p(P, \omega, \alpha_0)$, see Eq.(5)
s	(effective) semi-span of the wing
T	integration time
t	time
U_∞	free stream velocity
$w(P, t)$	vector form of time-dependent structural displacement
α_0	incidence of the stationary wing
$\hat{\alpha}$	amplitude of pitching oscillations $\alpha(t)$
$\hat{\gamma}$	amplitude of rolling oscillations $\gamma(t)$
ρ	air density
$\Phi_r(P)$	vector form of the r^{th} natural mode shape
ω	circular frequency
ω^*	reduced frequency, see Eq.(6)

Other notations:

$\text{Re}()$	real part of quantity ()
$\text{Im}()$	imaginary part of quantity ()

Coordinates:

x, y, z	cartesian coordinates, see Fig.3
$\bar{x}, \bar{y}, \bar{z}$	local cartesian coordinates of the wing, origin at the leading edge, see Fig.2

1. Introduction

For the solution of all types of dynamic aeroelastic problems adequate knowledge of the unsteady airloads induced by the structural vibrations is of fundamental importance. As long as these motion-induced unsteady airloads are associated with a potential flow, they can be predicted adequately by computation methods based on the concept of linearized small-perturbation theory. Inviscid linearized small-perturbation lifting surface theory has served the aeroelastician well in the majority of design applications for conventional aircraft operating under non-separated flow conditions. This theory has now been brought to a high degree of mathematical and numerical sophistication for proper use in potential-flow (classical) aeroelastic analyses.

With the development of highly manueverable fighter aircraft that operate well beyond the buffet onset boundary in transonic and post-stall flight under separated flow conditions, aircraft designers were faced with the problem of taking into account the buffeting characteristics of such aircraft. Hence, a challenging new domain of aeroelastic research emerged, i.e. aeroelasticity at separated flow [1]. Unsteady aerodynamic buffet loads associated with flow separations result in more or less pronounced pressure fluctuations which represent the driving forces in the aeroelastic buffeting response problem. The structural buffeting vibrations, in turn, generate motion-induced unsteady aerodynamic forces which play an important role in the overall aeroelastic problem, as they produce aerodynamic damping and hence limit the level of vibration.

Since the theoretical prediction of both types of unsteady airloads associated with and affected by flow separations is still in an early development stage, reliable aeroelastic buffeting response calculations are difficult to perform. For this reason, all buffeting prediction methods applied presently make use of wind tunnel model testing in some manner based, generally, on two different methods. In the first relatively simple method, see Refs. [2] to [5], a buffet excitation parameter is derived which appears to be, at least for fighter-type wing geometries, relatively insensitive with respect to variations in mode shape and frequency. The wind tunnel model acts as a selective analog filter, integrating the buffet excitation in space and time and combining this with modes of the model being excited. Extrapolation and application of these buffet excitation parameters from wind tunnel tests to in-flight buffeting response predictions for real aircraft, however, create special problems because assumptions must be made about the aerodynamic damping (of the motion-induced unsteady airloads) relative to the structural damping. The second method consists of the measurement of the aerodynamic buffet input forces (excitation) on a large number of points on the surface of a nominally rigid model. The buffet loads can then be integrated in space and time, together with the mode of interest, to give again the corresponding (generalized) buffet input parameter. On the other hand, the measured unsteady

aerodynamic buffet input forces can also be used to form generalized buffet input terms in a mathematical aeroelastic model in order to calculate the buffeting characteristics of the full-scale aircraft. In such an analytical approach, adequate knowledge of the (generalized) motion-induced unsteady airloads - the most significant physical effect of which is the generation of aerodynamic damping - is again of fundamental importance.

Detailed investigations of the motion-induced unsteady airloads on oscillating lifting systems at high angles of attack under separated flow conditions are rather poor. The main purpose of this paper, therefore, is to present and illuminate some characteristics of these unsteady airloads measured on a harmonically oscillating low-aspect-ratio trapezoidal half-wing at incidences of up to 40 degrees in incompressible flow. These investigations were part of a comprehensive aeroelastic wind tunnel research program, performed recently in the Institute for Aeroelasticity at DLR-Research Center Göttingen. Further results of the investigations will be presented by H. Zingel and P. Bublitz in their papers at this Specialists' Meeting.

2. Linearized Aeroelastic Buffeting Model Approach

The crucial point in predicting the aeroelastic buffeting behavior of aircraft is the knowledge of both the driving unsteady buffet airloads associated with flow separations, independent of any structural motion, and the motion-dependent unsteady airloads induced by the structural oscillations. Both types of unsteady airloads on aircraft lifting systems under separated flow conditions are highly dependent on many parameters, particularly on the wing geometry (profile and planform), angle of attack, Mach number and Reynolds number. When approaching the transonic speed range, the angle of attack and the Mach number become the governing parameters of buffet onset and intensity. The most important aspect, however, in establishing mathematical/physical models for an adequate description of the dynamic aeroelastic buffeting behavior of (elastic) lifting systems under separated flow conditions is the interaction between the highly non-linear unsteady flow processes on the stationary system, manifested in random-type pressure fluctuations as driving forces, and the motion-induced unsteady airloads due to the structural (buffeting) response. This interaction between the separated flow field and the motion of the elastic system is integral to the buffeting phenomenon.

In aeroelastic buffeting prediction techniques it is generally accepted to apply a linearized forced oscillator model approach, the functional diagram of which is illustrated in *Fig.1*. In this aeroelastic buffeting model the combination of structural response and motion-induced aerodynamic forces, indicated by a dashed line, forms a stable system which, left to itself, would settle down to a state of stable equilibrium. Here, the most significant physical effect of the motion-induced unsteady airloads is the generation of aerodynamic damping which (together with the structural damping) limits the dynamic response of the (elastic) structure excited by the motion-independent unsteady airloads due to flow separation. Practical application of this linearized forced vibration model approach in aeroelastic buffeting predictions is based on the following physical assumptions:

- The structural vibrations around a fixed steady mean angle of attack α_0 are relatively small, and hence the relationship between the system displacements and the motion-dependent (structural and aerodynamic) system forces is linear.
- The random-type driving forces, due to flow separation on the stationary system at α_0 , do not change significantly for small structural vibrations.
- The motion-induced unsteady airloads due to structural vibrations remain essentially unaffected by the (separated) flow field on the stationary system and can thus be derived from linearized inviscid potential-flow aerodynamic theory.

Hence, it is assumed that the buffet driving mechanism arises basically from a (virtually non-linear) flow phenomenon on the stationary system and the (linearized) structural buffeting response of the system about a fixed position α_0 may possibly modify but not significantly interfere with flow separation processes.

On the basis of this linearized forced vibration model approach, several more or less sophisticated semi-empirical aeroelastic buffeting prediction techniques have been elaborated adopting techniques of generalized harmonic analysis. Thereby, the displacement of the lifting system at a point $P(x, y, z)$ and time t in vector form can be expressed in terms of a set of normal coordinates $q_r(t)$ as

$$w(P, t) = \sum_{r=1}^n \Phi_r(P) q_r(t) \quad , \quad (1)$$

where $\Phi_r(P)$ is the r^{th} natural mode shape of the elastic structure. Applying mathematical concepts of the theory of random processes, the buffet (input) loads and the aeroelastic structural buffeting (output) response can be expressed in terms of power spectral densities, as fully described in Refs. [6] to [10]. Thereby, in the generalized aeroelastic transfer (admittance) functions - which relate the aeroelastic structural response to a harmonic driving force of unit amplitude and circular frequency ω - the generalized motion-induced unsteady airloads generally appear in the following form, or in a power spectral density form thereof:

$$A_{rs}(\omega, Ma, \alpha_0) = \iint_{(S)} \Phi_r(P) \cdot p_s^M(P, \omega, Ma, \alpha_0) dS ; \quad (2)$$

$$(r = 1, 2, \dots, n) , \quad (s = 1, 2, \dots, n) .$$

Here, $p_s^M(P, \omega, Ma, \alpha_0)$ is the vector of the motion-induced unsteady aerodynamic force per unit area arising in the s^{th} mode of vibration at a point P on the surface of the structure.

In the application of this generalized forced oscillation model approach neglect of aerodynamic mode coupling ($A_{rs} = 0$ for $r \neq s$) - which plays a vital role in classical potential-type aeroelastic stability (flutter) problems - and of structural damping coupling is common practice. Moreover, in the resulting single mode approach, the power spectral density of the buffet input loads is usually assumed constant in the neighborhood of the natural frequency, and the cross-correlation effects of the buffet driving forces are also usually neglected. It is difficult to assess the extent to which such drastic simplifications actually provide reliable results as long as no results of systematic investigations are available. Above all, we have almost no information concerning the effect of flow separation on the development of the motion-induced unsteady aerodynamic forces and their effective role in buffeting response predictions - even in the case of aerodynamically uncoupled single mode responses. Some characteristic features of these unsteady airloads on oscillating lifting systems under separated flow conditions at high angles of attack α_0 , obtained from wind tunnel model measurements, are presented and discussed in the following.

3. Wind Tunnel Model and Test Set-Up

The geometric details of the trapezoidal half-wing model under investigation, the coordinate systems used and the arrangement of the pressure pick-ups for the measurement of the aerodynamic loads on both the stationary and the oscillating wing are shown in *Fig. 2*. The model is equipped with 50 direct pressure sensors (KULITES) on the upper (suction) surface and 25 sensors on the lower (pressure) surface on the wing located on five spanwise measuring sections. The model is free to rotate about an axis at 25% root chord (y -axis) allowing (semi-rigid) pitching oscillations as well as an axis along the root chord in a streamwise direction (x -axis) allowing rolling oscillations. Each separate degree of freedom can be harmonically excited with an electro-hydraulic driving system. By means of dynamometers, the global unsteady aerodynamic pitching and rolling moments can be measured as well. A schematic of the complete wind tunnel test set-up is illustrated in *Fig. 3*.

The tests were performed in the $3 \times 3 \text{ m}^2$ Low Speed Wind Tunnel of DLR in Göttingen, Fed. Rep. of Germany, at mean incidences α_0 of the wing up to 40° and a wind speed of 60 m/s corresponding to $Ma \approx 0.2$. The Reynolds number based on this wind speed and the mean chord of the wing $\bar{c} = 0.61 \text{ m}$ is $Re = 2.4 \cdot 10^6$. The complete model, consisting of a "dummy" fuselage and the wing, was placed on a turntable so that the incidence α_0 of the model could easily be changed. The fuselage did not participate in the forced motion of the wing.

4. Motion-Induced Unsteady Airloads in Separated Flow

4.1 Main Characteristics of the Separated Flow Field on the Stationary Wing

To completely understand the effects of flow separation on the development of the motion-induced unsteady airloads on the oscillating wing and, vice versa, the effects of the motion of the wing on the flow separation behavior, deeper insight into the flow field on the stationary wing becomes mandatory. *Fig. 4*, first, shows the characteristic wall streamlines and the vortex skeleton on the upper side of the stationary wing at incidences $\alpha_0 = 7.5^\circ, 10^\circ, 15^\circ, 20^\circ, 25^\circ$ and 40° , obtained by an oil flow visualization technique. The corresponding steady mean pressure distributions,

$$\bar{c}_p(P) = \frac{1}{T} \int_0^T c_p(P, t) dt ; \quad c_p(P, t) = \frac{p(P, t) - p_\infty}{q_\infty} , \quad (3)$$

on the upper and lower sides of the wing are shown in *Fig. 5*. It can be seen that the wing exhibits the typical flow characteristics of a delta wing with the typical vortex formation at the leading edge. At $\alpha = 7.5^\circ$ flow separation has already started at the wing tip and extends from the leading edge to the trailing edge. At $\alpha_0 = 10^\circ$ separation of the flow now occurs along the entire leading edge of the wing with reattachment of the flow manifest in the formation of a concentrated vortex system. The well known pressure peaks (see *Fig. 5*) at the leading edge in the case of non-separated flow have disappeared, and, in the outer Sections ① and ② - where flow separation extends to the trailing edge - the Kutta condition (zero pressure) is no longer satisfied. The flow pattern at $\alpha_0 = 15^\circ$ and 20° are quite similar, and the flow separation now extends over the entire upper surface of the wing. The leading edge vortex assumes the character of a bubble and moves further in the

direction of the wing root. A ring vortex develops at the trailing edge rear the wing tip associated with the appearance of a secondary vortex at the leading edge. With the formation of the leading edge vortex system, relatively high underpressures appear in the pressure distributions (see Fig. 5) which result in maximum lift on the wing at $\alpha_0 = 20^\circ$. At $\alpha_0 = 25^\circ$ the leading edge vortex which dominates up to this point is almost completely displaced from the wing and the flow along most of the upper surface of the wing is now governed by the ring vortex, whereas the secondary vortex flow separation now extends along the entire leading edge. The corresponding chordwise pressure distributions (see Fig. 5) show nearly constant values. Finally, at $\alpha_0 = 40^\circ$, the leading edge vortex completely disappears and the flow separation pattern is entirely dictated by the now dominating ring vortex system. The pressure distribution (see Fig. 5) is practically constant over the entire upper surface of the wing.

The pressure distributions on the lower (pressure) side of the wing (see Fig. 5) show a clear potential-flow behavior, since no flow separation occurs on this side. The pressures increase with increasing angle of attack, retain their maxima at the wing leading edge and approach zero at the wing trailing edge.

Associated with these flow separation phenomena are more or less pronounced pressure fluctuations which form the buffet driving forces in the aeroelastic buffeting response problem. The time dependence of these pressure fluctuations can be expressed in the frequency domain in terms of amplitude spectra $\hat{c}_p(f)$ or $\hat{c}_p(\omega^*)$, respectively. These are defined as

$$\hat{c}_p(P, \omega^*, \alpha_0) = \sqrt{2 S_{c_p}^*(P, \omega^*, \alpha_0) \frac{1}{2\pi} \Delta\omega^*} \quad (4)$$

where

$$S_{c_p}^*(P, \omega^*, \alpha_0) = \frac{U_\infty}{\bar{c}} S_{c_p}(P, \omega, \alpha_0) \quad (5)$$

is the non-dimensional form of the power spectral density $S_{c_p}(P, \omega, \alpha_0)$ of the pressure coefficients $c_p(P, t, \alpha_0)$, and

$$\omega^* = \frac{\omega \bar{c}}{U_\infty} \quad (6)$$

a reduced frequency based on the mean chord \bar{c} of the wing with

$$\bar{c} = \frac{1}{S} \int_0^s c^2(y) dy \quad (7)$$

as a reference length. As a typical example, Fig. 6 shows the amplitude spectra $\hat{c}_p(f)$ and $\hat{c}_p(\omega^*)$, respectively, of the pressure coefficients $c_p(t)$ at the ten pressure measuring points of Section (4) on the upper side of the stationary wing at various incidences α_0 . It can be seen that the pressure fluctuations on the stationary wing generally exhibit broad-band random-type behavior with well pronounced maxima at relatively low frequencies.

4.2 Effect of Harmonic Motion on the Flow Separation Behavior

With regard to the application of the linearized forced oscillation model approach, the question as to the extent to which the flow separation processes on the stationary wing - and hence the buffet input loads - will be affected by (harmonic) motions of the wing is of fundamental importance. For the non-stationary wing performing harmonic pitching oscillations

$$\alpha(t) = \hat{\alpha} \exp(i\omega t) \quad (8)$$

and harmonic rolling oscillations

$$\gamma(t) = \hat{\gamma} \exp(i\omega t) \quad (9)$$

the amplitudes of the (complex) motion-induced unsteady pressure coefficients at a point P on the wing can be defined as

$$\hat{c}_{p,\alpha}^M(P) = \frac{\hat{p}_\alpha^M(P) - p_\infty}{q_\infty \hat{\alpha}} \quad (10)$$

and

$$\hat{c}_{p,\gamma}^M(P) = \frac{\hat{p}_\gamma^M(P) - p_\infty}{q_\infty \hat{\gamma}} \quad (11)$$

respectively. Correspondingly, the amplitudes of the (complex) unsteady motion-induced pitching moment and rolling moment coefficients may be expressed as follows:

$$\hat{c}_{M,\alpha}^M = \frac{\hat{M}_\alpha^M}{q_\infty S \bar{c} \hat{\alpha}} \quad (12)$$

and

$$\hat{c}_{L,\gamma}^M = \frac{\hat{L}_\gamma^M}{q_\infty S \bar{c} \hat{\gamma}} \quad (13)$$

Fig. 7 shows, as a typical example, the effect of a harmonic pitching motion on the amplitude spectrum $\hat{c}_p(f)$ of the pressure fluctuations $c_p(t)$ in Section ③. Here, the wing oscillates about a steady mean incidence $\alpha_0 = 20^\circ$ with a frequency $f = 8$ Hz (i.e. $\omega^* = 0.51$) and an amplitude $\hat{\alpha} = 1^\circ$. Compared to the stationary wing, the amplitude spectrum of the oscillating wing seems to remain essentially unaffected by the oscillatory motion. Only a well pronounced, very narrow-band peak appears at the frequency of forced oscillation $f = 8$ Hz. The same behavior can also be seen in Fig. 8, where the corresponding amplitude spectra $\hat{c}_L(f)$ of the rolling moment fluctuations $c_L(t)$ at $\alpha_0 = 20^\circ$ are illustrated.

From Figs. 7 and 8 it becomes evident that one basic assumption of the linear forced oscillation model approach seems indeed to be justified, namely, that the buffet driving forces due to flow separation do not change significantly for small oscillations of the wing. Moreover, at a first glance, it may also be supposed from Figs. 7 and 8 that the other generally accepted assumption, i.e. the motion-induced unsteady airloads remaining essentially unaffected by the separated flow field on the stationary wing, is also justified. This supposition, however, is incorrect as shown in the following.

4.3 Interaction of the Motion-Induced Unsteady Airloads with the Separated Flow Field

A much better insight into the rather complex interactions between the separated flow field phenomena on the stationary wing and the motion-induced unsteady airloads at high angles of attack α_0 can be obtained from the results of unsteady pressure distribution measurements on the (harmonically) oscillating wing, as shown in Fig. 9. Here, the amplitudes of the real parts $\text{Re}(\hat{c}_{p,\alpha}^M)$ and the imaginary parts $\text{Im}(\hat{c}_{p,\alpha}^M)$ of the motion-induced (complex) unsteady aerodynamic pressure coefficients on both the upper and lower sides of the wing performing harmonic pitching oscillations at $\alpha_0 = 5^\circ, 10^\circ, 20^\circ$ and 40° are illustrated. Δ^* , where no flow separation occurs on the stationary wing, the pressure distributions in the real and imaginary parts exhibit the well known potential-flow behavior (pressure peaks at the leading edge and zero pressure at the trailing edge). An exception to this appears only at the leading edge measuring point of Section ① on the upper side of the wing where the pressure shows a sudden change in sign. Evidently, as a consequence of the superimposed pitching motion of the wing, $\alpha = \alpha_0 \pm \hat{\alpha} \sin \omega t$, flow separation at the leading edge near the wing tip is just beginning and the phenomenon of "Dynamic Stall" with a periodic separation and reattachment of the flow around α_0 appears. This is clearly illustrated in Fig. 10, where the time history of the pressure signal $c_p(t)$ of this measuring point, its amplitude spectrum $\hat{c}_p(f)$ and the time history $\alpha(t)$ of the pitching motion are shown. It can be seen that the flow during one period of oscillation separates for $\alpha = \alpha_0 + \alpha(t)$ and reattaches for $\alpha = \alpha_0 - \alpha(t)$ as is manifest in the correlation between the pressure signal and the signal of the pitching motion, see Fig. 10b. This periodic dynamic stall phenomenon results in very pronounced higher harmonics of the unsteady pressure $c_p(t)$ in the amplitude spectrum $\hat{c}_p(f)$ in some multiple of the frequency of oscillation $f = 8$ Hz, see Fig. 10c.

In Fig. 9, at $\alpha_0 = 10^\circ$, where the flow on the stationary wing has separated along the entire leading edge (see Fig. 4), the suction peaks of $\text{Re}(\hat{c}_{p,\alpha}^M)$ at the points near the leading edge on the upper side of the wing have disappeared completely and the corresponding pressures have changed their sign due to the aforementioned dynamic stall events. Now the maxima of the negative pressures on the suction side of the wing appear in the real parts between the leading edge vortex center and the reattachment line (see Fig. 4) just where the stationary pressure distribution shows a maximum gradient (see Fig. 5). The imaginary parts $\text{Im}(\hat{c}_{p,\alpha}^M)$, on the other hand, are zero exactly at those points on the upper side of the wing where the real parts have their negative maxima, i.e. the negative pressure maxima are exactly in phase with the oscillatory motion of the wing. Moreover, the imaginary parts $\text{Im}(\hat{c}_{p,\alpha}^M)$ exhibit a positive maximum near those points on the suction side of the wing where the flow pattern in Fig. 4 shows a reattachment line. The level of negative pressure in the imaginary parts has increased considerably, indicating an increased amount of aerodynamic damping.

At $\alpha_0 = 20^\circ$, the pressure level on the upper side of the wing in the real parts $\text{Re}(\hat{c}_{p,\alpha}^M)$ has decreased on the whole, whereas the imaginary parts $\text{Im}(\hat{c}_{p,\alpha}^M)$ are still considerably larger than in the case of non-separated flow at $\alpha_0 = 5^\circ$. With increasing angles of attack α_0 the pressure distributions of both the real and imaginary parts on the upper side of the wing become more and more uniform, and the pressure level continues to decrease. Thus, at $\alpha_0 = 40^\circ$, the pressure level is of the same magnitude as for the rear part of the wing in non-separated flow at $\alpha_0 = 5^\circ$.

As in the case of the stationary wing (see Fig. 5), the motion-induced unsteady pressure distributions on the lower (pressure) side of the oscillating wing, see Fig. 9, remain practically unaffected by the flow separation processes on the upper wing side. The real parts $\text{Re}(\hat{c}_{p,\alpha}^M)$ show almost the same behavior as the \bar{c}_p -distributions

on the stationary wing with a change in sign at the rear part of the outer wing for $\alpha_0 = 10^\circ$ and 20° , see Fig. 5. The imaginary parts $\text{Im}(\hat{c}_{\mu, \alpha}^M)$ remain almost unchanged for all incidences α_0 and show the well known potential-flow behavior.

Quite similar behavior can be observed in Fig. 11 for harmonic rolling oscillations of the wing. For non-separated flow ($\alpha_0 < 5^\circ$), both the real and imaginary parts show again the behavior typical for potential flow. Near the leading edge, for $5^\circ < \alpha_0 < 10^\circ$, dynamic stall effects can be observed once more, and the pressure levels of the imaginary parts $\text{Im}(\hat{c}_{\mu, \alpha}^M)$ for $10^\circ < \alpha_0 < 20^\circ$ under separated flow conditions are considerably higher than for non-separated flow ($\alpha_0 < 5^\circ$).

4.4 Correlation with Analytical Potential-Flow Predictions

From these test results, it becomes clear that strong interactions exist between the flow separation processes on the stationary wing and motion-induced unsteady airloads on the oscillating wing. At specific points in the flow field of the oscillating wing - such as stagnation, separation and reattachment points - higher harmonics of the motion-induced unsteady pressures of considerable magnitudes may appear. This is a well known fact from unsteady transonic flow measurements. When the flow is completely separated, the circulatory part of the motion-induced unsteady flow field, which takes care of the Kutta condition and the influence of the non-stationary vortex wake, disappears and the generation of circulatory unsteady lift is no longer possible. Hence, it becomes evident that the prediction of motion-induced unsteady airloads from inviscid lifting surface theory must be a very crude approach in the case of flow separation. This is clearly demonstrated in Fig. 12, which shows as a typical example a comparison between the measured and calculated motion-induced unsteady pressure distributions in Section ② on the upper (suction) side of the wing undergoing harmonic pitching oscillations about various steady mean incidences α_0 . It can be seen that the theoretical prediction based on a velocity potential panel technique [11] agrees well with the experimental results as long as no flow separation occurs. However, in the case of flow separation at $\alpha_0 > 5^\circ$ inviscid potential flow theory leads to rather unrealistic and misleading results. Particularly the imaginary parts, which produce aerodynamic damping, appear to be considerably larger than those predicted by inviscid potential-flow theory. Thus, application of this theory would be too conservative in that it tends to underestimate the amount of aerodynamic damping and thus to overestimate considerably the dynamic response in practical buffeting calculations. This is clearly illustrated in Fig. 13 which shows a comparison between predictions and flight test data for the buffeting response acceleration power spectral density measured at 84% semi-span and 26% chord on the F-4E wing at $Ma = 0.82$ beyond the transonic boundary of buffet onset. The important effects of the motion-induced unsteady aerodynamic forces due to wing vibration can be clearly seen.

The same conclusions can also be drawn from Fig. 14, where a comparison is made between the measured and calculated unsteady pitching and rolling moment coefficients $\hat{c}_{m, \alpha}^M$ and $\hat{c}_{l, \alpha}^M$, respectively. The correlation between theory and experiment is only satisfactory for non-separated flow conditions ($\alpha_0 < 5^\circ$).

Generally speaking, no routine engineering technique presently exists to adequately determine the motion-induced unsteady airloads required for reliable buffeting response predictions for aircraft operating under separated flow conditions. Applying experimental techniques, a dynamically-scaled aeroelastic wind tunnel model - fully equipped with unsteady pressure pick-ups at a sufficient number of points on the flexible model - would be necessary. Due to static strength and stability requirements, the realization of such an aeroelastic model to be tested at high angles of attack under separated flow conditions, however, is practically impossible, particularly in the important transonic flow regime.

As repeatedly mentioned, the most important effect of the motion-induced unsteady airloads in aeroelastic response predictions is the generation of aerodynamic damping expressed by the imaginary parts, whereas, the real parts may be identified as virtual masses (or stiffnesses), the effects of which are negligibly small in aeroelastic response predictions. For completely separated flow, where the chordwise pressure distributions for both the steady mean pressures (see Fig. 5) and the motion-induced unsteady pressures (see Figs. 9 and 11) are almost constant over the entire upper surface of the wing and circulatory lift no longer exists, it appears reasonable to try to make use of a correction technique based on a quasi-steady approach applying the steady mean values measured on the stationary wing. Such semi-empirical correction techniques, applying the results of rigid and/or semi-rigid wind tunnel model measurements, offer perhaps the most promising way to evaluate motion-induced unsteady airload data for more reliable aeroelastic buffeting response predictions until corresponding results from CFD-techniques become available.

5. Concluding Remarks

Aeroelastic problems of aircraft associated with flow separations during operation at high angles of attack and/or in transonic flow are a challenging field of aeroelasticity. Due to a lack of reliable aerodynamic prediction techniques, use of experimentally derived unsteady airload data as input for semi-empirical methods seems to be the only feasible solution at the moment.

Based on this semi-empirical concept for buffeting response predictions of aircraft, the linearized forced oscillation model approach is generally acceptable. It has been shown in the present investigations that the buffet input forcing data for such buffeting calculations can be obtained relatively easily from ordinary rigid model wind tunnel measurements, and that the pressure fluctuations stemming from flow separation remain essentially unaffected by superimposed (structural) oscillations for relatively small amplitudes of vibration. In the evaluation and application of such data, scale effects (even with fixed transition on the model) and the effects of static aeroelastic distortion on the model and on the real aircraft may play an important role and must be kept in mind. The unsteady airloads induced by structural vibrations, however, are strongly affected by flow separation processes. Therefore, their prediction by inviscid potential-flow theory cannot be adequate and would lead to rather unrealistic and overly conservative results in buffeting response predictions. A semi-empirical derivation of these motion-induced unsteady airloads under separated flow conditions from measured steady-flow results and application of a quasi-steady approach is perhaps the most promising way, as long as more reliable theoretical prediction techniques are not available. This conclusion, however, requires further detailed investigation.

The theoretical prediction of the unsteady separated-flow pressure data at high incidences and/or under transonic flow conditions on the stationary wing or, even more importantly, of the motion-induced unsteady airloads under such conditions on the oscillating wing is a formidable task which can only be solved by application of the full Navier-Stokes equations or specific subsets thereof. In order to meet the special requirements of aeroelastic analysis in separated flow and, particularly, to improve the results of buffeting response predictions, computation of unsteady aerodynamic input data for such aeroelastic investigations presents a challenge to the CFD community.

6. Bibliography

- [1] Försching, H.: *Aeroelasticity at Separated Flow - Concepts and Prospects*. Int'l. Symp. on Aeroelasticity, October 5-7, 1981, DGLR-Report 82-01, 1982, pp.1-9.
- [2] Jones, J.G.: *A Survey of the Dynamic Analysis of Buffeting and Related Phenomena*. RAF Techn. Rep. 72197, 1973.
- [3] Mabey, D.G.: *Beyond the Buffet Boundary*. Aeron. Journal, April 1973, pp.201-215.
- [4] Mabey, D.G.: *Some Aspects of Aircraft Dynamic Loads Due to Flow Separation*. AGARD-Rep. No. 750, 1988.
- [5] Butler, G.F.; Jones, J.G.: *The Prediction of Buffeting Response in Flight from Wind Tunnel Measurements on a Model of Conventional Construction*. RAF Techn. Rep. 84045, 1984.
- [6] Houbolt, J.C.: *On the Response of Structures Having Multiple Random Inputs*. Jahrbuch der WGLR, 1957, pp.296-305.
- [7] Cunningham, A.M.; Benope, D.B.: *Prediction of Transonic Aircraft Buffeting Response*. In: "Unsteady Airloads in Transonic and Separated Flow", AGARD CP 226 (1977), pp.3-1 to 3-17.
- [8] Lee, B.H.K.: *A Method for the Prediction of Wing Response to Non-Stationary Buffet Loads*. NRCC AR 1.R-601, July 1980. See also: Journ. Aircraft, Vol.21, No.1, 1984, pp.85-87.
- [9] Zingel, H.: *Zur Bestimmung des aeroelastischen Verhaltens von Auftriebssystemen infolge Strömungsablösung. (On the Prediction of the Aeroelastic Behavior of Lifting Systems Due to Flow Separation.)* DfVLR-FB 86-35, 1986.
- [10] Försching, H.: *Aeroelastic Buffeting Prediction Techniques - A General Review*. DfVLR-FB 81-15, 1981.
- [11] Geißler, W.: *Non-Linear Unsteady Potential Flow Calculations for Three-Dimensional Oscillating Wings*. AIAA-Journal 16 (1978), pp.1168-1174.
- [12] Mullans, R.E.; Lemley, C.E.: *Buffet Dynamic Loads During Transonic Maneuvers*. AFFD Techn. Rep. AFFDL-TR-72-46, Sept. 1972.

Acknowledgement

The author is greatly indebted to Dr.H. Zingel (formerly DLR - Institute for Aeroelasticity and presently MBB-UT, Bremen) for providing most of the test results presented in this paper.

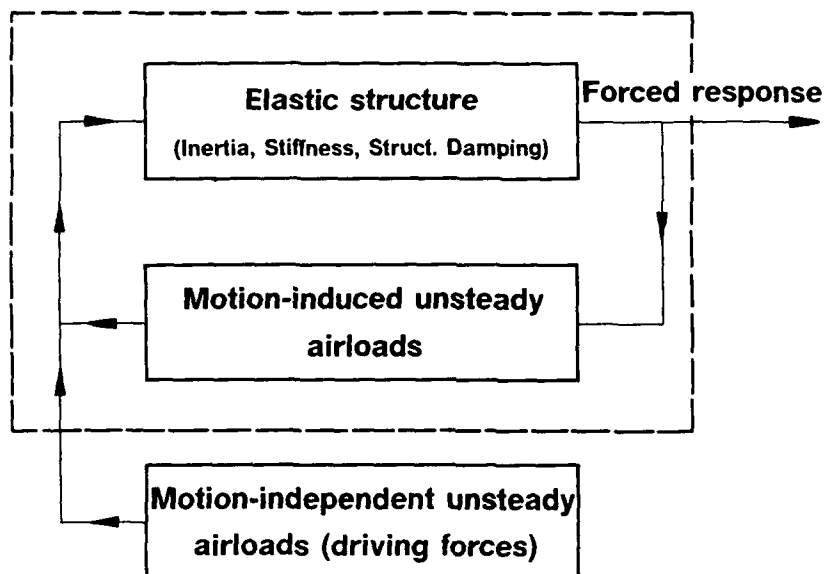


Figure 1. Aceroelastic functional diagram of the forced oscillation model approach.

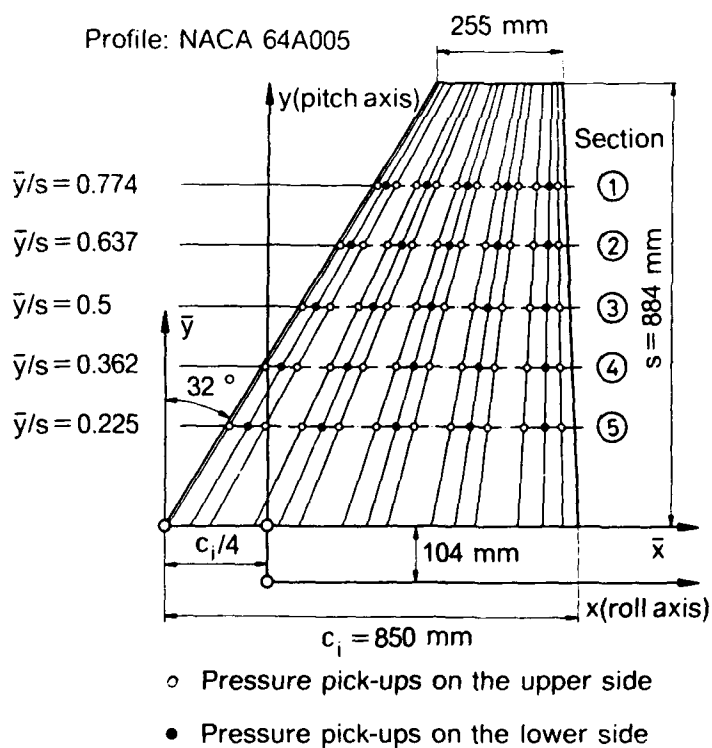


Figure 2. Geometric details of the half-wing wind tunnel model and arrangement of the aerodynamic pressure pick-ups.

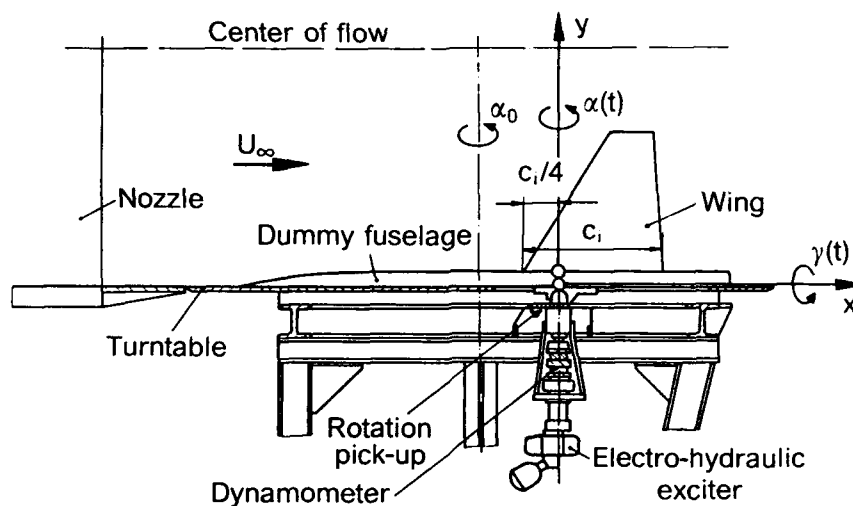


Figure 3. Schematic of the wind tunnel test set-up (for pitching excitation).

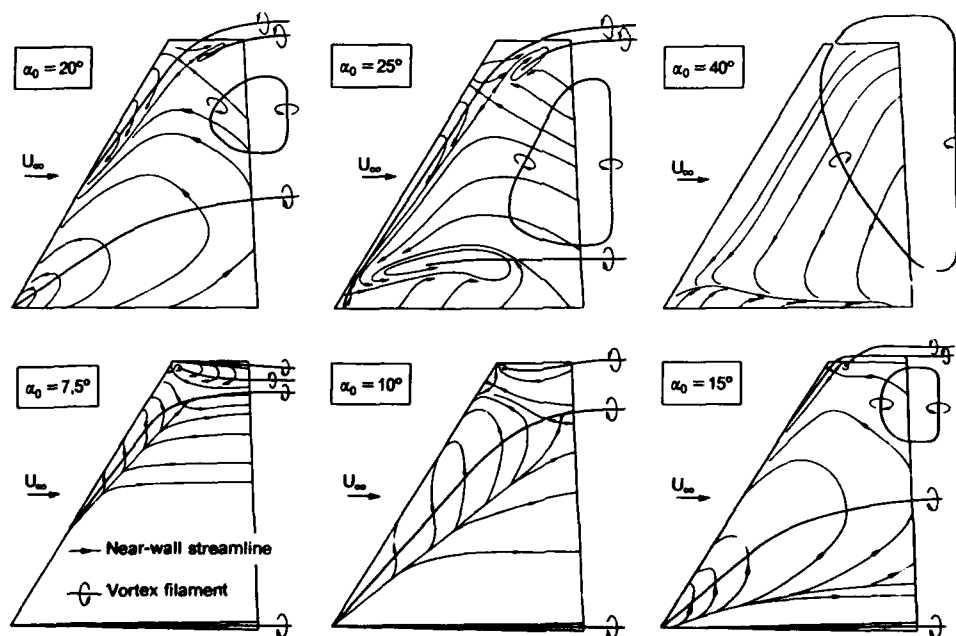


Figure 4. Characteristic near-wall streamlines and vortex skeleton at various steady mean incidences α_0 on the upper side of the stationary wing.

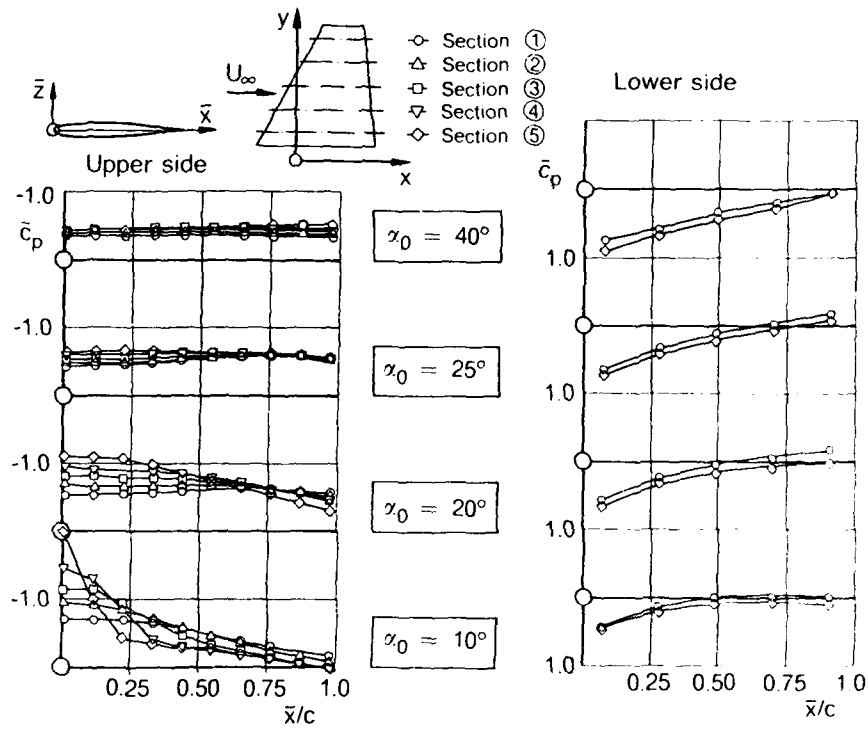


Figure 5. Steady mean pressure distributions \bar{c}_p at various incidences α_0 on the upper and lower sides of the stationary wing.

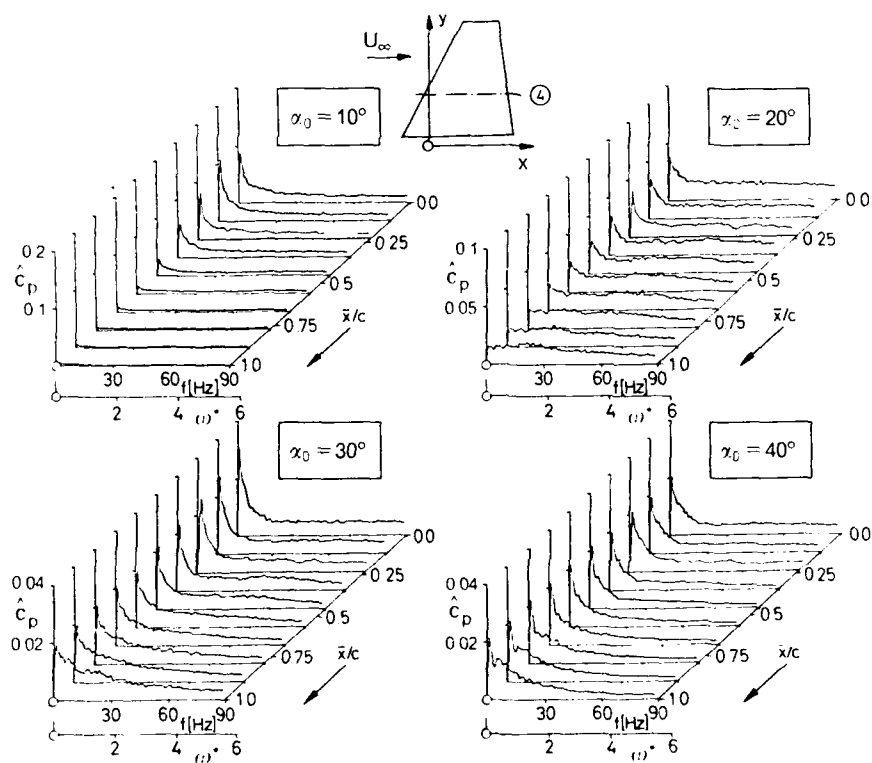


Figure 6. Amplitude spectra $\hat{c}_p(f)$ of the pressure coefficients $c_p(t)$ in Section ④ on the upper side of the stationary wing at various incidences α_0 .

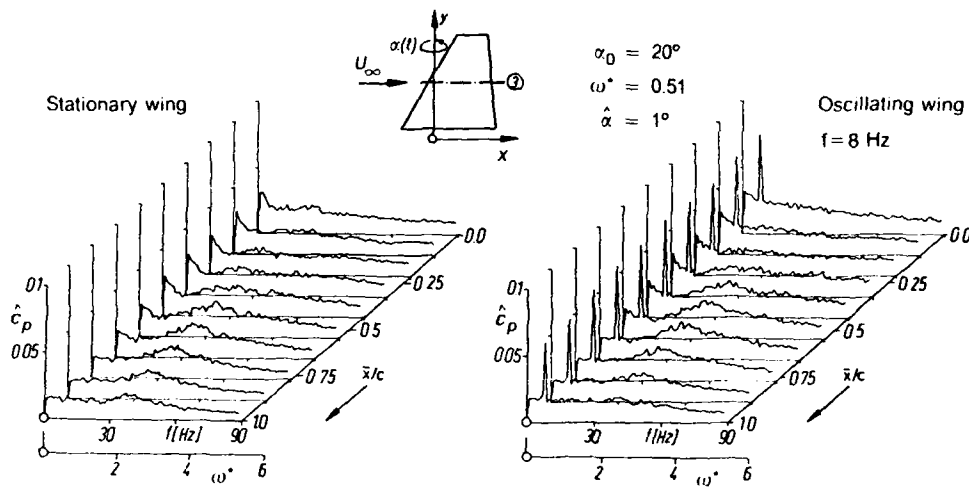


Figure 7. Effect of harmonic (pitching) motion on the amplitude spectrum $\hat{c}_p(f)$ of the pressure coefficients $c_p(t)$ in Section ③ on the upper side of the wing at an angle of attack $\alpha_0 = 20^\circ$.

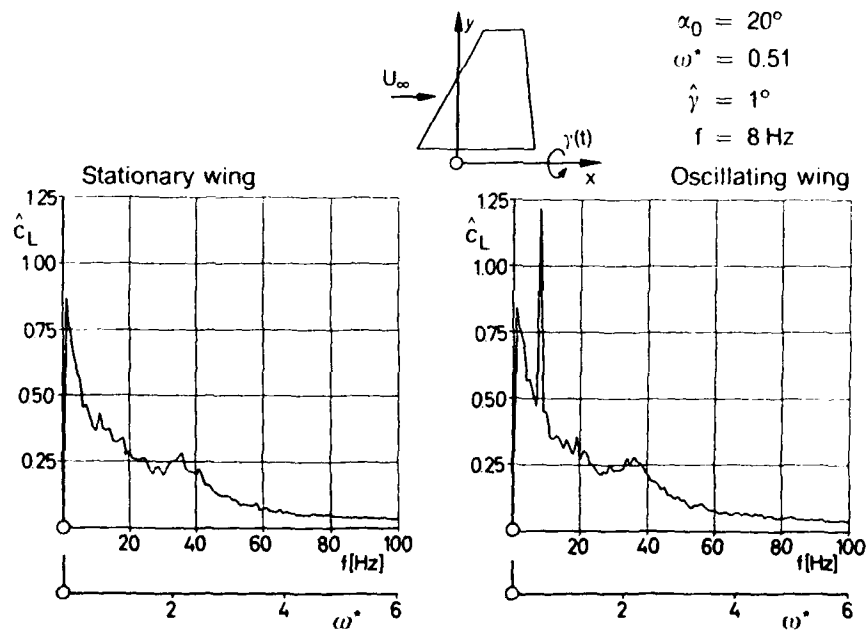


Figure 8. Effect of harmonic (rolling) motion on the amplitude spectrum $\hat{c}_l(f)$ of the rolling moment coefficient $c_l(t)$ at an angle of attack $\alpha_0 = 20^\circ$.

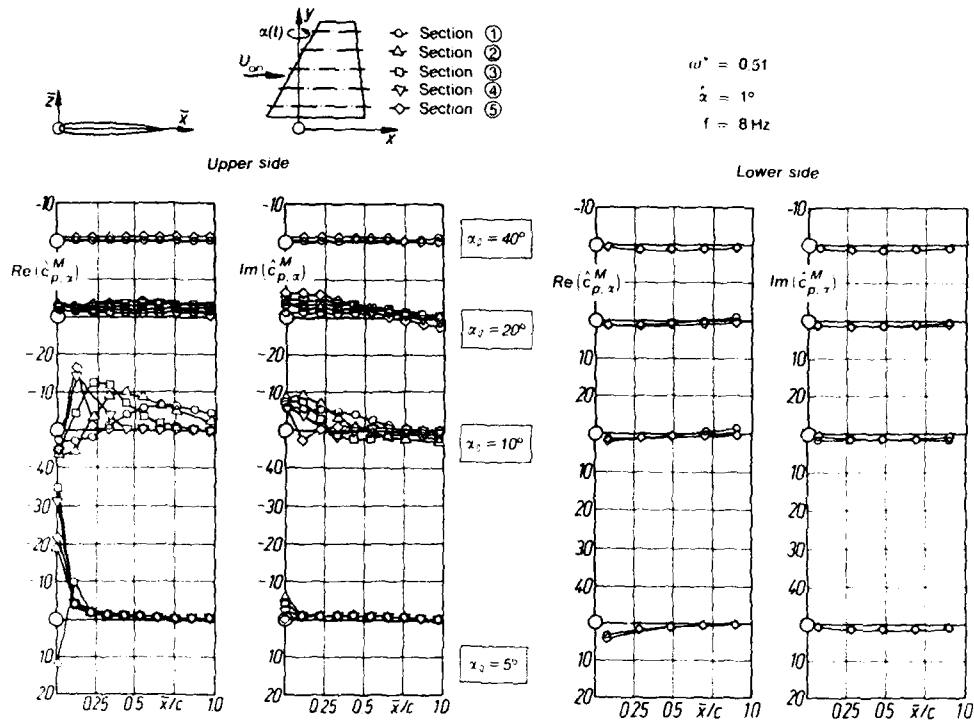


Figure 9. Amplitudes $\text{Re}(\hat{c}_{p,z}^M)$ and $\text{Im}(\hat{c}_{p,z}^M)$, respectively, of the motion-induced unsteady pressure distributions on the upper and lower sides of the wing performing harmonic pitching oscillations about various steady mean incidences α_0 .

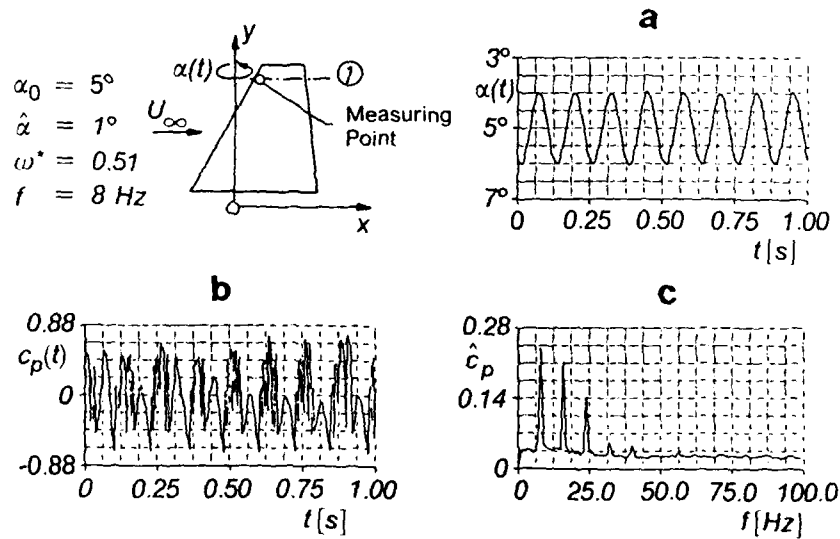


Figure 10. Dynamic stall events at a leading edge measuring point near the wing tip.

- Time history $\alpha(t)$ of the oscillating (pitching) wing.
- Time history $c_p(t)$ of the unsteady aerodynamic pressure signal.
- Amplitude spectrum $\hat{c}_p(f)$ of the pressure signal.

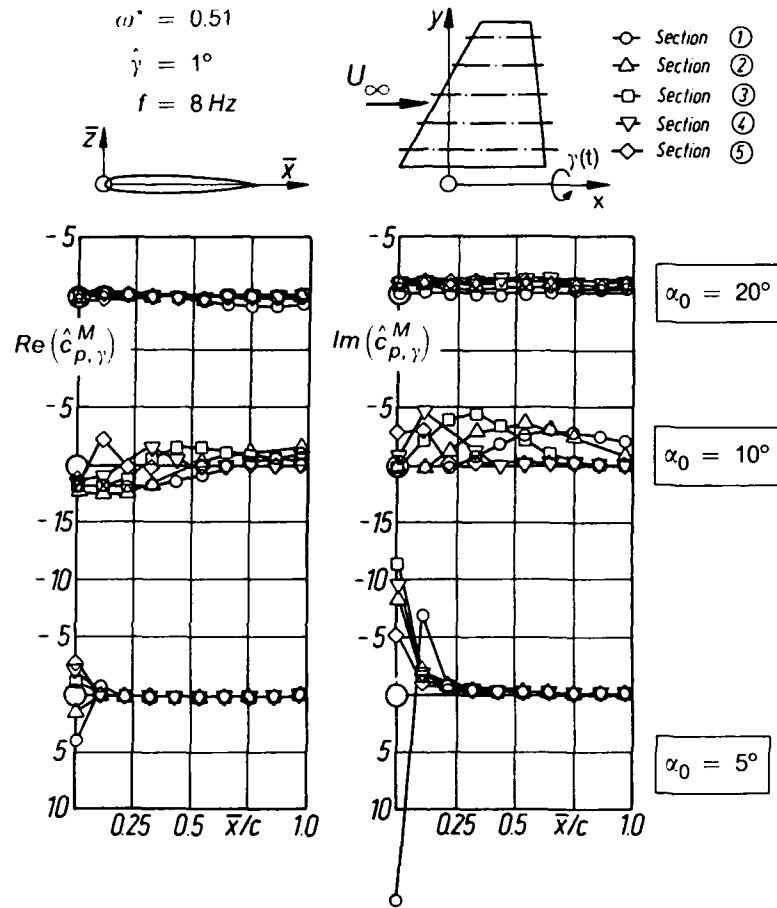


Figure 11. Amplitudes $\text{Re}(\hat{c}_{p,\gamma}^M)$ and $\text{Im}(\hat{c}_{p,\gamma}^M)$, respectively, of the motion-induced unsteady pressure distributions on the upper side of the wing performing harmonic rolling oscillations about various steady mean incidences α_0 .

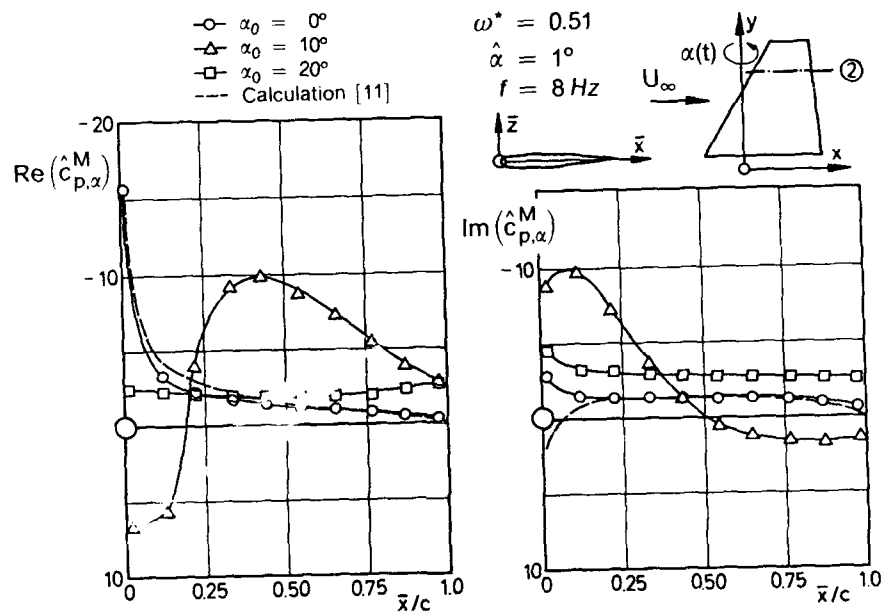


Figure 12. Comparison between measured and calculated amplitudes of motion-induced unsteady pressure distributions $\text{Re}(\hat{C}_{p,\alpha}^M)$ and $\text{Im}(\hat{C}_{p,\alpha}^M)$, respectively, in Section ② on the upper side of the wing performing harmonic pitching oscillations about various steady mean incidences α_0 .

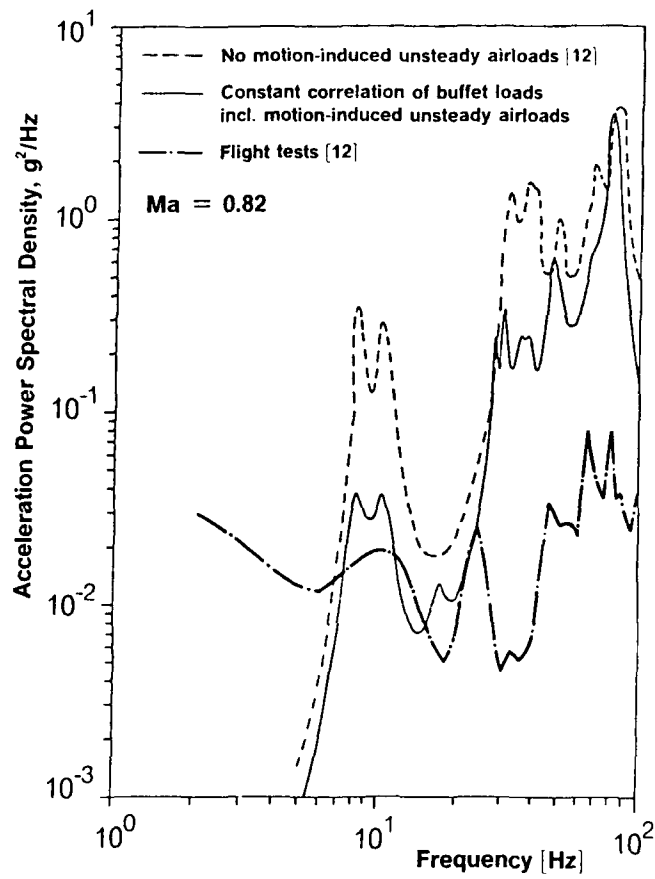


Figure 13. Comparison of transonic buffeting response acceleration power spectral density on an F-4E wing between theoretical predictions and flight tests (adapted from Ref. [8]).

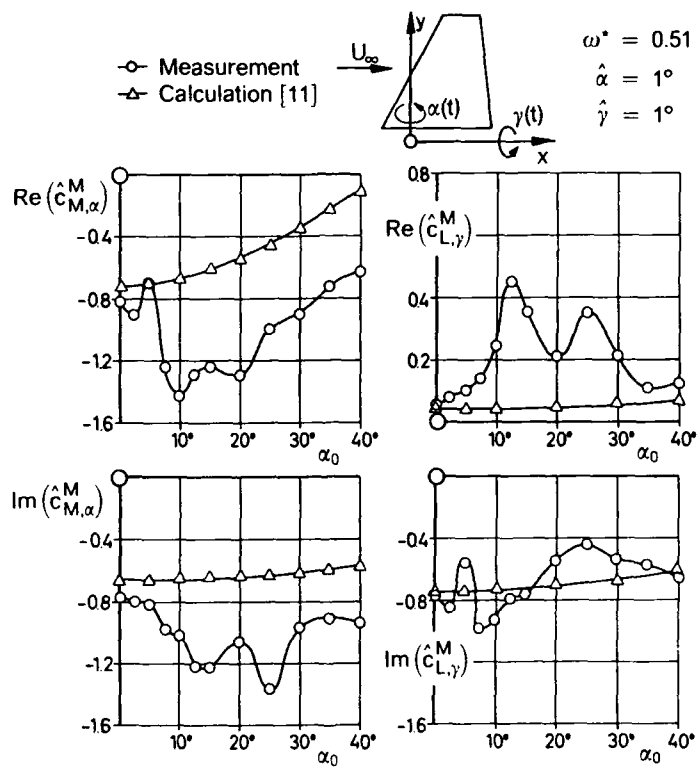


Figure 14. Comparison between measured and calculated amplitudes of motion-induced unsteady pitching moment and rolling moment coefficients ($\hat{C}_{M,\alpha}^M$) and ($\hat{C}_{L,\gamma}^M$), respectively, at various steady mean incidences α_0 .

The Forward Mounted Spoiler as a Source of Buffet Excitation

by

P.G. Myers & D.L. Birdsall

Department of Aerospace Engineering

University of Bristol

Queen's Building

University Walk

Bristol

BS8 1TR

United Kingdom

Summary

Tests have been made with fixed transition at low Reynolds Numbers (usually 0.56×10^6 , based on chord) on a wing with a spoiler of length 8% chord hinged at 13% chord. Different classes of flow leading to differing spoiler performance have been identified. However signal analysis has shown that the non-dimensional frequency n_1 can be used to correlate results from these classes of flow and that the peak frequencies will lie within a narrow band. Now $n_1 = fl_b/V$ where f is the frequency, l_b the length of separated flow from the spoiler free edge lying over the wing (in the case of a closed bubble, l_b is the bubble length) and V the freestream velocity. Since n_1 depends on l_b , a good idea of the nature of buffet excitation can be formed from an observation of the scale of separated flow lying over the wing.

With one class of flow, there was no change in steady state lift following spoiler deployment, but the formation of a separation bubble over much of the wing upper surface led to a high level of buffet excitation. This underlines the difficulty of trying to deduce the fluctuating component of lift from a steady mean.

Nomenclature

a_1	lift curve slope, $\partial C_L / \partial \alpha$
c	wing chord
C_L	2d lift coefficient
C_p	pressure coefficient
f	frequency
$F(n)$	spectral density function
h	projected height of a deflected spoiler
l_b	bubble length
L	representative length in definition of n
n	general frequency parameter based on L , fL/V
n_c	frequency parameter based on c , fc/V
n_1	frequency parameter based on bubble length, fl_b/V
\bar{p}	rms of fluctuating component of pressure fluctuations
$\Delta \bar{p}$	contribution to \bar{p} over analyser frequency bandwidth Δf
p_s	static pressure at a tapping on model
p_∞	tunnel reference pressure
q	dynamic pressure, $\frac{1}{2} \rho V^2$
$S(f)$	power spectral density function
V	tunnel velocity
x	streamwise coordinate
$(x/c)_c$	closure point of bubble in near wake
$(x/c)_r$	reattachment point of bubble
$(x/c)_s$	separation point of bubble
$x(t)$	general function in time domain (see Eqn 4.6)
$X(f)$	function in frequency domain resulting from an FFT
α	incidence
δ	spoiler deflection
ϵ	analyser bandwidth ratio, $\Delta f/f$
σ	square root of variance

1 Introduction

A study is being made within the Department of Aerospace Engineering, University of Bristol, into the static and dynamic characteristics of a wing fitted with a spoiler capable of rapid deployment. Many aircraft are fitted with spoilers mounted at a conventional position, hinged at about 70% chord back from the leading edge. However the present study has considered three positions in turn in order to investigate the effect on transient delays and loads (as well as static characteristics) of a change in spoiler chordwise position.

This paper is concerned with the nature of fluctuations associated with separated flow on a wing fitted with a statically deflected, forward mounted spoiler. In many cases, flow separating from the spoiler free edge and reattaching forward of the wing trailing edge formed a bubble. The emphasis is on providing a general, physical description of these separated flows.

2 Equipment

The major part of the research into spoiler aerodynamics at Bristol University for the last five years has been a study of transients (of lift) and delays during and after rapid spoiler movement. This was done by conducting tests in an open jet tunnel at low Reynolds numbers, taking measurements at high sampling rates from points around a wing profile using pressure transducers. Thus a priority was to ensure a large value in the pressure differences recorded by the transducers, leading inevitably to the use of a wing of large chord (and therefore low aspect ratio) fitted with large endplates. The wing had a NACA 0012 section with a basic aspect ratio of 2 and a span of about two thirds of the nominal jet diameter, the ratio (endplate height / wing chord) was 1.5 and a spoiler with a length 8% of wing chord was used. Transition was fixed upstream of the spoiler using a roughness strip. For these tests, the spoiler was hinged at a forward position, namely 13% of wing chord from the leading edge.

The preliminary tests described in Section 3 used a simple three component balance to generate static lift data for the cases of a clean wing and a wing with a statically deflected spoiler. All other tests used a pressure transducer system as a means of data collection. Data collection from the Setra transducers sampling at stations along the wing centreline was possible at rates ranging from 1kHz per tapping if about a dozen transducers were used, to 3.2kHz per tapping if just two transducers were used. Further details of the rig are given elsewhere (Ref 1).

3 Static Spoiler : Time Invariant Characteristics

A study was made of the steady state characteristics of a wing with a statically deflected spoiler. In this Department's other work on spoilers (studies of transients and delays following rapid spoiler deployment), pressure transducers have been used to record surface pressure histories with subsequent integration to give lift histories. In this Section, since only static lift measurements were required, a simpler scheme using tunnel balance measurements was adopted.

3.1 Clean Wing (No Spoiler)

Fig 1 shows the lift curve for a clean wing and the case of a spoiler at $x/c = 0.13$. Several points are of interest.

The data presented here have not been corrected for tunnel constraints, if only to allow certain comparisons with examples from Kalligas which were also free from corrections. Corrected data have been produced, using lifting surface theory and the endplate corrections recommended by Hoerner (Ref 2), to verify the lift curve slope a_1 . However, traditional correction procedures apply to static conditions and it must be assumed that localised phenomena - such as the strong starting vortex associated with the rapid opening of a spoiler - will not properly be accounted for. For such reasons, the static and dynamic data quoted are uncorrected.

Stalling of this aerofoil section (NACA 0012) at low Reynolds numbers was complex. A small change in transition fixing (particle size, width of roughness strip, etc) was seen to alter the lift curve noticeably. In general during these tests the stall was of the mixed leading edge, trailing edge type.

The other curves show the effect of deploying a spoiler hinged at $x/c = 0.13$ and deflected to $\delta = 20^\circ$ and $\delta = 40^\circ$. There are three types of flow apparent. To explain this observation it is convenient to consider an idealisation of an aerofoil with a spoiler and to observe the effect of changing the spoiler hinge position.

3.2 General Case : Flow about a Statically Deflected Spoiler

Consider the generalised case of a spoiler with hingeline at an arbitrary chordwise station on an aerofoil. Fig 2 shows that essentially there are three distinct flow regions : the portions on the upper surface fore and aft of the spoiler and the whole of the lower surface. For convenience we refer to these regions henceforth as A, B and C. From a consideration of each region in turn - and for the moment restricting the problem to one of maximising static spoiling - we shall see the conflicting requirements for choosing a chordwise position for a spoiler.

3.2.1 Region A

Pressures will always rise in region A forward of the deflected spoiler. Thus the change in lift in region A after spoiler deployment will always act to produce a net download on the aerofoil. Intuitively it would seem that in order for the spoiler to produce as large a lift decrement as possible in this region, the spoiler should have a large chord and be positioned to have greatest effect on those areas which usually have a strong suction. For positive angles of incidence, this implies that the hinge should be well forward.

3.2.2 Region B

Flow will always separate from the spoiler tip and often this divided flow will extend into the wake. However, given the right combination of sizes for the length of B as a fraction of chord, aerofoil incidence α and spoiler deflection δ , a different flow is observed. For example, if the length of B is a large fraction of chord, if α is small or negative and if δ is reasonably small then the separated shear layer will reattach forward of the trailing edge. A separation bubble is then formed in the front part of B. Region B is subjected almost exclusively to reduced pressures relative to conditions prior to spoiler deployment, and as a consequence contributes to increased lift. We must conclude that on this basis the hinge should not be well forward. Furthermore, the occurrence or otherwise of reattachment is an important consideration, because if the separated shear layer extends into the wake, the trailing edge pressure will be much reduced from conditions prior to spoiler deployment. This reduction in pressure will be transmitted around the trailing edge so that the entire lower surface, region C will be affected by a reduction and more lift will be lost. This again tends to argue in favour of the spoiler not being far forward at incidences where reattachment is a possibility.

3.2.3 Region C

The pressure drop sustained over this area after spoiler deployment (and provided that there is no flow reattachment on the upper surface) can provide strong conventional spoiling. The spoiling will be large when the pressure drop at the trailing edge is large. For this to happen, the spoiler must be far enough forward to generate a large pressure drop at the trailing edge - but not so far forward that reattachment can occur for the given combination of sizes of B, α and δ .

3.2.4 The Aerofoil as a Whole

For conditions which govern the pressure change in regions A and C, it seems that the farther forward the spoiler, the greater the ΔC_L - provided no reattachment occurs. If this proviso is not met, practically no spoiling would occur.

3.3 Forward Mounted Spoiler (Hinge at 13% Chord)

For the specific case of a spoiler mounted at $x/c = 0.13$ and deflected to $\delta = 40^\circ$, it is seen from Fig 1 that the spoiler was very effective at high α but less so as α was reduced. At negative α , the spoiler was ineffective as a lift reducing device. The figure implies that flow characteristics were totally different at $\alpha = +12^\circ$ and $\alpha = -12^\circ$, for example.

An analysis of the contributions to ΔC_L from upper and lower surfaces showed that at all positive values of α , the contribution to ΔC_L from the lower surface was large (of order -0.2 to -0.25) and apart from the stall region was substantially the major component of total spoiling action. However at negative values of α the lower surface contribution to ΔC_L rapidly fell away as the magnitude of α increased. The upper surface contribution to ΔC_L was sensibly constant for negative α . Over this range a separation bubble existed over the upper surface, or closed just aft of the trailing edge in the near-wake. As a means of

spoiling, the upper surface contribution was detrimental until α reached a value of about 8° , and was comparable in size to the lower surface contribution only at or near the positive stall.

The foregoing serves to explain the three characteristic regions of the lift curve of a wing fitted with a statically deflected, forward mounted spoiler.

Over an incidence range from negative stall to an angle α_1 , say, the spoiler is ineffective as a means of generating a ΔC_L . A moderate decrease in pressure is developed on the upper surface from the separation bubble and an even smaller decrease in pressure on the lower surface due to the ΔC_p at the trailing edge.

Over an incidence range from α_1 to α_2 , say, effectiveness increases rapidly. The separated shear layer originating from the spoiler free edge extends into the wake with an increasingly sizeable thickness at the trailing edge, which consequently leads to a progressively larger pressure drop at that edge. This in turn forces a rapid increase in the size of the contribution to spoiling from the lower surface. On the upper surface the pressure rise forward of the spoiler becomes more important and compensates for the pressure fall aft, so that over this incidence range the contribution to ΔC_L from this region falls from a low positive value to zero.

Over an incidence range from α_2 to near positive stall the separated flow field aft of the spoiler is fully developed. The pressure drop at the trailing edge is sensibly constant and therefore so is the contribution to ΔC_L from the lower surface. The contribution from the upper surface increases as the pressure rise in front of the spoiler increases up to near stall.

It will be seen that the static conditions resulting from a spoiler deployment have a profound effect on the levels of buffet excitation generated by the flow. Moreover this effect changes as the conditions change (in other words, as α and δ are varied) and generally cannot be inferred from static measurements.

4 Static Spoiler : Time Varying Characteristics

The time varying characteristics of the flow field about the upper surface of a wing with a forward mounted spoiler were investigated. During the development of the data collection and processing system, it was decided that for each pressure history, the record length and scanning frequency should be as high as possible. Existing software was modified so that maximum record length was increased from 500 measurements to nearly 2000 and maximum scanning frequency was increased from 1.0 to 3.2 kHz. The penalty for this increased performance per channel was a reduction in the number of channels sampled per run from eleven to two. So, for a particular configuration of α and δ , six tunnel runs had to be made to capture the pressure fluctuation history over the whole surface. Given that tunnel conditions were repeatable this was not seen to be a problem.

4.1 Data Analysis

After collecting pressure histories from various stations on the wing, some method was needed to convert the data and to allow a study to be made of the constituents of each pressure signal at discrete frequencies.

4.1.1 Analogue Method

A technique has been described by Owen (Ref 3) which was used at the RAE and can be termed an analogue method. Pressure signals were stored on tape at run time and played back through an analyser containing a bank of filters through which the signal was passed repeatedly. At every pass a particular reference frequency was selected ; a band-pass filter centred on that frequency then allowed only those constituents of the signal at frequencies within the pass band to pass through for analysis. With a careful choice of frequencies and a full sequence of analyses, spectral functions of several kinds would be obtained from the single original pressure signal.

As Owen noted, if a non-dimensional parameter n was defined with

$$n = fL/V \quad (4.1)$$

where f was the frequency, L a representative length and V the free stream velocity, a spectrum function $F(n)$ could be defined so that $F(n)\delta n$ would be the contribution to $(\bar{p}/q)^2$ in the frequency range n to $n+\delta n$. In the present work L was taken to be the wing chord c so that a specific reduced frequency n_c was defined specifically as

$$n_c = fc/V . \quad (4.1a)$$

Henceforth, n_c will be written as n except in cases where confusion is possible. Here, \bar{p} was the variance of the pressure fluctuation and q the dynamic pressure. Hence, $(\bar{p}/q)^2$ was the mean square value of the fluctuating component of C_p , since

$$C_p = (p_s - p_\infty)/q \quad (4.2)$$

with p_s being the static pressure measured at a surface pressure tapping and p_∞ the reference pressure. Integrating the spectral function over the full frequency range gave

$$\int_0^\infty F(n) dn = \int_{n=0}^{n=\infty} nF(n) d(\log n) = (\bar{p}/q)^2 . \quad (4.3)$$

With the analyser bandwidth ratio ϵ defined as

$$\epsilon = (\Delta f)/f , \quad (4.4)$$

and with $\Delta \bar{p}$ being the contribution to \bar{p} over the analyser bandwidth Δf , the final definition would be

$$\sqrt{[nF(n)]} = \Delta \bar{p}/(q\sqrt{\epsilon}) . \quad (4.5)$$

4.1.2 Digital Method

The analogue method was not suitable for the present work because at the earliest stage of data recording, signals were converted from analogue to digital form. The most obvious approach was to select a digital technique to match completely the analogue process. This was tried but was found to be inefficient and unlikely to provide acceptable accuracy because of associated computational problems. Rather it was found that the most convenient method was as follows.

The basis of the digital method was to use a discrete Fast Fourier Transform to convert a time history $x(t)$ (henceforth assumed to have a zero mean value) to a parallel function $X(f)$ in the frequency domain. Thus

$$x(t) \Leftrightarrow X(f) \quad (4.6)$$

and as a consequence of the associated theory (see for example Ref 4), the square of $X(f)$ had a mean equal to the variance of the original time signal. Thus

$$1/f_1 \int_0^{f_1} X^2(f) df = \sigma^2 \quad (4.7)$$

if f_1 = maximum value of f .

Now since by definition

$$\int_0^{f_1} S(f) df = \sigma^2 , \quad (4.8)$$

it followed that at every frequency f ,

$$S(f) = (1/f) X^2(f) . \quad (4.9)$$

It was therefore simple to generate $S(f)$ and $[fS(f)]/\sigma^2$. Finally, the $F(n)$ data could be generated just as easily from the identity

$$\int_0^{n_1} F(n) dn = \sigma^2 . \quad (4.10)$$

Bearing in mind that a large number of individual time histories would be analysed, a routine was written which read in files sequentially and which was capable of applying a selection of analyses to each one. The pressure history underwent block averaging, removal of the mean or 'dc component', and padding with zeros (addition of zeros in equal amounts to front and back of record). It was then passed through a discrete

Fast Fourier Transform routine. The frequency function so produced was then squared and multiplied by whatever frequency was implicit in the transform, to provide $\sqrt{[nF(n)]}$ for example.

In this way time histories in the form $C_p(t)$ were converted to functions in the frequency domain. Specifically, the following functions were generated :

$S(f)$ with f , $fS(f)/\sigma^2$ with $\log(f)$ and $\sqrt{[nF(n)]}$ with $\log(n)$.

The second form was useful for comparisons with data from wind engineering, for example that used by ESDU (Ref 5), whilst the third form was that used by Owen and in buffet analysis by amongst others, Mabey (Ref 6). At the heart of the frequency analysis routine was a discrete FFT subroutine written by Sehmi (Ref 7).

4.2 Typical Example : Bubble Closing Forward of Trailing Edge

To illustrate the method of analysis, consider the configuration of $\alpha = 4^\circ$, $\delta = 20^\circ$ where flow separated from the spoiler free edge but reattached forward of the wing trailing edge.

4.2.1 Total Broad Band Pressure Fluctuation : \bar{p}/q

Fig 3 shows the chordwise variation of \bar{p}/q . According to previous measurements, if the spacing between transducers had been small enough, a maximum recorded value for \bar{p}/q would have been observed just forward of reattachment. In fact, the closest transducer was at $x/c = 0.60$ and reattachment was judged to have occurred at about $x/c = 0.62$ based on flow visualisation. Allowing for the fact that the transducer was not at an optimum position relative to reattachment, the peak value for \bar{p}/q of 0.058 appears reasonable in view of published data on the subject. Mabey (Ref 6) observed that in general for a bubble class of flow, \bar{p}/q would lie within the range

$$0.04 \leq \bar{p}/q \leq 0.10 \quad (4.11)$$

and specifically for a bubble downstream of a spoiler the excitation should reach a maximum of

$$\bar{p}/q = 0.050 \quad (4.12)$$

4.2.2 Bubble Extent

The reattachment point was located using china clay surface flow visualisation after the method described by Moir (Ref 8), and verified using a nylon filament or wool tuft close to the surface in the indicated region. For all cases separation was taken to occur from the spoiler free edge giving the chordwise separation coordinate,

$$(x/c)_s = 0.13 + 0.08 \cos 20^\circ = 0.21 \quad (4.13)$$

For this case reattachment occurred at $(x/c)_r = 0.62$, which was just downstream of the recorded peak in \bar{p}/q . With the spoiler having a chord of $0.08c$, the length of the bubble l_b was given by the approximate relation

$$l_b/c = (x/c)_r - (x/c)_s = 0.41 \quad (4.14)$$

Note that if h was the height of the spoiler then for this test,

$$h/c = 0.08 \sin 20^\circ = 0.027 \quad (4.15)$$

giving the ratio of bubble length to projected spoiler height, l_b/h as

$$l_b/h = 0.41/0.027 = 14 \quad (4.16)$$

4.2.3 Spectral Plot of Pressure Close to Reattachment

An example of a spectral plot is shown in Fig 4. Gaussian smoothing (using five points to either side of each data point) was used to clarify the picture but still to retain some of the random element of the signal. The station selected was at $x/c = 0.60$, being close to the reattachment point of the separation bubble for this

configuration. The bell shape, characteristic of the $\sqrt{[nF(n)]}$ function for this class of flow near reattachment can be seen clearly. Of particular interest are the peak value of the function and the value of n at which it occurred.

As explained earlier, since bubble length is a variable dependant on α and δ , chord must be used as the characteristic length during the first part of the analysis. However, it is usual in correlating results to use bubble length, rather than model chord. Hence a slightly different reduced frequency, n_1 may be defined with

$$n_1 = fl_b/V \quad (4.17)$$

where l_b is the bubble length. There is no alteration to the $\sqrt{[nF(n)]}$ values because by definition,

$$fS(f) = nF(n) = n_1F(n_1). \quad (4.18)$$

From Fig 4, a peak value for $\sqrt{[nF(n)]}$ of 0.035 occurred at a value for n of 1.97. This is equivalent to a value of n_1 of 0.78. Mabey (Ref 6) correlated results for separated flows and stated that for stations close to reattachment n_1 should lie in the range

$$0.5 \leq n_1 \leq 0.8. \quad (4.19)$$

Clearly the peak value for a station close to reattachment is within this range.

Mabey (Ref 6) stated that for a leading edge separation bubble having a peak value for \bar{p}/q of 0.10, the peak value for $\sqrt{[nF(n)]}$ would be 0.06. Here (for the bubble behind a spoiler) the peak value for \bar{p}/q was 0.058 and so the peak value for $\sqrt{[nF(n)]}$ of 0.035 appears reasonable also.

4.2.4 Spectral Data From All Stations

Peak values of the function $\sqrt{[nF(n)]}$ were found for all eleven pressure measurement stations on the upper surface (for $\alpha = 4^\circ$, $\delta = 20^\circ$) and were plotted on Fig 3 along with the chordwise variation of \bar{p}/q mentioned before. Notice that the shapes of the two functions on this figure are very similar. Both have a maximum at the station $x/c = 0.6$, as well as can be judged with the resolution available. It would appear that the two functions are equally valid in predicting that reattachment has occurred and approximately where.

Values of n_1 for peaks of $\sqrt{[nF(n)]}$ were found for all stations sampled and the results are shown in Fig 5. It is clear that peaks of $\sqrt{[nF(n)]}$ lie at reduced frequencies within or close to the range (4.19), over a large proportion of the wing and not just close to reattachment.

4.2.5 Implications

A few key points from the preceding paragraphs of this section regarding the $C_p(t)$ at a station close to reattachment may be stated as follows :

- it will have a greater rms than any other $C_p(t)$;
- the peak value of the $\sqrt{[nF(n)]}$ function derived will be greater than the corresponding peaks derived from any other station ; and
- the frequency at which the function $\sqrt{[nF(n)]}$ shows a peak will be higher than for any other station within the bubble.

Now since the eleven $C_p(t)$'s could in principle be integrated to give the sectional lift along the centreline, it follows that :

- the rms of $C_L(t)$ will be significantly smaller than the rms of $C_p(t)$ at reattachment ;
- and
- comparing the $\sqrt{[nF(n)]}$ functions derived from $C_p(t)$ close to reattachment and from $C_L(t)$, the peak value of $\sqrt{[nF(n)]}$ will be larger and will occur at a larger frequency for the $C_p(t)$.

There are practical difficulties involved in generating a dynamic lift history, $C_L(t)$ - sufficiently accurate for spectral analysis - from the pressure coefficient histories $C_p(t)$. The eleven $C_p(t)$ records would have to be sampled exactly in parallel otherwise phase shifts would be incurred which would reduce rms values of the final signal as well as distorting the apparent relative sizes of constituents at discrete frequencies. However, a prediction as to the likely values of spectral parameters for the upper surface (broad band rms, peak value of $\sqrt{[nF(n)]}$ and n_1) was possible from an inspection of spectral values generated from the pressure coefficient histories.

4.2.6 Effect of a Change in Reynolds Number

Tests were carried out at a fixed configuration ($\alpha = 4^\circ$, $\delta = 20^\circ$) but with tunnel speed set to half and three quarters of the usual speed. All other test conditions (for example, roughness particle size) were left unaltered. Fixing reattachment was difficult for this case - more so than at lower reduced frequencies (ie at $\alpha = -12^\circ$ or at $\alpha = -4^\circ$) - but the bubble length was found to be very similar for all three tunnel speeds and, if anything, to show a slight reduction with decreasing Reynolds Number. This last trend was sensible but the limited accuracy of the test procedures allowed only a statement that the variation in n_1 was small.

4.2.7 Other Configurations with Closure Forward of the Trailing Edge.

Testing was carried out for several different configurations. Table 1a shows results collected from tests at those instances when a bubble extended from the spoiler and closed forward of the wing trailing edge. Generally, it was found easier to fix reattachment of the separation bubble for lower angles of incidence. Thus at $\alpha = -12^\circ$, reattachment was well defined and covered a narrow band since (by comparison with the other configurations) the streamwise pressure gradient was favourable. As α was increased, reattachment became less well defined as the pressure gradient became less favourable. Thus estimation of bubble length, l_b , was less accurate with $\alpha = 4^\circ$ than for configurations at the other two angles of incidence considered.

4.2.8 Peaks in \bar{p}/q

From Table 1 it is clear that there was a considerable variation in recorded peaks of the rms pressure fluctuation of

$$\bar{p}/q \text{ between } 0.038 \text{ and } 0.083. \quad (4.20)$$

Thus all peaks of \bar{p}/q fell (more or less) within the broader band (4.11) observed by Mabey (Ref 6). At the two moderate incidences of $\alpha = \pm 4^\circ$ it was found that levels of fluctuation increased with increasing spoiler deployment (and therefore bubble length). This was not found to be the case for a large negative incidence of $\alpha = -12^\circ$.

4.2.9 Peaks in $\sqrt{[nF(n)]}$

There was a similar variation in the values of recorded peaks in $\sqrt{[nF(n)]}$ within the range

$$0.024 \leq \sqrt{[nF(n)]}_{\max} \leq 0.056. \quad (4.21)$$

The respective values of n at which the peaks of $\sqrt{[nF(n)]}$ occurred were found and are recorded in Table 1. Having found respective values for bubble length, values for n_1 were found and are seen to be in the range

$$0.63 \leq n_1 \leq 0.81. \quad (4.22)$$

This was largely in agreement with the range (4.19) suggested by Mabey (Ref 6).

4.2.10 Bubble Extent

Estimation of bubble length, l_b , was approximate. However from Table 1 it can be seen that the ratio l_b/h (of bubble length to projected spoiler height) increased as α increased. This was to be expected since at a given value of x/c behind the spoiler the streamwise pressure gradient, dp/dx , would become more adverse with increasing α . Clearly in 2d inviscid flow with zero pressure gradient (on a flat plate rather than an aerofoil), l_b/h would be constant.

4.3 Configurations with Bubble Closure Behind the Wing.

The case of $\alpha = 4^\circ$, $\delta = 40^\circ$ was an instance where (using information from surface flow visualisation) the separation bubble did not appear to close over the wing surface. As shown by Fig 6, the chordwise variations of \bar{p}/q and $\sqrt{[nF(n)]}$ both showed a steady increase with increasing distance from the spoiler free edge, reaching peaks of 0.073 and 0.050 respectively at $x/c = 0.90$. Recalling the study of a static spoiler in Section 3.3, the spoiler was only marginally effective in decreasing lift for this configuration. However the indications

are that the bubble would close in the near wake and in the absence of any further information a guess was made that the bubble closed 0.1c downstream of the trailing edge. Hence l/c was taken to be 0.9, giving a value for l/h of 18 and (taking n to be 0.9 since this gave a peak for $\sqrt{[nF(n)]}$ at $x/c = 0.90$) giving a value for n_1 of 0.8.

A further example was $\alpha = 12^\circ$ and $\delta = 20^\circ$. The chordwise variations of \bar{p}/q and $\sqrt{[nF(n)]}$ are shown in Fig 7 to be different to the previous configuration: over the first half of the separated flow, both functions increased steadily and over the latter half remained almost unchanged at around 0.065 and 0.035 respectively. The earlier static study had shown that in this instance, the spoiler was effective as a lift reducing device. The length of separated flow over the wing was again used as the characteristic length in defining n_1 (no other length appearing to be appropriate). As for the previous configuration, l/c was 0.8, but the value for l/h was approximately 34, about twice the value for the previous case. This would be consistent with the observation that for the second configuration, the streamwise pressure gradient aft of the spoiler would be more adverse since incidence was greater. It was found that the value for n_1 at which $\sqrt{[nF(n)]}$ had a peak at stations near the trailing edge was again 0.8.

A comparison between these two configurations is instructive. Whilst they had practically the same peak values for \bar{p}/q (0.073 and 0.074) the peak value for $\sqrt{[nF(n)]}$ in the case of $\alpha = 12^\circ$, $\delta = 20^\circ$ was lower by 20% (0.041 as against 0.050). This is explained by the observation that for stations towards the rear of the wing, the variation of $\sqrt{[nF(n)]}$ with $\log(n)$ for this configuration had less of a pronounced bell shape, thus signal strength was not concentrated over as narrow a band as $\alpha = 4^\circ$, $\delta = 40^\circ$. Fig 8 illustrates this by comparing plots of $\sqrt{[nF(n)]}$ with $\log(n)$ for stations at $x/c = 0.80$ for the two configurations.

In short, the nature of separated flow over the rear 80% of the wing was different for the two cases and this provided an indication of the difference in spoiler performance for the two cases. However the reduced frequency, n_1 , for peaks in the function $\sqrt{[nF(n)]}$ was 0.8 in both cases.

5 Synopsis of Observations

Three distinct classes of flow were produced by a statically deflected forward mounted spoiler and could be identified by several criteria, including:

- the spoiler performance as a means of altering lift;
- the scale of the separated flow region caused by the spoiler; and
- the chordwise variation of broad band pressure fluctuation, \bar{p}/q .

For the first such class, the spoiler had practically no effect on lift, flow reattached forward of the trailing edge and the graph of \bar{p}/q with x/c had a well defined peak just forward of reattachment.

For the second class, the spoiler had only a small effect on lift (ie the configuration was in the transitional region on a C_L , α plot), flow just failed to reattach forward of the trailing edge and the graph of \bar{p}/q with x/c had an ill defined peak close to the trailing edge with little sign of a reduction in \bar{p}/q close to the trailing edge.

For the third class, the spoiler had a sizeable effect on lift, flow was fully separated from the spoiler free edge to the wake and the graph of \bar{p}/q with x/c showed a rapid rise aft of the spoiler free edge for about half the distance to the trailing edge, followed by a region of constant broad band pressure fluctuation.

Having thus identified the differences between the flows, similarities could also be observed. In general the peak value of \bar{p}/q was in a well-defined range (4.20). A length l_b was chosen for each flow. If flow reattached prior to the trailing edge, l_b was the bubble length whilst for the case of separated flow extending into the wake, l_b was the length of chord between the spoiler free edge and the trailing edge. A dimensionless frequency, n_1 , could be defined (Eqn 4.17), and at stations close to the end of the separated flow region the function $\sqrt{[nF(n)]}$ peaked at a frequency n_1 within the range (4.22).

6 Conclusions

A forward mounted spoiler may be fully or partially effective or completely ineffective as a means of reducing lift. The dynamic properties of the flow in each of these three states cannot be inferred from static measurements. In particular the case when the flow reattaches forward of the trailing edge much of the fluctuating component of the lift is concentrated over a narrow band of frequencies centred on a reduced frequency n_1 which may be predicted from the range (4.22). If this non-dimensional frequency corresponds to a frequency of buffet excitation, f , close to any structural mode, then serious buffeting may occur.

These observations underline the difficulties in all studies of separated flow fields of trying to deduce fluctuating characteristics from steady measurements.

References

- 1 Kalligas K.P., Department of Aeronautical Engineering, University of Bristol. The dynamic characteristics of two-dimensional spoilers at low speeds. PhD Thesis, 1985.
- 2 Hoerner S., *Fluid Dynamic Lift*. Hoerner Fluid Dynamics, 1975.
- 3 Owen T.B., Techniques of pressure fluctuation measurement employed in the RAE low speed wind-tunnels, 1958. AGARD Rep 172.
- 4 Brigham E.O., *The Fast Fourier Transform*. Prentice Hall, 1974.
- 5 ESDU, Characteristics of atmospheric turbulence near the ground. Item No 74031, 1974.
- 6 Mabey D.G., Some Aspects of Aircraft Dynamic Loads due to Flow Separation. AGARD Report 750, 1989.
- 7 Sehmi N., SDFFT, a subroutine for calculating the discrete Fast Fourier Transform. Department of Computer Science, University of Bristol, 1989.
- 8 Moir I.R.M., Recent Experience in the RAE 5 Metre Tunnel of a China Clay Technique for Indicating Boundary Layer Transition. *Aeronautical Journal*, Royal Aeronautical Society, 1986.

Acknowledgements.

The current research into spoilers within the Department of Aerospace Engineering, University of Bristol is under a contract funded by the Department of Trade and Industry and monitored by the Royal Aerospace Establishment, Bedford. A previous contract supported Kalligas.

The junior author thanks :

Mr Dennis Mabey for close monitoring of the research from its inception and for many constructive criticisms; and

Dr Kostas Kalligas for considerable developmental work in hardware and software.

Table 1 Parameters from Measurements of Bubbles of Different Types

(a) Bubble Closing Forward of the Trailing Edge

Effect of a Change in Configuration

α/deg	δ/deg	$(x/c)_r$	l/h	l/c	p/q_{max}	$\sqrt{[nF(n)]_{\text{max}}}$	n_c	n_1
-12	60	0.65	6.9	0.48	0.038	0.024	1.51	0.72
	40	0.56	7.2	0.37	0.065	0.049	1.83	0.67
-4	40	0.81	12.1	0.62	0.083	0.056	1.11	0.69
	20	0.51	11.0	0.30	0.038	0.024	2.14	0.63
4	20	0.62	15	0.41	0.058	0.035	1.97	0.81

Effect of a Change in Reynolds Number : $\alpha = 4^\circ$, $\delta = 20^\circ$

$V/(m/s)$	$(x/c)_r$	l/c	l/h	p/q_{max}	$\sqrt{[nF(n)]_{\text{max}}}$	n_c	n_1
10	0.56	0.37	14	0.082	0.061	2.34	0.86
15	0.57	0.38	14	0.064	0.045	2.09	0.80
20	0.62	0.41	15	0.058	0.035	1.97	0.81

(b) Bubble Assumed to Close in Near Wake : Effect of a Change in Configuration

α/deg	δ/deg	$(x/c)_c$	l/c	l/h	p/q_{max}	$\sqrt{[nF(n)]_{\text{max}}}$	n_c	n_1
4	40	1.0	0.9	18	0.073	0.050	0.9	0.8
12	20	1.0	0.9	34	0.074	0.041	0.9	0.8

(c) Spoiler geometry

δ/deg	20	40	60
$(x/c)_s$	0.21	0.19	0.17
h/c	0.027	0.051	0.069

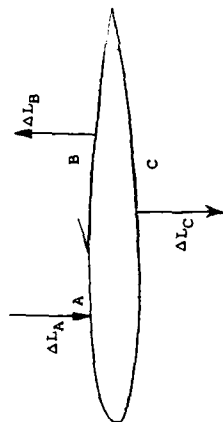


Fig 2 Three Flow Regions Around a Statically Deflected Spoiler

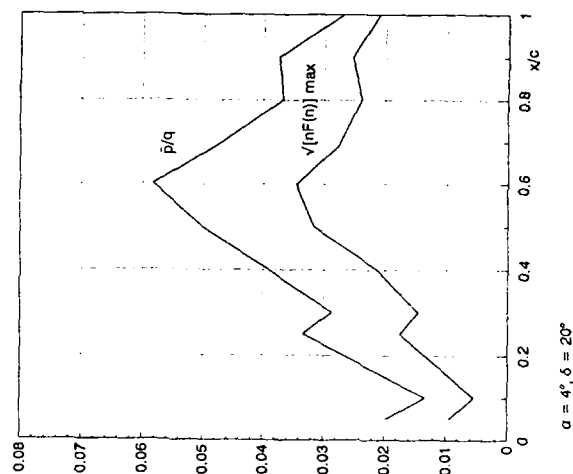
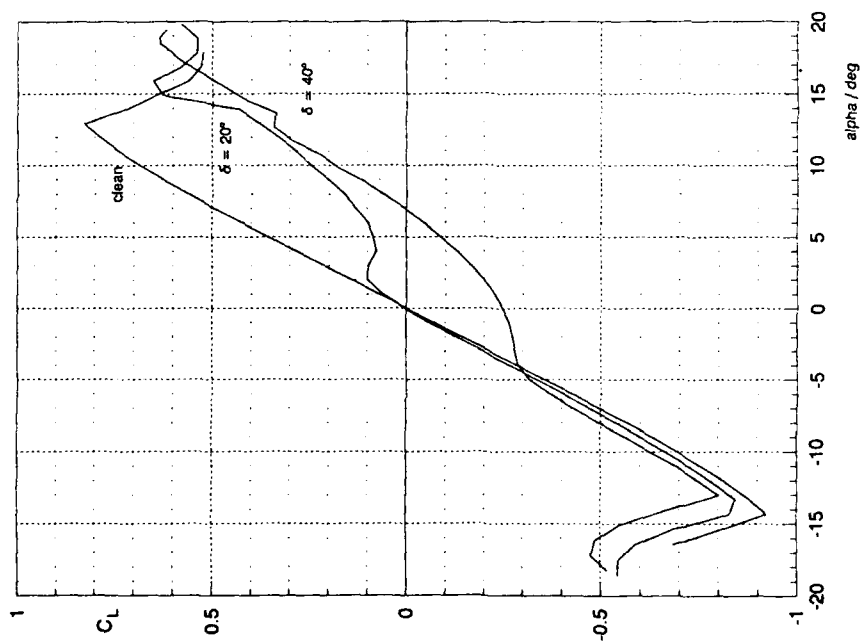
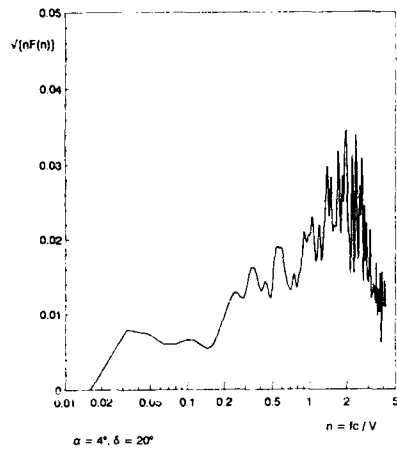
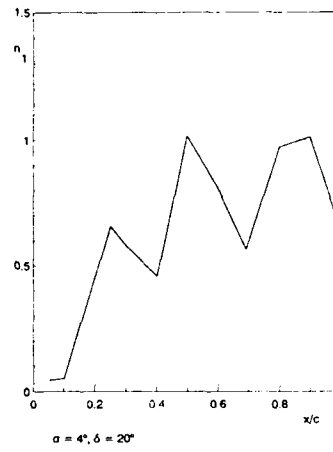
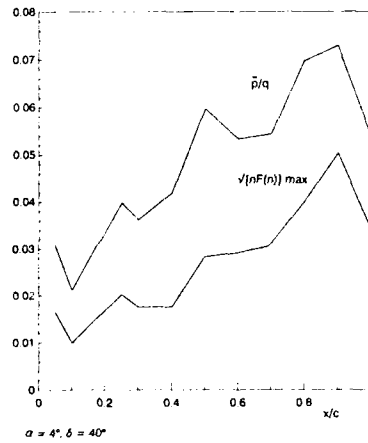
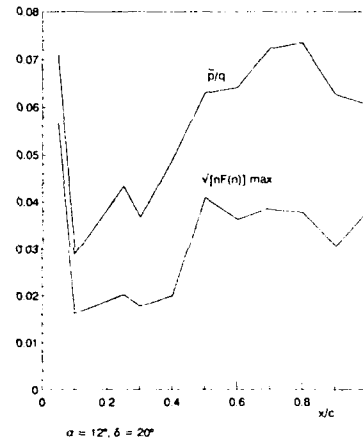
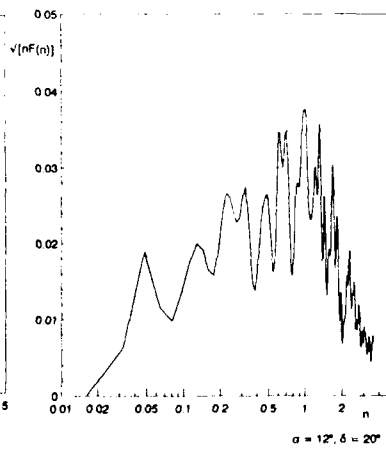
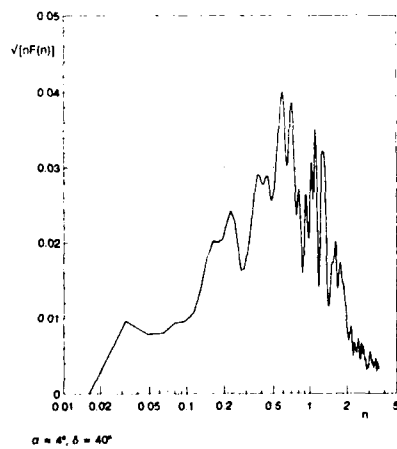
Fig 3 Chordwise Variation in \bar{p}/q and $\sqrt{[nF(n)] \text{ max}}$ 

Fig 1 Lift Curve for Clean Wing and 2 Spoiler Deflections

Fig 4 Spectrum of $\sqrt{[nF(n)]}$ at $x/c = 0.6$ Fig 5 Chordwise Variation in n_1 Fig 6 Chordwise Variation in \bar{p}/q and $\sqrt{[nF(n)]}$ maxFig 7 Chordwise Variation in \bar{p}/q and $\sqrt{[nF(n)]}$ maxFig 8 Spectrum of $\sqrt{[nF(n)]}$ at $x/c = 0.6$ for 2 Configurations

INVESTIGATION OF A SEMI-EMPIRICAL METHOD TO PREDICT LIMIT CYCLE OSCILLATIONS OF MODERN FIGHTER AIRCRAFT

by
J.J. Meijer, R.J. Zwaan
National Aerospace Laboratory (NLR)
P.O. Box 90502, 1006 RM Amsterdam
The Netherlands

Summary

Requirements of modern fighter aircraft to operate with high maneuverability in the transonic speed regime may lead under certain conditions to limit cycle oscillations (LCO), produced by a structural/aerodynamic interaction. Conditions of transonic LCO are moderate angle of attack and Mach numbers ranging from 0.9 to 1.1.

An analysis of steady wind tunnel data, obtained for a fighter-type aircraft in a typical configuration, has indicated that shock-induced separation plays a dominant role.

In the paper a semi-empirical prediction method is presented which makes use of these steady data, and some results are shown.

Possibilities are discussed to extend the method to the use of unsteady wind tunnel data.

1. Introduction

Requirements of modern fighter aircraft to operate with high maneuverability in the transonic speed regime may lead under certain flight conditions to limit cycle oscillations (LCO). These oscillations are self-sustaining and are caused by the interaction of separated flow and structural oscillations. The hindrance raised by LCO is a reduced operational capability, revealing itself in degraded ride comfort, targeting accuracy, and structural fatigue life.

The flow conditions for transonic LCO are Mach numbers ranging from 0.9 to 1.1, and moderate angles of attack depending on the Mach number, but usually less than 10 deg. Aircraft response appears in one or more weakly damped vibration modes for which the mode shapes admit a pronounced coupling with the separated flow pattern.

Reported cases of LCO for fighter aircraft were given in reference 1. Observations of LCO on other types of aircraft came also to the authors' knowledge.

LCO is experienced by swept wings as well, although different flow mechanisms may be involved. In references 2 and 3 such cases were analyzed in relation to wing bending oscillations.

LCO is characterized by an almost harmonic oscillation which sets in at a certain Mach number and angle of attack. When the Mach number gradually increases the amplitude initially also increases, then stabilizes and finally decreases after which LCO has disappeared. The regularity of the oscillation makes buffet as a forcing mechanism less obvious. Neither is the occurrence likely of an aerodynamic resonance mechanism at some specific frequency, which is known from wind tunnel tests with two-dimensional wings (Ref. 4). The argument is that the flow about fighter wings is strongly three-dimensional so that no discrete frequencies will prevail at which the resonance mechanism is able to develop. The most probable cause of LCO is a nonlinear aerodynamic damping which is able to destabilize the motion at small amplitudes. This conclusion may be a useful starting point for the development of a prediction method for LCO.

2. Basis of prediction method

A promising way to describe LCO may be found by considering this phenomenon as a nonlinear stability problem. In its simplest form LCO can be formulated as a one-degree-of-freedom (1-DOF) system. Its equation of motion is written as:

$$m\ddot{x} + d_s \dot{x} + kx + d_a(x, \dot{x}) = 0, \quad (2.1)$$

in which d_s is the structural damping coefficient and d_a is the nonlinear aerodynamic damping coefficient. The classical example is of course the Van der Pol equation, according to which:

$$d_a(x, \dot{x}) = -a\dot{x}(1 - b\dot{x}^2), \quad (2.2)$$

where a and b are positive constants. For small values of \dot{x} the aerodynamic damping is negative, so destabilizing, whereas for large enough values of \dot{x} the damping becomes positive. LCO will start whenever the condition is fulfilled:

$$d_s - a(1 - b\dot{x}^2) < 0. \quad (2.3)$$

Accordingly, in the general case of equation (2.1) the necessary condition for LCO is:

$$d_s \dot{x} + d_a(x, \dot{x}) < 0, \quad (2.4)$$

or in the simpler case where d_a only depends on \dot{x} :

$$d_s + d(d_a)/d\dot{x} < 0. \quad (2.5)$$

The latter condition was formulated by Den Hartog in his well-known explanation of galloping of slender structures (Ref. 5). In that case \dot{x} is proportional to the angle of attack. Assuming a dynamic damping force like indicated in figure 1, condition (2.5) may be satisfied in the interval of negative $d(d_a)/d\dot{x}$. A

self-sustaining constant-amplitude oscillation may develop over a larger interval when the energy influx from the air flow is compensated by the dissipative action of the structural damping force.

An important observation is that in the formulation of Den Hartog the relation between \dot{d} and \dot{x} is assumed independent of time and that this assumption does not prevent a satisfactory explanation of galloping.

The generalization of the principle of galloping to multi-DOF systems has been made the basis of the present prediction method. Accordingly the applicability of steady aerodynamic data of fighter aircraft has been accepted. The suggestion to use steady data was given already in references 2, 3 and 6. If by evaluating the method this applicability can be justified, at least for qualitative predictions, this would permit applications of the method early in the design process of the aircraft.

3. Aerodynamics for LCO

A crucial question of course is whether aerodynamic data of fighter-type wings exist which hold out a prospect of success in applying the galloping principle. In this connection steady pressure data for a full span wind tunnel model representing an advanced fighter wing were analyzed at NLR which were made available by the aircraft manufacturer. The pressures were integrated to sectional and overall forces. Results are presented here in the form in which they were used for the analysis. The wing planform of the wind tunnel model provided with the pressure orifices is shown in figure 2. Also shown is the panel distribution used in the chordwise and spanwise integration.

In figures 3 and 4 the steady normal force and moment coefficients are shown for stations 1 and 6 (most inboard and outboard, respectively) as functions of angle of attack (0 to 10 deg) and Mach number (0.90 to 0.96). The coefficient for the intermediate sections show a gradual transition. It is immediately clear that the coefficients in station 1 do not show any irregular behavior, whereas in station 6 both lift and moment coefficients show rapid changes in short intervals of the angles of attack (centered on about 7 deg) in the greater part of the Mach number interval. These rapid changes look similar to the hypothetical characteristic discussed in section 2, and might give rise to LCO.

Next the kind of pressure distributions are analyzed which lead to the rapid changes in the aerodynamic coefficients. To that purpose the pressure distributions on the upper and lower wing surface in station 1 and 6 at Mach number 0.92 are presented in figures 5 and 6. The pressure distribution at the upper surface in station 1 shows a very gradual development with angle at attack, with a small upstream shift of the shock along with a slight trailing edge flow separation at the highest angle of attack. In station 6 a strong upstream shift of the shock starts at 7 deg coupled with a rapidly developing flow separation at the trailing edge. The pressure distributions on the lower side show only very gradual developments.

Having established the cause of the rapid changes in the sectional coefficients, the question remains whether they are really able to provoke LCO. The answer should come from solving the equations of motion for the elastic aircraft structure.

4. Discussion of prediction method

It is assumed that the motion of the unrestrained elastic aircraft structure can be described by a number of rigid body modes and elastic modes. The equations of motion for these modes can be expressed in a usual matrix form:

$$\begin{bmatrix} \ddot{q}_R \\ \ddot{q}_E \end{bmatrix} + \begin{bmatrix} 0 & 0 \\ 0 & 2\zeta_E M_E \omega_E \end{bmatrix} \begin{bmatrix} \dot{q}_R \\ \dot{q}_E \end{bmatrix} + \begin{bmatrix} 0 & 0 \\ 0 & M_E \omega_E^2 \end{bmatrix} \begin{bmatrix} q_R \\ q_E \end{bmatrix} = \begin{bmatrix} L_R \\ L_E \end{bmatrix} \quad (4.1)$$

in which the indices R and E refer to the rigid body and elastic modes, while:

M, ζ, ω are generalized mass, damping factor and natural frequency,

q is generalized coordinate (total number is $N_R + N_E$),

L is generalized aerodynamic force on the wing (other lifting surfaces are not considered for simplicity).

The generalized aerodynamic force for the i -th coordinate is formulated as:

$$L_i = \frac{1}{2} \rho U^2 \int_S \phi_i(x, y) \Delta C_p(x, y, \alpha(t)) dS, \quad (4.2)$$

in which $\frac{1}{2} \rho U^2$ is the dynamic pressure, $\phi_i(x, y)$ is the natural mode shape and $\Delta C_p(x, y, \alpha(t))$ is the pressure difference distribution over the wing depending on the dynamic normal wash distribution α . This normal wash is expressed by:

$$\alpha = \alpha_0 + \Delta\alpha, \quad (4.3)$$

$$\Delta\alpha = \sum_{N_R + N_E} \left(\frac{\partial}{\partial x} + \frac{1}{U} \frac{\partial}{\partial t} \right) \phi_j(x, y) q_j(t). \quad (4.4)$$

α_0 is the initial angle of attack at which LCO is supposed to start and $\Delta\alpha$ the time-dependent variation during LCO.

The pressure distribution ΔC_p in expression (4.2) is in the present approach a time-independent nonlinear function of α . It is this relation by which the aerodynamic peculiarities discussed in section 3 may enter the equations of motion (4.1), possibly amplified by an appropriate mode shape ϕ_i . After substituting expressions (4.3) and (4.4) in expression (4.2), L_i can be written as:

$$L_i = Aq + B\dot{q}, \quad (4.5)$$

A and B being time-independent coefficients. This expression shows that \dot{q}_i does not only involve an aerodynamic damping term, $B\dot{q}_i$, but also an aerodynamic stiffness term, Aq_i . The relevance of the latter term is supported by the authors' experience that the start of LCO is sometimes accompanied by a small frequency shift.

In the numerical solution of the equations of motion the aerodynamic forces L_k are discretized as follows:

$$L_k = \frac{1}{2} \rho v^2 \int_{\Delta S_k} (C_p(x, v) - C_{p0}(x, v, \alpha)) dx \quad (4.6)$$

In which ΔS_k is the k-th panel area, and the product $(C_p - C_{p0})_k$ is taken constant over the whole k-th panel,

being evaluated at the (x, v) position of the k-th pressure orifice.

Before solving, the equations of motion are brought into a state space form.

Writing equations (4.1) as:

$$M \ddot{q} + D \dot{q} + K q = L(q, \dot{q}) \quad (4.7)$$

their state space form is:

$$\begin{cases} \dot{\hat{q}} = \{s\} \\ \dot{\hat{s}} = \{M^{-1} (L(q, \dot{q}) - D\{s\} - K\{q\})\} \end{cases} \quad (4.8)$$

These equations are solved by a step-by-step numerical method using the algorithm of Merson (Ref. 7). At each time step q_k is determined for each panel, after which the corresponding ΔC_{p_k} is interpolated in a data base in which the steady pressure distributions have been stored per combination of Mach number and wing angle of attack.

The result is the set of generalized coordinates q_i as functions of time. They can be reduced easily to quantities of practical interest, like wing tip amplitude, pilot seat acceleration, etc.

The last matter to discuss concerns the choice of the generalized coordinates. The need of keeping the calculations limited and the results easily understood would plead for a representation by a 1-DOF system. The observation that in the known cases the LCO can be correlated very well with one of the natural vibration modes supports this idea. A model on this basis has been illustrated recently in reference 6. The all-important question is of course what mode should be chosen. Some guidance may be derived from the results of flutter calculations for the complete multi-DOF system in attached flow, which are usually made in the design process. Then the natural vibration mode should be chosen that is dominating in the flutter solution with the least damping at a Mach number where LCO might be expected to occur. The risk, however, is that this dominance disappears when LCO sets in due to a rapidly changing aerodynamic load distribution.

The alternative is of course to accept various degrees of freedom. This will make the calculations more laborious, but has the advantages (1) that the system itself can filter out the mode(s) that will respond in LCO, and (2) that more modes are available to describe a possible shift in mean angle of attack due e.g. to static wing deflections. For it is also the mean angle of attack which has a major influence on the aerodynamic loads during LCO. Modes that contribute dynamically to LCO may differ from the modes that contribute to static deflections. The representation of the latter modes in the equations of motion may be simplified by the concept of modal residualization.

5. Applications

Two configurations of the fighter aircraft are considered to which the wind tunnel data presented in section 3 are applicable. Both configurations include the same wing tip launchers and underwing stores. Their difference is that configuration A has no wing tip missiles, whereas in configuration B tip missiles are installed. Model data of the two aircraft configurations were calculated using structural data provided by the aircraft manufacturer.

Further details for the LCO calculations are:

- Natural vibration modes were considered, antisymmetric and unrestrained with frequencies up to a maximum of 13 Hz. The maximum number of modes then for configuration A was 3 rigid body and 7 elastic modes, for configuration B 3 and 10 modes, respectively. Structural damping was taken into account.
- All aerodynamic loading were derived from the steady wind tunnel test data referred to in section 3. Only aerodynamic forces on the wings were considered. Mach number is 0.92. Altitude is at sea level. No deflections of wing flaps and control surfaces were assumed.
- The calculated responses are (1) the normal acceleration at the front end of the tip launcher, (2) the same at the rear end and (3) the lateral acceleration at the pilot seat. All accelerations in g.
- To investigate the sensitivity of LCO to changing flight conditions, calculations were carried out for varying angle of attack. Other flight conditions are the same as before.

For both configurations flight test data are available.

5.1 Configuration A

The two vibration modes which will turn out to be decisive for the development of LCO are shown in figure 7. The frequency difference is small. Both modes show a torsional deflection of the outer wing parts. The bending deflections are opposite.

a. 2 DOF system

The system consists of the two vibration modes shown in figure 7. The LCO calculations were started at an angle of attack of 8.5 deg, where in view of the sectional coefficients presented in figure 4 the occurrence of LCO was expected. An initial disturbance was given of the second vibration mode. Calculations were made of the three response accelerations during 10 s. The results are presented in figure 8. Acceleration 1 (tip launcher front end) first decays during 7 s and then passes very clearly into LCO with a frequency of 7.7 Hz and an amplitude of 0.8 g. Obviously the second vibration mode is dominating in the LCO.

Acceleration 2 (tip launcher rear end) stabilizes at 5 s and an amplitude of almost 0.3 g, while acceleration 3 (pilot seat) stabilizes at 5 s and almost 0.08 g. The "node" in the acceleration 2 signal is caused by the cancellation of opposite contributions of the two modes.

The response calculations were continued to 20 s to ensure that the LCO indeed remained unchanged.

b. Two 1-DOF system

Response calculations were made for the two vibration modes separately over a period of 20 s. The other conditions were the same as for the 2-DOF system. Surprisingly, neither of them show any LCO, the responses decay simply. The frequency of the first mode is 7.8 Hz (7.02 Hz in vacuum) and the second mode 7.5 Hz (7.81 Hz in vacuum). Possibly these small frequency shifts increased the sensitivity of the aircraft to LCO.

The conclusion is that (at least in this case) the interaction of the two vibration modes is indispensable for LCO to develop.

c. 8-DOF system

The response calculations for the system with vibration modes up to a frequency of 12 Hz lead to a result presented in figure 9. The responses are now decaying at a frequency of 7.7 Hz, although the rate of decay after 5 s is extremely small. The response calculations were continued to 20 s to confirm a lasting small decay. Obviously there is some damping influence of the other modes. The beats with a frequency of 3.5 Hz point to interaction with the fourth elastic mode with a natural frequency of 9.46 Hz (in vacuum).

The conclusion is that adding the remaining degrees of freedom leads to a near LCO.

d. 10-DOF system

The final LCO calculations for configuration A were intended as a search for the sensitivity of LCO to varying angle of attack. Results for the complete system are presented figure 10. The calculations were carried out over 30 s, while the angle of attack changed linearly from 1 to 10 deg. It appears that a much serious LCO occurs already at considerably lower angles of attack than 8.5 deg, contrary to what was assumed before. The frequency is again about 7.7 Hz.

Obviously it is advisable not to rely only on an interpretation of the aerodynamic loads to establish possible LCO conditions, but to include sufficiently variations of the flight conditions in the response calculations.

A demonstration that indeed LCO conditions were obtained is given in figure 11, where the response calculations were started in the same way as in figure 10, but after 7.5 s the angle of attack was kept constant at 3.5 deg.

It should be noted finally that the high response levels look unrealistically high. A more realistic result may be expected by taking account of wing flap scheduling, load factor limiting and non-zero altitude

The flight test results for configuration A yielded LCO at $M = 0.9$ and $\alpha = 4$ deg (during a wind-up turn at an altitude of 5K ft. The frequency of acceleration 1 was 7.5 Hz and the amplitude 5 g. The conclusion is that the calculated LCO and the flight test data seem to agree qualitatively.

5.2 Configuration B

a. 12-DOF system

Response calculations were made for a system with vibration modes up to a frequency of 12 Hz over a period of 10 s. The results are presented in figure 12.

The responses are very irregular, contrary to the responses of configuration A. They are lightly damped, but a clear indication for LCO is missing. Also these response calculations were continued to 20 s.

b. 13-DOF system

Results of response calculations for varying angle of attack are presented in figure 13. The calculations were carried out over 30 s, while the angle of attack changed linearly from 1 to 10 deg in the same way as for configuration A.

Again it appears that LCO is completely absent.

In flight tests of configuration B no LCO was observed, so that again the conclusion is that calculated LCO and flight test data correlate well in this respect.

The results of the preceding applications justify the conclusion that the proposed prediction method is promising, although further evaluation by applications to other configurations is necessary.

6. Improvements of the prediction method

The development of the present prediction method is still in progress. The following extensions are being realized or foreseen.

a. Use of unsteady wind tunnel data

It should be expected that the use of unsteady wind tunnel data obtained by pressure measurements with oscillating models will improve the accuracy of the predicted LCO. Especially the inherent phase differences between the aerodynamic wing loading and generating wing oscillations will influence the predicted sensitivity of the aircraft to LCO.

The chance to explore possible improvements will come in the near future after results have become available from unsteady transonic wind tunnel tests at NLR (Ref. 8). In these tests pressure distributions and overall aerodynamic loads will be measured on an oscillating semi-span wing model with the same planform as the model for which steady data were shown in section 3.

Unsteady aerodynamic loads due to harmonic model oscillations, however, are less appropriate for application in the prediction method as the equations of motion are solved in the time domain instead of in the frequency domain. A useful empirical technique to transform unsteady aerodynamic loads during dynamic stall to the time domain was developed by ONERA for two-dimensional wings (Ref. 9). This technique is based on splitting the aerodynamic force coefficients into a "linear" part F_1 and a "nonlinear" part F_2 (Fig. 14) which are modeled each of them by differential equations. The various parameters in these equations are deduced from matching with wind tunnel test data. A similar technique may be applicable to fighter type wings as well and will be tried out by NLR to transform the unsteady wind tunnel data mentioned before.

It should be mentioned that upgrading the prediction method by the use of unsteady wind tunnel data will generally be possible only later in the design process of the aircraft.

b. Improvement of numerical efficiency

The present numerical algorithm to integrate the equations of motion is too time-consuming. An improvement is expected from replacing the Merson algorithm by a more efficient integration procedure, e.g. by applying the transition matrix technique proposed in reference 10.

7. Conclusions

In this paper a semi-empirical method has been proposed to predict LCO of modern fighter aircraft. A limited evaluation has been performed. Some preliminary conclusions are drawn:

1. Calculated results show convincing LCO cases.
2. Data of steady wind tunnel tests are already sufficient to enable qualitatively correct predictions.
3. LCO is not a typical phenomenon of 1-DOF systems when these degrees of freedom are defined as in vacuum vibration modes. At least 2-DOF system may be necessary to arrive at LCO, just as in most "classical" flutter cases.

8. Acknowledgement

The authors are indebted to Dr. Atlee M. Cunningham, Jr., General Dynamics, for stimulating discussions.

9. References

1. Meijer, J.J. NLR contributions to the flutter certification of aircraft with external stores. NLR MP 86025 U, 1986.
2. Ericsson, L.E. Vortex-induced bending oscillation of a swept wing. J. Aircraft, Vol. 24, No. 3, March 1987, pp. 195-202.
3. Moss, G.F., Pierce, D. The dynamic response of wings in torsion at high subsonic speeds. AGARD-CP-226, 1977.
4. Boer, R.G. den, Houwink, R. Analysis of transonic aerodynamic characteristics for a supercritical airfoil oscillating in heave, pitch and with oscillating flap. AGARD-CP-374, 1985.
5. Hartog, J.P. den Mechanical vibrations. McGraw-Hill, New York, 4th Ed., 1956.
6. Cunningham, Jr., A.M. The role of shock induced trailing-edge separation in limit cycle oscillations. NASA-CP-3022, 1987.
7. NAG FORTRAN Library, Numerical Algorithms Group Ltd., NAG Central Office, Oxford, UK, 1987.
8. Cunningham, Jr., A.M., Boer, R.G. den Unsteady transonic wind tunnel testing of fighter type wings. 31st AIAA/ASME/ASCE/AHS/ASC Structures, Structural Dynamics, and Materials Conference, Long Beach, California, April 2-4, 1990.
9. Dat, R. Development of the basic methods needed to predict the aeroelastic behavior of helicopters. Rech. Aerosp. 1983-1.
10. Edwards, J.W., Bennett, R.M., Whitlow, Jr., W., Seidel, D.A. Time-marching transonic flutter solutions including angle-of-attack effects. J. Aircraft, Vol. 20, No. 11, Nov. 1983, pp. 899-906.

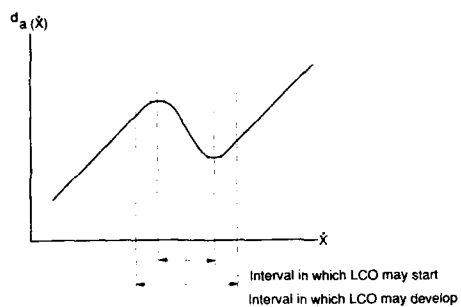


Fig. 1: Meaning of nonlinear aerodynamic damping force for occurrence of LCO.

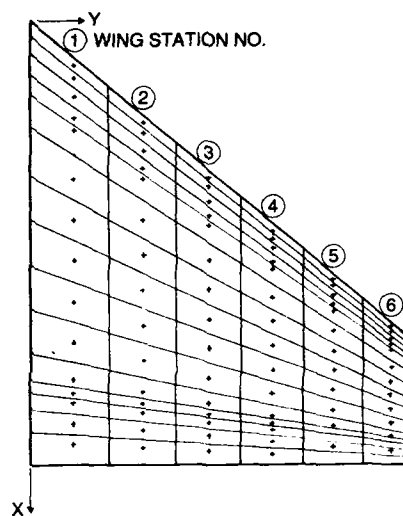


Fig. 2: Location of pressure orifices and corresponding panels on the model wing planform.

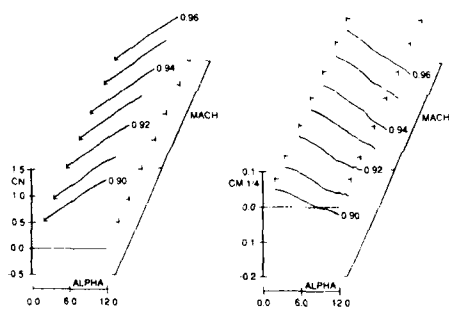


Fig. 3: Steady lift and moment coefficients in station 1 as functions of Mach number and angle of attack.

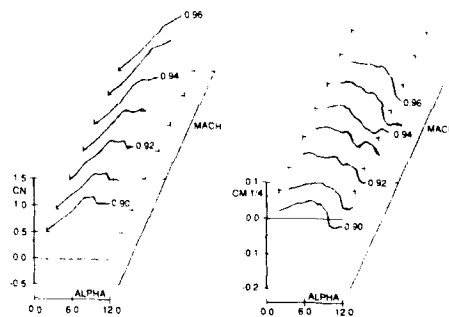


Fig. 4: Steady lift and moment coefficients in station 6 as functions of Mach number and angle of attack.

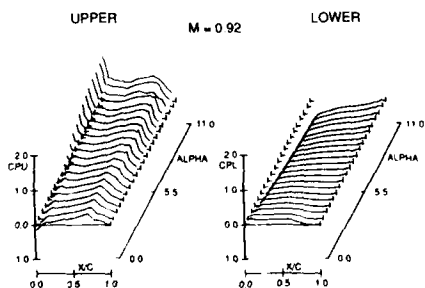


Fig. 5: Steady pressure distributions in station 1 as functions of angle of attack.

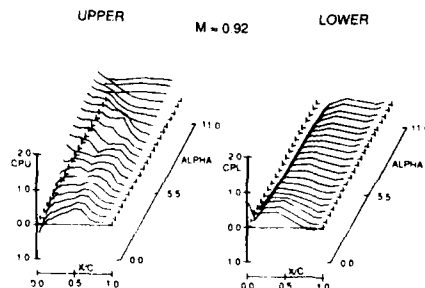


Fig. 6: Steady pressure distributions in station 6 as functions of angle of attack.

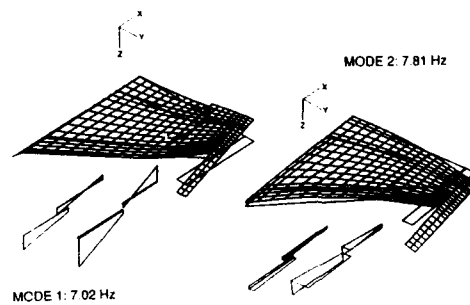


Fig. 7: First two vibration modes of configuration A.

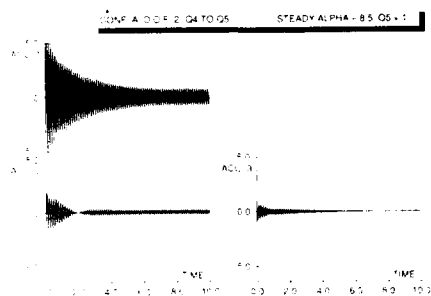


Fig. 8: Response calculations for configuration A; 2 DOF, $M=0.92$, $\alpha_0=8.5$ deg.

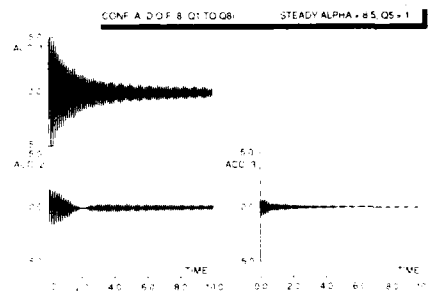


Fig. 9: Response calculations for configuration A; 8 DOF, $M=0.92$, $\alpha_0=8.5$ deg.

CONF. A D.O.F. 10: Q1 TO Q10; ALPHA LINEAR INCREASE FROM 1 TO 15 DEG. IN 30 SEC MACH NUMBER = 0.92 SEA LEVEL STRUCTURAL DAMPING $G=0.01$ Q5 = 0.5

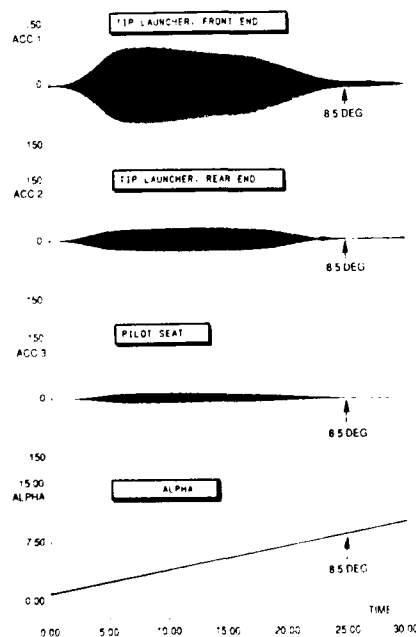


Fig. 10: Response calculations for configuration A; 10 DOF, $M=0.92$, α variable.

CONF. A D.O.F. 10: Q1 TO Q10; ALPHA LINEAR INCREASE FROM 1 TO 15 DEG. IN 7.5 SEC THEN CONSTANT MACH NUMBER = 0.92 SEA LEVEL Q5 = 0.5

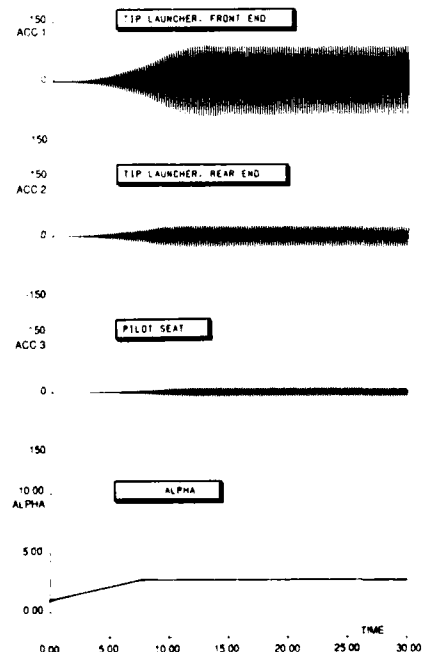


Fig. 11: Response calculations for configuration A; 10 DOF, $M=0.92$, α variable.

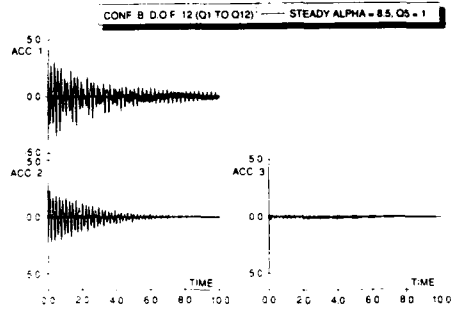
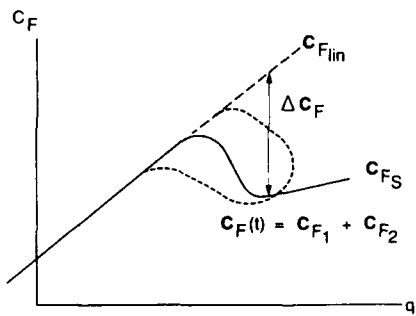


Fig. 12: Response calculations for configuration B;
DOF, $M=0.92$, $\alpha = 8.5$ deg.



$$C_F = C_{F1} + C_{F2}$$

$$\dot{C}_{F1} + a_1 C_{F1} = f_1(q, \dot{q}, \ddot{q})$$

$$\ddot{C}_{F2} + a_2 \dot{C}_{F2} + a_3 C_{F2} = f_2(q, \dot{q}, \ddot{q}, \Delta C_F)$$

Fig. 14: Generalized ONERA dynamic stall model.

CONF. A D.O.F. 10 (Q1 TO Q13), ALPHA LINEAR INCREASE FROM 1 TO 10 DEG
IN 30 SEC, MACH NUMBER = 0.92, SEA LEVEL, STRUCTURAL DAMPING $G=0.01$, $Q5=0.5$

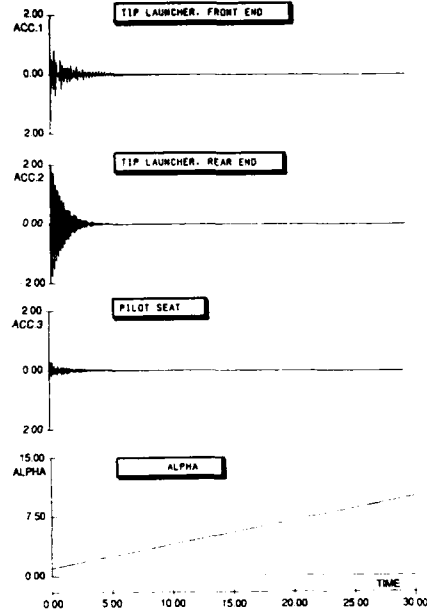


Fig. 13: Response calculations for configuration B;
13 DOF, $M=0.92$, α variable.

INTERACTION BETWEEN THE CANARD AND WING FLOWS ON A MODEL OF A TYPICAL COMBAT AIRCRAFT

by
D.G. Mabey
B.L. Welsh
C.R. Pyne
Procurement Executive, Ministry of Defence
Royal Aerospace Establishment
Bedford MK41 6AE
England

SUMMARY

The main features of canard/wing interaction were established by a comprehensive test of a half model of a typical combat aircraft in the RAE 13ft x 9ft Low Speed Wind Tunnel. The measurements comprised overall steady forces, buffeting on the wing and the canard, and steady and unsteady pressure distributions on the wing.

The results show that the canard effective incidence (determined by the canard setting and the body/wing upwash) controls the canard/wing interaction. With attached flow the canard produces a downwash field which has significant effects when the wing flow is attached. With separated flow on the canard, the downwash field is still produced but in addition there is vigorous mixing which inhibits the development of wing flow separations, increasing the overall lift, reducing the wing buffeting and reducing the drag. The process by which this favourable effect is achieved is illustrated by an analysis of the steady and unsteady pressure distributions on the wing at three spanwise sections.

These results have important implications with respect to the development and optimisation of other canard/wing configurations, particularly at high angles of incidence.

LIST OF SYMBOLS

C_{Mc}	static bending moment coefficient (Eq (1))
C_L, C_D, C_m	lift, drag and pitching moment coefficients
$C_{L_{max}}$	maximum lift coefficient
C_L	rolling moment coefficient
c	local chord
\bar{c}	aerodynamic mean chord of gross wing (868 mm)
C_p	pressure coefficient
f	frequency (Hz)
l	bubble length
$\sqrt{nG(n)}$	buffet excitation parameter (Eq (2))
m	generalised mass
n	frequency parameter (based on l or \bar{c})
$\sqrt{nF(n)}$	rms level of excitation at frequency parameter (defined in Ref 15)
\bar{p}	total broad band rms pressure fluctuations on wing
$q = \frac{1}{2}\rho U^2$	free stream kinetic pressure
S	gross wing area (1.031m ²)
S_w	exposed wing area (0.78m ²)
S_c	exposed canard area (0.136m ²)
s_c	exposed canard semi-span
s_w	wing semi-span from centre line
x	streamwise co-ordinate
y	spanwise co-ordinate
z	rms tip acceleration in mode
U	free stream velocity
α	wing and fuselage incidence
α_c	canard effective incidence (Eq (3))
ζ	total damping fraction critical (Eq (2))
$n = y/s_w$	semi-span ratio for wing pressure plotting sections
α_c	canard setting
ρ	free-stream density

1 INTRODUCTION

The next generation of advanced combat aircraft is likely to utilise small foreplanes or canards because of the large favourable effects of such canards on the overall static forces, such as improvements in $C_{L_{max}}$ [eg Refs 1 to 3] and because of the possible advantages of canards for Active Control Technology (ACT).

An additional advantage of close-coupled canards is that these generally reduce the wing buffeting⁴ but for certain restricted conditions they may increase it. These effects are still not understood completely, and it appeared desirable to study the interaction between canard and wing flows in more detail on a large well-instrumented half-model of a typical canard/wing configuration. The RAE High Incidence Research Model (HIRM 1) was chosen (Fig 1), because this had been used widely in a research programme shared between RAE and NASA. That investigation involved the comparison of both static and dynamic stability derivatives measured in wind-tunnel and flight tests⁵.

This paper gives the salient conclusions derived from tests of the HIRM 1 half-model in the RAE Bedford 13ft x 9ft Low Speed Wind Tunnel. Another Report⁶ describes some brief tests of the effects of a series of wing leading-edge notches on the static forces and buffeting at low speeds on this advanced wing design.

2 EXPERIMENTAL DETAILS

Although for time-dependent measurements a stiff model and a rigid support system are preferred a relatively flexible model design (section 2.1) was chosen to reduce the manufacturing time and this model was mounted on the half-model balance to allow overall force measurements (section 2.2). Section 2.3 describes the instrumentation used and the analysis of the time-dependent signals. Section 2.4 gives the test conditions.

2.1 Model

Fig 2 shows the general arrangement of the large half model. The model size was determined by the decision to make it from the same moulds as used for the complete models of the free-flight tests. The model was mounted vertically in the tunnel so that the effective ratio [model semi-span/tunnel width] = $1.3/2.7 = 0.48$. This is somewhat larger than the ratio recommended (< 0.40) for interference-free flow⁷. However in these tests the main emphasis was on comparative, rather than absolute measurements, so that this size of model was not unreasonable.

The fuselage has a steel frame and a moulded plastic skin of glass fibre laminate. The wing has two internal steel spars covered by a moulded skin of glass fibre laminate, which gives the required twisted and cambered wing section. The wing thickness/chord ratio varies from about 6% at the root to 4% at the tip. The wing construction must be described to explain the difficulties in the buffeting measurements. The skin is split into several different segments, as illustrated in the greatly simplified sketch in Fig 3. Inevitably, when the wing is loaded and vibrating, the relative movement between the many adjoining surfaces produces a large and variable structural damping. This variable structural damping dominates the total damping coefficient, because the aerodynamic damping coefficient is extremely small at low speeds. [The total damping coefficient is generally a function of the normal force on the wing.]

Steady and time-dependent pressure measurements on the wing supplemented the steady overall force measurements from the balance. Pressure transducers could be installed on the inside of the skin on both the suction and pressure surfaces at six spanwise sections ($\eta = 0.3, 0.4, 0.5, 0.6, 0.7$ and 0.8). For the present tests the 51 wing pressure transducers (17 per section) were installed at $\eta = 0.4, 0.6$ and 0.8 (Fig 2). The centre spar has top and bottom glass fibre laminate cover plates which carry pressure-transducer housings at $x/c = 0.30, 0.40, 0.50$ and 0.60 (Fig 3). The centre spar also supports a forward spar, which carries the leading-edge glove and the make-up piece. The leading-edge glove carries pressure transducers at $x/c = 0.05, 0.10$ and 0.20 on the upper surface and at $x/c = 0.05$ on the lower surface. The make-up piece carries the lower-surface pressure transducers at $x/c = 0.10$ and 0.20 . The steel centre spar also supports the plastic trailing-edge section, which carries the transducers at $x/c = 0.80$ on both surfaces and the transducer used to measure the trailing-edge pressure. This transducer is buried in the wing and connected to the thick trailing edge by a short length (< 60 mm) of 1 mm outer diameter hypodermic tubing.

The central spar of the wing only extends outboard to $\eta = 0.87$, so that the wing tip is relatively much more flexible than that of either an ordinary wind-tunnel model or a real aircraft. An accelerometer at $\eta = 0.80, x/c = 0.39$ gives an indication of the wing response. A wing-root strain-gauge bridge was provided but failed early in the tests. All the present tests were made with an undrooped leading edge, but a drooped leading edge (as used in all other tests on HIRM 1) is available.

The close-coupled canard (Fig 2) is symmetric and made by joining a pair of glass fibre skins, which are stiffened internally with polyurethane foam, just as for the free-flight models. The canard loads are diffused from this relatively weak structure into a steel root block which is integral with the drive shaft. The canard drive shaft is locked for the canard buffeting measurements, when the first-bending frequency is 67 Hz and the damping is constant at $\zeta = 3\%$ critical.

The canard drive system is described fully in Ref 8. The canard drive shaft is connected directly to an electromagnetic actuator (installed in the fuselage), which controls the desired mean static pitch angles ($-10^\circ, 0^\circ$ and $+10^\circ$ in the present tests) and reacts the corresponding aerodynamic loads. In addition, the actuator could be used to oscillate the canard for other tests.

The canard instrumentation consisted of:

- two accelerometers (to monitor the motion),
- two pressure transducers (on opposite surfaces of the canard) and a root strain-gauge bridge.

Although the canard drive system can be adjusted to provide three different heights (Fig 2), only the highest position is considered here.

As for the free-flight models, the wind-tunnel model could be provided with a tailplane, making it a 'three-surface' configuration. However, for simplicity the tailplane was not fitted for the present tests. Even with a 'two-surface' configuration the interaction between the canard and wing flows raises some difficult questions, as shown in section 3.3.

2.2 Model mounting

The model is bolted to the half-model balance in the floor of the RAE 13ft x 9ft Wind Tunnel (Fig 1). The turntable allows the angle of incidence to be varied over a wide range (from -10° to $+30^\circ$ in the present tests).

The advantage of using the turntable is that the overall static forces and moments can be measured directly on the balance. The disadvantage is that the balance flexibility provides additional degrees of freedom, which may contribute to the unwanted modes in the wing buffeting and to the variable structural damping. For small normal forces the wing first-bending mode is at a frequency of 21.6 Hz. This mode may involve some motion of the balance, yet it has constant total damping (about 2% of critical). For somewhat higher normal forces the predominant wing first-bending mode is at a frequency of 23.8 Hz. This mode is characterised by variable total damping, probably caused by motion between the skin and the steel spars. These variations in damping are undesirable in buffeting tests. They must be incorporated in the calculation of the buffet excitation parameter (section 2.3 below).

2.3 Analysis of measurements

The steady forces and moments sensed by the half-model balance were recorded and analysed by a computer.

The steady and time-dependent signals from the model transducers (for pressure, acceleration and root strain) were recorded for most conditions for a time of 34 s. These signals were analysed with the RAE Presto system³. The bandwidth of the measurements was from 0-100 Hz.

The canard-root bending moment coefficient is given by

$$C_{Br} = \frac{\text{canard bending moment}}{q S_c (0.46 S_c)} \quad (1)$$

where S_c = exposed canard area (0.136 m^2),
and s_c = exposed canard semi-span (0.328 m).

The factor 0.46 is introduced into the denominator of Eq (1) to make the measured bending moment equivalent to a lift coefficient, C_{Lc} , for a lift force acting at the centre of area.

As a safety precaution and as a measurement of the buffeting of the flexible wing, the wing accelerometer reading was recorded for every data point, using a spectrum analyser (Bruel and Kjaer Type 2120). The measurement time of 34 s gave about 750 cycles of buffeting at the wing first-bending frequency, so that accurate measurements of damping were possible from the signals recorded by the Presto system.

Buffet response is measured as output from the strain-gauge bridges in volts. Where applicable the buffet excitation parameter in any mode is given by the relation^{10,11}.

$$\sqrt{n\ddot{z}(n)} = \frac{2}{\sqrt{\pi}} \frac{m\ddot{z}}{qS} \zeta \quad (2)$$

where m = generalised mass in mode with respect to motion at tip,
 \ddot{z} = rms tip acceleration in mode,
 q = kinetic pressure,
 S = exposed reference area,
 ζ = total damping - as ratio to critical damping.

Before the tests the generalised masses (for the bending modes of both the wing and the canard) were measured and calibration factors established between tip acceleration in a particular mode and the strain gauge signal. Early in the tests the wing-root strain

gauge bridge failed. Hence the wing-tip acceleration applicable to the first-bending mode was deduced from the accelerometer reading at $\eta = 0.8$ according to the relation

$$(\text{acceleration at } \eta = 1) = 1.56 (\text{acceleration at } \eta = 0.8)$$

Damping coefficients were extracted from the spectra of the signals, using the half-power method. Knowing the generalised mass, the tip acceleration and the total damping the buffet excitation parameter could be calculated according to Eq (2) for both the wing and the canard.

2.4 Test Conditions

A roughness band 3 mm wide of 0.36 mm diameter ballotini was applied to fix transition at 3 mm from the leading-edges of both the wing and the canard. Most measurements were made at a speed of 60 m/s, giving a Reynolds number $R = 3.7 \times 10^6$ based on the wing aerodynamic mean chord, \bar{c} . Some additional measurements were made at a reduced speed of 40 m/s, with a corresponding Reynolds number of 2.5×10^6 . Unless otherwise stated, all the measurements presented are at 60 m/s.

No corrections were made for tunnel interference. In this closed working section, corrections would be large for such a large half model, particularly at angles of incidence from 15° to 30° when the wing flow is well separated. The uncorrected steady lift coefficient will have large errors (up to 0.1 in C_L) following flow separation. This is shown by the comparisons of uncorrected and corrected lift curves (Ref 12, Fig 26) for a combat aircraft half model of almost the same semi-span ($s_w = 1350$ mm compared to $s_w = 1300$ mm) and planform (compare Fig 8 of Ref 12 with Fig 2) also tested in the RAE 13ft x 9ft Wind Tunnel. However wall corrections are unlikely to affect the character of the interactions between the canard and wing flows, which is the main objective of these tests.

The static forces and moments were measured by the balance over the range of angle of incidence from $\alpha = -10^\circ$ to $+30^\circ$, in intervals of 1° . The steady and fluctuating measurements using the Presto system were restricted generally to $\alpha = 0^\circ, 5^\circ, 10^\circ, 12^\circ$ (buffet onset), $15^\circ, 20^\circ, 25^\circ$ and 30° . Some additional fluctuating measurements were made also at $\alpha = -10^\circ, -5^\circ$ and -3° .

3 RESULTS

The static force and buffeting measurements of the present tests conform to the general character of those found in previous experiments. It is convenient first to consider briefly the overall static forces and moments (section 3.1), the wing and canard buffeting (section 3.2) and the canard/wing flow interactions (section 3.3). The local steady pressures and buffet excitation on the wing are considered in detail (section 3.4) because this is the first time that such measurements have been made on a wing of this type at low speeds. [The measurements of Ref 3 are restricted to steady pressures and a single canard setting, although they cover the Mach number range from $M = 0.7$ to 1.2 .]

Although no surface flow visualisation was possible during the present tests, the results in section 3.4 may be used to infer the general character of the wing flow separations, both with and without the canard.

3.1 Overall static forces and moments

Fig 4 shows the overall static force and moment coefficients derived from the half-model balance, both with and without the canard. (These coefficients are based on the area and aerodynamic mean chord of the gross wing).

Fig 4a shows the variation of the lift coefficient C_L , with the angle of incidence, α . Without the canard C_L varies linearly with α up to about $\alpha = 14^\circ$ and the maximum lift coefficient ($C_{L_{\max}}$ about 1.15) is achieved at about $\alpha = 26^\circ$. With the canard

there is a small increase in the lift-curve slope up to about $\alpha = 14^\circ$, but beyond this incidence the lift coefficient still increases significantly to a maximum much higher than that for the isolated wing, a $C_{L_{\max}}$ of about 1.62 at $\alpha = 30^\circ$ for $\eta = 0^\circ$. In addition to

the large improvement in $C_{L_{\max}}$ the canard reduced the wing buffeting for a given angle of incidence. For reference, Fig 4a includes buffeting criteria for $\eta_c = -10^\circ$ and 'canard-off' derived from Fig 5a.

Fig 4b shows the variation of the pitching moment coefficient, C_m , with the lift coefficient. Without the canard the configuration is stable (dC_m/dC_L negative) up to about $C_L = 1$, then experiences a gentle pitch up, followed by a violent pitch down. With the canard, for lift coefficients above 0.4 the configuration is either neutrally stable ($dC_m/dC_L = 0$) for $\eta_c = -10^\circ$ up to $C_L = 0.95$ or unstable (dC_m/dC_L positive) for $\eta_c = -10^\circ$ ($C_L > 0.95$) or for $\eta_c = 0^\circ$ and $+10^\circ$ (all values of C_L). Overall pitching moment curves of this type would be ideal for ACT, apart from the curious and undesirable multi-valued loop for $\eta_c = -10^\circ$ observed for high angles of incidence. Fig 4b includes dashed lines suggesting buffeting contours based on Fig 5a. Manifestly, of the three canard settings

tested, $\alpha_c = 0^\circ$ is the most attractive for the buffeting characteristics and has acceptable trim characteristics. Some detailed measurements for this setting are discussed in section 3.4.

Fig 4c shows the variation of drag coefficient, C_D , with the lift coefficient, and includes no allowance for the additional drag required to trim at a particular C_L . Three detailed observations are made with respect to the canard-off configuration.

- (1) For all three canard settings and C_L above about 1, the canard increases lift and decreases drag.
- (2) The canard setting $\alpha_c = 0^\circ$ has only a small drag increment up to about $C_L = 0.75$. It therefore reduces wing buffeting with no significant drag penalty. The canard setting $\alpha_c = -10^\circ$ also has a small drag increment but has inferior buffeting characteristics.
- (3) The canard setting $\alpha_c = +10^\circ$ has a significant drag increment up to a $C_L = 1.0$. In addition it has increased buffeting with respect to either $\alpha_c = -10^\circ$ or $\alpha_c = 0^\circ$ and hence would be an unsuitable starting point for ACT.

Fig 4d shows the variation of rolling moment, C_l , with lift coefficient. The ratio C_l/C_L gives the position of the spanwise centre of lift. This is constant at about $\eta = 0.44$ up to about $C_L = 0.8$ (ie near to the onset of flow separations on the wing). Above $C_L = 0.8$ the centre of lift moves inboard, reaching $\eta = 0.38$ at $C_L = 1.3$ and remaining there up to $C_L = 1.6$. It follows from Fig 4d that the increase in interference lift obtained with the canard above $C_L = 1.0$ is centred more inboard, over the part directly influenced by the canard. This important inference will be confirmed by the sectional pressure distributions, summarized in section 3.4, and is consistent with previous observations (eg Refs 1-4). [This change in loading could have important implications with respect to the structural design of a wing.]

The overall force measurements of Fig 4 give no indication of buffet onset, even for an isolated wing. The process, known as 'kinkology', of inferring buffet onset from overall force measurements is unreliable, as discussed in Ref 13. However both the onset and severity of buffeting on the wing and the canard may be derived from measurements of tip accelerometers or unsteady-root strain, which are described below.

3.2 Wing and canard buffeting

The wing and canard buffeting measurements in the first-bending mode give a sensitive indication of the onset and severity of flow separations, as well as being important in themselves when flight buffeting limits must be predicted for an aircraft.

3.2.1 Wing buffeting

Fig 5 shows the buffet excitation parameter, $\sqrt{aG(H)}$, derived from the wing accelerometer readings according to Eq (2) for the wing first-bending mode at about 22 Hz. Consider first the variation with the angle of incidence (Fig 5a). Without the canard buffeting increases rapidly, reaching a maximum at about $\alpha = 20^\circ$. With the canard, buffeting is reduced for incidences greater than 12° . For $\alpha_c = -10^\circ$ and 0° buffet onset occurs at the same angle as with the wing alone, $\alpha = 12^\circ$. However for $\alpha_c = +10^\circ$ buffet onset occurs at a lower incidence, $\alpha = 6^\circ$. It will be shown later that this premature wing buffeting (before the wing flow has separated) is due to excitation provided by the well-separated flow on the canard. Considering next the variation of the buffet excitation parameter with the lift coefficient (Fig 5b), the increase in maximum lift combined with the reduction in buffeting makes a canard doubly attractive.

3.2.2 Canard static bending moments and buffeting

The canard root strain gauges provide simultaneously the static-bending moments and the buffeting. Hence it is helpful to consider these measurements together in Fig 6. These measurements all relate to the condition 'canard locked', when the freedom in pitch is suppressed by a pair of 'bump-stops' fitted into slots machined in the circumference of the drive shaft.

Following other measurements on canards, the present static bending moment coefficients, CBC , can be related in terms of an effective canard incidence, α_c (Fig 6a). This is a function of the wing incidence, α , and the canard setting α_c . It was found that for attached flows on the canard within the range $0^\circ < \alpha_c < 10^\circ$, measurements for all three canard settings were related by the expression

$$\alpha_c = 1.89\alpha + \alpha_c - 0.6^\circ \quad (3)$$

The factor 1.89 represents the effect of the wing and the body on the upwash at the canard and is in fair agreement with estimates. The third term, -0.6° , represents the upwash in the tunnel and the zero-lift angle of the wing.

Even when the canard flow is separated on the upper surface, Eq (3) provides a fair correlation of the static bending moments for $\alpha_c = -10^\circ$ and 0° ($12^\circ < \alpha_c < 40^\circ$), but not for $\alpha_c = +10^\circ$. This lack of correlation indicates that when a canard and a wing are closely coupled the passage of the canard wake close to the wing makes their interaction

more complex. For active control applications it is unfortunate that the canard static pitching moment coefficients are not correlated by α_c . [These measurements are derived from the DC excitation of the electromagnetic actuator and will be presented elsewhere⁸.]

When the canard flow is separated on the lower surface, Fig 6a shows that Eq (3) provides a good correlation of the static measurements for $n_c = -10^\circ$ and $+10^\circ$ but not for $n_c = 0^\circ$. Again, this anomaly is attributed to the strong interaction between the canard wake and the wing flow when the canard is closely coupled.

Fig 6b shows that Eq (3) also provides a fair correlation of the canard buffeting at the first-bending frequency of 67 Hz. Buffet onset is fairly well defined (at about $\alpha_c = \pm 12^\circ$), moderate buffeting is reached at about $\alpha_c = \pm 16^\circ$ and heavy buffeting is reached at about $\alpha_c = 23^\circ$. It should be noted that the maximum values of the buffet excitation parameter are very scattered and somewhat higher ($103/\sqrt{nG(n)} = 5$) than those for isolated wings ($103/\sqrt{nG(n)} = 3$). This can be attributed tentatively to the fact that the 'bump stops', provided to prevent rotation in pitch do not make the canard 'encastre' at the root, so that the calibration factor of the root-strain gauge is modified.

The uncertainty of the root fixing also affected the response measurements for $n_c = -10^\circ$ and negative angles of incidence for $10^\circ < \alpha_c < 0^\circ$. Here the buffeting in the first-bending mode at 67 Hz disappeared abruptly, and was replaced by a low level, random buffeting in the pitch mode at all frequencies below about 42 Hz. Similar buffeting in pitch was observed when the bump stops were removed and the actuator alone restrained the canard. These measurements are not presented here.

3.3 Interaction between the canard and the wing flows in the α , n_c domain

The concept of canard effective incidence helps to clarify the interaction between the canard and wing flows. When the canard is at such an incidence that the flow is separated ($\alpha_c > 12^\circ$ or $\alpha_c < -12^\circ$ here) there are large effects on the wing-flow separations and thus the wing buffeting is altered: these effects vary significantly with α_c . It follows that wing buffeting measurements on canard/wing configurations can be represented conveniently in the α , n_c domain, with lines superposed representing constant values of α_c according to Eq (3). Fig 7 shows the interaction between the canard and wing flows for the present configuration.

The wing-alone buffeting measurements may be represented by the line $\alpha_c = 0^\circ$ if thickness effects on the canard are ignored. The lines $\alpha_c = \pm 12^\circ$ represent the onset of buffeting and flow separation on the canard, i.e. the boundaries which mark the start of significant interference between the separated flows on the canard and the wing. The wing-buffeting measurements with canard settings of $n_c = -10^\circ$, 0° and $+10^\circ$ are represented directly in the α , n_c domain by points on the various contours of buffet intensity.

Fig 7 shows that a canard setting of $n_c = -10^\circ$ makes only a modest reduction in the severity of wing buffeting because large values of α_c (say 30°) and hence large separations on the canard are reached only at rather high angles of incidence ($\alpha = 22^\circ$). In contrast, a canard setting of $n_c = 0^\circ$ makes a large reduction of wing buffeting above $\alpha = 16^\circ$, because this angle of incidence already corresponds with a large value of α_c , (30°).

The rather poor wing buffeting characteristics for a canard setting of $n_c = +10^\circ$ present a paradox which is now explained. For this setting $\alpha_c = 30^\circ$ is reached at $\alpha = 10.5^\circ$, i.e. just before the onset of flow separations on the wing. Here the wake from the canard is so large that it excites the wing directly, even before the wing is excited by its own separated flow. Similarly for higher angles of incidence the relatively high level of direct excitation from the canard offsets the reduction in wing excitation due to the reduction in wing flow separations. However, even $n_c = +10^\circ$ offers a small reduction in wing buffeting in the first-bending mode relative to the wing alone once the wing flow separates.

This interpretation of Fig 7 is consistent with the general character of the static force characteristics given in Fig 4. Thus the increase in lift in Fig 4a relative to the wing alone is smallest for $n_c = -10^\circ$, because here α_c is relatively small and the full benefit of the canard is not achieved. The increase in lift is much larger for $n_c = 0^\circ$ because α_c is much larger than for $n_c = -10^\circ$. As with the buffeting measurements, the lift characteristic for $n_c = +10^\circ$ presents a paradox. With larger canard separations than for $n_c = 0^\circ$ the maximum lift coefficient at $\alpha = 25^\circ$ is lower, and may be even lower than that for $n_c = -10^\circ$. Presumably for $n_c = 10^\circ$, α_c has now become so large (56.7°) that the canard separations become large. The wake from a very large canard separation is probably less energetic than from a somewhat smaller one, and would therefore be less effective as a control of flow separations on the wing. However, there is currently no direct evidence (e.g. local shear stress measurements) to justify this suggestion.

An independent check of the validity of the assumption that 'canard-off' measurements are equivalent to $\alpha_c = 0^\circ$ is provided by the measurements of static pitching moment, which are reproduced in Fig 8 from Fig 4b. Fig 8 shows that for each of the three canard settings the points derived from Eq (3) for $\alpha_c = 0^\circ$ are close to, and the line joining them is parallel to, the 'canard-off' measurements. Fig 8 implies that the canard provides a small positive pitching moment for $\alpha_c = 0^\circ$ and that the assumption that 'canard-off' measurements correspond to $\alpha_c = 0^\circ$ is valid also for pitching moments. For reference, Fig 8 also includes the approximate contours for $\alpha_c = 12^\circ$ and 30° : manifestly these cannot be related directly with the measurements.

Fig 7 also has important implications with respect to the drag measurements of Fig 4c. For a fixed angle of incidence, α , changes in n_c provide relatively small changes in C_L (Fig 4a) but large changes in a_c (Fig 7). If it is assumed that a constant lift coefficient implies constant induced drag, variations in the total drag would be determined solely by the variations in a_c , which determine the drag due to the canard separations. Thus the total drag would be expected to remain constant when there are no separations on the canard, i.e. for $-12^\circ < a_c < 12^\circ$. However the total drag would be expected to increase steadily with a_c when the canard flow is separated, i.e. for $a_c > 12^\circ$. Fig 9 shows that C_D increases linearly with a_c when the canard flow is separated. If the variation in drag is attributed to the loss of leading-edge suction on the canard because of flow separations at buffet onset then the change in the drag coefficient is given approximately by

$$\Delta C_D = [(C_{BC}) \sin(\alpha + n_c)] (S_c/S) \quad (4)$$

Fig 9 shows that Eq (4) provides a good approximation to the measured drag variation up to $\alpha = 20^\circ$, but not at $\alpha = 25^\circ$.

Fig 9 also shows that when the drag coefficients measured with the canard are extrapolated to $a_c = +12^\circ$, (the lower bound for drag increments due to canard flow separations), the drag is close to the 'canard-off' value for the same fixed incidence (regarded as $a_c = 0^\circ$ in Fig 7) for $\alpha = 12^\circ$ and 15° . However the favourable influence of the canard on the wing flow is particularly marked for $\alpha = 20^\circ$ (C_L about 1.3) where the extrapolated drag for $a_c = 12^\circ$ is appreciably lower than the 'canard-off' value which develops a lift coefficient of only 1.1. (This discussion takes no account of any trim drag which might be required.)

Figs 8 and 9 suggest that the canard/wing flow interaction, as described in Fig 7, can help to optimise both the longitudinal stability and the overall drag characteristics of canard/wing configurations. Fig 7 also helps to explain the steady and unsteady pressure distributions on the wing measured with the canard locked, which are considered now.

3.4 Steady pressures and buffet excitation on the wing

The mean pressure distributions on the wing complement the overall force measurements and the unsteady pressure distributions complement the buffeting measurements. Steady and unsteady pressure measurements for $\alpha = 5^\circ, 12^\circ, 15^\circ, 20^\circ$ and 30° , with the three canard settings ($n_c = -10^\circ, 0^\circ, +10^\circ$) and without the canard have been analysed in detail. Salient points are summarised here.

3.4.1 Development of the wing flow

In the absence of separations on the wing (for $-3^\circ < \alpha < 12^\circ$) the principal effect of the canard at positive effective incidence is to create a positive downwash field at the wing. This reduces the suction a little on the wing upper surface (particularly for inboard sections), thus decreasing the wing lift. The overall lift is almost unchanged (Fig 4a) so that the small reduction in wing lift is almost balanced by the additional canard lift, just as observed in Ref 1. In contrast, once separations occur on both the wing and the canard (cf Fig 7) the mixing provided by the canard wake inhibits the spanwise and chordwise growth of the wing separations. This alters the pressures on the upper surface of the wing and increases the wing lift. Thus the increased overall lift shown in Fig 4a for $\alpha > 12^\circ$ is due to the combined effects of increased wing lift and the canard lift.

No flow visualisation was possible in the present tests*, but by analogy with two-dimensional bubbles¹⁴ a rough indication of the reattachment point is given by the peak level of \bar{p}/q at every section. The approximate loci of these points shown in Fig 10 marks the boundary between the attached and separated three-dimensional flows. [The area of separated flow may be regarded either as a swept bubble or a vortex/bubble.] Without the canard the leading-edge bubble extends progressively with increasing incidence from the leading edge to the trailing edge, so that for $n = 0.8$ the leading-edge bubble extends to the trailing edge at $\alpha = 15^\circ$. In contrast, with the canard at $n_c = 0^\circ$ (the 'optimum' value of the three settings tested) the bubble at $n = 0.8$ only extends to $x/c = 0.6$ at $\alpha = 15^\circ$. These reductions in the areas of separated flow are thus consistent with the improvements in overall forces and the reduction in wing buffeting.

In general on the lower surface the changes in both the steady and time-dependent pressure distributions are comparatively small.

3.4.2 Measurements illustrating the effect of the canard on the wing pressures ($\alpha = 20^\circ, n_c = 0^\circ$)

As an illustration of the strong, favourable effect of the canard on the wing flow (once that flow has separated), for $\alpha = 20^\circ$ pressure measurements are compared without the canard and with the canard set at $n_c = 0^\circ$. Without the canard ($a_c = 0^\circ$) the lift coefficient, C_L , is only 1.09 and the wing buffet excitation parameter $\sqrt{a_0(n)} = 4.0 \times 10^{-3}$.

*Subsequently the reattachment line suggested in Fig 10 has been confirmed by the observation of 'mini-tufts' on the same wing although with a different configuration.

With the canard set at $\alpha_c = 0^\circ$ ($\alpha_c = 37.2^\circ$) the lift increases to $C_L = 1.32$ and the wing buffet excitation parameter reduces to $\sqrt{n}G(n) = 1.4 \times 10^{-3}$. Fig 11 shows the origin of these favourable interference effects on the wing-pressure distributions. In addition to the increase in wing lift due to interference, the canard provides its own contribution to the overall lift, but this contribution was not measured directly.

Consider first the steady and unsteady pressure distributions for the inboard section (Fig 11a, $\eta = 0.4$). Without the canard the steady and unsteady pressure distributions suggest that the flow separates close to the leading edge and reattaches at about $x/c = 0.80$ (as indicated clearly by the peak in \bar{p}/q at $x/c = 0.80$). With the canard the steady pressure distribution indicates a large increase in suction at the leading edge and a greatly improved pressure recovery towards the trailing edge, consistent with almost complete suppression of separation but the overall lift on this section is reduced. This change in the steady pressure distribution is combined with a large reduction in pressure fluctuations for $x/c > 0.05$ which is a sure indication of the suppression of bubble separation. For the lower surface, where the boundary layer is attached for both conditions, there is a small increase in the steady pressure towards the trailing edge with the canard, but no corresponding change in the unsteady pressure distribution. On the lower surface of the wing the boundary layer is attached at all three sections so that the levels of \bar{p}/q in Fig 11 for the lower surface are much lower than for the upper surface.

For the centre section (Fig 11b, $\eta = 0.6$) the situation is completely different. Without the canard the steady and unsteady pressure distributions are consistent with a long bubble separation, which 'closes' in the wake well downstream of the trailing edge. Thus the pressure fluctuations are constant from the leading edge to $x/c = 0.80$ and then increase towards the trailing edge. With the canard the steady and unsteady pressure distributions are consistent with a bubble that reattaches at about $x/c = 0.80$ (where \bar{p}/q is a maximum). Hence there is a recovery in the static pressure coefficient at the trailing edge comparable with that observed for the inboard section.

For the outboard section (Fig 11c, $\eta = 0.8$) the situation is different again. Here the flow separation without the canard is so extensive that it is reduced by only a little with the canard. Thus the steady pressure distribution shows that with the canard flow remains completely separated (albeit with a small increase in suction on the upper surface), while the unsteady pressure fluctuations are reduced over most of the chord. This reduction in pressure fluctuations caused by the canard would be consistent with a reduction in the chordwise length of separation, which would move the excitation towards higher frequencies outside the bandwidth of the present measurements. (See discussion of the spectra given in Fig 12).

The changes in the pressure distributions shown in Fig 11 might be attributed to three possible causes:

- (1) The steady downwash field due to the canard. (This explanation is inapplicable outboard of the canard, where the downwash becomes an upwash).
- (2) The steady sidewash field due to the canard. (This explanation would be applicable across the complete wing and equally valid for attached and separated canard flows).
- (3) The vigorous mixing produced by the separated flow on the canard, i.e. the canard acts on the wing flow separations rather like a huge vortex generator.

Tentatively the latter appears the most likely explanation, because many other buffeting measurements suggest that the vigorous mixing produced by the canard separation is much the most important factor in improving the aerodynamic characteristics of close-coupled canard wing configurations. This suggestion is consistent with the spectra of the pressure fluctuations, which are now presented. The notation used is that suggested by Owen¹⁵ where the spectrum level $\sqrt{n}F(n)$ represents the rms level at a frequency parameter n .

Fig 12 shows some typical spectra of the pressure fluctuations corresponding with measurements of \bar{p}/q at $x/c = 0.05, 0.40$ and 0.80 . The test conditions are the same as for Fig 11 ($\alpha = 20^\circ$, canard off and canard at $\alpha_c = 0^\circ$).

For the inboard section (Fig 12a, $\eta = 0.40$) the flow is separated close to the leading edge (at $x/c = 0.05$) both with and without canard. For frequencies less than about 12 Hz the excitation is higher with the canard than without the canard, whereas for frequencies higher than 12 Hz the excitation is lower with the canard than without the canard. It is likely that the flow with the canard is close to reattachment, so that the flow separates and reattaches intermittently. This would give an increased level of low-frequency excitation and a reduced level of high frequency excitation as compared to the continuously separated flow without the canard. The flow reattaches upstream of $x/c = 0.40$ with the canard but remains separated without the canard. Hence for this position the level of pressure fluctuations is only about $\sqrt{n}F(n) = 0.001$ with the canard, compared to $\sqrt{n}F(n) = 0.007$ without the canard. Without the canard the flow reattaches at about $x/c = 0.80$. Hence the spectrum of the pressure fluctuations has a characteristic peak typical of the reattachment region of a bubble¹⁴. This peak occurs at a frequency parameter based on the local chord of $fc/U = 0.76$, or a frequency parameter based on the bubble length, $f = 0.8c$ of $f_1/U = 0.60$, which is in the same range as that for two-dimensional bubbles¹⁴. With the canard for $x/c = 0.80$, the flow remains attached and the excitation low at all frequencies.

For the centre section (Fig 12b, $\eta = 0.6$) the flow is separated both with and without the canard at $x/c = 0.05$ and 0.40 . Hence the level of pressure fluctuations is virtually identical and fairly high - typically about $\sqrt{np}(\eta) = 0.006$. This is about twice the peak level for an attached turbulent boundary layer on a flat plate (about $\sqrt{np}(\eta) = 0.002$ to 0.003). For $x/c = 0.80$, the flow reattaches with the canard but remains separated without the canard. The reattachment of the flow with the canard gives a characteristic peak in the pressure fluctuations at a frequency parameter based as the local chord of $fc/U = 0.76$ or a frequency parameter based on the bubble length $l = 0.80c$ of $fl/U = 0.60$, as for $\eta = 0.4$.

For the outboard section (Fig 12c, $\eta = 0.8$) the flows are completely separated both with and without the canard. However the level of pressure fluctuations without the canard is appreciably higher, and the peak level occurs at a lower frequency at every chordwise position. This change in the spectra due to the canard is significant for two reasons. The lower frequency of the peak excitation without the canard is due probably to a longer-length bubble¹⁴ (closing in the wake). However the lower level of the peak excitation with the canard must be due to some other factor. In the authors' view the most likely factor is the modification of the bubble structure on the wing by the vigorous mixing provided by the separated flow on the canard. An interesting feature of Fig 12c is that without the canard there is a peak in the pressure fluctuations at $f = 22$ Hz, which may indicate pressures generated by the wing-bending motion.

For completeness, a spectrum of the wing accelerometer signal is included in Fig 12d. The addition of the canard reduces the wing acceleration by a factor of about $1/3$, as has already been seen from the buffeting measurements (Fig 5a). This is roughly consistent with the reduction in the peak level of the lower surface pressure fluctuations (Fig 12e).

3.4.3 Classification of the wing alone flows and the effect of the canard

Fig 13 shows the classification of the steady and fluctuating pressure distributions on the wing upper surface derived from the measurements. Fig 13a shows how the types of pressure distributions vary across the span with the angle of incidence. Fig 13b gives a key showing the symbols associated with the five different types of steady (p/q v x/c) and unsteady (\dot{p}/q v x/c) pressure distributions. The description that follows refers to the changes caused by the canard from the pressure distributions without the canard.

For type 1 the canard induces essentially potential flow effects due to changes in downwash and sidewash in the absence of wing flow separations. Thus the steady pressure distribution indicates a progressive reduction in suction due to the canard as the canard setting increases from $\alpha_0 = -10^\circ$ to $+10^\circ$. There are no changes in the corresponding unsteady pressure distributions for $\alpha_0 = -10^\circ$ and 0° but there may be a small increase in pressure fluctuations for $\alpha_0 = +10^\circ$ due to high frequency excitation from the canard wake (wherever $\alpha_0 > 12^\circ$). Scale effects on the steady pressure distributions are likely to be small for this attached flow region.

For type 2 there is an important viscous effect in the trailing-edge region without the canard shown by an increase in trailing-edge pressure. With the canard there is defined upwash flow relative to the wing alone, shown by the decrease in trailing-edge pressure. The unsteady pressure distributions are similar to those in region 1. Scale effects on the steady pressure distributions are likely to be large close to the trailing edge particularly with the canard-off.

Type 3 was encountered only in the test at $\alpha = 10^\circ$ and $\eta = 0.4$. The canard was with potential and viscous flow effects over the whole chord. This is surprising, because the potential flow effects are characterised primarily by steady pressure distributions and the same as those of type 2. In contrast the viscous effects over the whole chord are shown by the sudden changes in the unsteady pressure distributions. For $\alpha_0 = -10^\circ$ and 0° there is a marked reduction in pressure fluctuations due to the suppression of the small separation, close to the leading edge, whereas there is a small increase for $\alpha_0 = +10^\circ$. (In type 2, for $\alpha_0 = 10^\circ$ the large values of α_0 are considered to generate large vigorous canard bubbles which are less effective in controlling the wing-flow separations as discussed above in section 3.4.1.) Scale effects on all the steady pressure distributions are likely to be large over the whole chord in this region.

For type 4 the canard causes a radical change in steady pressure distribution, in evidence of a strong interaction between the separated flow on the canard and the separated flow on the wing (see Fig 13a). The canard increases the suction on the forward part of the wing section and decreases the suction towards the rear of the section. The changes in the unsteady pressure distribution are complex: generally the pressure fluctuations are decreased for $\alpha_0 = -10^\circ$ and 0° and increased for $\alpha_0 = +10^\circ$. Type 4 is characterised by a strong interaction between two separated flows. Hence scale effects on the steady and unsteady pressure distributions are likely to be very large over the whole chord.

For type 5 the wing flow separations without the canard are so large that no significant reduction occurs when the canard is added (see Fig 13a). Hence the steady pressure distributions are only slightly changed by the canard. In this region the wing pressure fluctuations are generally increased by the canard. Scale effects are likely to be small over the whole chord in this region.

In summary, types 1 and 2 correspond with attached flow on the wing upper surface, i.e. $0^\circ < \alpha < 12^\circ$. Types 3, 4 and 5 correspond with varying areas of separated flow on the wing upper surface, i.e. $12^\circ < \alpha < 30^\circ$.

A tentative guess for the extent of the small region of type 3 is indicated by the shaded area Fig 13a. The boundaries of types 4 and 5 are fairly well defined and suggest a rapid growth of the area of separation as α increases, consistent with Fig 10. In particular, type 5 extends inboard rapidly at about $\alpha = 25^\circ$, when $C_{L_{max}}$ is approached for all the canard configurations. This is reasonable, because in type 5 the canard separated flow is no longer able to control the wing-flow separations (at least for the canard settings selected).

4 DISCUSSION

The comprehensive results of this experiment, presented in section 3.3 above confirm that the canard effective incidence, α_c , plays a crucial role in determining the interaction between the flows on the canard and the wing. Previously it had been shown on other configurations that the wing buffeting was represented best in the α_c, n_c domain for particular values of α_c . Now it has been shown that the same representation helps to explain the variations in overall forces (lift, pitching moment and drag), the wing steady pressure distributions and buffet excitation. It follows that the establishment of a relation for α_c equivalent to Eq (3) is a prerequisite to understanding the results of any experiment involving canard/wing interactions.

The present configuration is close-coupled and hence the leading term (1.89a) in Eq (3) includes contributions from both the wing and the body. The wing could not be removed to establish the upwash contribution due to the body alone. However some indication of the relative magnitude of the wing and body upwash effects is provided by tests with a smaller canard mounted further upstream on an extended fuselage. For that configuration the leading term in Eq (3) is only 1.43a. Thus the wing contribution is significant for the present configuration. This observation is consistent with theoretical estimates.

The large size of the model makes it possible to represent quite small details (such as the leading-edge notches described in Ref 6) and the effects of these details on the steady forces can be measured readily on the balance. The large size also makes it possible to install a sufficient number of pressure transducers to provide a detailed description of the steady and unsteady pressure distributions on both surfaces of the wing. For the lower surface of the wing the steady and unsteady pressure distributions warrant little comment except with separated flows on the upper surface when there are large pressure fluctuations close to the front stagnation point, particularly with leading-edge devices, as discussed in Ref 6.

For the upper surface of the wing the steady and unsteady pressure distributions for positive angles of incidence have many interesting features, which have been described fully in section 3.4.

The analysis of the results from this experiment suggest that three additions would be essential for definitive tests on a specific project model.

- (1) The canard setting (n_c) for the highest possible value of $C_{L_{max}}$ should be determined. [This test would be comparatively easy, for it could be made with small increments in n_c over a restricted range of incidence.]
- (2) The canard setting should be varied in small increments (say 1°) at every angle of incidence. This would give the canard effectiveness in quasi-steady flow. Apart from a great increase in measurement time this would require a more powerful actuator.
- (3) The possible effects of independent variations of Mach number and Reynolds number would need to be investigated carefully, because some of the flows will be sensitive to effects of compressibility and boundary layer thickness. This type of investigation is impossible in the RAE 13ft x 9ft Tunnel but could be done in pressurised tunnels such as the RAE 5m, 8ft x 8ft and 8ft x 6ft tunnels.

5 CONCLUSIONS AND RECOMMENDATIONS

This paper suggests five main conclusions.

- (1) The canard effective incidence, α_c , determines the canard flow. It also, in combination with α , determines the interaction between the canard and the wing flows, influencing both the wing buffeting (Fig 7) and the overall forces (Figs 8 and 9). Hence the derivation of the canard effective incidence is a prerequisite to understanding the results of other experiments involving canard/wing interactions.

- (2) The canard/wing interaction is complex and further detailed analysis of the present measurements is recommended. With separated flows on the canard the vigorous mixing is probably the major factor which inhibits the development of wing-flow separations (Fig 10).
- (3) The widely different types of flow observed (Fig 13) may have important implications both with respect to the siting of aerodynamic control surfaces on the wing and the fatigue life of the structure.
- (4) The canard has a strong favourable effect on both the overall forces and the buffeting with a canard setting of $\alpha_c = 0^\circ$ and consistent with the values of α_c , a much less favourable effect for $\alpha_c = +10^\circ$ (Fig 5).
- (5) The flows described could well be sensitive to scale effects and further investigations in a pressurised wind-tunnel, at constant Mach number, are recommended.

REFERENCES

- 1 B. B. Gloss, L. W. McKinney. 'Canard-wing lift interference related to manoeuvring aircraft at subsonic speeds', NASA TM X-2897 (1973).
- 2 J. F. Campbell, B. B. Gloss, J. E. Lamar. 'Vortex manoeuvre lift for supercruise configurations', NASA TM X-72836 (1976).
- 3 B. B. Gloss, K. E. Washburn. 'A study of canard-wing interference using experimental pressure data at transonic speeds', NASA TP 1355 (1979).
- 4 B. B. Gloss, W. T. Henderson. 'Effect of canard position and wing leading-edge flap deflection on wing buffet at transonic speeds', NASA TM X-72681 (1975).
- 5 G. F. Moss, A. J. Ross, G. F. Edwards, E. B. Jefferies. 'The use of free flight models for the prediction of departure control', AGARD CP 339 (1982) Paper 11.
- 6 D. G. Mabey, B. L. Welsh, C. R. Pyne. 'The development of leading-edge notches to improve the subsonic performance of wings of moderate sweep', RAE Technical Memorandum 2078 (1986).
- 7 H. C. Garner. 'Theoretical use of variable porosity in slotted tunnels for minimising wall interference on dynamic measurements', R&M 3706 February (1971).
- 8 B. L. Welsh, C. R. Pyne. 'An optimised control system for the inexorable excitation of wind-tunnel models using electromagnetic vibration', RAE Technical Memorandum Aero in preparation.
- 9 B. L. Welsh, D. M. McOwat. 'Presto - a system for the measurement and analysis of time-dependent signals', RAE Technical Report 79135 (1979).
- 10 J. G. Jones. 'A survey of the dynamic analysis of buffeting and related phenomena', RAE Technical Report 72197 (1972).
- 11 D. G. Mabey, B. E. Cripps. 'Some measurements of buffeting as a flutter model of a typical strike aircraft', Paper 13 AGARD CP 339 (1982).
- 12 P. R. Ashill, R. P. A. Keating. 'Calculation of tunnel wall interference from wall-pressure measurements', RAE Technical Report 85-086 (1985).
- 13 D. G. Mabey. 'Beyond the buffet boundary', Aeronautical Journal (1973).
- 14 D. G. Mabey. 'Analysis and correlation of data on pressure fluctuations in separated flow', AIAA Journal (1972).
- 15 T. B. Owen. 'Techniques of pressure fluctuation measurements employed in the RAE Low-Speed Wind Tunnels', RAE Technical Memorandum Aero 565, AGARD Report 172 (1958).



Fig 1 High incidence research model in RAE 13ft x 9ft Tunnel

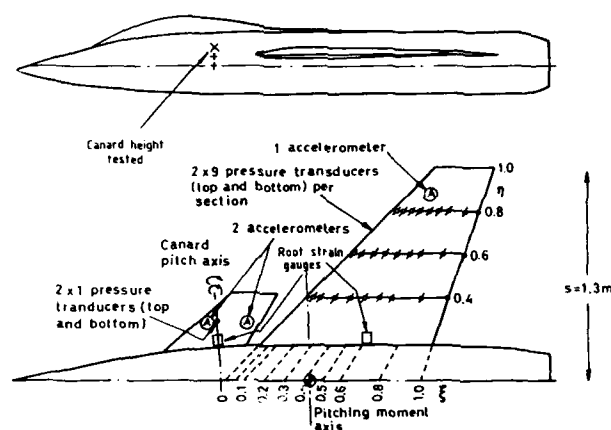


Fig 2 GA of half HIRM model for RAE 13ft x 9ft tunnel (4.0m x 2.7m)

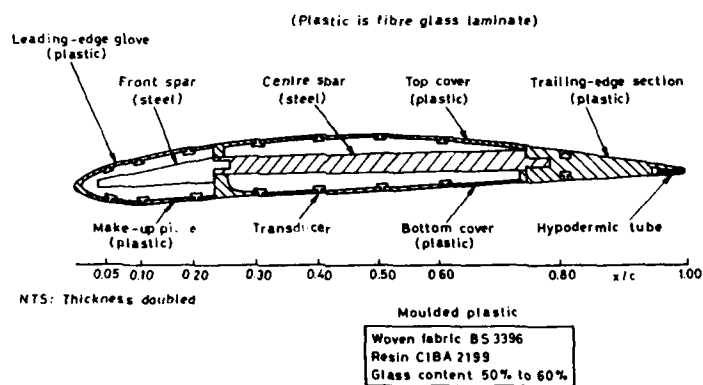


Fig 3 Simplified sketch of wing construction

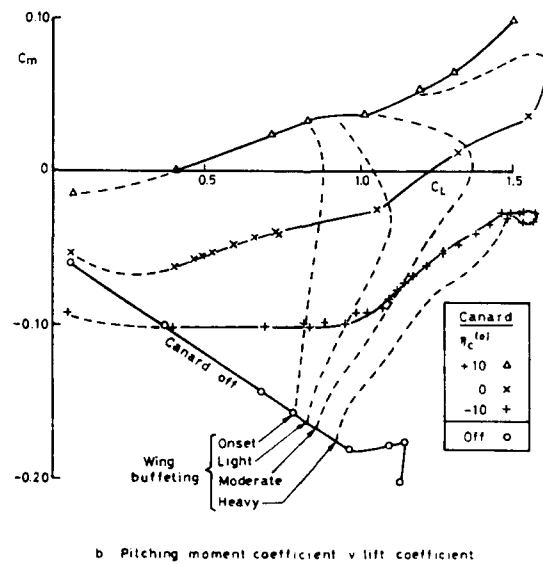
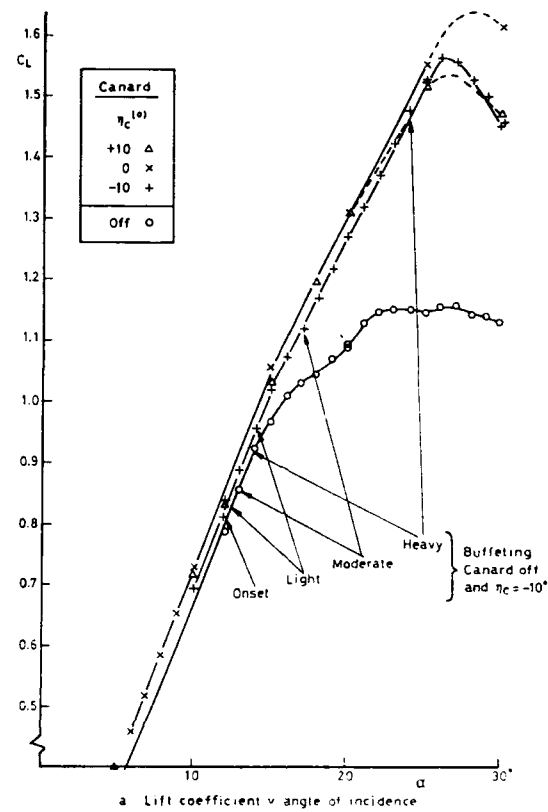


Fig 4 Static forces and moments

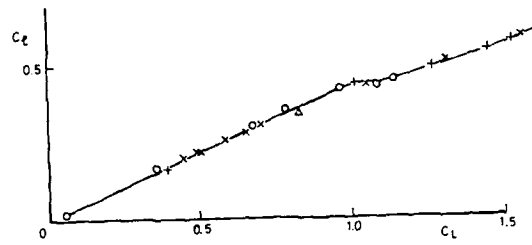
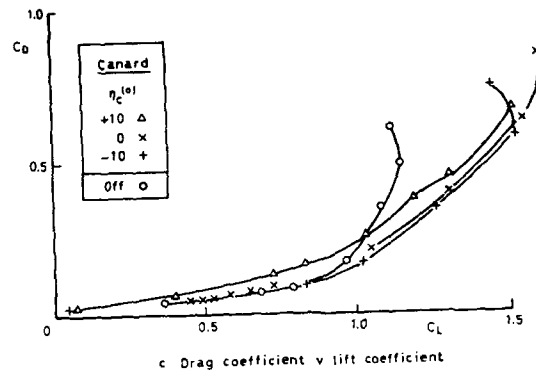


Fig 4(concld) Static forces and moments

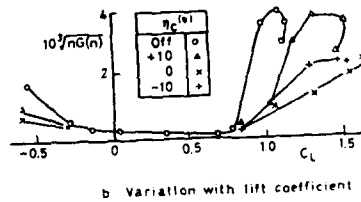
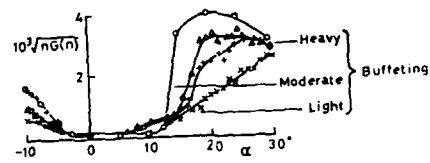


Fig 5 Buffet excitation parameter in wing first bending mode

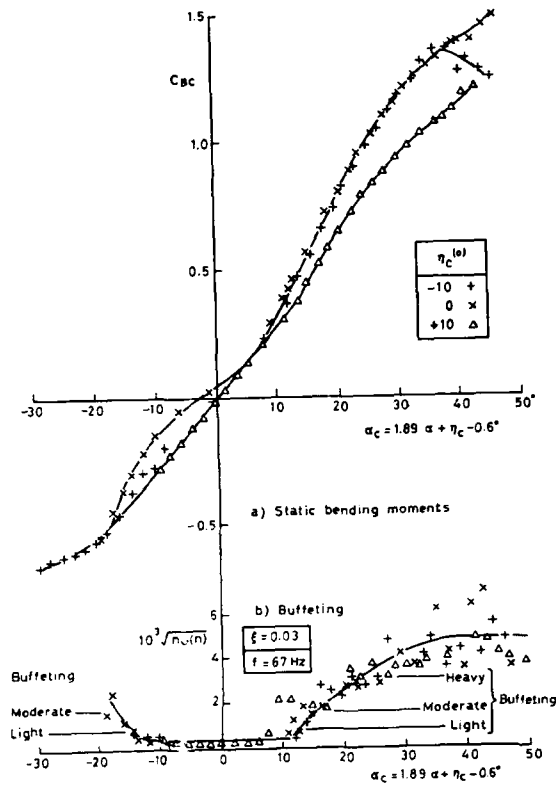
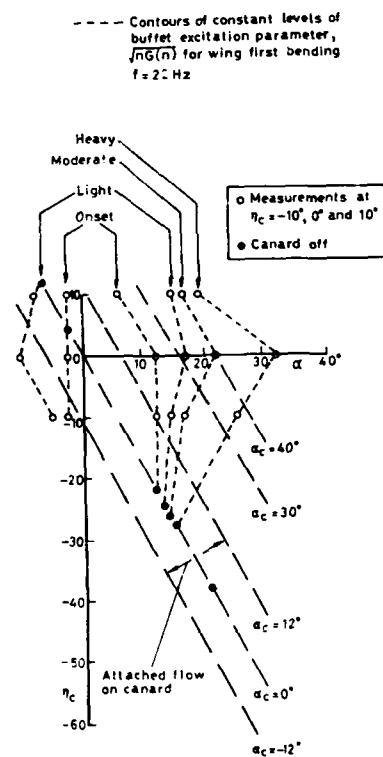


Fig 6 Canard static bending moment and buffeting in first bending mode

Fig 7 Interaction between canard flow and wing buffeting in $\alpha - \eta_c$ domain

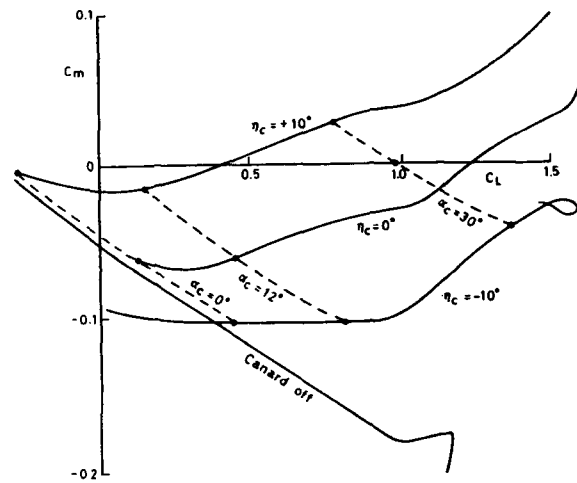


Fig 8 Interaction between canard and wing flows with respect to pitching moments

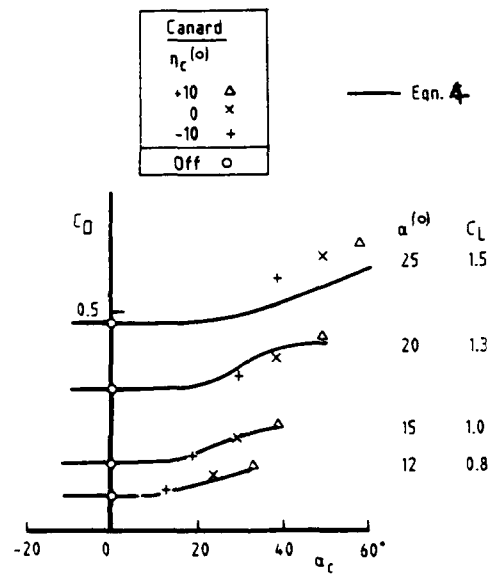


Fig 9 Variation of drag coefficient with canard effective incidence for constant wing incidence

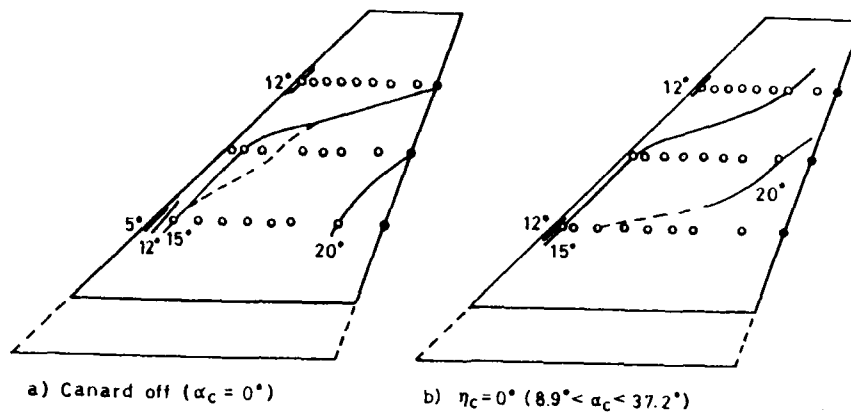


Fig 10 Approximate loci of $(\bar{p}/q)_{\max}$ for different angles of incidence

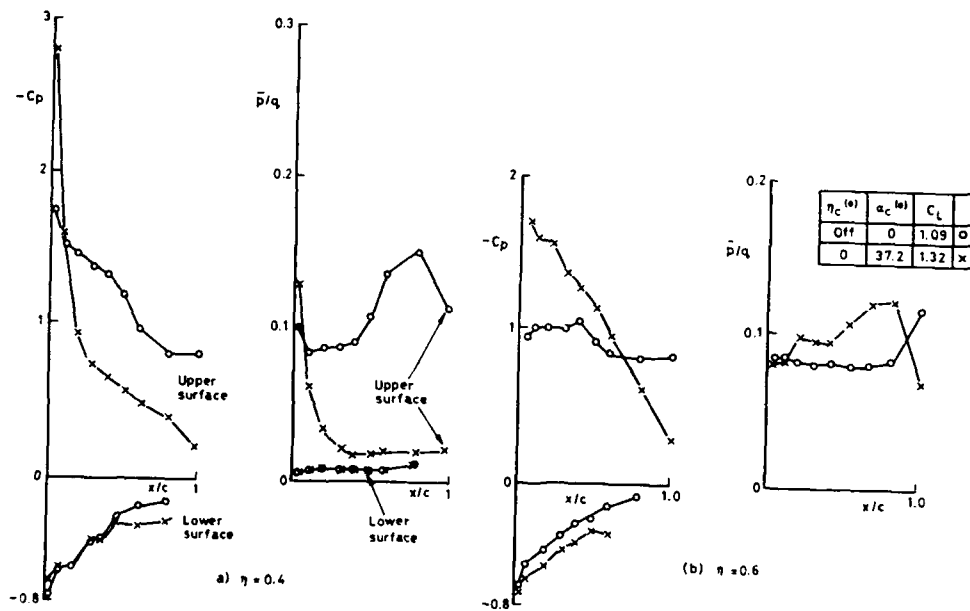
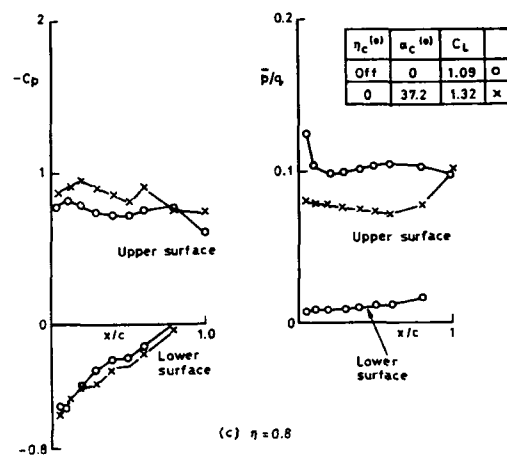
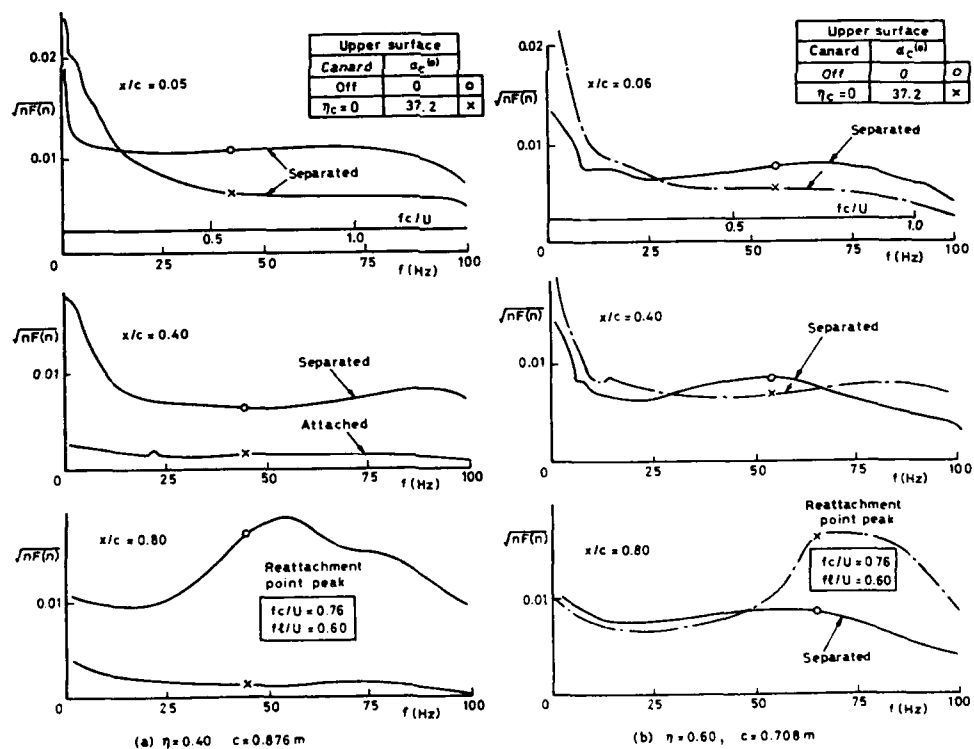


Fig 11 Typical pressure distributions showing effect of canard - $\alpha = 20^\circ$

Fig 11 Typical pressure distributions showing effect of canard $-\alpha = 20^\circ$ Fig 12 Typical spectra, $\alpha = 20^\circ$

PREDICTIONS OF F-111 TACT AIRCRAFT BUFFET RESPONSE*

by

Atlee M. Cunningham, Jr. and Charles F. Coe
 General Dynamics COE Engineering, Inc.
 Fort Worth, Texas 610 Cuesta Drive
 United States Los Altos, CA 94022
 United States

1.0 INTRODUCTION

Buffeting and the related flow phenomena that cause buffeting can strongly affect aircraft maneuvering characteristics and utility through various flight envelope restrictions. These restrictions, as discussed by John¹, include vibration level limits at critical airframe locations such as: (1) gyros or tracking radar antenna mountings; and (2) pilot's and other crew's seats. Fatigue damage to secondary structures such as leading or trailing edge flaps as well as primary structures such as horizontal and vertical tails, is not so much of an envelope restriction as it is a potential factor in reducing the service life of aircraft structures as was discussed by Cunningham and Benepe². Thus, because of the impact of buffet on aircraft operational capabilities, prediction methods are needed to allow aircraft designers to minimize the restrictions imposed by buffet phenomena.

A good review of the general principles of the aerostructural buffet problem and the basic features of the fluctuating aerodynamic pressures and elastically responding aircraft structure is given by Jones³. However, the complexity of the aerodynamic excitation and the aerostructural interaction has severely limited the ability to predict full-scale aircraft buffet characteristics. In a comprehensive review of buffet prediction methods, John¹ concluded that empirical methods were good for predicting buffet boundaries such as that of Mabey^{4,5}. He also concluded that wind-tunnel testing of dynamically scaled models should give the most accurate results for full-scale buffeting characteristics as demonstrated by Hanson⁶, however, this technique is severely limited due to cost and aerodynamic loads constraints on the model. A simpler and less costly method, originally suggested by Jones⁷ and applied by Butler and Spavins⁸, uses measured buffet response of nominally rigid wind tunnel models to calculate the buffet excitation and aerodynamic damping. These are then scaled to calculate the full-scale aircraft buffet characteristics, but predictions are limited to wing modes of vibration only. Another development described by Cunningham and Benepe², makes use of measured fluctuating pressure data from a rigid wind tunnel model to predict full-scale buffeting. This method is applicable to any aircraft vibration mode but assumes attached flow aerodynamic damping, and, because it uses power and cross-power spectra of the measured pressure data, it is expensive and difficult to apply.

In order to better understand both the aerodynamic and structural aspects of aircraft buffeting as well as develop a more practical approach for predicting buffet characteristics, a major effort was conducted as part of the F-111 TACT Program to investigate the many aspects of the buffet problem. NASA Ames Research Center, with support from General Dynamics, conducted this investigation with the objectives to: (1) verify the applicability of buffet excitation measurements obtained on nominally rigid wind tunnel models to full-scale elastic aircraft, (2) investigate effects of Reynolds number and static and dynamic aeroelasticity, and (3) to develop a more practical buffet prediction method and correlate structural response predictions with flight-test measurements. Two 1/6-scale semi-span models of the TACT aircraft were tested in the 11 foot by 11 foot transonic wind tunnel at NASA Ames. One model had a solid aluminum wing and the other a solid steel wing while both were extensively instrumented identically for steady and unsteady pressures as well as wing motion response. The aircraft was also instrumented in the same manner so that one-to-one correspondence of measurement locations existed between the aircraft and the two models. This aircraft was more completely instrumented for buffet testing than any previous aircraft. Flight testing was correspondingly improved to increase the statistical accuracy of flight measurements through long periods of sustained flying at buffet test points. The results of the buffet investigation were fully documented by Coe and Cunningham in a NASA report⁹.

This paper presents a summary of the prediction method development and correlations of predicted response with flight test measurements as discussed in Reference 9. The prediction method was based on refinements to the method described by Cunningham². One improvement made use of direct time integration of the correlated fluctuating pressure data to obtain buffet excitation for the various modes of interest. Another improvement incorporated a hybrid technique for scaling measured wind tunnel damping data to full-scale for the modes of interest. A third improvement made use of the diagonalized form of the fully coupled equations of motion. Finally, a mechanism was described for explaining an apparent coupling between the aircraft wing torsion modes and shock induced trailing edge separation that led to very high wing motion on the aircraft that was not observed on the wind tunnel model.

2.0 OVERVIEW OF THE PREDICTION METHOD

The three major functions involved in the method⁹ and their relationships to the prediction of buffeting are shown in Figure 1. There are three significant differences between the present method and previous fluctuating pressure methods. First, the measured fluctuating-pressure time histories were summed on a real-time basis to obtain the generalized aerodynamic forces for selected modes. This approach is simpler and more direct than that of Reference 2 which required the combining of a large number of spectra and

* Supported under NASA Contract NAS2-11420

cross-spectra to develop the complex spanwise and chordwise buffet excitation. Second, measured aerodynamic damping for major model modes of vibration were used in conjunction with a similarity analysis of damping to predict total damping for the selected full-scale aircraft modes. Third, eigenvalues from conventional flutter solutions were used to diagonalize the equations of motion representing the full-scale aircraft so that response calculations could be made on a small computer.

The data from the model tests included fluctuating-pressure and buffet response time histories. The fluctuating pressures were measured at sufficient locations on the model wing and horizontal tail for accurate integration of the overall buffet excitation. Figure 2 shows an example for the transducer distribution and corresponding prorated area panels for the wing upper surface. The normalized modal displacements at the panel centroids, for the aircraft modes used in the buffet response prediction, were provided by the aircraft structural dynamic analysis. The modal displacements, (h_i) , for the i^{th} mode were combined with the panel areas, $[A]$, and model fluctuating pressure time history data, (p) , to yield the total generalized aerodynamic force, Q_{ti} , for the i^{th} mode:

$$Q_{ti} = [h_i] [A] (b) = [Ah_i](p)$$

Because the pressures were measured on a semi-span model, it was assumed that they were symmetrical and uncorrelated for the right- and left-hand side. Thus,

$$Q_{ti} = (Q_{tir}^2 + Q_{til}^2)^{1/2} = [A(h_{iR}^2 + h_{iL}^2)^{1/2}] (p) \quad (1)$$

where Q_{tir} and Q_{til} are the right- and left-hand total generalized forces for the i^{th} mode and $[h_{iR}]$ and $[h_{iL}]$ are the right- and left-hand modal displacements at the panel area centroids.

The time integration of Equation 1 was accomplished with an analog computer as shown in Figure 3. The weighting factors applied with the attenuators accounted for transducer calibration factors, panel areas and mode displacements. The output time history for Q_{ti} was processed into a power spectral density, $G_{Q_{ti}}(f)$, with a spectral analyzer also shown in Figure 3. The motion-independent generalized force PSD, $G_{Q_{ii}}(f)$, was determined from $G_{Q_{ti}}(f)$ as

$$G_{Q_{ii}}(f) = G_{Q_{ti}}(f) - G_{Q_{di}}(f) \quad (2)$$

where $G_{Q_{di}}(f)$ is the motion-dependent generalized force PSD which will be discussed later. After $G_{Q_{ii}}(f)$ was determined, it was then reduced to the non-dimensional buffet excitation parameter⁷ for the i^{th} mode at the scaled resonant frequency for that mode, f_{mi} , as defined by Jones⁷

$$E_i(f_{mi}) = \frac{G_{Q_{ii}}(f_{mi}) V_{wt}}{S_A^2 q_{wt}^2 \bar{c}_m} \quad (3)$$

where

$$\begin{aligned} f_{mi} &= f_{Ai}(\bar{C}_A/\bar{C}_m) = \text{model scale modal resonant frequency} \\ f_{Ai} &= \text{full scale modal resonant frequency} \\ \bar{C}_A, \bar{C}_m &= \text{MAC for the aircraft and model respectively} \\ S_A &= \text{aircraft wing area} \\ V_{wt} &= \text{free stream velocity in wind tunnel} \\ q_{wt} &= \text{free stream dynamic pressure in wind tunnel} \end{aligned}$$

The value of $G_{Q_{ii}}$ for the full scale aircraft was obtained from E_i by solving for $G_{Q_{ii}}$ using V_A , \bar{C}_A and q_A as well as S_A for the aircraft

Analysis of the model buffet response data was also conducted as shown in Figure 3 to obtain response PSD's of the model accelerometers and total damping for the model first wing bending and torsion modes. Because of the higher response of the aluminum wing model, the better damping measurements were obtained from this model. Subtracting the experimentally determined structural damping, ζ_{sm} , for the model mode from the total damping, ζ_{tm} , yielded the aerodynamic damping, ζ_{am} , for the corresponding model mode. This was then used to determine the damping parameter, K_m , for each of the model modes as defined by Butler and Spavins⁸:

$$K_m = \frac{M_m \omega_m V_{wt} \zeta_{am}}{S_m q_{wt}} \quad (4)$$

where

$$\begin{aligned} M_m, \omega_m &= \text{generalized mass and frequency for the model mode} \\ S_m &= \text{model wing area} \end{aligned}$$

The aircraft structural dynamic analysis included the aerodynamic damping in a multiple degree-of-freedom analysis that accounts for full-scale modal coupling. The combination of the aerodynamic damping parameter, K_m , with the generalized masses, M_A , frequencies, ω_A , and normalized damping parameters, ζ_{aAn} , yielded the aerodynamic damping, ζ_{aA} for each aircraft mode at the selective flight conditions.

$$\zeta_{aA}(f,h) = \frac{K_m q_A S_A \zeta_{aAn}(f,h)}{M_A \omega_A(f,h) V_A} \quad (5)$$

where

q_A, V_A = aircraft dynamic pressure and free stream velocity

$\zeta_{aAn}(f,h)$ = normalized damping parameter relating the aircraft "pivot" mode with other similar aircraft modes as a function of forcing frequency, altitude and aircraft fuel weight

M_A = aircraft generalized mass as a function of aircraft fuel weight

$\omega_A(f,h)$ = aircraft mode frequency as a function of forcing frequency, altitude and aircraft fuel weight

Finally, the total damping, ζ_{ta} , was obtained as

$$\zeta_{ta} = \zeta_{aA}(f,h) + \zeta_{sA}$$

where ζ_{sA} is the structural damping for the aircraft mode. The normalized damping parameter for each mode is the theoretical aerodynamic damping for the mode divided by the theoretical aerodynamic damping for a pivotal mode on the aircraft. The pivotal modes are the primary aircraft wing bending and torsion modes that have shapes similar to those on the model. This concept will be discussed in more detail later in the paper.

The final step in the buffet prediction method in Figure 1 is the calculation of the power spectral density of the forced response of the aircraft. The generalized aerodynamic force coefficients, generalized masses, frequencies and total damping all defined for the flight condition of interest, are embodied in the PSD calculation for a range of frequencies that include the selected modes.

3.0 PRELIMINARY EVALUATION OF THE PREDICTION METHOD

The simplest and most direct approach to verify adequacy of the buffet prediction method is to apply it to the wind tunnel model and compare predictions with measured model response. This eliminates scale effects as well as differences in modes, damping and static aeroelasticity. Such an investigation was conducted by Moore, Cronin and Coe¹⁰ using the measured fluctuating pressure and damping data for the aluminum wing model to predict its buffet response for conditions covering pre-buffet, onset and heavy buffet as discussed below.

A typical buffet forcing function PSD is shown in Figure 4 for the model first wing bending mode at $\alpha = 12$ deg. The solid circles indicate the direct analog integration of the fluctuating pressures and first wing bending mode shape. At about 24 Hz, a dip in the PSD is noted which is a result of wing response and thus represents the effect of aerodynamic damping. In order to use measured aerodynamic damping in combination with a "rigid" input buffet forcing function as required by the prediction technique, this irregularity had to be removed for the evaluation study. Examination of many of the buffet forcing function spectra revealed a very smooth variation with frequency which justified a simple fairing through the regions of modal response. This fairing is indicated by the open diamonds in Figure 4 for the model modes. For airplane modes, this step was not generally necessary unless their scaled frequencies corresponded closely to that of a model mode. The dip in the PSD in Figure 4 also represents the $G_{Q_{11}}$ discussed previously in relation to Equation 2. Fairing through this dip as shown by the open diamonds represents satisfying the requirements of Equation 2. Thus, the open diamonds become $G_{Q_{11}}$.

Predictions for the model response given in Reference 10 were obtained using $G_{Q_{11}}$ and measured model damping for the model first wing bending and torsion modes. Because the modes were widely separated in frequency, it was possible to use single degree-of-freedom equations to calculate the wing response. A typical comparison of predicted and measured PSD's for the wing tip accelerometer is shown in Figure 5. The frequency range shown is in the vicinity of the first wing bending mode for the 26 deg. wing sweep at $\alpha = 8$ deg., just prior to buffet onset, and at $\alpha = 12$ deg., in heavy buffet. The predictions (open diamonds) are somewhat conservative in comparison to measured response (solid circles) at $\alpha = 8$ deg., however, the peaks are well matched at $\alpha = 12$ deg. The slight shift in frequency of the measured peaks is attributed to the increased stiffness due to aerodynamic springing which was ignored in this preliminary study.

Integrated RMS results for the model wing tip accelerometer are shown in Figure 6 for the first wing bending mode at 26 deg. and 35 deg. wing sweeps for the aluminum wing and $M = 0.8$. With measurements denoted by solid circles and predictions by open diamonds, the agreement in trend and magnitude is excellent for 26 deg. sweep. However, a slight conservatism is shown in predictions for the 35 deg. sweep case. Similar results are shown

in Figure 7 for the model first wing torsion mode at the same conditions. These predictions are more conservative, especially at 26 deg. sweep. It is also important to notice that the levels in both predictions and measurements are about five times those shown in Figure 6 for the first wing bending mode. The point will be of interest later when comparing predictions with the full scale aircraft.

In summary, the preliminary investigation to apply the buffet prediction technique to the wind tunnel model verified that the method is a reasonable approach. In this demonstration the buffeting pressures were essentially uncoupled from wing motion as is required by the basic assumptions.

4.0 STRUCTURAL DYNAMIC ANALYSIS

In order to predict full scale aircraft buffet characteristics using measured wind tunnel modes fluctuating pressure and damping data, the problems associated with scale effects as well as differences in modes, damping and static aeroelasticity must be addressed. These problems did not exist for the demonstration just discussed for the wind tunnel model buffet predictions, hence the correlations with measured response were excellent. Maintaining good correlation between predictions and measured flight test response, however, depends on how well the differences between model and aircraft are accounted for in the prediction method.

This section describes the approach used to account for the model/aircraft differences and to develop simplified but realistic equations of motion for the aircraft that could be used on small computers. Damping must be determined for all of the selected aircraft modes in such a way as to preserve the real flow effects that exist on the model as well as the modal coupling that exists for the full scale aircraft. A key to accomplishing this task is to minimize the miss-match between modes on the model and aircraft. In addition, the effects of altitude and fuel weight must be accounted for in the aircraft modal frequencies, damping and generalized masses that are inserted into the equations of motion. The solution to these final equations produces the predicted aircraft buffet response.

4.1 Equations of Motion

The basic working tool for the prediction method is the standard set of equations of motion for determining the dynamic response of a flexible aircraft. It is possible to utilize eigenvalues of this equation that are obtained in routine flutter analyses to reduce all of the matrices to a diagonal form that is easily programmed on small computers. This subsection describes the diagonalization process and implications of the assumptions needed to accomplish this diagonalization.

The equations of motion for an aircraft with flexible degrees of freedom can be expressed in a matrix equation for generalized coordinates which are the normal modes of vibration:

$$(\{M_i(\omega^2 - \omega_i^2 - i2\omega\omega_i\zeta_{is})\} + \{Q_{ij}\})\{r_i\} = \{Q_{iB}\} \quad (7)$$

where

- M_i = generalized mass of the i^{th} mode
- ω_i = undamped natural frequency of the i^{th} mode
- ω = exciting frequency
- ζ_{is} = structural damping for the i^{th} mode
- Q_{ij} = generalized aerodynamic force for pressures due to the j^{th} mode motion working on deflections of the i^{th} mode
- r_i = generalized coordinate response of the i^{th} mode
- Q_{iB} = generalized aerodynamic force for the buffeting pressures working on deflections of the i^{th} mode

For purposes of discussions, Equation 7 can be written in a more compact form:

$$[D - I]\{r_i\} = \left\{ \frac{Q_{iB}}{M_i\omega^2} \right\} \quad (8)$$

where

$$[D] = \left[\frac{-\omega_i^2 - i2\omega\omega_i\zeta_{is}}{\omega^2} \right] + \left[\frac{Q_{ij}}{M_i\omega^2} \right] \quad \text{and} \quad [I] = \text{identity matrix}$$

This form leads directly to the eigenvalue/eigenvector problem from which the diagonalization is evolved. The purpose of the diagonalization is to produce a set of equations that

are uncoupled mathematically but are effectively coupled through eigenvalues obtained from solutions to the fully coupled equations. The eigenvalue/ eigenvector form of Equation 8 is

$$[D - I \lambda_i] \{\phi_i\} = \{0\} \quad (9)$$

where λ_i and ϕ_i are the eigenvalue and eigenvector for the i th mode.

For most flight conditions, except near flutter, the damped natural modes are very close to their undamped counterparts. Under these conditions, the aerodynamic terms, Q_{ij} , are small which leads to

$$\phi_{ik} \ll \phi_{ii}, \phi_{ii} \approx 1 \quad (10)$$

Which is a mathematical statement of the assumption that aerodynamic coupling is a second order effect in modifying the mode shape. This is the key equation needed for diagonalizing Equation 7. Now, Equation 9 can be written in a more general form for all modes:

$$[D][\phi] = [\lambda \phi] \quad (11)$$

But from Equation 10, $[\phi]$ is very nearly a diagonal unit matrix, hence

$$[\phi] \approx [I] \text{ and } [\lambda \phi] \approx [\lambda] \quad (12)$$

Combining Equations 11 and 12 yields

$$[D][\phi] \approx [D][I] = [D] \Rightarrow [D] \approx [\lambda] \quad (13)$$

which is the desired diagonal form.

The eigenvalues are composed of a real part, frequency, and an imaginary part, damping, in the following form

$$\lambda_i = \frac{1}{\omega^2} (\bar{\omega}_i^2 + i2\omega \bar{\omega}_i \bar{\zeta}_i) \quad (14)$$

where the $\bar{\omega}_i$ and $\bar{\zeta}_i$ are a function of frequency, $\bar{\omega}_i(\omega)$ and $\bar{\zeta}_i(\omega)$, respectively. This dependency is a result of the Q_{ij} terms in the matrix which are a function of frequency, ω . These eigenvalues are readily available from routine flutter analyses and include all of the effects of aerodynamic coupling between modes. One drawback of using the flutter eigenvalues, however, is that the aerodynamic methods customarily used are based on linear theory and hence do not reflect the effects of separated or transonic flows. This point will be discussed later.

Substitution of Equations 13 and 14 into Equation 8 leads directly to the working form of the diagonalized equations of motion:

$$[M_i] \ddot{r}_i + \omega_i^2 r_i - i2\omega \bar{\omega}_i (\bar{\zeta}_i + \bar{\zeta}_{is}) \dot{r}_i = (Q_{iB}) \quad (15)$$

the solution to Equation 15 is simply the uncoupled form

$$\{r_i\} = \left[\frac{1}{M_i[\omega^2 - \omega_i^2 - i2\omega \bar{\omega}_i(\bar{\zeta}_i + \bar{\zeta}_{is})]} \right] (Q_{iB}) \quad (16)$$

This solution can be used to compute transfer functions for motion at any point on the aircraft from which response PSD's and integrated RMS values are obtained. Response calculations obtained from Equation 16 are for essentially un-correlated multiple degrees of freedom and are therefore added together on a mean-square basis.

4.2 Scaling of Measured Aerodynamic Damping

In order to scale measured damping from a wind tunnel model to a full-scale aircraft, the modes of each must be similar. The full-scale mode that most closely resembles the corresponding model mode is termed a "pivot mode". As an example, the first wing symmetric bending for the F-111 TACT aircraft was very similar to the first wing bending for the 1/6-scale aluminum wind-tunnel model. Thus, this mode was a logical choice for the "pivot mode" that represented the family of modes involving fundamental wing bending motion. Other aircraft modes belonging to this family included the first fuselage vertical bending and first wing antisymmetric bending.

In the case of torsion modes, the choice of a "pivot mode" was not so simple. The model wing first torsion mode had a node line that was further aft than the corresponding node lines for the torsion modes on the airplane. The torsion modes on the F-111 TACT aircraft were not typical of pure torsion modes and were actually a combination of first wing symmetric and antisymmetric torsion plus the second symmetric wing bending. This was a result of the distribution of the instrumentation mass which caused a mismatch between the right and left hand wings. The impossibility of matching one of the aircraft torsion modes with a model torsion mode significantly complicated the problem of scaling wind-tunnel model torsion mode aerodynamic damping data.

In order to remedy the problem of selecting an appropriate torsion pivot mode, a technique was developed for combining the airplane torsion modes to obtain a composite mode that was more like the model torsion mode. The technique was based on the assumptions that (1) the diagonalized equations of motion are valid and (2) separation and transonic effects scale similarly for similar mode shapes. The equations developed provided the generalized mass as well as damped and undamped natural frequencies for the composite mode. Equations were also developed for relating scaled aerodynamic damping values for the composite mode to those values of the "base modes" used to construct the composite mode. A summary of this development is given in the following discussion.

Let it be assumed that three base modes are to be combined to produce a final composite mode subject to some constraints on the mode shape. Let the modal deflections of the composite mode (h_C) be defined as

$$\begin{aligned} (h_C) &= p_1(h_1) + p_2(h_2) + p_3(h_3) \\ (h_C) &= (p_1 h_1 + p_2 h_2 + p_3 h_3) \end{aligned} \quad (17)$$

where: p_i are the real weighting numbers assigned to mode i as determined by shape constraints on (h_C); and (h_i) are the modal deflections for base mode i . Since the h_i vectors are orthogonal, i.e.,

$$\begin{aligned} \sum_k m_k h_{ik} h_{jk} &= 0, \quad i \neq j \\ &= \sum_k m_k h_{ik}^2 \neq 0, \quad i = j \end{aligned} \quad (18)$$

then it can be shown that the composite generalized mass is a simple sum of the generalized masses of the three base modes:

$$M_C = p_1^2 M_1 + p_2^2 M_2 + p_3^2 M_3 \quad (19)$$

Thus, once the weighting numbers, p_i , are obtained, M_C is readily calculated from M_i . This property (Eq. 19) will also play an important role in establishing the damping and frequency relationships.

In the absence of aerodynamic forces, the generalized stiffness of the equivalent mode must be equal to the weighted sum of the generalized stiffnesses of the base modes. Hence, the following must be true:

$$M_C \omega_C^2 = \sum_i p_i^2 M_i \omega_i^2 \quad (20)$$

This equation is exact because ω_C is the composite mode undamped frequency and the aerodynamic forces are the only source of off-diagonal terms. The remaining frequency and damping relationships derived in Reference 9 are

$$M_C \tilde{\omega}_C^2 \approx \sum_i p_i^2 M_i \tilde{\omega}_i^2 \quad \text{and} \quad M_C \tilde{\omega}_C \tilde{\zeta}_C \approx \sum_i p_i^2 M_i \tilde{\omega}_i \tilde{\zeta}_i \quad (21)$$

Also provided in Reference 9 are the equations required to calculate individual aircraft mode damping values from the scaled damping for the "pivot mode" whether it is composite or not. This relationship is expressed as

$$\tilde{\zeta}_i = \zeta_k \left(\frac{\tilde{\zeta}_i}{\tilde{\zeta}_k} \right)_T \quad (22)$$

Where the ratio of damping values is obtained from the theoretical flutter solution, hence, the subscript "T". This ratio is the same quantity as the ζ_{aan} parameter discussed in relation to Equation 5. The ζ_k is a scaled damping value for the pivot mode and $\tilde{\zeta}_i$ becomes the "scaled" damping for the i th mode member of the k th pivot mode group. For example, the k th mode could be the first symmetric wing bending and the i th mode could be the first antisymmetric wing bending. For the torsion mode group, the k th pivot mode is replaced by the composite pivot mode.

A composite first wing symmetric torsion mode for the F-111 TACT was developed using the above equations to combine the right and left hand wing torsion modes and the symmetric hybrid wing torsion/second wing bending mode. The result of this effort is shown in Figure 8 along with the first wing torsion mode for the wind tunnel model. The comparison is very good and far superior to that which involved the original aircraft modes. Weighting numbers to be applied to the modes involved in the composite mode were obtained by satisfying deflection constraints imposed by the model torsion mode. These conditions were satisfied at two leading and trailing edge points (inboard near the pivot and the outboard near the wing tip) on both wings which resulted in eight equations and led to a least squares solution. The weighting numbers obtained from the solution were

$$p_1 = 1.5272 \quad (\text{RWT}) \quad p_2 = 1.0284 \quad (\text{LWT}) \quad p_3 = -0.5865 \quad (\text{WST})$$

with a generalized mass, $M_c = 1041.6$ lbs., and undamped natural frequency, $f_c = 14.92$ Hz, for the composite mode. Although the eight boundary conditions were not exactly satisfied, this solution did produce a reasonable facsimile of the model torsion mode as shown in Figure 8.

4.3 Scale and Static Aeroelastic Effects

The most difficult aspect of buffet prediction to be accounted for is the scale effect due to Reynolds number dissimilarity between the model and full-scale aircraft. This effect significantly influences separated flow fields, particularly shock induced separation which is of primary importance for transonic buffet. The scale effect problem for the F-111 TACT aircraft was treated in the conventional manner of building the model as large as possible, hence the 1/6-scale was chosen. Testing at higher than ambient pressures increased the density and therefore Reynolds number so that a value of 14×10^6 was achieved with the steel model wing as compared with 25×10^6 for the aircraft. The comparison of wind tunnel and flight measured fluctuating pressures as fully discussed in Reference 9 showed that scale effects had been minimized as much as possible.

Static aeroelastic effects are also difficult to account for, but comparison of steel and aluminum wing fluctuating pressure data in Reference 9 provided some insight to these effects. Wing twist due to aeroelastic washout tended to lower the effective angle of attack for the wing and delay the development of the separated flow fields by about 1.0 deg. This delay tended to offset earlier development of the separated flow fields resulting from a lower Reynolds number, hence, static aeroelastic and scale effects almost canceled each other for the wind tunnel model as tested in this investigation. The aluminum wing data, however, were used in the buffet predictions since its aeroelastic properties better simulated the full-scale aircraft.

5.0 INPUT DATA FOR EQUATIONS OF MOTION

In order to predict full-scale aircraft buffet, the input data required for evaluating Equation 16 include modes, frequencies, damping and buffet excitation for the full-scale aircraft.

5.1 Aircraft Modes

The mode shapes employed in the present analysis for the generalized aerodynamic forces were numerically generated by General Dynamics Corp., Fort Worth Division, during the original structural dynamics analysis required for the TACT modification to the F-111 aircraft.¹¹ Six modes were selected to be included in the TACT aircraft buffet predictions as follows:

1. 1st wing symmetrical bending (WSB, 4.42 Hz)
2. 1st fuselage vertical bending (FVB, 7.30 Hz)
3. 1st wing antisymmetrical bending (WASB, 7.68 Hz)
4. 1st right-wing torsion (RWT, 14.09 Hz)
5. 1st left-wing torsion (LWT, 15.20 Hz)
6. 1st wing symmetrical torsion (WST, 17.14 Hz)

The mode shapes as well as masses and frequencies for both theoretical and experimental modes are given in Reference 9. The modes were selected to provide a variety of mode shapes (wing bending vs fuselage bending vs wing torsion), and because they were expected to dominate the TACT aircraft buffeting. Since, the differences in the natural frequencies for the FVB and WASB modes and the RWT, LWT and WST modes are small, it was considered necessary to include all modes in the close-frequency groupings because of the strong possibility of aerodynamic modal coupling.

5.2 Modal Masses, Frequencies and Damping

The generalized masses for each of the above modes were determined as a function of aircraft fuel weight for the specific flight test points. Factors were developed from analytical analyses to account for fuel weight that were applied directly to the analytically determined masses for the empty aircraft.

Modal frequencies as influenced by aerodynamic forces were determined from the eigenvalues taken from the flutter solution velocity/damping curves given in Reference 11. The aerodynamic damping factors, defined by the theoretical damping ratio in Equation 22, were also obtained from the eigenvalues in Reference 11. The effects of altitude and forcing frequency were inherent in these frequencies and damping factors as is illustrated in Figure 9 for the wing symmetric bending (WSB) and right wing torsion (RWT) modes. The effects of altitude are more significant for frequency than for damping in these plots because the effects are already accounted for in scaling of the model damping data. The influence of excitation frequency, f , is significant, however, particularly for the wing bending type modes such as WSB. These frequency effects are a direct result of the flutter eigenvalue variations with frequency. Similar curves as shown in Figure 9 were generated for the remaining four aircraft modes.

The scaled aerodynamic damping data for the aircraft pivotal modes were obtained from the measured damping for the aluminum model first wing bending and torsion modes. The corresponding aircraft pivot modes were the WSB and the composite torsion mode shown in Figure 8. Measured aerodynamic damping data from the two model modes are shown in Figure 10 as a function of incidence, α , for 26 deg. and 35 deg. wing sweeps. At both sweeps, bending mode damping shows a significant increase at buffet onset between 9 deg. and 10 deg. while torsion mode damping is little affected. The influence of wing sweep is not significant but the higher sweep shows a softening of the onset change for the bending mode and a slight overall increase for the torsion mode. These data in Figure 10 were scaled to the two aircraft pivot modes using the K_m factor defined in Equation 4 and the scaling relationships in Equation 5. They were further scaled to other modes in each pivot mode family using Equations 21 and 22 and damping factor curves for each mode as typified by those shown in Figure 9.

5.3 Buffet Excitation Coefficients

In order to conveniently account for the differences in the model and aircraft scale and wind-tunnel and flight conditions, the generalized aerodynamic forces were reduced to buffet excitation coefficients, E , (Eq. 3). The buffet excitation coefficients obtained from the aluminum- and steel-wing models are shown in Figure 11 versus angle-of-attack for two of the aircraft modes selected for analysis. The aluminum-wing data were obtained at test Reynolds numbers of 10.5×10^6 and the steel-wing data were obtained at test Reynolds numbers of 14.0×10^6 . Figure 11 shows that excitation coefficients evaluated from the aluminum- and steel-wing models were within a factor of 2 for all test points. This generally good agreement of E on a mean-square scale, substantiates the repeatability of data and adds confidence to the excitation coefficients.

With a lower Reynolds number, however, the aluminum wing data still reflected static aeroelastic effects. This is especially evident in the 35 deg. wing sweep results in Figure 11 where onset occurs at about 0.5 deg. higher for the aluminum wing. Thus, the aluminum wing pressure data were used in this investigation to represent the airplane partly because of this aeroelastic effect.

The effects of the wing and tail on buffet excitation were investigated for the aluminum wing model. The results as discussed in Reference 9, showed that the effects of the tail were important for five of the aircraft modes used in the analysis and negligible only for the WSB mode. The largest effect was felt by the FVB (fuselage vertical bending) mode. These two extremes are illustrated in Figure 12 for the same excitation parameter shown in Figure 11. The wing alone, tail alone and wing plus tail characteristics in Figure 12 clearly demonstrate these trends. Because tail contributions were significant for modes that had large fuselage and empennage motion, tail buffet excitation was a necessary part of this buffet response analysis. This is particularly important for determining buffet response at points other than on the wing as was discussed previously by Cunningham and Benepé².

6.0 AIRCRAFT BUFFET PREDICTIONS

The dynamic model developed in the previous sections was applied to predict the buffet response for the F-111 TACT aircraft at selected flight test conditions. This section presents and discusses the results of these predictions including correlations of predicted and measured damping. The correlation of predicted and measured buffeting are based on PDSs and integrated RMS values. The buffet response characteristics are correlated for the same range of angles of attack, altitude and wing sweep as the pressure-fluctuation correlations that were discussed extensively in Reference 9.

Details of the flight test program are described in Reference 9. The nominal conditions for the buffet response correlations are summarized as follows:

MACH NUMBER	0.8 for all buffet response correlations		
ALTITUDE	3.7 K m (12.0 K ft.)	6.1 K m (20.0 K ft.)	8.5 K m (28.0 K ft.)
DYNAMIC PRESSURE	28.0 K N/m (600 psf)	21.5 K N/m (450 psf)	14.4 K N/m (300 psf)
ANGLES OF ATTACK	7° - 10°	7° - 12°	7° - 12°
WING SWEEP	26° & 35°	26° & 35°	26° & 35°

6.1 Correlations of Damping

The amplitude of predicted buffet response for any given vibration mode is inversely proportional to the total damping value for that mode as indicated by Equation 16. Because of this sensitivity, a major effort was made in the F-111 TACT buffet investigation to correlate estimated modal damping with measured flight test values. Direct comparisons in Reference 9 showed that trends in estimated damping generally agreed with flight test data except that the predicted values had higher overall levels. One of the best correlations was shown for the RWT mode at both wing sweeps. In all cases, significant scatter was present in the flight test data, especially in the region of buffet onset. In view of the expected difficulty of predicting and measuring aerodynamic damping values for aircraft operating in separated transonic flow fields, these results were very encouraging.

6.2 Correlations of Power Spectral Densities

Complete sets of figures that include the predicted and measured PSDs of the wing tip and C.G. accelerations are given in Reference 9. Typical examples of wing tip accelerometer results are shown in Figure 13 for 26 deg. wing sweep and Figure 14 for 35 deg. wing sweep. The flight conditions are $M = 0.8$ for the middle dynamic pressure at about 20 K ft altitude. Two angles are shown representing pre-buffet at 9 deg. and heavy buffet at about 12 deg. The 26 deg. sweep predictions for the bending mode group from 3 to 10 Hz show very good correlations with flight test data at both angles in Figure 13. Predictions for the torsion mode group from 13 to 20 Hz, agree well at 9 deg. but are very low for heavy buffet at the higher angle. This characteristic was prevalent in all 26 deg. sweep predictions for both PSDs and integrated RMS values. For the 35 deg. sweep results in Figure 14, excellent agreement is seen between predicted amplitudes and flight test for all conditions with exception of the torsion mode group at 9 deg.

In summary, the predicted PSDs agreed quite well with flight measured PSDs with exception of the torsion mode group. The disagreement was most noticeable and consistent at 26 deg. sweep in heavy buffet.

6.3 Correlations of RMS Buffet Responses

In order to correlate the RMS values of the predicted and measured buffeting, the PSDs were integrated over several different frequency ranges. The frequency limits of the integrations and grouping of modes were as follows:

MODES	PREDICTION LIMITS	FLIGHT TEST LIMITS
WBS	3.45 - 6.25 Hz	3.22 - 6.14 Hz
FVB and WASB	5.95 - 9.46 Hz	5.95 - 9.46 Hz
RWT, LWT and WST	11.0 - 19.0 Hz	12.0 - 19.0 Hz

The FVB and WASB modes and RWT, LWT and WST modes were combined because the separate modes could not be isolated in flight test PSDs. A fourth integration was also performed where all responses listed above were combined into a total RMS over the full frequency range. As for the PSD comparisons, the RMS comparisons were made for both wing-tip and CG accelerations as a function of angle of attack, altitude and wing sweep at $M = 0.8$. Included in Reference 9 are all of the integrated RMS results corresponding to all of the PSDs given in that reference.

Examples of RMS results for the wing tip accelerometer for the WSB mode and the torsion mode group are shown in Figure 15. The effects of altitude, angle of attack, α , and wing sweep are illustrated in these results. As was observed in the PSDs, predictions for the WSB mode follow both α and altitude trends at both wing sweeps. Onset is well predicted and heavy buffet levels are reasonably well predicted. The torsion mode group predictions at 26 deg. sweep, however, are low by a factor of about 2.0 to 2.25 depending on altitude and α . There is also an interesting trend in the flight test data which shows an insensitivity to altitude. At 35 deg. wingsweep, the torsion mode group RMS predictions agree quite well with flight test data as was indicated earlier in the PSD comparisons.

The wide band RMS results for all six modes are shown in Figure 16 which includes the C.G. accelerometer as well as the wing tip accelerometer. For 26 deg. sweep, the wide band results are dominated by those for the torsion mode group, especially for the flight test data. This is expected on the basis of results shown in Figure 15 where the flight measured torsion mode group response was about three times the measured levels for the WSB mode. Trends noted in the wing tip accelerometer results are also seen in the C.G. accelerometer results but to a lesser degree for this wing sweep. At 35 deg. wing sweep, the agreement between predictions and flight measurements are quite good for both accelerometers, especially for buffet onset.

In summary, the predicted RMS buffet characteristics tracked flight test buffet measurements again with exception of the torsion mode group. At 26 deg. wing sweep, flight test torsion response dominated the trends and was higher than predictions by as much as 125%. In addition, a peculiar trend was noted in the torsion mode group wing-tip accelerometer response in that it was almost insensitive to altitude for 26 deg. sweep.

7.0 FACTORS THAT INFLUENCE THE CORRELATIONS

The basic factors that affect the correlations of wind-tunnel and flight-test buffet data were discussed in the Introduction; and in the body of this paper it was pointed out that the F-111 TACT program provided a significant improvement in the factors that affect the flight data. However, even with these improvements, the present correlations of predicted and measured buffeting still show some discrepancies. The questions arises then as to what factors were the most probable cause of the discrepancies.

Many factors were discussed in Reference 9 as being potential sources for the discrepancies between predictions and flight test results. It was decided in retrospect that a torsion family mode may have been ignored that should have been included to bring the total to seven modes to represent the full-scale aircraft. The dominant sensitivity of buffeting response to damping values also made the accuracy of damping estimates sus-

pect. However, correlations of estimated damping with flight measured damping showed that the technique for extrapolating measured tunnel damping data to full-scale airplane modes represents a satisfactory methodology. The fact that damping correlations were good where buffet predictions were not so good for the torsion modes suggested that other effects were responsible for differences in correlations between bending and torsion modes.

The accuracy of generalized masses and mode shapes was also questioned on the basis of comparison of the theoretical modes and masses used and those obtained from vibration tests of the aircraft. Reynolds number and static aeroelastic effects were suspect as well. Based on detailed analysis of the wind tunnel and flight measured pressure and other flow data in Reference 9, however, it was expected that these effects would not be significant for buffet response correlations. Pitch rate and maneuver time history effects were also considered as pointed out in Reference 2, however, the flight test techniques used in the investigation were aimed at minimizing these effects. Analyses of flight test results in Reference 9 verified that this goal was achieved.

All of the above factors were common to the predictions made at both 26 deg. and 35 deg. wing sweeps. Yet, at 26 deg. sweep, the predicted torsion mode group responses were very low compared with flight test measurements but were quite similar to those predicted and measured response levels at 35 deg. sweep. Therefore, the only data set that did not fit was the flight measured torsion mode group response at 26 deg. sweep as a result of two significant differences: (1) high levels of response over a narrow frequency band and (2) the insensitivity of response levels to altitude. This is clearly evident in the RMS results shown in Figures 15 and 16 and is opposite in trend to the results shown earlier in Figure 7 where the predicted model torsion response was higher than the measured values.

The possibility of any coupling between wing modes and fluctuating pressures on the aircraft could have a critical effect on the buffet correlations. For the F-111 TACT aircraft there were certain conditions when such a coupling may have affected the buffet response. This point was discussed in Reference 9 with regard to pronounced peaks observed in the flight data fluctuating pressure PSDs that occurred near the torsion mode frequencies for 26 deg. sweep. Similar peaks were not observed in the pressure PSDs for 35 deg. sweep. As a result it was proposed in Reference 9 that a potential coupling between the wing torsion modes and shock induced trailing edge separation (SITES) could produce a limited amplitude oscillation which would explain the anomalous behavior of the flight test buffet response. A more extensive discussion of this coupling mechanism is given by Cunningham in Reference 12 with regard to this case and several other types of limited amplitude oscillations (LCO) that may occur due to either aerodynamic or structural non-linearities. Thus, for the sake of completeness in this paper, a brief summary of the pertinent discussions in References 9 and 12 follows.

A clue to a possible means for the coupling was deduced from the static pressures in Reference 9 for 26 deg. wing sweep. The occurrence of trailing-edge pressure divergence at about $\alpha = 10$ deg. also corresponded to a large forward movement of upper surface main shock as shown by comparing pressure at $\alpha = 9$ deg. and at $\alpha = 10$ deg. It was also observed that the forward shock movement for the aircraft was much larger than that for the model. The condition of this transition is the occurrence of Shock-Induced Trailing Edge Separation (SITES) which is accompanied by a step change in pitching moment with either increasing or decreasing angle-of-attack. With increasing angle-of-attack, the forward shock movement produces a loss of lift toward the leading edge and the trailing edge divergence produces a gain of lift toward the trailing edge. The net result is to provide a step change in pitching moment that is nose down for increasing angle-of-attack, for decreasing angle-of-attack, the opposite occurs and produces a step change in pitching moment that is nose up. Such a step change in effect results in a nonlinear spring that could provide an increased resistance to wing motion past the point of SITES for either increasing or decreasing angle-of-attack.

The nonlinear spring described above can potentially produce a limited amplitude, self-sustaining oscillation, the existence of which could explain the higher torsion mode response exhibited by the full scale aircraft. How this is possible can be described by considering an airfoil with a torsion spring. Slowly increasing incidence at angles below that of SITES allows the torsion spring to attain a continuous state of equilibrium with aerodynamic pitching moment. When SITES is reached, a sudden nose-down increment is imposed on the aerodynamic pitching moment which will tend to reduce wing incidence. This will be a dynamic negative-pitch rate which will delay re-attachment and permit the nose-down moment to put work into the system. At some point, re-attachment does take place and the nose-down moment disappears. Accelerations become negative and the wing experiences a reducing pitch rate until it reaches zero and begins nose-up motion. Positive pitch rate now takes over which will produce a delay in SITES and allow an overshoot of the initial starting point due to stored elastic energy during the down stroke. When SITES does occur, the cycle then repeats itself.

The above concept was applied to the TACT aircraft as described in Reference 9. For simplicity, the RWT mode was chosen for a single degree-of-freedom model because of its dominant role in large amplitude responses measured on the aircraft at 26 deg. wing sweep. The appropriate equation of motion used was

$$M_{RWT} \ddot{x} + 2M_{RWT} \bar{\omega}_{RWT} \zeta_{RWT} \dot{x} + M_{RWT} \bar{\omega}_{RWT}^2 x = F(x, \dot{x}) \quad (23)$$

where M_{RWT} , $\bar{\omega}_{RWT}$, ζ_{RWT} are the mass, frequency and total damping for the RWT as used in the buffet response predictions. The forcing function, $F(x, \dot{x})$, was the generalized force

obtained by integrating over the wing the RWT mode shape with the change in static pressure distributions at 26 deg. sweep for α increasing from 9 deg. to 10 deg., that is $C_p(10 \text{ deg.}) - C_p(9 \text{ deg.})$. This function had the time varying characteristic of a step function where $F(r, \dot{r}) = 0$ for wing incidence less than that for SITES and $F(r, \dot{r}) = F$ for wing incidence greater than that for SITES. An aerodynamic lag parameter was assumed so that transition to SITES occurred at a higher angle for positive pitch rate and transition to attached flow occurred at a lower angle for negative pitch rate. The time varying RWT mode response, r , was obtained from a finite difference solution to Equation 23 in the time domain using the flip-flop forcing function characteristic.

Because the aerodynamic lag parameter was unknown, a range of values was assumed and time history solutions to Equation 23 obtained for each value. Right wing tip accelerometer responses clearly reached LCO in these time histories at levels ranging from about 1g to 2g's. This corresponds very well with the excess buffet levels noted in Figure 15 for the torsion mode group at 26 deg. sweep. A typical time history for $r(t)$ is shown in Figure 17 where the initial reaction of nose down is seen as a result of F (nose down generalized force) being applied at $t = 0$. In addition to producing reasonable levels of response, the math model also produced an increase in frequency for the RWT mode, resulting from the non-linear aerodynamic spring, in agreement with the flight test PSDs shown in Figure 13.

The math model was also applied to the wind tunnel model aluminum wing and was found to predict that no LCO would occur during the wind tunnel tests in agreement with observations. Thus, the concept was verified in two cases from a qualitative point of view and also produced quantitative response characteristics that were quite representative of observations. On the basis of these results it was concluded that the excess buffet response of the torsion mode group measured during flight test at 26 deg. wing sweep was most likely due to LCO of the torsion modes.

8.0 CONCLUDING REMARKS

A method has been presented for predicting buffet response from pressure-fluctuations on scale models in wind tunnels. The method embodies the following features:

1. The buffet forcing function is obtained by real time integration of pressure time histories with the natural modes.
2. Damping is obtained for pivot modes from model buffet response.
3. A hybrid method was developed and applied to extend the pivot-mode damping measurements to multiple modes by the use of theoretical damping data.
4. A technique was developed to form composite modes to obtain better one-to-one correspondence between model and aircraft modes to improve the scaling of damping.
5. Diagonalized equations of motion were derived and applied to simplify the multiple degree-of-freedom buffet response calculation.

The results presented have shown correlations of predicted and measured buffet response of the F-111 TACT aircraft at $M = 0.8$ with 26 deg. and 35 deg. wing sweeps for a range of angles-of-attack that includes buffet onset to high intensity buffeting. The correlations included comparisons of power spectral densities and integrated RMS results.

Generally the buffet predictions were considered to be quite good particularly in light of past buffet prediction experience. The most disappointing correlations of predictions and measurements were for the torsion modes at 26 deg. wing sweep at high buffet intensities. Generally the predictions were better at 35 deg. wing sweep than at 26 deg. wing sweep. Several factors could have affected the torsion-mode predictions such as damping predictions, generalized masses, mode shapes, Reynolds number, static aeroelasticity, and pitch rate. However, on the basis of an analytical investigation of a potential non-linear coupling between the torsion modes and aerodynamic forces, it was concluded that the high levels of flight measured response at 26 deg. wing sweep were most likely due to this coupling.

With regard to future developments, the use of digitally recorded fluctuating pressure data poses a significant simplification to calculating buffet forcing function time histories. This greatly increases the capability to treat more modes and more complex configurations through the use of digital processing as opposed to analog processing employed in this paper. More recently, the buffet prediction technique described in this paper has been applied in the U.S. to several launch vehicles, using both digitized and digitally recorded pressure data. Because of the advantages of digital processing, buffet analysis that included over a hundred mode shapes, has been successfully accomplished.

REFERENCES

1. John, H.: Critical Review of the Methods to Predict the Buffet Capability of Aircraft, AGARD Report No. 623, September 1974.
2. Cunningham, A. M., Jr. and Benepe, D. B., Sr.: "Prediction of Transonic Aircraft Buffet Response," AGARD-CP-226, April 1977.

3. Jones, J. G.; "Dynamic Response of Aircraft with Fluctuating Flow Fields," von Karman Institute for Fluid Dynamics Lecture Series 1981-4 on Unsteady Airloads and Aeroelastic Problems in Separated and Transonic Flow, March 9-13, 1981.
4. Mabey, D. G.; "Beyond the Buffet Boundary," Aeronautical Journal, Vol. 77, pp 201-215, April 1973.
5. Mabey, D. G.; "Some Remarks on Buffeting," von Karman Institute for Fluid Dynamics Lecture Series 1981-4 entitled Unsteady Airloads and Aeroelastic Problems in Separated and Transonic Flow, March 9-13, 1981.
6. Hanson, P. W.; Evaluation of an Aeroelastic Model Technique for Predicting Airplane Buffet Loads, NASA TN D-7066, February 1973.
7. Jones, J. G.; "Modeling of systems with high level of internal fluctuations," AGARD-CP-172, November 1974.
8. Butler, G. F. and Spavins, G. R.; The Prediction of the Transonic Buffeting Response of the Gnat Aircraft in Flight from Wind-Tunnel Tests on Models of Conventional Construction, RAE TR 81075, June 1981.
9. Coe, C. F. and Cunningham, A. M., Jr.; Predictions of F-111 TACT Aircraft Buffet Response and Correlations of Fluctuating Pressures Measured on Aluminum and Steel Models and the Aircraft, NASA CR-4069, May 1987.
10. Moore, J. W., Cronin, D. L. and Coe, C. F.; Predictions of Buffet Response of 1/6-Scale Models of F-111 TACT Wings, NASA TM 85858, October 1983.
11. Watts, D. and Haller, R. L.; F-111 TACT Final Flutter Analysis, Volume I, General Dynamics Corp., Fort Worth Division, FZS-595-021, October 1973.
12. Cunningham, A. M. Jr., "Practical Problems: Airplanes," Chapter 3, Unsteady Transonic Aerodynamics, edited by D. L. Nixon, AIAA Progress in Astronautics and Aeronautics Series, 1989.

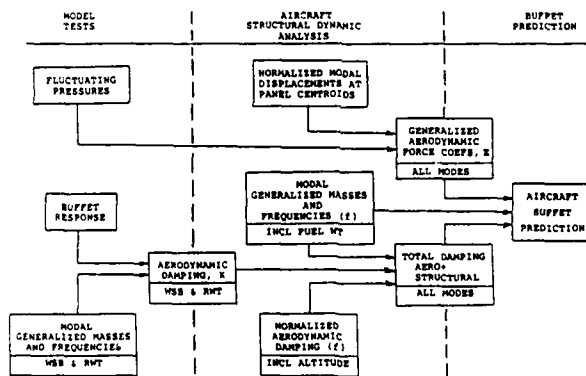


Figure 1 Buffet Prediction Method

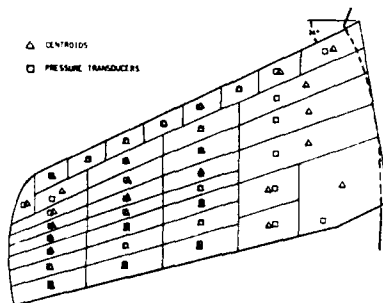


Figure 2 Pressure Transducers and Paneling on Wing Upper Surface

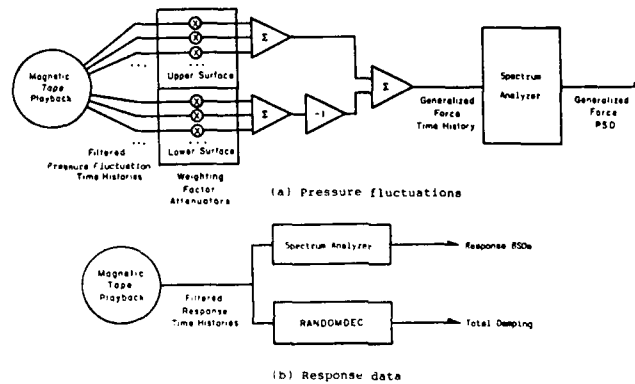


Figure 3 Flow Charts for Processing Wind Tunnel Pressure and Accelerometer Data

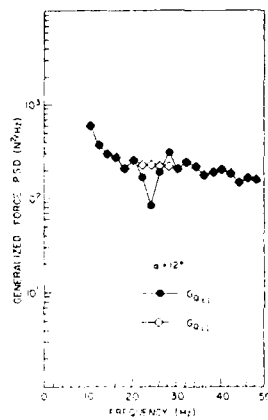


Figure 4 Generalized Aerodynamic Force on Model First Wing Bending Mode (from Reference 10)

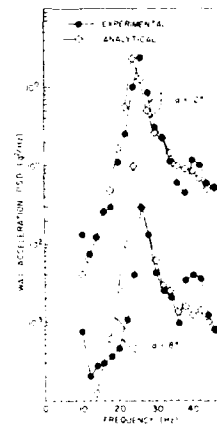


Figure 5 PSDs of Predicted and Measured Buffeting of the 1/6-Scale Model First Bending Mode (from Reference 10)

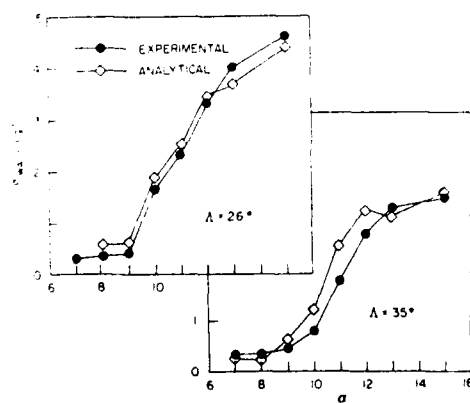


Figure 6 Wingtip Accelerometer RMS Response for Model First Bending Mode (from Reference 10)

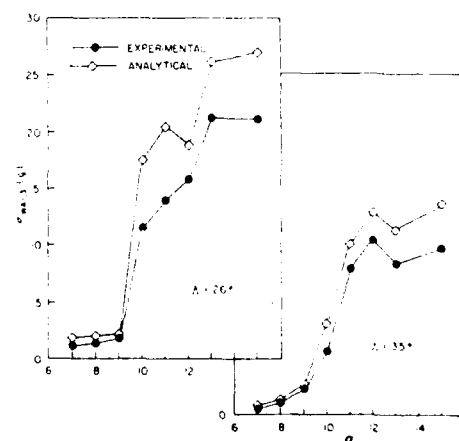


Figure 7 Wingtip Accelerometer RMS Response for Model First Torsion Mode (from Reference 10)

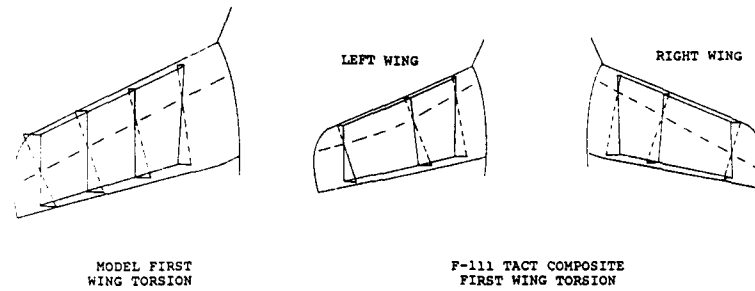


Figure 8 Composite Mode for F-111 TACT Aircraft "First Wing Torsion" Mode

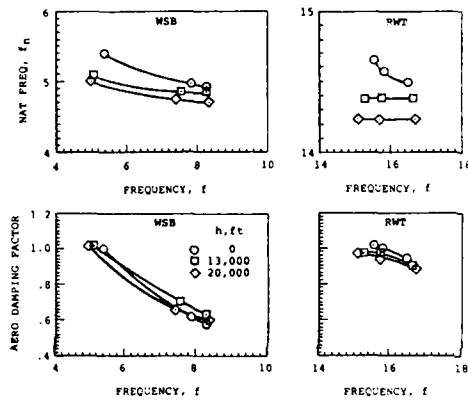


Figure 9 Natural Frequency and Aerodynamic Damping Variations with Forcing Frequency and Altitude

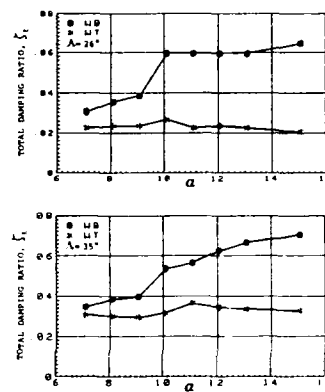


Figure 10 Total Damping Ratios from Model Buffeting Response

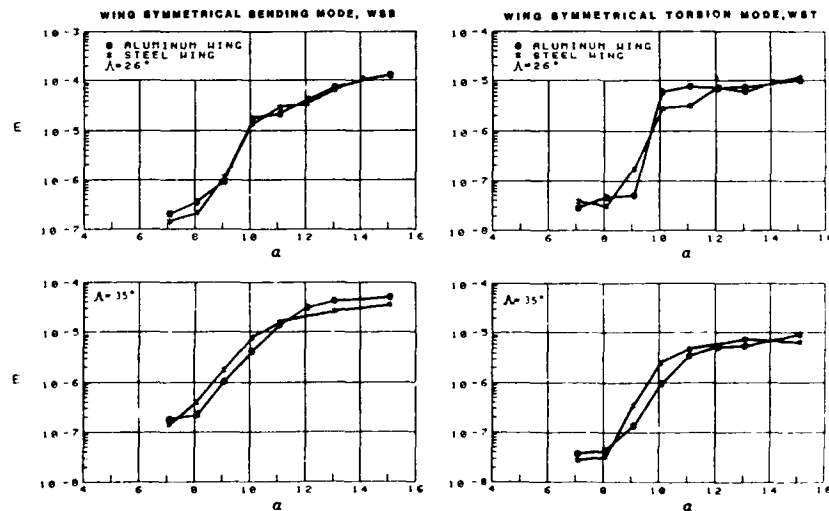


Figure 11 Generalized Forces from Pressures Measured on Aluminum and Steel Model Wings

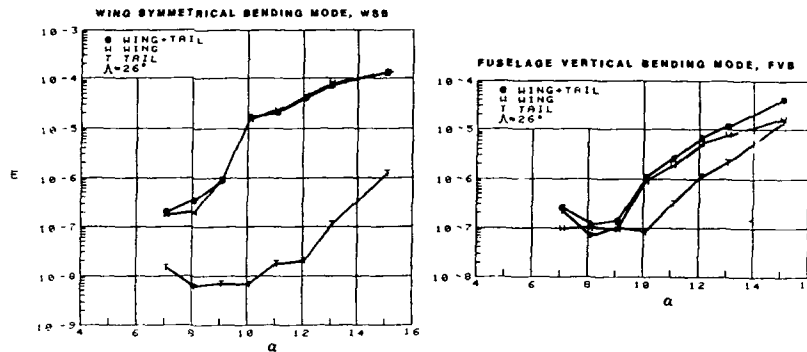


Figure 12 Generalized Forces on Wing and Tail

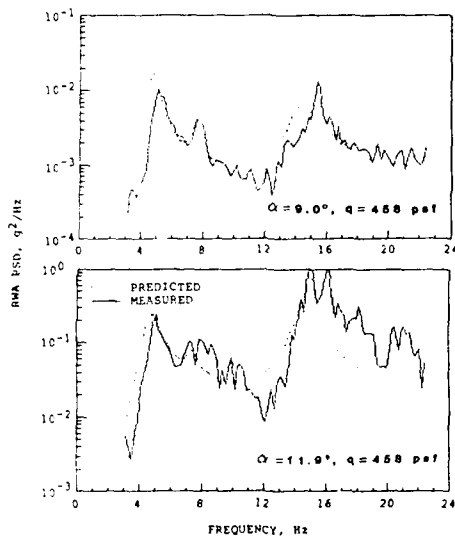


Figure 13 PSDs of Predicted and Measured Buffeting of TACT Aircraft for 26 Deg. Wing Sweep

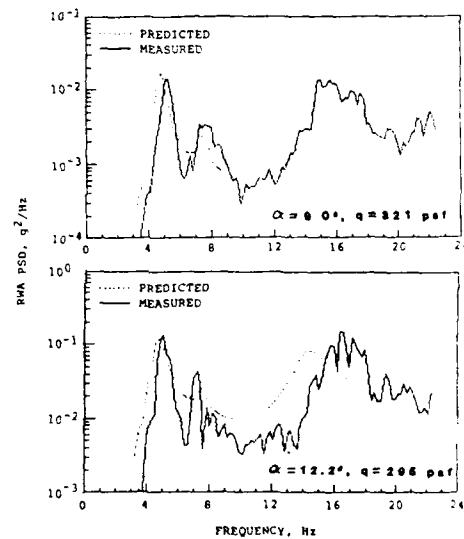


Figure 14 PSDs of Predicted and Measured Buffeting of TACT Aircraft for 35 Deg. Wing Sweep

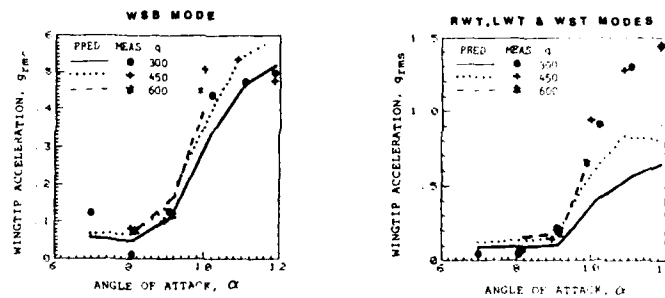
(a) $\Lambda=26^\circ$

Figure 15 Predicted and Measured RMS Accelerations Versus Angle of Attack - Wing Symmetric Bending and Torsion Mode Group

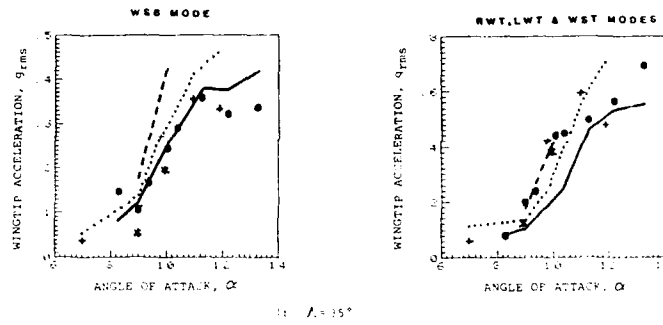


Figure 15 (continued)

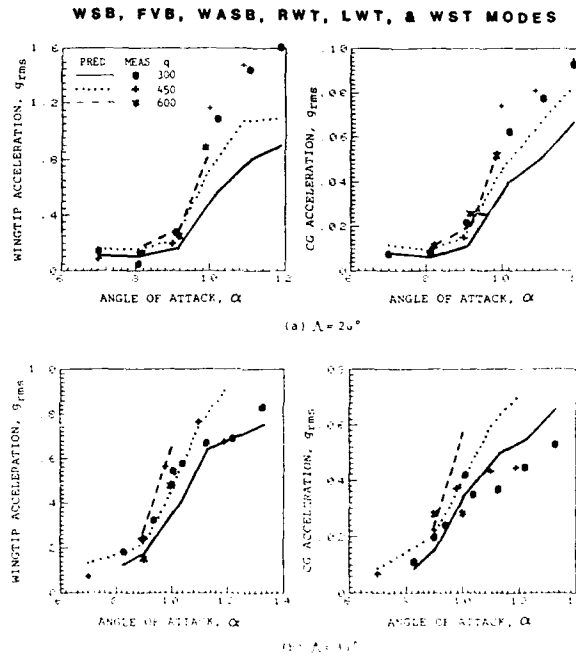


Figure 16 Predicted and Measured RMS Accelerations Versus Angle of Attack - All Modes

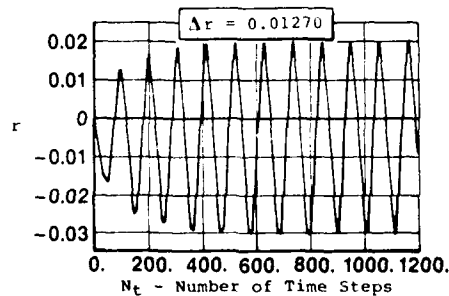


Figure 17 Sample of Predicted Limited Amplitude Oscillations for the RWT Mode

THE EFFECT OF WING PLANFORM
ON LOW SPEED BUFFET

by
S.J. Zan
Research Officer
National Aeronautical Establishment
Ottawa, Canada
K1A-0R6.

D.J. Maull
Reader
Cambridge University Engineering Department
Cambridge U.K.
CB2-1PZ.

1 SUMMARY

This paper is concerned with a parametric experimental investigation into low speed buffet. The influence of wing generalized mass, reduced frequency, aspect ratio, dynamic pressure and wing sweep on the buffet excitation parameter, $\sqrt{nG(n)}$ in the notation of Ref. 1, has been studied for a simple wing model with sharp leading and trailing edges. The investigation was limited to buffeting response in the fundamental bending mode. The angle of incidence range for the experiments was 0° to 40°, however the paper will concentrate on results at 10° incidence (near stall) and at 30° incidence. The influence of aspect ratio on the buffet excitation parameter was found to be significant at high incidences at values of reduced frequency below those common for subsonic flight.

2 LIST OF SYMBOLS

The following is a list of mathematical symbols used in this paper.

- b wing span (from root to tip)
- c wing chord (76 mm)
- f frequency (Hz)
- f_0 frequency of wing fundamental mode
- m mode generalized mass
- n reduced frequency $= \frac{fc}{V}$
- $\sqrt{nF(n)}$ modified spectra of unsteady pressure fluctuations
- $\sqrt{nG(n)}$ buffet excitation parameter
- q kinetic pressure
- z wing tip rms displacement
- \ddot{z} wing tip rms acceleration in a particular mode
- AR aspect ratio $= \frac{b^2}{S}$
- BM mean root bending moment
- C_l mean root bending moment coefficient
- E^2 dimensionless excitation power spectral density
- $G(n)$ dimensionless excitation power spectral density ($= E^2$)
- G_0 constant in Eqn. 4
- Re Reynolds number
- S wing area
- V mean flow velocity
- α wing incidence angle (deg)
- β constant in Eqn. 4
- ζ total damping
- Λ wing sweep angle (deg)
- $\Phi_p(f)$ spectral density of aerodynamic forcing

3 INTRODUCTION

In a recent AGARD Document (Ref. 2), a proposal is put forward that all measurements of wing buffeting should be standardized. It is proposed that buffeting measurements be presented using a dimensionless parameter called the buffet excitation parameter $\sqrt{nG(n)}$ where

$$\sqrt{nG(n)} = \frac{2 m \ddot{z}}{\sqrt{\pi} q S} \sqrt{\xi} \quad (1)$$

It is hoped that by standardizing buffet measurements, it will be easier to compare buffeting results from two separate investigations, be they flight test or wind tunnel investigations. Another function for such a parameter is that it could be used to estimate buffet loads on an actual aircraft based on results obtained in wind tunnel tests. The question that naturally arises, is how sensitive is the buffet excitation parameter to parameters such as Reynolds number, Mach number, lift coefficient and reduced frequency? In other words, which of these parameters must be matched in the wind tunnel to the values expected in flight?

Reference 3 attempts to address this issue discussing in detail two proposed models for the dynamics of a wing subject to buffet loads. The first of these models invokes the simple argument that the separated flow induces motion of the wing, but the responding wing does not in turn affect the flow field. If this is true, then buffeting can be modelled as a linear system for engineering purposes. Using spectral domain techniques, it is a simple matter to arrive at an expression relating the rms wing acceleration (at the tip for example) as a function of the power spectral density of the forcing. On dimensional grounds, it is argued that the power spectral density of the forcing $\Phi_r(f)$, can be written as

$$\Phi_r(f) = \frac{\bar{c} E^2}{V} (qS)^2 \quad (2)$$

The dimensionless excitation spectrum E^2 for a given wing was considered to be a function of incidence, Reynolds number and Mach number, and was considered to be approximately constant in the region of the wing natural frequency. This assumption enabled a simple derivation of the relationship between rms wing tip acceleration and E^2 (Ref. 3), and it is noted here that Equation (1) is derived as an extension of this relationship. In this paper the intention is to focus on the dependence of E^2 on frequency for various incidences. The experiments were conducted in an incompressible flow on wing models with sections insensitive to Reynolds number effects.

The second model proposed in Ref. 3 is a more complex one involving feedback from the responding wing into the flow, in all probability making the problem non-linear. Feedback of wing motion into the flow would imply that the number and complexity of scaling parameters required for similitude between scale model tests and full scale behaviour is likely to increase. It can easily be argued that full aeroelastic models would be beneficial in this case.

4 EXPERIMENTAL DETAILS

The experimental investigations were carried out in the 1.2 m x 1.7 m low speed wind tunnel in the Engineering Department at the University of Cambridge. This is a closed circuit wind tunnel with a maximum wind speed of about 60 m/s. The experiments were conducted using the 'semi-rigid' model technique as discussed in Ref. 4.

Seventeen wing models were tested (Table I), each at three values of dynamic pressure and hence reduced frequency. The models all had the same section as shown in Fig. 1, and with the exception of the aspect ratio 3 aluminium wing had the same chord. The chord for that wing was 127 mm and its thickness was scaled accordingly to satisfy geometric considerations. The models varied over a range of aspect ratios and sweep angles. Unswept wings had rectangular planforms and aspect ratios ranging from 3 to 8, aft swept wings ($\Lambda = 30^\circ$) had aspect ratios ranging from 4 to 8 and forward swept wings ($\Lambda = -20^\circ$) had aspect ratios ranging from 4 to 6. For all swept wings (forward and aft) the outboard edge of the wing was parallel to the free stream and the streamwise section was that indicated in Fig. 1. Throughout the remainder of this paper, wings denoted simply as 'swept' are understood to refer to the aft swept wings under investigation in this paper. Table I lists relevant details of all the wing models. Of particular note in Table I is the fact that while most models were machined from solid steel, some of the unswept wings are manufactured from solid aluminium. One model had a flush mounted lead insert near the tip to increase its generalized mass. Additionally, the effects of a tip tank were investigated on the buffeting response of an aspect ratio 4 unswept wing. The tip tank is shown in Fig. 2.

The sharp leading edge of the wing section should ensure that Reynolds number effects are minimized since flow separation will always occur from the leading edge. Minor Reynolds number effects may occur for small incidence angles $\alpha < 4^\circ$ as this wing section is subject to thin aerofoil stall and the growth of the separation bubble is obviously sensitive to Reynolds number. The experimental values of Reynolds number are low, only 0.1×10^6 to 0.5×10^6 .

Values of reduced frequency, n , based on the fundamental wing bending mode frequency ranged from 0.017 to 0.146. Values of n for the fundamental bending mode of an aircraft in flight generally are not less than 0.05 and not less than about 0.1 for subsonic flight. The low values of reduced frequency parameter are thus more relevant to rigid body modes although in these tests the wind tunnel models respond dynamically at low reduced frequencies, whereas the actual aeroplane wings in flight would respond in a quasi-steady fashion.

For the buffeting measurements, the wing models were mounted in a half-model configuration, cantilevered through the floor of the wind tunnel and rigidly clamped over a distance of 125 mm extending down from the wind tunnel floor. The clamping mechanism was mounted on a swivel base which permitted angle of incidence adjustment from 0° to 40° in 2° increments. No corrections were made to the results to account for wind tunnel blockage, as in these experiments the area blockage was never more than 1.5%.

Table 1: Wing Model Details

material	AR	tip tank	sweep (deg)	frequency (Hz)
steel	8	no	0	13.0
aluminium	8	no	0	13.3
aluminium with lead	8	no	0	9.75
steel	4	no	0	48.2
steel	6	no	0	22.9
aluminium	4	no	0	52.4
steel	5	no	0	32.8
aluminium	4	brass	0	29.3
aluminium	4	balsa	0	50.4
aluminium	3	no	0	38.8
steel	8	no	30	9.99
steel	6	no	30	17.8
steel	5	no	30	25.2
steel	4	no	30	39.1
steel	6	no	-20	20.3
steel	5	no	-20	28.6
steel	4	no	-20	43.3

In order to compute the buffet excitation parameter, measurements of generalized mass, root-mean-square (rms) wing tip acceleration and total damping are required. Wing generalized masses for the first bending mode were determined experimentally using the technique of adding small masses to the tip of the wing and measuring the resulting frequency change (Ref. 5). A linear relationship between the wing tip acceleration and strain gauge output was determined by experimental calibration with a reference accelerometer attached at the wing tip. The wing was sharply struck at the tip and both outputs were recorded. A calibration of this type is only valid at the frequency at which the wing was oscillated, in this case the fundamental wing bending mode. For a sampling rate of approximately 20 times the wing fundamental frequency, it was experimentally determined that time records of about 1600 cycles of wing motion would be required for the rms of the signal to converge in a statistical sense, especially for incidences well beyond that of the stall.

Estimation of total modal damping is a difficult task. Approximately 1000 estimates would be required during the course of the investigation, thus it was considered imperative to employ a reliable numerical technique to estimate the damping, which ranged from about one-half percent of critical to about three percent of critical. The Randomdec procedure (Ref. 6) was chosen for its simplicity, speed and accuracy, with the threshold level taken as the rms of the strain gauge signal. Three estimates of damping were made for each combination of wing model, incidence and dynamic pressure, the three estimates generally being within 10% of each other. Occasionally the Randomdec technique would produce erroneous results. Examination of the wing response power spectra in these cases would reveal the presence of a sharp spike of significant magnitude and not attributable to the mode under investigation (for example a higher order mode, wind tunnel fan electrical noise or blade passage frequency). These spurious signals were removed using a digital notch filter (Ref. 7), and the damping estimate obtained from the filtered data was satisfactory.

Reference 6 considered in depth the fractional accuracy associated with an estimate of the damping. Applying a similar approach to this investigation assuming a 95% confidence level, it was determined that for a damping estimate of 2.5% of critical the normalized standard deviation would be about 17% and for a damping estimate of 0.5% of critical the normalized standard deviation would be about 36%. Quantities such as generalized mass, and rms response can be measured to an order of magnitude better precision. Thus it is the error in the damping estimate that ultimately determines the precision of an estimate of the buffet excitation parameter. Using this result, the normalized standard deviation of an estimate of $\sqrt{nG(n)}$ is between 8% and 16%.

For buffeting measurements made in wind tunnels it is necessary to ensure that the level of unsteady pressure fluctuations in the empty wind tunnel is sufficiently smaller than the level of unsteady pressures that arise from the separated flow on the wing surface. Reference 8 suggests that the level of $\sqrt{nF(n)}$ not exceed 0.003 for any frequencies at which the models will be tested. $\sqrt{nF(n)}$ can be regarded as a normalized power spectral density of unsteady pressures inherent in the wind tunnel (Ref. 9). In the wind tunnel used for these experiments the levels of unsteady pressure fluctuations did not exceed the value of 0.003 for frequencies less than 100 Hz.

The floor boundary layer in this wind tunnel has a displacement thickness of about 6 mm for a typical test wind speed of 50 m/s. As the shortest models were 305 mm in span and root bending moments as recorded by a strain gauge are relatively insensitive to flow conditions near the wing root, it was thought that this boundary layer would not cause appreciable errors in the investigation.

5 RESULTS

5.1 Mean Root Bending Moment Coefficients

The mean root bending moment coefficients were measured for each wing model as a function of angle of incidence prior to the investigations of buffeting. These measurements were made on the semi-rigid models, and thus represent the mean output from the strain gauge whilst the wing is buffeting. The measurements were made at the middle value of the three dynamic pressures used in the buffeting investigation for a given wing model, and it was established that the results were insensitive to changes in velocity (i.e. Reynolds number). The results were normalized by computing a mean root bending moment coefficient C_l where

$$C_l = \frac{BM}{qSb} \quad (3)$$

Figure 3 presents the values of C_l as a function of angle of incidence for the unswept wings. The effect of aspect ratio on the mean aerodynamic loads is apparent, both in attached flow and in separated flow. From flow visualization studies in a smaller wind tunnel on an aerofoil with the same section, it was found that flow separation would begin at the leading edge for very small positive angles of incidence. The separation bubble would grow towards the trailing edge as incidence increased reaching the trailing edge at about four and one-half degrees of incidence. The mean root bending moment coefficient curve slope is seen to decrease at about this incidence, although the actual coefficient continues to rise until an incidence of 10° or so. This latter incidence will be referred to as the static stall angle for the purposes of this paper. Beyond the stall angle there is a slight drop in the magnitude of C_l , especially for the higher aspect ratios, and as incidence is further increased, C_l increases again.

Figure 4 is a plot of the mean root bending moment coefficients for the swept wings. It is seen that the moments are reduced compared to the unswept wing cases due in part to the reduction in wind speed normal to the leading edge. There is an abrupt change in the slope of the coefficient versus incidence near 4° incidence. At about this incidence the tip stalls reducing the overall bending moment. Beyond about 15° of incidence, C_l continues to rise with the exception of an occasional dip that occurs at higher incidences as aspect ratio increases.

Figure 5 plots C_l against incidence for the forward swept wings. For these wing models, flow separation originates near the root and moves spanwise towards the tip as incidence increases. This behaviour accounts for the more gentle variation in C_l as a function of incidence as compared to the unswept or swept wings. The shape of the curve for an aspect ratio of six near 30° incidence indicates that for this aspect ratio high suction are maintained at the tip. Flow visualization studies indicated that the suction was due to a vortex originating at the wing apex. Surface flow patterns revealed that at the trailing edge the influence of this vortex extended inboard approximately one-third of a chord. A smoke flow investigation established that the vortex was not stationary. At higher incidences, the influence of the vortex was not observed in the surface flow pattern.

5.2 Buffet Excitation Parameter

In earlier work by the authors (Ref. 10 & 11), and by other investigators (Ref. 1) the buffet excitation parameter is presented as a function of incidence. However this will not be the case for this paper. It is also shown in Ref. 11 that $\sqrt{nG(n)}$ depends on reduced frequency, which will form the initial basis for discussions in this work. Figures 6 to 9 are plots of the buffet excitation parameter for unswept wings in

a function of reduced frequency with the angle of incidence as a parameter. The connected data points are results from the same wing model, for which the aspect ratio is shown near the connecting line. A star beside the aspect ratio indicates that a tip tank was attached to the outboard edge of the wing. Two tip tanks were used in the investigation, one of balsa and one of brass, the reason being that brass tip tanks were effective in lowering the fundamental bending frequency of the wing model, but at the expense of possibly altering the wing tip aerodynamics. The balsa tanks have negligible effect on the wing model frequency, but incorporate the wing tip flow changes. In this way it was hoped that the influence of reduced frequency and of a tip geometry change on $\sqrt{nG(n)}$ could be studied separately. The effect of a tip tank on the mean root bending moment coefficient was to slightly increase the values above those for a bare wing.

For incidences of 10° and 20° the data collapse is very encouraging (Figs. 6,7), and there appears to be little if any influence of aspect ratio. This would imply that the linear model discussed above would be adequate for describing the physics of buffet and that the character of the unsteady forcing varies little along the span. It is significant that near the stall angle, the value of $\sqrt{nG(n)}$ is about twice the heavy buffet limit of 0.003 quoted in Reference 2. This may result from the unconventional 'nose' of this wing section which generates a larger separation bubble than would result from a more conventional wing section.

For typical flight values of n the magnitude of the buffet excitation parameter at 20° is reduced relative to the values at 10° . Flow visualization using smoke ($Re = 10,000$) showed that at an incidence of 10° the vortices generated from the leading edge separation would impinge on the upper surface but at 20° this did not occur. The influence of a tip tank is not large at either incidence, although values of $\sqrt{nG(n)}$ for wing models with a tip tank are consistently above those for a bare wing. Caution should be used in correlating this change with the changes in the mean root bending moment coefficients (Ref. 12).

At higher incidences (Figs. 8, 9) the dependence of $\sqrt{nG(n)}$ on n is rather weak for the higher values of n . These reduced frequencies correspond to values occurring in subsonic flight for a wing first bending mode ($n > 0.1$). There is a strong variation at lower values of n , corresponding to reduced frequencies below what is typical of aeroplanes in subsonic flight. There are also aspect ratio effects especially in the range $0.04 < n < 0.06$ where $\sqrt{nG(n)}$ values differ by a factor of two for a 50% increase in aspect ratio.

Figures 10 and 11 plot the buffet excitation parameter as a function of reduced frequency for the swept wing models. Again lines are used to join results obtained from the same wing model. It is clear that at typical flight values of n for a wing bending mode the buffeting at an incidence near stall is reduced by the introduction of sweep. There is an indication that aspect ratio effects may exist at this incidence, but considering the precision of the estimates of $\sqrt{nG(n)}$ these effects are probably small. At 30° incidence, there are probable aspect ratio effects and as is the case for the unswept wings, large values of $\sqrt{nG(n)}$ are evident at low values of reduced frequency. The effect of sweep however is still to reduce the buffeting under these conditions.

Plotted in Figs. 12 and 13 are the corresponding results for the forward swept wing models. The results are basically consistent with those presented above for an incidence of 10° . A sharp increase in $\sqrt{nG(n)}$ is observed for the aspect ratio 6 wing at 30° incidence, which may be related to its unusual mean root bending moment coefficient curve at the same incidence. A plot of buffet excitation parameter against incidence is shown for this wing model in Fig 14. The sharp decrease in buffeting between 30° and 32° has not been observed elsewhere in these experiments. In light of the comments made in section 5.1 about the vortex originating at the wing apex, it would seem reasonable to suggest that this tip vortex is responsible for the buffeting behaviour of this wing model at these incidences.

The influence of sweep on $\sqrt{nG(n)}$ is presented in Figure 15 for an incidence of 10° . Reduced frequency is a parameter on the graph, and the results are plotted without regard to the aspect ratio, which under these conditions is not considered to be a parameter on which buffeting is significantly dependent (Figs. 6, 10 and 12). Except for the lowest two values of reduced frequency, the similarity is encouraging. The results for all values of $n > 0.04$ lie in the shaded band in the figure. At the lowest values of reduced frequency, the reduction in $\sqrt{nG(n)}$ due to sweep is considerably less. It is inferred from this plot that the spectrum of aerodynamic loading must decrease more rapidly with increasing frequency for the wings with non-zero sweep.

The same plot but at 20° incidence (Fig. 16) reveals a consistent trend. Again the results are plotted without regard to aspect ratio. Values of the buffet excitation parameter decrease with increasing values of reduced frequency. The influence of sweep on $\sqrt{nG(n)}$ is reduced for increasing values of reduced frequency, and at $n = 0.114$ the effect is reversed as sweep is seen to slightly increase buffeting. At 30° incidence (Fig. 17), the reduction in $\sqrt{nG(n)}$ due to sweep for low values of reduced frequency is greater than at 10° or 20° . At moderate values of reduced frequency the effect of sweep is lessened, however for higher values of reduced frequency ($n > 0.06$) sweep

again slightly increases buffeting. The circled numbers in Fig. 17 indicate aspect ratio, as it has already been established that in at this incidence $\sqrt{nG(n)}$ is dependent on aspect ratio.

5.3 Spectra of the Forcing Functions

In order to better understand the nature of buffet, power spectral densities of the aerodynamic force acting on the wing models were calculated. In principle, the same information is contained in the graphs of $\sqrt{nG(n)}$ versus n , but the spectra provide a continuous curve as opposed to values only at discrete frequencies. The calculations were made for all wings at each value of dynamic pressure for angles of incidence of 10° and 30° . These spectra were determined indirectly from the time history of wing response as follows. The 32,768 data point time histories were transformed into a power spectral density of wing tip displacement using a standard Fast Fourier Transform (FFT) technique. Sixteen averages of a 2048 point time history were computed and averaged in order to minimize the total error in the spectral estimate (Ref. 13). The normalized standard deviation in the power spectral density estimates is about 0.27. A power spectral density of forcing could then be computed by dividing the power spectral density of displacement by a mechanical admittance function and taking due account of any data system gains including filter roll-off. The mechanical admittance function assumed was that for a simple single degree of freedom system and the calculation was made for the bandwidth $0.5 \leq f \leq 2f_0$. These spectral densities if for the were non-dimensionalized using Eqn. 2 above.

Parameters required for the mechanical admittance function were the wing bending frequency, total damping and wing stiffness. The wing frequencies were determined with the wind off and did not vary appreciably with the wind on. The total damping had already been determined via the Randomdec process, and the wing stiffness was taken to be the mode generalized mass multiplied by the square of the circular frequency. Finally it is noted that the power spectral densities of wing response had revealed only one other mode in the response spectra, that of the second bending mode at a frequency six times the fundamental which is well beyond the maximum frequency employed for these calculations.

In this paper the spectra are referred to as spectra of the forcing functions, and not force spectra. These spectra are computed from measurements on a *responding* wing, and the resulting spectra will thus reflect any non-linearities and/or feedback from the wing into the flow. Only if the system is linear and without feedback will these spectra match those obtained from a *rigid* wing, which are traditionally referred to as force spectra. Ref. 14 presents some force spectra obtained from a stalled rigid wing model in a wind tunnel, albeit at higher reduced frequencies.

For each wing model it was found that the dimensionless power spectral densities of the aerodynamic loads varied little with dynamic pressure. Figure 18 shows the power spectral densities of forcing for all unswept wings at 10° incidence. Note that the abscissa of the graph is reduced frequency. There is little difference between the results from various wing models, although it could be argued that the aspect ratio 3 wing has a greater power than the others at low reduced frequencies. This may be due to the fact that this wing model has a mode shape different from all other unswept wing models. The mode shape change is due to the fact that the wing is clamped over a 76 mm distance in the streamwise direction but the chord is 127 mm, and thus the wing model tends to respond more as a rigid model hinged at the root. The spectra in Fig. 18 are seen to be slowly varying functions of reduced frequency.

At 30° incidence (Fig. 19) the spectra of aerodynamic forcing for the unswept wing models are seen to vary more strongly with reduced frequency, and aspect ratio seems to influence the spectra particularly in the range $0.03 < n < 0.06$ (recall Fig. 8).

Figures 20 through 23 present the dimensionless spectra of forcing for the wing models with $\Lambda = 30^\circ$ and $\Lambda = -20^\circ$. For both sweep angles, the spectra at 10° incidence decrease with increasing frequency in a similar manner. The decrease is greater than for the unswept wing models (Fig. 18), and supports the inference made from Fig. 15. At 30° incidence, the wings with non-zero sweep define more clearly the effect of aspect ratio on the aerodynamic loading (Figs. 21 and 23). For the swept wings the effects are only observed at reduced frequencies less than about 0.06, whereas for the wing models with forward sweep, the aspect ratio effect is visible extending at least to $n = 0.12$, suggesting that the aerodynamics of this wing model are considerably different than those of the other forward swept wing models at this incidence. It can also be seen by comparison to Figs. 18 and 19 that the power spectral densities of forcing are greater for unswept wing models than for wing models with non-zero sweep.

6 DISCUSSION

Based on the results presented, it was argued that near the incidence of stall aspect ratio had little or no effect on the buffeting response of a wing model. This implies that the dynamic loads arising from the separated flow have little or no spanwise variation over the frequency range of this investigation. The same cannot be said at higher incidences such as 30° . At this incidence there are strong aspect ratio effects at low values of reduced frequencies for swept and unswept wings, and across the frequency bandwidth for the forward swept wings (Fig. 13). It is evident that significant variations in spanwise dynamic loading are occurring at these incidences. The fact that the buffeting increases with increasing aspect ratio implies that significant dynamic loads are acting at or near the wing tip. To investigate the actual

magnitudes, spanwise variations and correlations of these loads would require a series of wing models with a large number of flush mounted high frequency response miniature pressure transducers. This approach is beyond the scope of this investigation but is indicative of current practice in other research investigations (eg. Ref. 15).

It is clear that aspect ratio plays a major role in determining the buffeting response at these high incidences. It is experimentally difficult however to investigate the effect of doubling the aspect ratio for example while maintaining constant reduced frequency, similar Reynolds numbers and reasonable kinetic pressures. (With these simple models, doubling the aspect ratio from four to eight and maintaining constant reduced frequency would decrease the Reynolds number to as low as 25,000, and kinetic pressures to only 0.04 kPa.) An alternative approach is to indirectly obtain results for a particular aspect ratio over the reduced frequency range at which a wing model with a different aspect ratio was experimentally investigated. This can be done using the computed non-dimensional force spectra, $G(n)$ presented in Figures 18 through 23 as it is a straight forward procedure to compute $\sqrt{nG(n)}$ directly from $G(n)$. Presented here will be the results from the unswept wing models only. It is assumed that the non-dimensional spectra can be expressed using a piecewise power-law model for $G(n)$ of the form

$$G(n) = G_0 n^\beta \quad (4)$$

where G_0 and β are constants for a

particular wing at a particular incidence

with a break at $n = 0.06$ corresponding to the peak in the spectrum at 10° incidence and a break at $n = 0.01$ corresponding to a peak in the spectrum at 30° incidence. The non-dimensional spectra used for this calculation are those of the aspect ratio four wing.

Figure 24 shows the computed form of the buffet excitation parameter at 10° incidence for unswept wings derived using the arguments above. The experimental data points for the unswept wings are also included and the agreement is encouraging, indicating again that for an angle of incidence near stall, aspect ratio effects are unimportant and the variation in spanwise loading is insignificant. At 30° incidence, Fig. 25 indicates the magnitude of the aspect ratio effects that were first identified in Fig. 8. For low values of reduced frequency, differences in $\sqrt{nG(n)}$ of 50% to 100% are evident for an equivalent variation in aspect ratio, although the correlation of aspect ratio and buffeting is clearly not direct, in that if one is doubled so is the other.

It is of course more important to understand these aspect ratio effects at values of n that occur for subsonic flight. Unfortunately, it is not a straightforward matter to extrapolate the non-dimensional force spectra from the aspect ratio eight wing models to values of reduced frequency perhaps eight times that of the fundamental unless the mechanical admittance function for the model has been established over this wider frequency range via a proper ground resonance test. Additionally, one must be concerned with matters such as a low signal to noise ratio in the response power spectral densities at these higher frequencies. Such matters were beyond the scope of the current work, but in light of the apparent aspect ratio effects for the forward swept wing models at $n > 0.1$ (Fig. 23) should be investigated.

7 CONCLUSIONS

A detailed experimental investigation of the buffet excitation parameter has been made for a parametric series wings in incompressible flow. It was found that buffeting was reduced for swept or forward swept wings relative to unswept wings at low values of reduced frequency, but that at typical flight values of n (> 0.05) sweep had only a small influence on $\sqrt{nG(n)}$.

Aspect ratio effects were identified at high incidences (30°) and suggest an increase in the unsteady loads near the wing tip for higher aspect ratio models.

At typical subsonic flight values of n , the buffet excitation parameter was generally constant at about 0.003.

8 REFERENCES

- 1) Mabey, D.G. and Cripps, R.E., "Some Measurements of Buffeting on a Flutter Model of a Typical Strike Aircraft", 1983, AGARD-CP-339.
- 2) Mabey, D.G., "Some Aspects of Aircraft Dynamic Loads due to Flow Separation", 1988, AGARD-R-750.
- 3) Jones, J.G., "A Survey of the Dynamic Analysis of Buffeting and Related Phenomena", 1973, RAE-TR-72197.
- 4) Mabey, D.G., "An Hypothesis for the Prediction of Flight Penetration of Wing Buffeting from Dynamic Tests of a Wind Tunnel Model", 1971, ARC-CP-1171.
- 5) Hanson, P.W., "Structural and Aerodynamic Quantities of the Dynamic System, Similarity Laws, and Model Testing", 1975, AGARD-AR-82, Section 4.2.
- 6) Cole, H.A. Jr., "On Line Failure Detection and Damping Measurements of Aerospace Structures by Random Dec Signatures", 1973, NASA-CR-2205.

- 7) Zan, S.J., "An Investigation of Low Speed Wing Buffet", Ph.D. Dissertation (in progress), 1990, University of Cambridge.
- 8) Mabey, D.G., "Flow Unsteadiness and Model Vibration in Wind Tunnels at Subsonic and Transonic Speeds", 1970, RAE-TR-70184.
- 9) Owen, T.B., "Techniques of Pressure Fluctuation Measurements Employed in RAE Low Speed Wind Tunnels", 1958, AGARD Report 172.
- 10) Maull, D.J. and Zan, S.J., Proceedings - European Forum on Aeroelasticity and Structural Dynamics (Aachen), "An Investigation of the Buffet Excitation Parameter", 1989, DGLR-Bericht 89-01.
- 11) Zan, S.J. and Maull, D.J., Proceedings - First CASI Symposium on Aerodynamics (Ottawa), "An Experimental and Analytical Investigation of the Buffet Excitation Parameter", 1989.
- 12) Mabey, D.G. Welsh, B.L. and Pyne, C.R., "The Development of Leading-edge Notches to Improve the Subsonic Performance of Wings of Moderate Sweep", 1986, RAE-TM-Aero-2078 also DGLR-Bericht 89-01.
- 13) Bendat, J.S. and Piersol, A.G., Random Data: Analysis and Measurement Procedures, 2nd ed., New York, J. Wiley, 1986.
- 14) Lucas, A., "A Study of Wing Buffet", Ph.D. Dissertation, 1975, University of Cambridge.
- 15) Zingel, H., "On the Prediction of the Aeroelastic Behaviour of Lifting Systems Due to Flow Separation", 1987, ESA-TT-1043.

9 ACKNOWLEDGEMENTS

The research reported in this paper was funded by the Department of Trade and Industry (UK) under the technical direction of D.G. Mabey, RAE Bedford. S.J. Zan is currently on education leave from the NAE.

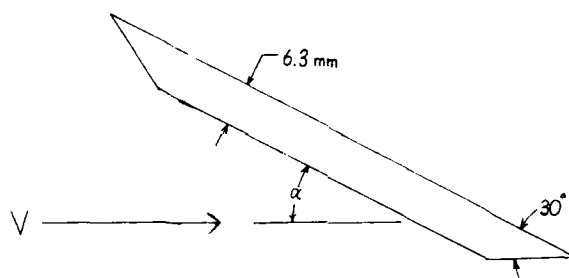


Fig 1 Wing Section

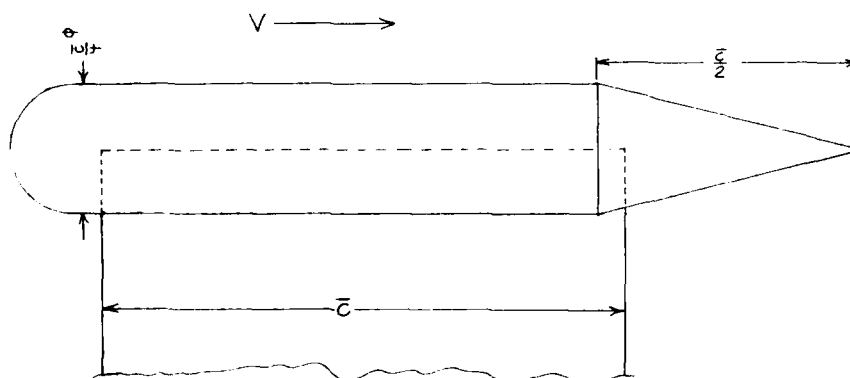


Fig 2 Wing Tip Tank Details

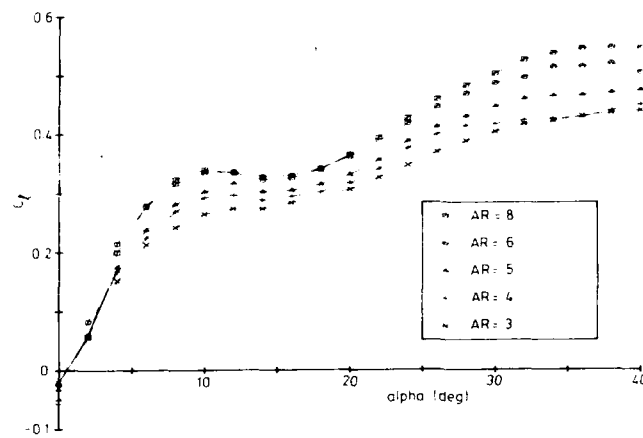


Fig 3 Mean Root Bending Moment Coefficients for Unswept Wings

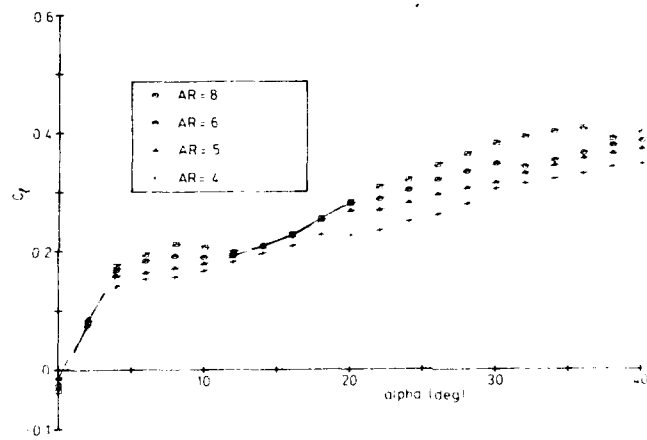


Fig 4 Mean Root Bending Moment Coefficients for Swept Wings

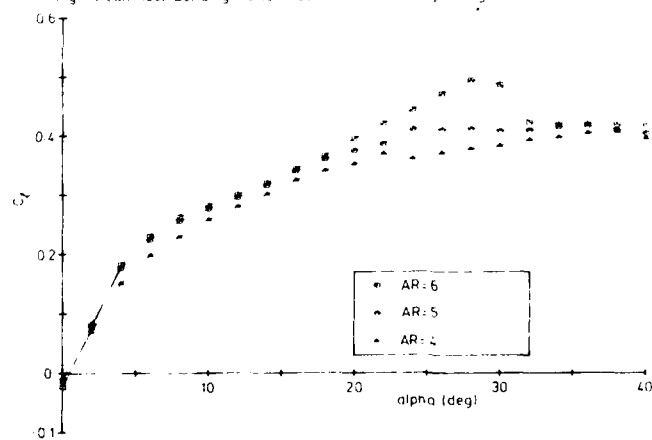
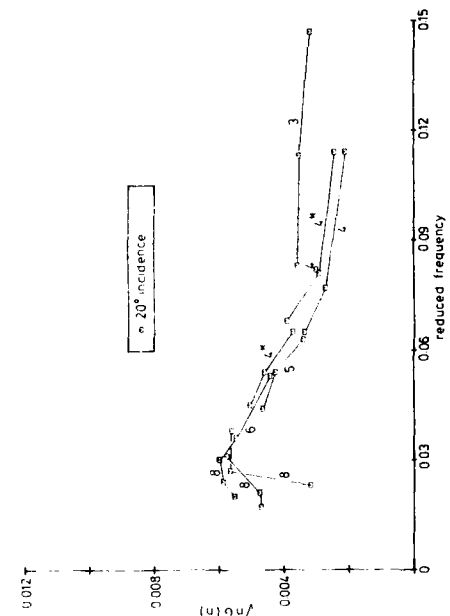
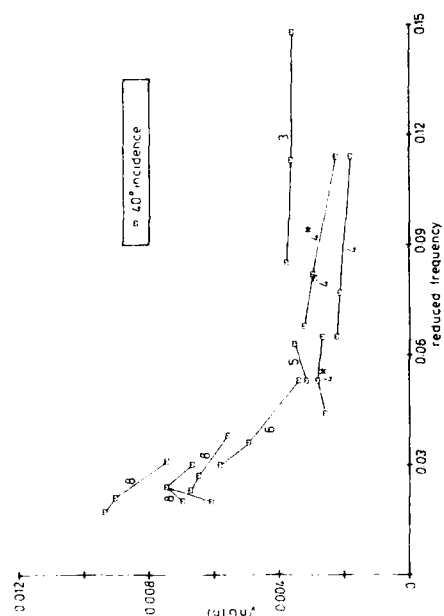
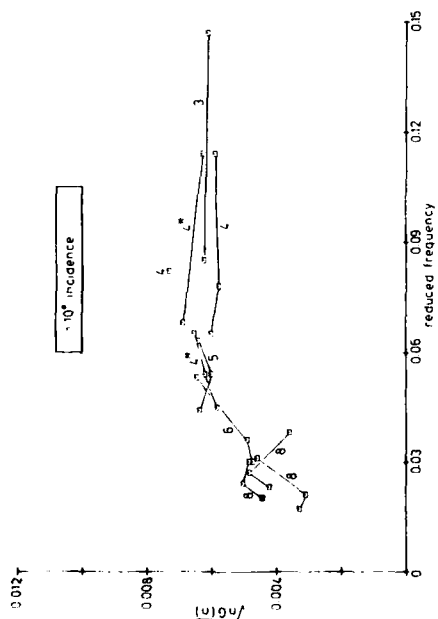
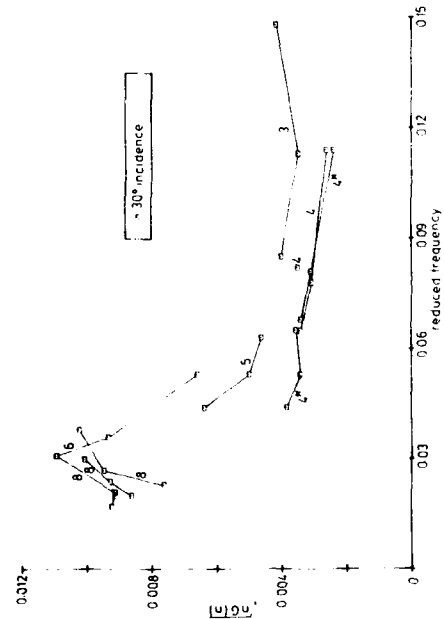


Fig 5 Mean Root Bending Moment Coefficients for Swept Forward Wings

Fig 7 Buffet Excitation Parameter as a Function of Reduced Frequency $\Lambda = 0^\circ$ Fig 9 Buffet Excitation Parameter as a Function of Reduced Frequency $\Lambda = 0^\circ$ Fig 6 Buffet Excitation Parameter as a Function of Reduced Frequency $\Lambda = 0^\circ$ Fig 8 Buffet Excitation Parameter as a Function of Reduced Frequency $\Lambda = 0^\circ$

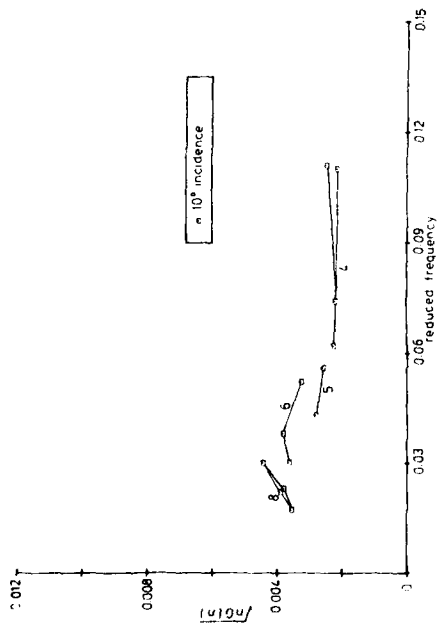


Fig 10 Buffet Excitation Parameter as a Function of Reduced Frequency $\Delta = 30^\circ$

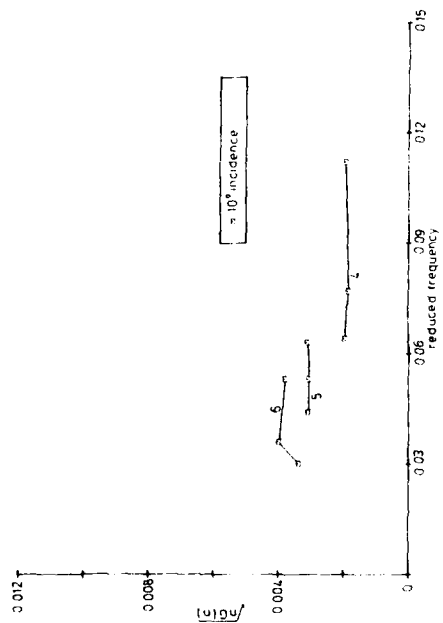


Fig 12 Buffet Excitation Parameter as a Function of Reduced Frequency $\Delta = 20^\circ$

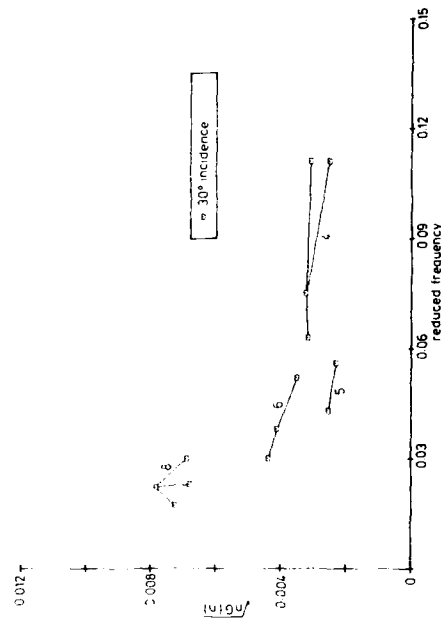


Fig 11 Buffet Excitation Parameter as a Function of Reduced Frequency $\Delta = 30^\circ$

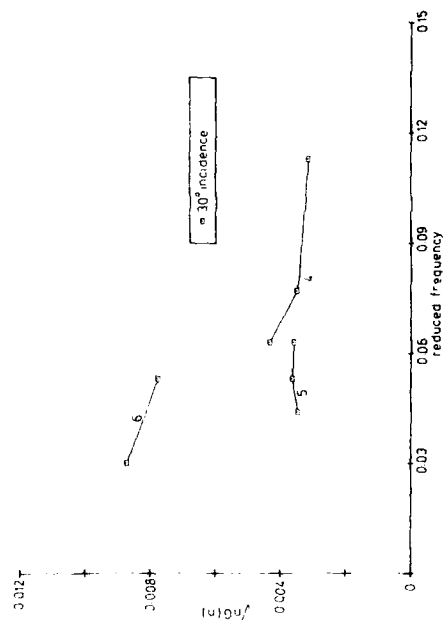
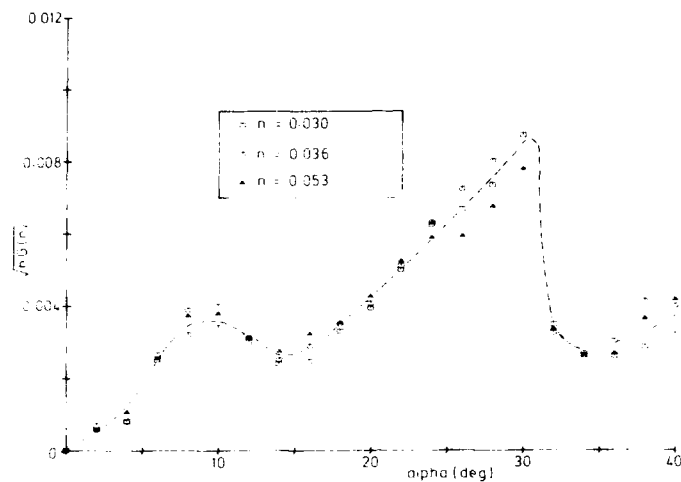
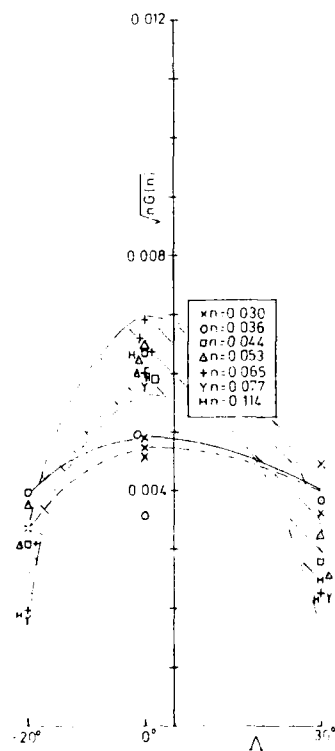
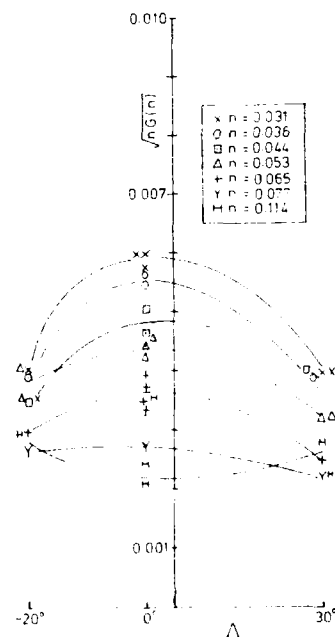
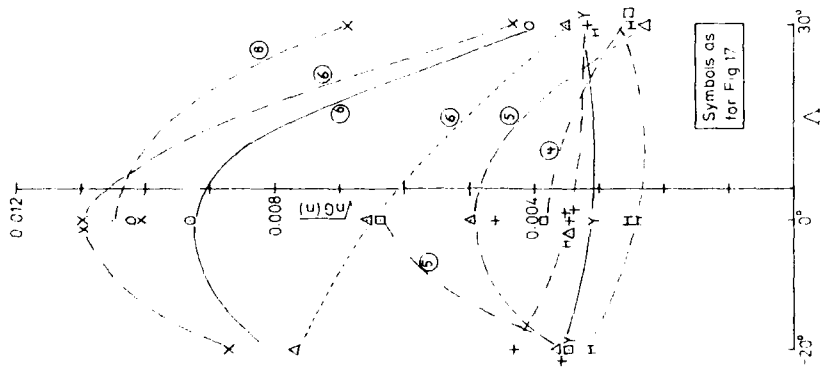
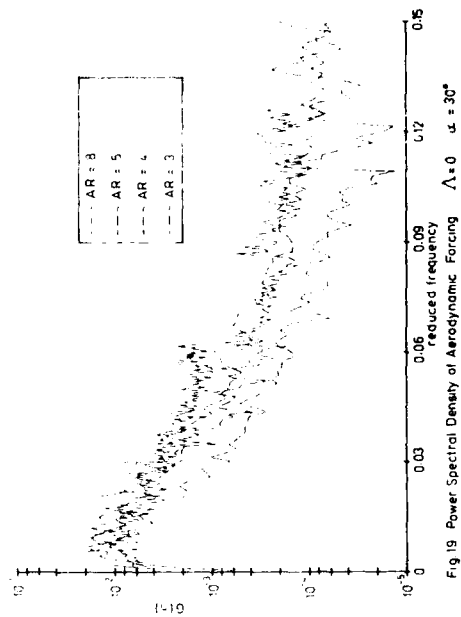
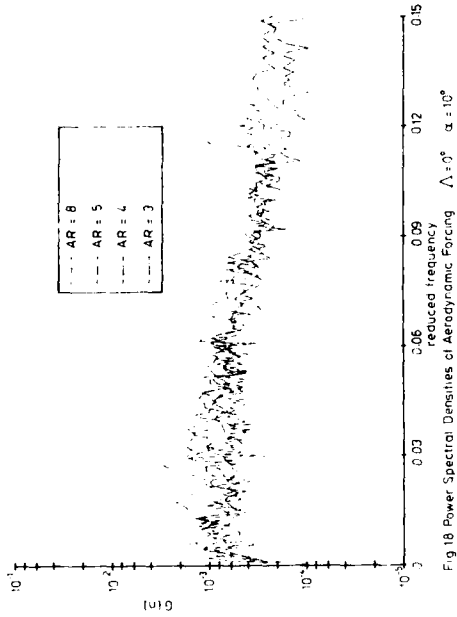
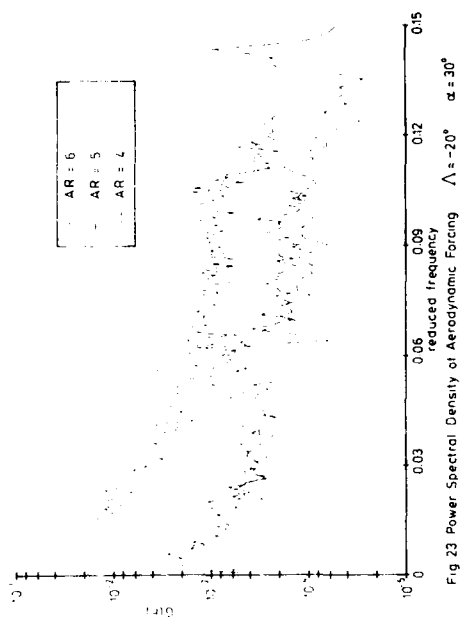
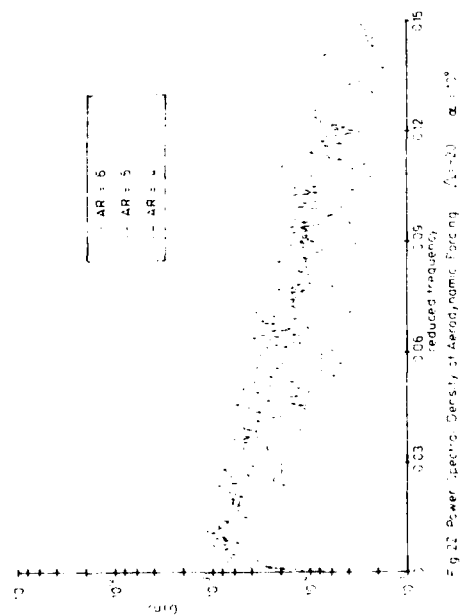
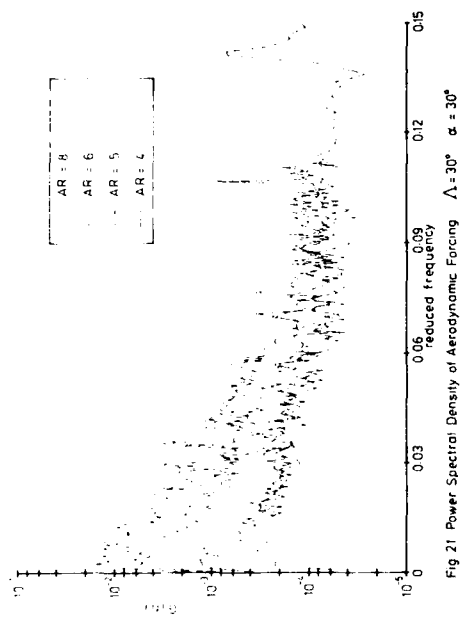
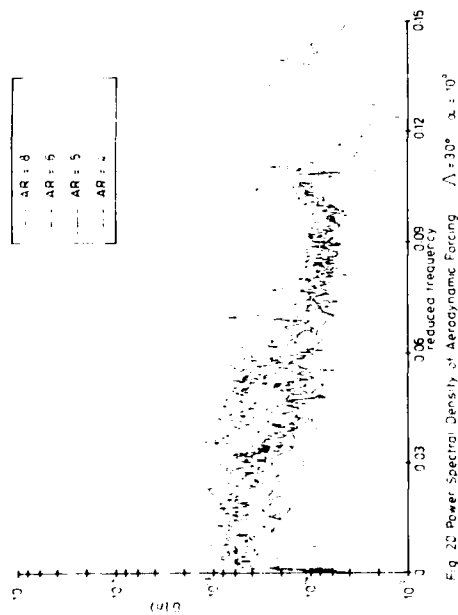
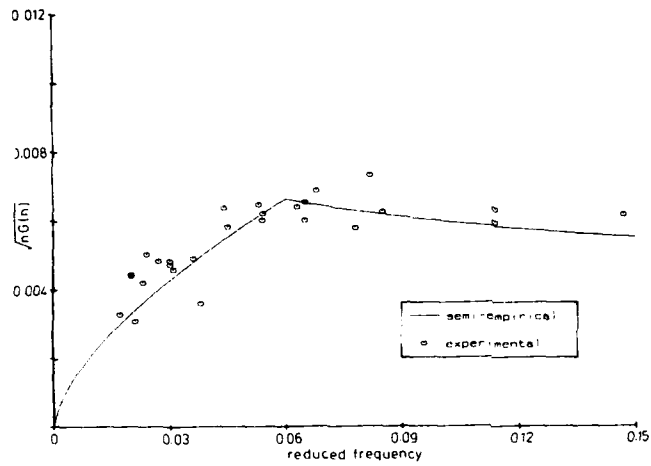
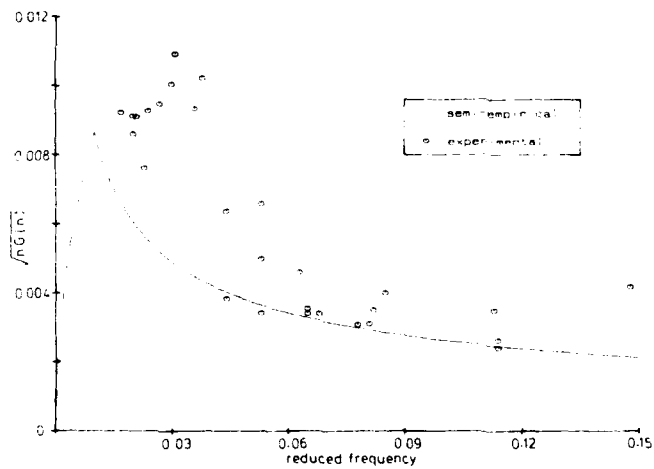


Fig 13 Buffet Excitation Parameter as a Function of Reduced Frequency $\Delta = 20^\circ$

Fig 14. Variation of Buffet Excitation Parameter with Incidence $\Lambda = -20^\circ$ $AR = 6$ Fig 15. Variation of Buffet Excitation Parameter with Sweep Angle $\alpha = 10^\circ$ Fig 16. Variation of Buffet Excitation Parameter with Sweep Angle $\alpha = 20^\circ$





Fig 24 Buffet Excitation Parameter for Unswept Wings $\alpha = 10^\circ$ Fig 25 Buffet Excitation Parameter for Unswept Wings $\alpha = 30^\circ$

NOUVELLE METHODE DE DETERMINATION DES FORCES DE TREMBLEMENT EN SOUFFLERIE

par

Roger Destuynder
ONERA, Châtillon
France

et

Roland Barreau
Aérospatiale
B.P.3153
316 Route de Bayonne
31060 Toulouse Cedex 03
France

RESUME

Parmi les critères usuels adoptés pour qualifier l'entrée en tremblement d'un avion il est courant d'utiliser la valeur de l'accélération mesurée au siège pilote et fixée à $\pm 0,2g$.

En réalité la vibration ressentie est le résultat de deux systèmes d'excitation, le premier terme indépendant des modes propres de l'avion est le champ de pression instationnaire aléatoire créée par les forces extérieures et qui s'étend dans une large gamme de fréquences (Ce sont les seules forces de tremblement) Le second terme est du aux forces induites par le mouvements de l'avion et caractérise principalement les vibrations des modes propres de la structure (Ce second terme agit sur l'évolution des fréquences et des amortissements).

Il a paru intéressant de tenter de séparer ces deux champs de pression afin d'affiner la prédiction du tremblement sur l'avion lui même. Pour cela un asservissement, lié au déplacement de l'aile mesuré par des accéléromètres, permet à l'aide d'un vérin de réduire de façon très importante le mouvement de l'aile.

La mesure du champ de pression caractérise alors les seules forces extérieures de tremblement (étant entendu que les déformations statiques de la maquette sous charge doivent être identiques à celles de l'avion).

Dans une deuxième phase, toujours dans le domaine du tremblement, une seconde excitation sinusoïdale celle là, créera un champ de pression sur l'aile, complètement décorrélé des pressions de tremblement qui permettra par une méthode de Fourier de remonter aux forces induites.

Quelques exemples de cette méthode seront montrés.

NEW METHOD TO DETERMINE IN WIND TUNNEL THE BUFFETING FORCES

ABSTRACT

Among the usual criteria used to qualify the airplane buffet onset, it is classical to use the acceleration values measured at the pilot seat and limited at $\pm 0,2g$.

This acceleration is the result of two excitation systems. The first one, due to the external forces, is created by the random unsteady field of pressure on the airplane and acting in a large frequency range. (That is the real buffet forces)

The second one excitation is due to the induced pressures coming from the airplane motions and characterizing principally the eigen modes of the structure.

It seems interesting to separate the two pressure fields to improve the buffet knowledge not only to have the correct buffet onset forces but also to obtain the forces distribution.

For this target a closed loop system using a parameter of the wing (unsteady bending moment or accelerometers) permits in wind tunnel to reduce the wing motion introducing damping forces, in the model with the help of actuator.

It is necessary to translate these results to the airplane, the static deformation of the model and plane being similar.

In a second phase, always under buffet conditions, sinusoidal excitations are applied on the wind tunnel model, giving a field of pressure uncorrelated with the buffeting pressure. In this manner we have the possibility to extract, using an FFT, the induced complex pressure and forces.

Some examples are given.

1. -INTRODUCTION

Le problème de la prévision du tremblement d'un avion civil est un problème important et difficile :

Il est important parce qu'il conditionne le domaine de vol de l'avion en tenant compte des marges, c'est à dire de la courbe $C_z(\alpha) = f(\text{mach})$.

Il est difficile à prévoir car il n'existe pas à l'heure actuelle de théorie capable de déterminer en tridimensionnel transsonique les efforts créés par le décollement sur une aile en fonction de l'incidence et de l'envergure.

Ce problème, très non linéaire n'a de signification qu'au sens statistique, les pressions engendrées par le décollement étant aléatoires et peu corrélées entr'elles.

Des essais en soufflerie effectués avec des maquettes de conception nouvelle et utilisant un équipement approprié permettent de réduire les différences entre les résultats de soufflerie et les essais en vol.

Beaucoup d'auteurs, dans différents pays, se sont penchés sur ce problème qui présente un certain nombre de difficultés de nature différentes (Ref.1-2-3-4).

Ces difficultés sont les unes inhérentes aux maquettes, ce sont :

- La grande différence entre le nombre de Reynolds de la maquette et celui de l'avion.

- La déformation statique sous charge qui diffère entre maquette et avion.

- Les critères de tremblement qui sont différents.

- Les modes propres de la structure qui ne sont représentatifs sur la maquette que pour les premiers modes. (Les modes de flexion par exemple).

- La difficulté de connaître avec précision la distribution dans le plan des fréquences des pressions dues aux décollements.

- Le fait que le système, hors l'origine du tremblement, est toujours soumis à deux champs de forces étroitement liés :

- L'un d'origine externe, c'est le tremblement proprement dit.

- l'autre d'origine induite, dû au mouvement de l'aile.

Ce sont ces différents problèmes que l'on va considérer l'un après l'autre.

2.-DEVELOPPEMENT DES METHODES ACTUELLEMENT UTILISEES

2.1.-INFLUENCE DU NOMBRE DE REYNOLDS SUR LE DECOLLEMENT

Il existe deux façons de vérifier l'influence du nombre de Reynolds sur les conditions de décollement :

2.1.1.-INFLUENCE DE LA PRESSION GENERATRICE.

On peut lorsque cela est possible, jouer sur la pression génératrice de la soufflerie. Dans ce cas on travaille à nombre de Mach constant et à pression génératrice variable. Pour cela, la maquette doit être extrêmement rigide afin de n'avoir que de très faibles déformations statiques que l'on peut négliger en première approximation. De tels essais ont été effectués à la NASA-Ames (Ref 5) sur un modèle bidimensionnel (Fig. 1).

On constate que dans ce cas la condition de début de décollement mesurée par les capteurs de pression instationnaires en fonction de l'angle d'incidence se stabilise très vite avec la pression dynamique \bar{q} , c'est à dire avec le nombre de Reynolds. A partir de $Re = 6.10^6$ le décollement initial est stabilisé à tous les nombres de Mach, de $Mach = 0,72$ à $Mach = 0,82$.

2.1.2.-INFLUENCE DE LA TEMPERATURE GENERATRICE

La seconde possibilité consiste à travailler à pression dynamique $\bar{q} = \frac{1}{2} \rho V^2$, et Mach constant et à faire varier la température génératrice dans une large gamme. Dans ce cas la déformation statique reste constante, (aux variations près des modules d'élasticité).

L'effet du nombre de Reynolds (Proportionnel à la température génératrice T_i) se stabilise très rapidement (Ref.6 - Fig.2).

Ces essais ont été effectués dans une soufflerie cryogénique avec des températures génératrices variant de 300° à 110° Kelvin. La maquette était du type tridimensionnel et était représentative d'une voilure d'avion civil. A partir de $R = 6.10^6$ à 7.10^6 c'est à dire les mêmes valeurs que dans le chapitre précédent la courbe $C_z = f(Mach)$ est figée.

Toutefois un inconvénient apparaît en instationnaire dans l'utilisation d'une soufflerie cryogénique pour déterminer le tremblement : Les fréquences réduites $\omega_r = \omega \frac{1}{V} = \omega \frac{1}{M\sqrt{\gamma RT}}$ varient avec l'inverse de la racine carrée de la température, dans le cas présent la variation serait de $\sqrt{3}$.

La figure 2, extraite d'un rapport de D Maybe (R.A.E) illustre très bien les deux conclusions ci-dessus.

2.2.-MAQUETTES

Il résulte des données précédentes que des maquettes de grande taille, telles que celles qui peuvent être réalisées par exemple pour la soufflerie S1 de L'ONERA Modane, conviennent aux essais de tremblement.

Par exemple, une maquette de 2,6 mètres de demi-envergure, ayant une corde aérodynamique moyenne de 1 mètre à un nombre de Mach de 0,80, à un nombre de Reynolds de 8.10^6 La figure 3 illustre une telle maquette utilisée pour des essais de tremblement (Ref. 7).

3.-DEFORMATION STATIQUE

Il est fondamental, dans le but d'avoir les mêmes positions de choc et de décollement sur la maquette et sur l'avion, que les déformations statiques sous charges aérodynamiques soient identiques. L'angle α de vrillage en envergure caractérise l'incidence locale qui détermine le décollement.

Les déformations en tout point doivent être dans le rapport des échelles $\lambda = \frac{l_{\text{maquette}}}{l_{\text{avion}}}$, ce qui imposera l'égalité des déformations angulaires. Pour cela partant des distributions de rigidités en flexion et en torsion de la voilure, calculées sur plan, on doit déterminer un caisson de voilure de maquette tel que le rapport suivant soit observé ;

$$\frac{\delta_{\text{maquette}}}{\delta_{\text{avion}}} = \frac{M_m g_m + q_m S_m C_{zm} L_m^3}{M_a g_a + q_a S_a C_{za} L_a^3} \cdot \frac{E_a I_a}{E_m I_m} = \lambda = \frac{L_m}{L_a} \quad (1)$$

avec $C_{zm} = C_{za}$; $\frac{S_m}{S_a} = \lambda^2$; $\frac{L_m}{L_a} = \lambda$; $E_m = E_a$; $\frac{I_m}{I_a} = \lambda^4$; $g_m = g_a$

L'équation (1) caractérise le rapport :

$$\frac{\delta_{\text{maquette}}}{\delta_{\text{avion}}} = \frac{\sum \text{Forces maquette}}{EI_{\text{maquette}}} \cdot \frac{EI_{\text{avion}}}{\sum \text{Forces avion}}$$

$C_{zm} = C_{za}$ du fait de l'égalité du nombre de Mach et du respect des déformées statiques.

$g_m = g_a$ caractérise l'égalité de l'accélération de la pesanteur pour la maquette et l'avion.

$E_m = E_a$ suppose que les caissons voilures et maquettes soient fabriqués dans le même matériau.

L'égalité (2)

$$\frac{\sigma_m}{\sigma_a} = \frac{\rho_m}{\rho_a}$$

ou ρ représente la densité de l'air et σ la densité structurale, montre que l'on peut négliger aussi bien pour l'avion que pour la maquette les quantités $M_m g$ et $M_a g$.

Exemple : Pour une maquette de $S = 2m^2$ à un nombre de Mach = 0,78 et un $C_z = 0,7$ la force statique de portance est de 3700 N environ. Simultanément le poids de l'aile sera de $M_m = \lambda^3 \cdot M_a = 58Kg$. Les forces de gravité de la voilure sont donc de l'ordre de 1 à 2% des forces aérodynamiques statiques.

On déduit finalement de (1) et (2) $\frac{E_a I_a}{E_m I_m} = \frac{G_a J_a}{G_m J_m}$ avec $E_m = E_a$ et $C_m = C_a$

Ce qui conduit à la relation bien connue :

$$\frac{I_m}{J_m} = \frac{I_a}{J_a}$$

avec

EI = Rigidité de flexion

GJ = Rigidité de torsion

et les indices

a pour avion et m pour maquette

Connaissant la distribution I_a et J_a de l'avion il est alors possible de calculer un caisson maquette équivalent sous forme d'une poutre.

Une autre propriété intéressante de cette similitude est de conserver l'égalité des contraintes :

On a
$$\sigma_m = \frac{M_t}{\frac{I_m}{V_m}} \quad \text{avec} \quad \frac{\sigma_m}{\sigma_a} = \frac{\frac{q_m}{q_a} + \frac{I_a}{I_m} + \lambda^4}{\frac{q_a}{q_a}}$$

À partir de (1) on peut écrire
$$\frac{E_a I_a}{E_m I_m} = \frac{1}{\lambda^4} + \frac{q_a}{q_m}$$

si $E_a = E_m$ on en déduit $\sigma_m = \sigma_a$

La similitude statique entre maquette et avion implique de plus le respect des conditions limites aile-fuselage, un exemple est donné dans la figure 4.

Pour cela un tube creux de section rectangulaire ou circulaire permet d'ajuster à l'emplanture de l'aile les raiders en flexion et en torsion ainsi que la position de l'axe élastique à l'aide de trois paramètres indépendants : Longueur du tube, diamètre extérieur et épaisseur du tube.

Dans tous les cas cette similitude n'implique rien sur les modes propres de la structure qui a priori ne sont pas semblables à ceux de l'avion. (Excepté, éventuellement, les premiers modes de flexion 1 et 2).

4.-DETERMINATION DES FORCES DUES AU TREMBLEMENT.

Lorsque les deux conditions précédentes sont remplies (même déformée statique de la maquette par rapport à l'avion au même nombre de Mach et de Reynolds) cela est suffisant pour obtenir les mêmes positions de choc et de décollement. On peut alors caractériser l'entrée en tremblement, mais pour pouvoir estimer la réponse de l'avion il faut outre sa base modale, pouvoir estimer et séparer les forces externes (tremblement) et les forces internes (celles dues au mouvement).

Considérons pour cela l'équation très générale suivante :

$$\begin{bmatrix} \mu \\ \alpha \\ \varphi \end{bmatrix} \ddot{q} + \begin{bmatrix} \alpha \\ \varphi \end{bmatrix} \dot{q} + \begin{bmatrix} \varphi \end{bmatrix} q + p v^2 \begin{bmatrix} A+iB \end{bmatrix} = F$$

dans laquelle μ , α et φ représentent dans une base orthonormée respectivement, les masses, amortissements et raiders généralisés, F les forces extérieures dues au décollement et $p v^2 \begin{bmatrix} A+iB \end{bmatrix}$ les forces induites par les mouvements de l'aile.

4.1.-FORCES EXTERIEURES.

La première condition à remplir est de séparer les forces induites des forces externes telles qu'elles apparaissent sur la figure 5. En fonction de l'incidence locale la force généralisée sur un mode de flexion, à partir des pressions instationnaires mesurées simultanément, montre à 55 Hz une participation de plus en plus importante du premier mode de flexion c'est à dire des forces induites. Il est clair que l'incidence locale doit être alors la somme de l'incidence de l'avion plus l'incidence locale de déformation due aux charges statiques plus les incidences dues aux déformées dynamiques. Pour éviter cette

difficulté, il est nécessaire d'immobiliser l'aile, autant que faire se peut, afin de n'avoir à mesurer avec les capteurs de pression que les termes dus aux forces extérieures.

Une boucle de contrôle permettant de reinjecter un amortissement important sur la structure atteint cet objectif.

Pour réaliser cet amortissement un puissant vérin hydraulique reinjecte un terme de moment sur l'aile en quadrature par rapport au mouvement de l'aile pris comme référence. Dans l'exemple de la figure 6 les deux premiers modes de flexion de l'aile en tremblement ont été ainsi traités, il faut noter que le cas choisi correspondait à un tremblement très violent bien au delà des limites admissibles pour un avion civil.

La mesure correcte des forces de tremblement et leur distribution en fonction de l'envergure s'effectue à l'aide d'un grand nombre de capteurs instationnaires. Dans un exemple réalisé sur une maquette de grandes dimensions, plus de 400 capteurs instationnaires répartis à l'intrados et surtout à l'extrados sur 20 cordes (coté du décollement), ont été utilisés.

Dans le même temps où le mouvement de l'aile est amorti et réduit à un très faible déplacement, on a vérifié que les pressions statiques locales étaient inchangées de même que la courbe $C_z = f(\alpha)$ (Fig. 7 & 8)

Le problème consiste à déduire section par section le torseur des efforts dus aux forces extérieures.

Il existe deux possibilités :

a)- On peut effectuer la somme temporelle de toutes les pressions de chaque section en utilisant deux matrices de pondération : L'une caractérisant la force, l'autre le moment ; puis effectuer la transformée de Fourier de chacune des sommes. (Les sommes de toutes les sections doivent être effectuées simultanément afin d'obtenir les phases relatives entre les différentes sections par rapport à une même référence.)

b)- On peut aussi mesurer numériquement toutes les pressions (ou tout au moins par groupe) par rapport à une référence donnée et échantillonnées dans le même temps. On effectue ensuite la transformée de Fourier pour avoir les composantes des pressions moyennées dans le plan des fréquences. (Cette méthode nécessite un équipement plus important). Les deux procédés sont comparés sur la figure 9 au nombre de Mach=0,80 dans une section comportant 18 capteurs de pression instationnaire.

La somme de la densité spectrale des pressions et la densité spectrale de la somme des pressions, c'est à dire la somme fréquentielle numérique ou la somme temporelle analogique donnent des résultats très voisins. Fig.9.

Le temps de moyennisation est le même dans les deux cas.

On a essayé de voir l'influence du nombre de moyennes, c'est à dire la durée de l'enregistrement sur le résultat final :

-En soufflerie il est aisé de maintenir les conditions de Mach, de pression, de température et d'incidence constantes durant un temps relativement long.

- En vol, les points de régime de tremblement s'obtiennent, pour un avion civil, en virage avec un facteur de charge compris, en général, entre 1 et 2. Il est difficile au pilote de maintenir longtemps l'avion avec des conditions de nombre de Mach, d'incidence et d'altitude constante.

En soufflerie trois durées d'enregistrement ont été choisies :

La première de 117 secondes représente un temps pratiquement infini. La figure 10 montre le résultat de la sommation des capteurs instationnaires d'une corde dans le domaine des fréquences à un nombre de Mach =0,80 pour une incidence de 5°.

La seconde courbe représente le même phénomène pendant une durée de 12 secondes, la troisième courbe représente le phénomène pendant 6 secondes.

L'erreur quadratique moyenne portée sur la figure 11 en fonction du temps montre que l'erreur qui atteint 30% pour une durée des moyennes de 6 secondes se réduit à 5% pour une durée des moyennes de 10 secondes. Ce qui permet de faire confiance aux données des essais en vol, ceux-ci étant en général moins perturbés par la turbulence atmosphérique que les essais en soufflerie ne le sont par la turbulence naturelle de la soufflerie.

4.2 - FORCES DUES AU MOUVEMENT DE L'AILE

La seconde partie du problème consiste à déterminer les forces induites par le mouvement de l'aile indépendamment des forces extérieures. Mais alors que les forces externes sont les mêmes pour l'avion et pour la maquette (Dans la mesure où les déformées statiques sont les mêmes et le nombre de Reynolds suffisant) les forces généralisées internes sont liées aux modes propres de la structure considérée.

On peut toutefois faire l'approximation suivante : Dans la mesure où le tremblement comporte une participation très importante de la première flexion et éventuellement de la deuxième flexion de l'aile (Ce qui est le cas le plus général pour des avions civil de grand allongement), on peut considérer que ces deux modes seront convenablement représentés par la maquette.

Comme il s'agit de modes de flexion avec un nœud en avant de l'aile, la contribution principale du mouvement de l'aile induit un amortissement aérodynamique, la rigidité structurale ne variant que très peu avec la partie réelle des forces induites, la fréquence propre du mode variera peu.

On peut étudier les forces induites soit à l'échelon global (variation de l'amortissement structural plus aérodynamique), soit à l'échelon local en excitant l'aile à l'aide d'un vérin hydraulique et en mesurant les pressions instationnaires induites par le mouvement de l'aile pris comme référence de phase.

a)- La première méthode figure.12 montre que lorsque l'incidence de l'aile augmente à partir d'une incidence nulle, la valeur de l'amortissement du mode de flexion a d'abord une valeur quasiment constante (ce qui caractérise des forces aérodynamiques instationnaires indépendantes de l'incidence), puis un choc apparaît sur l'aile (à l'extrados, dans le cas présent), la valeur de l'amortissement croît alors légèrement, lorsque le tremblement débute l'amortissement aérodynamique décroît rapidement pour passer par un minimum et croître à nouveau Ref.9.

Le résultat pour l'aile est d'abord une amplitude d'excitation constante, due en particulier en soufflerie au bruit de fond de celle-ci et à la turbulence dans la couche limite. Puis comme les forces extérieures croissent avec l'incidence en même temps que l'amortissement aérodynamique diminue, l'amplitude devient rapidement très grande. La figure.13 illustre ce résultat.

b)- La deuxième méthode consiste à exciter l'aile harmoniquement et à mesurer les pressions instationnaires, à en extraire la force généralisée correspondant au mode excité. La figure.14 montre la même tendance que l'évolution des amortissements à savoir un moment qui est d'abord constant, puis qui croît après l'apparition du choc et décroît ensuite lorsque l'incidence continue de croître. Ceci est caractérisé par les modules des deux ponts de jauges mesurant les moments de flexion sur l'aile à la fréquence de 80 Hz.

5. - CRITERE D'ENTREE EN TREMBLEMENT

Il existe de nombreux critères pour caractériser l'entrée en tremblement d'un avion ou d'une maquette. La figure 15 montre les différences qui peuvent exister entre un essai de tremblement déterminé en soufflerie sur une demi-maquette à la paroi et un essai en vol destiné à caractériser le même phénomène. Dans cet essai, où il ne s'agissait que de déterminer le point d'entrée en tremblement, il n'y a pratiquement aucun termes induits.

En soufflerie le critère d'entrée en tremblement se traduit par une variation de la pente de la courbe $C_x = f(\alpha)$ correspondant à une variation de l'angle d'incidence $\Delta \alpha = 0,1$ ou $0,2^\circ$. Il s'agit d'un critère statique.

En vol le critère le plus souvent utilisé pour les avions civils est un critère dynamique correspondant à une valeur R.M.S de l'accélération mesurée au siège pilote de l'ordre de $\pm 0,2g$. Il faut noter que ce critère dépend fondamentalement du couplage qui peut exister entre les vibrations de l'aile et celles de l'avant du fuselage. Le tableau de la figure.15 montre par exemple que les mouvements de roulis d'un réacteur sont très peu ressentis au siège pilote alors qu'ils donnent un mouvement important en bout d'aile, inversement le tangage du réacteur est peu ressenti en bout d'aile alors qu'il donne une grande amplitude au siège pilote.

Ce critère donne en général une faible amplitude, pour les modes symétriques, au siège pilote, par exemple la flexion fondamentale. De même le critère $\Delta\alpha = 0,1$ ou $0,2^\circ$ présente un écart important entre la maquette et l'avion, (dans le cas présent la maquette n'était pas de similitude élastique).

Il semble qu'un critère dynamique comme le moment de flexion de l'aile à l'emplanture, mesurable à la fois sur la maquette et sur l'avion, serait mieux approprié pour établir une comparaison car s'appliquant à des déplacements, c'est à dire à des quantités proportionnelles aux contraintes et non aux accélérations.

6.-CONTROLE DU TREMBLEMENT

Le tremblement peut très bien être contrôlé et l'amplitude de l'aile réduite dans un rapport important de l'ordre de 20 db (Ref. 11). La figure.6 illustre le contrôle du tremblement effectué sur une grande demi-maquette montée à la paroi, à l'aide d'un flapéron interne à un nombre de Mach = 0,50 ; Le contrôle consistait dans ce cas à reinjecter sur l'aile des forces instationnaires en quadrature avec le mouvement de l'aile. On peut noter que le tremblement très violent qui a été contrôlé pour une incidence de $\alpha = 8,5^\circ$ correspond à un angle moyen de quelques minutes. Il s'agissait dans ce cas de contrôler les deux premiers modes de flexion.

7.-COMPARAISON CALCULS ESSAIS

A partir des mesures de capteurs instationnaires effectuées lors du tremblement on a tenté de reconstituer le mouvement de l'aile. Le calcul a été effectué sur le premier mode de flexion d'une demi-aile à la paroi (fig.16 et 17). On peut noter aussi bien à Mach = 0,50 qu'à Mach = 0,78 (avec choc) que pour les faibles amplitudes, c'est à dire lorsque les forces extérieures de tremblement sont prédominantes, le calcul est plus correct que dans le cas à forte amplitude où le terme d'amortissement aérodynamique, qui décroît, devient important, l'estimation de ce terme très fortement non linéaire a été prise constante pour tous les angles d'incidence. L'accélération mesurée se présente sous la forme :

$$\ddot{q} = \frac{F}{2\mu} \quad \text{avec} \quad \alpha' = \alpha_u + \alpha_{\text{aéro}}$$

μ représente la masse généralisée, F = Forces extérieures calculée par les intégration des pressions.

8.-CONCLUSION

Pour réaliser une prévision raisonnable de la réponse d'un avion au tremblement à différents nombres de Mach et différentes incidences on est conduit à respecter les règles suivantes durant les essais en soufflerie :

a)- La maquette, ou plus généralement la demi-maquette à la paroi, doit avoir les mêmes déformées statiques que l'avion pour les mêmes charges, compte tenu bien évidemment des facteurs d'échelle.

b)- La maquette doit avoir un nombre de Reynolds ramené à la corde aérodynamique moyenne, au moins égal à 6×10^6 pour un nombre de Mach = 0,80.

Il existe trois possibilités :

b1)-Travailler en soufflerie cryogénique.

b2)-Travailler dans une soufflerie à pression génératrice importante et variable.

b3)-Travailler dans une soufflerie de très grande dimensions (Type S1 Modane).

Les trois méthodes présentant à la fois des avantages et des inconvénients.

c)- On doit séparer les forces externes, (tremblement dû au décollement), des forces de couplage (dûes aux forces induites), pour cela il est nécessaire d'introduire, par une loi de contrôle approprié, des forces d'amortissement sur l'aile, soit par l'intermédiaire d'une gouverne, soit par un mouvement d'ensemble de l'aile crée par un vérin hydraulique.

d)- On doit déterminer les forces de couplage.

d1)- Les forces de couplage induites peuvent être mesurées globalement par la variation de la fréquence propre et de l'amortissement aérodynamique, au moins pour le premier mode de flexion qui est le terme principal dans la réponse de l'aile dans la plupart des cas. Toutefois cette méthode reste très imprécise et ne fournit aucune information sur la distribution des forces en envergure.

d2)-On peut aussi exciter la maquette en régime harmonique durant le tremblement, après avoir amorti les premiers modes propres par une boucle de contrôle. L'excitation à fréquence fixe fournit alors un mouvement d'ensemble de l'aile dans lequel tous les points sont sensiblement en phase dans une large bande de fréquence. Les valeurs des capteurs de pression instationnaire donnent alors la possibilité de calculer la force généralisée en connaissant le mode sur lequel elles s'exercent. Ces pressions, qui sont référées au mouvement imposé à l'aile par l'excitation harmonique, sont complètement décorrélées des pressions de décollement.

e)-Enfin il est nécessaire d'avoir soit par calcul sur plan, soit par un essai au sol, une base modale de l'avion, incluant avec précision les amortissements structuraux et les masses généralisées. A l'aide de ces éléments on peut raisonnablement donner la réponse de l'avion au phénomène de décollement à partir d'essais en soufflerie, au moins pour le "Buffet onset".

9. BIBLIOGRAPHIE

1-H. FORSCHING

Aeroelastic Buffeting Prediction Techniques. A general review .
D. F. V. L. R. Göttingen F. B. 81615-1981

2- G. F. BUTLER, J. G. JONES

The Prediction of buffeting response in flight from wind tunnel measurements on model of conventional construction.
The Aeronautical Journal VOL. 877, 1984

3-A. M. CUNNINGHAM, D. B. BENEPE, P. G. WANER

A method for predicting full scale buffet response with rigid wind tunnel model fluctuating pressure data.
vol. 1 Prediction method development.
N. A. S. A. / C. R. 3035, 1978

4- C. F. COE, A. M. CUNNINGHAM

Predictions of F111TACT Aircraft buffet response and correlations of fluctuating pressures measured on aluminium and steel models and the aircraft.
N. A. S. A. / C. R. 4069, 1987

5-J. B. Mc DEVITT, A. F. OKONO

Static and dynamic pressures measurements on the N.A.C.A. 012 airfoil in the AMES high Reynolds number facility.
N. A. S. A. / T. P. 2485, 1985

6-D. G. MAREY

Some remarks on buffeting.
R.A.E. Bedford (G.B.) 1978

7-R. DESTUYNDER, V. SCHMIDT

O.N.E.R.A. (Chatillon)

J. BERGER, R. BARREAU

Aérospatiale

Des difficultés de prédire en soufflerie le tremblement d'un avion civil moderne.
A.G.A.R.D., Naples 1987 Conf.429

8P. NAUDIN

Avant projet d'une voilure pour étude du tremblement.
R. T. n°15/3425 O.N.E.R.A. 1985

9J. BECKE, A. GRAVELLE

Some results of experimental and analytical buffeting investigations on a delta wing.
International symposium on aeroelasticity.
Aachen (R.F.A.) April 1985

10 B. BENOIT, I. LEGRAIN

Buffeting prediction
A.I.A.A. Monterey (Ca) 1987

11 R. DESTUYNDER

Actif control of the buffeting response on a large modern civil airplane configuration in wind tunnel.
International symposium on aeroelasticity.
Aachen (R.F.A.) April 1985

10. LISTE DES FIGURES

fig-1 Début du décollement fonction du nombre de Reynolds

fig-2 Influence de la déformation statique

fig-3 maquette AS200-06 dans la soufflerie S1 de Modane

fig-4 Montage de demi maquette souple avec excitation

fig-5 Forces généralisées à Mach 0,5

fig-6 Contrôle de tremblement sur deux modes

fig-7 Invariance locale des données statiques avec et sans contrôle

fig-8 nvariance globales des données statiques avec et sans contrôle

fig-9 Somme temporelle et somme fréquentielle

fig-10 Influence du temps sur la sommation

fig-11 Erreur quadratique moyenne

fig-12 Variation de l'amortissement du mode fondamental durant la pénétration

en tremblement

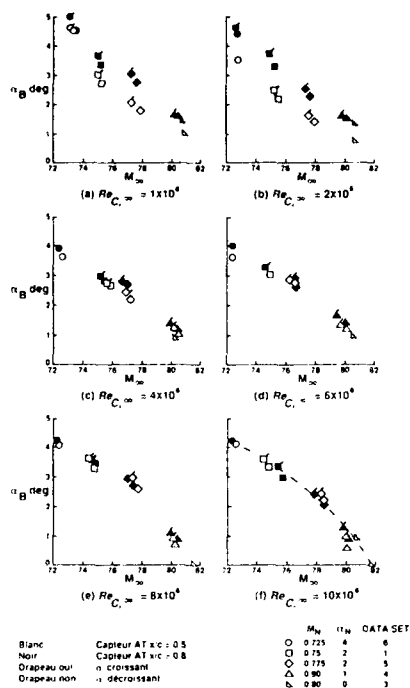
fig-13 Moment de flexion stationnaire et instationnaire

fig-14 Moment de flexion en instationnaire mesuré en deux points de l'aile

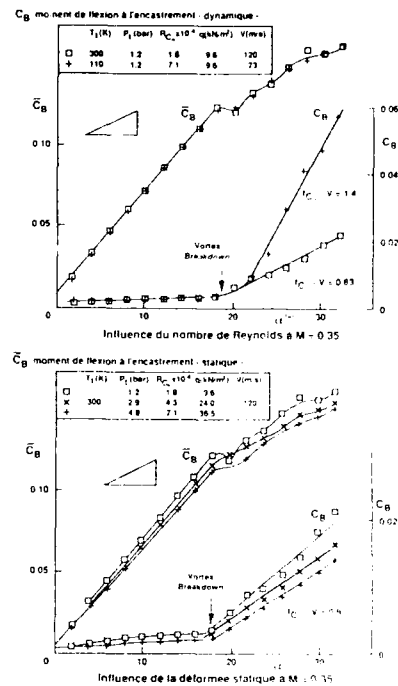
fig-15 Critère d'entrée en tremblement

fig-16 Comparaison test théorie de la réponse de l'aile à $M=0,5$

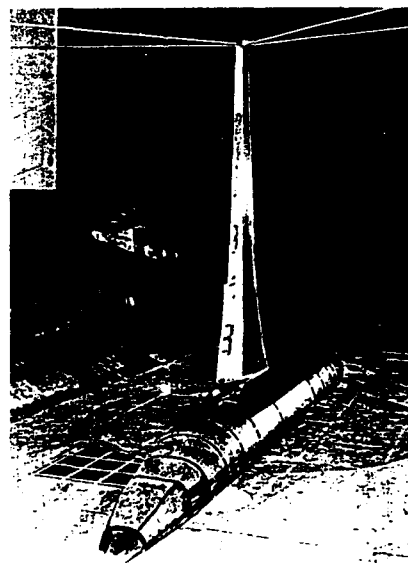
fig-17 Comparaison test théorie de la réponse de l'aile à $M=0,78$



DEBUT DU DECOLLEMENT FONCTION DU NOMBRE DE REYNOLDS - Fig 1 -

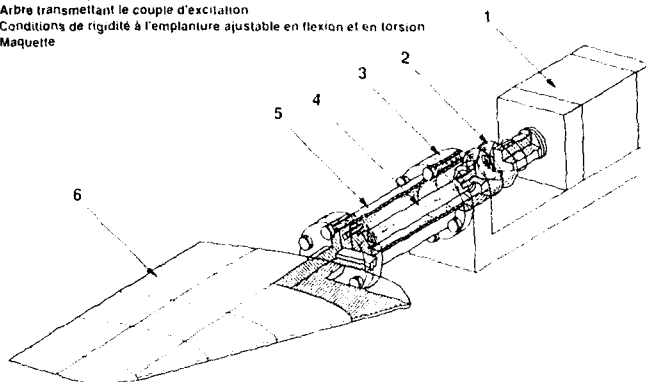


INFLUENCE DE LA DEFORMATION - Fig 2 -

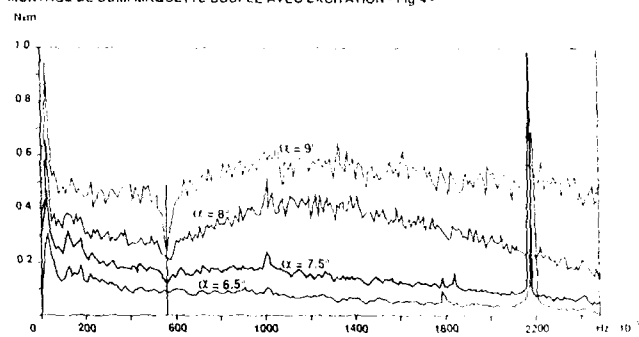


MAQUETTE AS200-06 DANS LA SOUFFLERIE S1 DE MODANE - Fig 3

- 1 Verin d'excitation - bruit blanc
- 2 Encastrement parfait
- 3 Encastrement parfait
- 4 Arbre transmettant le couple d'excitation
- 5 Conditions de rigidité à l'emplanture ajustable en flexion et en torsion
- 6 Maquette

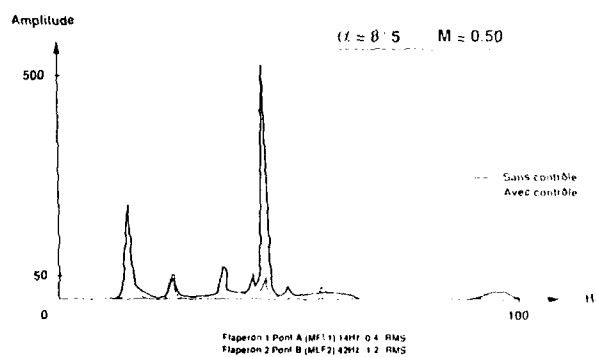


MONTAGE DE DEMI MAQUETTE SOUPLE AVEC EXCITATION - Fig 4 -

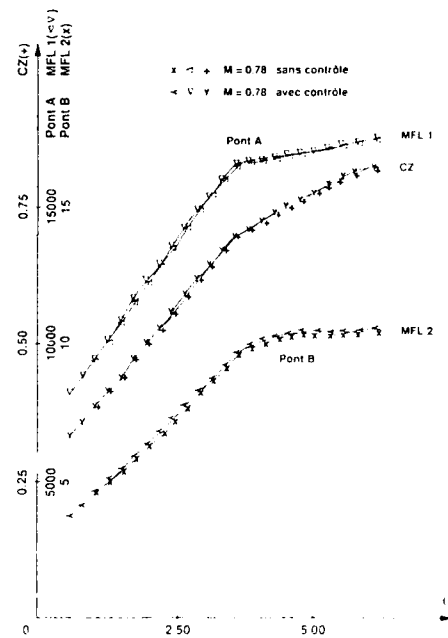
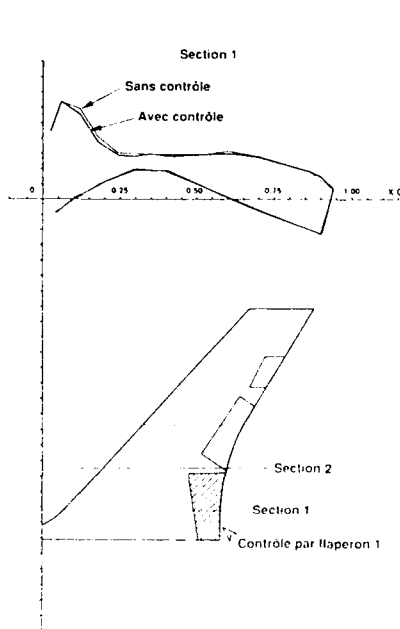


FORCES GENERALISEES A MACH 0.5 - Fig 5 -

Contrôle simultané sur les flaperons 1 et 2



CONTROLE DE TREMBLEMENT SUR DEUX MODES - Fig 6 -

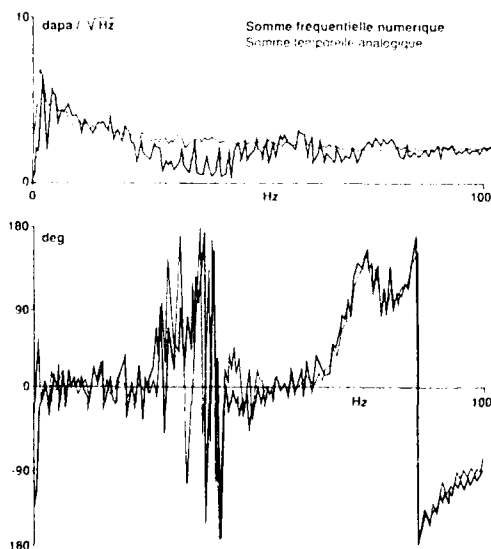


INVARIANCE LOCALE DES DONNÉES STATIQUES
AVEC ET SANS CONTRÔLE - Fig 7 -

SOMMATIONS SECTION 3

$M = 0.8$ $Pi = 0.95$

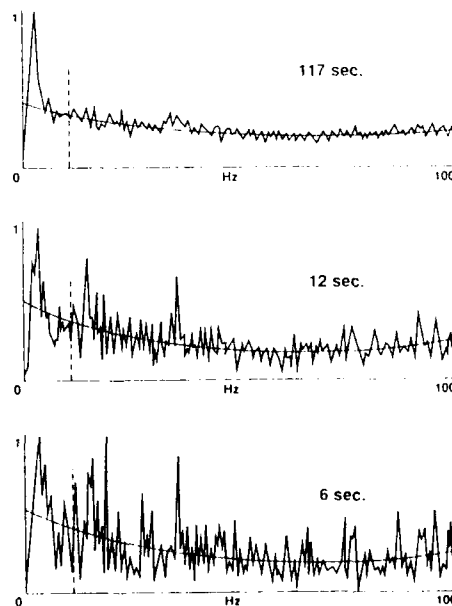
Phase : Accélération Missile



Somme fréquentielle numérique
Somme temporelle analogique

INVARIANCE GLOBALE DES DONNÉES STATIQUES
AVEC ET SANS CONTRÔLE - Fig 8 -

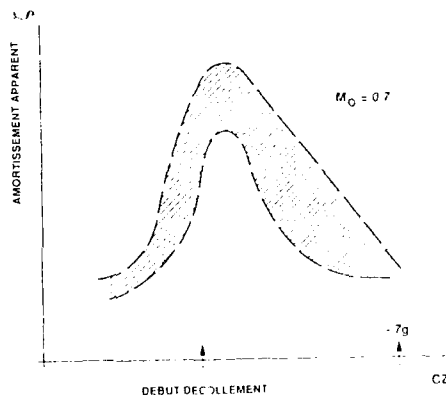
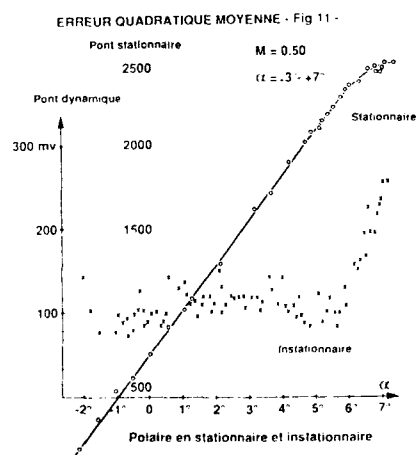
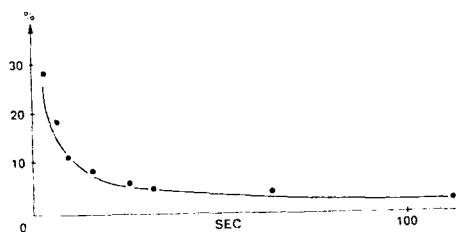
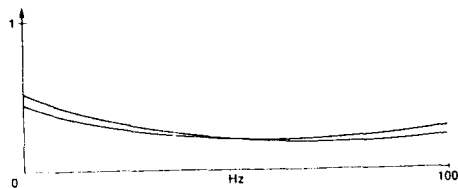
Moyennes d'une combinaison de capteurs



SOMME TEMPORELLE ET SOMME FREQUENTIELLE - Fig 9 -

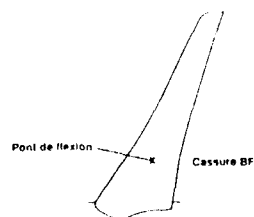
INFLUENCE DU TEMPS SUR LA SOMMATION - Fig 10 -

Lissage Temps d'enregistrement
6s 12s 117s

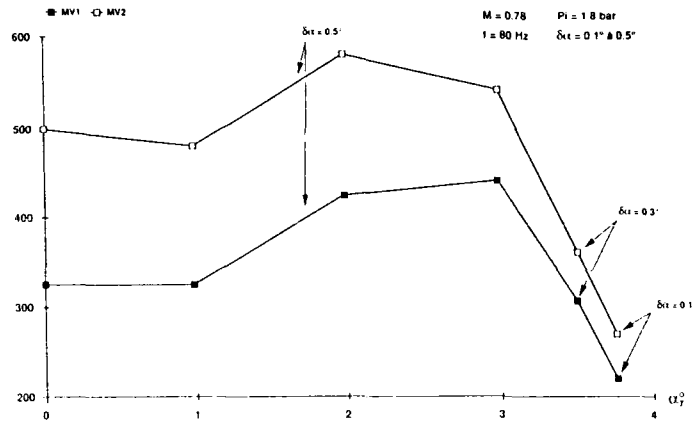


Ref 22 - The Dynamic Analysis of Buffeting and related Phenomena
Agard Conference CP 102 Paper-Fluid Dynamic of Aircraft Sizing 1972

VARIATION DE L'AMORTISSEMENT DU MODE FONDAMENTAL
DURANT LA PENETRATION EN TREMBLEMENT - Fig 12 -



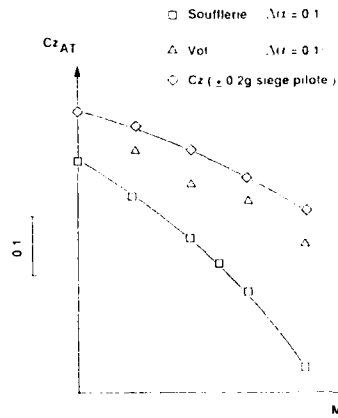
MOMENT DE FLEXION STATIONNAIRE ET INSTATIONNAIRE - Fig 13 -



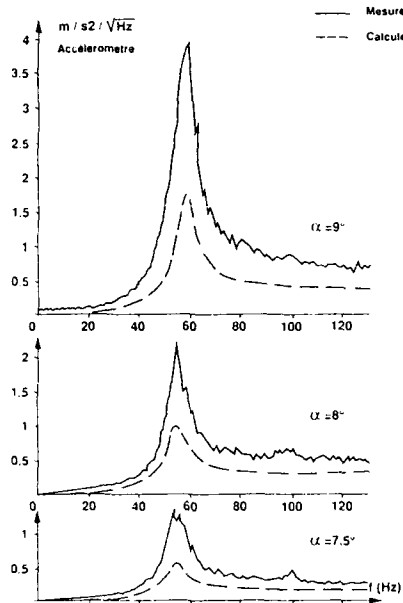
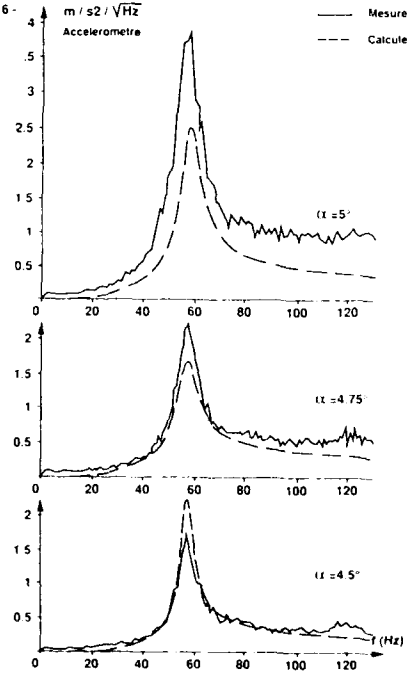
MOMENT DE FLEXION MESURE EN DEUX POINTS DE L'AILE EN INSTATIONNAIRE - Fig 14 -

DEPLACEMENTS MODAUX

Modes		Bout aile	Siege pilote
Flexion	$f = 2.11 \text{ Hz}$	7.0	0.5
Pendule reacteur	$f = 2.28 \text{ Hz}$	6.5	< 0.2
Tangage moteur	$f = 3.76 \text{ Hz}$	0.5	3.0
2 N Fuselage	$f = 4.87 \text{ Hz}$	5.0	1.0
Coplanaire	$f = 5.55 \text{ Hz}$	4.0	0.0



CRITERE D'ENTREE EN TREMBLEMENT - Fig 15 -

Réponse de l'aile à $M = 0.5$ COMPARAISON TEST THEORIE DE LA REPONSE DE L'AILE A $M = 0.5$ - Fig 16 -Réponse de l'aile à $M = 0.78$ COMPARAISON TEST THEORIE DE LA REPONSE DE L'AILE A $M=0.78$ - Fig 17 -

**FORCES AERODYNAMIQUES COUPLEES DUES AU
DECROCHAGE INSTATIONNAIRE SUR UNE AILE DE GRAND
ALLONGEMENT OSCILLANT A GRANDE AMPLITUDE**

par

J.-J. Costes et D. Pérot
ONERA
B.P.72 Châtillon Cedex
France

RESUME

Dans cet article on présente des résultats expérimentaux obtenus sur une aile rectangulaire pouvant osciller en tangage autour du quart avant. Par rapport au vent dans la soufflerie, l'aile est mise en attaque droite ou oblique. La comparaison avec une théorie simple utilisée pour les rotors d'hélicoptères met en évidence l'influence du tourbillon d'extrémité et l'importance de la composante de la vitesse du fluide le long de l'envergure de l'aile dans le cas de l'attaque oblique.

ABSTRACT

In this paper, experimental results which have been obtained on a rectangular wing oscillating in pitch around the quarter chord line are presented. Normal flow as well as skewed flow cases have been investigated. The comparison with a simple theory used in helicopter applications showed the influence of the tip wing vortex and the importance, in the skewed flow case, of the component of the wind velocity directed along the wing span.

I. INTRODUCTION

Le décrochage instationnaire sur une pale d'hélicoptère en rotation est un phénomène mal connu, c'est pourquoi des études fondamentales sur un cas plus simple ont été entreprises au département des structures de l'ONERA. On a choisi le cas d'une aile rectangulaire rigide et non vrillée oscillant en tangage autour de la ligne du quart avant. Cinq sections sur l'aile sont instrumentées avec des tubes de pression statique pour enregistrer la valeur moyenne de la pression et avec des capteurs à semi-conducteur pour en mesurer la partie instationnaire.

Des expériences ont été réalisées dans le cas d'un vent normal à l'aile ainsi que dans le cas d'une flèche avant ou arrière de 20 degrés. Les résultats expérimentaux ont été comparés avec ceux fournis par la théorie exposée au paragraphe suivant.

II. THEORIE

1. Présentation de l'étude théorique

Les profils utilisés pour les pales d'hélicoptères sont généralement conçus à partir de critères bidimensionnels. On effectue ensuite des expériences en soufflerie pour s'assurer que les critères demandés sont bien remplis. Dans le cas de grandes incidences où le phénomène de décrochage intervient, on se réfère presque exclusivement aux résultats expérimentaux bidimensionnels pour caractériser les profils. Il faut dans les expériences prendre soin de minimiser les effets tridimensionnels en effectuant les mesures dans la tranche centrale de la maquette. Il n'en reste pas moins que l'écoulement sur une aile ou sur une pale d'hélicoptère est tridimensionnel et qu'il faut par une théorie appropriée corriger les résultats expérimentaux.

La théorie aérodynamique linéaire classique est à la base des calculs qui seront présentés. Pour plus de détails, on se reportera aux références [1-3].

2. Etude stationnaire

2.1. Cas d'un profil bidimensionnel

On définit l'axe neutre d'un profil comme la direction du vent où la force de portance est nulle. L'angle compris entre l'axe de la soufflerie et l'axe neutre du profil est par définition l'incidence aérodynamique α du profil. Dans le cadre de la théorie du potentiel d'accélération pour un fluide linéarisé compressible, on peut calculer la vitesse induite au quart arrière du profil par un doublet d'intensité $q = \frac{-F}{\rho}$ placé au quart avant. F est la portance par unité de longueur sur le profil et ρ est la masse volumique du fluide non perturbé. La traduction d'une condition de glissement au quart arrière détermine l'intensité de la force de portance comme fonction de l'incidence α . On se limite ici à une schématisation du profil par un seul doublet en vue des extensions au cas non linéaire.

Lorsque l'incidence devient grande, le fluide décolle de l'extrados et chaque profil est caractérisé par une courbe de coefficient de portance $C_L(\alpha)$ (Fig 1). Supposons que le sillage et la poche de décollement à l'extrados du profil aient tous les deux une épaisseur modérée, on remplacera alors l'ensemble profil-poche de décollement par un pseudo-profil équivalent. Le sillage restant de faible épaisseur, les calculs linéaires usuels sont valables pour les vitesses induites. On peut alors écrire une sorte de condition de glissement pour l'axe neutre du profil fictif ce qui associe à la portance \bar{F} mesurée sur le profil une incidence efficace α_f . La relation entre \bar{F} et α_f est la relation linéaire classique :

$$\alpha_f = \frac{\bar{F} \sqrt{1-M^2}}{\pi \rho c V_\infty^2} \quad (1)$$

M = nombre de Mach, c = corde du profil, V_∞ = vitesse du vent à l'infini amont. La différence entre l'incidence du profil α et l'incidence efficace α_f est la perte d'incidence due au décrochage. Le produit $\Delta W = V_\infty(\alpha - \alpha_f)$ est la perte de vitesse induite.

2.2. Cas d'une aile rectangulaire

On considère une aile rectangulaire en attaque droite ou éventuellement oblique (fig 2). L'aile est schématisée par une ligne portante divisée en segments de longueurs éventuellement différentes. Sur chaque segment la portance est supposée constante. On remarque sur la figure 2 que dans le cas d'une attaque oblique l'extrémité de l'aile est d'autant plus mal représentée que l'angle de dérapage ϕ est grand. Augmenter le nombre de lignes portantes améliorerait la définition de l'aile mais on est limité ici à une ligne portante unique pour l'extension de la théorie au non linéaire.

Les vitesses induites peuvent être calculées par la théorie du potentiel d'accélération en des points dits de collocation situés sur la ligne du quart arrière. Comme en bidimensionnel, l'écriture d'une condition de glissement permet le calcul de la portance F le long de la ligne portante. Selon l'hypothèse de Prandtl on définit alors l'incidence aérodynamique locale par la relation (2) lorsque l'angle de dérapage est égal à ϕ

$$\alpha = \frac{F \sqrt{1-M_\phi^2}}{\pi \rho c V_\infty^2 \cos^2 \phi} \quad (2)$$

M_ϕ est le nombre de Mach correspondant à la vitesse $V_\infty \cos \phi$

Dans le cas de grandes incidences, on suivra la même démarche que celle utilisée dans le cas bidimensionnel (2.1). On supposera le sillage et la poche de décollement à l'extrados de l'aile comme étant d'épaisseur modérée. La position de l'axe neutre de l'ensemble profil plus poche de décollement détermine une incidence géométrique efficace θ_f le long de l'envergure de l'aile. La différence entre l'incidence géométrique réelle et l'incidence géométrique efficace peut être interprétée comme une perte due au décrochage. Dans la pratique, on modifiera la condition de glissement par un terme correctif tenant compte de la perte due au décrochage. On supposera que cette perte est la même que celle

constatée en bidimensionnel pour l'incidence α donnée par (2). C'est sur cette dernière hypothèse que repose les calculs qui seront présentés dans cet article. En bidimensionnel, la perte due au décrochage est connue, on l'obtient par le calcul à partir des courbes de portance comme il a été dit en 2.1.

Les termes correctifs qui viennent modifier la condition de glissement sont en général assez faibles. Le plus souvent, la recherche de la solution du système non linéaire qui détermine la portance \bar{F} le long de l'envergure de l'aile en régime décroché n'est pas trop difficile. Pourtant, on ne peut être assuré ni de l'existence ni même de l'unicité de la solution. C'est pourquoi on recherchera seulement une solution approchée minimisant une fonction d'erreur. Comme plusieurs minimums locaux sont possibles, la solution la plus proche de la solution de départ, c'est à dire du régime non décroché, sera retenue.

3. Etude instationnaire

3.1. Cas d'un profil bidimensionnel

On suppose que le profil est en oscillation autour de son quart avant, l'incidence étant donnée par $\alpha = \alpha_0 e^{i\omega t}$. De même qu'en stationnaire, le profil est schématisé par un point portant unique au quart avant. La condition de glissement exprimée au quart arrière permet le calcul de la portance qui cette fois dépend du temps, on aura $F(t) = F_0 e^{i\omega t}$. F_0 est un nombre complexe car la portance est déphasée par rapport au mouvement. Comme on s'est limité à un seul point portant, la méthode qui vient d'être exposée ne donne pas de bons résultats pour des valeurs élevées de la fréquence réduite ; $\frac{\omega c}{2V_\infty} > 0,3$.

Lorsque les variations d'incidence deviennent grandes, le phénomène de décollement intervient et les calculs linéaires ne sont plus valables. On les utilisera cependant pour calculer la perte de vitesse induite due au décrochage en supposant la portance expérimentale connue. Toutefois, il est nécessaire pour les utilisations ultérieures de pouvoir calculer cette perte de vitesse induite dans une gamme très large de nombres de Mach et de Reynolds ainsi que pour toute variation périodique de l'incidence. En soufflerie, on ne réalise le plus souvent que des oscillations harmoniques et seulement pour quelques nombres de Mach et de Reynolds. Il est alors nécessaire d'utiliser un modèle mathématique capable de fournir les portance et les moments sur le profil en interpolant à partir des résultats expérimentaux connus. Un tel modèle, fondé sur des hypothèses semi-empiriques, a été développé à l'ONERA au département des structures. On en donne ci-dessous les caractéristiques principales :

3.2. Modélisation bidimensionnelle

3.2.1. Principe

La façon la plus simple de prendre en compte le comportement des efforts aérodynamiques est d'écrire les équations différentielles qui relient ces efforts aux variables de position du profil.

Dans le cas du décrochage dynamique, les équations aérodynamiques exactes ne sont bien sûr pas accessibles. Les dynamiciens ont l'habitude de modéliser des structures complexes pour lesquelles on n'a pas non plus accès aux équations exactes, par des équations différentielles déterminées à partir de l'analyse du comportement de ces structures au voisinage des fréquences intéressantes.

Une telle démarche a été proposée par Dat [6] pour le décrochage dynamique. Cela a conduit à un modèle reproduisant bien le comportement des profils, et ce pour plusieurs types de mouvements (tangage, pompage et mouvement de tamis) et d'efforts (portance, moment et traînée) [7].

3.2.2. Mise en oeuvre

Des essais en soufflerie ont montré d'abord que les fonctions de transfert entre les efforts aérodynamiques et les variables de position d'un profil avaient bien un sens. On a en effet pu vérifier qu'un profil vibrant avec le mouvement $\alpha = \alpha_0 + \tilde{\alpha} e^{i\omega t}$ engendrait une réponse aérodynamique de la forme: $F = F_0 + \tilde{F} e^{i(\omega t + \phi)}$ pour laquelle le rapport $\tilde{F}/\tilde{\alpha}$ ainsi que la phase ϕ étaient indépendants de l'amplitude, pourvu que celle-ci ne soit pas trop forte (0.5 degré par exemple).

Les fonctions de transfert expérimentales ainsi obtenues dépendent de l'incidence moyenne à laquelle elles sont mesurées (ainsi que du Mach). Un jeu d'équations différentielles, écrit en temps réduit $\tau = V.t / (1/2 \text{ Corde})$, où C_q représente le coefficient de portance ou de moment, a particulièrement convenu pour approcher le comportement de ces fonctions de transfert:

$$\begin{aligned} Cq &= Cq_1 + Cq_2 \\ C\dot{q}_1 + \lambda.Cq_1 &= \lambda.Cq_L + (\lambda.s + \sigma).\dot{\alpha} + s.\ddot{\alpha} \\ C\ddot{q}_2 + a(\Delta Cz).C\dot{q}_2 + r(\Delta Cz).Cq_2 &= -[r(\Delta Cz).\Delta Cq + E(\Delta Cz).\dot{\alpha}] \\ (\text{Avec } E(\Delta Cz) &= 0. \text{ pour } \Delta Cz = 0.) \end{aligned}$$

Le terme Cq_1 prend la valeur du coefficient Cq en l'absence de tout décrochage. Il a un comportement toujours très proche de la théorie (plaque plane).

Le terme Cq_2 est la quantité (non petite) qu'il faut ajouter à Cq_1 pour obtenir la vraie valeur du coefficient Cq en cas de décrochage. Cq_2 répond remarquablement bien à une équation du second degré. Les coefficients de cette équation dépendent de α , mais on a préféré les faire plutôt dépendre de la quantité $\Delta Cz = Cz_L - Cz_S$ fonction de α , qui est la différence entre le coefficient de portance dans le domaine linéaire, extrapolé aux fortes incidences, et le coefficient de portance statique réel. C'est une quantité qui s'annule en dessous de l'angle de décrochage. Nous la considérons comme notre mesure du décrochage.

Ce modèle est valide par définition pour de petits mouvements autour d'une incidence moyenne. Nous l'appliquons à de grands mouvements, ce qui n'est valable que si les fonctions de transfert ne varient pas trop vite avec le temps.

-- C'est le cas avec les valeurs de $d\alpha/d\tau$ que l'on rencontre dans les applications.

-- Ce n'est pas le cas au moment du décrochage où la discontinuité des fonctions de transfert amène un problème. L'expérience montre que le décrochage de portance est alors retardé d'une certaine quantité. Ce phénomène particulier peut-être pris en compte dans nos équations en maintenant nulle la variable ΔCz pendant un certain temps ($\Delta\tau = 8$, exprimé en temps réduit).

Enfin, l'étude d'un grand nombre de profils nous a montré que les coefficients de ce modèle pouvaient être grandement simplifiés:

-- Les coefficients de l'équation en Cq_1 sont toujours très voisins d'un profil à l'autre.

-- Les coefficients de l'équation en Cq_2 sont très bien approchés par les expressions:

$$\begin{aligned} \sqrt{r} &= r_0 + r_2.\Delta Cz \\ a &= a_0 + a_2.\Delta Cz \\ E &= E_2.\Delta Cz \end{aligned}$$

Il ressort finalement de cette étude que les profils se comportent de façon assez semblable, dans le domaine linéaire où l'approximation plaque plane est toujours bonne, mais aussi dans le domaine décroché. En dehors du domaine transsonique, la forme du profil joue surtout à l'apparition du décrochage.

3.2.3. Modèle de portance bidimensionnel

Les équations utilisées dans cet article n'incluent pas l'extension du modèle au mouvement de tamis. Elles s'écrivent:

$$\begin{aligned} \text{Portance} &= 1/2 \rho \cdot S \cdot V^2 \cdot (Cz_1 + Cz_2) \\ \dot{Cz}_1 + \lambda \cdot Cz_1 &= \lambda \cdot Cz_L + (\lambda s + \sigma) \cdot \dot{\alpha} + s \cdot \ddot{\alpha} \\ \ddot{Cz}_2 + a(\Delta Cz) \cdot Cz_2 + r(\Delta Cz) \cdot Cz_2 &= -[r(\Delta Cz) \cdot \Delta Cz + E(\Delta Cz) \cdot \dot{\alpha}] \end{aligned}$$

Les valeurs numériques employées sont les suivantes:

$$\begin{aligned} \lambda &= 0,25 - 0,15 M^2 \\ s &= 0,08 (1 + M^2) \\ \sigma &= 0,105 - 0,08 M - 0,1 |\Delta Cz| - \lambda \cdot s \end{aligned}$$

$$\begin{aligned} \sqrt{r} &= 0,25 + 0,20 \Delta Cz^2 \\ a &= 0,40 + 0,45 \Delta Cz^2 \\ E &= -0,12 \Delta Cz^2 \end{aligned}$$

On peut voir qu'il a fallu corriger un peu la valeur de σ d'une quantité proportionnelle à ΔCz .

Ce modèle a été utilisé ici sans prendre en compte de retard au décrochage.

3.2.4. Modèle de moment bidimensionnel

De même que pour la portance, les équations utilisées dans cet article n'incluent pas l'extension du modèle au mouvement de tamis.

Les équations relatives au moment s'écrivent sous une forme particulière avec une expression directe de Cm_1 , ce que les équations de Theodorsen font déjà ressortir.

$$\begin{aligned} \text{Moment autour du quart avant} &= 1/2 \rho \cdot S \cdot 1/2 \text{corde} \cdot V^2 \cdot (Cm_1 + Cm_2) \\ Cm_1 &= Cm_L + (s + \sigma) \cdot \dot{\alpha} + s \cdot \ddot{\alpha} \\ \ddot{Cm}_2 + a(\Delta Cz) \cdot Cm_2 + r(\Delta Cz) \cdot Cm_2 &= -[r(\Delta Cz) \cdot \Delta Cm + E(\Delta Cz) \cdot \dot{\alpha}] \end{aligned}$$

Avec les valeurs numériques suivantes:

$$\begin{aligned} s &= -3\pi/16 [-1,26 - 1,53 \operatorname{atan}(15(M-0,7))] \pi/180 \\ \sigma &= -\pi/2 [1 + 1,4M^2] \pi/180 - s \\ \sqrt{r} &= 0,25 + 0,20 \Delta Cz^2 \\ a &= 0,15 + 0,45 \Delta Cz^2 \\ E &= 0,02 \Delta Cz^2 \end{aligned}$$

A partir du modèle mathématique qui vient d'être décrit on peut, tout comme en stationnaire, en utilisant la théorie linéaire calculer la perte de vitesse induite due au décrochage. Ceci est réalisable pour n'importe quelle incidence $\alpha(t)$ périodique.

3.3. Cas d'une aile rectangulaire

Comme dans le cas stationnaire, l'aile est schématisée par une ligne de segments portants. L'intensité des doublets de portance sur les segments est constante en envergure

mais dépend maintenant du temps $q(t) = -\frac{F_0 e^{i\omega t}}{\rho}$;

$q(t)$ est l'intensité du doublet et F_0 la portance (complexe), ces deux quantités étant données par unité de longueur.

En linéaire, la traduction de la condition de glissement sur la ligne du quart arrière permet le calcul des efforts aérodynamiques. Comme on est limité à une ligne portante unique, cette méthode ne s'applique qu'au cas de fréquences réduites assez faibles, inférieures à 0,3.

Lorsque le calage de l'aile atteint au cours du cycle d'oscillation des valeurs élevées, la valeur instantanée de l'incidence aérodynamique locale peut elle aussi devenir grande. C'est en particulier le cas au milieu de l'aile où les portances et donc aussi les incidences aérodynamiques sont les plus élevées. Dans ce cas, le phénomène du décrochage instationnaire se manifeste. Comme en stationnaire, on cherche alors à corriger la condition de glissement en supposant toujours que l'épaisseur du sillage et de la poche de décollement reste faible. Le calcul des vitesses induites se fait alors comme en linéaire.

Si $\alpha(y, t)$ est l'incidence aérodynamique de l'aile à l'envergure y et au temps t , la perte de vitesse induite due au décrochage sera supposée être celle calculée pour le profil bidimensionnel lorsque celui-ci subit la même variation d'incidence $\alpha(t)$. En un point de collocation donné, la vitesse induite par l'ensemble des segments de doublets qui schématisent l'aile, augmentée par la perte de vitesse induite locale, doit encore satisfaire à la condition de glissement. L'équation qui résulte de cette égalité sera écrite pour tous les points de collocation et pour différentes valeurs du temps équi-réparties sur la période d'oscillation. Il en résulte un système non linéaire dont la résolution est délicate. Comme on ne peut être sûr ni de l'existence ni de l'unicité de la solution, une fonction d'erreur sera calculée et minimisée en partant de la solution linéaire sans décrochage. Pour ce faire, on utilise une méthode de Newton généralisée en appliquant à chaque pas de l'itération un coefficient de relaxation de valeur inférieure ou égale à 1. Les dérivées nécessaires sont obtenues par différence finie ce qui rend la méthode indépendante du modèle aérodynamique utilisé pour la reconstruction des boucles de décrochage. Comme dans le cas stationnaire, les calculs sont poursuivis jusqu'au minimum local le plus proche de la solution linéaire ce qui fournit une solution approchée plausible.

III. EXPERIENCE, COMPARAISON AVEC LA THEORIE.

1. Présentation de la maquette.

Une aile rectangulaire, rigide et non vrillée a été construite pour l'étude des phénomènes dus au décrochage. Le profil utilisé est un OA 209 tout au long de l'envergure. Des mouvements d'oscillation en tangage autour de la ligne du quart avant peuvent être imposés à la maquette au moyen d'un vérin hydraulique. L'amplitude des mouvements est limitée à $\pm 5^\circ$ autour d'une incidence moyenne donnée. La valeur absolue de l'incidence ne peut dépasser 23° . Cinq sections (Fig 2) sont instrumentées chacune par 33 tubes de pression statique qui donnent la valeur moyenne de la pression et par 23 capteurs instationnaires qui fournissent la partie instationnaire de la pression. Les répartitions de pression à l'extrados et à l'intrados des sections instrumentées ont été enregistrées, mais seuls les résultats intégrés (portance et moment), peuvent être comparés avec les résultats fournis par la théorie simplifiée présentée au paragraphe précédent. Dans le dispositif expérimental, trois haubans rigidifiaient l'aile pour éviter, ou tout au moins minimiser, les flexions de celle-ci. Une expérience préliminaire a été effectuée en novembre 1983 et des résultats plus complets ont été obtenus en février et mars 1985 ainsi qu'en juillet et août 1986. Les deux premières expériences ont été réalisées dans la soufflerie S2 de Chalais-Meudon et la dernière dans la soufflerie S2 de Modane. Les résultats les plus complets ont été obtenus pour une vitesse de vent de 95 m/s c'est à dire pour un nombre de Mach proche de 0,3.

2. Décrochage stationnaire en attaque droite .

2.1. Résultats expérimentaux .

De nombreuses difficultés ont été rencontrées au cours de l'expérience . Après ces trois séries d'essais , on en a conclu que le décrochage n'est pas un phénomène réellement stationnaire . On a constaté une importante fluctuation des mesures en ce qui concerne la répartition de pression sur les profils instrumentés . Pour réduire autant que possible les effets de ces fluctuations , un grand nombre d'acquisitions (2000 ou 4000) sont moyennées . En dépit de cette procédure , les résultats obtenus pour la portance (fig 3) et pour le moment (fig 4) , présentent encore une dispersion importante lorsque l'incidence est supérieure à 15° . Il semble que ce phénomène soit caractéristique du décrochage stationnaire et que l'on ne puisse espérer une amélioration des résultats en raffinant le procédé expérimental .

On a également constaté que la manière - croissante ou décroissante - par laquelle les incidences désirées sont atteintes intervient beaucoup . Des incidences croissantes ont tendance à donner de plus hautes valeurs pour la portance et des incidences décroissantes de plus faibles valeurs . Comme on le voit sur les figures 3 et 4 pour la portance et le moment , il est possible de définir une limite supérieure et une limite inférieure par des courbes relativement lisses . On peut dire en ce qui concerne la limite supérieure que pour une raison physique indéterminée , le profil a "oublié" de décrocher , au contraire , pour la limite inférieure , le décollement le plus étendu possible s'est développé à l'extrados du profil . La possibilité de définir une limite inférieure pour les courbes de C_L et de C_M est d'un grand intérêt pour l'hélicoptère . En effet , les expériences réalisées avec des mouvements d'oscillation de grande amplitude ont montré , que dans tous les cas , les boucles de C_L et de C_M instationnaires sont approximativement centrées sur la limite inférieure des courbes de C_L et de C_M statiques . Les oscillations de grande amplitude semblent donc forcer le décrochage . Dans la suite de cet article , lorsque l'on parlera des courbes de C_L ou de C_M statique , on fera implicitement référence aux limites inférieures dans le cas des grandes incidences .

2.2. Comparaison théorie-expérience

Pour tenter une comparaison entre la théorie et l'expérience , il est nécessaire de disposer d'essais bidimensionnels stationnaires . Dans le cas de grandes incidences , les résultats expérimentaux dépendent beaucoup du nombre de Reynolds et sans doute aussi de la turbulence de la soufflerie . Comme on ne disposait pas des courbes correspondant aux conditions expérimentales pour le profil OA 209 , on a choisi d'utiliser les mesures effectuées sur la section 5 en attaque droite comme courbes bidimensionnelles de C_L et de C_M . La section 5 est la plus proche du plancher de la soufflerie et la présence de celui-ci double la longueur effective de la maquette . Le coefficient d'allongement effectif de celle-ci devient alors égal à 10 . Dans le cas linéaire , une correction simple [2] peut être apportée pour tenir compte de la position en envergure de la section 5 et de l'allongement fini de l'aile . Cette correction est également appliquée dans le cas des grandes incidences bien que l'on sorte de son domaine de validité . A partir des données bidimensionnelles , la théorie exposée au paragraphe II permet le calcul de la portance (fig 3) et du moment (fig 4) . Pour la portance , l'accord entre la théorie et l'enveloppe inférieure des mesures expérimentales est excellent pour toutes les sections , même pour la section 1 proche de l'extrémité libre . Pour le moment des forces de portance , si l'accord est bon pour les sections internes 3-4-5 , il n'en est pas de même pour la section 1 où les faibles incidences aérodynamiques ne peuvent induire le décrochage . De ce fait , la théorie donne une valeur quasi nulle pour le moment en section 1 . En cette section , la répartition de pression à l'extrémité de l'aile est profondément affectée par l'effet du tourbillon d'extrémité [4] mais la portance globale reste élevée ce qui explique le bon accord pour la portance et les erreurs pour le moment . Pour la section 2 , la différence entre les valeurs théoriques et expérimentales suggère que l'effet du tourbillon d'extrémité se fait encore sentir en cet endroit .

3. Décrochage instationnaire en attaque droite

3.1. Résultats expérimentaux .

La maquette peut osciller autour du quart avant , une fréquence fondamentale de 4,69 Hz a été choisie (fréquence réduite de 0,039) . L'amplitude des oscillations est limitée à $\pm 5^\circ$. L'incidence moyenne peut être choisie entre 0° et 18° . On ne présentera ici que deux cas d'oscillation harmonique pure . Dans le premier cas , l'incidence géométrique moyenne de l'aile est de 14° et le fluide se sépare et se rattache périodiquement à l'extrados de l'aile . Le second cas , pour une incidence moyenne de 18° est plus facile à traiter car l'aile reste dans le régime décroché tout au long du cycle d'oscillation . Le décrochage instationnaire n'est pas un phénomène strictement répétitif , au moins pour la partie du cycle correspondant aux incidences décroissantes au cours de laquelle le fluide se rattache à l'extrados . De ce fait , on est amené à moyenner un grand nombre (en général 40) d'enregistrements pour réduire la dispersion des résultats .

3.2. Comparaison théorie-expérience .

Pour une incidence moyenne de 14° et des oscillations sinusoïdales de $\pm 5^\circ$, on donne en figures 5 et 6 les valeurs expérimentales et théoriques de la portance et du moment . On a reporté en abscisse l'incidence géométrique de l'aile qui est la même en toute section puisque l'aile est non vrillée . L'accord théorie-expérience reste acceptable pour la portance en toute section bien que des différences significatives apparaissent pour les sections 4 et 5 . Pour le moment des forces aérodynamiques , l'accord est très satisfaisant pour les sections internes 3-4-5 . Pour les sections externes 1 et 2 , comme en stationnaire , la présence du tourbillon d'extrémité vient modifier la répartition de pression et ne peut être pris en compte par la théorie .

En figure 7 et 8 , on a reporté la portance et le moment pour une incidence moyenne de l'aile de 18° et des oscillations de $\pm 5^\circ$ degrés d'amplitude . Avec de telles valeurs , le fluide reste décroché tout au long du cycle d'oscillation et la corrélation théorie expérience est améliorée pour la portance (fig 7) . Pour le moment (fig 8) , on peut faire les mêmes commentaires que dans le cas précédent pour une incidence moyenne de 14° . Toutefois le désaccord est encore plus grand pour les sections 1 et 2 puisque le tourbillon d'extrémité est plus intense .

4. Décrochage stationnaire en attaque oblique .

4.1. Résultats expérimentaux .

L'aile peut être inclinée dans la soufflerie d'un angle de 20 degrés vers l'avant ou vers l'arrière . Les deux configurations ont été expérimentées . Ce qui a été dit en attaque droite sur la dispersion des mesures dans le cas de grandes incidences est encore vrai ici . Toutefois , on peut toujours définir une enveloppe inférieure pour la portance et pour le moment . Seule la borne inférieure est prise en compte pour les comparaisons théorie-expérience et c'est elle qui est donnée en figures 9 et 10 .

4.2. Données bidimensionnelles pour la théorie .

La théorie a été exposée au paragraphe II mais elle nécessite des données bidimensionnelles pour caractériser le profil . Ces données dépendent des conditions d'écoulement , des nombres de Mach et de Reynolds , de la turbulence etc ... Dans le cas de l'attaque oblique , le trajet des lignes de courant à l'extrados du profil est modifié . Le gradient de pression que subit une particule du fluide lors de son trajet est donc lui aussi affecté par l'angle de dérapage de l'aile ce qui change le moment d'apparition du décrochage . La variation d'épaisseur le long de la corde du profil est répartie sur une distance plus grande ce qui retarde le décrochage . Il serait nécessaire d'effectuer des expériences bidimensionnelles en attaque oblique , c'est à dire pour une aile non vrillée , d'allongement infini , en

dérage par rapport au vent de la soufflerie . De telles expériences sont difficiles à réaliser (effets de parois) mais la référence [5] donne une procédure simple pour introduire l'effet du dérage . Si Λ est l'angle de dérage et α l'incidence aérodynamique de l'aile mesurée suivant la normale à l'envergure ,

$$C_L(\alpha, \Lambda) = \frac{1}{\cos \Lambda} C_{L0}(\alpha \cos \Lambda) \quad (3)$$

où C_{L0} est le coefficient de portance en attaque normale c'est à dire pour $\Lambda = 0$

La formule 3 donne des valeurs identiques si Λ est changé en $-\Lambda$. On obtient donc la même chose en flèche avant ou en flèche arrière .

4.3. Comparaison théorie-expérience dans le cas d'une flèche arrière .

Des expériences ont été réalisées avec une flèche arrière de 20° . Comme il a été dit au paragraphe II , dans la théorie , on s'est volontairement limité à une modélisation de l'aile par ligne portante unique puisque l'on cherche à ramener le décrochage à un paramètre unique : l'incidence aérodynamique locale du profil d'aile . De ce fait , l'extrémité libre de l'aile rectangulaire est mal représentée ce qui fait que l'on n'obtient pas de bons résultats en section 1 même dans le cas de faibles incidences . En linéaire des calculs ont été effectués avec 4 lignes portantes , ils sont en bon accord avec l'expérience pour les incidences faibles mais on ne peut les étendre pour inclure le décrochage .

On trouve en figure 9 les résultats théoriques qui doivent être comparés avec la borne inférieure des points expérimentaux . Pour les grandes incidences , on constate que la théorie donne en section 5 des résultats trop faibles . Pour les sections 2 et 3 les résultats théoriques sont trop forts . La section 4 étant intermédiaire , en cet endroit on a des résultats convenables mais non significatifs . En section 1 le décrochage n'est pas un phénomène important , les erreurs constatées sont dues à la modélisation par ligne portante unique .

Tout se passe donc comme si un flux radial allant d'une zone à grande incidence (le pied de pale) vers une zone à incidence aérodynamique plus faible (l'extrémité libre) , induisait un déclenchement prématuré du décrochage . Le cas de la section 5 n'est pas clair car on ne peut négliger les effets de la paroi de la soufflerie .

4.4. Comparaison théorie-expérience dans le cas d'une flèche avant .

Les expériences ont été réalisées avec une flèche avant de 20° , les mesures sont données en figure 10 . La section 1 , toujours pour les mêmes raisons est mal modélisée . En section 5 la théorie est maintenant en bon accord avec l'expérience mais elle est trop pessimiste pour les sections 2-3-4.

Tout se passe donc comme si un flux radial allant d'une zone à faible incidence (l'extrémité libre) vers une zone à incidence aérodynamique plus grande (le pied de pale) , retardait le déclenchement du décrochage .

5. Décrochage instationnaire en attaque oblique

Comme on a pu le constater en figure 9 et 10 , le décrochage en attaque oblique n'est pas correctement prédit par la théorie . On ne peut donc espérer obtenir de meilleurs résultats en instationnaire . On trouvera cependant en figure 11 a et b à titre indicatif les courbes de portance théoriques et expérimentales dans le cas d'une oscillation de tangage de $\pm 5^\circ$ autour d'une incidence moyenne de 15° . En examinant les résultats expérimentaux , on constate que les boucles de décrochage sont beaucoup plus ouvertes dans le cas de la flèche arrière que dans le cas de la flèche avant . C'est particulièrement vrai pour les sections 3 et 4 qui sont les sections les plus bidimensionnelles . En ces sections , la théorie ne fait guère de différence entre la flèche avant et la flèche arrière puisque l'on ne prend pas en compte l'effet du gradient d'incidence sur le décrochage . Dans pratiquement tous les cas , sauf pour la section 1 , la théorie est trop optimiste pour la partie

correspondant aux incidences croissantes et trop pessimiste pour les incidences décroissantes lorsque le fluide se recolle à l'extrados de l'aile . Ceci est particulièrement vrai dans le cas de la flèche avant .

IV. SYNTHÈSE DES RESULTATS OBTENUS .

Dans cet article , on a cherché à développer une théorie qui serait capable d'étendre les résultats expérimentaux bidimensionnels sur profil au cas tridimensionnel d'une aile en attaque droite ou oblique . Cette théorie cherche à tout ramener un seul paramètre : l'incidence aérodynamique du profil . On peut s'interroger sur la validité d'une telle démarche . Comme on l'a vu au paragraphe précédent , l'aile en flèche avant se comporte différemment de l'aile en flèche arrière . Peut-on espérer améliorer les résultats en corrigeant les incidences aérodynamiques d'un effet de flèche ?

Supposons que cela soit possible . On corrige les incidences aérodynamiques des effets tridimensionnels , des effets de flèche , des effets de gradient d'incidence etc... Cette incidence corrigée détermine la somme et le moment des forces aérodynamiques sur le profil pris suivant la normale à l'envergure de l'aile . On peut alors tracer les courbes de coefficient de portance $C_L(\alpha)$ et de coefficient de moment $C_M(\alpha)$ en fonction de l'incidence aérodynamique locale corrigée . Puisque C_L et C_M ne dépendent que d'un seul paramètre α , on peut aussi tracer les courbes $C_M(C_L)$ où le coefficient de moment C_M est considéré comme fonction du coefficient de portance C_L . Ces courbes doivent être les mêmes pour les cinq sections instrumentées et doivent être indépendantes de l'angle de flèche si l'hypothèse du paramètre α unique est justifiée . Ces courbes , qui sont déduites des bornes inférieures des résultats expérimentaux sont données en figure 12 a-b-c pour l'attaque droite et pour la flèche avant ou arrière de $\pm 20^\circ$.

1. Aile en attaque droite .

Les courbes expérimentales $C_L(C_M)$ sont données en figure 12 a . Lorsque les incidences aérodynamiques sont faibles , le C_M reste voisin de zéro alors que le C_L croît . Au décrochage , le C_M varie très brusquement tandis que le C_L décroît . Ceci explique la forme des courbes obtenues pour les sections 2-3-4-5 où le coude très brutal qui apparaît pour $C_L \approx 1$ et $C_M \approx 0$ est caractéristique du début du décrochage . Si l'on augmente encore l'incidence , la valeur du moment se stabilise mais la portance continue de décroître ce qui explique le retour en arrière des courbes .

Pour la section 1 l'allure de la courbe $C_L(C_M)$ est toute autre . Le C_L ne cesse de croître et le C_M de décroître . Les incidences aérodynamiques restent faibles et il n'y a pas de décrochage mais le tourbillon d'extrémité de plus en plus intense fait reculer le foyer du profil et décroître le moment de façon presque linéaire .

Le fait que les courbes pour les sections 2-3-4-5 soient assez voisines les unes des autres explique que l'on ait pu obtenir des résultats convenables en attaque droite .

2. Aile en flèche avant

Les courbes expérimentales sont données en figure 12 b . Les courbes relatives aux sections 4 et 5 restent assez semblables aux courbes correspondantes de l'attaque droite . Il n'en est pas de même pour les sections 1 et 2 où le moment des forces aérodynamiques continue à décroître après le décrochage sans se stabiliser . Pour la section 1 , mis à part la pente de la courbe $C_L(C_M)$, l'effet caractéristique de la présence du tourbillon d'extrémité à lieu comme en attaque droite .

3. Aile en flèche arrière .

Sur la figure 12 c qui présente les résultats expérimentaux , toutes les sections , même la section 1 proche de l'extrémité libre de l'aile , ont des courbes qui présentent la forme caractéristique du décrochage . Ces courbes sont , entre elles , d'allure assez semblable mais elles ne sont pas superposables . On ne peut donc espérer obtenir de bons résultats dans les calculs théoriques .

V. CONCLUSION

Pour comprendre les phénomènes liés au décrochage instationnaire qui se produisent sur un rotor d'hélicoptère en vol avançant , des expériences plus simples , avec une aile rectangulaire en attaque droite ou oblique ont été réalisées .

Par ailleurs , les résultats obtenus ont été comparés avec ceux donnés par une théorie simple qui utilise les résultats bidimensionnels obtenus en soufflerie pour les étendre au cas tridimensionnel . Ce type de théorie est classiquement utilisé sous une forme ou sous une autre dans les calculs de rotors d'hélicoptère .

Comme on l'a vu dans cet article , si les résultats obtenus sont acceptables pour l'aile en attaque droite , il n'en est plus de même en attaque oblique . On a montré l'influence très importante du flux dirigé suivant l'envergure de l'aile , influence qui est différente suivant la direction de ce flux . Lorsque la vitesse du vent a une composante dirigée depuis une zone très décrochée vers une zone à faible incidence , c'est le cas de l'aile en flèche arrière , on constate un décrochage prématuré . A l'inverse , dans le cas de la flèche arrière , lorsque le vent a une composante de vitesse dirigée depuis une zone à faible incidence vers une zone à forte incidence , on a mis en évidence un certain retard à l'amorce du décrochage .

REFERENCES

- 1 - Costes C. , Costes J-J. and Pétot D. , *Unsteady stall modeling in three-dimensional flow* . La Recherche Aéronautique 1985-4 French and English editions .
- 2 - Costes J-J , *Etude du décrochage instationnaire tridimensionnel sur une aile rectangulaire* . La Recherche Aéronautique 1987-4 French and English editions .
- 3 - Costes J-J , *Equilibre aéroélastique d'un rotor d'hélicoptère en présence de forces aérodynamiques non linéaires* . La Recherche Aéronautique 1982-5 , French and English editions . See also AGARD conference proceedings 334 .
- 4 - Adler J. N. and Luttes M. W. , *Three-dimensionality in unsteady flow about a wing* . AIAA paper 85-0132, 23rd Aerospace Science Meeting , January 14-15 , Reno , Nevada , 1985 .
- 5 - Gormont R. E. , *A Mathematical model of unsteady aerodynamics and radial flow for application to helicopter rotors* . USA-AMRDL-TR-72-67 , May 1973 .
- 6 - Dat R, Tran CT, Petot D, *Modele phénoménologique de décrochage dynamique sur une pale d'hélicoptère*. 16ème colloque d'aérodynamique appliquée (AAAF). Lille, 1979.
- 7 - Petot D, *Modélisation du décrochage dynamique par équations différentielles*. La recherche Aéronautique 1989-5, éditions françaises et anglaises.

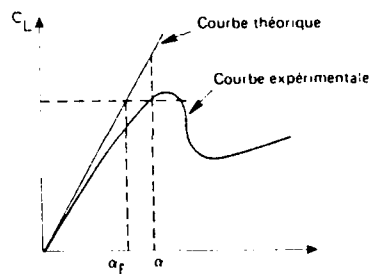


Fig. 1 - Coefficients de portance théoriques et expérimentaux
 α est l'incidence aérodynamique réelle, α_f est l'incidence aérodynamique effective. C'est l'incidence d'un profil théorique fictif dont le C_L serait égal au C_L mesuré sur le profil réel

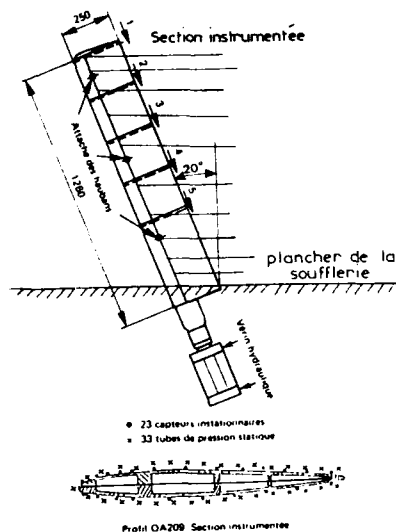


Fig. 2 - Maquette utilisée pour l'étude du décrochage instantané. 5 sections sont instrumentées. La maquette est représentée en attaque oblique de 20° vers l'avant.

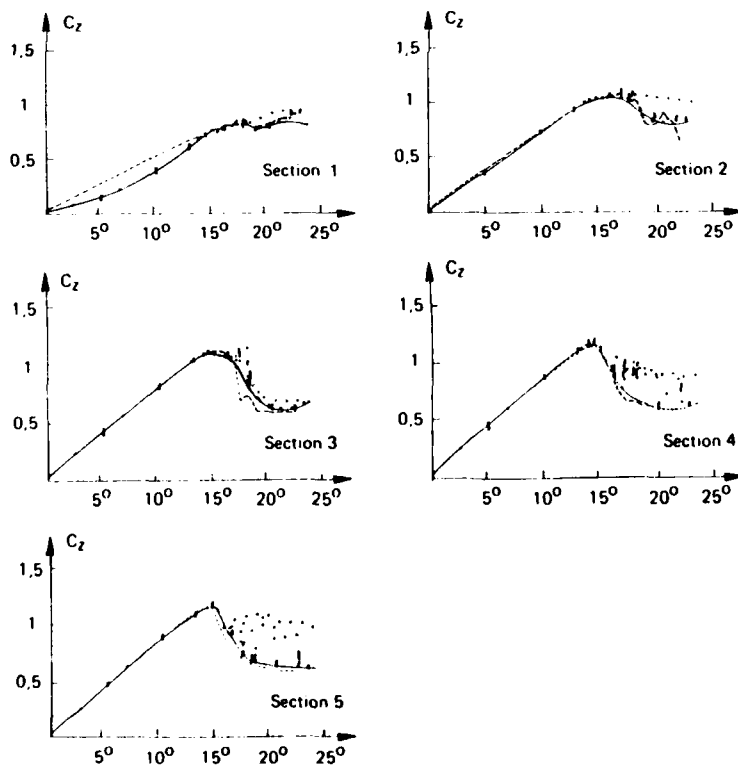


Fig. 3 - Coefficient de portance pour les cinq sections instrumentées. — Courbe expérimentale prise égale à la limite inférieure des points expérimentaux lors du décrochage. Théorie

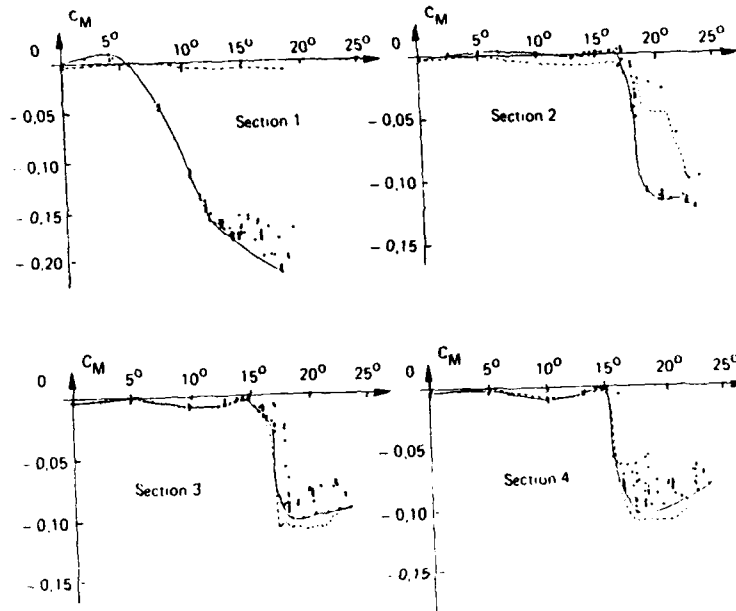


Fig. 4 - Coefficients de moment autour du quart avant mesurés et calculés pour les 5 sections instrumentées
 . Points expérimentaux
 - Courbe expérimentale, prise égale à la limite inférieure des points expérimentaux lors du décrochage
 --- Théorie

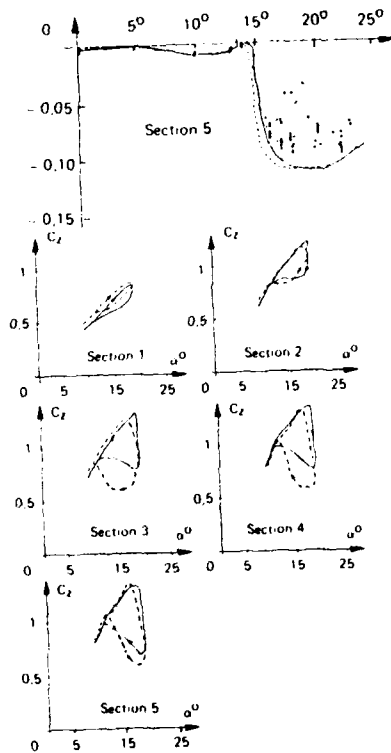


Fig. 5 Incidence $\alpha^\circ = 14 \pm 5^\circ$ fréquence 4.69 Hz.
 $Re = 1.72 \cdot 10^6$ — Exp S2 Ch 1985 ——— Théorie

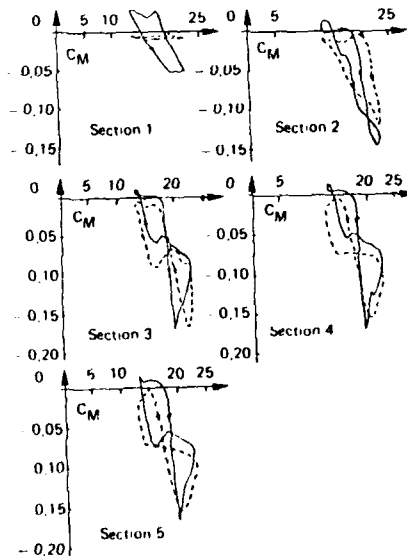


Fig. 6 Incidence $\alpha^\circ = 14 \pm 5^\circ$ fréquence 4.69 Hz.
 $Re = 1.72 \cdot 10^6$ — Exp S2 Ch 1985 ——— Théorie, coefficient de moment

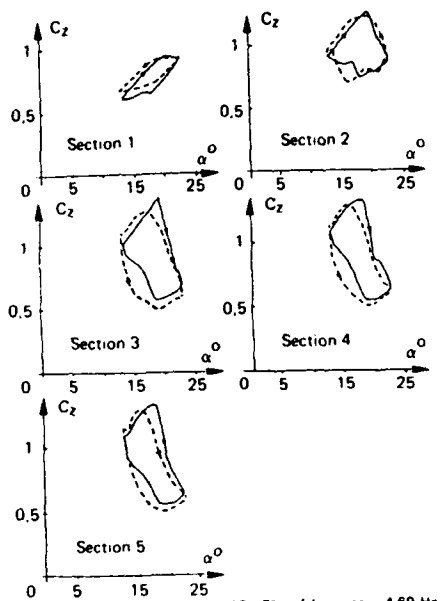


Fig. 7 - Incidence $\alpha = 18 \pm 5^\circ$, fréquence 4,69 Hz.
 $R_e = 1,72 \cdot 10^6$. — Exp. coefficient de portance S2Ch 1985. Théorie.

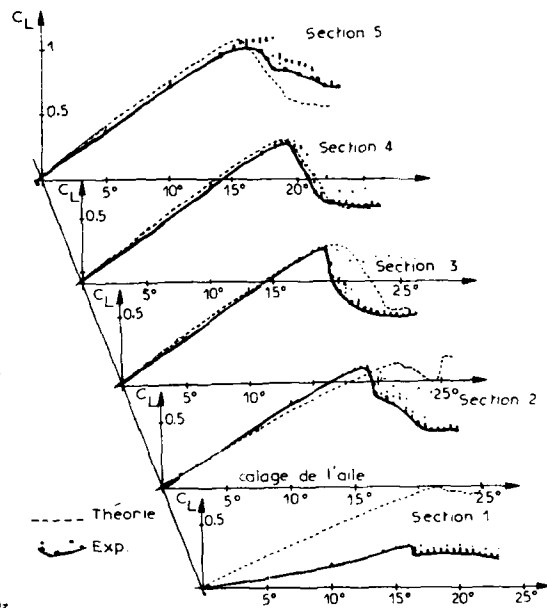


Fig. 9 - Aile avec 20° de flèche arrière.
 Coefficient de portance C_L en fonction
 du calage de l'aile pour les 5 sections
 instrumentées

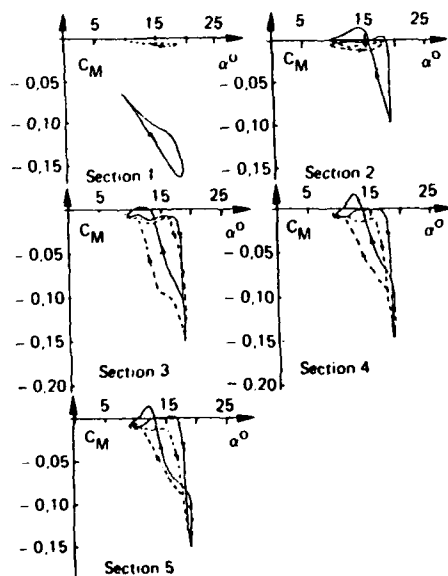


Fig. 8 - Incidence $\alpha = 18 \pm 5^\circ$, fréquence 4,69 Hz.
 $R_e = 1,72 \cdot 10^6$. — Exp. coefficient de moment S2Ch 1985. Théorie

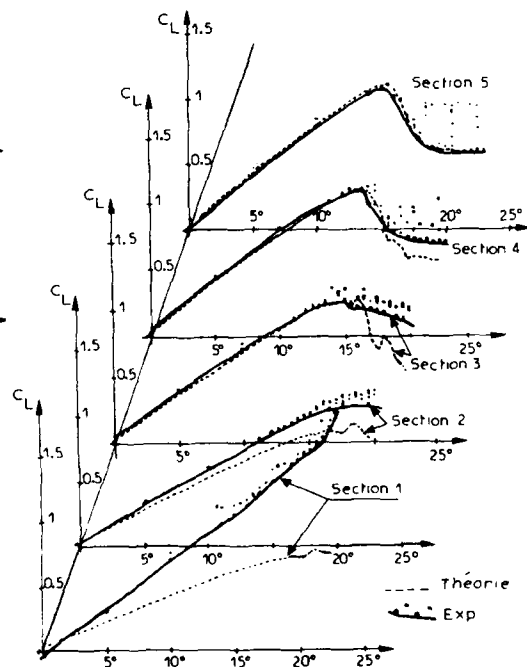


Fig. 10 - Aile avec 20° de flèche avant.
 Coefficient de portance C_L en fonction
 du calage de l'aile pour les 5 sections
 instrumentées.

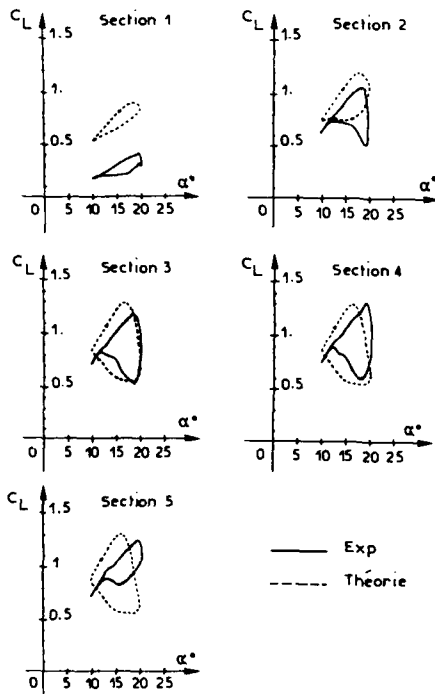


Fig. 11a - Aile avec 20° de flèche arrière
 $\alpha^\circ = 15 \pm 5^\circ$ $Fq = 4,69 \text{ Hz}$

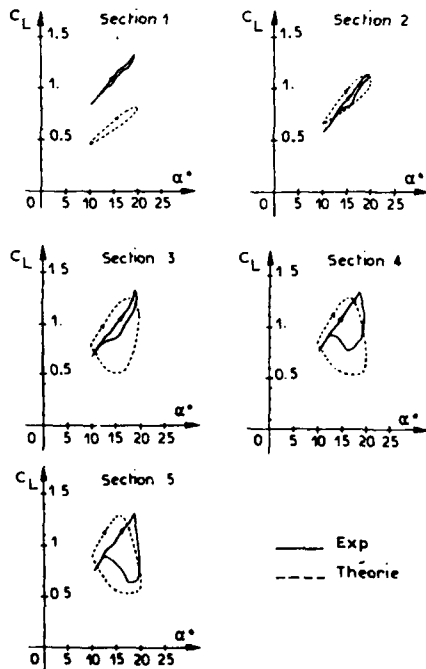


Fig. 11b - Aile avec 20° de flèche avant
 $\alpha^\circ = 15 \pm 5^\circ$ $Fq = 4,69 \text{ Hz}$

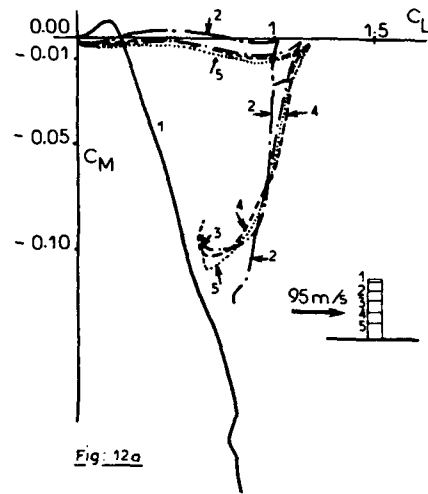


Fig. 12a

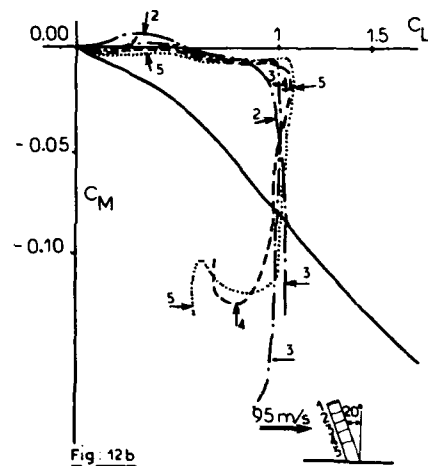


Fig. 12b

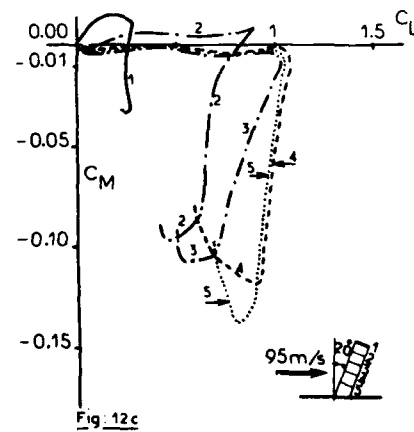


Fig. 12c

Fig. 12 - Courbes expérimentales $C_M(C_L)$ pour les 5 sections instrumentées.

UNSTEADY SEPARATED FLOW PHENOMENA CAUSING SELF-EXCITED STRUCTURAL OSCILLATIONS

by

L.E. Ericsson
Lockheed Missiles & Space Company, Inc.
P.O. Box 3504
Sunnyvale
CA 94088-3504
United States

SUMMARY

Because of steadily increasing performance demands, both aircraft and missiles operate at high angles of attack where separated flow often has a dominant influence on, especially, the unsteady aerodynamics. The penetration of the buffet boundary usually changes the structural response from the buffet-type to the self-excited type. This transfer occurs when the structural response starts interacting with the unsteady flow separation, generating negative aerodynamic damping. Separated flow aerodynamics are usually very nonlinear, and the self-excited response frequently takes the form of a limit-cycle oscillation.

NOMENCLATURE

c	two-dimensional chord length
d	sectional drag, coefficient $c_d = d/(\rho_\infty U_\infty^2/2)c$
f	frequency
h	cross-sectional height
K_1, K_2	proportionality constants, Eqs. (6) and (7)
l	sectional lift, coefficient $c_l = l/(\rho_\infty V_\infty^2/2)c$
m_y	sectional pitching moment, coefficient $c_m = m_y/(\rho_\infty V_\infty^2/2)c^2$
M	Mach number
M^*	highest Mach number for continuous subsonic aerodynamic characteristics
N	normal force, coefficient $C_N = N/(\rho_\infty U_\infty^2/2) S_r$
P	static pressure, coefficient $C_p = (P - P_\infty)/(\rho_\infty U_\infty^2/2)$
q	pitch rate
Re	Reynolds number, $Re = Vc/\nu_\infty$
S	Strouhal number, $S = fh/V$
S_r	reference area
t	time
U	horizontal velocity
V	crossflow velocity
\bar{V}	reduced velocity, $\bar{V} = S^{-1}$
x, y, z	cartesian coordinates
α	angle of attack
Δ	increment and amplitude
ϵ	rms wing root strain
ζ	damping, fraction of critical damping
ζ_0	structural damping
θ	perturbation in pitch and torsion

λ	wave length
ν	kinematic viscosity
ξ	dimensionless x-coordinate, $\xi = x/c$
ξ_{sp}	time lag effect of separation point movement
ξ_w	Karman - Sears wake lag parameter
ρ	fluid density
τ	dimensionless time, $\tau = V t/c$
$\omega, \bar{\omega}$	oscillation frequency, $\omega = 2 \pi f$; $\bar{\omega} = \omega c/U_\infty$

SUBSCRIPTS

a	attached flow
CR	critical
e	boundary layer edge condition
s	separated flow
SB	stability boundary
sp	separation point
v	vortex
w	wake
0	initial or trim condition
1,2	numbering subscript
∞	free stream condition

SUPERSCRIPTS

ⁱ	induced, e.g., $\Delta^i C_N$ in Fig. 9
-	time average, e.g., $\bar{c}_1(t)$ in Fig. 21

DERIVATIVE SYMBOLS

$\dot{\alpha}$	= $\partial \alpha / \partial t$
$\dot{C}_{m\alpha}$	= $\partial C_m / \partial \alpha$
\dot{C}_{mq}	= $C_{mq} + C_{m\dot{\alpha}}$; $C_{mq} = \partial C_m / \partial (\frac{c\dot{q}}{V})$; $C_{m\dot{\alpha}} = \partial C_m / \partial (\frac{c\dot{\alpha}}{V})$

1. INTRODUCTION

Until the recent demands on missiles and aircraft to maneuver at extremely high angles of attack, the structural response to unsteady separated flow was usually of the buffet type, i.e., the response to a forcing function of some type generated by flow separation. A very well documented source of buffet is shock-induced flow separation (Ref. 1), and methods have been established for prediction of the aircraft response to this buffet source (Ref. 2). One shortcoming of the methods in use (Refs. 2 and 3) is that they as a rule neglect the effect of flow separation on the aerodynamic damping. Early interpretation of the structural response in bending of a moderately swept wing showed that at buffet onset a large increase of the apparent aerodynamic damping occurred (Ref. 4). It was shown in Ref. 5 that such an increase of the damping could not be generated by shock-induced flow separation. A re-evaluation of the test data revealed that the originally extracted apparent aerodynamic damping was incorrect and that the corrected results (Ref. 3 and Fig. 1) were in good agreement with theoretical expectations (Refs. 5 and 6).

Thus, in the case of this wing buffet response to shock-induced boundary layer separation the separation-induced effect on the aerodynamic damping had not a significant impact on the structural response. However, the situation changes dramatically if the angle of attack is increased far beyond the value for buffet onset, as in the case of aircraft supermaneuvers (Refs. 7 and 8), when the vehicle aerodynamics become dominated by separated flow effects. Separation-dominated aerodynamics occur also at low angles of attack on components of missiles and launch vehicles, designed with little or no consideration to the aerodynamic environment. In these cases the dominant unsteady flow mechanism of concern is the separation-induced undamping, the negative aerodynamic damping.

2. ANALYSIS

The unsteady flow mechanism varies from the simple quasi-steady one to one in which time lag, accelerated flow and moving wall effects in various combinations supply the negative aerodynamic damping, with or without an interacting aerodynamic forcing function, such as the one supplied by Kármán vortex shedding. Examples of these different types of dynamic instability mechanisms will be presented.

2.1 Quasi-Steady Aerodynamics

The cable trays mounted on the main Space Shuttle booster (Ref. 9 and Fig. 2) are at transonic speeds subject to high velocity crossflow, induced by the solid rocket booster (Fig. 3). This creates the flow situation shown in Fig. 4. Figure 5 shows the aerodynamic characteristics of a similar cross-section, a $c/h=2$ rectangular profile (Refs. 10 and 11). The flow is separated at $\alpha = 0^\circ$, and a negative lift slope exists out to $\alpha=10^\circ$. For a cross-section in a plunging motion, generated by bending oscillation of the cable tray, the angle of attack is $\alpha = \dot{z}/V$ (see Fig. 6). Thus, the lift coefficient $C_L = C_{L\alpha} \dot{z}/V$ is negative, driving the plunging motion.

This negative damping will be generated until $\tan^{-1}(|\dot{z}|/V) > 10^\circ$, when $C_{L\alpha}$ becomes positive, and positive aerodynamic damping is produced. A limit-cycle oscillation results when the amplitude $\Delta z/h$ has reached the magnitude where the positive and negative damping contributions balance (cancel) each other. The limit cycle amplitude, determined in this manner (Ref. 12) by using experimental static test data (Refs. 10 and 11), like those in Fig. 5, agrees with experimental results (Ref. 13 and Fig. 7). Through an extension of the analysis in Ref. 12 the maximum possible limit-cycle amplitude for an arbitrary cross-section could be determined (Ref. 14). It bounds the available experimental data for galloping cables (Refs. 15, 16 and Fig. 8).

The negative aerodynamic damping discussed so far has been generated by classic quasi-steady theory, where the unsteady load is simply the product of the static derivative (e.g., $C_{L\alpha}$) and the instantaneous, equivalent angle of attack (e.g., \dot{z}/V). When one considers the torsional degree of freedom, θ in Fig. 6, one needs to add the time lag effect to the quasi-steady theory.

2.2 Time Lag Effect

In classic linearized theory the quasi-steady moment coefficient, $C_{m\alpha} \theta(t)$, gives no contribution to the out-of-phase θ -component, and can, therefore, not influence the aerodynamic damping in pitch, $C_{m\dot{\theta}} \dot{\theta}/V$. However, when accounting for the time lag effect the quasi-steady moment coefficient does affect the damping term. Through Taylor expansion one obtains

$$\begin{aligned} C_m(t) &= C_{m0} + C_{m\alpha} \theta(t-\Delta t) \\ &= C_{m0} + C_{m\alpha} \theta(t) - C_{m\alpha} \dot{\theta}(t) \Delta t \end{aligned} \quad (1)$$

For the negative nose load component discussed earlier one obtains the situation sketched in in Fig. 9. Even effects that are not truly due to convective time lag can often be expressed through

an effective time lag (Ref. 17). The figure shows how in the static case the separation-induced force $\Delta C_M(t)$ at $\alpha > 0$ is stabilizing. However, in the dynamic case the residual force, $\Delta C_M(t)$ at $\alpha = 0$, is generated by the flow separation created at the earlier time $t - \Delta t$, when $\alpha(t - \Delta t) > 0$, thus generating a force that drives the motion and, hence, is dynamically destabilizing. This property of the time lag, to make a statically stabilizing effect dynamically destabilizing, and vice versa, will exist for all cases where the quasi-steady concept is valid, in the present case for $c < \lambda/4$, i.e., for $\Omega = \omega c/V < \pi/2$.

From Ref. 17 one obtains the following expression for the effective phase lag

$$\left. \begin{aligned} \Delta \theta &= \dot{\theta} \Delta \tau = \Delta \tau \dot{c} \theta / V \\ \Delta \tau &= \xi_w + \xi_{sp} \end{aligned} \right\} \quad (2)$$

$\xi_w = 1.5$ and $\xi_{sp} = 0$ for a sharp-edged, rectangular cross-section (Ref. 17). Combining Eqs. (1) and (2) gives

$$\Delta C_{M\dot{\theta}} = \frac{\partial C_M(t)}{\partial \left(\frac{\dot{c} \theta}{V} \right)} = -C_{M\alpha} \Delta \tau \quad (3)$$

Equation (3) displays the opposition between static and dynamic stability discussed above and gives a quantitative expression for the negative damping illustrated in Fig. 9.

For the cable tray cross-section with rounded corners (Fig. 4), ξ_{sp} takes the following values (Ref. 17).

$$\xi_{sp} = \begin{cases} 0.75 \text{ turbulent stall} \\ 3.0 \text{ laminar stall} \end{cases} \quad (4)$$

Using Eqs. (2) - (4), with $C_{M\alpha}$ determined by static experimental results (Refs. 10, 11 and 18), the stability boundary shown in Fig. 10 was obtained for the Space Shuttle cable tray (Ref. 9). As the structural damping (ξ_0) was less than 5%, the cable tray was aerelastically unstable in its first torsional mode.

The results of the above analysis indicated that the structural integrity of the LO_2 cable tray could not be ensured with the existing design. The same was also true for the two aft SRB cable trays, which were directly exposed to the full axial flow over the HO tank. It was, therefore, decided that on the first Space Shuttle flight vehicle 20-deg flow ramps would be applied as upstream wind shields for the LO_2 and SRB cable trays, and also for some sections of the LH_2 cable trays (Ref. 9 and Fig. 11). The ramps for the different cable trays are visible in the pictures of the roll out of the first flight vehicle (Refs. 20, 21). They are still used (Fig. 12).

The analysis was by necessity very conservative, as neither static nor dynamic test results were available at the time for the actual cable tray cross section. However, the final analysis (Ref. 22), in which such experimental data was used, led to the same conclusion in regard to the need for aerodynamic fixes. The dynamic test (Ref. 23) also verified the soundness of the time lag concept used in the initial analysis, as is illustrated by the comparison in Fig. 13 between the "old" prediction (Fig. 10) and the aerelastic stability boundary obtained using the measured (Ref. 23) aerodynamic characteristics for the original LO_2 cable tray cross section. The agreement is remarkably good. The main difference is the change of the limiting Mach number for continuous subsonic aerodynamic characteristics, from the assumed value $M^* = 0.9$ to $M^* = 0.66$. The results in Fig. 10, obtained through linear analysis, are only valid for $M < M^*$, where $M^* < 1$. At $M > M^*$, the aerodynamics become nonlinear, and a different analytic method has to be used, as will be shown.

§ A simple method for determining the boundary for such "beam flutter" is described in Ref. 19.

2.3 Nonlinear Analysis

The linear analysis produces stability boundaries (Figs. 10 and 13), providing information similar to that for buffet-onset boundaries, warning the designer of possible problems if the boundary is crossed. In reality, the aerodynamic characteristics are often nonlinear^{##}, and structural failure occurs only if a certain response amplitude is exceeded. The aerodynamic effects of separated flow are usually nonlinear in character and a nonlinear analysis is needed to determine the amplitude of the limit cycle oscillation resulting when the total damping, aerodynamic plus structural, is zero.

In the initial cable tray analysis (Ref. 9) the presence of the ground plane surface of the main fuel tank was neglected (Fig. 14a). A later cable tray design, with its added heat protection material, brought the ground plane surface much closer (Fig. 14b), and its presence could no longer be neglected. Consequently, static and dynamic tests (Refs. 23-25) were performed in a more or less two-dimensional flow arrangement. The torsional moment around a mid-chord axis showed a discontinuous dependence on the angle of attack from $M = 0.7$ through $M = 1.45$ (Fig. 15). At $M = 0.7$, the cause of the moment discontinuity is a sudden complete separation of the flow on the underside of the cable tray when the angle of attack is changed from $\alpha = -3^\circ$ to $\alpha = -4^\circ$ (see Fig. 16). Pitch oscillations of the cable tray around the angle of attack where the discontinuity occurred (Ref. 23), gave the results shown in Fig. 17. Because of the problem of dynamic scaling, it was essential that the nonlinear dynamic test results in Fig. 17 could be predicted using corresponding static experimental data (Figs. 15 and 16).

In the nonlinear analysis the energy dissipation during one cycle of oscillation is computed, accounting for the nonlinear aerodynamics, including any discontinuity. In this manner an effective damping derivative is determined as a function of amplitude (see Ref. 26 for a detailed description).

The effective damping derivative, $C_{m\dot{\alpha}}$, determined in this manner, is inversely proportional to the amplitude in the case of a pure discontinuity without any associated static alpha-hysteresis.

In presence of such hysteresis $C_{m\dot{\alpha}}$ is also inversely proportioned to the reduced frequency, Ω . As a 50% increase of the pitching frequency had no measurable effect on the experimental results (Ref. 23), no consideration of static hysteresis effects was needed. Using the moment discontinuity in Fig. 15 the analysis (Refs. 22 and 24) gave the results represented by the solid line in Fig. 17.

Based upon this agreement between prediction and dynamic experimental results the aeroelastic characteristics shown in Figs. 18a and 19a could be predicted with the needed confidence level for $M = 0.7$. In a similar manner (see Ref. 27), the aeroelastic characteristics at $M = 0.92$ were also determined (Figs. 18b and 19b). The results indicate that, for the maximum measured structural damping $\zeta_0 = 1\%$, the resulting limit cycle amplitudes are 0.55 and 0.70 deg at $M = 0.70$ and 0.92, respectively. This is well beyond the structural capability of the cable-tray/thin-shell booster structure. Thus, the final aeroelastic analysis confirmed the need for protective flow ramps for the LO₂ and SRB cable trays established in the preliminary analysis (Ref. 9).

2.4 Accelerated Flow and Moving Wall Effects

The dynamic effects discussed so far have had no effect on the magnitude of the static force or moment vector. The effect of time lag is only to cause a phase lag between the motion vector and the force or moment vector. In this section dynamic effects that change the magnitude of the force and moment vectors will be discussed.

2.4.1 Accelerated Flow Effect.

The non-stationary Bernoulli equation gives

^{##} Structural nonlinearities are not considered here.

$$dp_e/d\xi = (\partial p_e/\partial \xi)_{\alpha=0} + (\partial p_e/\partial \alpha) (c\dot{\alpha}/V_e); \quad (5)$$

i.e., the local pressure gradient is less in the dynamic case than in the static case (at the same α) by the amount $-(\partial p_e/\partial \alpha) (c\dot{\alpha}/V_e)$. Thus, the boundary layer at separation has in the unsteady case a more favorable upstream time-history. As a result, the boundary layer is improved and can stand a higher pressure gradient before separating. It has been shown by Shamroth and McDonald (Ref. 28) that the quasi-steady pressure distribution prescribed by Eq. (5) gives the full unsteady boundary layer characteristics for frequencies and pitch rates as high as $\omega c/V = 2.0$ and $c\dot{\alpha}/V = 0.20$, respectively. As a result of the boundary layer improvement, the static stall angle can be exceeded by an amount $\Delta \alpha_{s1}$, giving a corresponding overshoot of static c_{lmax} (see Ref. 17)

$$\begin{aligned} \Delta c_{lmax} &= c_{la} \Delta \alpha_{s1} \\ \Delta \alpha_{s1} &= K_1 \frac{c\dot{\alpha}}{V} \end{aligned} \quad (6)$$

That is, the static lift vector at lift maximum is increased in magnitude by Δc_{lmax}

2.4.2 Moving Wall Effect

The other dynamic-stall-overshoot component, $\Delta \alpha_{s2}$, is caused by the "leading-edge-jet" (Fig. 20). As the airfoil leading edge moves upward during the "upstroke", the boundary layer is strengthened and stall delayed due to the vastly different tangential wall velocities between the stagnation point and the top of the airfoil, a short distance downstream. Thus, the boundary layer has a fuller profile and is, therefore, more difficult to separate. The "rolling leading edge" analogy used in Fig. 20 to describe the "leading edge jet" effect is investigated in detail in Ref. 29. In a first approximation, $\Delta \alpha_{s2}$ is proportional to the leading edge plunging velocity \dot{z}_{LE} , (Ref. 17). That is

$$\Delta \alpha_{s2} = -K_2 \frac{\dot{z}}{V} \quad (7)$$

2.4.3 Dynamic Experimental Results

Figure 21 shows the results obtained by Halfman et al (Ref. 30) when oscillating an airfoil in pitch at angles of attack well beyond the static stall angle. It is shown in Ref. 17 how convective time lag and accelerated flow effects can delay flow separation. However, in the case of 6° amplitude pitch oscillations around $\alpha = 22^\circ$, the minimum angle of attack is 16 deg, well above the static stall angle, $\alpha_s < 12^\circ$. Thus, a flow mechanism acting in the nose region to cause flow reattachment is needed. The oscillating airfoil provides such a mechanism through the so called moving wall effect, the moving wall/wall jet analogy shown in Fig. 20.

Note that the moving wall effect in Fig. 20 is reversed in the case of a plunging airfoil, promoting flow separation when \dot{z}/U_∞ increases during the downstroke, producing the negative damping generated by dynamic stall for plunging oscillations (Ref. 31 and Fig. 22). The moving wall effect influences transition in the same manner (Fig. 23). That is, it generates negative damping for the experimentally observed divergent bending oscillations of a 25 deg swept wing (Refs. 32, 33 and Fig. 24). One fix is, of course, to fix the location of transition, as was done in the test (Ref. 33) by use of blowing (the "turbulent boundary layer" portion of the time trace in Fig. 24a was the result of applying blowing at 5% chord to fix transition).

In all the cases discussed so far the flow mechanism generating negative aerodynamic damping is unaffected by the presence of a forcing function: of the buffet type, for example. That is, there is no interaction causing a change of the aerodynamic forcing function. However, there are cases in which such interaction does take place.

2.5 Aerodynamic Coupling with Forcing Function

Of the flow ramps placed on the Space Shuttle to protect the cable trays (Fig. 11) the SRB cable-tray fairings complicated the Shuttle stacking procedure and required very time-consuming manual work on the launch pad to complete the installation. Thus, the SRB trays were redesigned to eliminate this time delay of approximately two days.

The new design moved the rectangular ($c/h = 1.96$) SRB cable tray closer to the surface of the external tank, resulting in a much stiffer support structure. The natural frequencies, both in bending and torsion, then fell in the Kármán vortex shedding range, and a new analysis had to be performed to determine how the aeroelastic stability of the new SRB cable tray was affected by Kármán vortex shedding (Ref. 34).

The coupling between the cable tray motion and Kármán vortex shedding (Ref. 35) was assumed to be similar to the coupling between the motion and associated moving wall effects of a circular cylinder in translational oscillations and the Kármán vortex shedding, resulting in the so called lock-on phenomenon (Refs. 36 and 37). This is, of course to be expected. However, for oscillation frequencies above the Strouhal frequency, i.e., for $\bar{V} < \bar{V}_{cr} \approx 11$, where $\bar{V} = S^{-1}$, the response amplitude goes to zero (Fig. 25). It is shown in Ref. 35 that the lock-on of Kármán vortex shedding on rectangular cylinders provides damping at $\bar{V} < \bar{V}_{cr}$ (Fig. 26). For torsional oscillations, there are also \bar{V} -regions with positive aerodynamic damping (Ref. 37 and Fig. 27). The stability boundaries for the SRB cable tray corresponding to those in Figs. 26 and 27 are shown in Figs. 28a and 28b, respectively. Similarly, the coupling between airfoil motion and Kármán vortex shedding provides the experimentally observed high frequency flutter boundary at $Q = \omega c/U_\infty \approx 2$ for the straight wing of the first Space Shuttle Orbiter configuration (Refs. 40, 41 and Fig. 29).

3. SCALING

The problem of using subscale test results for prediction of full-scale characteristics increases in difficulty as the aerodynamics become more and more dominated by separated flow effects. Because of the strong coupling existing between vehicle motion and boundary layer transition (Ref. 42), dynamic simulation of viscous flow effects in a ground test facility is only possible if the test is performed at the full-scale Reynolds number (Ref. 43). The problem is complicated further by the strong interdependence of Reynolds number and compressibility effects (Refs. 44 and 45).

In spite of these difficulties it is sometimes possible to extrapolate from dynamic subscale tests to full-scale dynamics using analytical means (Refs. 46 and 47). A necessary condition for this extrapolation is that the test and full-scale Reynolds numbers are located on the same side of the critical range. Before the method described in Refs. 46 and 47 is extended to include moving wall effects, it is also required that such effects be small, which in turn depends upon geometric details and ambient flow conditions.

4. CONCLUSIONS

The conclusion to be drawn from the shown examples of self-excited oscillations, caused by separated flow, is that when the buffet boundary is penetrated much closer cooperation and interaction than before is needed between structural and aerodynamic dynamicists.

5. ACKNOWLEDGEMENTS

The author is indebted to J. Peter Reding, with whom he has performed numerous analyses in the past under contracts to NASA and Navy DOD, the summarized results of which form a substantial part of the present paper.

6. REFERENCES

1. Pearcy, H. H., "A Method for the Prediction of the Onset of Buffeting and other Separation Effects from Wind Tunnel Tests on Rigid Models," AGARD Report 223, Oct. 1958.
2. John, H., "Critical Review of Methods to Predict the Buffet Capability of Aircraft," AGARD-R-623, Sept. 1974.
3. Mabey, D. G., "Prediction of the Severity of Buffeting," Paper 7, AGARD LS-94, Three-Dimensional and Unsteady Separation at High Reynolds Numbers, 1973.
4. Jones, J. G., "The Dynamic Analysis of Buffeting and Related Phenomena," Paper 23, AGARD-CP-102, 1972.
5. Ericsson, L. E., "Dynamic Effects of Shock-Induced Flow Separation," J. Aircraft, Vol. 12, No. 2, Feb. 1975, pp. 86-92.
6. Ericsson, L. E., "Erratum: Dynamic Effects of Shock-Induced Flow Separation," J. Aircraft, Vol. 18, No. 7, July 1981, p. 608.
7. Herbst, W. B., "Future Fighter Technology," J. Aircraft, Vol. 17, No. 8, Aug. 1980, pp. 561-566.
8. Herbst, W. B., "Supermaneuverability," Proceedings of Workshop on Unsteady Separated Flow, Aug 11, 1983, Francis and Luttges editors (1984), pp. 1-9.
9. Ericsson, L. E. and Reding, J. P., "Aeroelastic Stability of Space Shuttle Protuberances," J. Spacecraft and Rockets, Vol. 19, No. 4, July-Aug. 1982, pp. 307-313.
10. Nakamura, Y. and Mizota, T., "Aerodynamic Characteristics and Flow Patterns of a Rectangular Block," Reports of Research Institute for Applied Mechanics, Kyushu University, Japan, Vol. XIX, No. 65, March 1972.
11. Nakamura, Y. and Tomonari, Y., "Pressure Distributions on Rectangular Prisms at Small Incidence," Transactions of the Japan Society for Aeronautical and Space Sciences, Vol. 21, No. 54, 1979, pp. 205-213.
12. Ericsson, L. E., "Hydroelastic Effects of Separated Flow," AIAA Journal, Vol. 21, No. 3, March 1983, pp. 452-458.
13. Parkinson, G. V., "Aeroelastic Galloping in One Degree of Freedom," Proceedings of the Conference on Wind Effects on Buildings and Structures, National Physics Laboratory, England, June 1963, Vol. II, London, 1965, pp. 582-609.
14. Ericsson, L. E., "Limit Amplitude of Galloping Bluff Cylinders," AIAA Journal, Vol. 22, No. 4, April 1984, pp. 493-497.
15. Laneville, A. and Parkinson, G. V., "Effect of Turbulence on Galloping of Bluff Cylinders," Proceeding of Conference on Wind Effects on Buildings and Structures, 1971, pp. 787-797.
16. Nakamura, Y. and Mizota, T., "Unsteady Lifts and Wakes of Oscillating Rectangular Prisms," J. Eng. Mech. Div., Proceedings of the American Society of Civil Engineers, Vol. 101, No. EM6, Dec. 1975, pp. 858-871.
17. Ericsson, L. E. and Reding, J. P., "Fluid Mechanics of Dynamic Stall. Part I. Unsteady Flow Concepts," J. Fluids and Structures, Vol. 2, 1988, pp. 1-33.
18. Polhamus, E. C., "Effect of Flow Incidence and Reynolds Number on Low-Speed Aerodynamic Characteristics of Several Non-Circular Cylinders with Applications for Directional Stability and Spinning," NASA TR R-29, 1959.
19. Ericsson, L. E., "Engineering Approximation of Beam Flutter," J. Spacecraft and Rockets, Vol. 21, No. 1, Jan-Feb 1984, pp. 6-8.
20. Aviation Week, Jan. 5, 1981, p. 51.
21. Time, Jan. 12, 1981, front page.
22. Ericsson, L. E. and Reding, J. P., "Aeroelastic Analysis of the Space Shuttle External Tank Cable Trays, Final Technical Report," Lockheed Missiles & Space Company, Inc., Sunnyvale, CA, LMSC-D766543, April 1981.
23. Orlik-Bückemann, K. J. and LaBerge, J. G., "Dynamic Wind Tunnel Tests of the Simulated Shuttle External Tank Cable Trays," J. Spacecraft and Rockets, Vol. 20, Jan.-Feb. 1983, pp. 5-10.
24. Reding, J. P. and Ericsson, L. E., "Analysis of Static and Dynamic Wind Tunnel Tests of the Space Shuttle Cable Trays," J. Spacecraft and Rockets, Vol. 19, Sept.-Oct. 1982, pp. 412-418.
25. Ericsson, L. E. and Reding, J. P., "Separated Flow Dynamics of the Space Shuttle Cable Trays," AIAA Paper No. 81-1880, Aug. 1981.

26. Ericsson, L. E., "Unsteady Aerodynamics of Separating and Reattaching Flow on Bodies of Revolution," Recent Research on Unsteady Boundary Layers, Vol. 1, IUTAM Symposium, Laval University, Quebec, May 24-28, 1971, pp. 481-512.
27. Ericsson, L. E. and Reding, J. P., "Aeroelastic Characteristics of the Space Shuttle External Tank Cable Trays," J. Spacecraft and Rockets, Vol. 22, No. 3, May-June 1985, pp. 289-296.
28. Shamroth, S. J. and McDonald, H., "Application of Time-Dependent Boundary Layer Analysis to the Problem of Dynamic Stall," J. Applied Mech., Vol. 39, 1972, pp. 823-825.
29. Modi, V. J. and Mokhtarian, F., "Joukowski Airfoil with Circulation Control," AIAA Paper 85-1772-CP, Aug. 1985.
30. Halfman, R. L., Johnson, H. C., and Haley, S. M., "Evaluation of High Angle-of-Attack Aerodynamic Derivative Data and Stall Flutter Prediction Techniques," NACA TN 2533 (1951).
31. Liiva, J., Davenport, F. J., Gray, L. and Walton, I. C., "Two-Dimensional Tests of Airfoils Oscillating Near Stall," TR 68-13, US Army Aviation Laboratories, Fort Eustis, Virginia (1968).
32. Ericsson, L. E., "Transition Effects on Airfoil Dynamics and the Implications for Subscale Tests," J. Aircraft, Vol. 26, No. 12, Dec. 1989, pp. 1051-1058.
33. Mabey, D. G., Ashill, P. R., and Welsh, B. L., "Aeroelastic Oscillations Caused by Transitional Boundary Layers and Their Attenuation," J. Aircraft, Vol. 24, No. 7, July 1987, pp. 463-469.
34. Ericsson, L. E. and Reding, J. P., "Aeroelastic Stability Analysis of the New SRB Cable Tray," Lockheed Missiles & Space Company, Inc., CA, Tech. Rept. LMSC-D059412, Contract AS 2-65-0323, May 1983.
35. Ericsson, L. E., "Karman Vortex Shedding: Friend or Foe of the Structural Dynamicist?", J. Aircraft, Vol. 23, No. 8, Aug. 1986, pp. 621-628.
36. Ericsson, L. E., "Karman Vortex Shedding and the Effect of Body Motion," AIAA Journal, Vol. 18, Aug. 1980, pp. 935-944.
36. Ericsson, L. E., "Circular Cylinder Response to Karman Vortex Shedding," J. Aircraft, Vol. 25, No. 9, Sept. 1988, pp. 769-775.
38. Nakamura, Y. and Mizota, T., "Unsteady Lifts and Wakes of Oscillating Rectangular Prisms," J. Engineering Mechanics Div., ASCE, Vol. 101, No. EM6, Dec. 1975, pp. 855-871.
39. Otsuko, Y., Washizu, K., Tomizawa, H., Ohya, A., and Fujii, K., "Experiments on the Aeroelastic Stability of Prismatic Bars with Rectangular Section," Proceedings of the Third International Conference on Wind Effects on Buildings and Structures, Suikon Co., Ltd., Tokyo, Japan, Sept. 1971, pp. 891-898.
40. Ericsson, L. E., "Effect of Karman Vortex Shedding on Airfoil Stall Flutter," J. Aircraft, Vol. 24, No. 12, Dec. 1987, pp. 841-848.
41. Goets, R. C., "Exploratory Study of Buffet and Stall Flutter of Space Vehicle Wing Concepts," NASA LMP-072, May 1970.
42. Ericsson, L. E., "Review of Transition Effects on the Problem of Dynamic Simulation," AIAA Paper 88-2004, May 1988.
43. Ericsson, L. E. and Reding, J. P., "Scaling Problems in Dynamic Tests of Aircraft-Like Configurations," Paper 25, AGARD CP-227, Feb. 1978.
44. Ericsson, L. E. and Reding, J. P., "Stall Flutter Analysis," J. Aircraft, Vol. 10, No. 1, Jan. 1973, pp. 5-13.
45. Ericsson, L. E. and Reding, J. P., "Fluid Mechanics of Dynamic Stall. Part II. Prediction of Full Scale Characteristics," J. Fluids and Structures, Vol. 2, No. 2, March 1988, pp. 113-143.
46. Ericsson, L. E. and Reding, J. P., "Dynamic Simulation through Analytic Extrapolation," J. Spacecraft and Rockets, Vol. 10, No. 2, March-April 1982, pp. 160-166.
47. Ericsson, L. E. and Reding, J. P., "Analytic Extrapolation to Full-Scale Aircraft Dynamics," J. Aircraft, Vol. 21, No. 3, March 1984, pp. 222-224.

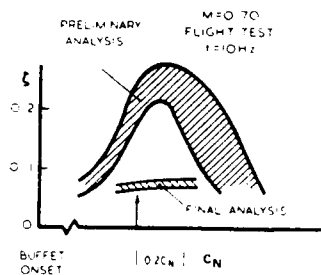


Fig. 1 Apparent damping of first wing-bending mode (Ref. 3)

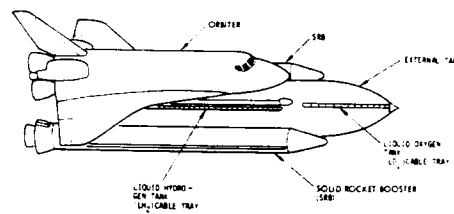


Fig. 2 Space Shuttle booster (Ref. 9)

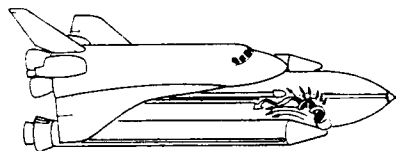


Fig. 3 Interpretative flow sketches of oil flow photographs (Ref. 9)

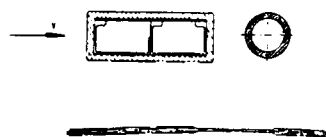


Fig. 4 Initial LO₂ tank cable tray configuration

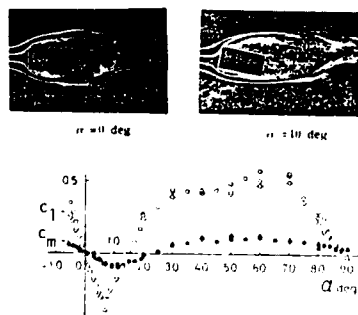


Fig. 5 Aerodynamic characteristics of a rectangular prism (Ref. 10)

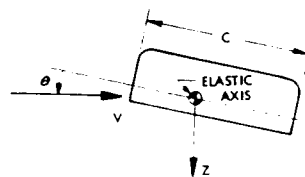


Fig. 6 Definition of cable tray coordinates

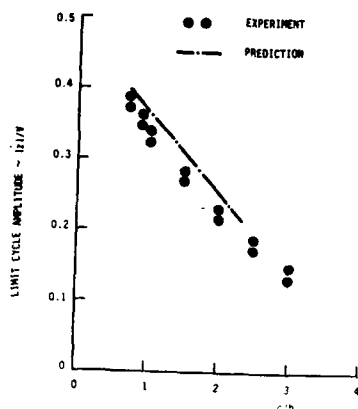


Fig. 7 Limit cycle amplitude of rectangular prisms describing plunging oscillations

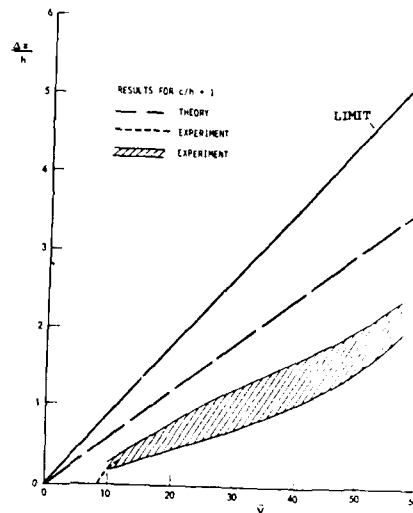


Fig. 8 Limit amplitude as a function of reduced velocity

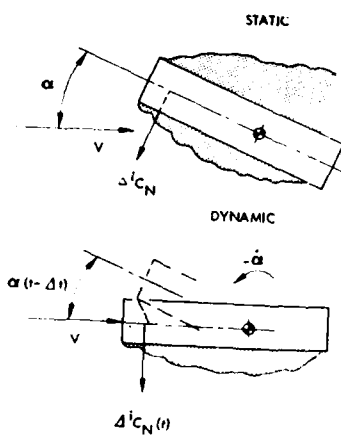


Fig. 9 Sketch of effective time lag effect

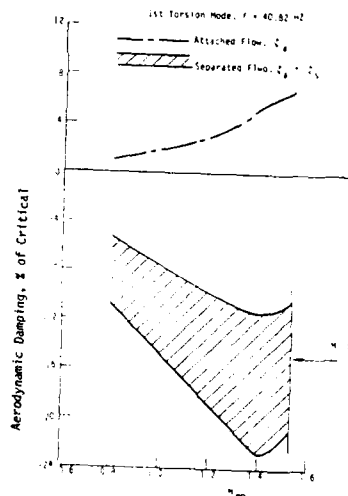


Fig. 10 Computed aerodynamic damping of cable tray torsional oscillations in subsonic local crossflow



Fig. 11 Cable tray protective flow ramps used on Space Shuttle

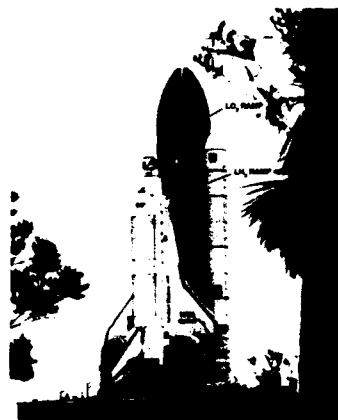


Fig. 12 Aerodynamic fixes on Space Shuttle flight vehicle

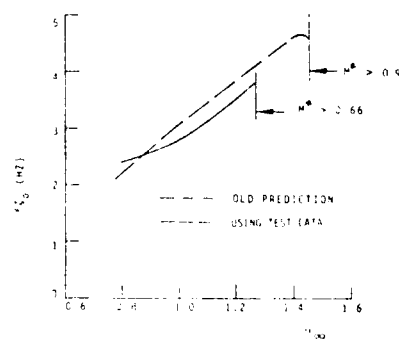
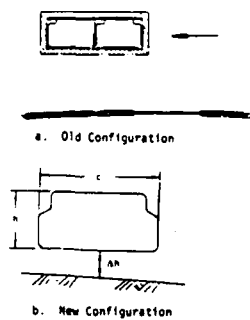
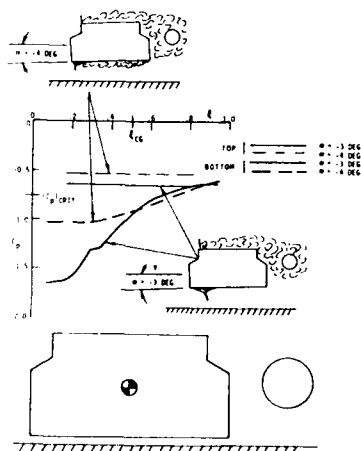
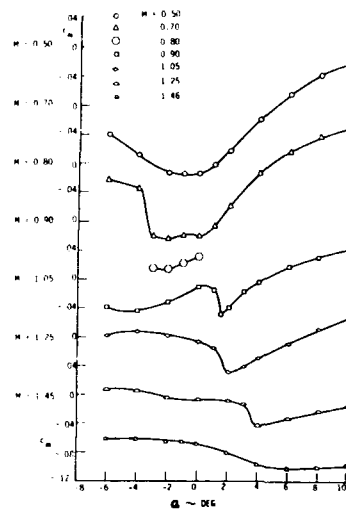
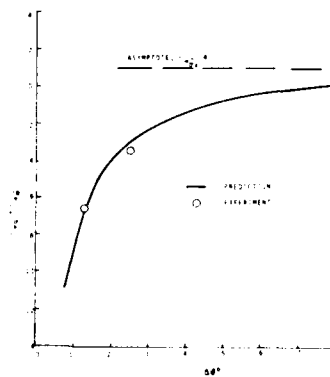


Fig. 13 Comparison between old and new stability boundaries for the LO₂ cable tray

Fig. 14 L O₂ cable tray geometriesFig. 16 Static pressure distribution on the L O₂ cable tray at $M=0.7$ Fig. 15 Static wind tunnel data for L O₂ cable trayFig. 17 Maximum adverse damping of the L O₂ cable tray as a function of amplitude at $M=0.7$

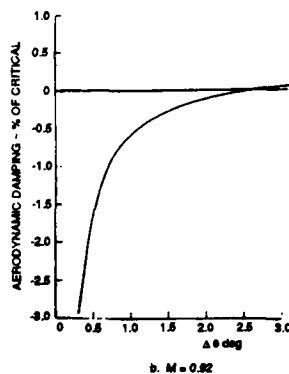
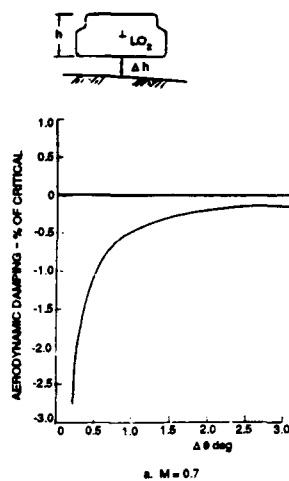


Fig. 18 Nonlinear aeroelastic characteristics of the LO₂ cable tray, $\Delta h/h = 0.55$

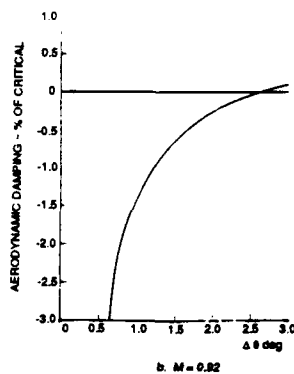
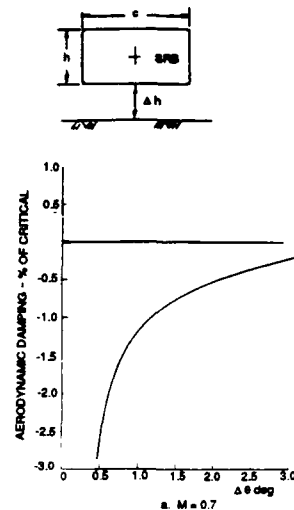


Fig. 19 Nonlinear aeroelastic characteristics of the SRB cable tray, $\Delta h/h = 1.41$

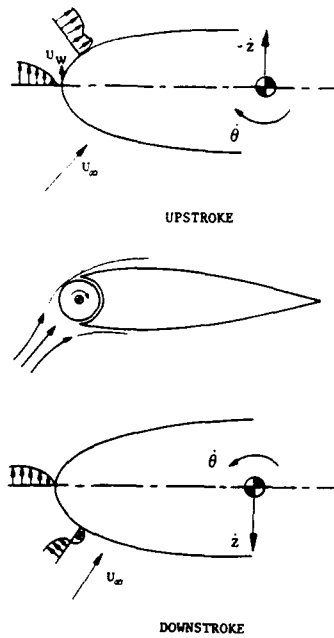


Fig. 20 Moving-wall/leading-edge-jet analogy

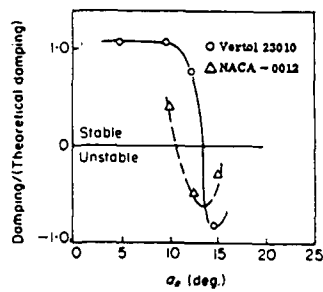


Fig. 22 Plunging-induced negative aerodynamic damping at stall-penetration (Ref. 31)

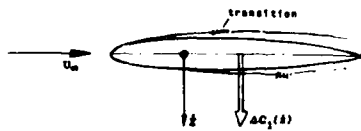


Fig. 23 Transition characteristics for plunging oscillations

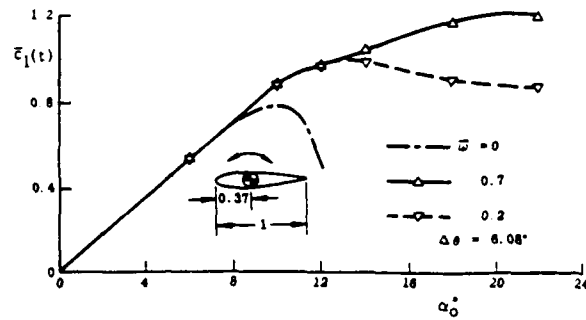
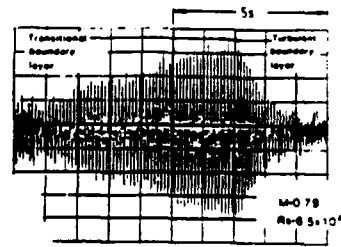
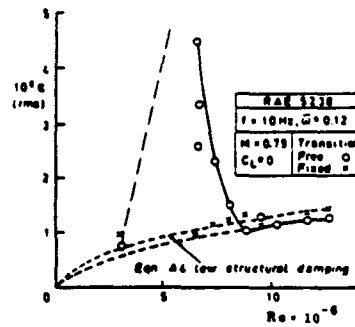


Fig. 21 Time-average lift of a thin airfoil describing pitching oscillations at $Re = 10^6$ (Ref. 30)



a. Typical Response of Wing-Tip Accelerometer



b. Variation of Unsteady Wing-Root Strain with Reynolds Number

Fig. 24 Self-excited wing bending oscillations (Ref. 33)

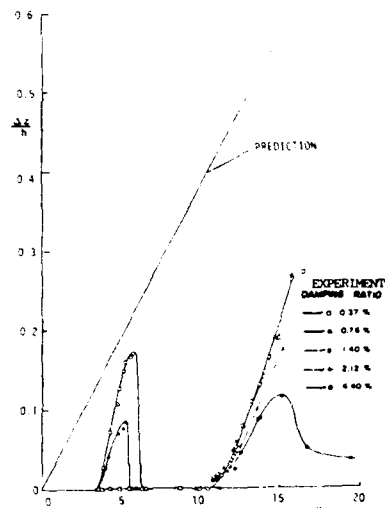


Fig. 25 Response characteristics of a $c/h = 2$ rectangular prism (Ref. 35)

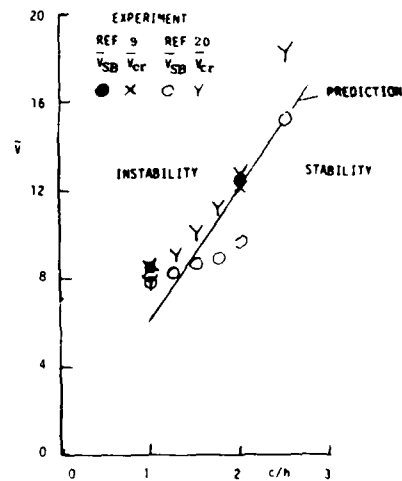


Fig. 26 Predicted and measured stability boundaries of galloping rectangular cylinders (Ref. 35)

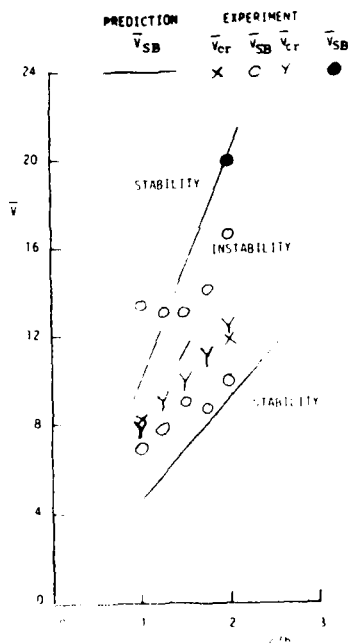


Fig. 27 Predicted and measured stability boundaries for torsional oscillations (stall flutter) of rectangular cylinders (Ref. 35)

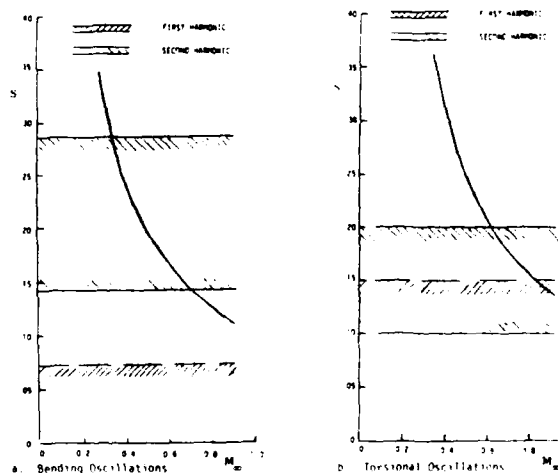
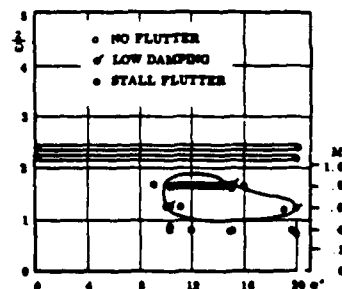


Fig. 28 Stability boundaries of the $c/h = 2$ rectangular SRB cable-tray cross section (Ref. 35)

Fig. 29 Stall flutter boundaries of a NACA-0012 airfoil (Ref. 41)



UNSTEADY AIRLOADS DUE TO SEPARATED FLOW ON AIRFOILS AND WINGS

John W. Edwards
NASA Langley Research Center
Hampton, Virginia 23665-5225

SUMMARY

Experimental and computational studies of airloads due to separated flows over airfoils and wings conducted at the NASA Langley Research Center are surveyed. Results are presented for cases involving local flow separation such as shock-induced separation, for the initiation of leading-edge vortex flows, and for cases involving unsteady airloads due to flows separating over remote aircraft components. Good correlation is obtained between experiment and computation for cases of locally separating flow and steady computations of vortex flows over delta wings and complex forebody geometries are shown. Physical flow modeling issues and computational requirements for the case of vertical tail buffeting are developed.

1. INTRODUCTION

Unsteady airloads due to flow separation are involved in a number of cases critical to the structural integrity of aircraft. As speed increases for moderate angles of attack typical of maneuvering flight near trimmed flight conditions, local transonic flow effects are encountered which lead to separated flow over the aft portions of lifting surfaces. Minimum flutter speed indices are often encountered in this transonic region, in conjunction with the onset of separated flow. The ability to predict these minimums is obviously tied to the ability to treat such "local" separated flows on wings.

For slightly lower speeds where more aggressive maneuvering is possible, unsteady airloads due to flow separation over "remote" components (e. g. main wing panel) leads to issues of buffet and structural fatigue on aft aircraft components. For these cases, as speed and/or angle of attack increase, smooth air flow over lifting surfaces breaks down in a variety of ways depending strongly upon the geometry. For lower sweep angles and blunt leading edges, flow separation may initiate near the trailing edge or near shocks and progress to completely separated and stalled conditions. For higher sweep angles and less blunt leading edges, leading edge flow separation bubbles foreshadow the development of leading edge vortex flows. At higher angles, unsteady and burst vortex flow in the vicinity of the wing and downstream lifting surfaces leads to strong unsteady airloads and buffeting. Flow conditions near the boundaries of these regions of different flow phenomena can be sensitive to a number of conditions and an understanding of these effects is called for in order to avoid adverse aeroelastic effects such as stall flutter, buzz and structural buffeting.

Research in these areas requires the comparison of experimental and computational results with the goal of achieving accurate predictive capability. Edwards^{1,2} provides surveys of these efforts for the transonic flutter problem while Mabey³ discusses the physical phenomena associated with unsteady transonic flow. Bobbitt's⁴ review of the issues involved in obtaining accurate results both from experiment and from computation is particularly noted. Regarding higher angle, vortex dominated flows, a trend of increasing interest by the aerodynamics community in unsteady flows is also noted. This is due to the inherent unsteadiness of such flows and to the ability of emerging computational fluid dynamics (CFD) methods to simulate their details. Newsome and Kandil⁵ discuss physical modeling issues involved in the computational prediction of vortex dominated flows and survey numerical results.

Experimental research in this area has been pursued separately by the aerodynamics and structures communities until recently. Mabey⁶ gives a recent assessment of dynamic loads due to flow separation while references 7-9 report buffeting tests on the F/A-18, F-15, and F-111 TACT aircraft. Cunningham¹⁰ documents unsteady pressure and flow visualization tests on an oscillating straked-delta wing model. Doggett and Cazier¹¹ give examples of recent experimental aeroelasticity studies at the NASA Langley Research Center including cases of aeroelastic response due to local and remote flow separation.

While the above research efforts focused on the flow unsteadiness in order to gain understanding of buffeting structural response, parallel efforts by the aerodynamics community have been directed at understanding the physics of separated vortical flows and the gathering of data bases for the validation of CFD codes. The experiments have involved detailed measurements on static, rigid models. Most of the basic research has studied vortex flows about idealized shapes; for instance, highly swept delta wings, sharp leading-edges, etc. Eisenaar et al.¹² summarize results from the International Vortex Flow Experiment, a joint program studying vortex flow development on a 65 degree cropped delta wing. Tests were conducted between Mach numbers of 0.4 and 4.0. Both sharp and rounded leading-edges were tested for validation of Euler and Navier-Stokes codes, respectively. Also sweep effects were studied with the inclusion of a 55 degree swept wing and configuration effects studied with the addition of a canard. Hummel¹³ summarizes another extensive series of basic wind tunnel tests including an aspect ratio 1.0, 75 degree swept, sharp-edged delta wing and a double-delta (80-60 deg.) wing.

Recognizing the need for higher quality flowfield data for code validation, Kjølgaard et al.¹⁴ and Pagan and Solignac¹⁵ utilized nonintrusive laser Doppler velocimetry (LDV) for off-the-surface flow measurements. Reference 14 gives data for the 75 degree delta wing at 20.5°. Reference 15 studied in detail the bursting of vortices generated by a 75 degree delta wing, giving root-mean-square (rms) velocity components in addition to mean velocities.

Recent wind tunnel investigations of vortex flows are beginning to show a merging of interest of the two communities upon the problem of tail buffeting. Sellers et al.¹⁶ describe LDV surveys of the flow over a YF-17 model in a low speed wind tunnel, giving mean and rms velocities for burst flows in the vicinity of twin vertical tails. Still, there remains a scarcity of data bases suitable for the validation of CFD computations of buffeting flows. More fundamentally, knowledge of the required level of detailed flow modeling is incomplete. For instance, compressibility and transonic effects at high subsonic speeds and high angles are largely unknown. The appendix to reference 12 discusses recent results on vortex bursting at high subsonic speeds, indicating that there is much that is not known about such flows.

Turning finally to the computation of vortex dominated flows, we note the use of the thin-layer Navier-Stokes equations to compute: unsteady vortex shedding over dynamically moving airfoils¹⁷, steady vortex flows about the 75 degree delta wing^{18,19}, detailed calculations of the flow about the F/A-18 forebody-leading edge extension configuration²⁰, and the calculation of steady vortex breakdown over the 75 degree delta wing^{18,21}. In addition, calculations of the flow over the complete F-16A configuration

have been presented in references 22 and 23. Edwards²⁴ assesses the status of these CFD methods for use in the prediction of tail buffeting and concludes that at least a three order of magnitude increase in computational efficiency is needed to make these methods viable as design tools.

This paper gives details of experimental and computational experience with unsteady airloads due to separated flows on airfoils and wings at the NASA Langley Research Center. First, studies involving airloads due to locally separating flows are discussed: airloads on a flexible wing responding to transonic shock-induced separation, aileron buzz, and the calculation of periodic oscillating flows over rigid airfoils. This is followed by cases involving the generation of vortical flows over airfoils, wings and bodies: vortex shedding over airfoils and bodies, and vortex formation over delta wing and forebody configurations. Next, two studies involving airloads due to remotely separating flows are discussed: buffeting tests on a twin-tailed fighter and LDV flowfield measurements of vortex flow about a twin-tailed fighter. Finally, a discussion of the computer resources which would be required for the computational prediction of tail buffet is given.

2. DESCRIPTION OF WIND TUNNEL FACILITIES

The experimental studies described herein were conducted in two of Langley's wind tunnels, the Transonic Dynamics Tunnel (TDT) and the Basic Aerodynamics Research Tunnel (BART). The TDT is a closed circuit, single return wind tunnel with a large slotted-wall test section (16-foot-square). Mach number and dynamic pressure can be varied simultaneously or independently, with either air or a heavy gas as the test medium. The Mach number may be varied continuously to a maximum of 1.2. The TDT is used almost exclusively for aeroelastic and structural dynamics research.

The BART facility²⁵ is an open-return wind tunnel with a test section 28 inches high, 40 inches wide and 10 feet long. It was developed to acquire the detailed flowfield data required for computational code validation and is ideally suited for flowfield surveys over complex aircraft configurations. The maximum flow velocity in the test section is 220 ft/sec, yielding a Reynolds number of 1.4 million per foot. Instrumentation includes a two-axis traverse system (used for pressure probe surveys and for the LDV seeding system) and a three-component LDV system to enable nonintrusive measurements.

3. FLUID DYNAMIC FLOW MODELS

Most of the computational results to be presented were obtained from computer codes implementing the following two algorithms.

3.1 Navier-Stokes Equations

Rumsey and Anderson¹⁷ give the thin-layer approximation to the Reynolds averaged Navier-Stokes equations for two-dimensional flow. In the thin-layer approximation viscous terms are resolved in a layer near the body where viscous terms in ξ , the direction along the body, are neglected and only terms in η , normal to the body, are retained. The equations are written in generalized coordinates and conservation form;

$$\frac{\partial}{\partial t}(\hat{Q}) + \frac{\partial}{\partial \xi}(\hat{G}) + \frac{\partial}{\partial \eta}(\hat{H} - \hat{H}_v) = 0 \quad (1)$$

$$\hat{Q} = \frac{Q}{J} = \frac{1}{J} \begin{bmatrix} \rho \\ \rho u \\ \rho v \\ e \end{bmatrix}, \quad \hat{G} = \frac{1}{J} \begin{bmatrix} \rho U \\ \rho U u + \xi_x p \\ \rho U v + \xi_y p \\ (e + p)U - \xi_x p \end{bmatrix}, \quad \hat{H} = \frac{1}{J} \begin{bmatrix} \rho V \\ \rho V u + \eta_x p \\ \rho V v + \eta_y p \\ (e + p)V - \eta_y p \end{bmatrix} \quad (2)$$

The shear stress and heat flux terms contained in \hat{H}_v are given in reference 17. The curvilinear generalized coordinates (ξ, η) correspond to the coordinates parallel and normal to the body surface, respectively, and are related to Cartesian coordinates (x, y) via the transformation

$$\xi = \xi(x, y, t), \quad \eta = \eta(x, y, t), \quad \tau = t \quad (3)$$

Note that the transformation is time-dependent, allowing the grid to move to follow body motion and giving rise to grid metric terms such as η_t in eq. (2).

Boundary conditions are applied explicitly. No slip, adiabatic wall conditions, as well as zero normal pressure gradient conditions are applied on the body where

$$u = v = 0 \quad (4)$$

For turbulent calculations, turbulence modeling such as the algebraic eddy viscosity model of Baldwin and Lomax²⁶ is used. Thomas et. al¹⁸ describe the three-dimensional implementation of the above algorithm in the CFL3D code.

3.2 Transonic Small Disturbance Potential Equation

The Transonic Small Disturbance (TSD) Potential equation is derived from the inviscid Euler equations assuming that the flow is a small perturbation of a steady uniform flow, U , in the x direction. The TSD velocity potential function, ϕ , describes the perturbed velocity components u, v, w .

$$u = \frac{\partial \phi}{\partial x}, \quad v = \frac{\partial \phi}{\partial y}, \quad w = \frac{\partial \phi}{\partial z} \quad (5)$$

where the total velocity in the x direction is $U + u$. References 27 and 28 give the modified TSD potential equation in conservation form as

$$\frac{\partial \phi_0}{\partial t} + \frac{\partial \phi_1}{\partial x} + \frac{\partial \phi_2}{\partial y} + \frac{\partial \phi_3}{\partial z} = 0 \quad (6)$$

where

$$\begin{aligned} \phi_0 &= -A\phi_1 - B\phi_x & \phi_2 &= \phi_y + H\phi_x\phi_y \\ \phi_1 &= E\phi_x + F\phi_x^2 + G\phi_y^2 & \phi_3 &= \phi_z \end{aligned} \quad (7)$$

The coefficients A-H are given by Batina²⁷. The TSD equation (6) is distinguished from the higher equation level flow models in that, within the small disturbance assumption, the computational grid is not required to move with the body since boundary conditions are imposed at the mean plane, usually $z = 0^\pm$. The wing flow tangency boundary condition is

$$\phi_z^\pm = f_x^\pm + f_y^\pm \quad (8)$$

where $f^\pm(x, y, t) = 0$ describes the upper and lower body surfaces. The trailing wake boundary conditions are

$$[\phi_x + \phi_1] = 0 \quad ; \quad [\phi_z] = 0 \quad (9)$$

where $[-]$ indicates the jump in the indicated quantity across the wake. The pressure coefficient may be computed using either linear or nonlinear forms of the Bernoulli equation in the algorithm as implemented in the CAP-TSD code.²⁸

Viscous-Inviscid Interaction. The inviscid TSD equation (6) does not incorporate viscous effects which can be important for high speeds and for lower speeds at higher angles. It is possible to account for unsteady viscous effects by coupling a viscous boundary-layer model with an otherwise inviscid analysis. As commonly implemented, the inviscid outer flow solution provides the surface pressure distribution needed to solve the boundary layer equations. This yields the boundary-layer displacement thickness distribution which is used to modify the airfoil surface tangency boundary condition for the next iteration of the outer inviscid flow solution.

Howlett and Bland²⁹ describe such a method implemented in a two-dimensional TSD code. The effect of a viscous boundary layer for attached turbulent flow is modeled in a quasi-steady manner by means of Green's lag-entrainment equations. In this integral method the displacement thickness δ^* is computed as a function of the boundary-layer momentum thickness θ and the shape factor H :

$$\delta^* = \theta \cdot H \quad (10)$$

Coupling between the boundary-layer and inviscid analysis is through the boundary conditions on the airfoil and wake, eqs. (8) and (9), which are modified to

$$\phi_z^\pm = f_x^\pm + f_y^\pm + (\delta^*/\delta c)_x^\pm \quad ; \quad [\phi_z] = [(\delta^*/\delta c)_x] \quad (11)$$

4. UNSTEADY AIRLOADS DUE TO LOCALLY SEPARATING FLOW

In this section, several studies of unsteady airloads due to shock-induced boundary layer separation are discussed. In each case, the relevant unsteady airloads are those on the lifting surface about which the flow is separating.

4.1 Unusual High Response Region For Transport Wing Configuration

The purpose of this research³⁰ was to investigate an unusual transonic aeroelastic response boundary of a wing model representative of an advanced transport configuration tested in the TDT. The supercritical wing had a design cruise Mach number of 0.80. A photograph of the model mounted in the wind tunnel is shown in Figure 1. The model exhibited high response in its wing first-bending mode at dynamic pressures well below the analytically predicted conventional flutter boundary. The region of high response occurred over a narrow range of Mach number and could be penetrated without the amplitude of the oscillations diverging. The motion begins to increase rapidly at about $M=0.85$, reaches a maximum near $M=0.92$, and then decreases rapidly. Autospectra results indicated that the response was primarily in the first bending mode which had a wind-off frequency of about 8.2 Hz. The response was effected by changes in angle of attack but no consistent pattern was observed. The response at a given angle of attack was proportional to the dynamic pressure. Tufts installed on the wing surfaces during the test indicated large regions of flow separation on both the upper and lower surfaces above $M=0.9$.

The model was instrumented with unsteady pressure transducers and Figure 2 gives some illustrative data at four Mach numbers: below the response onset, as the response was increasing, at the maximum response condition, and above the region of wing response. At the top of the figure, the mean chordwise pressure distributions at 87 percent span are shown. At $M=0.92$, where the maximum response occurred, there are strong shocks on both surfaces and the mean pressures indicate that the flow is near separation. Seidel et al.³¹ show that in actuality the flow at this condition is alternately separating and reattaching aft of the shocks. In the lower portion of the figure pressure time histories at four chordwise locations are shown for these four Mach numbers. At $M=0.80$ some unsteadiness is apparent in the flow, most noticeably at station 1. At $M=0.88$ the flow is smooth at station 1 and is considerably unsteady at station 2 on the upper surface and at stations 3 and 4 on the lower surface. These three transducers indicate large pressure fluctuations but the frequency is well above that of the first bending mode. In contrast, at $M=0.92$, transducers 2 and 4 pick up the dominant first bending mode frequency (the shocks are oscillating across these two transducers at this condition). At $M=0.96$ the flow is supersonic over the entire wing chord and the pressure traces indicate smooth flow. At $M=0.92$ the reduced frequency of the oscillations is approximately 0.10 (based on wingtip semichord).

The characteristics of this case make it an interesting one for CFD code validation involving as it does strong transonic flow effects, alternately separating and reattaching flow, and large aeroelastic wing motions. An early attempt to calculate this response³² with an inviscid transonic small disturbance code was unsuccessful. The code was unable to predict the correct steady pressures for the loaded and deformed wing for the Mach number range in which the oscillations occurred indicating that viscous boundary layer modeling will be required to treat this case.

4.2 Control Surface Buzz

This term refers to a type of control surface instability sometimes encountered at transonic speeds. A single degree of freedom limit cycle (limited amplitude of oscillation) behavior is typically observed and is apparently due to the interaction of local shocks on the upper/lower surfaces in the vicinity of the control surface and the control surface dynamics. Steger and Bailey³³ give a summary of a well known case involving the wing ailerons of the P-80 aircraft and provide an early computational demonstration of the use of CFD methods in aeroelasticity. They used a two-dimensional Navier-Stokes code to perform a strip analysis of the P-80 wing/aileron section. The code implemented the Beam-Warming implicit Approximate Factorization solution algorithm, using an algebraic eddy viscosity turbulence model. A novel shearing transformation of the coordinate normal to the aileron was used to allow the aileron to deflect during the calculation and the experimental buzz boundary, in terms of Mach number versus angle of attack, was successfully calculated.

The expense of Navier-Stokes calculations is such that it is of interest to determine if the buzz instability might be treated with lower level CFD methods. Howlett³⁴ has shown that the P-80 buzz case may be successfully treated using the TSD potential equation in conjunction with an interacted boundary layer model. Figure 3a shows the steady pressure distribution for one case at $M=0.80$ and $\alpha=-1$ degree. Figure 3b shows the aileron response when it is released. A limit cycle oscillation of approximately 6 degrees amplitude develops at a reduced frequency of $k_b = 0.4$. Figure 3c shows that the calculated buzz boundary is in good agreement with the experimental and Navier-Stokes code boundaries, indicating that this level of CFD code can be used to predict the onset of this form of control surface buzz. It is interesting to note the similarity in the mean pressure distributions shown in Figures 2 and 3a for cases where maximum aeroelastic response incidents have been observed. In both cases there are nearly coincident strong shocks well aft on the upper and lower surfaces.

4.3 Periodic Aerodynamic Oscillations

This last case of unsteady airloads due to locally separated flow again involves transonic shock-induced separation of the boundary layer. Edwards and Thomas¹ discuss the experimental and computational studies of these oscillatory flows over circular arc airfoils. For an 18 percent thick airfoil, periodic unsteady flows have been observed over the narrow Mach number range of $0.73 < M < 0.78$ at a reduced frequency of $k_b = 0.48$. Figure 4 shows calculations¹ for $M=0.78$ and $Re=11 \times 10^6$ of Mach contours about the airfoil through one-half cycle of oscillation indicating the forward movement, disappearance, and subsequent formation near the trailing edge of the lower surface shock. The reduced frequency is $k_b = 0.406$ in close agreement¹ with other Navier-Stokes calculations for this case.

These cases of unsteady airloads due to locally separated flow indicate the relative maturity of CFD methods for such effects in two-dimensional flows. They also illustrate an important point relating to aeroelastic analysis: critical cases, such as minimum flutter speed indices and maximum transonic aeroelastic response occur for conditions of incipient flow separation where regions of the flow are near separation. For such cases, the structural response can interact with the flow to induce intermittent separation and reattachment, and "resonance"-like interactions can occur between the structure and the airflow. These cases require some type of viscous modeling for accurate predictions and, for airfoils in two-dimensional flow, CFD methods have been developed which can predict these interactions. For wings in three-dimensional flow the situation has not yet matured to this level.

5. VORTICAL FLOW OVER AIRFOILS, WINGS AND BODIES

In this section attention will be given to the generation of vortical flows. Computational studies are beginning to delineate the required levels of effort to produce accurate computations for such flows. It should be self-evident that such accurate flow modeling of the initiation of separated flows will be required for similar accuracies when unsteady airloads due to separated flows impinging on remote aircraft components are considered.

5.1 Unsteady Vortex Shedding Over Airfoils

Rumsey and Anderson¹⁷ used the Navier-Stokes equation model given above to calculate separating vortical flows over the NACA 0012 airfoil undergoing sinusoidal pitching oscillations and the NACA 0015 airfoil undergoing constant pitch rate ramping motions. The former calculations were for a Reynolds number of 4.8×10^6 and turbulent flow was modeled. The Mach number was 0.6, $\alpha = 4.86^\circ + 2.44^\circ \sin \omega t$ and $k_c = 0.162$. (Confusion over the reference length used for reduced frequency will be dealt with by subscripting -c for chord and -b for semichord; obviously $k_c = 2 k_b$.) The latter calculations modeled a ramping motion from 0 to 60 degrees and were for a Reynolds number of 45,000 where laminar flow was assumed for the calculations. The numerical sensitivity of the solutions was investigated by varying a number of key parameters. For both cases, the sensitivity to grid density was studied. In addition, the sinusoidal oscillation case was used to investigate effects of time step size, spatial accuracy in the finite-difference algorithm and turbulence model.

Three different grid densities were studied: 257×97 , 129×49 , and 65×25 . Each grid was of the same extent, fifteen chordlengths, and the coarser grids were obtained by deleting every other point from the finer grid. Figure 5 is typical of the results for the sinusoidal oscillation case, showing that the coarsest grid does not provide accurate results for this case, while the medium grid results are in good agreement with the fine grid results. Similarly, by varying the grid extent and time step size it was determined that accurate results were obtained with a minimum grid size of 15 chordlengths and maximum nondimensionalized time steps of 0.1 (based on chordlength and the speed of sound). For this case involving only mild shock-induced separation, an equilibrium, zero-equation turbulence model predicted the unsteady lift coefficients accurately but underpredicted the moment coefficients. A nonequilibrium, "half-equation" model predicted higher moment coefficients in better agreement with experiment, but gave shock locations too far forward.

The constant rate pitching motion study was for the much larger angles of 0 to 60 degrees and showed details of leading edge vortex formation and shedding. Figure 6 shows the effect of grid density on the instantaneous flowfield for $\alpha = 30$ and 45 degrees. In Figure 6(a), the finer mesh solution shows a shed vortex near the leading edge at $\alpha = 30^\circ$, similar in character to the corresponding experimental flowfield³⁹. The coarser mesh shows attached flow. At $\alpha = 45^\circ$, Figure 6(b), the shed leading-edge vortex for the finer mesh has convected farther downstream than that for the coarse mesh, in better agreement with experiment. At higher angles, the computed vortices on both meshes are too far upstream in comparison with experiment. This is attributed to lack of grid density in the region into which the vortex is convecting and grid refinement methods are regarded as necessary to continue to accurately track the vortex.

The issue of accurately calculating vortical flows convecting over significant distances deserves further discussion as it must play a critical role in attempts to compute aeroelastic responses such as tail buffeting. For calculations of vortex flows, where the vortex is calculated as a part of the solution and not imposed on the solution, a significant problem is that conventional differencing schemes possess enough artificial dissipation to smear and dissipate the vortex very rapidly. In general, the coarser the grid used to perform the calculation, the greater the distortion of the vortex. Rai³⁵ indicates that conventional spatially second-order-accurate finite-difference schemes are too dissipative for calculations involving vortices that travel large distances. Studying the model problem of a two-dimensional, cross-flow vortex being convected by the freestream, the effect of higher order spatial- and time-accurate differencing was evaluated. The commonly used Beam-Warming differencing algorithm was shown to dissipate more than 20% of the vortex core pressure in only 5 vortex core radii of travel, making it unsuitable for such calculations. Increasing the time-accuracy to second order is very effective, decreasing the pressure dissipation to 20% in 45 core radii. Increasing spatial accuracy is also required to further decrease the numerical dissipation. Acceptable accuracies also require adequate grid densities and reference 35 indicates that an approximate minimum grid density is at least 8-10 grid points per core diameter of the vortex. No similar study of accuracy and grid density requirements for streamwise vortices, such as leading-edge vortices, has been made.

5.2 Vortical Flows Over Bodies and Wings

Unsteady conical flow. In the high angle of attack range, the vortical flow over forebodies and wings may become asymmetrical and, for some range of flow conditions, show evidence of random or periodic shedding, similar to the von Karman vortex shedding in two-dimensional flows around cylinders. The extent to which this mechanism is involved in unsteady buffet loads is largely unknown. Computations similar in spirit to those of reference 17 are given by Kandil et al.³⁶ for supersonic conical flows. The "locally" conical flow assumption reduces the computer resources required to treat such flows, allowing a significant number of such calculations to be made. An implicit, central-difference, finite-volume algorithm was developed to solve the thin-layer Navier-Stokes equations. Calculations with this algorithm and that of reference 17 for circular and elliptic section cones are given³⁶ for $1.4 < M < 1.8$ and for $10^\circ < \alpha < 34^\circ$.

For a circular cone at $M = 1.8$ and $\alpha = 10^\circ$, the two algorithms yielded the same steady, symmetric results. When the angle of attack is increased to 20° , both codes converge upon the same steady, asymmetric vortex flow solution. This solution could be induced by truncation round-off disturbances or by forcing with transient side-slip conditions. When the angle was further increased to 30° , periodic asymmetrical shedding of the vortices was observed. The time step size was 10^{-3} , $Re = 10^5$ (based upon unit root chordlength and freestream velocity) and the oscillations repeated in 1400 time steps giving a Strouhal number of 4.488.

Similar calculations were made for an elliptic cone with fineness ratio of 0.2 in order to study such oscillations for wing-like sections. Figure 7 gives results for this case for which $\alpha = 34^\circ$, $Re = 2 \times 10^6$, $\Delta t = 0.002$ and $M = 1.4$. Shown are the time history of the residual error, the lift coefficient, and snapshots of the total-pressure loss contours through one-half period of oscillation. The pressure contours show that, at $n = 15,000$, the left-side vortex is stretched, while the right-side vortex has expanded covering a large region of the left side of the flow domain over the wing. Under the right-side vortex, a strong secondary vortex has formed. At $n = 15,200$ the top vortex is shed into the flow field. Between $n = 15,300$ to $15,400$ the left vortex expands to the right, the right vortex strengthens and stretches upward, and a secondary vortex begins forming under the left vortex. The oscillation repeats after 1050 steps giving a Strouhal number of 2.992. These calculations were obtained on grids of 161×81 points whose extent for the circular cone was 21 radii.

Vortical flow over delta wings. Moving to fully three-dimensional vortical flows, it is necessary to establish the accuracy with which the development of leading-edge vortex flows may be computed. In this section, two such studies are surveyed. In the first study, CFD calculations are compared with steady measurements made on the wing surface while in the second, CFD calculations are compared with off-the-surface flow measurements. Hsu and Liu³⁷ made calculations for three delta wing planforms using an incompressible Navier-Stokes equation code. The wings were: a 60° delta wing, an $80^\circ - 60^\circ$ double-delta wing and an $80^\circ - 40^\circ$ cropped double-delta wing. Calculations for $\alpha = 12^\circ$ and 20° are given and the flow is assumed to be laminar. Effects of grid density, Reynolds number and planform are discussed. For the double-delta wing with 955,000 points in the finest grid, the surface pressure suction peaks under the vortices were not well predicted due to lack of grid resolution in the vicinity of the vortex cores. However, the integrated lift and moment coefficients were in excellent agreement with the experimental values; generally within 1% except for the cropped double-delta wing at $\alpha = 20^\circ$ where the moment was off by 4%. Reference 38 gives further results for the double-delta wing for angles from 6-40 degrees including calculations at $\alpha = 35^\circ$ and 40° indicating unsteadiness and bubble-type vortex breakdown. Whereas the calculations contain reversed axial flow in the burst vortex region starting at $x/c = 0.95$ for $\alpha = 35^\circ$ and $x/c = 0.85$ for $\alpha = 40^\circ$, the experimental results show bursting at $x/c = 0.6$ starting at $\alpha = 30^\circ$. Figure 8³⁷ shows the effect of planform and angle-of-attack upon the vortex flows for angles of 12° and 20° . A clear well-organized vortex is indicated for the delta wing which moves inboard with increasing angle. The double-delta wing adds an additional vortex formed at the strake-wing juncture which interacts with the wing vortex, intertwining with it over the wing. For the cropped double-delta wing, an additional vortex appears due to the flow separating from the side edge and at $\alpha = 20^\circ$ all three vortices 'angle' together in the wing-tip region.

The second study, by Kjelgaard and Sellers¹⁴, addressed the need for detailed off-the-surface flowfield data for code validation by performing tests on a 75 degree swept flat plate delta wing using a pitot pressure probe, a 5-hole pressure probe and three-component LDV measurements. Data were obtained for Reynolds numbers between 0.5 and 1.5 million and with the most extensive data being taken at 1.0 million (based on root chordlength). The accuracy of each instrumentation system is discussed and several methods of calculating vorticity are applied. Thomas et al.¹⁸ have performed CFD computations for this wing using the CFL3D code. A grid containing 850,000 points modeling the half-span was used and results obtained for angles of 0-40 degrees. The predicted maximum lift coefficient of 1.10 at 35 degrees agrees closely with the measured maximum lift of 1.06 at 33 degrees. At 40 degrees a steady, bubble-type reversed flow region (due to breakdown) extending from $x/c = 0.6$ to just downstream of the trailing-edge was observed. The experimental burst location for this condition is $x/c = 0.4$. Detailed comparisons with experiment for $\alpha = 20.5^\circ$ show good agreement of minimum pressure coefficients under the primary and secondary vortices. Additional calculations for this

wing are reported by Taylor et al.³⁹ Comparisons with the 3-D LDV flowfield measurements for $\alpha = 20.5^\circ$ show that the CFD code predicts the physics of the flow well, such as the position of the primary and secondary vortex cores and the position of the secondary separation line. However, differences in the magnitudes of pressure, velocity and vorticity in the region of the primary vortex core were noted. Krist et al.¹⁹ show that these deficiencies are due to grid resolution in that region. Using a grid embedding technique to achieve high grid density there without the necessity of global grid enrichment, they show that the deviation from the experimental core velocity approaches zero as the minimum grid spacing in the core region is decreased. Figure 9 shows the experimental and computed streamwise velocity contours for $x/L = 0.7$, $Re = 0.5 \times 10^6$ and $\alpha = 20.5^\circ$. The experimental measurements were made with a five-hole probe and the accuracy was checked with independent LDV measurements. The two techniques agreed in regions of low shear and flow angularity, but the measurement errors were large in the vortex core region. The peak streamwise velocity was 2.25 with the probe whereas the LDV measurements led to a corrected value of ~ 3.1 . The CFD results were obtained on a baseline global grid with $65 \times 65 \times 37$ points ($\sim 156,000$ points). Two levels of grid embedding were obtained by successively halving the global grid and extracting the needed regions for the embedded grid calculations. The first level of refinement encompassed the entire upper surface and part of the lower surface of the wing while the second level occupied only the vortex core region. The results indicate that the physical size and shapes of the computed vortices agree with the experimental results and an increase in resolution is apparent with each level of refinement. The maximum streamwise velocities predicted on the three grids are 1.5, 1.86 and 2.04 in reasonable agreement with the probe measurement but lower than that estimated using the LDV data.

Vortical flow over a forebody configuration. One final example of Navier-Stokes computations of the generation of vortex flows over bodies is given by Thomas et al.²⁰ Vortex flow patterns over the F/A-18 forebody and wing leading-edge-extension (LEX) were calculated for a low speed condition ($M = 0.3$) at $\alpha = 30^\circ$. Both laminar and turbulent calculations were made with the CFL3D code and compared with low Reynolds number, low speed wind tunnel tests and high Reynolds number flight tests. In terms of surface flow patterns, primary and secondary forebody surface separation lines were well predicted. Figure 10(a) shows the surface flow pattern from the laminar calculations at $Re = 740K$ which agreed well with the wind tunnel results at $Re = 200K$. Figure 10(b) shows the turbulent calculations for $Re = 10^7$ which agreed well with the flight test results at the same Reynolds number. The two calculations show significant differences in surface flow patterns indicating the effect of laminar versus turbulent flow conditions. The downstream convection of these vortical flows under buffeting conditions can be expected to show evidence of transition and turbulence effects on buffet.

Transonic Vortex Flow Visualization

Most of the vortical flow research which has been discussed has been for low speed conditions. The appendix of reference 12 discusses recent results on vortex bursting at high subsonic speeds and indicates that there is much that is not known about such flows. For instance, off-the-surface transonic features, such as terminating center-line shocks and shock-vortex structures, are known to occur and to have strong influences. Seidel et al.⁴⁰ describe vortex flow visualizations from a test of a clipped delta wing oscillated in pitch at $M = 0.92$. Figure 11(a) shows the model installed in the TDT and Figure 11(b) presents photographs of the instantaneous flowfield illuminated by a laser light sheet at four instants during a period of oscillation. The wing was oscillated $\pm 5^\circ$ about a mean angle of 15° at a frequency of 3.35 Hz. Arrows indicate the direction of the motion for each instant. The white image near the left-center of each frame is the corner flow at the junction of the wing with the splitter plate. The leading-edge vortex flow is seen, viewed from the rear, above the light sheet trace on the wing in the right-center of each frame. The details shown in the visualizations will provide good cases for comparison computations with CFD methods.

6. BUFFET FLOWFIELDS AND BUFFETING RESPONSE

A primary application of the computation of unsteady separated airloads is the prediction of buffeting response. This paper has indicated the level of complexity which such computations have achieved. No CFD calculations of tail buffeting have been reported, indicating that the capability to reliably predict such responses has not yet been achieved. In two-dimensions, significant progress has been made in the calculation of unsteady separated flows. For three-dimensional flows, major issues remain unresolved, as indicated by the types of flows which have been studied: detailed forebody flows, demonstration calculations of separating vortical flows over idealized planforms and shapes, a few calculations indicating instabilities of leading-edge vortices. At issue are the computer resources required for more realistic problems and additional physical flow modeling details needed for accurate prediction of such flows. The computer resource issue will be addressed in the following section. Key flow modeling issues involve: i.) grid densities necessary for accurate calculation of vorticity convected over significant distances, ii.) detailed modeling necessary for accurate calculations of vortex instability, iii.) dynamic turbulence modeling for free shear layers, iv.) unsteady flow separation for moderately swept, rounded leading-edge wings, and v.) vortex flows about wings at high subsonic speeds. In this section, two experimental studies directed at these issues are discussed.

6.1 Buffeting Flowfield Measurements

Recent wind tunnel investigations of vortex flow are beginning to show a merging of interest of the aerodynamics and structural dynamics communities upon the problem of tail buffeting. Many earlier wind tunnel studies of vortex flows are not germane to this issue for a variety of reasons: i.) vortex systems were steady/stable, ii.) unsteadiness was not addressed or measured, iii.) idealized configurations (sharp-edges, highly swept wings, etc.) were tested. To obtain detailed measurements of a buffet flowfield Sellers et al.¹⁶ performed LDV surveys of the flow over a YF-17 model in the BART low speed wind tunnel. Figure 12 shows mean and rms component velocities for $\alpha = 25^\circ$ at a station just ahead of the vertical tail. The strake vortex has burst ahead of this station and the mean streamwise velocity component, u , shows a region of reversed flow centered on the vertical tail location. The maximum rms velocity fluctuations reach levels of approximately 40%, 35%, and 30% for the u , v and w components and mean crossflow angles at the tail vary from -30° at the root to $+15^\circ$ at the tip. While such detailed flowfield surveys are necessary to provide data for code validation, they still do not provide the level of global, instantaneous measurements probably required. For example, knowledge of the instantaneous surface pressure distribution over the vertical tail is required in order to calculate the tail buffeting response. Time correlated measurements of these pressures are needed along with off-the-surface flowfield measurements in order to begin to understand the interaction between the tail structure and the oncoming buffet flow. This constitutes extremely large data sets and presses the current limits of nonintrusive measurement techniques.

6.2 Twin Vertical Tail Airplane Model Buffeting Response

Recent experiences from the operational use of high performance, twin vertical tail airplane configurations have shown that relatively large dynamic response of the tail structure occurs at certain high angle of attack flight conditions. These buffeting-like responses may be larger than those anticipated in the structural design and can have an adverse effect on service life. Doggett and Cazier¹¹ discuss a test in the TDT undertaken to better understand the characteristics of these undesirable responses. A full span, "rigid," sting mounted model of a high performance twin vertical tail airplane was equipped with an elastic vertical tail and buffet tested over a range of angle of attack and Mach number. A photograph of the model mounted in the wind tunnel is shown in Figure 13. Although the elastic tails did not precisely scale the dynamic characteristics of a specific full scale design, their stiffness and mass were chosen so that the dynamic characteristics were representative of full-scale values.

Some of the experimental buffet response data that were obtained are shown in Figure 14 as the variation of a normalized rms bending moment response parameter with angle of attack for several different Mach numbers. The commonly used response parameter is the one derived from using generalized harmonic analysis considerations. In normalizing the data it is assumed that the aerodynamic damping was very small compared to the structural damping. The response of the tails was primarily in one structural mode as shown by the typical autospectrum included on the figure. The data for all Mach numbers are similar in that the bending moment is small and relatively constant up to an angle of attack of about 15°, where a relatively sharp increase in bending moment begins to occur. Although the details of the data are different at the various Mach numbers, it does appear that the peak response occurs in the neighborhood of about 30 to 35 degrees angle of attack. The magnitude of the maximum values, however, appears to be a function of Mach number. Data such as those presented here provide a basis of assessing the Mach number effects on the buffet characteristics of twin vertical tail airplane configurations.

7. COMPUTATIONAL RESOURCES FOR PREDICTION OF TAIL BUFFETING

In the past, steady maneuver loads on aircraft have been predicted based upon a combination of model test data and analysis while dynamic buffeting loads could only be estimated from model tests by means of suitable scaling procedures. For strong vortical flowfields such as that shown in Figure 11, even empirical scaling or predictive methods are largely lacking. This has led to a desire for improved prediction methods for such dynamic buffet loads, which emerging CFD methods might be expected to fulfill. In order to assess the magnitude of the task, Edwards²⁴ discussed the computational resources which would be required to perform a direct CFD calculation of the buffeting response of a twin vertical tail fighter configuration. The goal was to obtain a ballpark estimate of the computer memory size and computer run time for the calculation of a single buffeting response in order to yield reliable measures (e. g. stable bending moment power spectral densities). Until recently, computer memory size was the pacing item in CFD calculations, with the allowable number of grid points being restricted by available memory sizes. The currently available supercomputers, with memories ranging from 32-256 million words of core memory, have made job run times the pacing item as the estimates below will show.²⁴

The Computer Processing Unit (CPU) run time for a CFD calculation can be estimated from the relation

$$T_{cpu} = N_{st} * N_{gp} * \tau \quad (12)$$

relating computer CPU time, T_{cpu} , to the number of computational steps, N_{st} ; the number of grid points, N_{gp} ; and the algorithm speed, τ , given in microseconds per grid point per time step.

Selection of suitable values for the parameters of eq. (12) are discussed in the following sections.

Algorithm Speed. The parameter, τ , is a common measure of the speed of an algorithm and typically ranges from 10-100 microseconds per grid point per time step. Lower values of τ are associated with less complex algorithms, such as explicit methods, while more complex algorithms yield larger values. However, the higher level algorithms (e. g. implicit, upwind-biased, etc.) allow larger time steps and are generally favored for calculations requiring time-accuracy. A value of $\tau = 40$ microseconds was assumed for the following estimates and is representative of the speed for an implicit, upwind-biased code.

Number of Computational Time Steps. The parameter N_{st} depends on the time step size, Δt , and the total real time length necessary for the calculation T_{tot}

$$N_{st} = T_{tot} / \Delta t \quad (13)$$

The maximum time step size, Δt , is limited by the numerical stability of the algorithm and by the required accuracy for the aerodynamic results. To perform a buffet calculation, the frequency bandwidth of interest must be specified. Let f_{min} and f_{max} designate these limits with the corresponding maximum and minimum periods of oscillation given by $T_{min} = 1/f_{max}$ and $T_{max} = 1/f_{min}$. Now the time step, Δt , is chosen as

$$\Delta t = T_{min} / N_{st/cy} \quad (14)$$

where $N_{st/cy}$ is the number of computational steps per cycle of oscillation. For Euler codes $N_{st/cy}$ can be assumed to be in the range 100-200 whereas for Navier-Stokes codes, where smaller time steps are demanded for stability (due to the smaller minimum grid cell size used in order to resolve the boundary layer), values of 1000 and higher are needed.

The total real time length, T_{tot} required for buffeting calculations will be set by the number of cycles of oscillation, N_{cy} , at the lowest frequency, f_{min} , in order to obtain stable, converged results:

$$T_{tot} = N_{cy} * T_{max} \quad (15)$$

Since the buffeting flowfield is inherently nonsteady and nonperiodic, convergence will have to be measured in some statistical sense such as the attainment of stabilized power spectral densities of selected structural response parameters. Edwards²⁴ estimates a

reasonable range of N_{cy} to be 10-50 and picks $N_{cy} = 10$ for his estimates. (This choice is almost certainly on the very optimistic side but, even so, leads to prohibitive run time estimates.) Finally, assuming a bandwidth of 10-40 Hz. (i. e. $f_{min} = 10$ Hz., $f_{max} = 40$ Hz.) estimates of $N_{st} = 8,000$ for an Euler code calculation and $N_{st} = 40,000$ for a Navier-Stokes code are developed.

Number of Grid Points. To estimate the number of grid points, N_{gp} , the concepts of "local accuracy" and "remote accuracy" are introduced. The former term refers to the typical CFD gridding strategy wherein grid points are clustered near the wing to resolve details there and grid point densities are rapidly decreased away from the body. Such local grid densities are required in order to resolve boundary layers and capture the flowfield separating off of the forward aircraft components (wing, forebody, etc).

Turning now to buffet computations, the issues of unsteadiness and the convection of vorticity must be addressed. Now the fast grid stretching away from the body cannot be used since accuracy at remote locations is required (the effect of disturbances originating in the wing region must be accurately resolved at the tail). For this purpose, the computational domain is treated as three regions. In Region I, the boundary layer region of the wing, fuselage, and tail, thin-layer Navier-Stokes grid densities are assumed, leading to an estimate of 196,000 grid points per body component. In Region II, the near-field of the aircraft containing unsteady separated vortical flow, grid densities adequate to resolve and convect the flow for the frequency bandwidth of interest will be assumed. Region III comprises the outer flow field (inviscid and irrotational) necessary to capture to correct global flow. Thus the total number of grid points is

$$N_{gp} = N_{gp,I} + N_{gp,II} + N_{gp,III} \quad (16)$$

The number of grid points required for Region III will be a small fraction of the total number and will be assumed to be $N_{gp,III} = 50,000$.

Figure 14 illustrates this concept of the near-field Region II for the F-15 aircraft. It is assumed that the correct amount of unsteady vorticity has already been injected into the flow (e. g. via the viscous boundary layers, Region I). Hence, in Region II, the Euler equation flow model will be assumed capable of accurately convecting the flow. The grid cell sizes for this region, Δx , Δy and Δz , are determined assuming that the vortical flow is convected at the freestream velocity. Then the spatial wavelength due to the highest frequency components at f_{max} can be calculated and the number of grid points per wavelength, $N_{gp/wl}$, set for the desired level of accuracy. For the following estimates, $N_{gp/wl} = 50$ is used. Finally, for the large flow angularities found in buffet flows, it is assumed that the spatial resolution needed for the crossflow directions is the same as that for the streamwise direction. For a freestream Mach number of $M = 0.5$ this leads to $\Delta x = \Delta y = \Delta z = 0.25$ ft. and the number of grid points in Region II is calculated to be approximately 1.5×10^6 .

Thus from eq. (16) the estimate of the total number of grid points for a buffet calculation is

$$N_{gp} = 568,000 + 1,500,000 + 50,000 \\ = 2,138,000$$

and the total CPU run time for one buffet calculation (full span), assuming that the thin layer Navier-Stokes equations are used is estimated to be

$$T_{cpu} = 40,000 \times 2,138,000 \times (40 \times 10^{-6}) / (3600 \text{ sec/hr}) \\ = 950 \text{ hrs}$$

If an Euler equation calculation is assumed ($N_{gp,I} = 0$, no viscous boundary layer, $N_{st} = 8,000$) the estimate reduces to $T_{cpu} = 132$ hrs. However, reference 24 discusses the inadequacies of the Euler equations for such flows.

Equations 12-16 are summarized in Table 1. While these extremely long run times would seem to be quite impractical, they are likely to indicate the range within which solutions with sufficient accuracy to be useful in design decisions will be found. Reference 24 discusses a number of ways in which these estimates may be reduced. Also discussed is the large amount of uncertainty underlying a number of the assumptions. For instance, the assumption that all vorticity generation occurs in the boundary layers adjacent to aircraft body components is crucial in limiting the total number of grid points. If it is necessary to model viscous effects occurring in free shear layers within the Region II volume, and off of body surfaces, then the required number of grid points would increase greatly. Also, in this case the thin layer assumption would probably not be applicable, further compounding the problem. A further concern is that nonlinear mechanisms are likely to be involved, leading to the likelihood of large sensitivity to initial conditions and calling for extensive calculations to cover reasonable ranges of conditions. Finally, there is the possibility of chaotic responses, in which there is no repeatability in the response.

Equation (12) for the total CPU run time for a buffeting calculation can be rearranged to give

$$T_{cpu} = N_{cy} N_{st} \frac{f_{max}}{f_{min}} + [196,000 N_{bod} + \frac{V_{\infty}^2 N_{gp}^2}{U_{\infty}^2}] + 50,000 \quad (17)$$

This expression indicates a strong dependence of T_{cpu} upon f_{max} and U_{∞} due to the grid density in the near field, Region II. For this example, increasing f_{max} from 40 to 60 Hz increases T_{cpu} by a factor of 3.5 while halving the freestream speed, U_{∞} from $M = 0.5$ to 0.25 results in a six-fold increase in T_{cpu} . The CPU run time estimate for the thin-layer Navier-Stokes equations needs to be reduced by approximately three orders of magnitude (from 1000 hours to approximately one hour) before such buffet calculations

will be viable. Then the number of cases, the job turn-around time and the computational expense would be at levels that could support efforts leading to reliable engineering tools. These run time improvements can probably be anticipated due to expected increases in computer speed and memory and increases in algorithm speed and efficiency.

It would not be proper to leave this discussion of computational resources without raising an issue regarding the detail with which buffet flowfields need to be calculated. It should be born in mind that, ultimately, the structural designer needs to know the worst case buffeting response. Accurate simulations of subcritical buffeting response conditions are virtually useless. Thus, it seems likely that the optimum use of computational predictions of buffet flows might be in guiding empirical determination of such worst case conditions.

8. CONCLUSIONS

Experimental and computational experience at NASA Langley Research Center with unsteady airloads due to separated flows has been surveyed. Studies have been grouped into three categories depending upon the spatial separation between the location at which unsteady loads are measured and the location of flow separation. Structural dynamic response due to shock-induced separating flow, control surface buzz and periodic aerodynamic oscillations are examples of locally separating flows for which a number of cases show good predictive ability. Vertical tail buffeting is an example of unsteady airloads caused by flow separating over remote aircraft components. Predictions of unsteady airloads due to this second type of separated flow is much more difficult than the former, involving as it does several more troublesome numerical steps. No direct calculations of such buffeting response have yet been made. The formation of vortical flows over wings and forebody geometries presents a situation of intermediate difficulty and a number of studies show good agreement for steady features of such flows.

Cases of control surface buzz and periodic aerodynamic oscillations have been successfully treated using both Navier-Stokes and potential-plus-boundary layer codes in two-dimensional strip analyses. However, the application of such methods to treat the aeroelastic response of wings in the presence of separating flows is not yet mature.

Experimental flow field data about complete fighter configurations at high angles of attack are available and are being compared favorably with steady computational results. However, the problem of obtaining time-correlated off-the-surface flow field data for validating unsteady computational predictions remains to be addressed.

Steady Navier-Stokes computations of stable vortex flows about delta wings and forebody geometries agree very well with experiment. Here, studies of grid refinement, turbulence modeling and algorithm studies are providing guidance in the selection of numerical methods. Computer run times for these cases range from several to 40 hours per case.

An assessment of the computer resources which would be required to perform a computational prediction of one vertical tail buffeting response for a twin tailed fighter configuration leads to an estimate of at least 1000 hours per case for the calculation of stabilized buffeting response spectra. This estimate assumed the use of a thin-layer Navier-Stokes code, over 2×10^6 grid points, and a bandwidth of 10-40 Hz. There is a large amount of uncertainty in this estimate, reflecting the number of modeling issues to be resolved.

9. REFERENCES

1. Edwards, J. W.; and Thomas J. L.: Computational Methods for Unsteady Transonic Flow, Chapter 5 in Unsteady Transonic Aerodynamics, Edited by David Nixon, Vol. 120 of AIAA Progress in Astronautical and Aeronautics, 1989.
2. Edwards, J. W.: Unsteady Aerodynamics: Physical Issues and Numerical Prediction. Presented at the Third International Congress of Fluid Mechanics, Cairo, Egypt, January 2-4, 1990.
3. Mabey, D. G.: Physical Phenomena Associated with Unsteady Transonic Flows, Chapter 1 in Unsteady Transonic Aerodynamics, Edited by David Nixon, Vol. 120 of AIAA Progress in Astronautical and Aeronautics, 1989.
4. Bobbitt, P. J.: The Pros and Cons of Code Validation. AIAA Paper No. 88-2535. Presented at the AIAA 6th Applied Aerodynamic Conference, Williamsburg, Virginia, June 6-8, 1988.
5. Newsome, R. W.; and Kandil, O. A.: Vortical Flow Aerodynamics - Physical Aspects and Numerical Simulation. AIAA Paper No. 87-0205. Presented at the AIAA 25th Aerospace Sciences Meeting, Reno, Nevada, January 12-15, 1987.
6. Mabey, D. G.: Some Aspects of Aircraft Dynamic Loads Due to Flow Separation. AGARD-R-750.
7. Zimmerman, N. H.; Ferman, M. A.; and Yurkovich, R. N.: Prediction of Tail Buffet Loads for Design Application. AIAA Paper No. 89-1378, presented at AIAA Structures Structural Dynamics and Materials Conference, Mobile, Alabama, April 3-5, 1989.
8. Triplett, W. E.: Pressure Measurements on Twin Vertical Tails in Buffeting Flow. AFWAL-TR-82-3015, Volume I, April 1982.
9. Coe, C. F.; and Cunningham, A. M., Jr.: Predictions of F-111 TACT Aircraft Buffet Response and Correlations of Fluctuating Pressures Measured on Aluminum and Steel Models and the Aircraft. NASA CP 4069, May 1987.
10. Cunningham, A. M., Jr.; den Boer, R. G.; Dogger, C. S. G.; Geurtis, E. G. M.; Persoon, A. J.; Retel, A. P.; and Zwaan, R. J.: Unsteady Low-Speed Wind Tunnel Test of a Straked Delta Wing, Oscillation in Pitch. Part 1 General Description and Discussion of Results, AFWAL TR-87-3098, April 1988.
11. Doggett, R. V., Jr.; and Cazier, F. W., Jr.: Aircraft Aeroelasticity and Structural Dynamics Research at the NASA Langley Research Center - Some Illustrative Results, NASA TM 100627, May 1988.

12. Elsenaar, A. Hjelmberg, L.; Butefisch, K. and Bannick, W. J.: The International Vortex Flow Experiment. AGARD CP-437. Vol. I, 1988.
13. Hummel, I. D.: Documentation of Separated Flows for Computational Fluid Dynamics Validation. AGARD CP-437. Vol. II, 1988.
14. Kjølgaard, S. O.; and Sellers, W. L., III: Detailed Flowfield Measurements Over a 75° Swept Delta Wing for Code Validation. AGARD CP-437. Vol. II, 1988.
15. Pagan, D.; and Soligna, J. L.: Experimental Study of the Breakdown of a Vortex Generated by a Delta Wing. Rech. Aérop. (English Edition) 1986-3.
16. Sellers, W. L., III; Meyers, J. F.; and Hepner, T. E.: LDV Surveys Over a Fighter Model at Moderate to High Angles of Attack. SAE TP Series 881448, Aerospace Technology Conference and Exposition, Anaheim, California, October 3-6, 1988.
17. Rumsey, C. L.; and Anderson, W. K.: Some Numerical and Physical Aspects of Unsteady Navier-Stokes Computations Over Airfoils Using Dynamic Meshes. AIAA Paper No. 88-0329. Presented at the AIAA 26th Aerospace Sciences Meeting, Reno, Nevada, January 11-14, 1988.
18. Thomas, J. L.; Taylor, S. L.; and Anderson, W. K.: Navier-Stokes Computations of Vortical Flows Over Low Aspect Ratio Wings. AIAA Paper No. 87-0207. Presented at the AIAA 25th Aerospace Sciences Meeting, Reno, Nevada, January 12-15, 1987.
19. Krist, S. L.; Thomas, J. L.; Sellers, W. L., III and Kjølgaard, S. O.: An Embedded Grid Formulation Applied to a Delta Wing. AIAA Paper No. 90-4029. Presented at the 28th Aerospace Sciences Meeting, Reno, Nevada, January 8-11, 1990.
20. Thomas, J. L.; Walters, R. W.; Reu, T.; Ghaffari, F.; Weston, R. P.; and Luckring, J. M.: A Patched-Grid Algorithm for Complex Configurations Directed Towards the F/A-18 Aircraft. AIAA Paper No. 89-0121, presented at the 27th Aerospace Sciences Meeting, Reno, Nevada, January 9-12, 1989.
21. Ekaterinaris, J. A.; and Schiff, L. B.: Vortical Flows Over Delta Wings and Numerical Prediction of Vortex Breakdown. AIAA Paper No. 90-0102. Presented at the AIAA 28th Aerospace Sciences Meeting, Reno, Nevada, January 8-11, 1990.
22. Flores, J.; and Chaderjian, N. M.: The Numerical Simulation of Transonic Separated Flow About the Complete F-16A. AIAA Paper No. 88-2506, presented at the AIAA 6th Applied Aerodynamics Conference, Williamsburg, Virginia, June 6-8, 1988.
23. Huband, G. W.; Shang, J. S.; and Aftosmis, M. J.: Numerical Simulation of an F-16A at Angle of Attack. AIAA Paper No. 90-0100. Presented at the AIAA 28th Aerospace Sciences Meeting, Reno, Nevada, January 8-11, 1990.
24. Edwards, J. W.: Assessment of Computational Prediction of Tail Buffet. NASA TM 101613, January 1990.
25. Sellers, W. L., III; and Kjølgaard, S. O.: The Basic Aerodynamics Research Tunnel - A Facility Dedicated to Code Validation. AIAA Paper No. 88-1997. Presented at the AIAA 15th Aerodynamic Testing Conference, San Diego, California, May 18-20, 1988.
26. Baldwin, B.; and Lomax, H.: Thin Layer Approximation and Algebraic Model for Separated Turbulent Flows. AIAA Paper No. 77-257, 1978.
27. Batina, J. T.: An Efficient Algorithm for Solution of the Unsteady Transonic Small-Disturbance Equation. AIAA Paper No. 87-0106. Presented at the AIAA 25th Aerospace Sciences Meeting, Reno, Nevada, January 12-15, 1987. Also NASA TM 89014, December 1986.
28. Batina, J. T.; Seidel, D. A.; Bland, S. R.; and Bennett, R. M.: Unsteady Transonic Flow Calculations for Realistic Aircraft Configurations. AIAA Paper No. 87-0850-CP. Presented at the AIAA/ASME/ASCE/AHS, 28th Structures, Structural Dynamics and Materials Conference, Monterey, California, April 6-8, 1987. Also NASA TM-89120, March 1987.
29. Howlett, J. T., and Bland, S. R.: "Calculation of Viscous Effects on Transonic Flow for Oscillating Airfoils and Comparisons with Experiment." NASA TP-2731, September 1987.
30. Eckstrom, C. V.; Seidel, D. A.; and Sandford, M. C.: Unsteady Pressure and Structural Response Measurements on an Elastic Supercritical Wing. AIAA Paper No. 88-2277. Presented at the AIAA/ASME/ASCE/AHS/ACS 29th Structures, Structural Dynamics, and Materials Conference, Williamsburg, Virginia, April 18-20, 1988.
31. Seidel, D. A.; Eckstrom, C. V.; and Sandford, M. C.: Investigation of Transonic Region of High Dynamic Response Encountered on an Elastic Supercritical Wing. AIAA Paper No. 87-0735-CP. Presented at the AIAA/ASME/ASCE/AHS/ASC 26th Structures, Structural Dynamics and Materials Conference, Monterey, California, April 6-8, 1987.
32. Bennett, R. M.; Seidel, D. A.; and Sandford, M. C.: Transonic Calculations for a Flexible Supercritical Wing and Comparison with Experiment. AIAA Paper No. 85-0665. Also, NASA TM 86439, May 1985.
33. Steger, J. L.; and Bailey, J. E.: Calculation of Transonic Aileron Buzz. *AIAA Journal*, vol. 18, no. 3, March 1980.
34. Howlett, J. T.; in Smith, J. G. and Gardner, J. E.: Structural Dynamics Division Research and Technology Accomplishments for FY 1989 and Plans for FY 1990. NASA TM 101683, January 1990, pp. 90-91.
35. Rai, M. M.: Navier-Stokes Simulations of Blade-Vortex Interaction Using High-Order Accurate Upwind Schemes. AIAA Paper No. 87-0543, presented at the AIAA 25th Aerospace Sciences Meeting, Reno, Nevada, January 12-15, 1987.
36. Kandil, O. A.; Wong, T. C.; and Liu, C. H.: Prediction of Steady and Unsteady Asymmetric Vortical Flow Around Cones. AIAA Paper No. 90-0598, Presented at the 28th Aerospace Sciences Meeting, Reno, Nevada, January 8-11, 1990.

37. Hsu, C. -H.; and Liu, C. H.: Upwind Navier-Stokes Solutions for Leading-Edge Vortex Flows. AIAA Paper No. 89-0265. Presented at the 27th Aerospace Sciences Meeting, Reno, Nevada, January 9-12, 1989.
38. Hsu, C.-H.; and Liu, C. H.: Navier-Stokes Computation of Flow Around a Round-Edged Double-Delta Wing. AIAA Paper No. 88-2560-C., presented at the AIAA 6th Applied Aerodynamics Conference, Williamsburg, Virginia, June 6-8, 1988.
39. Taylor, S. L.; Kjelgaard, S. O.; Weston, R. P.; Thomas, J. L.; and Sellers, W. L., III: Experimental and Computational Study of the Subsonic Flow About a 75° Swept Delta Wing. AIAA Paper No. 87-2425, presented at the AIAA Atmospheric Flight Mechanics Conference, Monterey, California, August 17-19, 1987.
40. Seidel, D. A.: in Gardner, J. E.: Structural Dynamics Division Research and Technology Accomplishments for FY 1988 and Plans for FY 1989. NASA TM 101543, January 1989, pp. 94-95.

Table I
Computer Time Requirement for One Buffeting Response Calculation

values used herein

total computer run time	$T_{cpu} = N_{s1} N_{gp} \tau$	
algorithm speed	$\tau = 10 - 100 \mu\text{sec/grid-point/time step}$	40 μsec
number of computational steps	$N_{s1} = N_{cy} N_{s1/cy} \frac{t_{max}}{t_{min}}$	
bandwidth for buffeting analysis	t_{min}, t_{max}	10, 40 Hz.
number of grid points	$N_{gp} = N_{gp,I} + N_{gp,II} + N_{gp,III}$	
	$N_{gp,I} \equiv (100 \times 20 \times 49) \times 2 \times N_{bod}$	588,000
	$N_{gp,II} \equiv V_H / (\Delta x \cdot \Delta y \cdot \Delta z)$	2,138,000
	$N_{gp,III} \equiv 50,000$	50,000
minimum spatial wavelength	$\lambda_{min-x} = U_{\infty} / t_{max}$	
grid spacing for Region II	$\Delta x = \lambda_{min-x} / N_{gp/w1} = U_{\infty} / (N_{gp/w1} t_{max})$	
	$\Delta x \equiv \Delta y \equiv \Delta z$	0.25 ft.
number of cycles at t_{min}	$N_{cy} = 10 - 50$	10
number of steps per cycle	$N_{s1/cy} = \begin{cases} 100 - 200 & \text{(Euler)} \\ \geq 1000 & \text{(RNS)} \end{cases}$	100 1000
number of grid-points per spatial wavelength	$N_{gp/w1} = 50 - 100$	50



Figure 1. High aspect ratio flexible wing mounted in TDT test section.³⁰

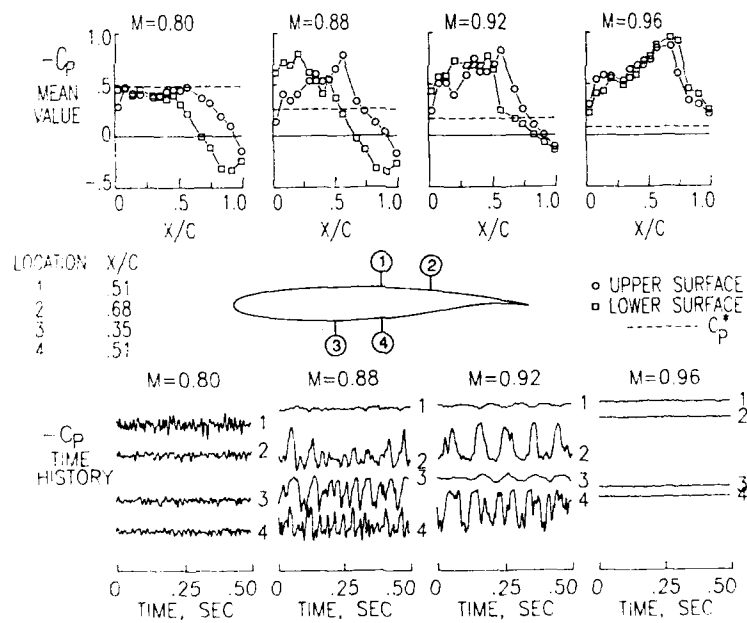


Figure 2. Mean value chordwise pressure distributions and sample pressure measurement time histories for four Mach numbers, $\alpha = 0.87.30$

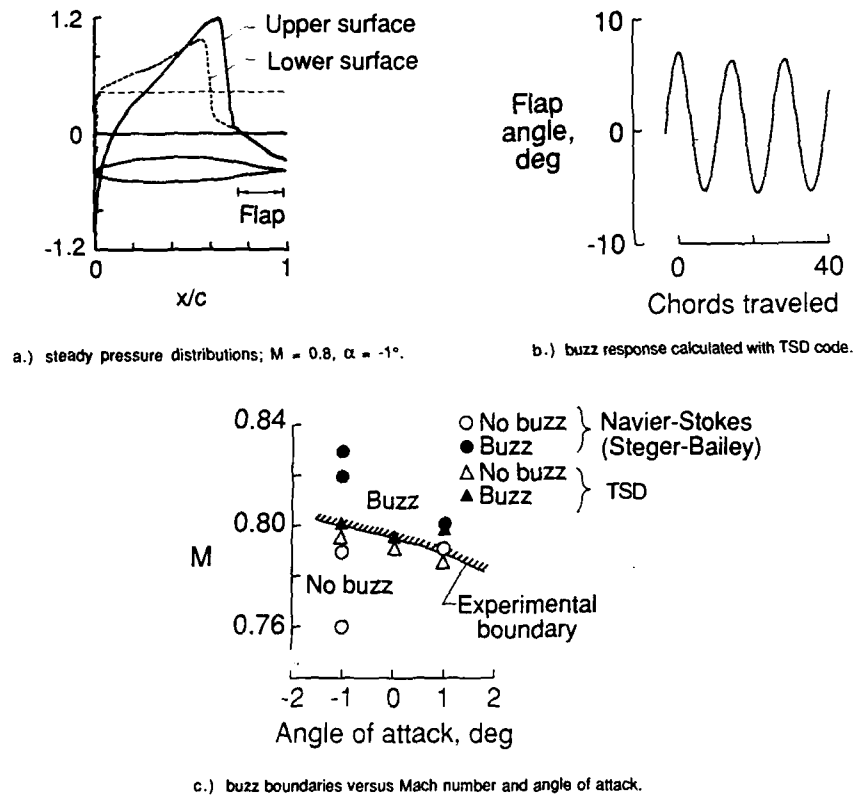


Figure 3. Comparison of experimental and calculated aileron buzz conditions for the P-80 airplane.³⁴

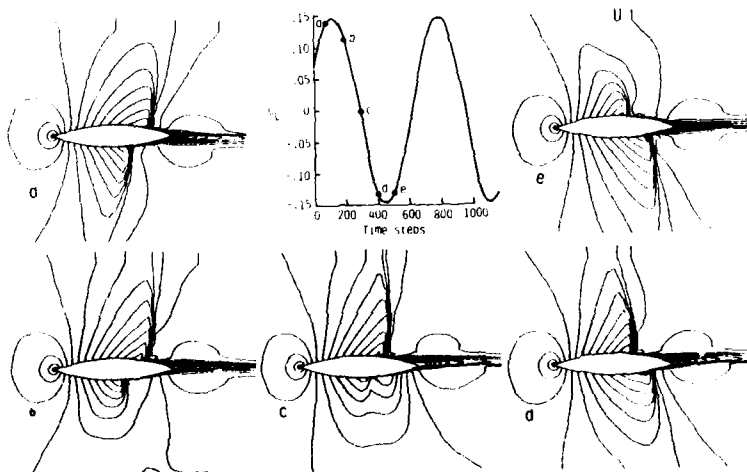


Figure 4. Calculated periodic aerodynamic oscillation for 18% biconvex airfoil using implicit thin-layer Navier-Stokes code; $M = 0.78$, $Re = 11 \times 10^6$, and $k_b = 0.406$.¹

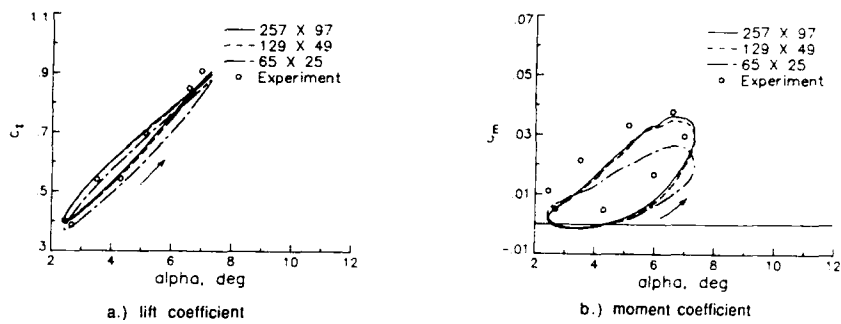


Figure 5. Effect of grid density on lift and moment coefficients for an NACA 0012 airfoil oscillating in pitch; $M = 0.6$, $\alpha = 4.86^\circ + 2.44^\circ \sin \omega t$, $k_\theta = 0.081$, thin-layer Navier-Stokes code with algebraic turbulence model.¹⁷

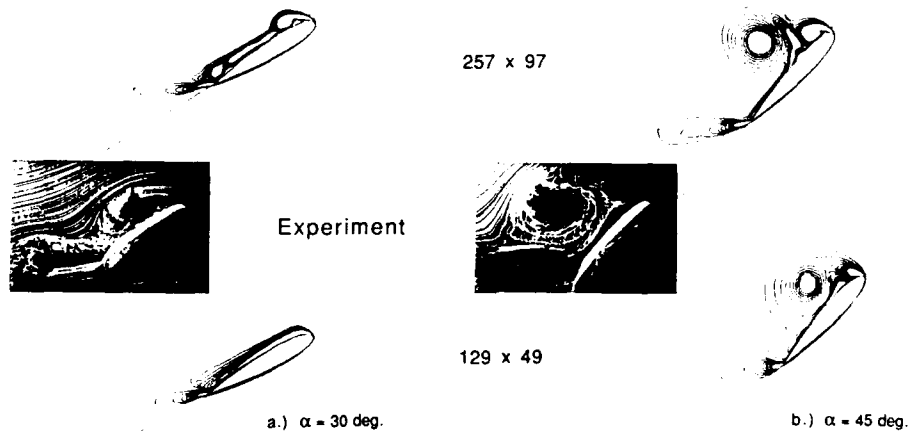


Figure 6. Grid density effect on vortex shedding for the NACA 0015 airfoil undergoing ramping motion from 0° to 60° ; $M = 0.2$, $Re = 45,000$, thin-layer Navier-Stokes code.¹⁷

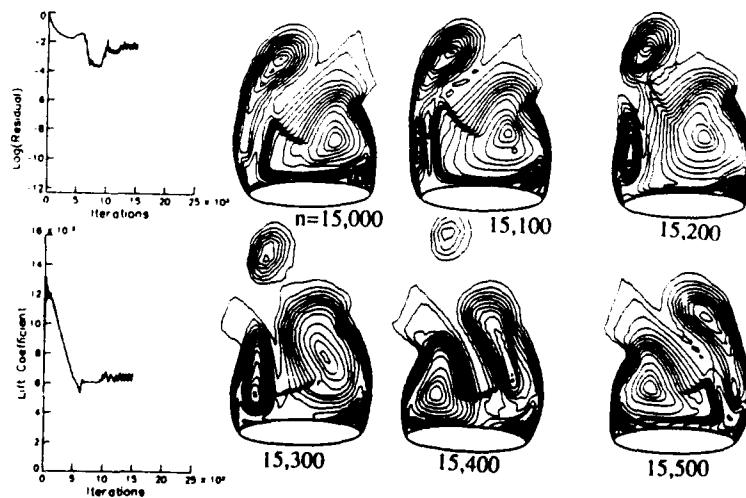


Figure 7. Unsteady asymmetric vortex shedding for an elliptic-section cone; $M = 1.4$, $\alpha = 34^\circ$, $Re = 2 \times 10^6$, thin-layer Navier-Stokes code, "locally" conical flow solution.³⁷

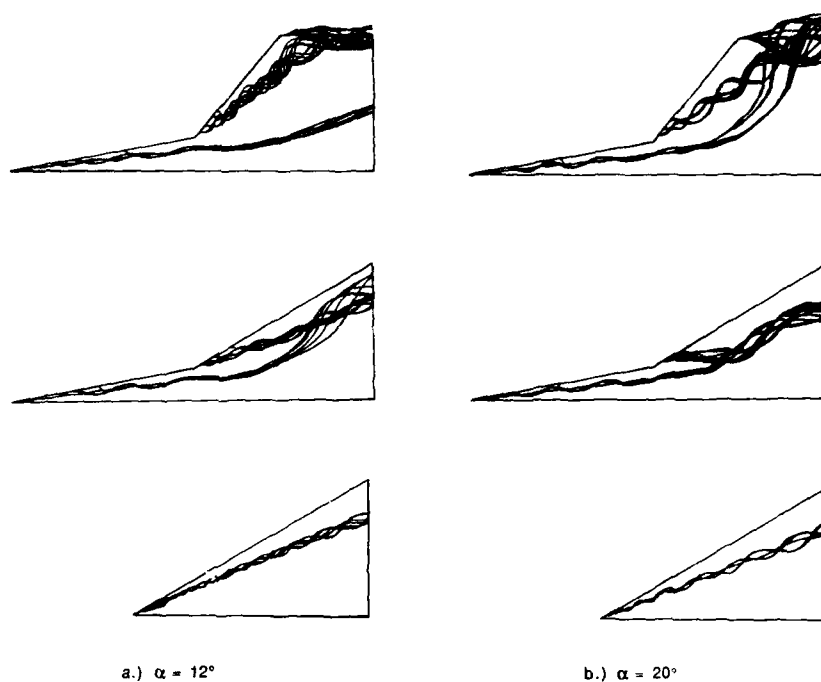


Figure 8. Wing planform and angle of attack effects upon vortical flow over three wing planforms. Top view of off-surface partial traces. $Re = 1.3 \times 10^6$, incompressible Navier-Stokes code.³⁷

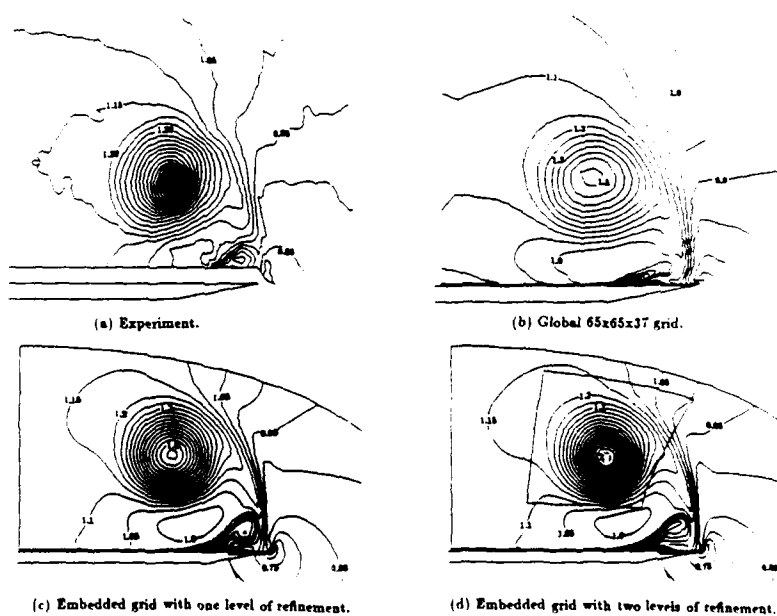


Figure 9. Effect of embedded grid enrichment on streamwise velocity contours for a 75° swept delta wing; $x/L = 0.7$, $M = 0.3$, $\alpha = 34^\circ$, $Re = 500,000$, thin-layer laminar Navier-Stokes code.¹⁹

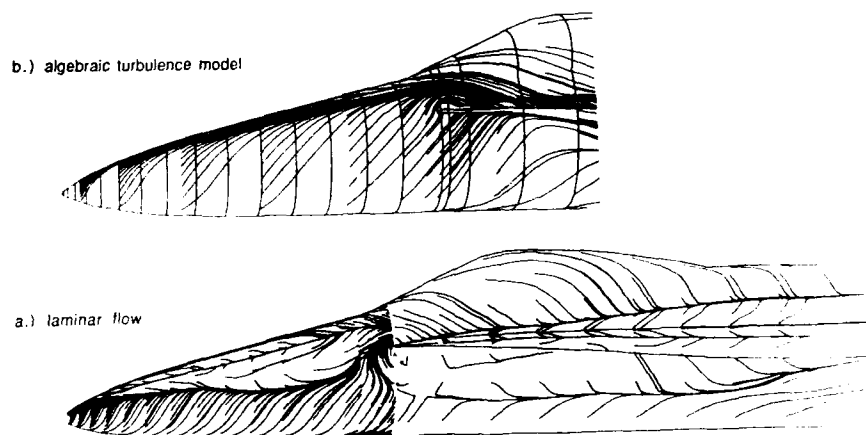


Figure 10. Effect of turbulence modeling on calculated surface particle traces c/o the forebody of an F/A-18 airplane model: $M = 0.3$, $Re = 200,000$, $\alpha = 30^\circ$, thin-layer Navier-Stokes code.²⁰

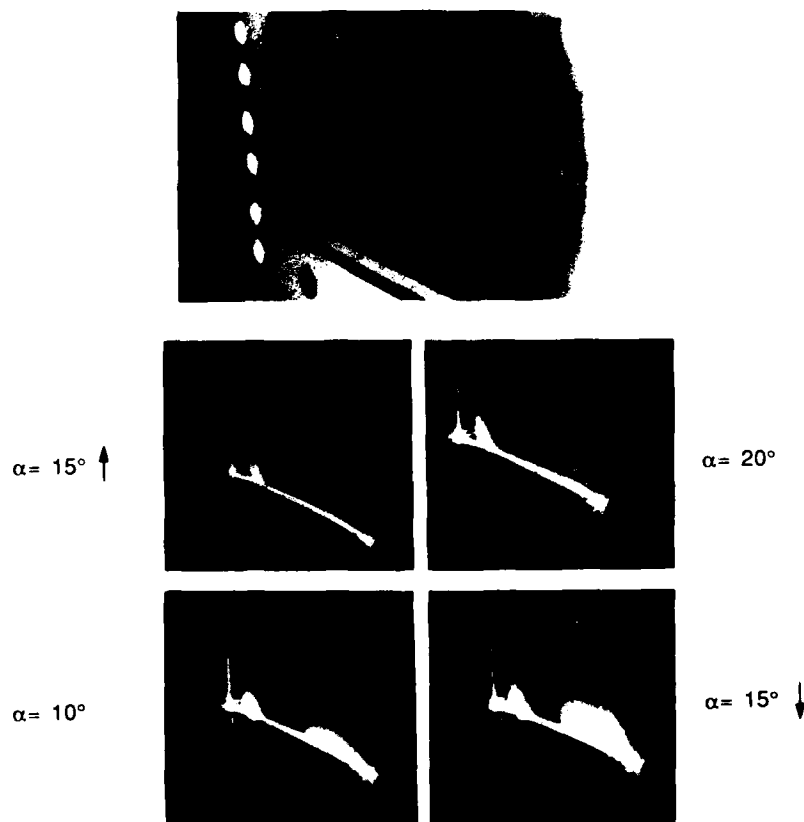


Figure 11. Flow visualization of vortex flow over an oscillating clipped delta wing: $\Lambda = 50.5^\circ$, $M = 0.92$, $\alpha = 15^\circ + 5^\circ \sin(2\pi 3.35t)$.⁴⁰

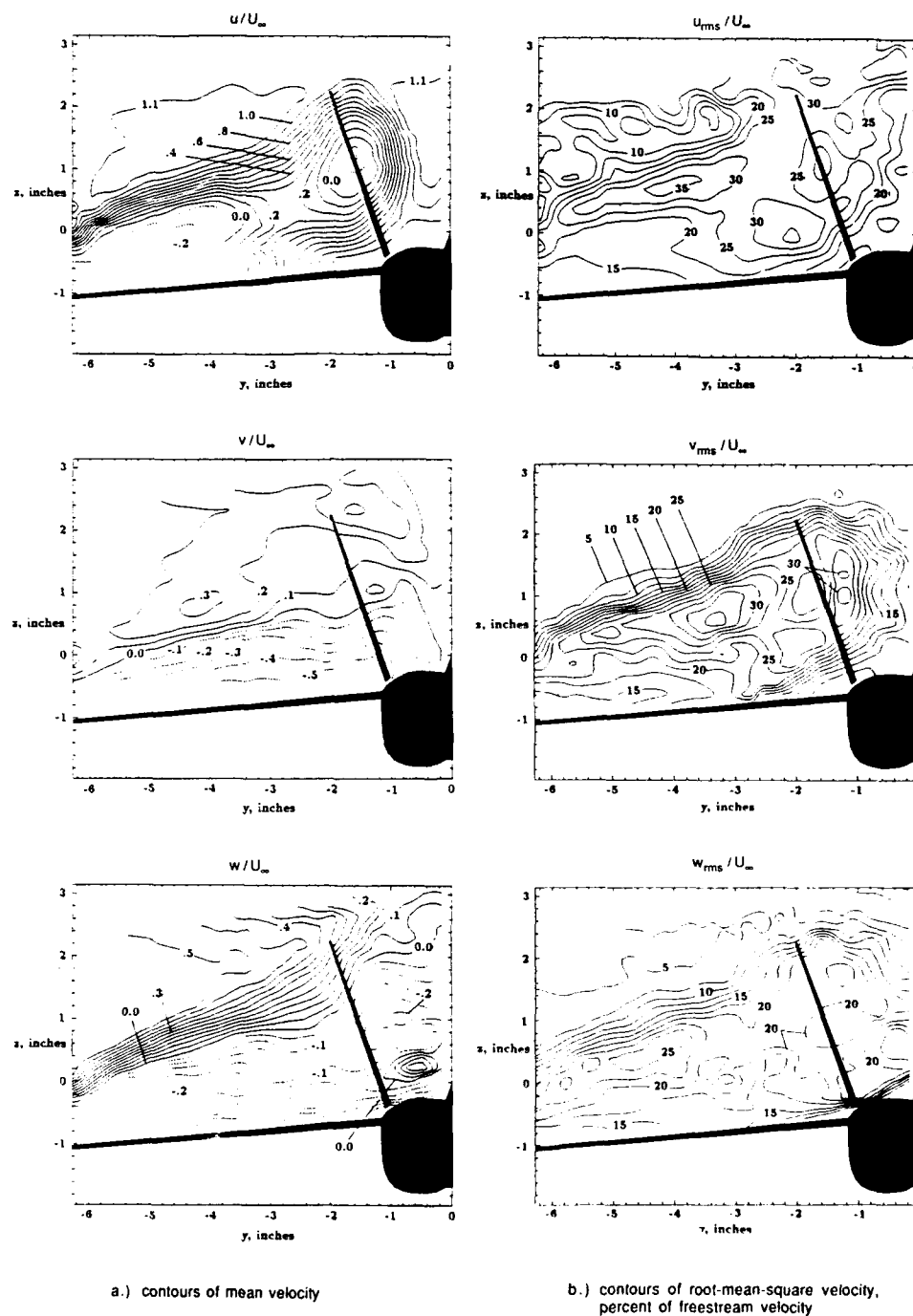


Figure 12. Three-dimensional laser velocimetry flow survey for a YF-17 model in the BART low speed wind tunnel; $\alpha = 25^\circ$, $Re = 326,000.16$

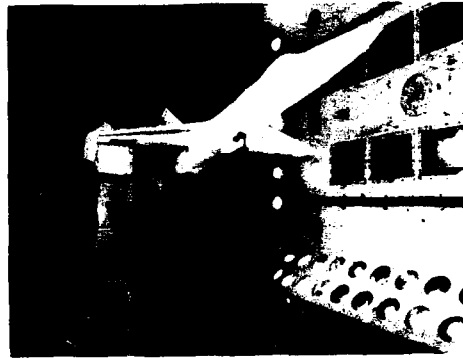


Figure 13. Twin tailed fighter configuration in TDT.¹¹

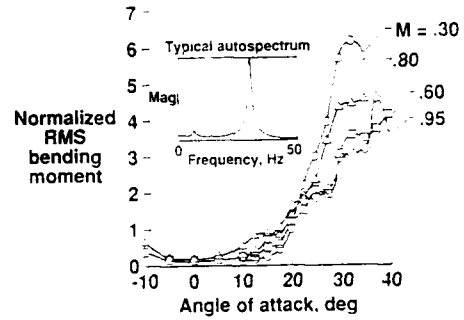


Figure 14. Variation of buffeting response of vertical tail of a twin tail fighter model with angle of attack and Mach number.¹¹

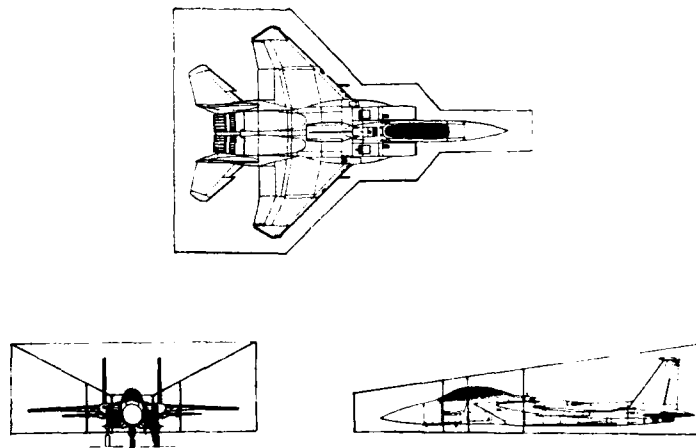


Figure 15. Nearfield volume, Region II, for the F-15 aircraft requiring grid density sufficient for accurate vorticity convection calculations.²⁴



REPORT DOCUMENTATION PAGE			
1. Recipient's Reference	2. Originator's Reference	3. Further Reference	4. Security Classification of Document
	AGARD-CP-483	ISBN 92-835-0582-4	UNCLASSIFIED
5. Originator	Advisory Group for Aerospace Research and Development North Atlantic Treaty Organization 7 rue Ancelle, 92200 Neuilly sur Seine, France		
6. Title	AIRCRAFT DYNAMIC LOADS DUE TO FLOW SEPARATION		
7. Presented at	the 70th Meeting of the AGARD Structures and Materials Panel, held in Sorrento, Italy on 1-6 April 1990.		
8. Author(s)/Editor(s)	Various		9. Date September 1990
10. Author's/Editor's Address	Various		11. Pages 278
12. Distribution Statement	This document is distributed in accordance with AGARD policies and regulations, which are outlined on the Outside Back Covers of all AGARD publications.		
13. Keywords/Descriptors	<div style="display: flex; justify-content: space-between;"> <div style="width: 45%;"> Aeroelasticity Buffeting </div> <div style="width: 45%;"> Aerodynamic loads Separated flow </div> </div>		
14. Abstract	<p>This publication reports the papers presented to a Specialists' Meeting held by the Structures and Materials Panel at its Spring 1990 Meeting.</p> <p>The Meeting was intended to provide a "state-of-the-art" review of all types of separated-flow dynamic problems to be encountered in present and future aircraft. In particular, the Meeting concentrated on the following topics:</p> <ul style="list-style-type: none"> — Evaluation of aerodynamic buffet input characteristics — In-flight and wind tunnel buffeting measurements — Aeroelastic buffeting prediction techniques. 		

<p>AGARD Conference Proceedings No.483 Advisory Group for Aerospace Research and Development, NATO AIRCRAFT DYNAMIC LOADS DUE TO FLOW SEPARATION Published September 1990 278 pages</p> <p>This publication reports the papers presented to a Specialists' Meeting held by the Structures and Materials Panel at its Spring 1990 Meeting.</p> <p>The Meeting was intended to provide a "state-of-the-art" review of all types of separated-flow dynamic problems to be encountered in present and future aircraft. In</p> <p>P.T.O.</p>	<p>AGARD-CP-483</p> <p>Aeroelasticity Buffeting Aerodynamic loads Separated flow</p>	<p>AGARD Conference Proceedings No.483 Advisory Group for Aerospace Research and Development, NATO AIRCRAFT DYNAMIC LOADS DUE TO FLOW SEPARATION Published September 1990 278 pages</p> <p>This publication reports the papers presented to a Specialists' Meeting held by the Structures and Materials Panel at its Spring 1990 Meeting.</p> <p>The Meeting was intended to provide a "state-of-the-art" review of all types of separated-flow dynamic problems to be encountered in present and future aircraft. In</p> <p>P.T.O.</p>	<p>AGARD-CP-483</p> <p>Aeroelasticity Buffeting Aerodynamic loads Separated flow</p>
<p>AGARD Conference Proceedings No.483 Advisory Group for Aerospace Research and Development, NATO AIRCRAFT DYNAMIC LOADS DUE TO FLOW SEPARATION Published September 1990 278 pages</p> <p>This publication reports the papers presented to a Specialists' Meeting held by the Structures and Materials Panel at its Spring 1990 Meeting.</p> <p>The Meeting was intended to provide a "state-of-the-art" review of all types of separated-flow dynamic problems to be encountered in present and future aircraft. In</p> <p>P.T.O.</p>	<p>AGARD-CP-483</p> <p>Aeroelasticity Buffeting Aerodynamic loads Separated flow</p>	<p>AGARD Conference Proceedings No.483 Advisory Group for Aerospace Research and Development, NATO AIRCRAFT DYNAMIC LOADS DUE TO FLOW SEPARATION Published September 1990 278 pages</p> <p>This publication reports the papers presented to a Specialists' Meeting held by the Structures and Materials Panel at its Spring 1990 Meeting.</p> <p>The Meeting was intended to provide a "state-of-the-art" review of all types of separated-flow dynamic problems to be encountered in present and future aircraft. In</p> <p>P.T.O.</p>	<p>AGARD-CP-483</p> <p>Aeroelasticity Buffeting Aerodynamic loads Separated flow</p>

<p>particular, the Meeting concentrated on the following topics:</p> <ul style="list-style-type: none"> — Evaluation of aerodynamic buffet input characteristics — In-flight and wind tunnel buffeting measurements — Aeroelastic buffeting prediction techniques. 	<p>particular, the Meeting concentrated on the following topics:</p> <ul style="list-style-type: none"> — Evaluation of aerodynamic buffet input characteristics — In-flight and wind tunnel buffeting measurements — Aeroelastic buffeting prediction techniques.
<p>ISBN 92-835-0582-4</p>	<p>ISBN 92-835-0582-4</p>
<p>particular, the Meeting concentrated on the following topics:</p> <ul style="list-style-type: none"> — Evaluation of aerodynamic buffet input characteristics — In-flight and wind tunnel buffeting measurements — Aeroelastic buffeting prediction techniques. 	<p>particular, the Meeting concentrated on the following topics:</p> <ul style="list-style-type: none"> — Evaluation of aerodynamic buffet input characteristics — In-flight and wind tunnel buffeting measurements — Aeroelastic buffeting prediction techniques.
<p>ISBN 92-835-0582-4</p>	<p>ISBN 92-835-0582-4</p>